ASME
SETTING THE STANDARD

Journal of Engineering for Gas Turbines and Power

Published Monthly by ASME

VOLUME 132 • NUMBER 5 • MAY 2010

Transactions of the ASME, Journal of Engineering for Gas Turbines and Power (ISSN 0742-4795) is published monthly by The American Society of Mechanical Engineers, Three Park Avenue, New York, NY 10016. Periodicals postage paid at New York, NY and additional mailing offices.
POSTMASTER: Send address changes to Transactions of the ASME, Journal of Engineering for Gas Turbines and Power, c/o THE AMERICAN SOCIETY OF MECHANICAL ENGINEERS, 22 Law Drive, Box 2300, Fairfield, NJ 07007-2300.
CHANGES OF ADDRESS must be received at Society headquarters seven weeks before they are to be effective. Please send old label and new address.
STATEMENT from By-Laws. The Society shall not be responsible for statements or opinions advanced in papers or ... printed in its publications (B7.1, par. 3).

RESEARCH PAPERS

(Contents continued on inside back cover)

This journal is printed on acid-free paper, which exceeds the ANSI Z39.48-1992 specification for permanence of paper and library materials. ♾™
♻ 85% recycled content, including 10% post-consumer fibers.

Journal of Engineering for Gas Turbines and Power MAY 2010

Volume 132, Number 5

TECHNICAL BRIEFS

The ASME Journal of Engineering for Gas Turbines and Power is abstracted and indexed in the following:

AESIS (Australia's Geoscience, Minerals, & Petroleum Database), Applied Science & Technology Index, Aquatic Sciences and Fisheries Abstracts, Civil Engineering Abstracts, Compendex (The electronic equivalent of Engineering Index), Computer & Information Systems Abstracts, Corrosion Abstracts, Current Contents, Engineered Materials Abstracts, Engineering Index, Enviroline (The electronic equivalent of Environment Abstracts), Environment Abstracts, Environmental Science and Pollution Management, Fluidex, INSPEC, Mechanical & Transportation Engineering Abstracts, Mechanical Engineering Abstracts, METADEX (The electronic equivalent of Metals Abstracts and Alloys Index), Pollution Abstracts, Referativnyi Zhurnal, Science Citation Index, SciSearch (The electronic equivalent of Science Citation Index), Shock and Vibration Digest

A New Kind of Multifunctional Energy System Based on Moderate Conversion of Chemical Energy of Fossil Fuels

Wei Han
e-mail: hanwei@mail.etp.ac.cn

Hongguang Jin
e-mail: hgjin@mail.etp.ac.cn

Institute of Engineering Thermophysics,
Chinese Academy of Sciences,
Beijing 100190, China

This paper proposes a new kind of multifunctional energy system (MES) using natural gas and coal to more efficiently and more economically produce methanol and power. Traditional chemical processes pursue high conversion ratios of chemical energy of fuels. The new MES focuses on the moderate conversion of the chemical energy of fuels. To do this, about 50% of the coal is partially gasified with pure oxygen and steam as oxidant, and then the unconverted residuals (char) and natural gas are utilized synthetically by char-fired reforming to generate syngas. The combustion of char drives the methane/steam-reforming reaction. Here, the reforming reaction is also moderately converted, and the reforming temperature is decreased 100–150°C compared with that of the conventional method. The carbon-rich syngas from the partial gasifier of coal and hydrogen-rich syngas from char-fired reformer are mixed together and converted into methanol at a proper conversion ratio (lower than that of the conventional chemical process). Finally, the unconverted syngas is used in a combined cycle as fuel for power generation. As a result, the total exergy efficiency of the new system is 55–60%. Comparing to individual systems, including the integrated gasification combined cycle and the natural gas-based methanol synthesis plants, this new system can generate 10–20% more electricity with the same quantity of fossil fuel input and methanol output. In addition, the possibility of reducing the size of gasifier, reformer, and methanol synthesis reactor may reduce investment costs accordingly. These results may provide a new way to use coal and natural gas more efficiently and economically. [DOI: 10.1115/1.3205025]

1 Introduction

The world's primary energy consumption has increased consecutively for several decades, with fossil fuels serving as the main energy source. Considering the human track record, this trend will continue into the future. Currently, the consumption of coal and natural gas continues to grow and account for nearly half of the global energy consumption [1]. Given the low reserves-to-production ratios, efficient use of fossil fuels has become an arresting issue.

As far as the consumption of coal and natural gas (NG) goes, a large portion is converted to electricity and chemicals through power plants and chemical processes. Coal gasification is considered a promising and effective technology to provide fuel gas for combined cycles [2–4] and to produce syngas for catalytic conversion to chemicals or clean fuels [5–8]. Full gasification pursues high-carbon conversion ratios, which requires a large coal gasifier. The investment cost of a gasifier is extremely high, thus limiting the application of coal gasification technology. Compared with full gasification, the concept of partial gasification of coal offers a promising way [9,10]. The advanced idea of partial gasification converts coal based on the chemical activities of different components [11,12]. The components of shorter hydrogen-rich branches, which have high chemical activities, can be converted into hydrogen-rich gas easily and quickly, and the components of longer carbon-rich branches will change into char instead of syngas. In this way, the size of the coal gasifier can be decreased considerably. Several combined-cycle power plants using partial gasification of coal with air as oxidant were investigated, and the limitations observed include high-temperature cleanup of the syngas from the gasifier and the flue gas from the pressurized char combustor. The components of syngas from the partial gasifier are hydrogen and carbon monoxide, which make good raw materials for chemical synthesis. Presently, most partial gasification investigations focus on power generation, and a paucity of literature addresses using the syngas for chemical production.

Natural gas is another major fossil fuel used for power and chemical production. In a combined cycle, natural gas is directly burned in the combustion chamber, and the exergy destruction of combustion accounts for about half of the total exergy destruction of the cycle [13,14]. In a chemical process, natural gas must first be transformed into syngas through methane/steam reforming, and the high conversion ratio from natural gas to syngas also occurs. Since higher temperatures favor the reforming reaction, large amounts of natural gas, which account for about 30% of the natural gas, should be burned in the reformer to provide high-temperature conditions—usually the temperature of the one-stage reformer is higher than 900°C [15]. Because of the high temperature and large size of the reformer, the investment cost of the reformer is extremely high. Partial oxidation of methane and auto thermal reforming have been proposed to decrease the high temperatures, but these technologies require more complex reactors and/or more equipment such as air separation units (ASUs) [16].

A newly proposed multifunctional energy system (MES), in which coal combustion, instead of natural gas combustion, provides the high-temperature thermal energy for the reforming reaction. The reforming products are then used to cogenerate chemicals and power [17–19]. The research results show that the MES can save 10–15% of fossil fuels compared with the single systems. Since the coal is directly burned regardless of components in MES, the big potential is to efficiently use the active components of coal before burning.

The objective of this paper is: (1) to propose a new principle to

Manuscript received April 7, 2009; final manuscript received April 10, 2009; published online March 4, 2010. Review conducted by Dilip R. Ballal.

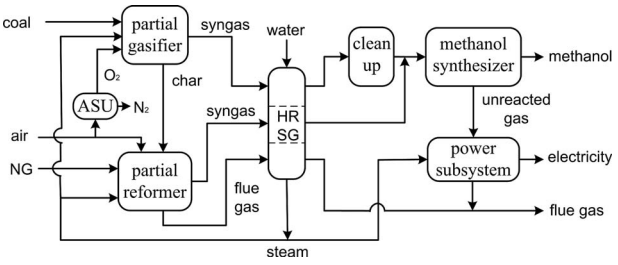

Fig. 1 Schematic of the multifunctional energy system with moderate conversion of coal and natural gas

convert coal and natural gas to chemicals and power based on the concept of moderate conversion of the chemical energy of fuels; (2) to synthesize a novel energy system using coal and natural gas as fuel; and (3) to demonstrate the role of the new approach in the improvement of overall efficiency.

2 An Innovative Multifunctional Energy System Based on the Moderate Conversion of Fossil Fuels

2.1 Conceptual Design of the Multifunctional Energy System. Figure 1 illustrates the schematic of the multifunctional energy system using moderate conversion of coal and natural gas based on two basic concepts:

(1) to use efficiently different components of coal (hydrogen-rich branches and carbon-rich branches) based on chemical activities
(2) to integrate the chemical process and power plant to use syngas efficiently

Coal is fed to a partial gasifier along with steam from the heat recovery steam generator and oxygen from the air separation unit. The gasifier coal conversion ratio is an important parameter that evaluates the transfer from coal to gas. It is the ratio of carbon converted to syngas components to the total carbon input. In a full gasification process, the high conversion ratio of carbon is more important (usually over 95%) because higher conversion ratios mean lower energy loss. However, in partial gasification, the emphasis has focused on converting the chemically active components of coal into syngas. The carbon conversion ratio can be changed from 30% to 70% by controlling the quantity of steam and oxygen and the detention time. The volatile components in coal and active carbon-rich components are converted into syngas quickly, and the inactive carbon-rich components and ash are changed into char [9]. As opposed to the conventional partial gasifier, the oxidant used in the new gasifier is pure oxygen instead of air. Therefore, the syngas is not diluted with nitrogen; the concentration of H_2 and CO in syngas of the new approach can be increased, which favors converting syngas to chemicals in the next step.

The char from the coal partial gasifier is introduced to a partial methane/steam reformer and is burned in outside reaction tubes. Inside the reaction tubes, the methane/steam-reforming reaction occurs—which is a major method of producing syngas from natural gas and is widely used by the chemical industry. The process is based on two independent equilibrium-limited reactions, as follows:

$$CH_4 + H_2O \rightarrow 3H_2 + CO \quad \Delta H^0_{298} = 206 \text{ kJ/mol} \tag{1}$$

$$CO + H_2O \rightarrow CO_2 + H_2 \quad \Delta H^0_{298} = -41 \text{ kJ/mol} \tag{2}$$

Reaction (1) is an endothermic steam-reforming reaction, and the typical reaction temperature is around 900°C. The second, often known as the water-gas shift reaction, is a lightly exothermic reaction. As a whole, the reforming of methane by steam will absorb a large amount of high-temperature thermal energy. In the conventional reforming process, the reaction heat is provided by the combustion of natural gas, which accounts for about 30% of the reacted natural gas. In this new approach, however, the combustion of char from a partial gasifier supplies the reaction heat and the natural gas burnt in the conventional reforming process is used as a reactant of reforming. Of note here is that a partial methane/steam reformer is adopted in the new approach, and the conversion ratio of methane is decreased from the conventional method's 92.5% to 66.5%. Along with the decrease in the conversion ratio, the reforming temperature is decreased from 950°C to 800°C, thus making it possible to decrease the size of the reformer and prolonging the life of reaction tubes.

Syngas, including the products of coal partial gasification and natural gas reforming, consists of large amounts of CO and H_2—the active material for methanol synthesis. The new system integrates the power plant and chemical process: the clean syngas from the gasifier is first mixed with syngas from the reformer, and then the active components are moderately converted to methanol using the methanol synthesizer. In the conventional methanol synthesis process, to get a high-methanol conversion ratio, large amounts of unreacted syngas must recycle through the synthesizer, hence increasing the size of the synthesizer and consume additional compression work. In the new system, only a part of the components is converted into methanol and the recycle ratio (ratio of mole flow of recycled syngas to that of fresh syngas) is decreased from the original 4.8 to 1.5. Finally, the unreacted gas enters a combined cycle to generate electricity.

During the partial gasification, most of the harmful compositions, such as sulfur and alkali metals enter the syngas. This means that the syngas must be treated carefully before methanol synthesis to protect the catalyst. The newly proposed system implements a low-temperature cleanup technology. Since carbon and ash make up the main components of char, the combustion of char in the reformer has little negative effect on the conventional reaction tubes. Only the structure of the char-fired reformer need be redesigned to adapt the coal combustion system.

2.2 Configuration of the New MES. Figure 2 shows the flowchart of the new system based on the moderate conversion of chemical energies of both coal and natural gas. This system is mainly composed of three subsystems, including the syngas production and heat recovery subsystem, the chemical synthesis subsystem, and the power generation subsystem. Coal along with oxygen pressed by the compressor 4 and steam extracted from the steam turbine, enters the partial gasifier, where the chemically active components are converted to syngas, and the inactive components are converted to char. In the new system about 50% of carbon is converted into raw syngas, which consists of ash, hydrogen sulfide, alkali metals, carbon monoxide, hydrogen, and carbon dioxide. The high-temperature syngas is first cooled in a heat exchanger (HE1) and generates superheated steam for a steam turbine at the same time. During the cooling process, the alkali metals coagulate on the surface of the ash, and then the ash and alkali metals are removed from the syngas through a precipitator. Finally, the hydrogen sulfide is separated by a flue gas desulfurization (FGD) unit and by clean syngas results. To protect the catalysts used in the downstream synthesis step, sulfur level below 1 ppmv in the syngas is required. Several technologies, such as the Selexol solvent absorption, are commercially available to capture H_2S [5].

The residual char from the gasifier is transmitted to the char-fired methane/steam reformer by the nitrogen from the ASU like a conventional circulating fluidized bed done. The char is burned with preheated air outside the reaction tubes, and released thermal energy is absorbed by the reforming reaction occurring inside the reaction tubes. The surplus heat of flue gas is used to generate steam for the steam turbine in heat exchangers (HE2 and HE3) and to preheat the combustion air (HE4). Since most of the sulfur derived from coal has been transformed into H_2S in syngas, the sulfur removal from the flue gas of char combustion can be elimi-

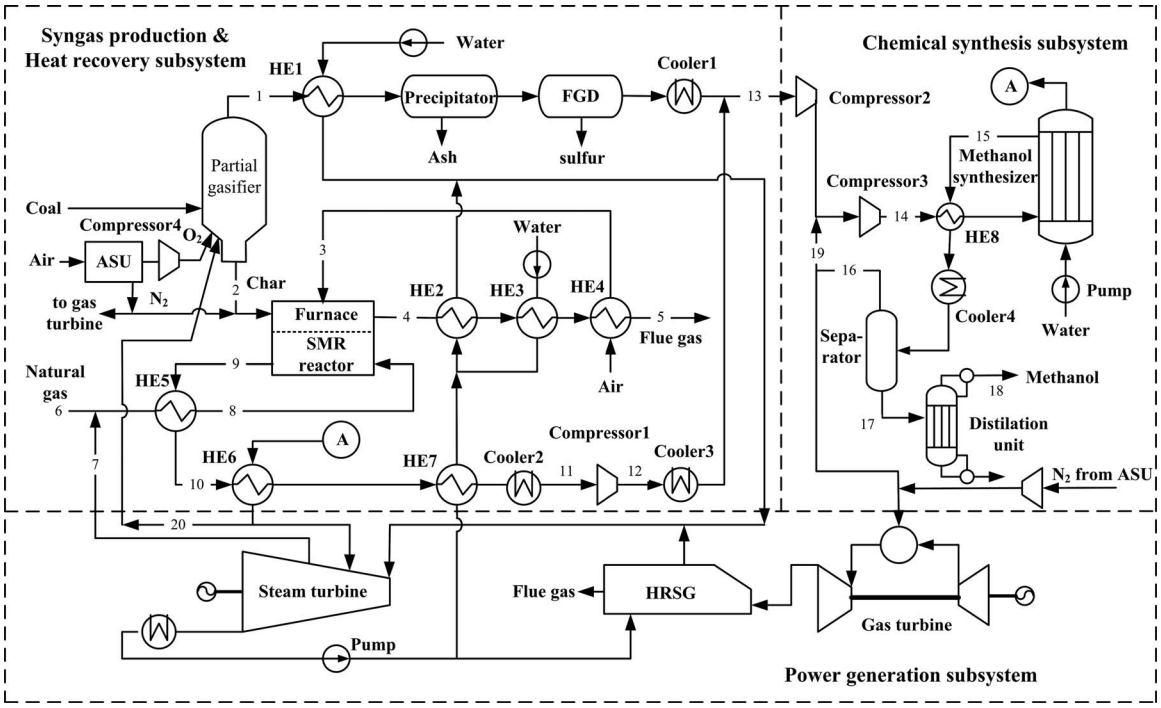

Fig. 2 System configuration of the new MES with moderate conversion of chemical energy of coal and natural gas

nated by adding limestone. The syngas, a product of the reforming reaction, preheats the mixture of natural gas and steam (HE5), to superheat steam from the methanol synthesizer (HE6), and to vaporize water (HE7). After cooling to near-ambient temperature, the syngas from the reformer is pressured, and then mixed with the cooled syngas from the partial gasifier.

The mixed syngas is compressed further and mixed with circulating gas from the separator. The mixed gas is then compressed to the pressure of methanol synthesis. After being preheated by a heat exchanger (HE8), the high-pressure mixture enters a methanol synthesizer. The products of the methanol synthesis are cooled, and raw methanol is separated. Then the raw methanol is refined to a high-purity methanol in the distillation unit, which is a tricolumn refiner. The unreacted gas from the separator is divided into two streams: one stream acts as a circulating gas for the methanol synthesis and the other stream is sent to a combined cycle as fuel. Because the main components of the unreacted gas are H_2 and CO, the combustion of such fuels may result in an extremely high NO_x emission. In the MES the fuel is first diluted by the nitrogen generated in the ASU and then is burnt in the combustor of the gas turbine. This method can reduce the NO_x emission efficiently even if the fuel is pure hydrogen [20]. The steam used in the reforming and distillation is extracted from the steam turbine.

2.3 Brief Description of the Reference Systems. The energy system proposed in this paper has multi input of fossil fuels and multi output of products: we thus estimated the performance of the MES based on the comparison to the reference systems, which included the integrated gasification combined cycle (IGCC) for power generation and the methanol synthesis plant based on natural gas (MSN). The IGCC is assumed as an integration of Texaco's gasification process, gas cleanup, and heat recovery system with a gas turbine generator, a heat recovery steam generator (HRSG), and the steam turbine generator [7]. The MSN system consists of a methane/steam-reforming process and Japan Petroleum Institute's (JPI's) methanol synthesis process and methanol refining [14].

3 Evaluation of the MES

3.1 Assumptions and Operating Conditions. The partial gasifier is based on a fluidized bed and does not refer to any particular technology. The simulation assumes that the chemical equilibrium well represents the outlet condition from the gasifier. The pressure in the gasifier is 4.5 MPa, and the carbon conversion ratio is set at 0.5. The tar and oil vapors are not considered in the syngas exiting the gasifier. Coal composition is listed in Table 1. The used ASU delivers O_2 at a purity of 96% at a pressure of 5 bars with a specific electricity consumption of 0.27 kWh/kg-O_2. The nickel-based catalyst is used in the char-fired reformer. The ratio of steam to methane is 3.0 and the reforming temperature and pressure, respectively, are 800°C and 2.0 MPa. The high-reforming temperature produces chemical equilibrium [21] from the reformer. The surplus air ratio of char combustion in the char-fired reformer is 1.2.

The operating conditions in the chemical synthesis subsystem and the power generation subsystem are representative of state-of-the-art technologies, as shown in Table 2. The single systems, including the IGCC and the MSN, have also been simulated and the assumptions in chemical syntheses and power generation meet those of the MES. The gasification pressure and temperature in the

Table 1 Coal composition

Ultimate analysis (by wt %)	
Ash	16.03
Carbon	63.93
Hydrogen	4.26
Oxygen	5.63
Nitrogen	1.18
Sulfur	3.98
Water	5.00
Coal LHV (MJ/kg)	25.75

Table 2 Assumptions for calculation

Chemical synthesis subsystem	
Synthesis pressure of methanol, MPa	10
Synthesis temperature of methanol, °C	270
Pressure loss of synthesizer, %	5
Pressure loss of heat exchangers, %	3
Pressure loss of reformer of cold side, %	10
Pressure loss of reformer of hot side, %	1
Isentropic syngas compressor	0.75
Power generation subsystem	
Pressure ratio of compressor	15
Turbine inlet temperature, °C	1308
Pressure loss of heat exchangers, %	3
Isentropic efficiency of air compressor	0.88
Isentropic efficiency of gas turbine	0.89
Isentropic efficiency of pump	0.8
Pinch point in HRSG, °C	10
Approach point in HRSG, °C	30
Pressure loss of HRSG (gas-side), %	3
Pressure loss of HRSG (steam, water)	10
Condensation pressure, MPa	0.0085

IGCC are 2.6 MPa and 1350°C, respectively. The reforming temperature, pressure, and ratio of steam to methane, respectively, are 950°C, 2.0 MPa, and 3.0, respectively.

3.2 Evaluation of the New System. To evaluate the new MES, we assumed that the MES and the reference systems consume the same quantity of natural gas and coal. Since the methanol output of the MES can be controlled by changing the flow rate of the circulating gas to the synthesizer, we kept the methanol output of the MES equal to that of the single methanol synthesis plant based on natural gas. Hence, the more electricity output will denote the advantages of the MES. The MES and the reference systems are simulated by means of the commercial software ASPEN. The pressure, temperature, mass flow, and composition of the key points in Fig. 2 are listed in Table 3.

Table 4 shows energy balance results and the overall efficiency of the new and single systems. The thermal efficiency based on lower heating value (LHV) of the IGCC and MSN are, respectively, 43.1% and 61.4%. The overall efficiency is defined as the ratio of a product's energy (electricity and methanol) to the energy of fossil fuels based on lower heating value. The energy input of coal was almost equal to that of natural gas, and the energy of methanol was about 23% more than that of electricity. The overall efficiency of the MES reached 57.1%—about 5 percentage points higher than that of the single systems.

Table 4 Results for the MES and the single systems (MW)

		Reference systems		
Items	MES	IGCC	MSN	Total
Natural gas	315.9		315.9	315.9
Coal	312.8	312.8		312.8
Methanol	198.6		195.1	195.1
Power	160.5	134.9	−1.1	133.8
Overall efficiency (LHV), %	57.1	43.1	61.4	52.3

Table 5 shows the exergy distributions of the MES and the single systems. The MES can generate about 20.0% (26.7 MW) more electricity than that of the reference systems. The increase in electricity of the MES comes mainly from the decrease in the exergy destruction in the coal gasification subsystem, the methane/steam-reforming subsystem, and the methanol synthesis subsystem.

This paper uses the energy-utilization diagram (EUD) methodology developed by Ishida [17,22]. The EUD is determined by the energy level (A) versus the energy-transformation quantity (ΔH). The energy level (A) is equal to the exergy change ($\Delta\varepsilon$) divided by the energy change (ΔH), that is, $A=\Delta\varepsilon/\Delta H$. For an energy-transformation system, the energy is released by the energy donor and is accepted by the energy acceptor. In the EUD, the exergy destruction can be obtained easily from the area between the curves for the energy donor (A_{ed}) and energy acceptor (A_{ea}).

4 Discussions

4.1 Significant Role of the Moderate Conversion of Chemical Energy of Coal. In the MES coal is moderately converted to syngas and char through partial gasification. In Table 5 we see that the exergy destruction of the coal gasification subsystem in the MES is decreased by 44.26 MW (63%) compared with the IGCC. Because only 50% of the carbon component of

Table 3 Parameters of key points of the MES

				Percent molar composition (%)										
Point	G (kg/s)	p (MPa)	T (°C)	C	CH_4	C_2H_6	CH_4O	CO	CO_2	H_2	H_2O	O_2	N_2	H_2S+COS
1	8.82	4.5	908.8	-	21.6	-	-	46.0	3.8	21.2	2.3	-	1.8	3.3
2	3.69	4.5	908.8	100	-	-	-	-	-	-	-	-	-	-
3	50.63	0.11	212	-	-	-	-	-	-	-	-	21	79	-
4	54.32	0.104	900	-	-	-	-	-	17.5	-	-	3.5	79	-
5	54.32	0.101	140.3	-	-	-	-	-	17.5	-	-	3.5	79	-
6	6.37	2.58	38.0	-	90	10	-	-	-	-	-	-	-	-
7	21.71	2.6	352.0	-	-	-	-	-	-	-	100	-	-	-
8	28.08	2.39	500	-	21.0	2.3	-	-	-	-	76.7	-	-	-
9	28.08	2.16	800.0	-	5.2	-	-	7.2	6.3	45.2	36.1	-	-	-
10	28.08	2.10	603.2	-	5.2	-	-	7.2	6.3	45.2	36.1	-	-	-
11	13.62	2.0	38.0	-	8.0	-	-	11.3	9.2	71.2	0.3	-	-	-
12	13.62	4.42	132.2	-	8.0	-	-	11.3	9.2	71.2	0.3	-	-	-
13	21.8	4.3	37.3	-	11.4	-	-	19.9	8.1	60.0	0.2	-	0.4	-
14	59.2	10.5	92.4	-	11.4	-	-	19.9	8.1	60.0	0.2	-	0.4	-
15	59.2	10.0	270.0	-	23.2	-	8.6	8.4	12.4	46.1	1.1	-	0.2	-
16	48.32	9.8	38.0	-	25.6	-	0.5	9.2	13.7	50.9	0.1	-	-	-
17	10.87	9.8	38.0	-	-	-	86.7	-	-	-	11.0	-	2.3	-
18	9.97	1.1	60.0	-	-	-	99.8	-	-	-	0.02	-	-	-
19	37.40	9.8	38.0	-	25.6	-	0.5	9.2	13.7	50.9	0.1	-	-	-
20	0.42	4.5	354.6	-	-	-	-	-	-	-	100	-	-	-

Table 5 Exergy distributions of the MES and the single systems

Exergy, MW	MES	IGCC	MSN	Total of sing.
Natural gas input	328.1	-	328.1	328.1
Coal input	314.1	314.1	-	314.1
Coal gasification subsystem				
Coal gasifier	19.10	46.45	-	46.45
Air separation unit	2.05	10.17	-	10.17
Syngas coolers	2.02	10.48	-	10.48
Cleanup unit	2.79	3.12	-	3.12
Methane/steam-reforming subsystem				
Reformer	48.08	-	52.91	52.91
Syngas and flue gas coolers	27.14	-	36.10	36.10
Methanol synthesis subsystem				
Syngas compressors	2.36	-	2.05	2.05
Syngas mixture	1.22	-	2.58	2.58
Methanol synthesizer	3.49	-	4.30	4.30
Distillation unit	4.85	-	6.07	6.07
Power subsystem	132.54	102.43	1.63	104.06
Exhaust gas	14.07	6.55	4.49	11.04
Methanol output	221.97	-	219.03	219.03
Power output	160.50	134.90	−1.10	133.8
Total	642.2	314.1	328.1	642.2

coal is transformed into syngas, the quantity of pure oxygen consumed in the partial gasifier is about 20% of that in the full gasifier. Hence, the exergy destruction of the ASU is decreased by 8.12 MW, as shown in Table 5. The partial gasifier generates less quantity of syngas with a lower temperature (908.8°C) compared with the full gasifier (1350°C), the exergy destruction in the syngas coolers decreases by 8.46 MW compared with the IGCC. More importantly, with the same coal input, the exergy destruction of the partial gasifier is decreased by 27.35 MW (58.8%) compared with that of the full gasifier. Notably, these benefits come from the moderate conversion from coal to syngas in the partial gasification process.

Figures 3(*a*) and 3(*b*) show the energy-utilization diagram for the partial gasification in the MES and full gasification in the IGCC, respectively. The partial oxidation of coal acts as an energy donor, represented by the curve A_{ed}. The energy acceptors included the gasification reaction (curve A_{ea4}) and three streams of pure oxygen (curve A_{ea1}), steam (curve A_{ea2}), and coal (curve A_{ea3}), which are preheated to the specific gasification temperature of 908.8°C. As is the case with the partial gasifier, the energy donor of full gasification is also the partial oxidation of coal (curve A_{ed}), as shown in Fig. 3(*b*). However, the energy acceptors include heating pure oxygen (curve A_{ea1}), water (curve A_{ea2}), and coal (curve A_{ea3}) to the gasification temperature of 1350°C and the gasification reaction (curve A_{ea4}). Comparing Figs. 3(*a*) and 3(*b*), we see that the average energy level of the energy acceptor in the partial gasifier (0.621) is a little lower than that in the full one (0.629) because the temperature of the partial gasification is lower than that of the full gasification. However, the energy-transformation quantity (ΔH) in the partial gasifier is only 42% of that in the full one. Although the difference in the energy level between the energy donor and the acceptors in the partial gasifier is larger, the decrease in energy transfer makes the exergy destruction in the partial gasifier decrease by 58%. The benefits of coal gasification in the MES result from the moderate conversion of coal in the gasification process.

4.2 Significant Role of the Moderate Conversion of Chemical Energy of Natural Gas. The char-fired reformer integrates the char combustion and natural gas reforming. The exergy destruction of the reforming subsystem in the MES is decreased by 13.4% compared with that in the MSN. As mentioned above, about 30% of the natural gas will burn outside the reaction tubes in the conventional reforming process. However, the MES substitutes the combustion of char for natural gas, and furthermore, the natural gas burned in the conventional reformer is used as a reactant. Similarly with coal gasification, natural gas is also moderately converted to syngas through the char-fired reformer. In the MES, the reforming temperature decreases from 950°C (conventional reformer) to 800°C and, accordingly, the methane conversion ratio decreases from 92.4% to 66.5%. Since the thermal energy for reforming reaction decreases, the surplus heat recovered from the syngas and the flue gas generated from char combustion decreases. Therefore, the exergy destruction in the syngas and flue gas coolers decreases by 8.96 MW (24.8%) compared with the conventional reforming process.

Table 5 shows that the exergy destruction in the reformer of the MES decreased by 4.83 MW (9.1%) compared with the single methanol synthesis system. Figure 4(*a*) is the EUD for the char-fired reformer. The oxidation of char act as an energy-donating reaction (curve A_{ed}), and the methane/steam-reforming acts as an energy-accepting reaction (curve A_{ea3}). In addition the heating process of the two streams (curve A_{ea1} represents the preheating process of the air for combustion and curve A_{ea2} represents the preheating process of the natural gas and steam mixture) also acts as energy acceptors, which are preheated to the specific reaction temperature of 800°C. Figure 4(*b*) gives the EUD for the conven-

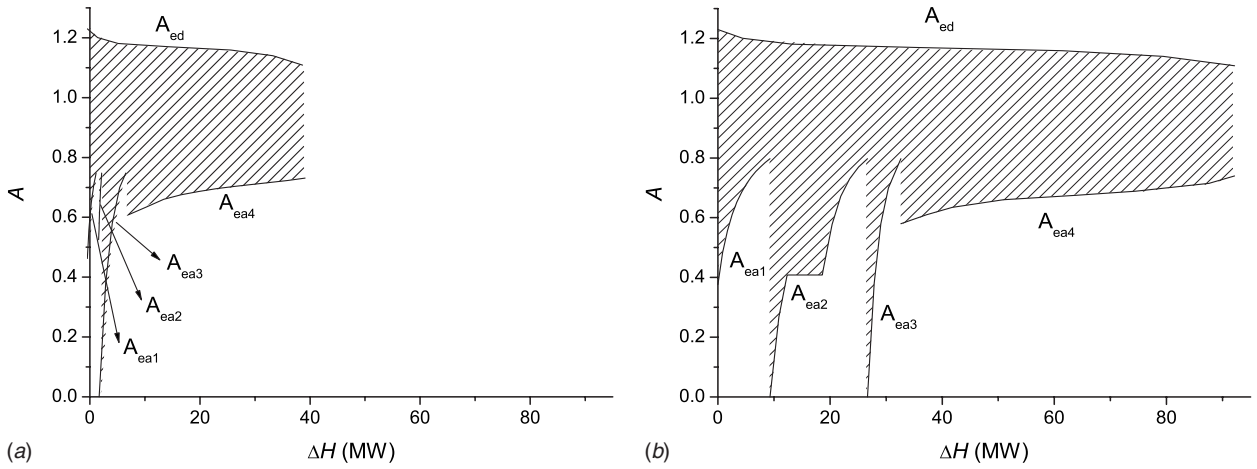

Fig. 3 (*a*) EUD for partial gasification and (*b*) EUD for full gasification

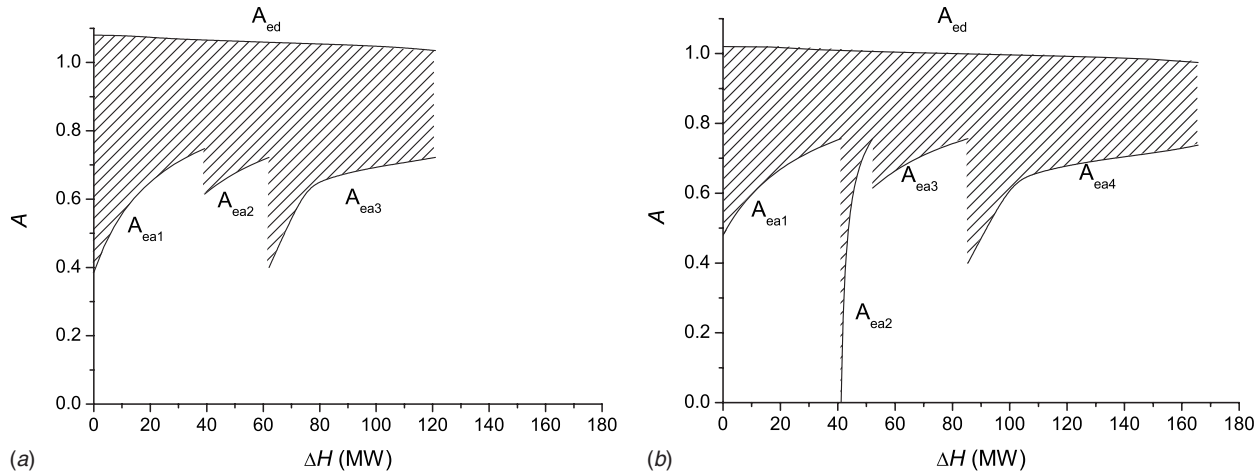

Fig. 4 (*a*) EUD for char-fired partial reformer and (*b*) EUD for conventional reformer

tional reformer of a single system. The curve A_{ed} represents the oxidation reaction of natural gas and the preheating processes of three streams (curves A_{ea1}–A_{ea3}, respectively, represent the preheating process of air, natural gas as fuel, and a mixture of natural gas and steam) act as energy acceptors, which are preheated to the reforming temperature of 950°C. Additionally, the methane/steam-reforming reaction acts as an energy acceptor as well.

Comparing Figs. 4(*a*) and 4(*b*), the energy level of char combustion is higher than that of the combustion level of natural gas. Because of the lower reforming temperature, the energy level of the energy acceptors of the char-fired reformer is lower than that in the conventional reformer. Hence, the difference in the energy level in the char-fired reformer is higher than that in the conventional reformer. However, the energy transferred from the energy donors and acceptors decreased from the MSN's 165.7 MW to the MES's 127.9 MW because of the lower conversion ratio from natural gas to syngas. The advantages of the char-fired reforming derive from the moderate conversion of natural gas in the reforming process.

4.3 Advantages of the Integration of Chemical Process and Power Plant. By integrating the methanol synthesis plant and power plant, the new system can use the syngas from coal and syngas from natural gas in a mutually beneficial way. The exergy destruction of the methanol synthesis subsystem in the MES decreases by 20.5% compared with that in the MSN. The main components of the syngas from gasifier are CO, H_2, and CO_2, which are raw materials for methanol synthesis. However, they are directly burned in the combustion chamber of the gas turbine for power generation in the single IGCC. Since the chemical process and power plant are integrated in the MES, the syngas from the gasifier can be used in methanol synthesis and convert the active components to methanol. The synthetic use of the syngas from the gasifier and from the reformer has additional gains. The syngas from the coal gasifier is rich in carbon monoxide and the hydrogen-carbon ratio $((H_2-CO_2)/(CO+CO_2))$ is 0.35, based on the data in Table 3. On the other hand, the syngas from the reformer is rich in hydrogen: the hydrogen–carbon ratio is 3.0. When the syngas from the gasifier and the syngas from the reformer are mixed, the hydrogen–carbon ratio becomes 1.85—close to the ideal hydrogen–carbon ratio of 2.0 for methanol synthesis. In the single methanol synthesis plant based on natural gas, to get the high conversion of CO to methanol, a large amount of unreacted gas must be recycled to the reactor. A partial methanol synthesizer is adopted in the MES, and about 47% of active components in the fresh gas are converted to methanol. The lower conversion ratio will decrease the quantity of the recycling gas greatly in the synthesizer. In the case of the MSN, the flow rate of fresh gas is 1.61 kmol/s, and the flow rate of the recycling gas is 7.83 kmol/s. However, in the MES, the flow rate of fresh gas is 1.77 kmol/s, and the flow rate of recycling gas is only 2.69 kmol/s. Table 5 shows the exergy destruction of the mixing process of fresh gas. The recycling gas in the MES decreased by 1.36 MW compared with that in the MSN because less fresh gas and recycling gas are mixed before the synthesizer in the MES. The exergy destruction in the methanol synthesizer of the MES decreases by 0.81 MW compared with that of the MSN (see Table 5).

Figures 5(*a*) and 5(*b*) show the EUD for the methanol synthesis process in the MES and the MSN, respectively. The synthesis reaction acts as the energy donor (A_{ed} in the two figures), and the two heating processes, including the preheating of the reactant (curve A_{ea1}) and the steam generating (curve A_{ea2}), act as energy acceptors. Benefiting from the rational hydrogen–carbon ratio, the energy level of the methanol synthesis and the energy transferred between the energy donor and acceptors in the MES decreases noticeably, compared with that in the MSN, which decreases the exergy destruction in the methanol synthesizer of the MES. At the same time, the steam generated in the synthesis reaction also decreases, which means the raw methanol consists of less water. Hence, with the same methanol output, the energy consumption for methanol refining decreases from the MSN's 19.9 MW to the MES's 16.1 MW, and the exergy destruction in the distillation unit decreases by 1.22 MW.

4.4 Advantages of a Moderate Conversion on Economic Aspects. The advantages of moderate conversion of fossil fuel are not only to increase the efficient use of fossil fuel, but it also has a great potential to decrease the size and investment costs of key equipments, such as coal gasifier, methane/steam reformer, and methanol synthesizer—usually large and expensive in the single systems.

In the MES, the carbon conversion ratio of the partial gasifier was 0.5, which is much lower than that of the full gasifier (over 95%) in the IGCC. As we know, the higher reactivity parts react faster and the remainder slow considerably. To reach a high-carbon conversion ratio, the coal must remain in the gasifier for a considerable amount of time, requiring a large volume of reactor. The effects of the carbon conversion ratio on the reactor volume and the reaction time were investigated in Ref. [11], and the results show that the reactor volume can be decreased by 66% when the carbon conversion ratio is reduced from 0.9 to 0.5. At the same time, the reaction temperature of partial gasification is 908.8°C, which is much lower than that of full gasification (1350°C). Hence, the partial gasifier and the heat recovery steam generator can use relatively inexpensive material. Given the small

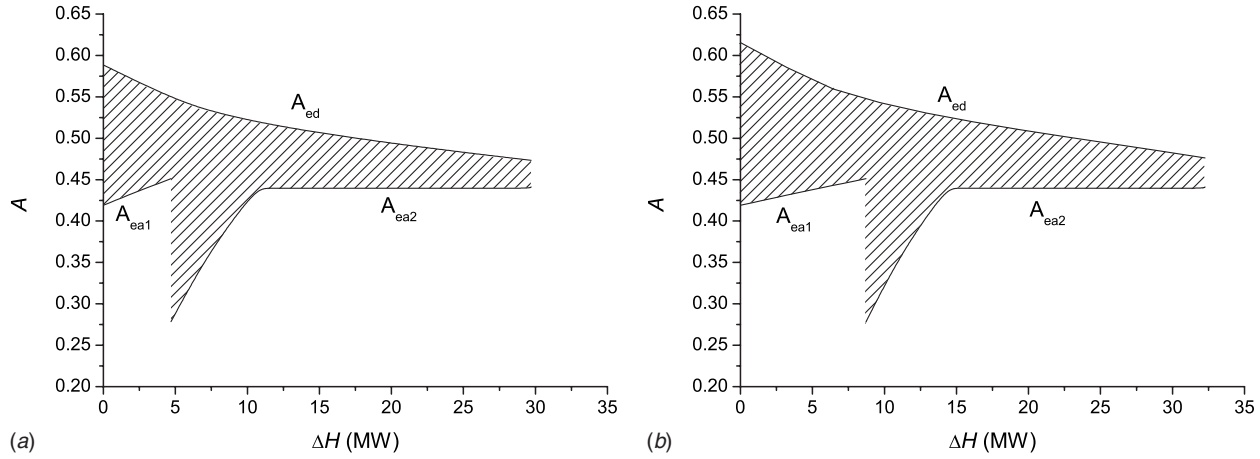

Fig. 5 (***a***) **EUD for methanol synthesis in MES and** (***b***) **EUD for methanol synthesis in MSN**

size and low cost of the material, investment outlay of the partial gasification process will be significantly decreased compared with the costs of full gasification.

To increase the methane conversion ratio in the conventional chemical process, the reaction requires a high reaction temperature and a high steam/methane ratio. For example, for the conventional one-stage reformer, the reaction temperature and steam/methane ratio should be 950°C and 3, respectively, to achieve a conversion ratio as high as 92.4%. In the MES, natural gas is moderately converted into syngas with the steam/methane ratio of 3, and the methane conversion ratio decreases to 66.5%. As in the gasifier, the reaction rate will increase with the reduction in the methane conversion ratio, which results in a smaller reaction volume in the MES. According to the low conversion ratio, the reaction temperature in the MES decreases to 800°C. The relatively low reaction temperature also can prolong the life of the reaction tubes in the reformer. Again, the partial reformer has the desirable potential of reducing investment as well as operating costs.

The concept of moderate conversion is also used in the methanol synthesizer of the MES. The conversion ratio of CO in the fresh gas is decreased from the MSN's 71.0% to the MES's 46.5%. The lower conversion ratio results in a fast reaction rate. Accordingly the flow rate of syngas, which enters the synthesizer, decreases from the MSN's 9.44 kmol/s to the MES's 4.46 kmol/s. With the same methanol production, the size and the investment costs of the partial synthesizer used in the MES are much lower than that of the conventional one used in the MSN because of the high reaction rate and low flow rate of syngas.

5 Conclusion

This paper proposes a new kind of MES based on the moderate conversion of chemical energy of fossil fuel including coal partial gasification, char-fired NG partial reforming, and partial methanol synthesis. With the same coal and natural gas input and same methanol output, the new system can generate about 21% more electricity than the single systems. The overall thermal efficiency of the new system can reach 57.1%, about 5 percentage points higher than that of the single systems. The graphical exergy analysis based on EUD methodology reveals that the moderate conversion of fossil fuels is the main contributor to the greater efficiency fuels in the MES. The exergy destruction in the coal gasification subsystem, the methane/steam-reforming subsystem, and the methanol synthesis subsystem in the MES, decrease by 63.9%, 15.5%, and 20.5%, respectively, compared with that in the single systems. In addition, the new system has great potential to decrease investment costs since the volume of key expensive equipments such as gasifier, reformer, and synthesizer could be reduced appreciably. The proposed MES provides a new and promising approach to using fossil fuels more efficiently and more economically.

Acknowledgment

This study was supported by the National Natural Science Foundation of China (Contract Nos. 50520140517 and 50706051).

References

[1] BP Group, 2008, "BP Statistical Review of World Energy 2008."
[2] Cai, R., Lin, R., Xiao, Y., and Xu, D., 1993, "Coal-Fired Combined Cycle Power Generation Technology With High Efficiency, Low Pollution, and Low Water Consumption," UNESCO, Senior Conference of Cleaning Coal-Fired Technology, Beijing, China.
[3] Longwell, J. P., Rubin, E. S., and Wilson, J., 1995, "Coal: Energy for the Future," Prog. Energy Combust. Sci., **21**, pp. 269–360.
[4] Rukes, B., and Taud, R., 2004, "Status and Perspectives of Fossil Power Generation," Energy, **29**, pp. 1853–1874.
[5] Larson, E. D., and Ren, T., 2003, "Synthetic Fuels Production by Indirect Coal Liquefaction," Energy for Sustainable Development, **7**(4), pp. 79–102.
[6] U.S. Department of Energy and the Gasification Technologies Council, 2000, "Gasification-Worldwide Use and Acceptance."
[7] Gao, L., Jin, H., Liu, Z., and Zheng, D., 2004, "Exergy Analysis of Coal-Based Polygeneration System for Power and Chemical Production," Energy, **29**, pp. 2359–2371.
[8] Lange, J., 2001, "Methanol Synthesis: A Short Review of Technology Improvements," Catal. Today, **64**, pp. 3–8.
[9] Lozza, G., Chiesa, P., and De Vita, L., 1996, "Combined-Cycle Power Stations Using "Clean-Coal Technologies:" Thermodynamic Analysis of Full Gasification Versus Fluidized Bed Combustion With Partial Gasification," ASME J. Eng. Gas Turbines Power, **118**, pp. 737–748.
[10] Foster Wheeler Development Corporation, 2003, "Development of Pressurized Circulation Fluidized Bed Partial Gasification Module (PGM)," Department of Energy, Contract No. DE-FC26-00NT40972.
[11] Tang, Z., and Wang, Y., 2000, "Efficient and Environment Friendly Use of Coal," Fuel Process. Technol., **62**, pp. 137–141.
[12] Xu, Y., Jin, H., Lin, R., and Han, W., 2008, "System Study on Partial Gasification Combined Cycle With CO2 Recovery," ASME J. Eng. Gas Turbines Power, **130**, p. 051801.
[13] Jin, H., Ishida, M., Kobayashi, M., and Numokawa, M., 1997, "Exergy Evaluation of Two Current Advanced Power Plants: Supercritical Steam Turbine and Combined Cycle," ASME J. Energy Resour. Technol., **119**, pp. 250–256.
[14] Jin, H., 1994, "Development of Thermal Power Systems Based on Graphical Exergy Analysis," Ph.D. thesis, Department of Environmental Chemistry and Engineering, Tokyo Institute of Technology, Tokyo, Japan.
[15] Japan Petroleum Institute, 1983, "Design of Methanol Synthesis."
[16] Rosen, M. A., and Scott, D. S., 1998, "Comparative Efficiency Assessments for a Range of Hydrogen Production Process," Int. J. Hydrogen Energy, **23**, pp. 653–659.
[17] Han, W., Jin, H., and Xu, W., 2007, "A Novel Combined Cycle With Synthetic Utilization of Coal and Natural Gas," Energy, **32**, pp. 1334–1342.
[18] Jin, H., Han, W., and Gao, L., 2007, "Multi-Functional Energy System (MES) With Multi Fossil Fuels and Multi Products," ASME J. Eng. Gas Turbines Power, **129**, pp. 331–337.

[19] Jin, H., Han, W., and Gao, L., 2008, "A Novel Multifunctional Energy System (MES) for CO_2 Removal With Zero Energy Penalty," ASME J. Eng. Gas Turbines Power, **130**, p. 021401.
[20] Chiesa, P., Lozza, G., and Mazzocchi, L., 2005, "Using Hydrogen as Gas Turbine Fuel," ASME J. Eng. Gas Turbines Power, **127**, pp. 73–80.
[21] Kesser, K. F., Hoffman, M. A., and Baughn, J. W., 1994, "Analysis of a Basic Chemically Recuperated Gas Turbine Power Plant," ASME J. Eng. Gas Turbines Power, **116**(2), pp. 277–284.
[22] Ishida, M., and Kawamura, K., 1982, "Energy and Exergy Analysis of a Chemical Process System With Distributed Parameters Based on the Energy-Direction Factor Diagram," Ind. Eng. Chem. Process Des. Dev., **21**, pp. 690–695.

Effects of a Reacting Cross-Stream on Turbine Film Cooling

Wesly S. Anderson
Marc D. Polanka
Joseph Zelina

Air Force Research Laboratory,
Propulsion Directorate,
Wright Patterson AFB,
Dayton, OH 45433

Dave S. Evans
Naval Air Systems Command,
NAS,
Patuxent River, MD 20670

Scott D. Stouffer
Garth R. Justinger

University of Dayton Research Institute,
Dayton, OH 45469

Film cooling plays a critical role in providing effective thermal protection to components in modern gas turbine engines. A significant effort has been undertaken over the last 40 years to improve the distribution of coolant and to ensure that the airfoil is protected by this coolant from the hot gases in the freestream. This film, under conditions with high fuel-air ratios, may actually be detrimental to the underlying metal. The presence of unburned fuel from an upstream combustor may interact with this oxygen rich film coolant jet resulting in secondary combustion. The completion of the reactions can increase the gas temperature locally resulting in higher heat transfer to the airfoil directly along the path line of the film coolant jet. This secondary combustion could damage the turbine blade, resulting in costly repair, reduction in turbine life, or even engine failure. However, knowledge of film cooling in a reactive flow is very limited. The current study explores the interaction of cooling flow from typical cooling holes with the exhaust of a fuel-rich well-stirred reactor operating at high temperatures over a flat plate. Surface temperatures, heat flux, and heat transfer coefficients are calculated for a variety of reactor fuel-to-air ratios, cooling hole geometries, and blowing ratios. Emphasis is placed on the difference between a normal cylindrical hole, an inclined cylindrical hole, and a fan-shaped cooling hole. When both air and nitrogen are injected through the cooling holes, the changes in surface temperature can be directly correlated with the presence of the reaction. Photographs of the localized burning are presented to verify the extent and locations of the reaction. [DOI: 10.1115/1.3204616]

1 Introduction

Film cooling is the primary means of maintaining turbine surface temperatures below the critical melting temperature. The most common cooling hole configurations are normal cylindrical holes, angled cylindrical holes, and fan-shaped holes. Countless studies have been conducted over the past forty years that have investigated the merits of different cooling schemes under nearly all conditions encountered in a turbine. A review article by Bogard and Thole [1] addresses many of the relevant issues. The impact of the inclination angle was studied by Baldauf et al. [2] revealing that at low blowing ratios the angled holes exhibit better performance because the coolant flow remains attached to the surface over a longer distance. At the higher blowing ratios, the relative differences between normal and angled holes diminish and the normal holes can be more effective. The relative benefits of cylindrical, fan-shaped, and laidback fan-shaped holes were also studied by Saumweber et al. [3]. The laidback fan-shaped hole ejects more coolant flow at a lower blowing ratio. Because of the increasing area of the hole near the exit, this configuration also reduces the tendency of the jet to separate. These benefits associated with shaping are dramatic, particularly at high blowing ratios, resulting in higher effectiveness.

One area that has not been investigated thoroughly is the impact of combustion gases on the film cooling process. Historically, the combustion sections of gas turbine engines operated at overall equivalence ratios (Φ) much less than one [4]. Additionally, a relatively long flow path within the combustor (in the order of 25–50 cm) compared with chemical and mixing times ensured that reactions were complete before leaving the combustor. Therefore, no unburned species enter the turbine and subsequently little concern has been expressed in literature. Recently, however, the desire to increase performance has led to the development of combustors that operate at a Φ much closer to one. With these designs, the chance of fuel-rich streaks entering the turbine increases. At the same time, advanced combustors are being designed more compact to increase the thrust to weight ratio [5]. One such design is the ultracompact combustor/interturbine burner (UCC/ITB) currently being developed at the Air Force Research Laboratories (AFRL) [5,6]. Figure 1 contains images of a conventional annular combustor (left) and the UCC (right). This concept directs the flow of combustion air into a circumferential cavity for providing sufficient residence times while at the same time reducing the axial length of the component. Fuel is injected into this cavity, where combustion occurs in a fuel-rich regime [5]. The flow is then entrained into a radial cavity that is integrated with the vane. Because of the close proximity, the gases in this cavity still contain intermediate combustion products.

The possibility of unburned fuel entering the turbine, therefore, can no longer be ignored. The primary location where the fuel can find an oxygen rich stream to complete the reaction is at the film cooling hole. The chances of reactions occurring in the turbine vastly increase. When the unburned fuel mixes with oxygen rich compressor bleed air in the turbine cooling film, the conditions become conducive for burning in the turbine. Heat release in the cooling film, whether it results from the recombination of dissociated species or from the combustion of unburned fuel, would drastically reduce the cooling effectiveness of the turbine cooling scheme with potentially severe effects on engine component durability. The challenges presented by this design require a fuller understanding of the interaction between turbine cooling films and incomplete combustion products as well as the relationship between boundary layer reactions and turbine durability.

The potential effect of heat release in the turbine was studied by Lukachko et al. [7] who found that the potential local temperature rise depends strongly on the amount of chemical energy remaining in the flow. The research showed that the local temperature increase in a flow simulating a fuel streak in a future combustor at a stoichiometric fuel-to-air ratio could become large and potentially

Manuscript received March 23, 2009; final manuscript received June 2, 2009; published online March 3, 2010. Review conducted by Dilip R. Ballal.

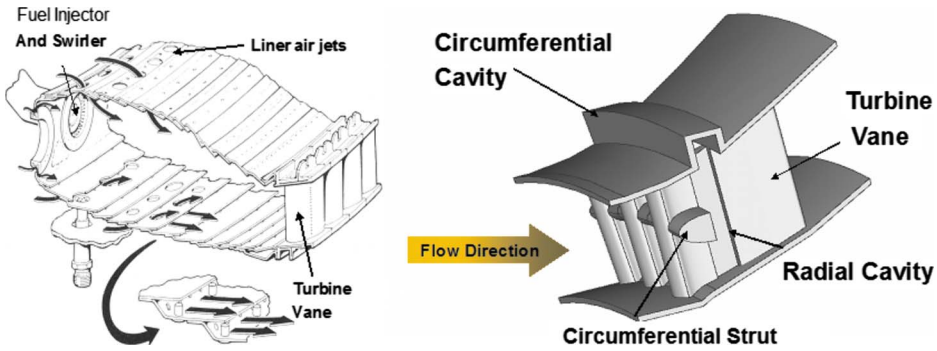

Fig. 1 Conventional axial combustor (left) and ultracompact combustor (right) [5]

catastrophic. In a subsequent effort by Kirk et al. [8], a series of shock tube experiments were conducted that examined the impact of near wall reactions in a cooling film. Their experimental setup allowed concurrent heat flux measurements for a reacting (air) coolant flow and a nonreacting ($N2$) coolant flow through a 35 deg injection angle into a freestream mixture of ethylene and argon. Blowing ratios in the test ranged from 0.5 to 2.0, for a range of unburned fuel concentrations. Their research showed that at high concentrations of unburned fuel, as much as a 30% increase in heat flux may occur. At moderate CO concentrations, the increase reaches approximately 10%. At low concentrations, the difference between reacting and nonreacting flows is insignificant. The objective of the present research is to explore the effect of reactions on turbine film cooling. Specifically, the impact of blowing ratio, equivalence ratio, and cooling hole shape on the occurrence of heat release on a flat plate geometry are quantified. A well-stirred reactor (WSR) was employed to provide a well characterized source of combustion products utilizing propane as a fuel source. Propane was chosen due to its similar heat release as liquid jet fuel while being more chemically accurate to the molecular weight of the species expected to be present within the turbine section. This research will serve as an incremental step toward understanding the physics of reacting boundary layers as they relate to compact combustion systems such as the UCC, where the turbine vane is integrated into the combustor design. The ultimate goal of this program is to provide a sufficient understanding for the development of turbine cooling schemes that will enable the application of the UCC/ITB to future systems.

2 Experimental Setup

A WSR, as developed by Nenniger et al. [9] and modified by Zelina and co-workers [10–12], was used to simulate the turbine entry conditions of a notional combustor. In a WSR, a high rate of mixing of products and incoming reactants is induced, which results in a very nearly uniform distribution of temperature and species within the reactor and at the exit. Because of the uniformity of the flow at the exit, it is possible to assume a uniform species and temperature distribution at a given distance within the test section. The mass flow rate and Φ into the reactor were controlled by thermal mass flow controllers.

The reactor is composed primarily of two toroidal half sections of cast zirconia-oxide ceramic, an Inconel® jet ring, and a metal housing. A schematic of the WSR is shown in Fig. 2. Premixed air and fuel is fed through the fuel-air tubes into the jet ring, into the jet ring manifold, and through 48 fuel-air jets into the reactor toroid. The two toroidal half sections fit together on the top and bottom of the jet ring, forming a 250 ml internal volume. Once in the reactor, the fuel-air mixture reacts and then exits through eight exhaust ports. The flow then enters a common exhaust section, which turns the flow upwards into the test section. A temperature limit of 1970 K restricted the use of the reactor at equivalence ratios close to one at the high overall air flow rates that were desired to match the inlet Reynolds number. A gas sample was fed from the WSR to a standard emissions test bench for characterization of gas concentrations. CO_2 and CO were measured with a California Analytical Instruments Fourier transform infrared (FTIR) analyzer. O_2 was measured with a Horiba magnetopneumatic analyzer.

From the WSR the exhaust flowed upwards through a shaped ceramic chimney, over a forward facing step that served as a turbulent trip, and into the test section. The test section consisted of a thick flat plate base that was enclosed by three quartz window side walls. Slots were machined in the piece to allow for the insertion of two cooling air assemblies and four heat transfer gauge assemblies. Each of these assemblies was inserted through the back of plate with their surfaces flush with the surface of the plate.

The cooling air assemblies were made up of the cooling hole slot inserts and the plena. The cooling air or nitrogen was fed to the plena from the facility supply. In the plena, the cooling air temperature and pressure were measured. The plena were attached to the cooling hole inserts and sealed with a high temperature adhesive sealant. Thermocouples were inserted to a location 5.1 mm from the outside surface of the cooling hole inserts. The cooling air assemblies were inserted through the back of the flat plate. The cooling hole geometries were machined into the surface of the inserts. Three film cooling configurations were tested as part of this study: normal holes, angled holes, and fan-shaped laidback holes (Fig. 3). All the holes were 0.51 mm in diameter. The normal holes had a length to diameter ratio (L/D) of 5. The spacing between the holes was 3.81 mm.

The angled holes were machined at an angle of 30 deg to the surface. To maintain a L/D of 5, the surface was thinner. The fan-shaped laidback holes were based on the angled hole geometry, being equal in size, angle, and depth. However, at the surface

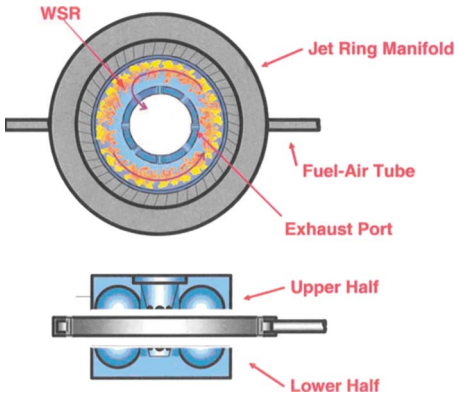

Fig. 2 WSR schematic, modified from Stouffer [12]

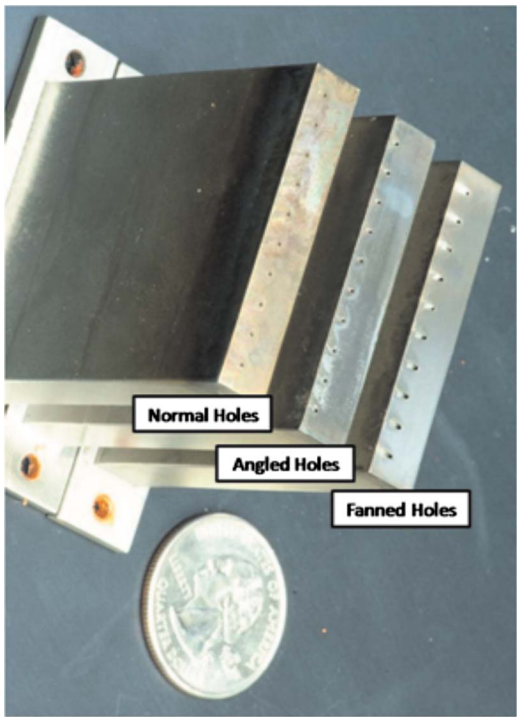

Fig. 3 Cooling insert geometries

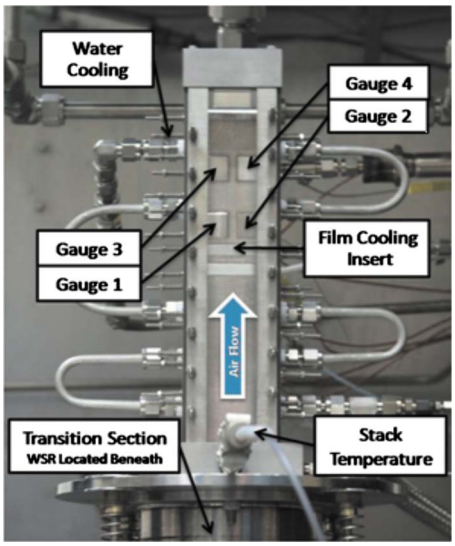

Fig. 4 Flat plate heat transfer gauge and cooling hole insert location

that sees the flow, the sides of the hole flared out 10 deg and lay back 10 deg and provided an exit hole length of 0.91 mm on the surface.

In the current study, the heat transfer to the surface is utilized to determine the amount of heat release in the film. The heat transfer is calculated from measurements of two thermocouples embedded in instrumentation blocks downstream of the film cooling holes. The upper gauge was located 3.8 mm from the surface of the block. A second thermocouple was inserted through the bottom of the block to a depth of 19.1 mm from the surface. This provided a known distance between these thermocouples (15.3 mm). The conductivity of the Hastelloy-X® was determined locally by utilizing a linearization of the conductivity of Hastelloy-X® as a function of temperature from the manufacturer's material property data sheets. With these parameters being known, the heat flux can be determined directly from Fourier's Law. Steady, one dimensional conduction was confirmed by analyzing a typical set of boundary conditions with an ANSYS thermal conduction solver. Within the instrumentation blocks the temperature was determined to be nearly one dimensional. Based on this result, the surface temperature was extrapolated using the embedded measurements and the calculated heat transfer. Four instrumentation blocks were installed, two at nominally 20 hole diameters downstream of the film coolant hole and the other two at approximately 75 diameters downstream. The surface of the flat plate with all inserts installed is shown in Fig. 4. Also shown in this figure is the location of the film cooling row of 11 holes and the location of a second, upstream, film cooling port that was intended to simulate an upstream coolant row that will be used in future tests. What was not shown in Fig. 4 is a trip strip that was installed at the leading edge (bottom of the picture) of the plate to ensure a turbulent boundary layer at the film cooling hole location.

One necessary addition to the test section was water channels to maintain the entire film cooled surface below the melting temperature of the material. A simple heat balance calculation indicated that the Hastelloy-X® would achieve a surface temperature of 1600 K without active cooling. Because of the uncooled leading edge section and the desire to run at low coolant flow rates, it was necessary to water cool this surface. As shown in Fig. 4, a five pass water circuit was included. To maintain a one-dimensional temperature profile in the area of interest, the wall thickness was 5.1 cm and the circuits were 6.4 mm in diameter and installed about 13 mm from the bottom of the flat plate. The impact of the water circuit was investigated by Evans et al. [13]. The water circuit controlled the temperatures between 850 K on the hot surface and 450 K at the deep thermocouple location.

For a comparison with the current literature it was beneficial to calculate the heat transfer coefficient in the presence of film cooling h_f. The traditional means of determining h_f in a film cooling layer would be with the use of Eq. (1) where T_f is the driving temperature for the heat transfer and is the temperature of the film located adjacent to the surface and T_s is the temperature of the surface.

$$q'' = h_f(T_f - T_s) \tag{1}$$

It is a goal of this program to be able to experimentally measure T_f locally above the surface with the use of laser diagnostics, but at the current time T_f has not been measured. Therefore, Eq. (1) is modified with T_∞ as the reference temperature, and h_f is replaced with the effective heat transfer coefficient, h_{eff}. This effective heat transfer coefficient will therefore take into account changes locally of the film temperature due to heat release as this cannot currently be separated. Equation (2) is the form of the convective heat transfer equation used in the analysis of the results of this study.

$$q'' = h_{\text{eff}}(T_\infty - T_s) \tag{2}$$

Many fluid mechanical factors influence the film cooling behavior. The current study explores a number of these in addition to the chemistry of the flow: blowing ratio, injection angle, and hole shape. The blowing ratio M, also referred to as the mass flux ratio, is given in Eq. (3) as a ratio of densities and velocities.

$$M = \frac{\rho_c U_c}{\rho_\infty U_\infty} \tag{3}$$

The calculation of M directly from Eq. (3) requires precise knowledge of the density of the gases. The determination of this property in reacting systems is imprecise. Therefore, M was calculated in this experiment using the conservation of mass for a constant area flow in an incompressible fluid for both coolant flow and reactor exhaust flow. This yields the following:

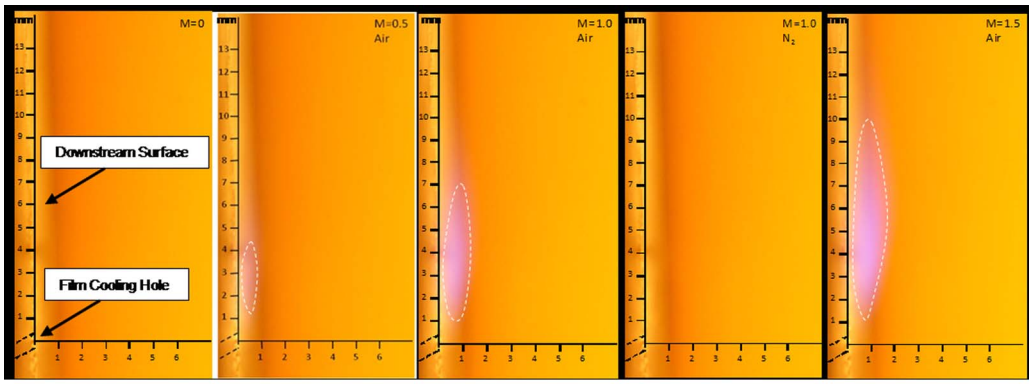

Fig. 5 Angled hole visible burning for (*a*) *M*=0, (*b*) *M*=0.5, air, (*c*) *M*=1.0, air, (*d*) *M*=1.0, N2, and (*e*) *M*=1.5, air

$$M = \frac{\dot{m}_{c,\text{total}} A_\infty}{\dot{m}_\infty A_{c,\text{total}}} \tag{4}$$

Here, $\dot{m}_{c,\text{total}}$ is the total mass flow of the coolant through all cooling holes, $A_{c,\text{total}}$ is the metered area of all cooling holes, A_∞ is the cross-sectional area of the test rig, and $\dot{m}_\infty$ is the mass flow of the reactor exhaust, equaling the sum of $\dot{m}_{\text{fuel}}$ and $\dot{m}_{\text{air}}$.

The ratio of $\dot{m}_{\text{fuel}}$ to $\dot{m}_{\text{air}}$ is the fuel-air ratio. This ratio compared with the value at the stoichiometric condition is the equivalence ratio. This ratio is given as

$$\Phi = \frac{\left(\frac{\dot{m}_{\text{fuel}}}{\dot{m}_{\text{air}}}\right)}{\left(\frac{\dot{m}_{\text{fuel}}}{\dot{m}_{\text{air}}}\right)_{\text{stoich}}} \tag{5}$$

where the stoichiometric value of the fuel-air ratio is 0.06395 for propane. With this definition, a Φ greater than one would be fuel-rich and, conversely, a Φ less than one would be fuel lean. More details of the measurements and calculations can be found in Evans et al. [13].

3 Results

An extensive test matrix was built to understand the impact of heat release on a film cooled surface. This matrix focused on investigating the three typical film cooling hole arrangements shown in Fig. 3. For each of these test plates, a series of experiments was performed with both nitrogen as the film coolant and then with air ejecting from the holes. A sequence of blowing ratios was established covering $M=0$, 0.5, 1.0, 1.5, and 2.0. Each test configuration was performed at equivalence ratios of 0.6, 0.8, 1.5, 1.6, and 1.7 at a relatively high air flow of 1020 g/min. This set the freestream velocity to be 34 m/s, which correlated with a freestream Reynolds number of about 60,000 based on the channel height or 600 based on the hole diameter. Equivalence ratios closer to 1.0 could not be achieved at this air flow rate because of the resultant WSR and stack exit temperature being too high. The materials used in the reactor were not capable of withstanding these higher temperatures. Therefore, a few cases were performed at equivalence ratio of 0.8 and 0.95 at lower air flows of 720 g/min and 480 g/min. These lower air flows were also repeated at the $\Phi=1.5$ condition to permit comparison. A previous effort, Evans et al. [13], provides the impact of main airflow on the results.

In performing these tests, a prominent white flame was evident just downstream of the coolant holes for the higher equivalence ratios. The flame was not present for any condition of Φ less than 1.0. While readily visible to the naked eye, it was somewhat challenging to capture digitally mainly because of the viewing angle and the amount of light saturating the camera. The photographs were taken from the side of the rig with the field of view restricted to the area immediately around the cooling holes. One good set of images was captured in Fig. 5 for the angled hole case at a $\Phi=1.5$ showing the differences between the blowing ratio of 0, 0.5, 1.0, and 1.5 for the air flow and the stark contrast at $M=1.0$ for the nitrogen coolant flow. As the coolant jet met and mixed with the reactor exhaust flow, local combustion occurred. The combustion is visible as a white plume emanating from the coolant hole and progressing downstream.

These photographs demonstrate that boundary layer reactions can occur in fuel-rich conditions as a result of the introduction of air from cooling holes. The reactions happen in close proximity to the surface and cause significant heat transfer to the surface in the immediate vicinity of the cooling holes. This visual evidence is proof of the cause for the heat transfer augmentation that will follow and is discerning to the turbine cooling designer. Instead of the film cooling flow serving to maintain the airfoil surface below a specific temperature, this oxygen rich flow is serving as a flame holder for any remaining combustion products to reach completion. As shown for this fuel-rich condition, as the blowing ratio is increased, the amount of burning is also increased. One small benefit is that for these angled holes at the higher blowing ratio, the jet itself is lifted off the surface. Therefore, the highest temperatures are achieved away from the airfoil surface.

While the photographs of the visible flame provide qualitative proof of what was occurring in the flowfield, the measurements of temperature within the block and the subsequent reduction in heat flux provided the quantitative impact of that flame. The primary comparison made was a relative comparison between the air coolant flow and the nitrogen coolant flow. These two conditions were always obtained on the same day of testing for each configuration and the order was often alternated as the blowing ratio was varied to ensure that the trends were consistent. Also a given blowing ratio was occasionally repeated later in the test program to verify that the facility was not changing throughout the testing window. This was done for a number of reasons, the most significant was that the two set of blocks on either side of the rig often produced results with a substantial side to side variation. That is while the changes between gauges 1 and 3 were consistent with the changes between gauges 2 and 4 within approximately 5 K, gauge 1 could be higher or lower than block 2 by 20 K or more for a given test day or period within a test. It was thought that some residual variation within the well-stirred reactor occurred because of some localized plugging of some of the feed holes that caused different flow to the different areas of the rig. Over the course of a test window, the characteristics of this distribution could change. Laser diagnostics are planned to further quantify these localized variations in the inlet condition.

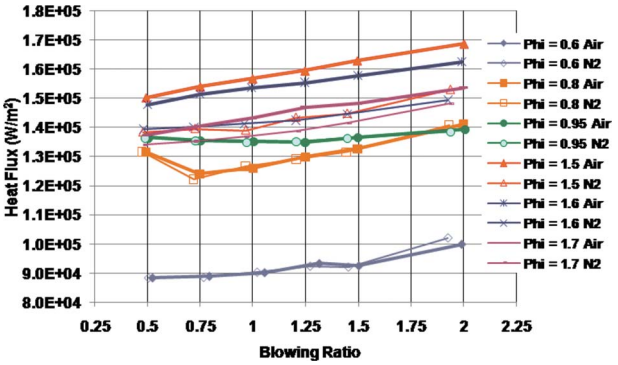

Fig. 6 Angled hole heat flux as a function of equivalence ratio and coolant gas at $x/D=20$

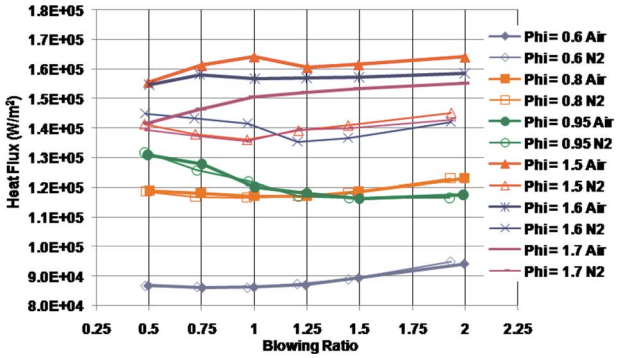

Fig. 8 Fan shaped hole heat flux as a function of equivalence ratio and coolant gas at $x/D=20$

What was ultimately verified was that the side to side trend in the blocks held true throughout when the results for air were compared with those for nitrogen. An uncertainty of about 1% was measured in surface temperature and subsequent heat flux between repeat points within a test period. A greater variation of closer to 5% occurred in an individual surface temperature with about a 4% change in the resultant heat flux when trying to reestablish the same condition on a different day. This was often due to changes in the WSR exit stack temperature and or the coolant exit temperature, which were both difficult to control day to day. However the difference between the air results and the nitrogen results was consistent, with variation within 2%. To account for some of the overall variation, the results presented in the following figures are mean values of measurements for gauges 1 and 2 for the 20 D location and between gauges 3 and 4 for the 75 D location.

The heat flux for the three cooling hole arrangements at an $x/D=20$ is provided in Figs. 6–8. In Fig. 6 the angled hole results are shown for Φ of 0.6, 0.8, 0.95, 1.5, 1.6, and 1.7. It is noted that the $\Phi=0.95$ data were obtained at a lower overall airflow of 720 g/min. Two primary results were realized. First, the overall heat flux levels differ at the different equivalence ratios, which is mostly due to the difference in the freestream temperature as Φ was changed. There was some variability between test days for this value but Table 1 provides the nominal variation in stack temperature with equivalence ratio. Again, this is the temperature achieved at the lower overall airflow for the $\Phi=0.95$ case. This variation was absorbed by utilization of the effective heat transfer coefficient to be discussed in detail later. The second result was the marked difference in heat flux between the air and nitrogen coolant gases at the same Φ and blowing ratio for the equivalence ratios greater than 1.0. This is attributed to the local heat addition due to the reaction chemistry shown in Fig. 5. It is likely that the reactions were initiated by auto-ignition as the inlet temperatures run in the experiment were well above those necessary for auto-ignition in hydrocarbon fuels. It is also possible that the flame contained in the WSR propagated into the test section causing ignition.

A similar result is depicted in Fig. 7 for the normal hole case. Here, the heat flux at each equivalence ratio for nitrogen is somewhat higher than that found for the angled holes, which is consistent with literature (Baldauf et al. [2], for example). What is different is that the heat flux augmentation was substantially higher for the angled holes than for the normal holes when the equivalence ratio was over 1.0. This can be directly attributed to the poorer film cooling coverage of the normal holes. Since, particularly at higher blowing ratios, the normal holes separate from the airfoil surface, the reaction is occurring off the surface, thus transferring less additional heat to the wall. Laser diagnostic measurements are planned in later experiments to try to determine exactly where the reactions are taking place for all three test conditions.

A contrary result is revealed in Fig. 8 for the heat flux for the shaped hole configuration. Here, the heat flux values are lower than those for the angled hole configuration because of the more effective spread of coolant as is often observed in literature (Saumweber et al. [3], as an example). But as clearly seen in Fig. 8, when the equivalence ratio was over 1.0, the augmentation experienced by the air fed cooling condition is the greatest of any case because the coolant flow was maintained very close to the surface. An attached flow is traditionally desirous for an effective cooling arrangement. However, in this case, having air close to the wall caused the heat release due to reaction to also be maintained near the wall. This resulted in a marked increase in the heat transfer.

Looking further downstream for the shaped holes, Fig. 9 reveals that the reaction still has an impact at 75 hole diameters. The difference between the air and nitrogen injections has diminished at this distance but it is still prevalent causing about a 5–10% enhancement with air particularly at the lower blowing ratios. At the higher blowing ratios, little coolant would be expected at this downstream location, so it is not surprising to see little variation. One note is that the overall heat flux is calculated to be higher at this location than at $x/D=20$. This is attributed to the greater amount of cooling water present downstream pulling more heat out of the test surface. The actual surface temperatures are 30–80 K lower at $x/D=75$ than at $x/D=20$. Table 2 gives the varia-

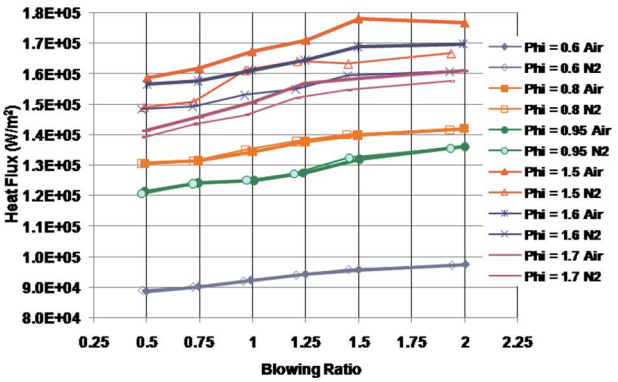

Fig. 7 Normal hole heat flux as a function of equivalence ratio and coolant gas at $x/D=20$

Table 1 Comparison of stack temperatures at different equivalence ratios

Equivalence ratio	0.6	0.8	0.95	1.5	1.6	1.7
Stack temperature (K)	1525	1777	1827	1845	1805	1760

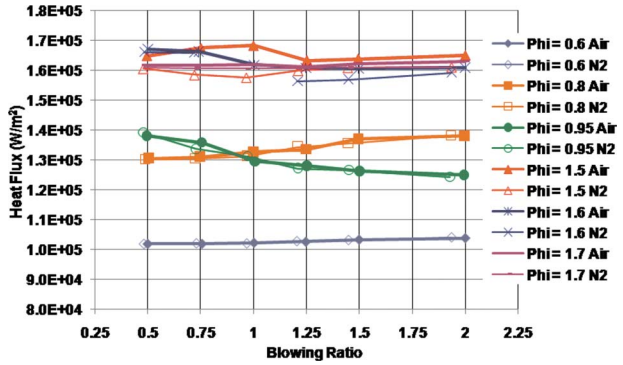

Fig. 9 Fan shaped hole heat flux as a function of equivalence ratio and coolant gas at $x/D=75$

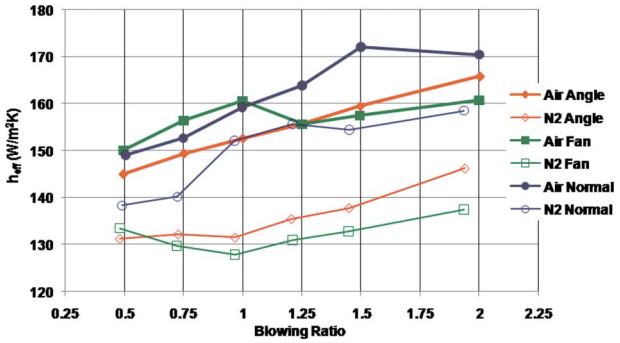

Fig. 11 Comparison of cooling hole geometries: dependence of h_{eff} on M, $\Phi=1.5$, and $x/D=20$

tion in surface temperature for the fan holes for four different equivalence ratios at a blowing ratio of 1.0. Readily apparent is the larger differences at the higher Φ.

One means of normalizing the differences in these results for the various cooling configurations was to utilize an effective heat transfer coefficient (h_{eff}). The values of h_{eff} for each of the geometries are compared in Figs. 10–12. Figure 10 displays h_{eff} for the angled, fan-shaped, and normal holes at $\Phi=0.6$. The data for cooling air (closed symbols) and cooling nitrogen (open symbols) are nearly coincident for the three geometries, indicating that boundary layer reactions had no effect on h_{eff} at this Φ. Furthermore, the basic trends of the data show the angled holes performed better (maintained a lower h_{eff}) than the normal holes at lower M, however performance degrades at higher M due to separation. The fan-shaped hole design provided much lower h_{eff} over the entire range of tested values of M.

Figure 11 shows the h_{eff} data for the same cooling geometries at $\Phi=1.5$. The effect of boundary layer reactions can be clearly observed by comparison of the air and nitrogen data. When air is introduced, a significant increase in effective heat transfer coefficient was experienced for each geometry. The h_{eff} of the normal jets increased by an average of 8% when coolant was switched from nitrogen to air. The h_{eff} for angled holes increased by an average of 14%, while the fan-shaped holes increased by 19%. This caused the fan-shaped holes, which were the most effective in the nonreactive flow conditions, to be the least effective (highest h_{eff}) for the lower blowing ratios. Interestingly, the shape of the curve changed for the fan-shaped holes as well. The previous minimum value of h_{eff} at $M=1$ has increased by 25% to one of the highest levels of h_{eff}. This reemphasizes that the fan-shaped holes which, by design, maintain the film coolant close to the wall, has a negative impact in a reacting flow. Any reactions that occur do so next to the wall for this cooling scheme, resulting in a significant increase in the surface temperature.

Looking farther downstream to the 75 D location, Fig. 12 provides similar results at the equivalence ratio of 1.5. While the overall levels have been reduced, the same trends are readily apparent, which suggests one of two potential drivers. One explanation is that the reaction times are sufficiently long to last an additional 55 hole diameters downstream. In other words the Dahmkohler number (Da), near 0.68 for this experiment, is such that this reaction was still completing over this surface length. Some simple reaction rate calculations were performed, which shows that the carbon and air reaction would require about 1.62 ms to complete in this experiment and that the flow would take about 1.1 ms to traverse from the cooling hole to the downstream set of gauges so it is possible the reaction was still occurring at the downstream location. The second potential driver stems from the belief that the reaction was only occurring on the edge of the coolant jets. Literature showed (Moore et al. [14], for example) that high vorticity is generated along the interface with the freestream and this mixing zone is where combustion is likely to

Table 2 Comparison of surface temperatures at different equivalence ratios for $M=1.0$ for the shaped holes

Φ	X	$T_{s,Air}$ (K)	$T_{s,N2}$ (K)	Difference (%)
1.7	20D	790.0	767.1	3.0
	75D	730.4	725.4	0.7
1.5	20D	813.6	764.7	6.4
	75D	739.2	717.5	3.0
0.8	20D	720.2	719.5	0.1
	75D	671.7	669.7	0.3
0.6	20D	632.2	631.5	0.1
	75D	597.9	597.4	0.1

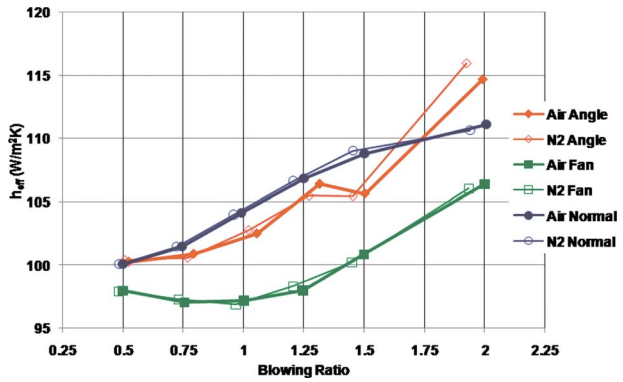

Fig. 10 Comparison of cooling hole geometries: dependence of h_{eff} on M, $\Phi=0.6$, and $x/D=20$

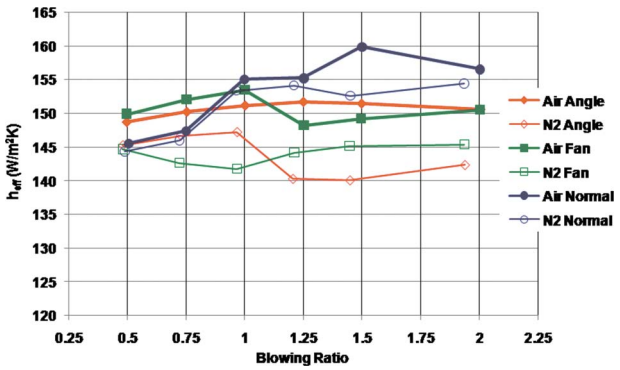

Fig. 12 Comparison of cooling hole geometries: dependence of h_{eff} on M, $\Phi=1.5$, and $x/D=75$

occur. As the jet progresses downstream, more oxygen was convected out of the core where it could react with the fuel-rich freestream. This process continued with downstream distance until the air was depleted from the core. The fact that the normal holes show little enhancement at this downstream position for low blowing ratios further reinforces these drivers. The normal jet ejected the flow further away from the wall leaving less oxygen near the wall at the downstream location.

4 Conclusions

This study has focused on the potential for heat release to occur within a turbine as a result of the interaction of air rich cooling flow with the exhaust of a fuel-rich well-stirred reactor operating at high temperatures over a flat plate. A test rig was designed and constructed with modular components to allow the study of different cooling hole geometries. This investigation focused on three common configurations used in modern turbines—normal holes, angled holes, and fan-shaped cooling holes. The cooling holes could be fed with either air or nitrogen, which enabled a direct comparison of the impact of the reactions to be isolated. The heat flux and effective heat transfer coefficient were calculated for a variety of equivalence ratios and blowing ratios for the three cooling hole geometries.

This investigation has shown that reactions do occur downstream of the introduction of cooling film in the presence of a combustor exhaust stream containing unburned fuel. These reactions occurred close to the surface and resulted in augmented heat transfer to the metal and only happened for equivalence ratios above stoichiometric. The relative impact of the reactions on the surface heat transfer was quantified for the three cooling arrangements. The normal holes resulted in the lowest enhancement of heat transfer to the surface. This was attributed to the high amount of separation resulting in the reactions occurring off the wall surface. The angled holes were more susceptible to reaction as the coolant was introduced along the wall, thus significantly raising the local driving temperature to the wall. The fan-shaped holes exhibited the greatest degradation of performance since the well attached film of coolant that was produced by this design resulted in reactions occurring even closer to that wall and more spread along the wall. This resulted in the highest overall heat load and the greatest difference between the nitrogen injection and the air injection. Overall, the results were consistent with blowing ratio from the perspective of understanding where the jet would be located for the specific case. A turbine cooling scheme designed to take advantage of the improved performance of the fan-shaped holes in a nonreactive condition could underpredict the magnitude of augmented heat release due to fuel streaks, potentially resulting in turbine durability degradation.

Further investigations are planned to better understand the two main areas of concern. First, an improved quantification of the inlet chemistry in the upstream boundary condition to the film cooling jet is desired. Laser diagnostics will be used to aide in the identification of the species that has a significant impact on the reaction. Second, diagnostic lasers will also be used to help quantify the location of the reaction and, more precisely, the extent of the reaction. Clearly reactions can occur in a configuration such as an intra turbine burner and further investigations are needed to address relevant design issues.

Acknowledgment

The authors are grateful to Dr. Jeff Brown and Lt. Joe Beck of the Air Force Research Laboratory Structures Branch in the Turbine Engine Division for their model of the temperature distributions within the test block. We are further grateful to Dr. Paul King of the Air Force Institute of Technology for his advice during this project. We also wish to acknowledge Chuck Abel of ISSI and Mike Arstingstall of UDRI for their assistance in machining the test pieces and running the experiments, respectively.

Nomenclature

A = area (m^2)
D = diameter (m)
Da = Damkohler number
H = heat transfer coefficient (W/m^2 K)
M = blowing ratio
$\dot{m}$ = mass flow rate (g/min; g/s)
q'' = heat flux (W/m^2)
T = temperature (K)
U = velocity (m/s)
x = location; distance (m)
Φ = equivalence ratio
ρ = density (kg/m^3)

Subscripts

∞ = freestream; reactor exhaust stream
c = coolant; convection
eff = effective
f = film
s = surface

References

[1] Bogard, D. G., and Thole, K. A., 2006, "Gas Turbine Film Cooling," J. Propul. Power, **22**, pp. 249–269.
[2] Baldauf, S., Schulz, A., and Wittig, S., 2001, "High-Resolution Measurements of Local Effectiveness From Discrete Hole Film Cooling," ASME J. Turbomach., **123**, pp. 758–765.
[3] Saumweber, C., Schulz, A., and Wittig, S., 2003, "Free-Stream Turbulence Effects on Film Cooling With Shaped Holes," ASME J. Turbomach., **125**, pp. 65–73.
[4] Mattingly, J. D., Heiser, W. H., and Daley, D. H., 1987, *Aircraft Engine Design*, AIAA, Washington, DC.
[5] Zelina, J., Sturgess, G. J., Shouse, D. T., 2004, "The Behavior of an Ultra-Compact Combustor (UCC) Based on Centrifugally Enhanced Turbulent Burning Rates," AIAA Paper No. 2004-3541.
[6] Zelina, J., Shouse, D. T., and Hancock, R. D., 2004, "Ultra-Compact Combustors for Advanced Gas Turbine Engines," Paper No. 2004-GT-53155.
[7] Lukachko, S. P., Kirk, D. R., Waitz, I. A., 2002, "Turbine Durability Impacts of High Fuel-Air Ratio Combustors, Part 1: Potential For Intra-Turbine Oxidation of Partially-Reacted Fuel," Paper No. GT-2002-30077.
[8] Kirk, D. R., Guenette, G. R., Lukachko, S. P., and Waitz, I. A., 2002, "Gas Turbine Engine Durability Impacts of High Fuel-Air Ratio Combustors Part 2: Near Wall Reaction Effects on Film-Cooled Heat Transfer," Paper No. GT-2002-30182.
[9] Nenniger, J. E., Kridiotis, A., Chomiak, J., Longwell, J. P., and Sarofim, A. F., 1984, "Characterization of a Toroidal Well Stirred Reactor," *Twentieth Symposium (International) on Combustion*, Combustion Institute, pp. 473–479.
[10] Zelina, J., "Combustion Studies in a Well-Stirred Reactor," Ph.D. thesis, University of Dayton, Dayton OH, 1995.
[11] Stouffer, S. D., Striebich, R. C., Frayne, C. W., and Zelina, J., 2002, "Combustion Particulates Mitigation Investigation Using a Well-Stirred Reactor," AIAA Paper No. 2002-3723.
[12] Stouffer, S., Pawlik, R., Justinger, G., Heyne, J., Zelina, J., and Ballal, D., 2007, "Combustion Performance and Emissions Characteristics for a Well-Stirred Reactor for Low Volatility Hydrocarbon Fuels," AIAA Paper No. 2007-5663.
[13] Evans, D. S., King, P. I., Polanka M. D., Zelina, J., Anderson, W. S., and Stouffer, S. D., 2009, "The Impact of Heat Release in Turbine Film Cooling," AIAA Paper No. 2009-298.
[14] Moore, K., Wolff, J. M., Polanka, M. D., and Sondergaard, R., 2005, "A Large Scale Investigation of a Flat Plate Vortex Generator Jet in Crossflow Using PIV," 41st AIAA/ASME/SAE/ASEE Joint Propulsion Conference and Exhibit, Tucson, AZ, July 10–13, Paper No. AIAA-2005-4221.

Nicole Donato
Christopher Aul
Eric Petersen

Department of Mechanical Engineering,
Texas A&M University,
College Station, TX 77843

Christopher Zinner
Department of Mechanical, Materials and
Aerospace Engineering,
University of Central Florida,
Orlando, FL 32816

Henry Curran
School of Chemistry,
National University of Ireland Galway,
Galway, Ireland

Gilles Bourque
Rolls-Royce Canada,
Montreal, Canada H8T 1A2

Ignition and Oxidation of 50/50 Butane Isomer Blends

One of the alkanes found within gaseous fuel blends of interest to gas turbine applications is butane. There are two structural isomers of butane, normal butane and isobutane, and the combustion characteristics of either isomer are not well known. Of particular interest to this work are mixtures of n-butane and isobutane. A shock-tube experiment was performed to produce important ignition-delay-time data for these binary butane isomer mixtures, which are not currently well studied, with emphasis on 50-50 blends of the two isomers. These data represent the most extensive shock-tube results to date for mixtures of n-butane and isobutane. Ignition within the shock tube was determined from the sharp pressure rise measured at the end wall, which is characteristic of such exothermic reactions. Both experimental and kinetics modeling results are presented for a wide range of stoichiometries ($\phi = 0.3 - 2.0$), temperatures (1056–1598 K), and pressures (1–21 atm). The results of this work serve as a validation for the current chemical kinetics model. Correlations in the form of Arrhenius-type expressions are presented, which agree well with both the experimental results and the kinetics modeling. The results of an ignition-delay-time sensitivity analysis are provided, and key reactions are identified. The data from this study are compared with the modeling results of 100% normal butane and 100% isobutane. The 50/50 mixture of n-butane and isobutane was shown to be more readily ignitable than 100% isobutane but reacts slower than 100% n-butane only for the richer mixtures. There was little difference in ignition time between the lean mixtures. [DOI: 10.1115/1.3204654]

1 Introduction

Fuel-flexible gas turbines are of interest to the power generation industry due to the increasing level of variation in hydrocarbon fuel composition. It is very important that the combustion chemistry is well understood to avoid problems in the combustion system such as flashback, blowoff, instabilities, and autoignition [1,2]. Thus, there is a need to perform experiments to validate the detailed chemistry mechanisms for various higher order hydrocarbons. The focus of this paper is on the chemistry of a butane fuel blend comprised of 50% *n*-butane with 50% isobutane in air. Although this blend may not be a practical fuel for use on its own, its chemistry is a fundamental part of other hydrocarbon fuels such as liquefied natural gas (LNG) and refinery fuels used in industrial applications. Most importantly, the present work provides the validation of chemistry models at practical engine conditions.

Previous work has shown that butane isomers have different combustion characteristics. Structurally, *n*-butane is the unbranched alkane with four carbon atoms, while isobutane, also known as 2-methylpropane, is the branched structure of butane, as seen in Fig. 1 [3]. Although *n*-butane and isobutane have many similar properties, for example, molar mass, they also have dissimilar properties such as boiling point and autoignition temperature. Normal butane has been shown to be more readily ignitable than isobutane [4].

Butane, like many other complex hydrocarbons, exhibits interesting combustion characteristics such as cool flames, negative temperature coefficient regions [5], two-stage autoignition, and product formation at low temperatures [6]. Logically, it follows that understanding butane will give insight to other more complex hydrocarbons. To date, there have been many studies investigating the behavior of *n*-butane oxidation [5–21], while only a few examine isobutane [5,8]. It is important to investigate butane because its two isomers have been shown to have different combustion characteristics [4,5,8,21]. Previous investigations have utilized many different techniques such as shock tubes [14], rapid compression machines (RCMs) [5,6,10,17], spark ignition engines [11], jet stirred reactors [12], and homogeneous charge compression engines [13]. In general, there is a lack of data for blends of the two isomers, particularly at pressures of interest to gas turbines and with undiluted fuel-air mixtures.

In the present study, shock-tube experiments have been performed to determine ignition delay times over a wide range of conditions for 50/50 *n*-/isobutane blends in theoretical air ($O_2 + 3.76N_2$), as seen in Table 1. The range of conditions includes equivalence ratios of $0.3 \leq \phi \leq 2.0$, where the equivalence ratio is the mass-based fuel-to-oxidizer ratio to the stoichiometric fuel-to-oxidizer ratio, target pressures of around $1 \leq P$ (atm) ≤ 21, and temperatures of 1056–1598 K. The results from this work are important to validate chemistry models.

A discussion on the chemical kinetics modeling follows, along with a comparison of the model to experimental results. Additionally, details of the experimental setup and a discussion concerning the approach used to determine ignition delay times are provided

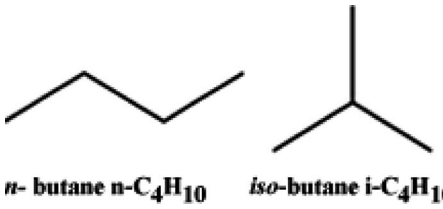

Fig. 1 ***n*-butane and isobutane chemical structures. Normal butane carbon atoms are arranged in one row, while isobutane has a carbon atom in the middle [4].**

Contributed by the International Gas Turbine Institute of ASME for publication in the JOURNAL OF ENGINEERING FOR GAS TURBINES AND POWER. Manuscript received March 26, 2009; final manuscript received April 7, 2009; published online March 4, 2010. Review conducted by Dilip R. Ballal. Paper presented at the ASME Gas Turbine Technical Congress and Exposition, Orlando, FL, June 8–12, 2009.

Table 1 Mixture compositions in percent volume

Mixture	ϕ	n-C_4H_{10} (%)	iso-C_4H_{10} (%)
1	0.3	50	50
2	0.5	50	50
3	1.0	50	50
4	2.0	50	50

in the following sections. Lastly, a thorough discussion of the results is provided as well as results from developed correlations. A sensitivity analysis is also presented to give insight to the important reactions for ignition under varying conditions.

2 Chemical Kinetics Model

The chemical kinetics mechanism was developed, and simulations were performed using the HCT (Hydrodynamics, Chemistry, and Transport) program [22]. The detailed chemical kinetics model is based on that used to describe methane/propane [23] and methane/ethane/propane mixtures [24], but some changes have been made, and these are discussed here. The thermochemistry of a number of species has been taken from the CHEMKIN thermochemistry library [25] or recalculated using THERM [26] with updated groups based on the work of Lay et al. [27] and Sumathi and Green [28] (Table 2). In the mechanism, reactions obey the thermodynamic equilibrium, and thus changes in thermochemistry have led to changes in rate constants of reactions involving these species.

Figure 2 shows how well the model performs over wide ranges

Table 2 Sample of thermochemistry data for species that were changed for the present mechanism, where H_f^0 is the standard heat of formation, S_f^0 is the entropy, and C_p is specific heat under constant pressure

SPECIES	H_f^0 at 298 K (kcal mol^{-1})	S_f^0 at 298 K (cal K^{-1} mol^{-1})	C_p (cal K^{-1} mol^{-1}) 300	400	500	600	800	1000	1500
CH_2[a]	92.49	46.72	8.25	8.55	8.88	9.23	9.93	10.57	11.74
C_2[a]	171.31	37.76	4.98	4.98	4.97	4.97	4.97	4.97	4.97
CH_2CO[a]	−12.40	57.79	12.43	14.17	15.67	16.91	18.79	20.24	22.44
HCCO[a]	42.45	60.74	12.65	13.47	14.23	14.92	16.07	16.83	17.98
HCCOH[a]	20.43	58.71	13.22	14.78	16.16	17.35	19.15	20.30	22.29
C_2H_5CHO[b]	−45.36	72.75	19.82	23.24	26.77	30.28	36.85	42.35	50.07
C_2H_5CO[b]	−7.96	73.87	19.31	21.77	24.62	27.65	33.64	38.76	45.41
HO_2CH_2OCHO[b]	−110.29	90.89	25.72	30.04	33.61	36.54	40.88	43.74	47.49
$HOCH_2OCO$[b]	−82.59	81.62	19.83	22.28	24.60	26.74	30.41	33.18	36.77
CH_3OCHO[b]	−85.68	68.10	15.62	18.97	22.09	24.95	29.73	33.22	37.35
CH_3OCO[b]	−39.37	68.94	14.74	17.57	20.20	22.60	26.56	29.38	32.53
CH_2OCHO[b]	−37.42	70.63	14.64	17.57	20.24	22.62	26.52	29.28	32.46
C_3H_8[b]	−25.06	64.29	17.90	22.77	27.08	30.89	37.16	41.95	49.33
n-C_3H_7[b]	23.94	69.08	17.13	21.39	25.17	28.50	34.00	38.20	44.68
iso-C_3H_7[b]	21.29	68.80	16.56	20.48	24.11	27.42	33.12	37.58	44.33
C_3H_6[b]	4.87	63.82	15.45	19.32	22.74	25.75	30.72	34.51	40.34
C_3H_5-a[b]	40.97	60.69	14.88	18.70	21.94	24.68	28.96	32.07	36.88
C_3H_5-t[b]	61.78	65.63	15.09	18.09	20.80	23.24	27.37	30.59	35.58
C_3H_5-s[b]	63.98	65.21	15.26	18.51	21.36	23.85	27.92	31.01	35.82
C_3H_4-a[b]	47.64	57.95	14.25	16.97	19.46	21.71	25.45	28.20	32.06
C_3H_4-p[b]	45.77	58.90	14.51	17.06	19.40	21.54	25.16	27.90	31.79
C_3H_3[b]	83.05	61.49	15.84	17.74	19.47	21.01	23.43	25.00	27.55
C_3H_6OOH2-2[b]	1.00	88.11	26.02	31.08	35.29	38.78	44.14	47.97	54.08
$C_3H_5$1-2,3OOH[b]	−20.00	104.98	33.45	39.90	45.21	49.55	56.01	60.37	66.48
$C_3H_5$2-1,3OOH[b]	−17.98	103.80	33.05	39.02	44.08	48.35	54.95	59.59	66.07
C_2H_3OOH[b]	−7.59	72.50	18.43	22.06	25.07	27.55	31.25	33.75	37.25
C_4H_{10}[b]	−30.04	73.71	23.34	29.68	35.27	40.17	48.21	54.27	63.52
$p$$C_4H_9$[b]	18.96	78.50	22.57	28.30	33.36	37.79	45.05	50.53	58.86
$s$$C_4H_9$[b]	16.31	79.52	21.81	27.37	32.37	36.84	44.27	49.92	58.31
C_4H_8-1[b]	0.07	73.51	20.62	26.22	31.06	35.25	41.98	47.00	54.71
C_4H_8-2[b]	−2.78	71.03	20.67	25.84	30.45	34.53	41.29	46.45	54.32
C_4H_8OH-1[b]	−19.71	90.39	24.82	30.85	36.15	40.80	48.37	54.03	62.47
C_4H_8OH-2[b]	−24.08	88.39	25.43	31.55	36.89	41.53	49.02	54.58	63.00
$C_2H_3COCH_3$[b]	−30.40	78.20	21.23	26.36	30.77	34.55	40.53	44.88	51.30
iso-C_4H_{10}[b]	−32.07	70.11	23.33	29.79	35.44	40.38	48.41	54.49	63.86
iso-C_4H_9[b]	16.93	75.21	22.54	28.40	33.53	37.99	45.26	50.74	59.21
$t$$C_4H_9$[b]	12.33	75.35	22.45	27.38	31.98	36.22	43.59	49.46	58.47
iso-C_4H_8[b]	−4.21	71.37	21.58	26.74	31.30	35.31	41.90	46.91	54.64
iso-C_4H_7[b]	31.89	69.62	20.99	26.11	30.47	34.20	40.10	44.44	51.16
$t$$C_3H_6OH$[b]	−24.40	76.94	20.50	24.97	28.79	32.06	37.24	41.06	47.12
$t$$C_3H_6O_2CHO$[b]	−39.73	93.50	30.47	36.84	42.27	46.88	54.07	59.18	66.46
$t$$C_3H_6O_2HCO$[b]	−38.93	94.40	31.74	38.35	43.91	48.56	55.63	60.46	66.91
iso-$C_3H_5O_2HCHO$[b]	−26.83	96.70	31.82	38.41	43.96	48.59	55.63	60.44	66.90

[a]Kee et al. [25].
[b]Ritter and Bozzelli [26], Lay et al. [27], and Sumathi and Green [28].

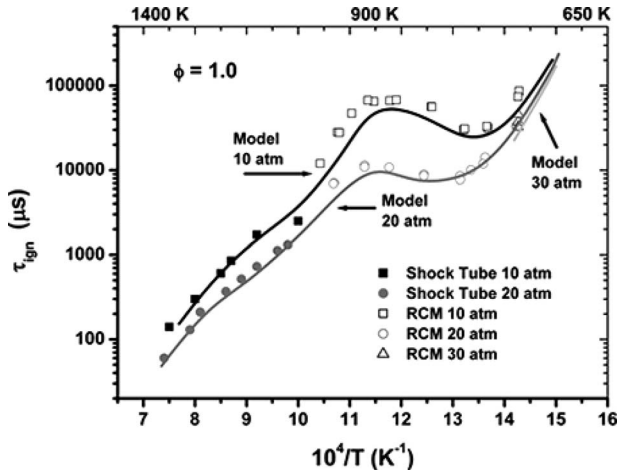

Fig. 2 Validation of model for 100% *n*-butane in air (ϕ=1) over a wide range of conditions. Points are experimental results; lines are model simulations. Data are from Ref. [29].

of temperatures (650–1400 K) and pressures (10–30 atm) for pure *n*-butane/air mixtures. The data shown in Fig. 2 were taken from a recent study by the authors, presented elsewhere [29]. A complete listing of the detailed kinetic mechanism, together with thermochemical parameters and transport data, is available on the NUI Galway combustion chemistry website.[1]

3 Experiment

As mentioned above, shock-tube experiments were performed over a wide range of conditions to better understand the ignition behavior of various 50/50 blends of *n*-/isobutane. The experiments were performed using two separate shock tubes as described later in this section. Pressure traces from the experiment were analyzed to determine ignition time. The ignition-delay data were then used to help validate the chemical kinetics mechanism.

3.1 Apparatus and Procedure. Two shock-tube facilities capable of achieving the high pressures and temperatures needed for the present study are described in this section. Both facilities measure the incident-shock velocity at the test region to determine the overall conditions behind the reflected shock by way of one-dimensional shock relations. The incident-shock measurement is facilitated by five pressure transducers (PCB 113) set in series along the side of the shock tube, which feed signals to four Fluke PM 6666 timer counter boxes, which in turn are used to extrapolate the incident-shock velocity directly to the end wall.

The first facility, described in greater detail by Petersen et al. [30], used in generating all of the data in the intermediate- to high-pressure region, has a driven section length of 10.7 m with a circular profile internal diameter of 16.2 cm. The driver section of this first facility is 3.5 m in length and has a smaller internal diameter of 7.62 cm, which is then expanded through a nozzle cone to the driven diameter directly after the diaphragm location. The second facility, presented by Aul et al. [31], has a driven section length and inner diameter dimensions of 4.72 m and 15.24 cm, respectively, and a driver section length and an inner diameter of 4.93 m and 7.62 cm, respectively. A schematic of the second facility is shown in Fig. 3. Both facilities are constructed entirely of stainless steel 304, which is wholly inert to the test gases used in this study.

Ignition-delay-time measurements are determined from the highly exothermic pressure rise present during reaction via PCB 134A and Kistler 603B1 pressure transducers located at the sidewall and end wall of each shock-tube facility. Measurements of the emission of OH^* chemiluminescence are made at both the sidewall and end wall locations through CaF_2 windows and are focused onto a 307 ± 5 nm bandpass filter in sequence with a Hamamatsu 1P21 photomultiplier tube in a home-made housing. Each of the data signals is processed through a 14 bit GageScope digital oscilloscope board with sampling rates of 1 MHz or greater per channel.

3.2 Ignition Time Definition. The ignition time is measured from the end wall as the sudden rise in pressure behind the reflected-shock wave. For these real fuel-air mixtures, a sharp rise is seen in the pressure trace during ignition, which also coincides with the onset of OH^* emission, as shown in Fig. 4(*a*). The end wall pressure trace was used quantitatively to determine ignition time, while the end wall emission trace was used qualitatively to verify the ignition event. For the mixtures analyzed in this work, no significant pressure rises before ignition were observed, even under colder temperatures and longer test times, as seen in Fig. 4(*a*). Figure 4(*b*) shows the pressure and emission traces for a different temperature and stoichiometry and is representative of all test cases. No pre-ignition pressure rises, such as those sometimes seen in lower-temperature, higher-pressure experiments,

[1]http://c3.nuigalway.ie/butane.html

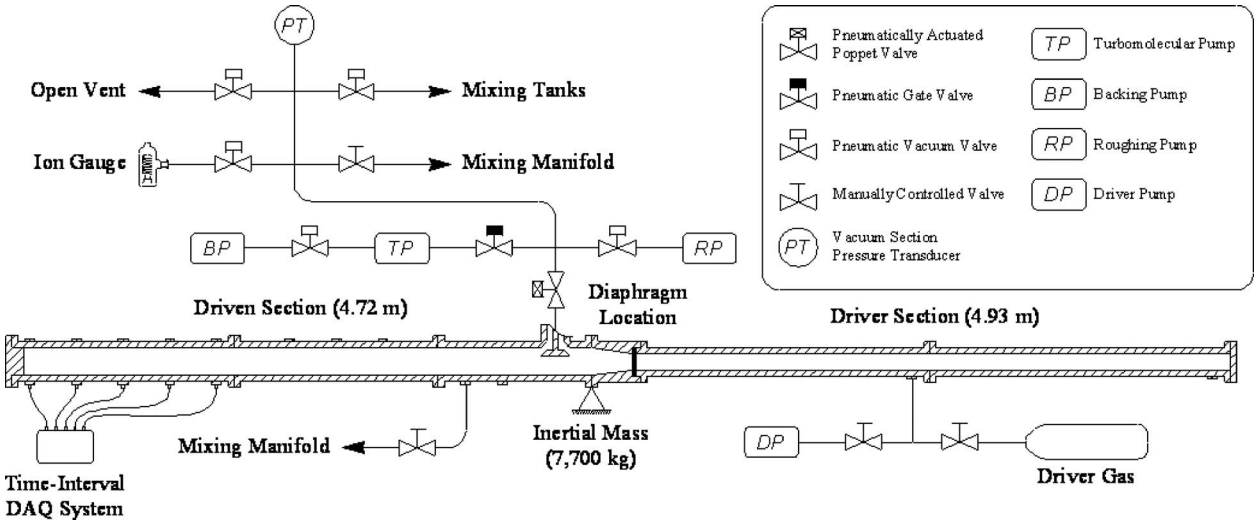

Fig. 3 Schematic of shock-tube facility presented in Aul et al. [31]

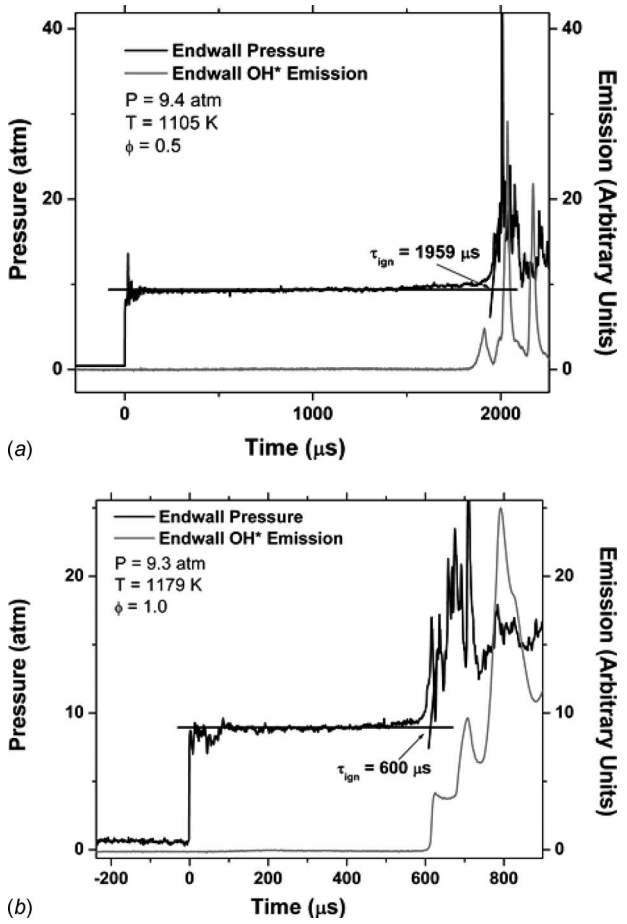

Fig. 4 Typical end wall pressure and emission traces used to determine ignition delay time. No early reaction leading to accelerated main ignition is seen in either the pressure or OH* traces. (*a*) Long test time example: T=1105 K and τ_{ign} =1959 μs. (*b*) Typical test time example: T=1179 K and τ_{ign} =600 μs.

were observed in any of the data presented herein. Such early pressure increases have been linked to faster-than-expected ignition events in some studies [32].

4 Results

The experimental results for the entire range of conditions are provided in Table 3, where the definition of ignition delay time for each case was defined as the inflection point between the test pressure achieved after compressing the mixture and the steep rise in pressure at the time of ignition, as described above.

The experimental data for all four mixtures are plotted in Figs. 5–8 on Arrhenius-type plots that give the ignition delay time on a log scale as a function of the reciprocal reflected-shock temperature. Predicted ignition times from the C4 mechanism are shown on each plot as well. The effect of temperature on the ignition times can be discerned from the data. For temperatures above about 1175 K, the ignition trend becomes more linear, and the slope is steeper. This trend is noticeable for all the mixtures herein. In general, the model is in excellent agreement with the measured ignition delay times, particularly at the higher pressures.

There is a small but noticeable ignition delay time uncertainty that is apparent for measurements lower than 200 μs and has been statistically averaged throughout the collection of data to be ± 8 μs. This uncertainty in time is the result of inherent uncertainties in selecting the specific pressure and/or emission features at the time of the ignition event and also in the repeatability of the

Table 3 Shock-tube ignition-delay-time data for 50/50 *n*-/isobutane mixtures in air

T (K)	P (atm)	τ_{ign} (μs)	ϕ
1354	1.9	166	0.3
1321	2.0	318	
1282	2.0	511	
1255	2.0	725	
1248	2.0	895	
1253	8.6	335	
1151	9.1	1396	
1307	7.9	169	
1102	8.9	2380	
1190	8.5	878	
1266	17.7	223	
1211	18.9	421	
1148	19.5	804	
1099	19.9	1287	
1362	16.9	79	
1383	1.7	130	0.5
1307	1.7	410	
1282	1.9	650	
1263	1.9	973	
1235	1.8	1404	
1363	1.8	199	
1409	1.7	111	
1105	9.4	1959	
1147	8.9	1292	
1239	8.2	444	
1321	7.6	164	
1195	8.6	746	
1323	16.9	89	
1240	17.9	247	
1167	18.5	543	
1115	19.5	846	
1079	20.3	1191	
1406	16.3	42	
1278	1.9	773	1.0
1266	1.8	1045	
1303	1.8	714	
1336	1.8	469	
1355	1.8	380	
1350	1.8	395	
1274	1.9	1053	
1179	9.3	600	
1096	9.3	1662	
1258	7.9	318	
1366	7.1	123	
1111	8.8	1652	
1178	9.3	812	
1220	18.3	266	
1158	19.4	441	
1099	20.0	727	
1062	21.0	987	
1297	16.9	129	
1407	15.4	48	
1300	1.7	784	2.0
1368	1.6	403	
1445	1.5	178	
1517	1.3	115	
1262	1.7	1449	
1194	8.1	637	
1119	8.7	1369	
1076	9.2	2030	
1266	7.4	369	
1361	6.9	165	
1421	6.3	100	
1119	19.1	488	
1056	19.1	871	
1182	18.6	317	
1259	17.4	187	
1317	16.0	107	

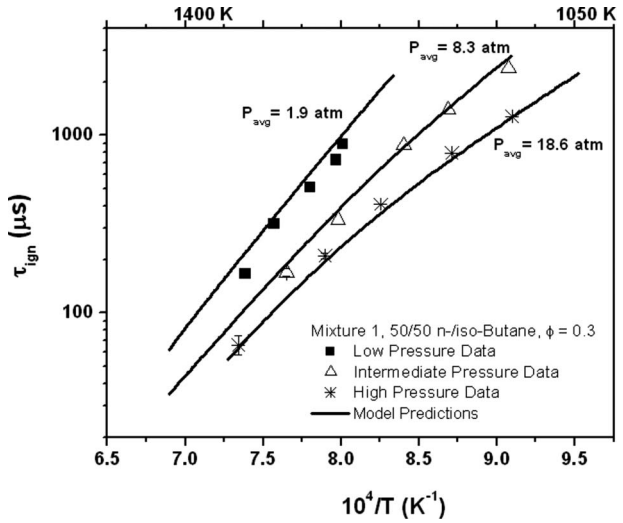

Fig. 5 Ignition-delay-time data compared with model results for mixture 1: 50% n-C_4H_{10} and 50% iso-C_4H_{10} at ϕ=0.3

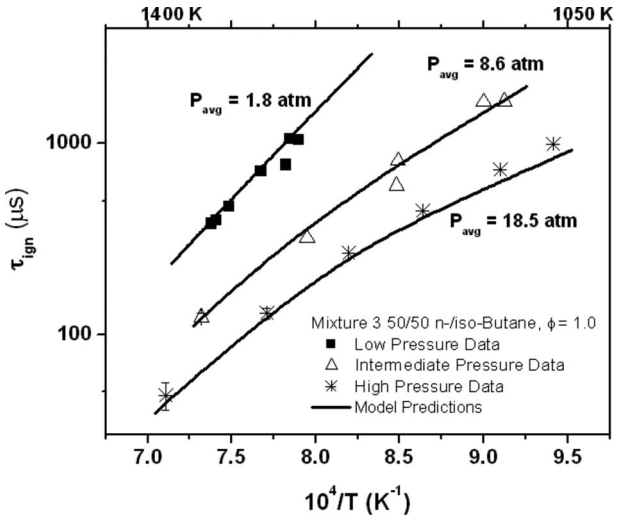

Fig. 7 Ignition-delay-time data compared with model results for mixture 3: 50% n-C_4H_{10} and 50% iso-C_4H_{10} at ϕ=1.0

ignition event itself from test to test. This variation is almost insignificant for longer ignition times and is thus only shown in error bars for the faster ignition results.

5 Discussion

The experimental results are in agreement with the present C4 mechanism over the entire range of temperatures, pressures, and stoichiometries, as seen in Figs. 5–8. Any slight disagreement that does exist between the model and the data occurs at the lower pressure (Fig. 8), where the model overpredicts the ignition at higher temperatures. Since the model is validated over the conditions of the experiment, it can be used to explore the effect of mixtures and conditions not directly measured in the experiment.

Figure 9 compares the results from the model for the cases of 100% n-butane, 0% isobutane all the way to the case of 0% n-butane, 100% isobutane in 25% increments for various stoichiometries (ϕ=0.3, 0.5, 1.0, and 2.0) at P=8 atm. An interesting effect is seen at fuel lean conditions (Figs. 9(a) and 9(b)), where there is little variation in ignition times between 100% n-butane and 100% isobutane. There becomes a clear distinction in ignition times of the two different isomers when the fuel blend is stoichiometric, as seen in Fig. 9(c). This difference becomes even more exaggerated under fuel rich conditions, where in Fig. 9(d) n-butane is seen to ignite significantly faster than isobutane. A sensitivity analysis was performed to further examine this effect and is presented later in this section.

In other ongoing work, the authors have performed an extensive series of rapid compression and shock-tube ignition-delay-time experiments for the cases of 100% isobutane as well as 100% n-butane [29]. This work agrees with the predicted results shown in Fig. 9 and was also mentioned above with regard to Fig. 3. Correlations have been developed from the experimental results to predict ignition delay times. Each correlation determines ignition times for a given temperature, pressure, and amount of n-butane and isobutane. The correlations help to give an understanding of the complex chemistry by providing simplified physical relationships. Following traditional hydrocarbon fuel ignition time behavior, it is seen that the ignition time is exponentially dependent on the inverse temperature and directly dependent on the mixture concentration to some power. The basic form of the correlation is as follows:

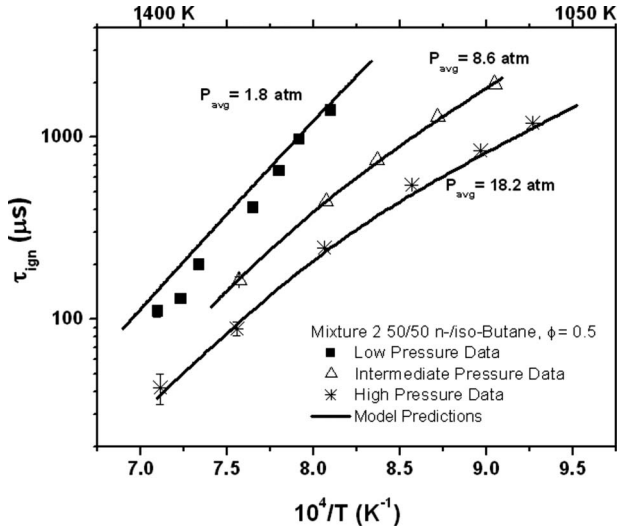

Fig. 6 Ignition-delay-time data compared with model results for mixture 2: 50% n-C_4H_{10} and 50% iso-C_4H_{10} at ϕ=0.5

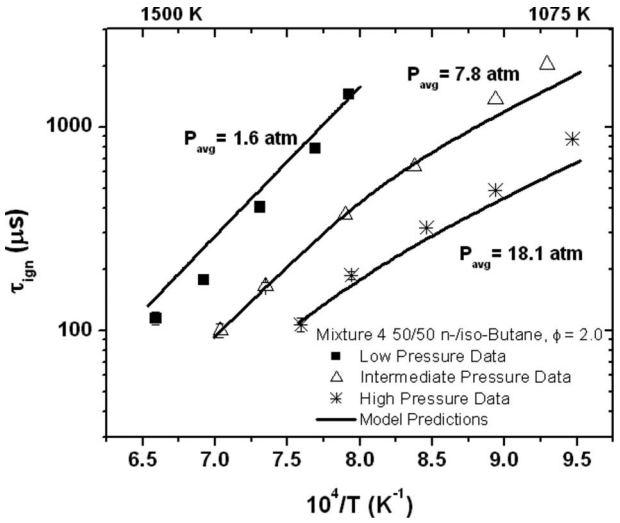

Fig. 8 Ignition-delay-time data compared with model results for mixture 4: 50% n-C_4H_{10} and 50% iso-C_4H_{10} at ϕ=2.0

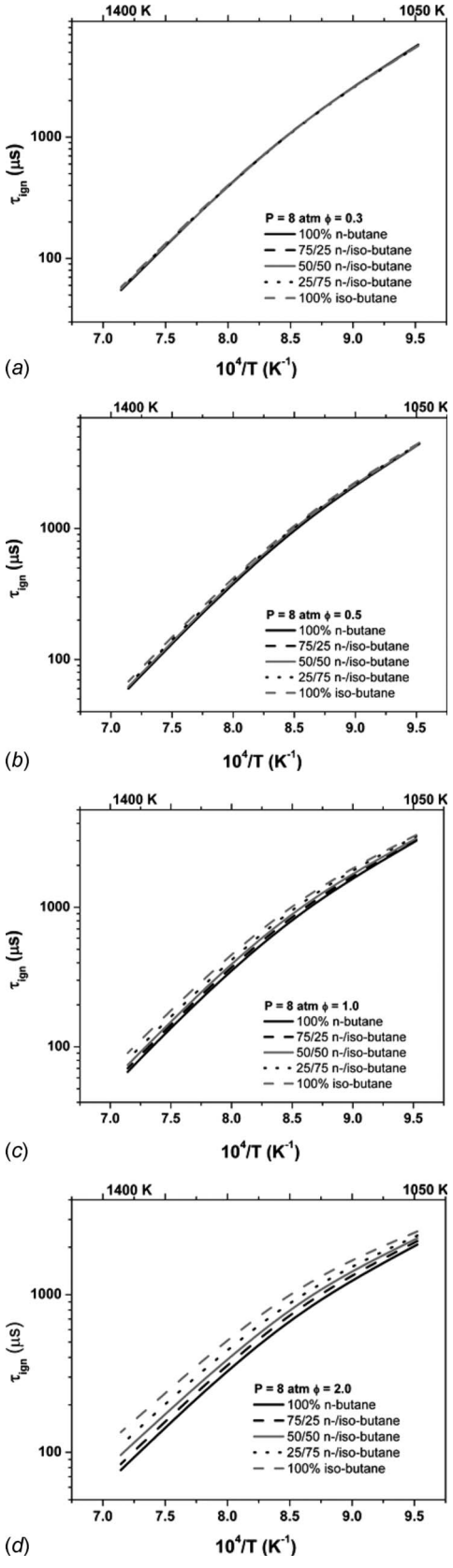

Fig. 9 Ignition delay times obtained from the mechanism are plotted against inverse temperature at 8 atm for a wide range of stoichiometry. Fuel lean conditions show similar ignition times for n-C_4H_{10} and iso-C_4H_{10}; however, under stoichiometric and fuel rich conditions, n-C_4H_{10} and iso-C_4H_{10} have significantly different ignition times. (*a*) ϕ=0.3, (*b*) ϕ=0.5, (*c*) ϕ=1.0, and (*d*) ϕ=2.0.

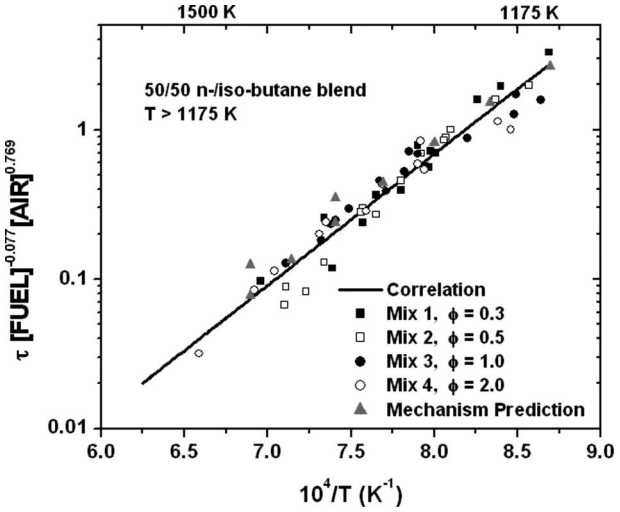

Fig. 10 High-temperature correlation from Eq. (2). Experimental data, correlation results, and mechanism predictions plotted against inverse temperature show good agreement for high temperatures (τ in μs; [fuel] and [air] in mol/cm^3).

$$\tau_{ign} = A[\text{fuel}]^x[\text{air}]^y \exp\left(\frac{E}{RT}\right) \tag{1}$$

where τ_{ign} is the ignition delay time or kinetic time in μs; fuel is 50/50 n-C_4H_{10} plus iso-C_4H_{10} in mol/cm^3; air is also in mol/cm^3; E, A, x, and y are constants. The constant E is commonly referred to as an ignition activation energy, which is in kcal/mol, and R is the ideal gas constant in kcal/mol K units. As noted above, there is a shift in temperature dependence between the higher-temperature and lower-temperature data, so two correlations were found to best fit the data.

The first correlation was developed for temperatures greater than 1175 K (Eq. (2)). When using the data to obtain the correlation, data that were close to 1175 K were used in both the high- and low-temperature correlations, so that the correlations will overlap,

$$\tau_{ign} = 6.734 \times 10^{-8}[\text{fuel}]^{0.077}[\text{air}]^{-0.769} \exp(40.1/RT) \tag{2}$$

The pressure dependence of ignition delay can be estimated as the pressure raised the sum of the exponents of the fuel and air terms since the fuel and air concentrations both depend linearly on the

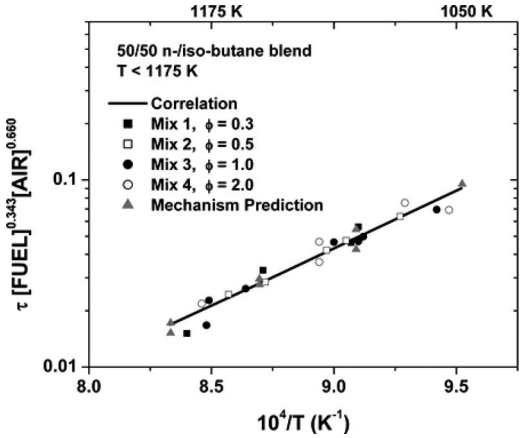

Fig. 11 Low-temperature correlation of Eq. (3). A shallower slope is seen for the lower temperature experimental data, correlation, and mechanism predictions when plotted against inverse temperature (τ in μs; [fuel] and [air] in mol/cm^3).

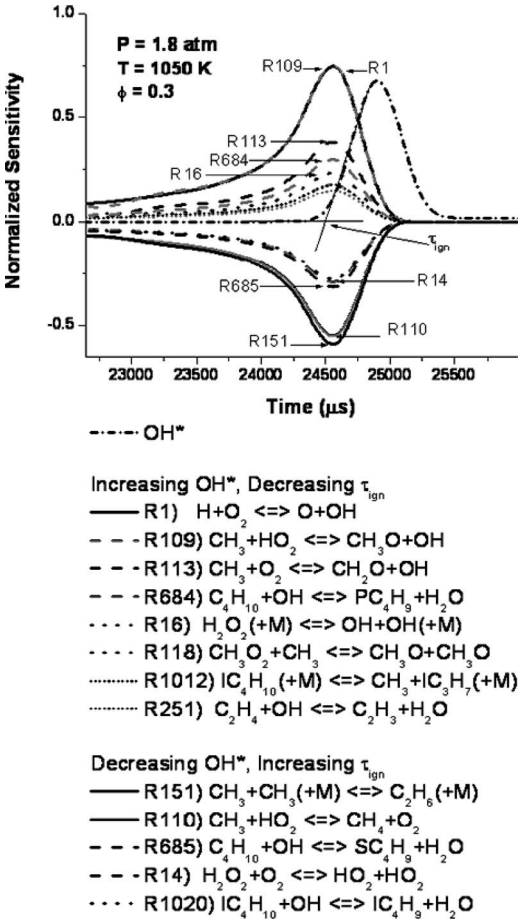

Fig. 12 Sensitivity analysis results from OH* show the most important reactions as a function of time during ignition. Sensitivity results for low pressure (1.8 atm) and low temperature (1050 K).

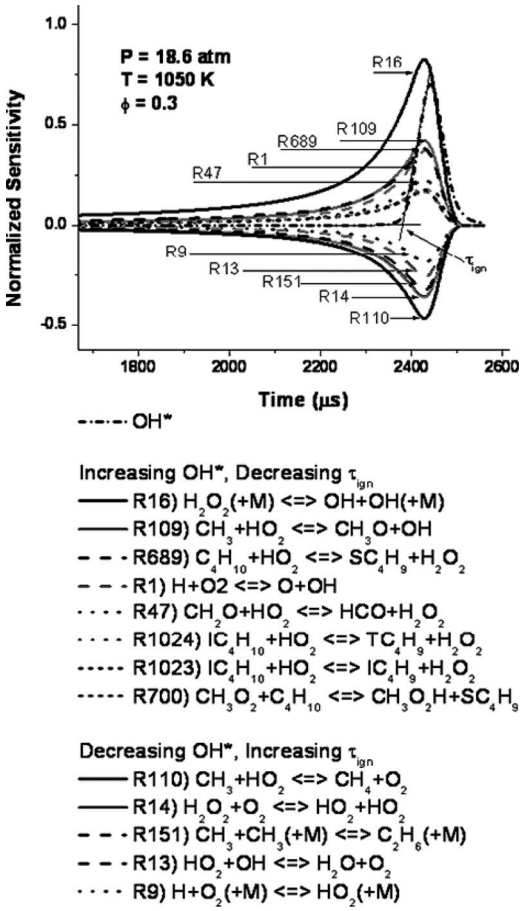

Fig. 13 Sensitivity analysis results from OH* show the most important reactions as a function of time during ignition. Results shown for high pressure (18.6 atm) and low temperature (1050 K).

pressure. The above equation gives an overall pressure dependency of $P^{-0.69}$. The negative exponents of fuel and air show that ignition will become faster with increasing amounts of fuel and air. Results from the high-temperature correlation compared with the experimental results and mechanism predictions show good agreement, as seen in Fig. 10, with an $R^2=0.93$.

The mechanism was run over the conditions of the experimental range to determine predicted ignition delay times. The results from the mechanism were then compared with the correlation. Figures 10 and 11 show excellent agreement between the predicted results and the correlation for the same range of temperatures, pressures, and equivalence ratios.

In a similar fashion, a low-temperature correlation was developed for temperatures less than 1175 K,

$$\tau_{\text{ign}} = 1.335 \times 10^{-7}[\text{fuel}]^{-0.343}[\text{air}]^{-0.660}\exp\left(\frac{28.0}{RT}\right) \qquad (3)$$

Here, a pressure dependence of $P^{-1.003}$ was seen. Once again, good agreement, $R^2=0.96$, is seen between the correlation, experimental data, and mechanism predictions, as shown in Fig. 11.

The activation energy, E, for the high-temperature correlation (40.1 kcal/mol) is larger than that of the lower-temperature correlation (28.0 kcal/mol). This difference corresponds to a steeper slope when plotted against an inverse temperature, as seen in Figs. 10 and 11.

To gain further insight to the chemical processes occurring during ignition, a sensitivity analysis was performed. A range of stoichiometries from lean to rich for 50/50 *n*-/isobutane mixtures was investigated in the sensitivity study. Within the mixtures, high (1400 K) and low (1050 K) temperatures were chosen as well as high (18.6 atm) and low (1.8 atm) pressures. Using CHEMKIN [33], a sensitivity analysis was performed on the species OH*. Although this is not the same as performing a direct ignition-delay sensitivity, it is qualitatively similar since there is a sudden buildup of the radical OH* at ignition and because OH* chemiluminescence is a marker of ignition in the experiments. The majority of the key reactions that mostly affect ignition will show up in the excited hydroxyl radical sensitivity. It should be noted that reactions that have a positive or increasing effect on OH*, which is a highly reactive species, lead to decreasing ignition time, while reactions that have a negative or decreasing effect on OH* will increase ignition time.

Figures 12 and 13 show normalized sensitivities for the top reactions at a given condition versus time. Figure 12 provides the low-pressure, low-temperature case, while Fig. 13 shows the high-pressure, low-temperature results, both for fuel lean conditions. The OH* mole fraction is also shown on the plot and used to determine ignition. At the time of ignition, the most important reactions are listed. The reaction numbering scheme used in this paper follows that used in the C4 mechanism.

The OH* sensitivity analysis for the fuel lean cases revealed that the top reactions for all cases are well known reactions from the methane and hydrogen mechanisms. Under most conditions, the chain branching reaction R1 ($H+O_2=OH+O$), which helps to speed up ignition, is the most important reaction. At low pressures (both at high and low temperatures), the most influential reactions in speeding up ignition time other than R1 were R109,

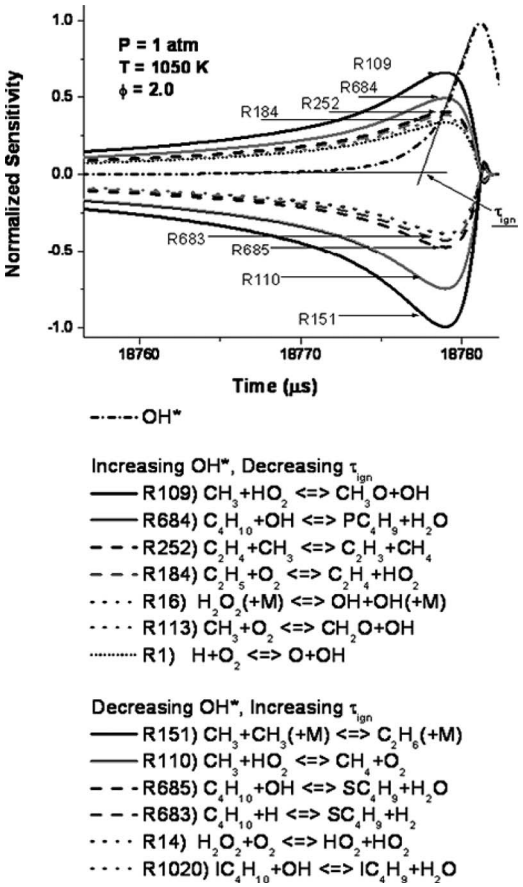

Fig. 14 Sensitivity analysis results from OH* show the most important reactions as a function of time during ignition. Sensitivity results show that the key reactions for fuel rich conditions are different from those reactions for fuel lean conditions at low pressure (1 atm) and low temperature (1050 K).

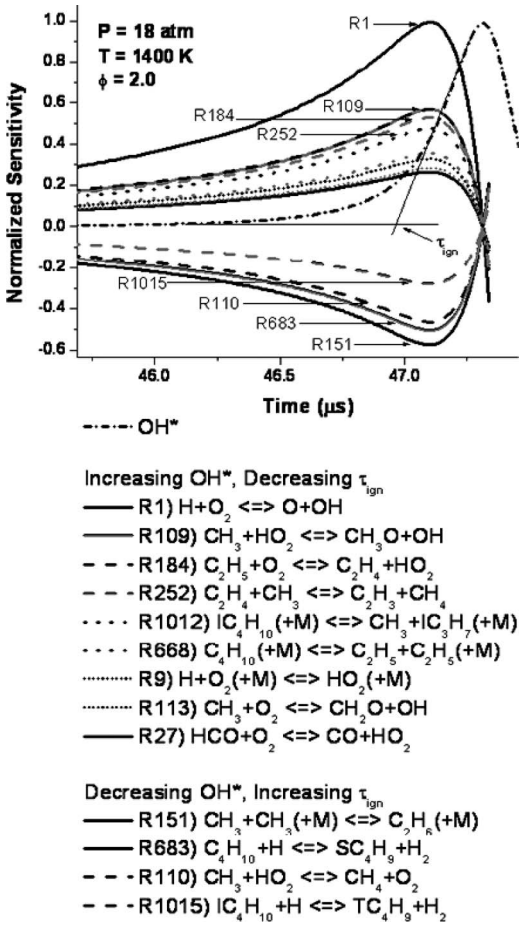

Fig. 15 Sensitivity analysis results from OH* show the most important reactions as a function of time during ignition. Sensitivity analysis results show that the important reactions for fuel rich conditions are different from those reactions for fuel lean conditions at high pressure (18 atm) and high temperature (1400 K).

$$CH_3 + HO_2 = CH_3O + OH$$

and R113,

$$CH_3 + O_2 = CH_2O + OH$$

At high pressures and low temperatures (Fig. 13), R1, while still influential, is not the most important reaction in accelerating ignition. Of more importance at these conditions is reaction 16, the hydrogen peroxide decomposition reaction that forms two of the highly reactive radical OH,

$$H_2O_2 + M = OH + OH + M$$

When looking at high pressures and low temperatures, peroxide reactions become most important, as expected.

Interestingly, the only C4 reactions that show up as being important for lean ignition at the conditions of interest herein are the hydrogen abstraction reactions of the butanes with OH at the lower pressures (R684, R685, and R1020 in Fig. 12) and with HO_2 at the higher pressures (R689, R1023, and R1024 in Fig. 13). Isobutane pyrolysis also has some importance at the lower pressure (R1012, Fig. 12).

As previously mentioned, the composition of the fuel blend has an increasingly greater effect on the ignition time at fuel rich conditions than at fuel lean conditions, as seen in Figs. 9(*a*)–9(*d*). A sensitivity analysis on OH* at fuel rich conditions (ϕ=2.0) confirms that the key reactions vary between fuel lean and fuel rich conditions. Figure 14 provides the low-pressure, low-temperature case, while Fig. 15 shows the high-pressure, high-temperature results, both for fuel rich conditions. Figure 14 shows that the most important reactions in speeding up ignition at low pressures and low temperatures are different from those of the fuel lean case (Fig. 12). The oxygen-containing, chain branching reaction, R1, is no longer the most important reaction. Two new reactions show up as being important at these conditions, R252,

$$C_2H_4 + CH_3 = C_2H_3 + CH_4$$

and R184,

$$C_2H_5 + O_2 = C_2H_4 + HO_2$$

These hydrocarbon reactions become more important under fuel rich conditions.

The examination of sensitivity analysis results for fuel rich conditions at high pressure (18 atm) and high temperature (1400 K), as seen in Fig. 15, reveals that some of the most influential reactions on ignition time are different from the reactions that were most important at fuel lean conditions. For high pressures and high temperatures, the two most important reactions for decreasing ignition time, R1 and R109, are the most important reactions for both fuel lean and rich conditions. However, the next two most important reactions are different. At fuel rich conditions, the hydrocarbon reactions R184 and R252 prove to be important. Additionally, the butane decomposition reaction R668 becomes influential in accelerating ignition,

$$C_4H_{10}(+M) = C_2H_5 + C_2H_5(+M)$$

While many of the same reactions that increase ignition time show up for both fuel lean and fuel rich conditions, the influence of the most significant reactions changes.

6 Conclusion

Shock-tube experiments have been performed over a wide range of conditions to validate the chemical kinetics mechanism for a blend of 50/50 *n*-/isobutane in air at pressures up to approximately 20 atm. This study marks the first of its kind to perform such an extensive investigation into this isomer fuel blend. A very good agreement has been demonstrated between the chemical kinetics model developed herein and the data. Additionally, useful correlations were developed to gain insight on the fundamental behavior of the system including important physical relationships such as the effect of stoichiometry on ignition times for different fuel blends and the pressure dependence of the ignition delay time. At lean conditions, the butane type has little effect on ignition time, whereas at stoichiometric and rich conditions, differences between *n*- and isobutane become apparent.

Acknowledgment

This work was supported primarily by Rolls-Royce Canada. Additional support came from the National Science Foundation (Grant No. CBET-0832561) and from The Aerospace Corporation.

References

[1] Richards, G. A., McMillian, M. M., Gemmen, R. S., Rogers, W. A., and Cully, S. R., 2001, "Issues for Low-Emission, Fuel Flexible Power Systems," Prog. Energy Combust. Sci., **27**, pp. 141–169.

[2] Lieuwen, T., McDonell, V., Petersen, E., and Santavicca, D., 2008, "Fuel Flexibility Influences on Premixed Combustor Blowout, Flashback, Autoignition and Stability," ASME J. Eng. Gas Turbines Power, **130**, p. 011506.

[3] Von Richer, V., 1947, *Chemistry of the Carbon Compounds; Or, Organic Chemistry*, Blakiston, New York, p. 74.

[4] Ogura, T., Nagumo, Y., Miyoshi, A., and Koshi, M., 2007, "Chemical Kinetic Mechanism for High Temperature Oxidation of Butane Isomers," Energy Fuels, **21**, pp. 130–135.

[5] Griffiths, J. F., Halford-Maw, P. A., and Rose, D. J., 1993, "Fundamental Features of Hydrocarbon Autoignition in a Rapid Compression Machine," Combust. Flame, **95**, pp. 291–306.

[6] Minetti, R., Ribaucour, M., Carlier, M., Fittschen, C., and Sochet, L. R., 1994, "Experimental and Modeling Study of Oxidation and Autoignition of Butane at High Pressure," Combust. Flame, **96**, pp. 201–211.

[7] Pitz, W. J., and Westbrook, C. K., 1986, "Chemical Kinetics of the High Pressure Oxidation of *n*-Butane and Its Relation to Engine Knock," Combust. Flame, **63**, pp. 113–133.

[8] Fotache, C. G., Wang, H., and Law, C. K., 1999, "Ignition of Ethane, Propane, and Butane in Counter Flow Jets of Cold Fuel Versus Hot Air Under Variable Pressures," Combust. Flame, **117**, pp. 777–794.

[9] Chandraratna, M. R., and Griffiths, J. F., 1994, "Pressure and Concentration Dependence of the Autoignition Temperature for Normal Butane+Air Mixtures in a Closed Vessel," Combust. Flame, **99**, pp. 626–634.

[10] Kojima, S., 1994, "Detailed Modeling of *n*-Butane Autoignition Chemistry," Combust. Flame, **99**, pp. 87–136.

[11] Smith, J. R., Green, R. M., Westbrook, C. K., and Pitz, W. J., 1984, "Experimental and Modeling Study of Engine Knock," 20th International Symposium on Combustion, The Combustion Institute, Pittsburgh, p. 91.

[12] Proudler, V. K., Cederbalk, P., Horowitz, A., Hughes, K. J., and Pilling, M. J., 1991, "Oscillatory Ignitions and Cool Flames in the Oxidation of Butane in a Jet-Stirred Reactor," Philos. Trans. R. Soc. London, Ser. A, **337**(1646), pp. 211–221.

[13] Yudai, Y., and Norimasa, I., 2003, "Numerical Analysis of Autoignition and Combustion of *n*-Butane and Air Mixtures in Homogeneous-Charge Compression-Ignition Engine Using Elementary Reactions," JSME Int. J., Ser. B, **46**, pp. 52–59.

[14] Burcat, A., Scheller, K., and Lifshitz, A., 1971, "Shock-Tube Investigation of Comparative Ignition Delay Times for C1-C5 Alkanes," Combust. Flame, **16**, pp. 29–33.

[15] Buda, F., Bounaceur, R., Warth, V., Glaude, P. A., Fournet, R., and Battin-Leclerc, F., 2005, "Progress Toward a Unified Detailed Kinetic Model for the Autoignition of Alkanes From C4 to C10 Between 600 and 1200 K," Combust. Flame, **142**, pp. 170–186.

[16] Wilk, R. D., Pitz, W. J., Westbrook, C. K., Addagarla, S., Miller, D. L., Cernansky, N. P., and Green, R. M., 1990, "Combustion of *n*-Butane and Iso-Butane in an Internal Combustion Engine: A Comparison of Experimental and Modeling Results," Sym. (Int.) Combust., [Proc.], **23**, pp. 1047–1056.

[17] Kojima, S., and Suzuoki, T., 1993, "Autoignition-Delay Measurement Over Lean to Rich Mixtures of *n*-Butane/Air Under Swirl Conditions," Combust. Flame, **92**, pp. 254–265.

[18] Griffiths, J. F., and Nimmo, W., 1985, "Spontaneous Ignition and Engine Knock Under Rapid Compression," Combust. Flame, **60**, pp. 215–218.

[19] Pekalski, A. A., Terli, E., Zevenbergen, J. F., Lemkowitz, S. M., and Pasman, H. J., 2005, "Influence of the Ignition Delay Time on the Explosion Parameters of Hydrocarbon-Air-Oxygen Mixtures at Elevated Pressure and Temperature," Proc. Combust. Inst., **30**, pp. 1933–1969.

[20] Marengo, S., Comotti, P., and Galli, G., 2003, "New Insight Into the Role of Gas Phase Reaction in the Partial Oxidation of Butane," Catal. Today, **81**, pp. 205–213.

[21] Morley, C., 1987, "A Fundamentally Based Correlation Between Alkane Structure and Octane Number," Combust. Sci. Technol., **55**, pp. 115–123.

[22] Lund, C. M., and Chase, L., 1995, "HCT-A General Computer Program for Calculating Time-Dependent Phenomena Involving One-Dimensional Hydrodynamics, Transport, and Detailed Chemical Kinetics," Lawrence Livermore National Laboratory, Report No. UCRL-52504.

[23] Healy, D., Curran, H. J., Dooley, S., Simmie, J. M., Kalitan, D. M., Petersen, E. L., and Bourque, G., 2008, "Methane/Propane Mixture Oxidation at High Pressures and at High, Intermediate and Low Temperatures," Combust. Flame, **155**, pp. 451–461.

[24] Healy, D., Curran, H. J., Simmie, J. M., Kalitan, D. M., Zinner, C. M., Barrett, A. B., Petersen, E. L., and Bourque, G., 2008, "Methane/Ethane/Propane Mixture Oxidation at High Pressures and at High, Intermediate and Low Temperatures," Combust. Flame, **155**, pp. 441–448.

[25] Kee, R. J., Rupley, F. M., and Miller, J. A., 1987, Sandia National Laboratories, Report No. SAND87-8217.

[26] Ritter, E. R., and Bozzelli, J. W., 1991, "THERM: Thermodynamic Property Estimation for Gas Phase Radicals and Molecules," Int. J. Chem. Kinet., **23**, pp. 767–778.

[27] Lay, T., Bozzelli, J. W., Dean, A. M., and Ritter, E. R., 1995, "Hydrogen Atom Bond Increments for Calculation of Thermodynamic Properties of Hydrocarbon Radical Species," J. Phys. Chem., **99**, pp. 14514–14527.

[28] Sumathi, R., and Green, W. H., Jr., 2003, "Oxygenate, Oxyalkyl, and Alkoxycarbonyl Thermochemistry and Rates for Hydrogen Abstraction From Oxygenates," Phys. Chem. Chem. Phys., **5**, pp. 3402–3417.

[29] Healy, D., Curran, H. J., Petersen, E. L., Aul, C. J., Zinner, C. M., and Bourque, G., 2009, "*n*-Butane: Ignition Delay Measurements at High Pressure and Detailed Chemical Kinetic Simulations," Combust. Flame, submitted.

[30] Petersen, E. L., Rickard, M. J. A., Crofton, M. D., Abbey, E. D., Traum, M. J., and Kalitan, D. M., 2005, "A Facility for Gas- and Condensed-Phase Measurements Behind Shock Waves," Meas. Sci. Technol., **16**, pp. 1716–1729.

[31] Aul, C. J., de Vries, J., and Petersen, E. L., 2007, "New Shock-Tube Facility for Studies in Chemical Kinetics at Engine Conditions," Eastern States Fall Technical Meeting of the Combustion Institute, Charlottesville, VA, Oct. 21–24.

[32] Petersen, E., Lamnaouer, M., de Vries, J., Curran, H., Simmie, J., Fikri, M., Schulz, C., and Bourque, G., 2007, "Discrepancies Between Shock Tube and Rapid Compression Machine Ignition at Low Temperatures and High Pressures," 26th International Symposium on Shock Waves, Göttingen, Germany, Paper No. 0911.

[33] Kee, R. J., Rupley, F. M., Miller, J. A., Coltrin, M. E., Grcar, J. F., Meeks, E., Moffat, H. K., Lutz, A. E., Dixon-Lewis, G., Smooke, M. D., Warnatz, J., Evans, G. H., Larson, R. S., Mitchell, R. E., Petzold, L. R., Reynolds, W. C., Caracotsios, M., Stewart, W. E., Glarborg, P., Wang, C., and Adigun, O., 2000, CHEMKIN Collection, Release 3.6, Reaction Design, Inc., San Diego, CA.

Experimental Analysis of the Combustion Behavior of a Gas Turbine Burner by Laser Measurement Techniques

Holger Ax[1]
e-mail: holger.ax@dlr.de

Ulrich Stopper

Wolfgang Meier

Manfred Aigner

Institute of Combustion Technology,
German Aerospace Center (DLR),
Pfaffenwaldring 38-40,
D-70563 Stuttgart, Germany

Felix Güthe
Alstom Ltd.,
CH-5401 Baden, Switzerland

Experimental results from optical and laser spectroscopic measurements on a scaled industrial gas turbine burner at elevated pressure are presented. Planar laser induced fluorescence on the OH radical and OH chemiluminescence imaging were applied to natural gas/air flames for a qualitative analysis of the position and shape of the flame brush, the flame front and the stabilization mechanism. The results exhibit two different ways of flame stabilization, a conical more stable flame and a pulsating opened flame. For quantitative results, one-dimensional laser Raman scattering was applied to these flames and evaluated on an average and single-shot basis in order to simultaneously determine the major species concentrations, the mixture fraction, and the temperature. The mixing of fuel and air, as well as the reaction progress, could thus be spatially and temporally resolved, showing differently strong variations depending on the flame stabilization mode and the location in the flame.* [DOI: 10.1115/1.3205033]

Keywords: laser diagnostics, Raman scattering, gas turbine combustor, flame stabilization

1 Introduction

The lean premixed combustion concept is widely applied in stationary gas turbines (GTs) in order to achieve low NO_x levels. However, these flames are prone to combustion instabilities in the form of unsteady flame stabilization or thermoacoustic pulsations [1–5]. These phenomena arise from a complex interaction between the turbulent flow field, the flame reactions, and the combustor geometry. Furthermore, effects of unmixedness have a significant influence on the flame stabilization and emissions [6,7]. Different approaches have been reported to reduce or even to eliminate the unsteady effects, e.g., active or passive control mechanisms [8–13] or fuel staging [14]. However, a fundamental understanding of the underlying mechanisms has not been reached so far, and further experimental and numerical studies are necessary before the potential of lean premixed combustion can be fully exploited.

In recent years, detailed laser diagnostic studies in GT-relevant combustors have contributed significantly to a better understanding of processes such as flame stabilization, combustion instabilities, pollutant formation and finite-rate chemistry effects. Frequently used measuring techniques were particle image velocimetry (PIV) or laser Doppler velocimetry (LDV) for the flow field; laser induced fluorescence (LIF) for flame radicals, tracers, pollutants, or temperature; coherent anti-Stokes Raman scattering (CARS) for temperature; and laser Raman scattering for species concentrations. Overviews and detailed descriptions of the different laser measurement techniques can be found in Refs. [15–18]. In some research groups, high-pressure test rigs have been equipped with optical access in order to apply these techniques to GT combustion processes under realistic conditions, i.e., preheated air, elevated pressure, high thermal loads, high turbulence levels, and relevant combustor geometries, see for example Refs. [19–28]. Here, challenges arise from the limited optical access and especially from window contamination by the high thermal loads or particles in the flow [29]. Particularly for single-shot one-dimensional (1D) Raman measurements, which require high laser pulse energies, a high laser fluence can lead to window damage or optical breakdown in the focal region.

In the investigations presented here, a scaled industrial GT-burner was installed in the high-pressure test rig at the Institute of Combustion Technology of the German Aerospace Center (DLR) in Stuttgart and investigated using different laser measuring techniques in combination with chemiluminescence imaging, exhaust gas analysis, and dynamic pressure recording. The combustor was operated with natural gas (NG) and preheated air ($T=400\,^{\circ}C$), and the flame settings were varied in a wide range of thermal power, equivalence ratio, and fuel staging. Main goals of the study were a detailed characterization of the combustion process, the influence of fuel staging on the flame stabilization, the quantification of the degree of mixing, the identification of effects of turbulence-chemistry interactions, and the investigation of transient flame behavior. Planar laser induced fluorescence (PLIF) of OH and OH* chemiluminescence imaging were applied to determine the flame structures and the stabilization region. Further, 1D-laser Raman scattering was used to quantitatively measure the major species concentrations (N_2, O_2, H_2O, C_xH_y, CO_2, CO, and H_2) and the temperature. By this technique, the local mixture fraction and the reaction progress could be determined, revealing effects of unmixedness and turbulence-chemistry interactions.

The focus of this paper lies on the comparison of two different flames in terms of their shape and stabilization on the burner. Detailed quantitative results from single-shot 1D-Raman measurements on a scaled industrial GT-burner under realistic conditions are presented for the first time to our knowledge.

2 Experimental Setup

2.1 Burner and Test Rig. The experiments were conducted on a geometrically downscaled version of a gas turbine burner

[1]Corresponding author.

Contributed by the International Gas Turbine Institute of ASME for publication in the JOURNAL OF ENGINEERING FOR GAS TURBINES AND POWER. Manuscript received April 8, 2009; final manuscript received May 14, 2009; published online March 5, 2010. Review conducted by Dilip R. Ballal. Paper presented at the ASME Gas Turbine Technical Congress and Exposition, Orlando, FL, June 8–12, 2009.

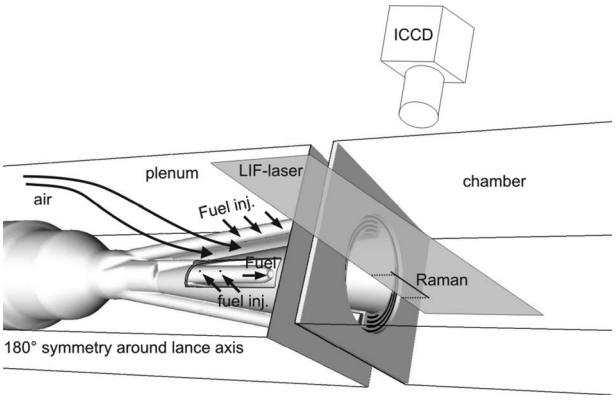

Fig. 1 Schematic drawing of the burner and the measurement positions of the different laser diagnostic techniques

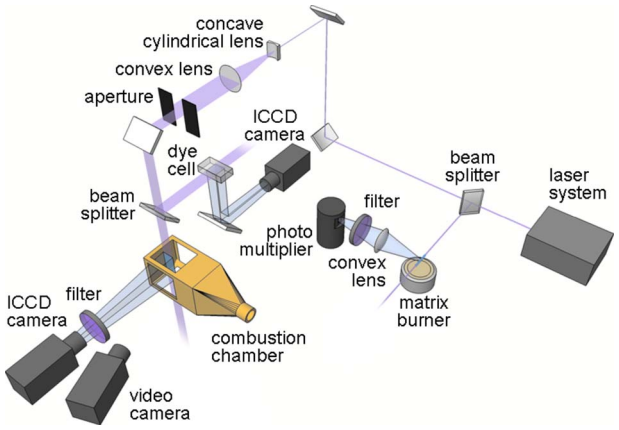

Fig. 2 Schematic drawing of the experimental setup for OH-PLIF measurements

(Alstom EV burner) [30,31]. The burner has already been the object of various experimental and numerical investigations with respect to the flow field, the flame behavior, emissions, the flame stability, and the mechanism of flame stabilization, see Refs. [14,32]. A schematic drawing of the burner is shown in Fig. 1. The positions of the laser sheet for LIF measurements and the radial profiles where the Raman measurements were taken are also indicated. It should be noted that the laser beam for the 1D-Raman measurements was directed orthogonally to the LIF laser sheet; the line in Fig. 1 refers to the middle of the imaged range, which intersects the LIF sheet.

The design of this swirl-stabilized burner is based on two halves of a cone, which are radially shifted apart. This generates two tangential slots of constant width, through which the combustion air enters the cone. By this concept, a tangential velocity component is induced in the flow, with an increasing swirl strength downstream and which results in a vortex breakdown close to the burner exit ($D=70$ mm). The fuel is injected through small holes along the tangential slits and mixes with the entering air. Additional fuel can be injected through the tip of a pilot lance, which protrudes on the axis 54 mm upstream from the burner mouth. The two fuel flows (tangential slots and pilot lance) can be controlled separately for different fuel staged operation conditions. The staging ratio is defined as the ratio of the fuel mass flow through the lance to the total fuel mass flow. For the present study, the EV type burner was operated and investigated in the high-pressure combustion test facility HBK-S (Hochdruckbrennkammerprufstand-Stuttgart) at the DLR Stuttgart. The test rig and the specially designed rectangular combustion chamber (99×129 mm^2) were both equipped with large quartz glass windows to provide full optical access on all four sides. The outer windows in the pressure vessel were exposed to elevated pressure but only at intermediate to low temperatures, while the inner ones were directly exposed to the flame but only moderate pressure variations. The inner windows were installed in a double-glazed configuration with cooling air flowing between the glass plates in order to reduce the thermal load of the windows. So, there were three windows in total both on the laser entrance and the exit side, as well as on the two sides in line of the detection. The burner plate was cooled by air streaming through small holes into the combustion chamber.

2.2 Flames. The burner was operated with natural gas/air flames with a thermal power up to 370 kW at different values of air equivalence ratio λ and staging ratios. The NG was taken from the public power supply. The composition of the NG hardly varied during the period of the measurement campaign with a mean composition of 94.14% CH_4, 2.955% C_2H_6, 0.557% C_3H_8, 0.064% C_4H_{10}, 0.07% isobutane, 2.124% N_2, and 0.09% CO_2. The air preheat temperature was kept constant to 673 K, the pressure inside the combustion chamber was 3 bars. It has been observed in the flow field that the burner can exhibit two different ways of flame stabilization, depending on the several conditions, as it has been reported from several investigations, both experimental and theoretical [14,32,33]. One is a conical and more stable flame with respect to pulsations, which is anchored inside the burner cone. The other one is stabilized just downstream the burner exit. In this case, the flame is more opened and the outer recirculation zone (ORZ) is more pronounced compared with the cone stabilized flame. The opened mode has better mixing leading to lower NO_x, but it is also more prone to pulsations. Generally speaking, the transition from the cone stabilized to the opened flame takes place with increasing λ (decreasing reactivity) with a relatively small range in which the flame alternates between the two states, or with a reduced staging ratio. The transition to the opened flame is accompanied by a reduction of NO_x emissions and a pressure drop across the burner, both in the case of increasing λ and the case of a reduced staging ratio. In this study, the results of 1D-Raman measurements of two selected flames are presented, one of each way of stabilization, and compared with the according LIF and OH^* chemiluminescence measurements. The two flames are referred to as flames A and B in this paper. Flame A is a cone stabilized flame with a thermal power of 345 kW, a staging ratio α_A of 0.23, and $\lambda_A \approx 1.3$. Flame B is an opened flame with 317 kW, $\alpha_B=0.17$, and $\lambda_B \approx 1.7$. The corresponding mixture fractions f are $f_A=0.044$ and $f_B=0.034$ for flames A and B, respectively.

2.3 PLIF/OH^* Chemiluminescence Imaging. For the OH-PLIF measurements a flashlamp pumped frequency doubled Nd:YAG laser (Quanta Ray, DCR-2) was used to pump a frequency doubled tunable dye laser (Lumonics, HD-500) at 10 Hz. The UV beam (pulse duration of 8 ns and line width of 0.4 cm^{-1}) had a pulse energy of approximately 2.5 mJ at the exit of the laser and was tuned to the $Q_1(8)$ transition of OH at approximately 283 nm in the $\nu''=0\rightarrow\nu'=1$ vibrational band of the A $^2\Sigma^+$-X$^2\Pi$ system. The population of the laser-coupled ground state of the selected line varied by approximately 9% in the temperature range of interest (1400–2200 K). Subsequent OH fluorescence in the $\nu'=1\rightarrow\nu''=1$ and $\nu'=0\rightarrow\nu''=0$ bands near 310 nm was detected through an interference filter in the wavelength region 295–340 nm. This enabled suppression of light scattered from the incident laser beam and background radiations. The output beam from the dye laser was expanded into a vertical sheet by means of cylindrical lenses, as shown in Fig. 2. The laser sheet inside the combustor was 60 mm in height and approximately 400 μm in thickness. By means of a beam splitter, a small portion of the incoming laser beam was directed into a CH_4/air reference flame on a matrix burner, operated under laminar conditions. The LIF produced

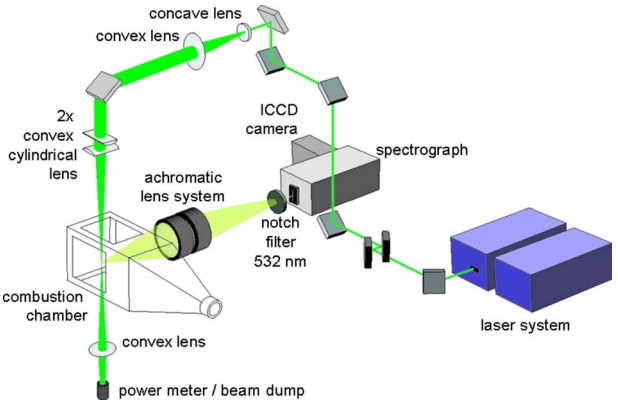

Fig. 3 Schematic drawing of the setup for 1D-Raman experiments

by that flame was used for the online monitoring of the excitation line wavelength.

The OH-PLIF detection system consisted of an image-intensified charge coupled device (ICCD) camera (Roper Scientific, 512×512 pixels) with achromatic UV lens (Halle, $f/2$, $f=100$ mm). Part of incoming laser sheet was deflected into a quartz cell filled with fluorescent dye solution by means of a beam splitter. The dye cell fluorescence profile was simultaneously imaged using another ICCD camera (Roper Scientific, 512×512 pixels) equipped with a Nikon lens ($f/4.5$, $f=105$ mm). This dye cell profile was used for correcting the laser sheet profile inhomogeneities. The image intensifier was set to an exposure time of 400 ns for both the OH-PLIF and the dye cell fluorescence camera. In this experiment, an arrangement for the correction of absorption [34,35] was not applied. The same detection system along with the filter combination was used for the OH^* chemiluminescence measurements. The exposure time for the image intensifier was set to 40 μs to capture the integrated (along the line of sight) spontaneous emission from OH in the electronically excited state (OH^*). The timing between the laser pulses and the camera gate openings were synchronized by means of a pulse delay generator (DG535, SRS Inc., Sunnyvale, CA).

2.4 1D-Laser Raman Scattering. Single-shot vibrational Raman scattering was applied to simultaneously determine the major species concentrations (N_2, O_2, H_2O, NG, CO_2, CO, and H_2) along a line 7 mm in length. The NG was treated as one species in the detection and evaluation procedure. The various hydrocarbons within the NG all contribute to the Raman-active C–H stretch vibration, which was detected at around 630 nm. The inaccuracy associated with this simplification is relatively small because the maximum NG mole fractions measured in the investigated premixed flames were approximately 0.1. Thus, the mole fractions of the minor constituents of the NG are below 0.01. The main components of the experiment were a laser system consisting of five Nd:YAG lasers, a pulse stretcher, beam forming optics, the detection optics, a spectrograph, and an ICCD camera, as shown in Fig. 3. The Nd:YAG lasers provided five temporally separated pulses at a wavelength of $\lambda=532$ nm of 7 ns duration, each at a repetition rate of 10 Hz, which were combined to one beam [36]. In order to reduce the intensity at the windows and to avoid optical breakdown in the focal region the pulses were elongated by a pulse stretcher, and furthermore the laser beams were focused by a combination of two perpendicularly arranged cylindrical lenses ($f=300$ mm) to generate a "blurred" focus of an average diameter of 0.5 mm [29]. In this way, a total pulse energy of 0.8 J could be irradiated into the combustor. The pulse stretcher consisted of two beam splitters and six mirrors, which divided each pulse into several individual pulses, which were recombined again after having traveled different path lengths, generating a total pulse duration of about 350 ns [37]. The Raman scattered light was collected at 90 deg by a custom designed achromatic lens system, with an aperture of 150 mm configured for line imaging of Raman scattering at 532 nm [36] and relayed onto the entrance slit of the spectrograph (SpectraPro 300i, Acton Research, $f=300$ mm, 490 lines/mm, $f_{\#}=4$, and dispersion ~6 nm/mm). For the rejection of elastically scattered light, a holographic notch filter was placed in front of the entrance slit. A slit width of 1 mm, a slit height of 14 mm, and a magnification of the detection optics of 2 resulted in an imaged probe volume of 7 mm in direction of the laser beam and 0.5 mm in diameter. After spectral separation, the Raman bands from the different major species were detected by an intensified CCD camera (1340×1300 pixels) along the line of 7 mm. The images were binned on chip to superpixels (268 in the direction of the spectral separation and 28 in spatial direction). This yielded a partition of 28 measurement volumes along the laser line with 0.25 mm length. The laser was introduced from the top of the combustor, and the focus was always kept in the middle of the combustion chamber in vertical direction. The measuring location within the combustion chamber was changed in the direction of the detection line by translating the laser beam optics and detection optics simultaneously via computer controlled translation stages. Due to restrictions of the optical access, the measuring location closest to the burner mouth was 22 mm. For the measurements presented in this paper, 500 single shots were recorded per location.

One of the main challenges in performing the Raman measurements was the degradation of the combustor windows, which were directly exposed to the flame. At high flame temperatures, quartz begins to soften and its surface becomes rough and increasingly opaque leading to decreasing transmittance and, in the worst case, to window damage by the laser beam. The degradation was not uniformly distributed over the window and most severe where the flame hit the quartz surface. As a result, the effective laser pulse energy at the measuring location could not always be determined accurately. However, this quantity is usually needed to ratio the Raman signals in order to determine the species concentrations quantitatively. A similar uncertainty arose from the unknown (time and position dependent) transmission of the window on the detection side. Therefore, it was necessary to find an appropriate method to compensate for the lacking information.

2.5 Raman Data Evaluation. In order to deduce the species number densities from the Raman signals, calibration measurements were performed. Temperature dependent calibration and crosstalk factors were determined in laminar flat flames (1150–2200 K) with known temperature and gas compositions operated at atmospheric conditions in the GT combustion chamber. The coefficients for the low temperature range ($T=300-1000$ K) were determined in cold and electrically heated gas flows. The temperature is deduced from the total number density using the ideal gas law and the measured pressure in the combustion chamber. The measured signals from the GT flames were evaluated using these calibration curves. Because the signals have to be weighted by the laser pulse energy (on a single-shot basis), the uncertainty of the determination of the laser energy caused by degraded windows led to a significant uncertainty in the determination of the species number densities. Although the relative species composition was hardly affected by this uncertainty, the total number density and thus the temperature are. Therefore, the following procedure was applied to determine the temperature. All C and H atoms in the combustion chamber stem from the fuel and all N and O atoms from the air supply (except for a negligible contribution from the natural gas). During all processes in the combustion chamber (transport and chemical reactions) the atomic ratios C/H and N/O remain unaltered in every volume element, i.e., 0.26 for C/H and 3.73 for N/O. A correct Raman measurement must therefore yield these numbers. On the other hand, the Raman calibration curves for the different molecular

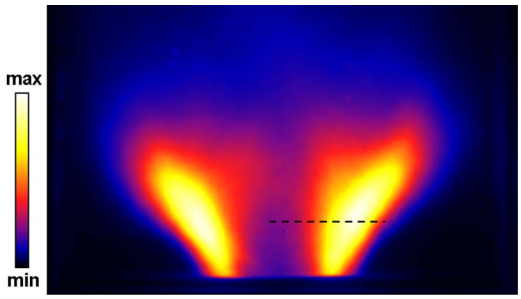

Fig. 4 Mean distribution of the OH* chemiluminescence of flame A (averaged over 200 single shots). The dotted line indicates the position of the radial profile that was measured by 1D-Raman scattering.

species exhibit different temperature dependencies. Fortuitously, the temperature dependencies vary in a way that the C/H and N/O ratios deduced from the measurements are a unique and noticeable function of T. Taking the relative Raman signal intensities from each single-shot measurement, it turned out that only for one temperature value the ratios C/H and N/O assumed the expected values. The Raman-spectrum was therefore scaled to match the optimum value of both the C/H and the N/O ratio. The species number density and the temperature were then calculated based on the scaled spectrum.

The precision of the Raman results can be estimated by the single-shot evaluation and shot noise analysis of measurements on the stable calibration flames. The relative standard deviations in the postflame region of a flat CH_4/air flame at atmospheric pressure are typically around 4% for N_2, 13% for H_2O, 20% for CO_2, and 7% for the temperature and the mixture fraction. The absolute temperatures of the calibration flames were reproduced by an accuracy better than 5%. The flame temperatures had been determined beforehand using CARS with an accuracy of 3%. The temperature data for flat calibration flames obtained by CARS measurements have been published in Refs. [38,39]. As the Raman signals scale linearly with pressure, the signals from the GT flames (3 bars) are a factor of 3 higher than in the calibration flames. The precision should therefore be improved by a factor of $\sim\sqrt{3}$. However, systematic uncertainties due to shifts in alignment or signal correction might impair the accuracy.

3 Results

3.1 Cone Stabilized Flame A. The measurement results of the two different flames are presented one after another. First, the cone stabilized flame A is discussed. In Fig. 4 the mean OH* chemiluminescence of this flame is shown, averaged over 200 single shots. The electronically excited OH is formed by the flame reactions in the region of the highest heat release rates and is therefore a good marker for the position of the flame front. In all shown pictures, the flow is from the bottom up. One can clearly see that the flame brush has a conical shape and is mainly concentrated in a distinct layer in the outer region of the swirled flow exiting the burner. The combustion of the fresh gas already takes place inside the burner and just outside the burner exit. One should keep in mind, however, that the detected signal of the chemiluminescence is integrated over the whole flame in the line of sight and gives no information about the flame structure details with an appropriate spatial resolution. The slight asymmetry in the intensity distribution might partly be due to inhomogeneities in the transparency of the combustor windows. However, the combustor geometry is not axial symmetric, so that the observed asymmetry of the flame might be real.

The PLIF measurements on OH reveal the hot regions in the combustion chamber where the OH radical is present ($\geq$1400 K). The results of the PLIF measurements of flame A are

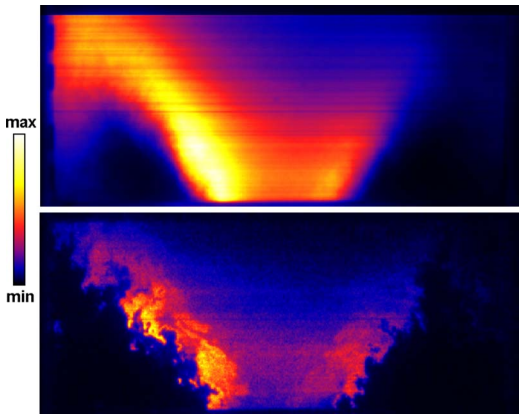

Fig. 5 OH-PLIF measurements of flame A. Top: mean OH distribution (averaged over 200 single shots). Bottom: single-shot OH-PLIF measurement.

shown in Fig. 5. On top, the mean OH distribution is shown, averaged over 200 single shots. The asymmetry is caused by absorption of the laser radiation by OH radicals and thus attenuation of the laser light sheet, which enters the combustion chamber from the left side. The hot inner recirculation zone (IRZ) reaches back into the burner, where it promotes the ignition of the fresh gas and stabilizes the flame. The bottom picture shows a single shot of the OH-PLIF measurements. Like the OH* chemiluminescence measurements, it also shows the conical shape of the flame and reveals a strongly wrinkled flame front due to the turbulence of the flow. Regions of high signal intensity (red and yellow) indicate the location of the flame front, where OH is formed in superequilibrium concentrations [40].

Such a qualitative analysis of this flame by OH-PLIF and OH* chemiluminescence has already been reported elsewhere [14]. The new component in the present study is the successful application of laser Raman scattering, which allows for a quantitative analysis with respect to the major species, the temperature, and the mixture fraction. The results of the evaluated mixture fractions f in flame A at different radial positions 22 mm downstream are shown in Fig. 6. The symbols represent the ensemble averaged values of the measuring volume in the plane of the PLIF laser sheet over 500 single shots. As expected for a technically premixed flame, the mixture fraction is not constant, however, the variation in the mean values is rather moderate over a large region. Close to the burner axis (-5 mm$\leq r \leq 5$ mm), the mixture fraction is slightly increased and asymmetric, which is presumably due to the asymmetry of the flow field, as the burner is not rotationally symmetric.

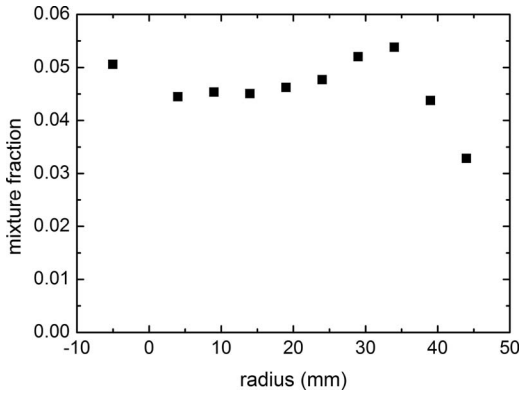

Fig. 6 Radial profile of the mean mixture fraction in flame A 22 mm downstream from the burner mouth; for comparison, the stoichiometric mixture fraction of the NG is 0.057

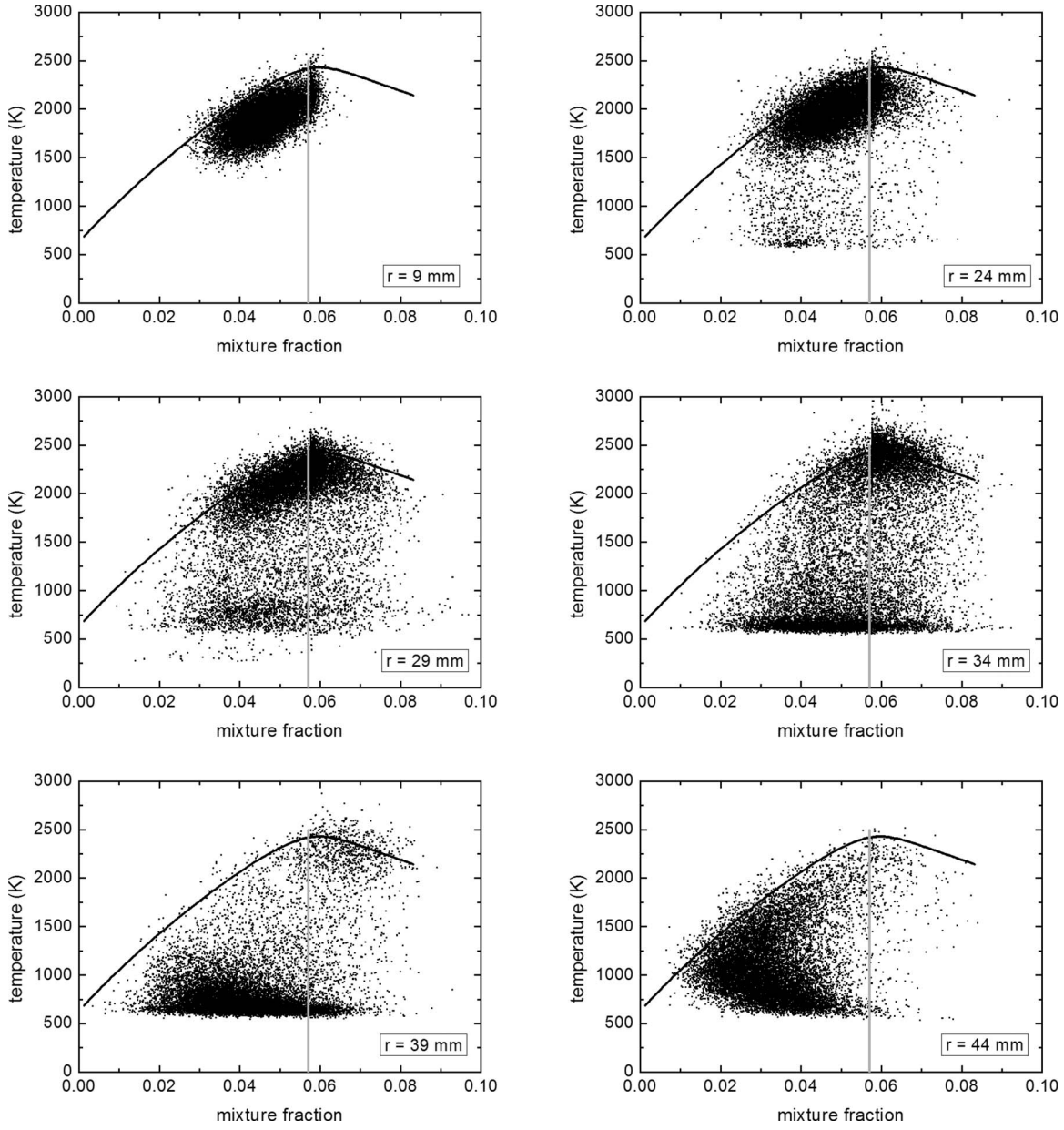

Fig. 7 Scatter plots of single-shot Raman measurements in flame A at different radial positions 22 mm downstream from the burner mouth. Adiabatic equilibrium (black) and stoichiometric mixture fraction (light gray) are indicated by lines.

From $r=5$ mm outwards, the mixture fraction remains almost constant until it starts to increase at a radius of $r=25$ mm. It reaches the maximum value at $r=34$ mm, which is also the region where the highest signal intensities can be found in the PLIF and OH^* chemiluminescence measurements at this distance from the burner mouth. Farther outwards the mixture fraction strongly decreases, which can be explained by the hot gas in the outer recirculation zone mixing with the cooling air for the burner plate, which streams into the combustion chamber through the burner plate. In Fig. 7 scatter plots are displayed showing the correlation between the temperature and mixture fraction at some of the prior shown radial positions at the same downstream location (22 mm). The data points represent the results of the single-shot measurement from all 28 measuring volumes along the laser line. In addition, the indicated black curve shows the correlation at adiabatic equilibrium conditions, which was calculated with GASEQ [41]. It is not expected that the investigated flame is in a state of adiabatic equilibrium, however, the curve helps to assess the thermochemical state of the flame. The light gray vertical line indicates the stoichiometric mixture fraction for the given NG composition. In general, the scatter plots reflect a significant variation in f, which changes with the radial position. For an industrial GT-burner, it is the first time that this variation could be determined quantitatively on a single-shot basis, i.e., without temporal or spatial averaging. The second general feature, which becomes immediately obvious from the scatter plots, is the significant variation in temperatures reflecting different states of reaction progress. In the following the different radial positions are discussed in more detail. At $r=9$ mm, the temperatures are high with little fluctuations and the samples are close to adiabatic equilibrium. This is typical for the IRZ, where the residence time was long enough for the gas to (almost) completely react before being transported back to the burner mouth. The small temperature depression compared with equilibrium might be due to strain effects, temperature loss by

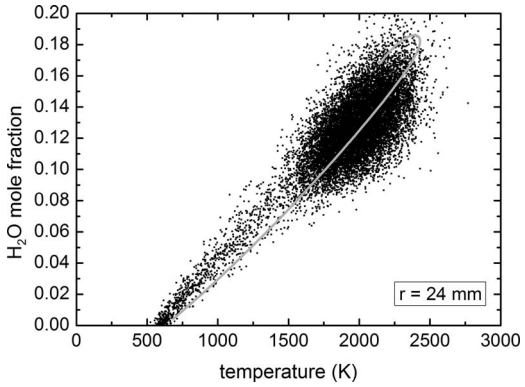

Fig. 8 Scatter plot of H_2O versus temperature in flame A at a radius of $r=24$ mm, 22 mm downstream from the burner mouth. The light gray line indicates the adiabatic equilibrium state.

radiation or contact to cold surfaces or also to measurement uncertainties. A detailed analysis of these effects would exceed the scope of this paper; however, the approach to such an analysis is, e.g., outlined in Ref. [42]. The further outwards ($r=24$ mm to $r=34$ mm) the more cold fresh gas is detected and the mean of the mixture fraction increases, as it was seen in Fig. 6. The local variation in the mixture fraction also increases, reaching from lean ($f\approx0.02$) to rich ($f\approx0.08$) mixtures due to a not perfect mixing of fuel and air. With increasing radius the number of samples with cold temperatures ($T\approx630$ K) increases. Although many of them have near-stoichiometric mixture fraction values, they have not reacted yet.

In addition, a large number of samples with intermediate temperatures is seen, which reflects a state of "partially reacted." They most likely represent mixtures of hot reacted gas from the recirculation zones with fresh cold gas from the burner, which have not reacted yet due to ignition delay [42]. Other reasons for the partially reacted state might be local flame extinction or that the flame front crossed the measurement volume. However, in any case, these samples reflect effects of finite-rate chemistry. At $r=39$ mm, most samples are in cold states with a smaller mean but still strongly varying mixture fraction.

The detected hot (burned) states have a higher mixture fraction compared with the cold states. This can be explained by the higher reactivity of richer mixtures. At $r=44$ mm the mixture is even leaner but hotter in the mean. The characteristics of the scatter plots from the different radial regions are closely related to the different flow regions. Close to the flame axis, in the IRZ, the gas is mainly reacted, as explained before. Close to the ORZ ($r\geq40$ mm), the gas is rather fuel lean and cold due to the influence of the cooling air from the burner plate. In the regions of the shear layers between the fresh gas injection and the IRZ or the ORZ, a large variation in mixing and reaction progress is present.

A representative scatter plot of the measured species concentrations is shown in Fig. 8 for H_2O in correlation with the temperature. One can see that the formation of water correlates well with the temperature, as expected, and that the results are in reasonable agreement with the equilibrium state calculation. The samples from the intermediate temperature range tend to exhibit lower temperatures as for the equilibrium. This might be due to heat loss or to effects of flame strain exerted by the high turbulence levels known from this kind of flames. The mole fractions from the other main species have also been evaluated but are not displayed and discussed here due to the limited space available.

3.2 Lifted Flame B. Flame B is a pulsating opened flame, which is stabilized farther downstream than flame A, just after the burner exit. The mean OH^* distribution is shown in Fig. 9, indicating the position of the flame brush. The images were taken with the same camera intensifier gain as for the flame A and were also averaged over 200 single shots.

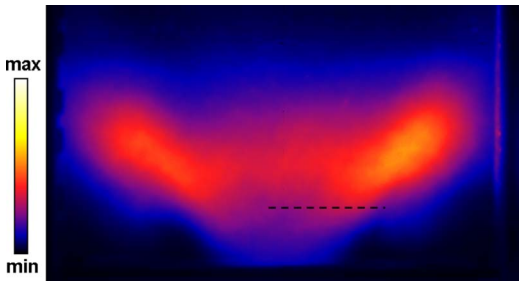

Fig. 9 Mean distribution of the OH^* chemiluminescence of flame B (averaged over 200 single shots). The dotted line indicates the position of the radial profile that was measured by 1D-Raman scattering.

In comparison to flame A, one can see that the flame zone is not so distinct and that the flame is more open and wider. The regions of the highest signal intensities lie further downstream and are less intense than in flame A.

The according OH-PLIF measurements of flame B are shown in Fig. 10, again, the mean OH distribution on top, averaged over 200 single shots, and a representative single-shot picture beneath. It is clearly visible in both images, that flame B stabilizes just outside the burner and that the ORZ contains more OH than in flame A. In the single-shot exposure it can be seen that the flame front is highly wrinkled and is also partially located in the ORZ, indicated by the spots of high signal intensities (red and white) due to the superequilibrium concentrations of the OH in the reaction zone. The contribution of the ORZ to the ignition and stabilization of the flame is therefore significantly higher than in flame A.

The radial profile of the mixture fraction f in flame B is shown in Fig. 11. As for flame A, the mean values of f are plotted against the radial position 22 mm downstream for the measuring volume in the plane of the laser sheet for the PLIF experiment. Around the burner axis (-5 mm$\leq r\leq5$ mm), the mixture fraction is relatively high, similar to flame A. The peak value, however, is hardly dislocated from the burner axis.

In the intermediate and outer radius range (from $r=10$ mm outwards), the values of f slowly increase up to the peak value at

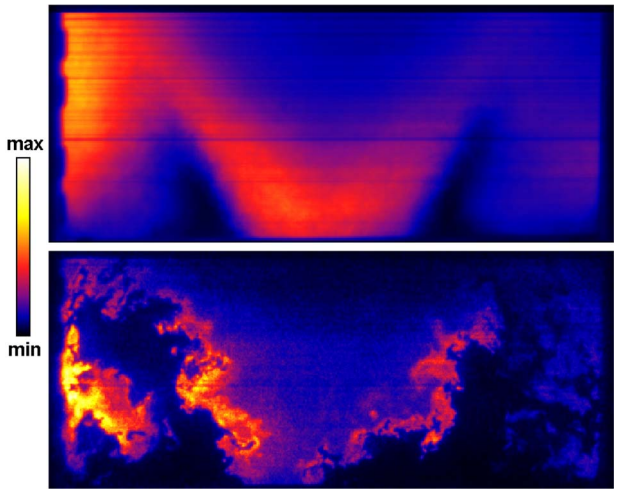

Fig. 10 OH-PLIF measurements of flame B. Top: mean OH distribution (averaged over 200 single shots). Bottom: single-shot OH-PLIF measurement.

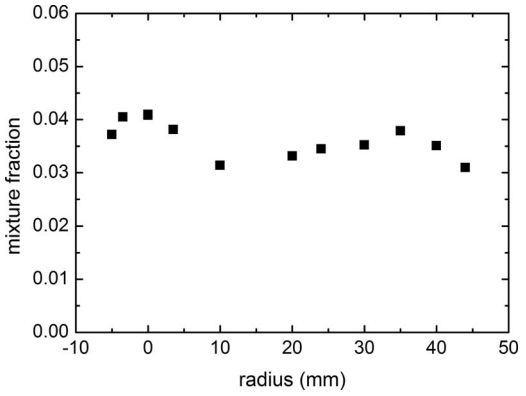

Fig. 11 Radial profile of mean mixture fraction in flame B 22 mm downstream from the burner mouth

$r=35$ mm and then decrease again in the ORZ. In comparison to flame A, the values of f are generally lower due to the higher global air equivalence ratio of flame B and also more evenly distributed, especially in the outer region ($r \geq 30$ mm).

Results of the single-shot evaluation are displayed as scatter plots in Fig. 12. The mixture fractions in all 28 measuring volumes are plotted against the temperature for different radial positions 22 mm downstream together with the equilibrium state curve (black line) and the stoichiometric mixture fraction for the NG (light gray line). As in flame A, one can see the strong variations in the mixture fraction, changing with the radial position. Partly, the measured temperature of the burned gas lies above the equilibrium curve, e.g., at $r=30$ mm. This deviation is possibly due to an inaccuracy of the measurement. However, a detailed analysis has not yet been performed and is in preparation.

In the following, the scatter plots for the different radial positions in flame B are analyzed in more detail. At $r=10$ mm, most

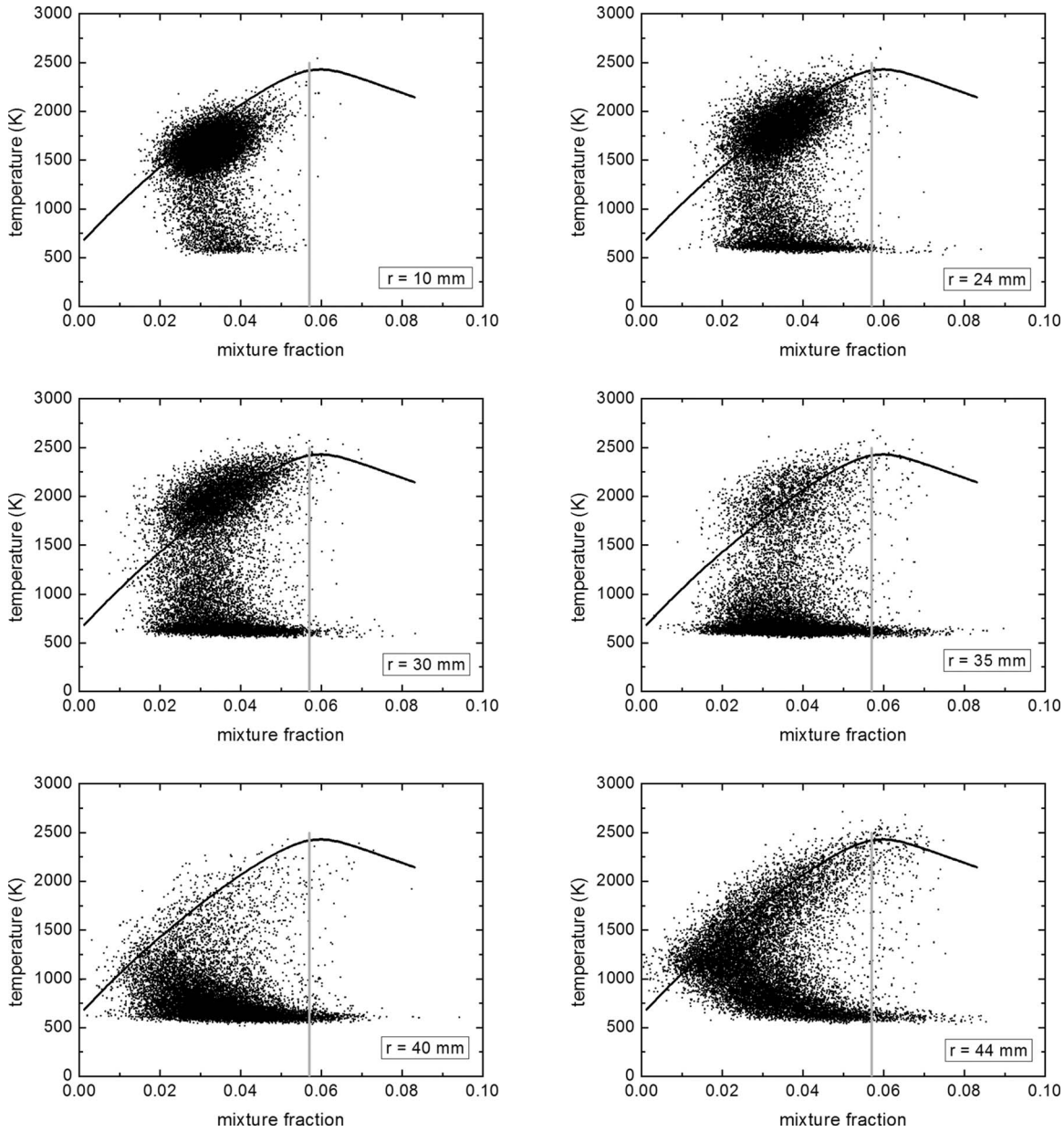

Fig. 12 Scatter plots of single-shot Raman measurements in flame B at different radial positions 22 mm downstream from the burner mouth. The adiabatic temperature (black) and the stoichiometric mixture fraction (light gray) are indicated by lines.

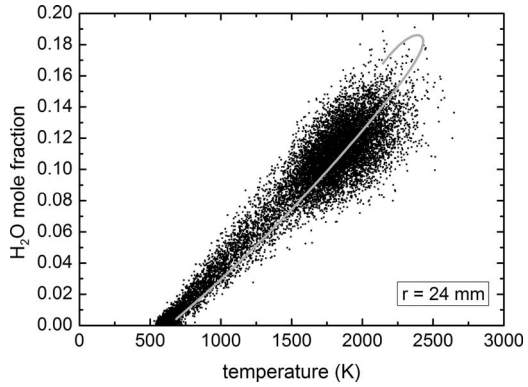

Fig. 13 Scatter plot of H_2O versus temperature in flame B at a radius of $r=24$ mm. The light gray line indicates the adiabatic equilibrium state.

measurements show high temperatures with relatively low variations in the mixture fraction. A minor part of the samples is detected at cold or intermediate temperatures, which indicates that this position is not fully inside the IRZ as it was in flame A. With increasing distance from the burner axis the variation in the mixture fraction increases due to the effects of the not perfect mixing of fuel with air, as well as the cooling air for the burner plate, which mixes with the gas in the ORZ. The portion of cold samples also increases steadily up to a radius of $r=40$ mm. At $r=44$ mm the mean temperature increases again due to the influence of the ORZ, where hot gas is transported back to the burner.

As a representative result of the single-shot evaluations of the major species, the correlation of the H_2O concentration with the temperature is shown in Fig. 13 together with the adiabatic equilibrium state. For a better comparison to flame A, the results at the same radius ($r=24$ mm) are displayed. In general, the H_2O concentration is in good agreement with the equilibrium state for the complete temperature range. The mean value of the H_2O concentration for the burned state ($T \geq 1500$ K) is smaller then in flame A, as expected, according to the lower global mixture fraction. There are also far more samples in the intermediate to cold temperature range as in flame A, where the ignition has not set in yet, or the gas is only "partially" burned due to the afore mentioned reasons.

4 Summary

A downscaled industrial gas turbine burner was equipped with an optical combustion chamber and installed in a high-pressure test rig. It was operated at different flame conditions at elevated pressure. Laser spectroscopic and optical measurements have been performed to investigate the flame behavior and to provide data for validation purposes of numerical simulations. Planar OH-LIF and OH^* chemiluminescence were applied to reveal the structure of the reaction zones and hot regions and the position and shape of the flame brush, respectively. 1D-laser Raman scattering has been applied to measure the major species concentrations, the temperature and the mixture fraction along a line of 7 mm length. The application of this technique to a high-pressure test rig of this size was challenging and problems related to the high laser intensities, and stained windows had to be overcome. Two different flames in terms of shape and stabilization (flames A and B) were selected and investigated in more detail. The OH-PLIF and OH^* chemiluminescence measurements revealed that flame A, which was stabilized within the burner cone, has a smaller and more distinct flame zone than the lifted and more unstable flame B. The single-shot Raman measurements enabled a detailed characterization of the mixing and reaction progress of these flames. Although it was known before that the degree of premixing in GT burners is limited, it could now be quantified for the first time without spatial or temporal averaging. In both flames, the mixture fraction exhibited a significant scatter at a distance of $\sim 1/3$ of the burner exit diameter, and its distribution varied with the radial position. The scatter plots also revealed that the thermochemical state of the flames varied from nonreacted via partially reacted to fully burned. The partially reacted mixtures had intermediate temperatures and stemmed probably from the mixing of hot burned gas with cold fresh gas before ignition has set in. The characteristics of the scatter plots from different radial regions were in accordance with the different flow field regions, i.e., the inflow of fresh gases, the recirculation zones, and the shear layers.

Acknowledgment

The authors would like to thank A. Koch, R. Sadanandan, and their colleagues from the DLR test rig for their support and contributions to the investigations. The financial support from the State Baden-Württemberg, the EnBW Energie Baden-Württemberg AG and ALSTOM Power within the research program KW21 is gratefully acknowledged.

References

[1] Paschereit, C. O., Gutmark, E., and Weisenstein, W., 1998, "Structure and Control of Thermoacoustic Instabilities in a Gas-Turbine Combustor," Combust. Sci. Technol., **138**, pp. 213–232.
[2] Lefebvre, A. H., 1999, *Gas Turbine Combustion*, Taylor & Francis, Philadelphia, PA.
[3] Lee, J. G., and Santavicca, D. A., 2003, "Experimental Diagnostics for the Study of Combustion Instabilities in Lean Premixed Combustors," J. Propul. Power, **19**, pp. 735–750.
[4] Sattelmayer, T., 2003, "Influence of the Combustor Aerodynamics on Combustion Instabilities From Equivalence Ratio Fluctuations," ASME J. Eng. Gas Turbines Power, **125**, pp. 11–19.
[5] 2006, *Combustion Instabilities in Gas Turbine Engines: Operational Experience, Fundamental Mechanisms, and Modeling*, T. Lieuwen and V. Yang, eds., American Institute of Aeronautics and Astronautics, Reston, VA.
[6] Syed, K. J., and Buchanan, E., 2005, "The Nature of NO_x Formation Within an Industrial Gas Turbine Dry Low Emission Combustor," ASME Paper No. GT2005-68070.
[7] Meier, W., Weigand, P., Duan, X. R., and Giezendanner-Thoben, R., 2007, "Detailed Characterization of the Dynamics of Thermoacoustic Pulsations in a Lean Premixed Swirl Flame," Combust. Flame, **150**, pp. 2–26.
[8] Docquier, N., and Candel, S., 2002, "Combustion Control and Sensors: A Review," Prog. Energy Combust. Sci., **28**, pp. 107–150.
[9] Emiris, I., and Whitelaw, J. H., 2003, "Control of Combustion Oscillations," Combust. Sci. Technol., **175**, pp. 157–184.
[10] Richards, G. A., Straub, D. L., and Robey, E. H., 2003, "Passive Control of Combustion Dynamics in Stationary Gas Turbines," J. Propul. Power, **19**, pp. 795–810.
[11] Mongia, H. C., Held, T. J., Hsiao, G. C., and Pandalai, R. P., 2003, "Challenges and Progress in Controlling Dynamics in Gas Turbine Combustors," J. Propul. Power, **19**, pp. 822–829.
[12] Zinn, B. T., 2005, "Smart Combustors—Just Around the Corner," ASME Paper No. GT2005-69138.
[13] Schneider, E., Staudacher, S., Schuermans, B., and Ye, H., 2008, "Model Based Active Combustion Control Concept for Reduction of Pulsations and NO_x Emissions in Lean Premixed Gas Turbine Combustors," ASME Paper No. GT2008-50326.
[14] Geigle, K.-P., Meier, W., Aigner, M., Willert, C., Jarius, M., Schmitt, P., and Schuermans, B., 2006, "Phase Resolved Laser Diagnostic Measurements of a Downscaled, Fuel Staged Gas Turbine Combustor at Elevated Pressure and Comparison With LES Predictions," ASME Paper No. GT2006-90875.
[15] Eckbreth, A. C., 1996, *Laser Diagnostics for Combustion Temperature and Species*, Taylor & Francis, New York.
[16] Kohse-Höinghaus, K., 2002, *Applied Combustion Diagnostics*, Taylor & Francis, New York.
[17] Wolfrum, J., 2000, "Lasers in Combustion: From Basic Theory to Practical Devices," Proc. Combust. Inst., **27**, pp. 1–42.
[18] Barlow, R. S., 2007, "Laser Diagnostics and Their Interplay With Computations to Understand Turbulent Combustion," Proc. Combust. Inst., **31**, pp. 49–75.
[19] Lee, S.-Y., Seo, S., Broda, J. C., Pal, S., and Santoro, R. J., 2000, "An Experimental Estimation of Mean Reaction Rate and Flame Structure During Combustion Instability in a Lean Premixed Gas Turbine Combustor," Proc. Combust. Inst., **28**, pp. 775–782.
[20] Meier, U. E., Wolff-Gassmann, D., and Stricker, W., 2000, "LIF Imaging and 2D Temperature Mapping in a Model Combustor at Elevated Pressure," Aerosp. Sci. Technol., **4**, pp. 403–414.
[21] Löfström, C., Engström, J., Richter, M., Kaminski, C. F., Johansson, P., Nyholm, K., Nygren, J., and Aldén, M., 2000, "Feasibility Studies and Application of Laser/Optical Diagnostics for Characterisation of a Practical Low-

Emission Gas Turbine Combustor," ASME Paper No. 2000-GT-0124.
[22] Gord, J. R., Brown, M. S., and Meyer, T. R., 2002, "Optical Diagnostics for Characterizing Advanced Combustors and Pulsed-Detonation Engines," 22nd AIAA Aerodynamic Measurement Technology and Ground Testing Conference, St. Louis, MI, Jun. 24–26, Paper No. AIAA2002-3030.
[23] Kojima, J., and Nguyen, Q.-V., 2004, "Measurement and Simulation of Spontaneous Raman Scattering in High-Pressure Fuel-Rich H_2-Air Flames," Meas. Sci. Technol., **15**, pp. 565–580.
[24] Willert, C., Hassa, C., Stockhausen, G., Jarius, M., Voges, M., and Klinner, J., 2006, "Combined PIV and DGV Applied to a Pressurized Gas Turbine Combustor Facility," Meas. Sci. Technol., **17**, pp. 1670–1679.
[25] Griebel, P., Siewert, P., and Jansohn, P., 2007, "Flame Characteristics of Turbulent Lean Premixed Methane/Air Flames at High Pressure: Turbulent Flame Speed and Flame Brush Thickness," Proc. Combust. Inst., **31**, pp. 3083–3090.
[26] Janus, B., Dreizler, A., and Janicka, J., 2007, "Experiments on Swirl-Stabilized Non-Premixed Natural Gas Flames in a Model Gas Turbine Combustor," Proc. Combust. Inst., **31**, pp. 3091–3098.
[27] Stopper, U., Aigner, M., Meier, W., Sadanandan, R., Stöhr, M., and Kim, I. S., 2008, "Flow Field and Combustion Characterization of Premixed Gas Turbine Flames by Planar Laser Techniques," ASME Paper No. GT2008-50520.
[28] Strakey, P. A., Woodruff, S. D., Williams, T. C., and Schefer, R. W., 2008, "OH-Planar Fluorescence Measurements of Pressurized, Hydrogen Premixed Flames in the SimVal Combustor," AIAA J., **46**, pp. 1604–1613.
[29] Wehr, L., Meier, W., Kutne, P., and Hassa, C., 2007, "Single-Pulse 1D Laser Raman Scattering Applied in a Gas Turbine Model Combustor at Elevated Pressure," Proc. Combust. Inst., **31**, pp. 3099–3106.
[30] Döbbeling, K., Hellat, J., and Koch, H., 2005, "25 Years of BBC/ABB/ALSTOM Lean Premix Combustion Technologies," ASME Paper No. GT2005-68269.
[31] Zajadatz, M., Lachner, R., Bernero, S., Motz, C., and Flohr, P., 2007, "Development and Design of ALSTOM's Staged Fuel Gas Injection EV Burner for NO_x Reduction," ASME Paper No. GT2007-27730.
[32] Schmitt, P., Poinsot, T., Schuermans, B., and Geigle, K.-P., 2007, "Large-Eddy Simulation and Experimental Study of Heat Transfer, Nitric Oxide Emissions and Combustion Instability in a Swirled Turbulent High Pressure Burner," J. Fluid Mech., **570**, pp. 17–46.
[33] Biagioli, F., Schiessel, P., and Fischer, L., 2008, "Investigation of Flame Stability Characteristics of the EV Burner on the GT13E2 Engine," ASME Paper No. GT2008-50274.
[34] Versluis, M., Georgiev, N., Martinsson, L., Aldén, M., and Kröll, S., 1997, "2-D Absolute OH Concentration Profiles in Atmospheric Flames Using Planar LIF in a Bi-Directional Laser Beam Configuration," Appl. Phys. B: Lasers Opt., **65**, pp. 411–417.
[35] Giezendanner-Thoben, R., Meier, U., Meier, W., Heinze, J., and Aigner, M., 2005, "Phase-Locked Two-Line OH Planar Laser-Induced Fluorescence Thermometry in a Pulsating Gas Turbine Model Combustor at Atmospheric Pressure," Appl. Opt., **44**, pp. 6565–6577.
[36] Karpetis, A. N., and Barlow, R. S., 2002, "Measurements of Scalar Dissipation in a Turbulent Piloted Methane/Air Jet Flame," Proc. Combust. Inst., **29**, pp. 1929–1936.
[37] Ax, H., Kutne, P., Meier, W., König, K., Maas, U., Class, A., and Aigner, M., 2009, "Low Pressure Premixed CH_4/Air Flames With Forced Periodic Mixture Fraction Oscillations: Experimental Approach," Appl. Phys. B: Lasers Opt., **94**, pp. 705–714.
[38] Weigand, P., Lückerath, R., and Meier, W., "Documentation of Flat Premixed Laminar CH4/Air Standard Flames: Temperatures and Species Concentrations," http://www.dlr.de/vt/datenarchiv/
[39] Prucker, S., Meier, W., and Stricker, W., 1994, "A Flat Flame Burner as Calibration Source for Combustion Research: Temperatures and Species Concentrations of Premixed H_2/Air Flames," Rev. Sci. Instrum., **65**, pp. 2908–2911.
[40] Sadanandan, R., Stöhr, M., and Meier, W., 2008, "Simultaneous OH-PLIF and PIV Measurements in a Gas Turbine Model Combustor," Appl. Phys. B: Lasers Opt., **90**, pp. 609–618.
[41] http://www.arcl02.dsl.pipex.com/
[42] Meier, W., Duan, X. R., and Weigand, P., 2006, "Investigations of Swirl Flames in a Gas Turbine Model Combustor. Part II: Turbulence-Chemistry Interactions," Combust. Flame, **144**, pp. 225–236.

Hybrid Wireless-Wired Optical Sensor for Extreme Temperature Measurement in Next Generation Energy Efficient Gas Turbines

Nabeel A. Riza
Mumtaz Sheikh
Frank Perez[1]

Photonic Information Processing Systems Laboratory,
CREOL, The College of Optics and Photonics,
University of Central Florida,
4000 Central Florida Boulevard,
Orlando, FL 32816

Accuracy, reliability, and long lifetimes are critical parameters for sensors measuring temperature in gas turbines of clean coal-fired power plants. Greener high efficiency next generation power plants need gas turbines operating at extremely high temperatures of 1500°C, where present thermocouple temperature probe technology fails to operate with reliable and accurate readings over long lifetimes. To solve this pressing problem, we have proposed the concept of a new hybrid class of all-silicon carbide (SiC) optical sensor, where a single crystal SiC optical chip is embedded in a sintered SiC tube assembly, forming a coefficient of thermal expansion (CTE) matched all-SiC front-end probe. Because chip and host material are CTE matched, optimal handling of extreme thermal ramps and temperatures is possible. In this article, we demonstrate the first successful industrial combustor rig test of this hybrid all-SiC temperature sensor front-end probe indicating demonstrated probe structural robustness to 1600°C and rig test data to ~1200°C. The design of the rig test sensor system is presented and data are analyzed. [DOI: 10.1115/1.3204509]

Keywords: temperature sensor, extreme environments, gas turbines, optical sensor

1 Introduction

Coal continues to be the dominant fossil fuel around the world used for electric power production. The increasing thirst for energy consumption, particularly in developing economies such as China and India, is leading to rapid deployment of large (>300 MW) coal-fired power plants. Per 2008 data, China was building two or more power plants a month. Given the negative environmental effects of coal technology, the research community and power plant technology manufacturers are developing methods for greener energy production via cleaner coal-based fuels [1–4]. Even the jet engine industry is pushing for super-hot turbines to enable faster, longer range, and more fuel efficient planes [5]. In addition, maritime transportation can also benefit from more efficient on-board power and propulsion systems [6,7]. Specifically, the next generation power plants are being designed using cleaner natural gas produced by coal gasification systems. Compared with older combustion systems operating near the 1000°C temperature with on average 32% efficiencies, the new combined-cycle power plants are being designed for operations at much higher 1500°C temperatures. Recent studies are showing that operating the gas turbines at these elevated temperatures will not only produce energy with higher on average 60% efficiencies of scale per laws of thermodynamics, but operating the combustor at higher temperature can produce greener plant designs with improved methods for waste product removal and storage [8]. Given the rationale that clean coal power production will be the reality for many years to come, innovators are being pushed to develop a reliable, accurate, and long lasting (>10,000 h) temperature measurement technology to operate in the hostile environment of combustion chambers of gas turbines. Today, in test engines, the dominant temperature measurement technology is the classic thermocouple (TC) probe. Although precious metal platinum–rhodium TC probes can handle the extreme temperature measurement range, these probes require special packaging to increase operational accuracy and lifetimes. A common problem that inherently plagues TC technology in these extreme environments is that the insulating ceramic in which the TC wires are embedded develops tiny cracks that eventually lead to insulation breakdown. Specifically, the large thermal ramps and mechanical stresses the TC probe suffers cause the multimaterial probe to suffer mechanical failure due to CTE mismatch of probe materials [9]. In addition, TCs via the electromotive force (EMF) voltage-based effect have an inherent repeatability/accuracy tolerance that is a certain percentage of the temperature measured, essentially linked to the intrinsic unavoidable differences in the thermoelectric properties along the length of the wires due to the intrinsic variations in the wire alloy compositions and their annealing state [10].

Researchers have attempted designing various optical methods [11,12], specifically sapphire crystal and sapphire-fiber-based fiber-optic temperature sensors for these extreme environment applications [13–16]. Fundamentally, this approach requires the special packaging of the mechanically fragile optical fiber wire and fiber tip sensing element, again forming a multimaterial CTE mismatched assembly that is fundamentally prone to mechanical failure over plant service-time durations. Optical pyrometry [17–19] is also an attractive option for measuring extreme temperatures, in particular, when the black-body radiation emissitivity factor is constant or calibratable, such as for clean metal surfaces. As the gas mixtures in advanced gas turbines is a dynamic soup of gases, corrosive liquids, solid waste, and specific plant conditions, development is required of better emissivity models over engine lifetime operational conditions for reliable readings via active calibration. Pyrometers also face the multimaterial probe packaging limitations as radiation capture lens and/or fiber-optics has to be protected from the harsh environment of gas turbines. SiC is an excellent material for handling extreme conditions, hence previous attempts using SiC thin films on other substrates have been proposed as optically implemented temperature sensors that are again limited via their multimaterial designs [20,21].

[1]Nuonics, Inc., 1862 Royal Majesty Court, Oviedo, FL 32765.

Manuscript received March 5, 2009; final manuscript received June 2, 2009; published online March 3, 2010. Review conducted by Allan Volponi.

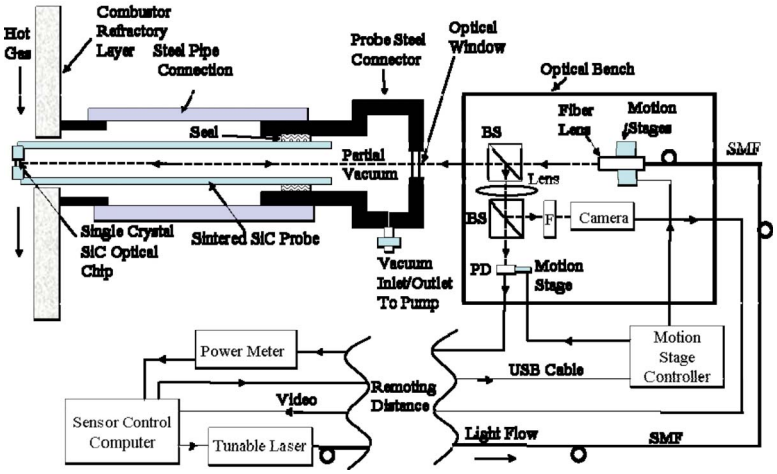

Fig. 1 All-SiC front-end probe-based optical sensor system for extreme gas temperature measurements in combustion engines

Given the mentioned challenging conditions, recently proposed is a temperature sensor innovation [22–29] that circumvents the inherent limitations of prior works. The fundamental design innovation involves three novel aspects. First, a single material is used to form the front-end probe, in our case, the material is SiC. By doing so, one places the vital SiC optical chip for temperature sensing within a SiC packaging tube, thus providing a CTE-matched materials scenario that is ideal in handling extreme temperature, pressure, and chemical conditions. Second, a freespace laser beam that forms a noncontact life-time reliable temperature reading mechanism is used to thermally isolate the temperature sensitive optics from the hot probe. In this way, the prior-art life-time limited wire conduit (electrical or fiber-optical) that transports the temperature information to the temperature reader (e.g., Volt-meter in the case of TCs) is eliminated. Third, active alignment fiber-optics with vacuum sealing of tube is used to target the hot chip within a confocal microscope geometry, thus forming a robust operation probe that combines the best of laser (wireless) and fiber (wired) remoting via a hybrid optical design solution.

2 Sensor System Design

Figure 1 shows the basic research design and method of the proposed all-SiC front-end probe sensor system used for extreme gas temperature measurement within the combustor section of a gas turbine. The system is subdivided into three thermally isolated subsystems forming a hybrid optical design engaging both wired and wireless optics. The first subsystem represents the sensor controls and processing station that is remotely located at a safe site for human interface. This subsystem includes the sensor control computer, optical power meter, and tunable laser. The remoting distance depending on the electrical signal drive requirements and can range from tens of meters to near a hundred meters. The second subsystem consists of the optical transceiver module containing targeting light beam and detection optics, active mechanics, and electronics. This transceiver module is located in close proximity (e.g., a few centimeters) from the front-end probe that forms the third subsystem that is uniquely passive, i.e., contains no lasers, detectors, electronics, or other electrically controlled device. The physical link between the controls subsystem and the transceiver subsystem is via one single mode fiber (SMF) optical cable and three electrical (USB style) cables, providing significant environmental isolation between the two sites. More importantly, the hot front-end probe subsystem is thermally decoupled from the transceiver subsystem with the only physical connection established via a single wireless optical link interfacing the hot SiC optical chip with the laser beam emerging from the SMF-coupled fiber lens (FL). The transceiver module is preferably enclosed in an environmentally protected chamber to minimize moisture, dust, and air currents. The transceiver module is designed for under 70°C operation that is ideally compatible with turbine manufacturer external safety and technician operational environment requirements. Furthermore, this friendly $<70^\circ$C temperature range is also compatible with temperature limits for standard fiber-optics, mechanics, and electronics. The transceiver module is mechanically interfaced to a thermally isolated cooler part of the turbine housing. The front-end probe subsystem consists of a steel connector that forms a pressurized fitting at the inlet to the engine combustor section, where gas temperature sensing is desired. This steel connector via a high temperature pressure seal connects to a long all-SiC probe that extends slightly into the hot gas section of the combustor. At the tip of this probe is embedded a thick single crystal SiC optical chip packaged within the sintered SiC material thus forming the much desired CTE-matched front-end. As shown, a steel pipe is used as an interface assembly between the probe steel pressurized connector and the hot gas section within the thermally isolating refractory layer. The probe steel connector has a high temperature window through which the laser beam travels but equally important, the connector has a vacuum inlet/outlet that connects to an on-demand vacuum pump. Maintaining a partial vacuum within the front-end probe structure is a critical innovation as it essentially eliminates laser beam turbulence along the long thermal ramp influenced probe path that, due to air currents within probe, can ruin beam alignment between chip and the FL. Furthermore, the partial vacuum prevents the unwanted convection-based cooling of the SiC optical chip from within the probe cavity. In addition, the presence of a vacuum cavity eliminates elevated temperature oxidization of the SiC sensor chip and the sintered SiC probe internal structure. Although Fig. 1 shows a single refractory layer between the hot gas section and the inlet to the combustor where the probe connector is attached (the scenario for our experiment), a typical deployed commercial combustor has several (e.g., >5) thick refractory layers such that there is a gradual temperature gradient between the extremely hot (say 1500°C) gas section and the probe insertion point where temperatures are under 200°C. Keeping the overall system design as three independent subsystems improves system maintenance efficiencies as repairs can be made by independent removal of subsystems, in particular, the front-end probe that will suffer the most from the harsh environment of the gas turbine.

The sensor system operates as follows. The computer controls

the required wavelength and power of the laser, as well as providing control signals for the remote motion controller. The computer also stores the received optical power readings for the given wavelength, as well as the received infrared (IR) beam video images from the alignment camera. To measure the gas temperature, the computer instructs the laser to provide optical power of a given infrared wavelength (e.g., 1550 nm) and amount (e.g., 10 dBm) to the SMF that in-turn feeds the FL operated in the low freespace-SMF coupling loss self-imaging condition between SiC chip plane and FL [30]. This light is launched toward the SiC chip sitting at the tip of the probe. The IR beam position at the SiC chip plane is electronically manipulated using piezo-actuators that control the FL translational and tip/tilt conditions such that the IR beam strikes after passing through the first beam splitter (BS) and optical window strikes the SiC chip for optimal retroreflection. Using the first BS coupled with another second BS, the SiC chip reflected light is routed toward two separate optical detection optics. A lens is used to produce focused beam spots on both the two dimensional (2D) camera, e.g., charge-coupled device (CCD) and the large area point photodetector (PD). The PD is also translated in unison with the FL controls such that the spot stays aligned on the PD active area. The computer processes the optical power and CCD image data and provides feedback control signals to the motion stage controller to adjust the optics for optimal interrogation of the SiC chip. The infrared band filter F (e.g., bandwidth of 1530–1560 nm) blocks the black-body (BB) radiation produced by the SiC optical chip that is captured by the lens optics, thus allowing only the laser beam to pass through to the CCD, and hence preventing camera saturation. In short, the sensor system operates to actively target the SiC optical chip and then to properly recover the received retroreflected temperature coded beam to deduce the SiC chip, and hence the gas environment temperature. The SiC chip acts as a temperature sensitive Fabry–Pérot (FP) cavity and previously described multiwavelength signal processing techniques implemented via the control computer can be used to deduce the optical chip temperature [23,26,28]. In short, the SiC chip reflected light optical power is given by the classic FP expression:

$$R_{FP} = \frac{R_1 + R_2 + 2\sqrt{R_1 R_2}\cos\varphi}{1 + R_1 R_2 + 2\sqrt{R_1 R_2}\cos\varphi} \tag{1}$$

where $\varphi = 4\pi/\lambda n(\lambda, T)t(T)$. Here $n(\lambda, T)$ is the chip refractive index at wavelength λ, T is the chip temperature, $t(T)$ is the chip thickness at temperature T, and R_1 and R_2 are the classic Fresnel power coefficients for the SiC-air interface given by $R_1 = R_2 = [(1-n)/(1+n)]^2$. Do note the SiC chip is of a thick (e.g., 400 μm) single crystal SiC material that is optically flat and mechanically robust for handling high (e.g., 160 atm) pressures [23] and high temperatures (e.g., 1500°C). The SiC material that makes the chip and front-end probe is also robust to chemical attack with excellent thermal properties for handling extreme temperatures [25].

3 Sensor Assembly and Experimental Turbine Rig Test

Figure 2 shows the Nuonics, Inc. (Oviedo, FL) provided all-SiC front-end probe displayed in its unassembled and assembled fashions. The point to note is the harsh environment front-end probe assembly consists of three parts, namely, (a) the all-in-one SiC probe consisting of sintered SiC tube assembly with an embedded single crystal SiC optical chip, (b) the pressure sealed steel connector housing that the probe is inserted into to form an interface with pressurized turbine chamber, and (c) the connector flange with an optical window and vacuum connection housing that can connect to the vacuum pump. The probe uses a 400 μm thick single crystal SiC chip of 1×1 cm^2 size embedded with a nonporous sintered SiC tube of 41.5 cm length, and 2.1 cm and 3.3 cm inner and outer diameters, respectively. The pressure seal between the sintered SiC tube and the steel connector is of Viton material with a maximum sealing temperature of 205°C. The window (with 3 deg wedge angle) is made of a 2.54 cm diameter and 6.35 mm thick magnesium fluoride (MgF_2) material with a specified high temperature handling of 500°C and 800°C in moist and dry conditions, respectively. The wedge design eliminates interference effects from the window acting as a wavelength and temperature sensitive cavity. A Mityvac model EW-79301-20 hand operated vacuum pump is connected to the probe vacuum valve and a 25 in.-Hg (~85 kpa) partial vacuum is established within the probe. A cold test of the probe indicates a vacuum drop to 19 in.-Hg and 2 in.-Hg after 62.5 h and 240 h (10 days), respectively. The probe is thermally treated over 30 thermal treatment cycles using an oven with a room temperature (~20°C) to 1100°C thermal cycle consisting of a ramp up time of 4.5 h and cool time of 12 h.

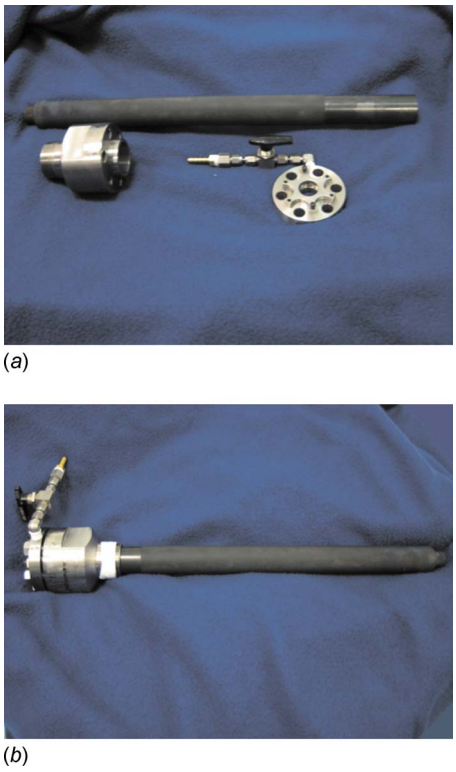

(*a*)

(*b*)

Fig. 2 SiC temperature front-end probe shown in an (*a*) unassembled and (*b*) assembled fashion

Next, the described all-SiC front-end probe along with its Fig. 1 transceiver is deployed in a Siemens (Orlando) combustion test rig facility (see Fig. 3) to form an industrial scenario gas turbine temperature sensing system for a proof-of-concept industrial harsh

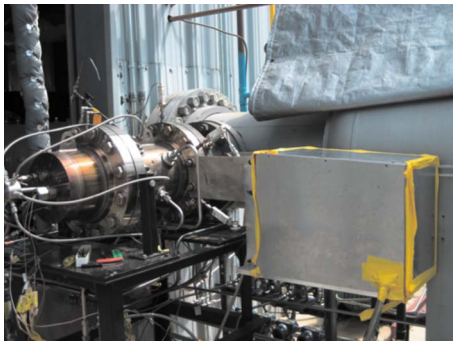

Fig. 3 All-SiC temperature sensor deployed for a first test at Siemens rig facility

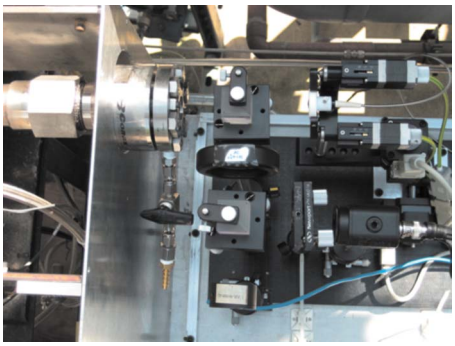

Fig. 4 The assembled sensor optical transceiver module top view

environment sensor technology test. The test combustor is engaged with six 30 cm long reference type-B platinum–rhodium TCs with ceramic and platinum sheath shields for protection and support and a $\pm 0.25\%$ uncertainty, and 1 s response and data recording time. In addition, the all-SiC probe is located in the combustor exhaust section in close proximity (within ~ 14 cm) to the TCs that are located at the midsection of the combustor. A 23 cm length of each TC sits within the combustor encasing while a 5 cm length of the SiC probe sits within the hot section of the combustor. The 35.5 cm(length) $\times$ 20 cm(width) transceiver optical bench is boxed in a water proofed 48 cm(length) $\times$ 30 cm(width) $\times$ 37.5 cm(height) aluminum housing that includes a moisture absorbing desiccant bag to counter the rainy high humidity weather in Florida. The housing is also earthed to counter the lightening strikes common in Florida.

The bench optical layout (see top view in Fig. 4) distances are as follows. Fiber lens to first BS: 5.25 cm; fiber lens to SiC optical chip: 60 cm; first BS to probe window: 6.25 cm; first BS to focusing lens: 5 cm; lens to PD: 11.25 cm; lens to camera: 15 cm. The focal length of the lens is 10 cm. Beam diameter size of 0.8 mm is detected on CCD with <0.8 mm diameter beam on the PD. The PD is a Newport model 818-IR large 3 mm diameter active area point detector, while the BB radiation reduction filter F is centered at 1550 nm with a 30 nm (full-width half-max) passband. The camera is a video rate IR 2D CCD, while Standa piezoelectric translation and tip/tilt motion stages are used to optimize beam alignment. A laser spot size of 550 μm $1/e^2$ beam size forms on the SiC chip. The test rig and control room hardware are connected via 15 m of one SMF and three 10 m electrical cables. The control room contains other rig operational systems such as TC and pressure data reading electronics, as well as combustor flame and fuel monitoring systems. The probe passes through a single 7.62 cm thick combustor refractory layer that for a sample test indicated an external refractory temperature of 426°C when the combustion chamber maximum gas temperature reached 1370°C, indicating the large (in this case, 944°C) temperature drop and high intrinsic thermal insulation of the deployed refractory.

The rig operation begins with an initial warm-up and operational check period, when the hot air blowers are turned on and the combustor is pressurized to a desired ~ 100 psi (or 7 atm) as shown in Fig. 5. For the performed hot rig tests, this warm-up time varied greatly due to various changing on-ground rig conditions and ranged from 20 min to 5 h. Once the rig has reached stable warm-up operational conditions with a fuel-air ratio ~ 0.05, the combustor flame is lit. At this stage, the combustor flame ignited localized gas temperature drastically ramps up over a 1000°C in ~ 3 s. In effect, the entire combustor and all its inserted temperature measuring instruments suffer a great thermal shock. In our case of first rig flame lighting, one reference TC completely failed (no electrical signal out), while another gave drastically wrong temperature readings. The remaining four TCs continued to supply appropriate temperature readings to the remote data acquisition system. This unwanted behavior of these high performance type-B TCs was expected, and hence six TCs were deployed for redundancy. The all-SiC probe survived the thermal shock as optical data readings from both the PD and IR CCD continued to register. In fact, the CCD camera recording at the video rate of 30 fps produced a rapid sequence of an on/off blinking laser spot (see Fig. 6) that spatially darted around a 1 mm diameter around the original alignment point before settling to a beam position within 0.25 mm diameter from its original spot on the camera. The darting around is due to the thermal shock the probe front-end suffers on flame ignition causing the SiC chip surface to temporally deform causing the retroreflected beam to misalign from its original on-axis position of the camera. In addition, the flame ignition also slightly misaligns the probe mechanical assembly causing the retroreflected beam to be slightly off its cold alignment position. Nevertheless, both dynamic and settled beam positions stay within the 3 mm diameter active area of the PD, and furthermore are well within the CCD image zone to allow

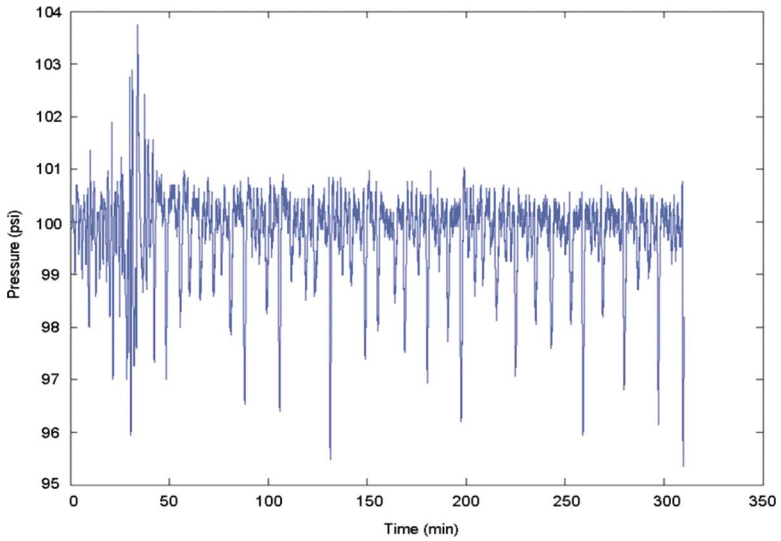

Fig. 5 Combustor average pressure readings of ~ 100 psi (7 atm) measured during rig operations

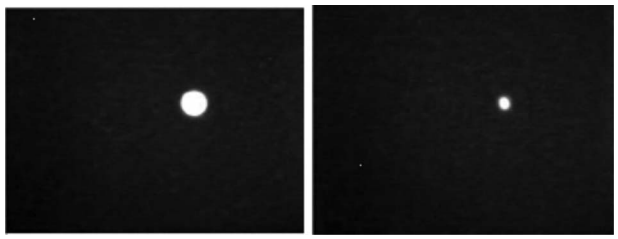

Fig. 6 IR CCD camera (8.8×6.6 mm² active area view) received laser beam snap shots during thermal shock stage indicating on/off oscillatory Fabry–Pérot étalon behavior of SiC optical chip due to the rapid thermal gradient. Left photo: power max and right photo: power min.

the piezo-actuators to optimize beam alignment. The PD's power meter coupled to the control computer is set to take optical power readings after every 78 ms. After the flame light-up, the rig gas temperature near the TC after a ~23 min time interval (see TC data) settles into its expected high temperature operational range with measured TC maximum temperatures reaching 1239°C. Do note that for this particular test rig, one could not set or stabilize the combustor to a given high temperature; thus each time the rig is operated, one finds the combustor temperature sitting in a range between 1100°C and 1239°C.

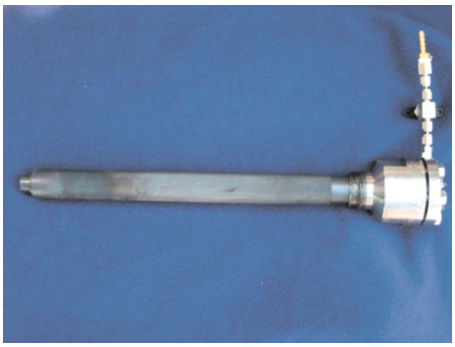

Fig. 7 After first rig test of probe, expected part front-end discoloration is seen due to chemical exposure in combustor refractory section

4 Rig Test Results and Discussion

Over a 28 day period, the probe was subjected to combustor operations on 6 days, with each given day the combustor turned on and then off after test operations. After the first rig test, the probe is removed from the rig and inspected for optical and mechanical failures. The probe showed no damage apart from some expected discoloration (see Fig. 7) of part of the front-end due to chemical treatment in the hot soup of the combustor refractory zone. The probe is reinserted into the system to continue rig test operations.

Figure 8 shows the raw optical data provided by the PD for one of the test days. For the same test, Fig. 9 shows the equivalent temperature readings provided by one of the four working TCs in the rig. Both TC and PD data acquisition systems are synchronized via a computer clock's locked time counter, so one can have direct one-to-one mapping of probe optical power to TC measured temperature to enable probe calibration. Ideally, the optical probe must be calibrated using a temperature measuring device that has far better measurement accuracy than today's high temperature TCs. In addition, the probe calibration must be done at a much slower temporal rate versus an uncontrolled thermal shock mechanism of the rig.

One can clearly see the expected Fabry–Pérot effect oscillatory behavior of the optical power during thermal ramping. In addition, the optical power picks up an increasing bias level due to increasing BB radiation during ramping. In addition, the optical power continues to oscillate depending on the rig temperature fluctuations at the set higher temperature zone. This is so as the optical sensor is designed to be sensitive to high temperature zone changes in a 20°C increment indicating that optical power goes from a peak to a null if temperature changes by 10°C. This feature points to the fact that the optical sensor can measure temperature to a very high accuracy given the optical power meter is highly sensitive.

Figure 10 shows a 15 min snap shot of the probe optical power data taken in the stable ~1107°C region of the rig operation. This data indicates that the probe temperature measurement standard

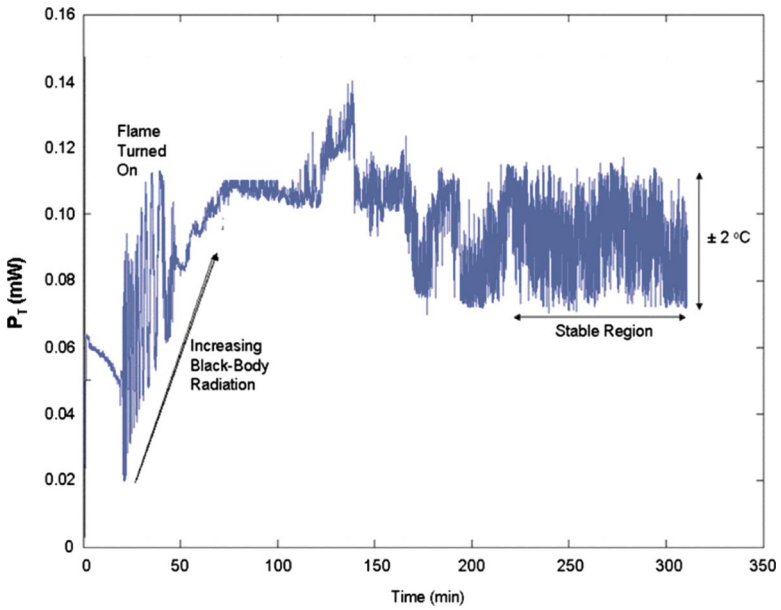

Fig. 8 Raw optical data recorded by the probe PD indicating the rig thermal ramp zone and the relative high temperature stabilization zone. Vertical axis is measured optical power in mW and horizontal axis is a time counter.

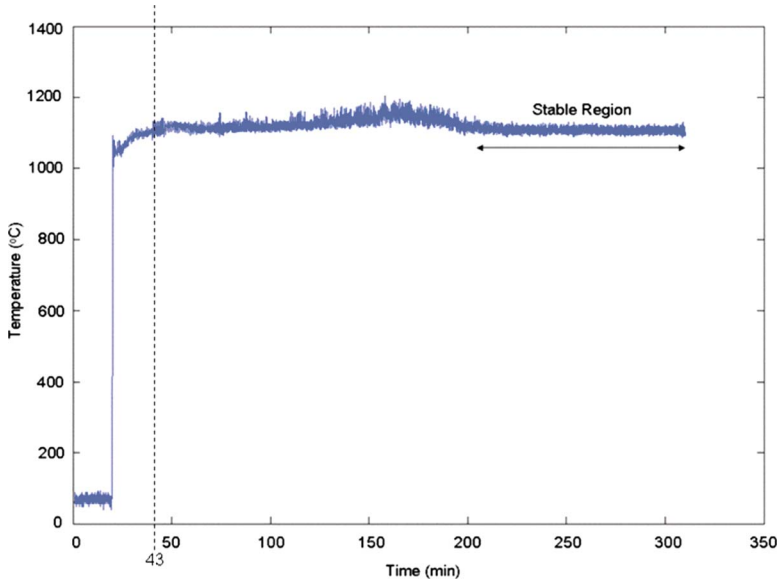

Fig. 9 Rig TC provided temperature reading during the Fig. 8 optical data acquisition period. This TC data is used for optical probe calibration. Vertical axis is measured temperature and horizontal axis is a time counter. A 43 min marker line indicates when the rig gas temperature near TC settles down in its high temperature range that is 23 min after thermal shock.

deviation (SD) is ±2°C for time snap shots of 30 min, 15 min, and 1 min sections. Given the deployed power meter accuracy of 1 μW, the given optical sensor has a calculated sensing accuracy of 0.18°C. Figure 11 shows the Fig. 10 data of 15 min time period TC data. This TC data indicates temperature measurement SD of ±8.3°C, ±8.1°C, and ±9.9°C for time snap shots of 30 min, 15 min, and 1 min sections, respectively. Given that the TC indicates an averaged temperature of 1107°C, the specified TC measurement accuracy for this data is ±2.8°C, indicating a possible limitation of TCs compared with the proposed optical probe that has the potential to deliver much better measurement resolution.

BB radiation fundamentally depends on Planck's law that relates the amount of BB radiation to the temperature of the BB source and the wavelength of radiation and is given by:

$$L_b(\lambda, T) = \frac{C_1}{\pi\lambda^5} \frac{1}{e^{C_2/\lambda T} - 1} \tag{2}$$

where $L_b(\lambda, T)$ is the spectral radiance, λ is the wavelength of radiation, T is the temperature of the BB, while C_1 and C_2 are radiation constants given by $C_1 = 2hc^2$ and $C_2 = hc/k$. The total amount of BB radiation is given by the area under the spectral radiance versus wavelength curve. As the temperature increases the peak of this curve moves to higher intensities and shorter wavelengths, resulting in an increase in the total amount of BB radiation. The actual amount of BB radiation detected depends on the wavelength response of the PD used.

Fig. 8 optical data after the flame light-on region indicates that the rig cavity, and hence the optical probe take a considerable time

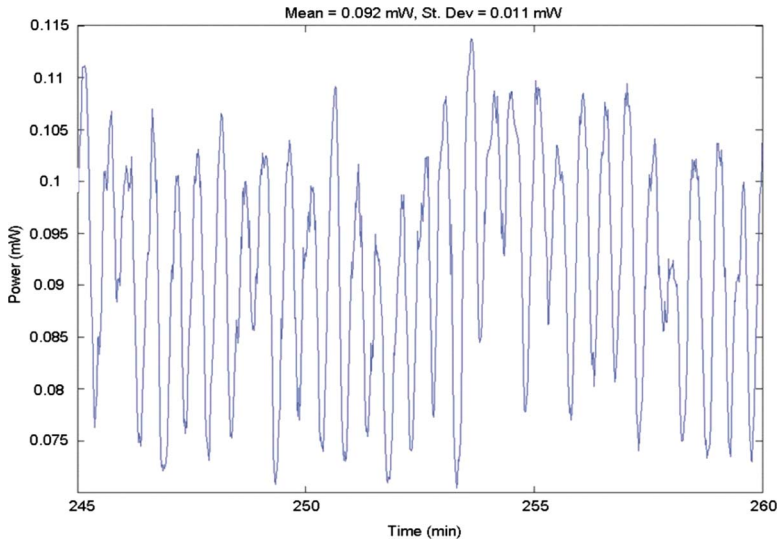

Fig. 10 15 min snap shot of optical power readings from probe during the stable ~1107°C region of the rig operation with a standard deviation of ±2°C.

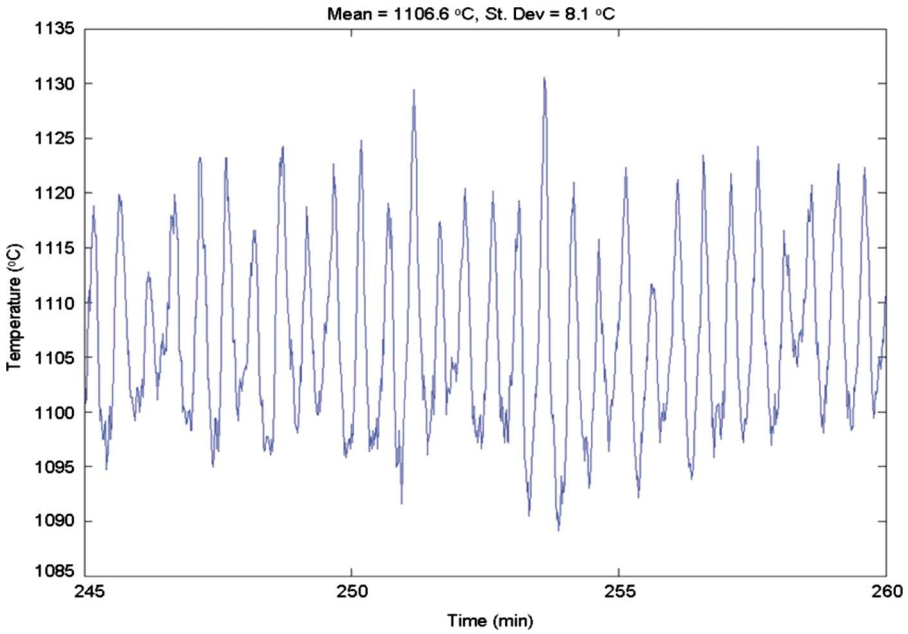

Fig. 11 TC data during the Fig. 9 data 15 min time period with a standard deviation of ±8.1°C

after thermal shock to give stabilized PD-based optical power readings. This is mainly due to the fact that the presently designed all-SiC probe has a partial externally exposed SiC chip optical window that allows BB radiation from the rig hot copper internal walls to pass through the probe cavity in-line path to the PD optics. As the combustor rig is a large BB radiation cavity, a significant time of 48 min after thermal shock is taken for the entire rig to reach the stable high temperature given by its increasing BB radiation signature, thereby producing a slow build-up of the PD optical power data shown in Fig. 8. Note that compared with the TC that is mostly encased within the combustor, the SiC probe generates a large thermal mass due to its large highly conducting (thermal) heat sink structure that at present mostly sits outside the hot zone of the combustor. In effect, the probe thermal mass due to its physical size and nonoptimal single refractory layer placement in combustor limits the dynamic response of the probe temperature measurement. One can note that once the rig has reached its stable high temperature, the optical probe is quick to pick up small temperature changes. Nevertheless, the mentioned probe thermal mass at present has a clipping effect on the actual temperature readings, where the shown ±8.1°C TC readings are clipped to ±2°C probe temperature readings. The solution for reducing this current experimental probe performance limitation is to reduce the probe thermal mass by (a) placing most of the SiC probe within the combustor section including within the highly insulating refractory layers that is typical of a deployed combustion turbine and (b) to design a physically smaller sintered SiC probe package with slow thermal sinking between the SiC optical chip and the sintered SiC probe package. Do note that in the thermal shock region, the all-SiC optical probe did respond in real-time (or video rate) indicated by the rapidly pulsating on/off laser beam images with a 33 ms video time interval.

Fig. 12 shows the optical probe measured temperatures over the whole duration of the rig operation. The signal processing method to find the Fig. 12 temperature plot using the Fig. 8 optical probe data is detailed in the Appendix. The Fig. 12 curve shows that the stable region average temperature of the gas in the rig is 1107°C and the SD in the indicated 60 min stable region is ±6.3°C and ±2°C given by the TC and SiC probe, respectively. Do note that to ensure high temperature measurement sensitivity around the detected laser power maximas and minimas, the optical probe can be calibrated for a second slightly different wavelength that would ensure that for any given temperature, the received laser power reading for at least one of the two calibration wavelengths is in the highly sensitive region for laser power-based temperature signal processing. Fig. 13 shows data from the Fig. 12 zoomed in region around the thermal shock time zone indicating that the measurement response of the TC is under-damped, whereby it oscillates around the temperature of the gas. In contrast, the temperature measurement response of the optical probe is heavily damped, whereby after a fast initial response due to thermal shock, the response slowly (in ~16 min) approaches the temperature of the gas (see Fig. 13). Assuming that the heat is transferred from the hot gas to the TC or the optical probe at an exponentially slow rate (a valid assumption for convective heat transfer thermal systems [31]), thermal time constants can be determined to give a measure of the thermometer response time τ. Hence, one can write measured elevated temperature $T(°C)=[T_f-T_i][1-\exp(-t/\tau)]+T_i$, where T_i and T_f are the initial and final temperatures, respectively.

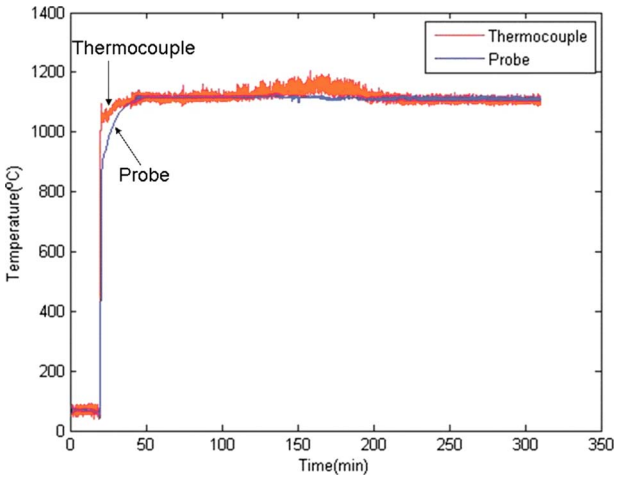

Fig. 12 Comparative optical probe and TC measured temperatures over the duration of the rig operation

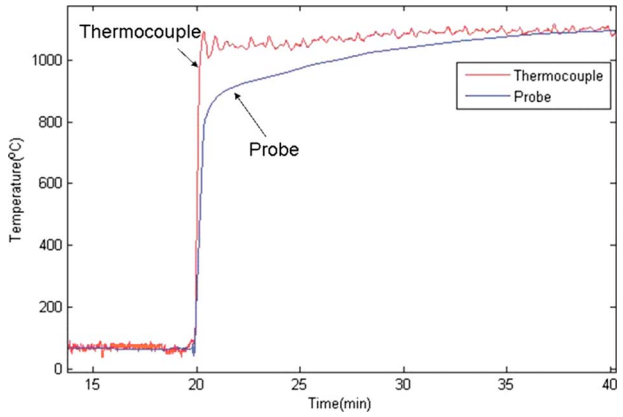

Fig. 13 Comparative optical probe and TC measured temperatures over the zoomed in thermal ramp duration of the rig operation

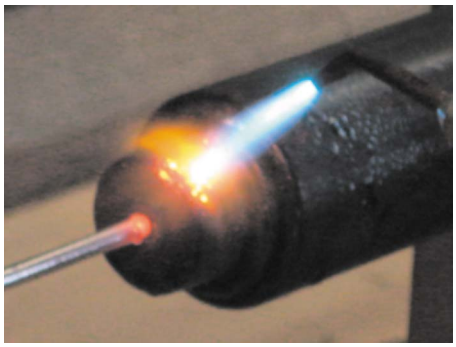

Fig. 14 All-SiC probe and type-R high temperature thermocouple under oxyacetylene flame thermal and localized thermal ramp joint test with temperatures reaching 1600°C

Using Fig. 13, a thermal time constant of 10 s is computed for the TC as this is the time it takes for the TC to reach 63.2% (or 1–1/e) of the difference between the thermal ramp start and end temperatures or for $T=0.632\cdot(1050-87)+87=695°C$. In comparison, using Fig. 13, the thermal time constant for the all-SiC probe is computed as a TC comparable 18 s. As mentioned earlier, this limited dynamic temperature measurement response of the SiC probe owes its behavior to the probe's large thermal mass via its present physical size and its current nonoptimal thermal refractory insulation experimental conditions. Nevertheless, the present rig test of the proposed all-SiC probe technology has proven its operational robustness in the harsh conditions of a commercial test combustion rig.

Specifically, Table 1 shows the conducted key operational parameters for the probe rig test. For example, the probe survived eight thermal up-ramps of 1000°C, each ramp of ~3 s. The probe also survived localized thermal shock (see Fig. 14) and maintained mechanical integrity when subjected to an oxyacetylene flame that produced temperatures near 1600°C. In fact, the R type thermocouple began to melt using the oxyacetylene flame setup, while the all-SiC probe stayed intact. It is important to note that the on/off modulation depth of the retroreflected signal off the SiC optical chip varied from 20:1 to 2:1 during the 28 days of rig tests as different parts of the external chip zone were optically spoiled to a different degree by the hot chemical soup in the combustor. Using the active beam alignment system in the probe, one was highly effective in finding a high modulation depth spot on the chip for effective optical power data recording, again proving the versatility of the smart beam targeting probe design when operating under harsh conditions of a commercial gas turbine. As the optical power meter is highly sensitive, even a 2:1 optical power ratio between a 10°C temperature change provides significant signal processing resolution to calculate the measured temperature with high (e.g., 0.2°C) accuracy.

The probe operated successfully for 28 days, eventually developing a vacuum seal breakage (see Fig. 15) in the pressurized connector on the lower temperature side of the probe. This led to unwanted combustor cooling water entry into the probe at high temperatures (~1200°C) and stoppage of probe operations. A higher (>200°C) temperature insulating pressure seal needs to be deployed to prevent seal breakdown. Do note that during operations, the temperature of the external part of the probe steel connector registered a 200°C reading, indicating that heat from the combustor was efficiently traveling via the probe structure to the external connector chamber. This can indeed be prevented in a deployed combustor using many more thermally insulating refractory layers between probe front-end and connector zone. This would lead to a much lower connector external temperature, and also a much lower temperature experienced by the Viton seal in the connector. In addition, the thermal mass of the probe would be greatly reduced thereby improving the dynamic temperature measurement response of the probe.

Figure 16 shows the probe condition after 28 continuous days in the rig. One can notice the (blue) copper sulfate deposits on the probe front-end. This is indeed so as the combustor chamber was made from copper and the cooling water had sulfur content in it.

5 Conclusion

To our knowledge, for the first time, a single material front-end temperature sensing probe using sintered and single crystal forms of SiC has been assembled and tested in a combustion rig. The probe features a hybrid optical design using a standard silica fiber in the cooler section and a thermally isolated wireless optical link that engages the hot section of the combustor. The probe showed mechanical robustness, surviving eight near 1000°C over 3 s thermal shocks during flame lightings. The probe provided the appropriate optical signal for temperature sensing and signal processing with rig temperatures reaching 1200°C. As the rig operated with greatly reduced thermal refractory layers that would otherwise be present in gas turbines, the deployed Viton gas seal in the probe assembly was exposed to elevated temperatures above the 200°C seal design temperature, thus leading to seal damage and gas leakage into the probe. Rig operations indicate that the SiC chip optical response of the direct gas exposed zone is affected by the combustor dirt; nevertheless, the chip zone within the probe assembly that has surface protection continues to provide a strong

Table 1 Summary of all-SiC probe test at Siemens rig

Combustion rig flame active operation	6 days
No. of times probe experienced flame light and thermal shock (temperature ramp of 1000°C in 3 s)	8 (1 day, 3 flame lights, 5 days, 1 flame light/day)
Operation with flame on	26 h
Operation with flame off and blower on	13.5 h
Number of combustion heat and cool cycles	8
Days in external rig environment	28 days

Fig. 15 Condition of Viton seal used in the probe connector before and after 28 days in rig

optical signal. The probe also survived several localized thermal shocks of 1600°C using a flame torch. Future work requires probe front-end redesign for optimal chip protection with direct signal processing and probe miniaturization and appropriate placement in combustor to reduce thermal mass and improved probe temporal response. Unlike EMF-based TCs used for extreme temperature sensing, the proposed probe does not suffer from the intrinsic limit of temperature measurement error being a percentage of the temperature measured. In addition, unlike TCs, the probe front-end is a single material package, thus pointing to the promise of the proposed all-SiC temperature probe technology for gas turbine extreme temperature sensing.

Acknowledgment

This paper was prepared with support of the U.S. Department of Energy. Equipment and design support was provided by Nuonics, Inc., including the Nuonics SiC temperature probe. Part of the paper describes work conducted at Nuonics, Inc. with collaboration from Siemens Power Generation, Orlando, FL. The authors also thank S. Azer Reza of PIPS Lab. UCF for experimental support, and R. Bunce, D. Sheldon, and Dr. N. Ulerich of Siemens for rig support.

Appendix: Measuring Temperature via Probe Raw Photodetector Data

The raw photodetector data P_T (Fig. 8) contains both BB radiation P_{BB} and laser reflected power P_L off the SiC chip leading to the expression:

$$P_T = P_{BB} + P_L \tag{A1}$$

Equation (A1) can be further written in terms of its dc or $P_{T(dc)}$ and ac or $P_{T(ac)}$ components giving

Fig. 16 Probe condition showing copper sulfate deposits after 28 continuous days in the rig (available in color online)

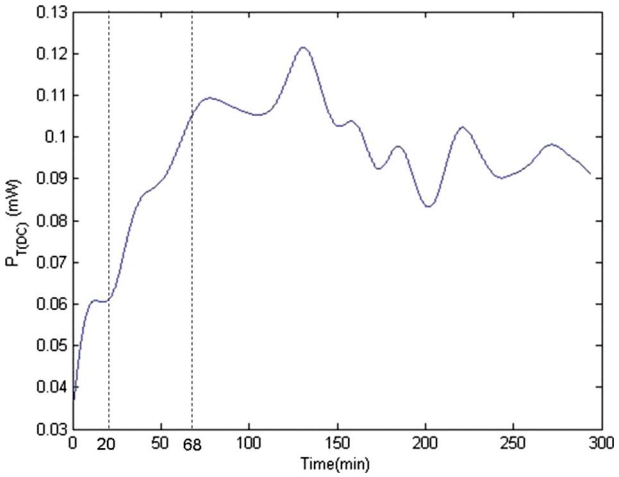

Fig. 17 Photodetector dc value $P_{T(dc)}$ generated from filtering P_T Fig. 8 experimental data against time

$$P_T = P_{T(dc)} + P_{T(ac)} \tag{A2}$$

Here, the dc and ac contributions to the total PD optical power came from both the laser and BB optical powers. The dc contributions of the total optical power due to BB and laser are given as $P_{BB(dc)}$ and $P_{L(dc)}$, respectively. Similarly, the ac contributions of the total optical power due to BB and laser are given as $P_{BB(ac)}$ and $P_{L(ac)}$, respectively. Hence one can write

$$P_T = (P_{BB(dc)} + P_{L(dc)}) + (P_{BB(ac)} + P_{L(ac)}) \tag{A3}$$

One can further write

$$P_{BB(ac)} + P_{L(dc)} + P_{L(ac)} = P_T - P_{BB(dc)} \tag{A4}$$

Since $P_{BB(ac)} \ll P_{L(ac)}$ for the given experimental conditions in the stable region of the present rig temperature measurement scenario (e.g., for a 10°C change at 1100°C, P_L changes by 70 μW, while P_{BB} changes by 8 μW, Eq. (A4) can be approximated as

$$P_{L(dc)} + P_{L(ac)} \approx P_T - P_{BB(dc)}$$

$$P_L = P_T - P_{BB(dc)} \tag{A5}$$

Note that P_L can be used to find the SiC probe tip temperature, and hence the gas temperature at or near the probe tip. P_L is determined by subtracting $P_{BB(dc)}$ from P_T. To determine $P_{BB(dc)}$ shown in Fig. 17, first $P_{T(dc)}$ is determined by passing the Fig. 8, P_T data through a computer implemented low-pass filter. The low-pass filter used is a 5th order type Butterworth filter with an angular cutoff frequency of 0.005π rad/sample or equivalently, 0.2 rad/s, since the power readings are taken 78 ms apart.

Note that the BB radiation compared with the laser power is significant only for temperatures >700°C in the present experimental scenario (at 700°C, the BB radiation is 7.5 μW compared with the average laser power of 57 μW determined from the complete min/max cycles that occur just after the thermal ramp. This is consistent with Planck's black-body radiation law (Eq. (2)), according to which the black-body spectrum shifts to lower wavelengths and higher powers as the temperature goes up. Hence, one can assume that before the thermal ramp at the 20 min timer mark, $P_{BB(dc)}=0$. After the near 3 s flame lit thermal shock at the ~20 min time marker, the entire rig and its internal constituents (e.g., gas soup, SiC probe, TCs, and combustor copper wall) experience thermal ramps. In turn, $P_{T(dc)}$ starts to increase, and this increase is entirely due to BB radiation. This is because

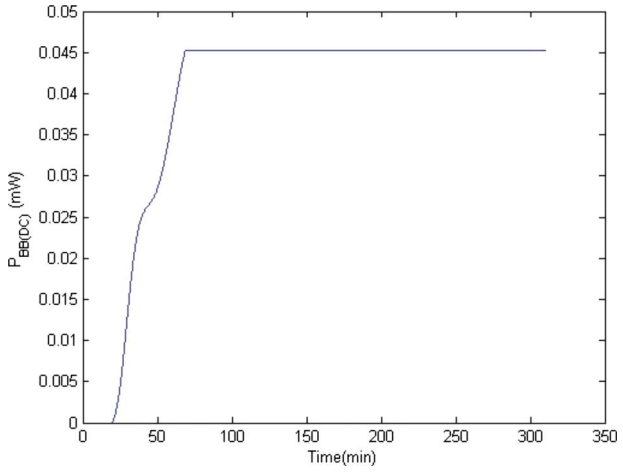

Fig. 18 Clamped photodetector dc value $P_{BB(dc)}$ against time after considering received laser power max/min swing

the thermal shock causes the laser power to rapidly go through many rapid complete power max/min cycles that leads to $P_{L(dc)}$ remaining a constant level.

The max-to-min laser power P_L swing is determined from the complete min-to-max P_T cycles that occur just after the thermal ramp (see Fig. 8), when there is no BB radiation (i.e., when temperature $<700°C$) and gives a P_L swing of 75 μW with $P_L(\text{minimum})=20$ μW and $P_L(\text{maximum})=95$ μW. Since the maximum value of P_T recorded is 140 μW after the thermal ramp settles (see Fig. 8), it implies that the $P_{BB(dc)}$ can be no smaller than 45 μW in the stable temperature region after the thermal ramp. Similarly, the minimum value of P_T recorded is 70 μW after the thermal ramp settles, which implies that the $P_{BB(dc)}$ can be no larger than $70-20=50$ μW in the stable temperature region after the thermal ramp. Within this range, i.e., 45–50 μW, a $P_{BB(dc)}$ value of 45 μW that occurs at the 68 min time marker in Fig. 8 is picked as that conforms most to the P_L max/min cycles occurring nearest to the stable temperature region. To implement signal processing for temperature measurement, $P_{BB(dc)}$ data in Fig. 17 are clamped to its value at the 68 min mark to produce Fig. 18, as 45 μW is the value $P_{BB(dc)}$ can reach if one assumes that the laser power P_L completes a max-to-min swing subsequently.

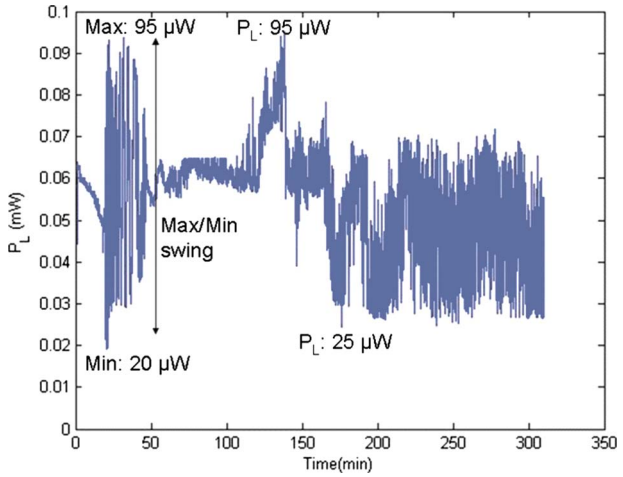

Fig. 19 Computed laser power P_L from raw power P_T data using Eq. (A5) and plotted against time

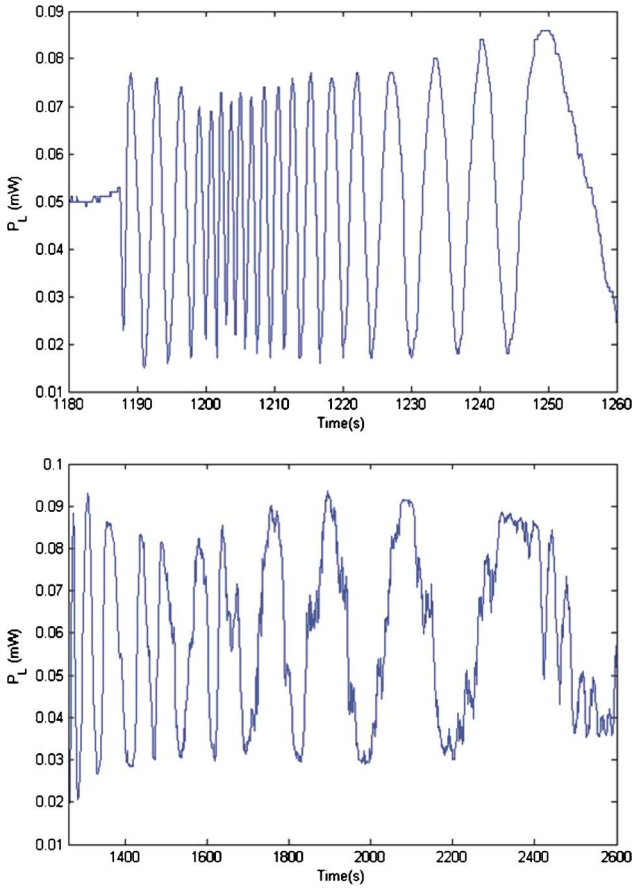

Fig. 20 Zoomed in versions of Fig. 19 around the thermal ramp region

As the temperature of the combustor rig given by the reference TC does not change by much (i.e., it fluctuates around 1120°C) after the 68 min time marker, $P_{BB(dc)}$ is taken to be constant value of 45 μW after this time instant. As $P_{BB(dc)}$ is now determined, P_L is simply determined according to Eq. (A5) to produce the Fig. 19 P_L data.

Near the probe tip, the all-SiC probe measured coarse temperature of the gas in a ~20°C range can be determined from Fig. 19 data by finding the number of laser power min-to-max cycles that have passed starting from the initial (i.e., time marker of zero) rig temperature (87°C) and comparing that to a previously calibrated laser power P_L against temperature probe calibration curve [23].

Figures 20(*a*) and 20(*b*) show the zoomed in snapshots of these P_L laser power cycles at different time instants after the flame ignited thermal shock. Within each 20°C window, the exact temperature is found by comparing the Fig. 19 actual power reading against the calibrated P_L curve to get the Fig. 12 probe provided temperature values. Note that the laser reflected power off the SiC chip varies with temperature according to Eq. (1).

References

[1] Pacala, S., and Socolow, R., 2004, "Stabilization Wedges: Solving the Climate Problem for the Next 50 Years With Current Technologies," Science, **305**(5686), pp. 968–972.

[2] Hoffert, M. I., Caldeira, K., Jain, A. K., Haites, E. F., Harvey, L. D. D., Potter, S. D., Schlesinger, M. E., Schneider, S. H., Watts, R. G., Wigley, T. M. L., and Wuebbles, D. J., 1998, "Energy Implications of Future Stabilization of Atmospheric CO_2 Content," Nature (London), **395**, pp. 881–884.

[3] Hawkins, D. G., Lashof, D. A., and Williams, R. H., 2006, "What to Do About Coal," Sci. Am., **295**(3), pp. 68–75.

[4] Langston, L. S., 2007, "Fahrenheit 3600: Everywhere You Look, The Gas Turbine Industry is Running Hot," ASME Mechanical Engineering Magazine, **129**(4), pp. 34–37.

[5] Manley, D. K., McIlroy, A., and Taatjes, C. A., 2008, "Research Needs for Future Internal Combustion Engines," Phys. Today, **61**(11), pp. 47–52.
[6] Bonafoux, J., 2004, "Propulsion System Requirements for High Speed Naval Ship Designs," RENK Symposium, Paper No. 42.
[7] O'Rourke, R., 2006, "Navy Ship Propulsion Technologies: Options for Reducing Oil Use-Background for Congress," Congress Research Service (CRS) Report No. RL33360.
[8] Ausubel, J. H., 2004, "Big Green Energy Machines," Ind. Phys., **10**(5), pp. 20–24.
[9] Bentley, R. E., 1998, "Thermocouple Materials and Their Properties," *Theory and Practice of Thermoelectric Thermometry: Handbook of Temperature Measurement*, Springer-Verlag, Singapore, Chap. 2, pp. 25–81.
[10] Ripple, D., 2000, "Thermocouples and Thermocouple Wires," Tutorial in NIST Thermocouple Workshop, IEEE Conference on Advanced Thermal Processing of Semiconductors.
[11] Lee, B., 2003, "Review of the Present Status of Optical Fiber Sensors," Opt. Fiber Technol., **9**(2), pp. 57–79.
[12] Winz, M., Stump, K., and Plant, T. K., 2002, "High Temperature, Stable Fiber Bragg Gratings," *Proceedings of the 15th Optical Fiber Sensors Conference Technical Digest (OFS 2002)*, p. 195.
[13] Grobnic, D., Smelser, C. W., Mihailov, S. J., and Walker, R. B., 2004, "Isothermal Behaviour of Fiber Bragg Gratings Made With Ultrafast Radiation at Temperatures Above 1000°C ," Opt. Commun., **2**, pp. 130–131.
[14] Hai, X., Wei, Z., Lockhard, R., and Anbo, W., 1997, "Absolute Sapphire Optical Fiber Sensor for High Temperature Applications," Proc. IEEE, p. 351.
[15] Grobnic, D., Mihailov, S. J., Smelser, C. W., and Ding, H., 2004, "Ultra High Temperature FBG Sensor Made in Sapphire Fiber Using Isothermal Using Femtosecond Laser Radiation," Opt. Commun., **2**, pp. 128–129.
[16] Zhang, Y., Pickrell, G. R., Qi, B., Safaai-Jazi, A., and Wang, A., 2004, "Single-Crystal Sapphire-Based Optical High-Temperature Sensor for Harsh Environments," Opt. Eng., **43**(1), pp. 157.
[17] Dewitt, D. P., and Nutter, G. D., 1988, *Theory and Practice of Radiation Thermometry*, Wiley, New York.
[18] Ng, D., and Fralick, G., 2001, "Use of a Multiwavelength Pyrometer in Several Elevated Temperature Aerospace Applications," Rev. Sci. Instrum., **72**(2), pp. 1522–1530.
[19] Bonzani, J. P. J., Florczak, E. H., Scire, J. J. J., and Markham, J. R., 2003, "Improvement to a Bench Top Instrument for Measuring Spectral Emittance at High Temperatures," Rev. Sci. Instrum., **74**(6), pp. 3130–3136.
[20] Beheim, G., 1986, "Fibre-Optic Thermometer Using Semiconductor-Etalon Sensor," Electron. Lett., **22**(5), pp. 238–239.
[21] Cheng, L., Steckl, A. J., and Scofield, J., 2003, "SiC Thin-Film Fabry-Perot Interferometer for Fiber-Optic Temperature Sensor," IEEE Trans. Electron Devices, **50**(10), pp. 2159–2164.
[22] Riza, N. A., and Perez, F. A., 2008, "High Temperature Minimally Invasive Optical Sensing Modules," US Patent No. 7,327,472.
[23] Riza, N. A., Arain, A., and Perez, F., 2006, "Harsh Environments Minimally Invasive Optical Sensor Using Free-Space Targeted Single-Crystal Silicon Carbide," IEEE Sens. J., **6**(3), pp. 672–685.
[24] Riza, N. A., Ghauri, F., and Perez, F., 2007, "Wireless Pressure Sensor Using Laser Targeting of Silicon Carbide," Opt. Eng., **46**(1), p. 014401.
[25] Riza, N. A., Ghauri, F., and Perez, F., 2007, "Silicon Carbide-Based Remote Wireless Optical Pressure Sensor," IEEE Photonics Technol. Lett., **19**(7), pp. 504–506.
[26] Riza, N. A., and Sheikh, M., 2008, "Silicon-Carbide-Based Extreme Environment Temperature Sensor Using Wavelength-Tuned Signal Processing," Opt. Lett., **33**(10), pp. 1129–1131.
[27] Sheikh, M., and Riza, N. A., 2008, "Experimental Studies of an All-Silicon Carbide Hybrid Wireless-Wired Optics Temperature Sensor for Extreme Environments in Turbines," *Proceedings of the Optical Sensors 2008*, Strasbourg, France, Vol. 7003, p. 70030C.
[28] Sheikh, M., and Riza, N. A., 2009, "Direct Measurement High Resolution Wide Range Extreme Temperature Optical Sensor Using an All-Silicon Carbide Probe," Opt. Lett., **34**(9), pp. 1402–1404.
[29] Riza, N. A., and Sheikh, M., 2009, "All-Silicon Carbide Hybrid Wireless-Wired Optics Temperature Sensor: Turbine Tests and Distributed Fiber Sensor Network Design," *Proceedings of the Optical Sensors 2009*, Prague, Czech Republic, Vol. 7356, pp. 73560O.
[30] Van Buren, M., and Riza, N. A., 2003, "Foundations for Low-Loss Fiber Gradient-Index Lens Pair Coupling with the Self-Imaging Mechanism," Appl. Opt., **42**(3), pp. 550–565.
[31] Lewis, R. W., Nithiarasu, P., and Seetharamu, K. N., 2004, *Fundamentals of the Finite Element Method for Heat and Fluid Flow*, Wiley, New York, p. 151.

Active Compressor Stability Management Via a Stall Margin Control Mode

Yuan Liu[1]

Manuj Dhingra

J. V. R. Prasad

School of Aerospace Engineering,
Georgia Institute of Technology,
270 Ferst Drive,
Atlanta, GA 30332

An active engine control scheme for protection against compressor instabilities such as rotating stall and surge is presented. Compressor stability detection is accomplished via a parameter known as the correlation measure, which quantifies the repeatability of the pressure fluctuations in the tip region of a compressor rotor. This work investigates the integration of the correlation measure with an aircraft engine control system through the use of a stall margin control mode. The development and implementation of the stall margin mode are described. The effectiveness of the overall active control framework—an active compressor stability management system—is assessed using a computer simulation of a high-bypass, dual-spool, commercial-type turbofan engine.
[DOI: 10.1115/1.3204652]

1 Introduction

The control system for gas turbine engines used on modern, commercial aircraft consists of a controller for measurable parameters closely related to thrust, such as spool speeds or pressure ratios, and a protection system against violation of critical operational limits. In general, this protection system is a cascade of limit regulators for overtemperature/-pressure prevention and fuel rate limiters for avoidance of compressor aerodynamic instabilities. These compressor instabilities, such as rotating stall and surge, play a large role in restricting the operating envelope of gas turbine engines. This limitation can be represented as the surge line on a typical compressor map (Fig. 1). The precise location of the surge line is uncertain since it is sensitive to factors such as inlet distortion, manufacturing tolerances, and component deterioration due to aging. To compensate for this uncertainty, the engine protection system is designed to maintain a conservative stall margin throughout the operating envelope, generally at the expense of engine performance and operability.

An active engine control system would permit the engine to utilize excessive stall margin as necessary while protecting it from compressor instabilities. A possible approach to an active control framework is through the use of a control mode based on compressor stall margin. Studies performed on engine simulations have demonstrated the potential benefits of such a stall margin control mode [1]. Abidhatla and Lewis [2] assessed the effectiveness of a fan stall margin regulator on a low-bypass turbofan engine model known as the XTE46. However, stall margin is sensitive to engine and operating conditions and is not directly measurable. Consequently, since such control modes inherently require stall margin to be a feedback parameter, they are only feasible in scenarios such as model-based control or as "research-purpose" controllers in engine simulations. For instance, the modular aeropropulsion system simulation (MAPSS) [3], a model of a generic, low-bypass, military-type turbofan engine developed by the NASA Glenn Research Center, utilizes a controller with stall margin feedback.

This work investigates a realistic implementation of a stall margin control mode through the use of a stability detection parameter known as the correlation measure. Developed by Dhingra et al. [4], the correlation measure is a parameter rooted in the unsteady flow field characteristics of the compressor rotor tip region. Experiments conducted on several laboratory compressor rigs, as well as a modern aircraft engine, have shown that the measure is able to signal increased proximity between the compressor operating point and its stability limit [5]. A stochastic model of the correlation measure, which emulates the statistical properties of the parameter, was also developed [6]. Recent research employed Boolean-type (on/off) control logic along with this statistical model to investigate different methods of incorporating the correlation measure into the engine control system [7]. The combination of the correlation measure with a stall margin control mode was determined to be the most favorable route toward an active control system.

This paper presents the design and implementation of an active compressor stability management system through use of a stall margin control mode. The effectiveness of the control scheme is evaluated with the commercial modular aeropropulsion system simulation (C-MAPSS). This simulation models a high-bypass, dual-spool, commercial-type turbofan engine. The studies involve degrading certain engine components within reasonable levels but to the point at which the engine will encounter compressor instabilities for a step throttle command from idle to full power at sea-level static conditions. The design of the stall margin control mode for this engine is described. The theoretical effectiveness of this controller is demonstrated by running the deteriorated engine through the aforementioned transient with the stall margin mode in place of the conventional stall protection system. Stall margin feedback is then replaced with the correlation measure, forming the active stability management system. The results show that stability management and stall margin feedback control are equally effective in protecting against compressor instabilities in the degraded engine whereas the unmodified control system is not.

2 Engine Simulation

The testbed used for the implementation and assessment of active compressor stability management is the commercial modular aeropropulsion system simulation [8]. Developed by the NASA Glenn Research Center, C-MAPSS is a computer simulation of a high-bypass turbofan engine representative of those used on a large commercial aircraft. C-MAPSS utilizes a dynamical system implemented in the MATLAB/SIMULINK environment to model the engine and control system. However, low-level calculations for the main engine components are accomplished using C. As a result, the simulation can be run at faster-than-real-time speeds. The

[1]Corresponding author.

Contributed by the International Gas Turbine Institute of ASME for publication in the JOURNAL OF ENGINEERING FOR GAS TURBINES AND POWER. Manuscript received March 25, 2009; final manuscript received April 9, 2009; published online March 4, 2010. Review conducted by Dilip R. Ballal. Paper presented at the ASME Gas Turbine Technical Congress and Exposition, Orlando, FL, June 8–12, 2009.

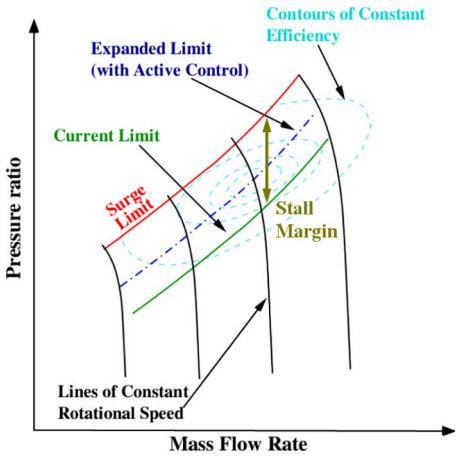

Fig. 1 Generic compressor map demonstrating notions of surge line and stall margin

simulation increments in 15 ms time-steps. Degradation of major engine components is modeled through the use of variable health parameters.

The C-MAPSS engine is a high-bypass, dual-spool turbofan engine with a maximum thrust of approximately 90,000 lbs. The engine is represented as a component-level dynamic model. Engine components are modeled independently using thermodynamic equations and performance maps, and interconnected via the SIMULINK block diagram syntax. The major components (Fig. 2) are the inlet, fan, bypass nozzle, low-pressure compressor (LPC), high-pressure compressor (HPC), combustor, high-pressure turbine (HPT), low-pressure turbine (LPT), and core nozzle. The health parameters, which simulate deterioration and/or faults in the five rotating components, include flow, efficiency, and pressure ratio modifiers for each of the compression components (fan, LPC, and HPC); and flow and efficiency modifiers for the turbine components (HPT and LPT). The state variables of the dynamic engine model are fan speed and core speed. Thus, C-MAPSS can simulate transient engine operation but cannot capture stall or poststall characteristics. However, stall margins of the fan, LPC, and HPC are available through their respective component maps. Since the focus of this study is compressor instability avoidance (as opposed to recovery), the lack of a stall model is not a significant limitation. Stall onset is taken to be the instant any one of the three stall margins become nonpositive.

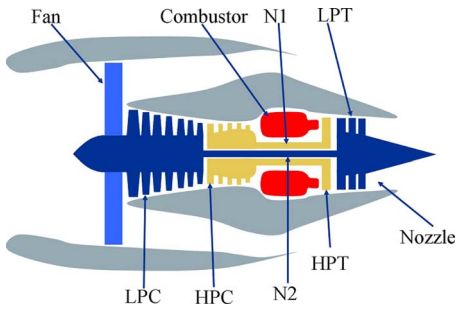

Fig. 2 Simplified representation of the C-MAPSS high-bypass, dual-spool turbofan engine [8]

A high-level diagram of the C-MAPSS engine control system is shown in Fig. 3. The control system calculates fuel flow rate (w_f) to the engine from throttle input profiles provided by the user in terms of throttle resolver angle (TRA) values. The TRA range 0–100 deg represents idle to full engine power. TRA is translated into a demanded fan speed based on ambient conditions. A scheduled-gain fan speed controller calculates $\dot{w}_f$, the incremental change in fuel flow rate necessary to meet the demanded fan speed. This $\dot{w}_f$ value is then cascaded through minimum/maximum logic with limit regulators to avoid excursions beyond design limits on HPT exit temperature, combustor static pressure, and core speed; acceleration and deceleration limiters to prevent compressor stall. A suite of sensors provides necessary information on engine parameters for the controller and limit regulators. Afterwards, $\dot{w}_f$ is integrated to form a w_f command for the fuel actuator. First-order transfer functions model the dynamics of the actuators and sensors.

3 Compressor Stability Detection

This section highlights the principles behind the compressor stability detection parameter, the correlation measure, and its implementation in the engine simulation environment.

3.1 Correlation Measure. Previously developed at the School of Aerospace Engineering, Georgia Institute of Technology, the stability detection method utilized in this work is based on experimental observations of the pressure fluctuations in the compressor rotor tip region. Namely, the repeatability of this pressure signature, as measured by a sensor fixed to the casing, deteriorates as the compressor is loaded toward its stability limits. Thus, a "correlation measure" is used to quantify the periodicity level of the sampled signal. The correlation measure [4] is calculated as

$$C(n) = \frac{\sum_{i=n-\text{wnd}}^{n} p_i p_{i-N}}{\sqrt{\sum_{i=n-\text{wnd}}^{n} p_i^2 \sum_{i=n-\text{wnd}}^{n} p_{i-N}^2}} \tag{1}$$

where $C(n)$ is correlation measure, n is sample index, i is index, N is the number of samples per shaft rotation, and wnd is the window size in number of samples.

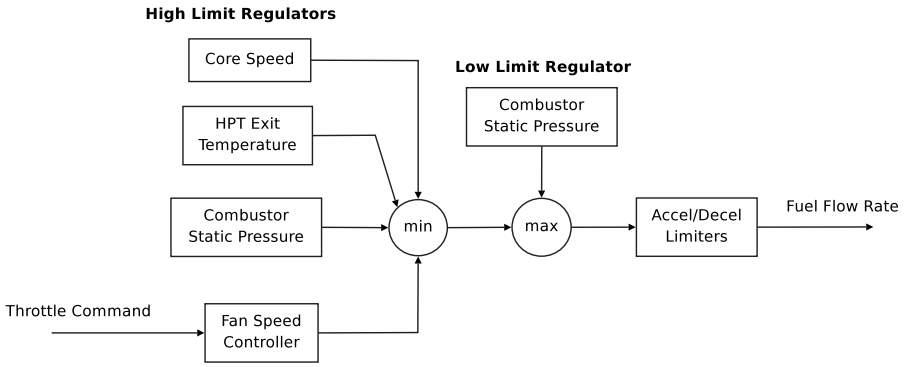

Fig. 3 C-MAPSS control system architecture

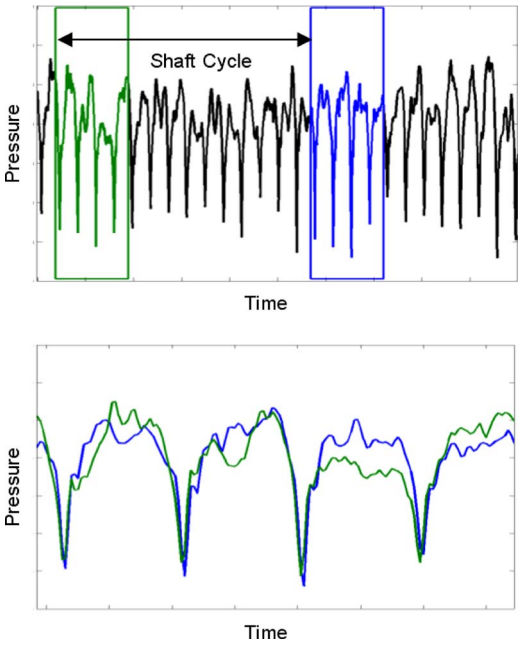

Fig. 4 Example illustrating the notion of the correlation measure, which compares two moving windows of pressure samples separated in time by one shaft cycle

As Eq. (1) suggests, the correlation measure compares two moving windows of pressure samples separated in time by one shaft revolution. Figure 4 depicts a visualization of this process applied to a representative pressure signal. Both windows contain wnd number of data points. Technically, the measure is bounded by -1 and 1, with the latter representing a perfectly periodic signal. However, the quantity usually stays between 0 and 1 during typical compressor operation. Previous applications of the correlation measure to engine control [9,7] involve monitoring for and responding to "events," which are defined as drops in the correlation measure below some specified threshold. Resulting from the deterioration of the pressure signature's repeatability, an increase in event frequency is indicative of proximity to the limit of stable compressor operation.

3.2 Stochastic Model. Since the correlation measure is determined from the pressure fluctuations over a compressor rotor, it is not feasible to directly calculate the quantity from the dynamic engine simulation alone. Instead, a stochastic model of the correlation measure is used to implement the stability detection technique in the simulation environment. In particular, this model utilizes compressor stall margin, readily available from the engine simulation, to replicate correlation measure events. The details of model formulation and validation are provided in Refs. [6,10].

Analysis of experimental data obtained from various compressor platforms has shown that there exists a relationship between stall margin and the statistical properties of event occurrences. Specifically, the rate at which events occur (i.e., events/s) is a function of compressor stall margin. Figure 5 illustrates this relationship for a particular research compressor rig. It has been found that although the magnitudes of the event rates may vary among different machines, the overall trend of the relationship is consistent. Furthermore, the time separation between event occurrences (TBE) can be approximated with an exponential probability distribution function

$$F_{\mathrm{TBE}}(\tau) = P(\mathrm{TBE} < \tau) = 1 - e^{-\mu_{cm}\tau} \tag{2}$$

In this expression, μ_{cm} is the event rate. Figure 6 shows the agreement between this mathematical model and experimental data.

These correlation measure-based phenomena are emulated us-

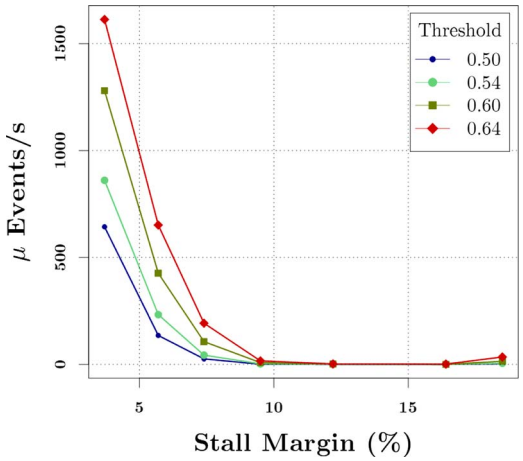

Fig. 5 Relationship between event rate and stall margin for different thresholds on correlation measure. Experimental data from tests conducted on a research compressor [10].

ing threshold-crossings of a pseudorandom number generator (RNG). For given stall margin, the corresponding event rate is determined from a particular set of experimental data, such as that depicted in Fig. 5. An algorithm maps this event rate to threshold levels for a pseudo-RNG such that the statistical distribution of TBE is replicated. Specifically, Cramer and Leadbetter [11] showed that for any random process and a threshold value, the distribution of the time between threshold-crossings is

$$F_{\mathrm{TBE}}(\tau) = 1 + \mu^{-1} D^{+} u_0(\tau) \tag{3}$$

where μ is the average number of threshold-crossings, D^{+} is the right hand derivative, and u_0 is the probability that no threshold-crossings are observed in the time interval $0-\tau$. Numerical investigations showed that level-crossings of an exponentially distributed pseudo-RNG yield an exponentially decaying probability of "no event," that is $u_0 = e^{-\mu\tau}$. Moreover, if the threshold level is chosen based on the natural logarithm of μ_{cm}, μ becomes μ_{cm}, hence reducing Eq. (3) to Eq. (2). As a result, instead of explicitly calculating the correlation measure, this stochastic model utilizes compressor stall margin values obtained from the engine model to generate level-crossings that simulate correlation measure events.

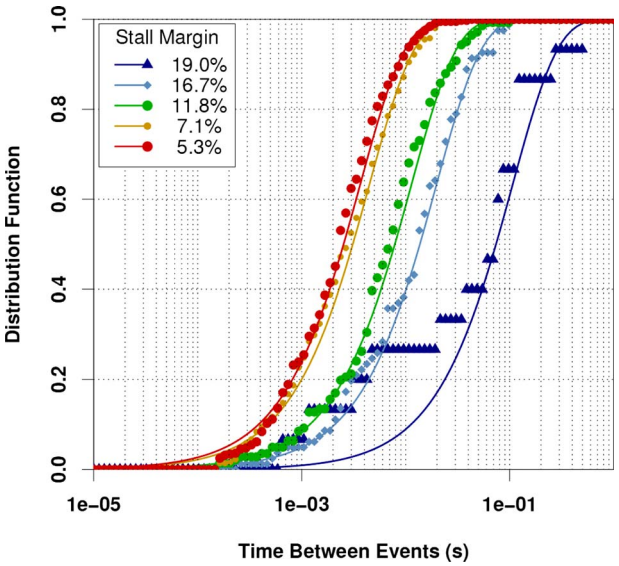

Fig. 6 TBE is exponentially distributed regardless of stall margin level [6]

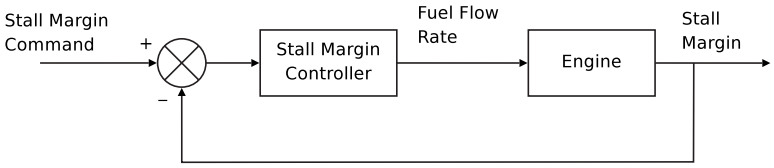

Fig. 7 Connection between stall margin controller and engine

4 Active Compressor Stability Management

Active compressor stability management represents the integration of the stability detection technique with the engine control system. In this study, this integration is done through a stall margin control mode. This control mode consists of a stall margin controller driven by correlation measure-based events. The development and implementation of the stall margin control mode are described.

4.1 Stall Margin Controller. The stall margin control mode requires a controller that can drive the engine to some reference compressor stall margin value. The "model-matching" method, by Edmunds [12], is used to design this stall margin controller. This technique, also referred to in literature as the "*KQ* method," has been previously used in the design of model-based engine control systems [13] as well as full flight envelope, multivariable engine controllers [14]. Detailed mathematical formulations of this controller design method are provided in Refs. [12,15]. For simplicity, the stall margin controller is single-input, single-output, and localized at one point (sea-level static) in the operation envelope. Figure 7 shows the intended connection between the stall margin controller and the engine. The input to this controller is the difference between the reference and actual stall margin. The output is the corresponding $\dot{w}_f$ value.

The model-matching method involves first selecting Q, a dynamical system representing the desired closed-loop response characteristics of the parameter to be controlled on. The goal is then to find K, the controller which, when connected with the plant, will produce a closed-loop response that closely matches the response of Q. To do this, the poles of K are selected to fix the denominator structure of the transfer function. The numerator is calculated from a least-squares algorithm that minimizes the discrepancy between the desired response and actual closed-loop response. The C-MAPSS application provides a MATLAB-based algorithm that performs the KQ method for the purpose of designing customized limit regulators on core speed, engine pressure ratio, turbine exit temperature, and combustor static pressure. This code is extracted and modified to design the stall margin controller.

For this work, both K and Q are selected to be second-order. The form of K is chosen based on the structure of the limit regulators already present in the C-MAPSS engine control system

$$K = \frac{as^2 + bs + c}{(s - p_1)(s - p_2)} \tag{4}$$

In this expression for K, p_1 and p_2 are defined a priori, while a, b, and c are unknown parameters to be solved for. Q is defined by specifying its damping ratio (ζ) and undamped natural frequency (ω_n). Hence, Q has the form

$$Q = \frac{\omega_n^1}{s^2 + 2\zeta\omega_n s + \omega_n^2} \tag{5}$$

The model-matching method is then applied to a linearized model of the C-MAPSS engine. The equilibrium point used for the linearization corresponds to a TRA of 0 deg with a deteriorated engine at sea-level static conditions. This point was chosen since the equilibrium fan speed is relatively close to the fan speed at which the HPC stall margin reaches a minimum during a burst transient from 0 deg to 100 deg TRA. The details of this transient and the engine deterioration level are presented in Sec. 7.

A qualitative and somewhat informal procedure is used to determine appropriate values for the four design variables: placement of the two poles of K, and the damping ratio and natural frequency of Q. The selection is based on the closed-loop response using the stall margin controller to a demanded increase in HPC stall margin of approximately 8%. The parameters are chosen such that the response is relatively quick while minimizing oscillations and overshoot as much as possible. It is important to note that although the controller is designed with a linearized model, its performance is judged utilizing the nonlinear engine model. It has been observed that certain controllers, which produce favorable, closed-loop responses with the linear model, actually destabilize the nonlinear system. For this work, both poles of K are placed at -20; the damping ratio and natural frequency of Q are chosen to be 0.7 and 40 rad/s, respectively. The performance of this stall margin controller is presented in Fig. 8, which depicts the response of the nonlinear engine model running at 0 deg TRA and sea-level static conditions. The stall margin controller is activated at the 20 s mark.

5 Implementation

The ideal implementation of the stall margin controller would involve feeding back actual HPC stall margin to the controller. However, this is not realistic since stall margin is an unmeasurable parameter. Instead, correlation measure events are used as a representative feedback input for the controller. The implementation method utilized in this work is a combination of event-based stall margin estimation and control mode blending.

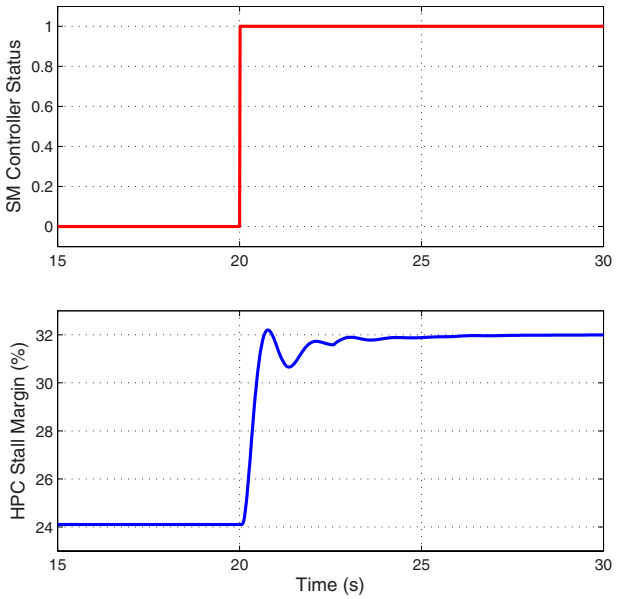

Fig. 8 Stall margin controller is activated at 20 s. Response of nonlinear engine model to a demand of an extra 8% HPC stall margin.

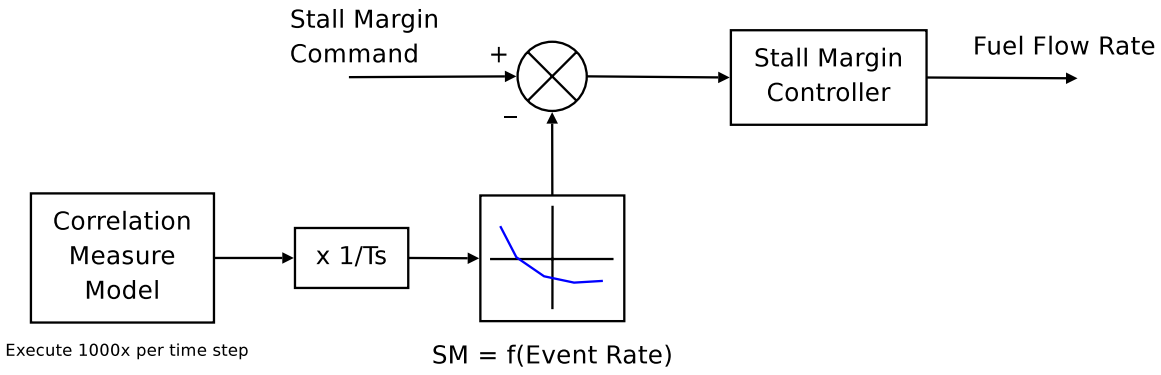

Fig. 9 Stall margin control mode driven by correlation measure

The structure of the stall margin mode is summarized in Fig. 9. The estimation process exploits the experimentally observed relationship between stall margin and event rate. The data set utilized is shown in Fig. 10 and corresponds to the 0.64-threshold case from the experiments conducted on the research compressor (Fig. 5). At each controller time-step, the stochastic model is executed 1000 times. The stall margin for a particular time-step is then estimated from the event rate for that time interval, which is obtained by dividing the number of events by the time-step value. This estimated stall margin value is then routed to the stall margin controller. For instance, suppose for a particular time-step, the stochastic model produced 15 events. C-MAPSS has an update rate of 15 ms. Hence, the corresponding event rate for this time-step is 1000 events/s. From Fig. 10, this corresponds to an estimated stall margin of approximately 5%.

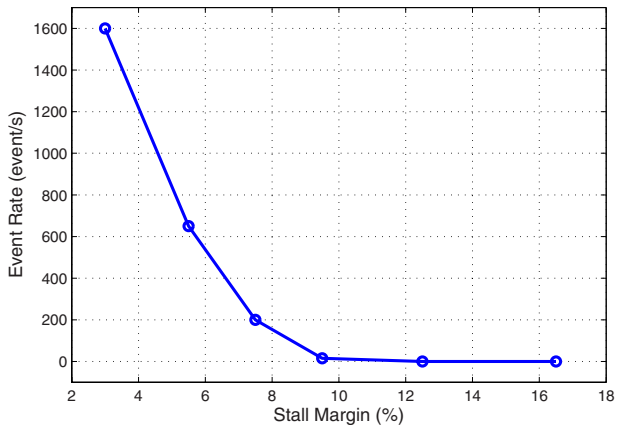

Fig. 10 Event rate/stall margin data set used for stall margin control mode

The combination of the stall margin controller, the correlation measure, and the event-based estimation technique forms the structure of the stall margin control mode. A blending procedure is used to facilitate switching between this mode and the conventional engine control logic. In this case, the conventional control mode is defined as all the original components of the C-MAPSS control system excluding the acceleration limiter (Fig. 11). This comprises of the fan speed controller and the limit regulators on HPT exit temperature, combustor static pressure, and core speed. The acceleration limiter is omitted since the stall margin mode is used for compressor stall/surge protection. The blending process is essentially a weighted average of the $\dot{w}_f$ values calculated by both modes

$$\dot{w}_f = \dot{w}_{f,\text{conv}}(1 - W) + \dot{w}_{f,\text{SM}}(W) \tag{6}$$

The weighting factor W is based on the estimated stall margin value (Fig. 12). This relationship implies that the stall margin mode has no effect if the estimated stall margin is greater than 8%. On the other hand, the stall margin mode has full control authority if stall margin is estimated at less than 3%. For the sector between 8% and 3%, the relative authority of the stall margin mode varies inversely with estimated stall margin.

6 Numerical Experiments

The effectiveness of the stall margin control mode can only be assessed when the compressor of the C-MAPSS engine operates near its stability limit. To this end, a combination of transient engine operation and component degradation has been employed. No inlet distortions are assumed. The metrics for evaluation are (1) the ability of the stall margin mode to prevent compressor

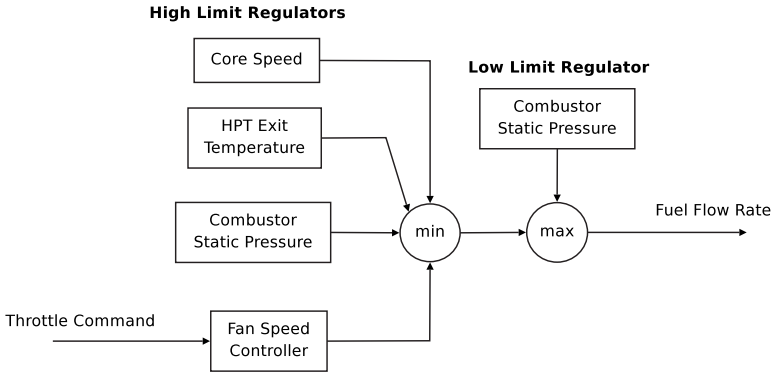

Fig. 11 Conventional engine control mode. Identical to original engine control system with omission of acceleration limiter.

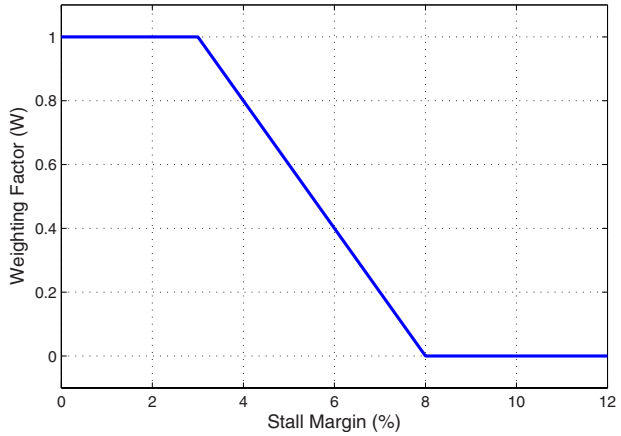

Fig. 12 Relationship between weighting factor and stall margin determines relative control authority of the stall margin control mode

stall, and (2) the time taken by the engine to complete the desired transient.

The rapid increase in fuel flow during an engine acceleration causes the compressor to operate at lower stall margins. Accordingly, the experiments conducted using the engine simulation involve a large step command in TRA from 0 deg (idle) to 100 deg (full power) at standard sea-level static conditions. The thrust response of a nominal engine to this input is shown in Fig. 13. Additionally, Fig. 14 depicts the time history of the HPC stall margin and the trajectory of the transient on the compressor map. As expected, the HPC operates closer to its stability threshold during the transient, causing a significant loss in available stall margin during the acceleration process. This run with the nominal engine acts as the baseline case against which the stall margin control mode is evaluated.

As evidenced by this nominal engine response, the C-MAPSS engine and control system are designed to maintain an excess of HPC stall margin even for a demanding TRA command. The minimum stall margin value attained during the acceleration is approximately 11%. However, when the engine components are degraded, the HPC stall margin is further decreased. Therefore, the stall margin mode is evaluated on a degraded engine. Table 1 lists typical component efficiency modifier values after 3000 and 6000 operation cycles.

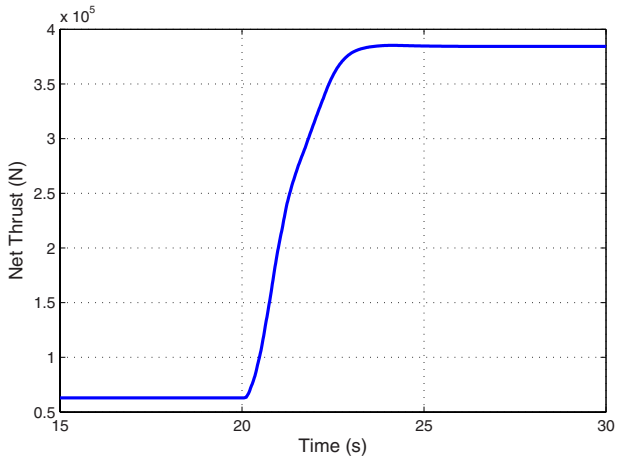

Fig. 13 Nominal engine: net thrust response to step TRA command (step time at 20 s) from 0 deg to 100 deg at standard sea-level static conditions

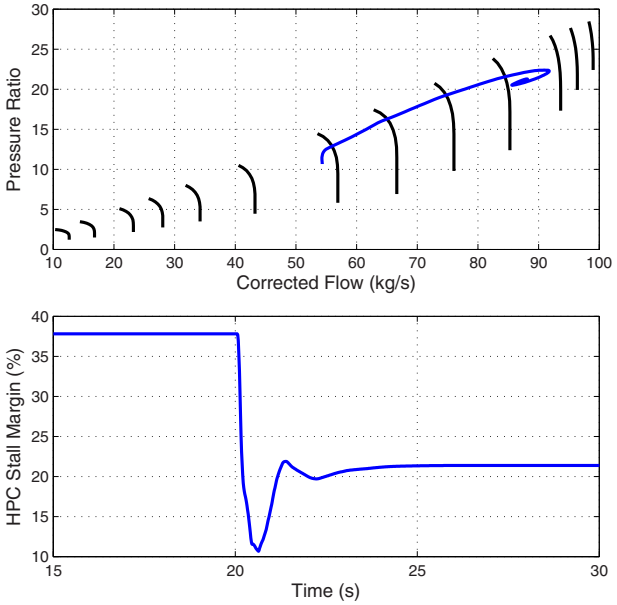

Fig. 14 Nominal engine: trajectory of burst transient represented on compressor map; HPC stall margin response

For this work, HPC and HPT efficiencies are degraded by 5% and 3%, respectively. Moreover, HPC pressure ratio is decremented by 6%, which is in accordance with previous studies [9]. The trajectory of the transient and the corresponding time evolution of the HPC stall margin for this deteriorated engine are shown in Fig. 15. As a result of component degradation, the operating point prior to the transient is now closer to the stability threshold. Furthermore, stall margin attains a nonpositive minimum value, suggesting that the control system, specifically the acceleration limiter, is unable to protect the engine from compressor instabilities for this level of deterioration. Since the engine simulation lacks a poststall model, any information on the engine obtained after the stall margin reaches a nonpositive value (shown as the dotted portion of the plots) is considered invalid. By the same reasoning, the net thrust response for this deteriorated case is omitted.

Three simulation studies are performed utilizing this engine model. First, the baseline case is the aforementioned burst transient from 0 deg to 100 deg TRA at sea-level standard conditions with the nominal engine. Next, the transient is performed with the degraded engine, but enhanced with the stall margin control mode. However, the stall margin mode and blending procedure operate on a true stall margin for this case, representing an ideal but unattainable active control scenario. This is to independently evaluate the effectiveness of the control mode before introducing the correlation measure. Last, the degraded engine is run with active compressor stability management: The stall margin mode is both activated and driven by correlation measure-based events.

Table 1 Typical efficiency modifiers for engine component deterioration [16]

Component	3000 cycles (%)	6000 cycles (%)
Fan	−1.50	−2.85
LPC	−1.46	−2.61
HPC	−2.94	−9.40
HPT	−2.63	−3.81
LPT	−0.54	−1.08

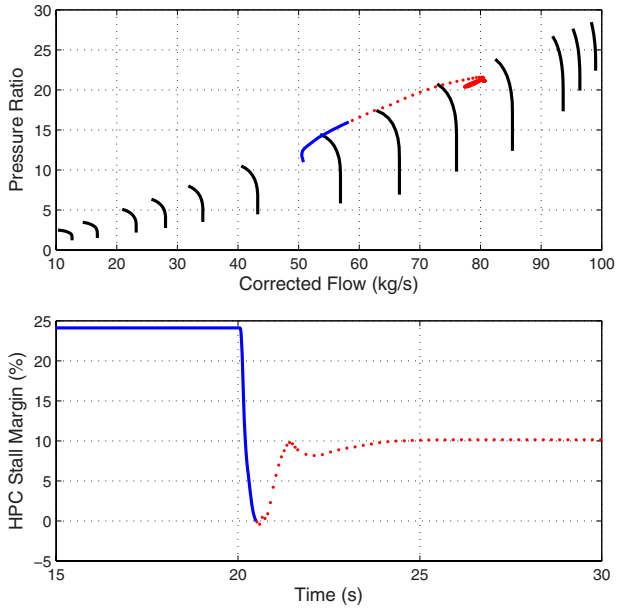

Fig. 15 Degraded engine: trajectory of burst transient represented on compressor map; HPC stall margin response. The dotted portion represents the data considered invalid after stall margin has reached a nonpositive value.

7 Results and Discussion

The effectiveness of the stall margin control mode and active stability management is analyzed in this section. To do so, it is useful to define a rise time metric as the time between the TRA step time (20 s mark) and the point at which the engine reaches 95% steady-state net thrust. The baseline case, which uses the nominal engine and whose results are shown in Figs. 13 and 14, has a rise time of approximately 2.70 s.

7.1 Stall Margin Control Mode. The stall margin mode is first evaluated independently. Instead of the correlation measure events, true HPC stall margin is fed back to the stall margin controller. Figure 16 compares the time evolution of the net thrust and stall margin during the burst transient for this case with the baseline run. The large difference between the steady-state stall margin values, both before and after the transient, represents the effects of engine degradation. The rise time attained is approximately 3.05 s. Hence, the stall margin mode is able to protect the degraded engine from compressor instabilities, with a minimal increase in acceleration time.

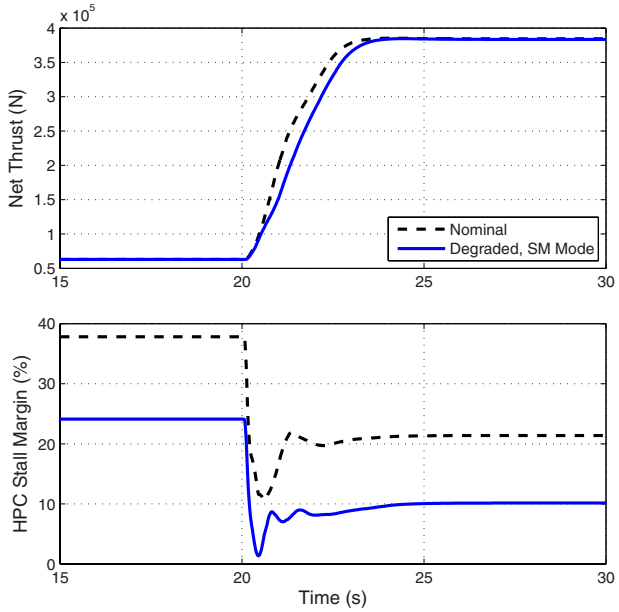

Fig. 16 Independent stall margin mode (degraded engine): net thrust and HPC stall margin

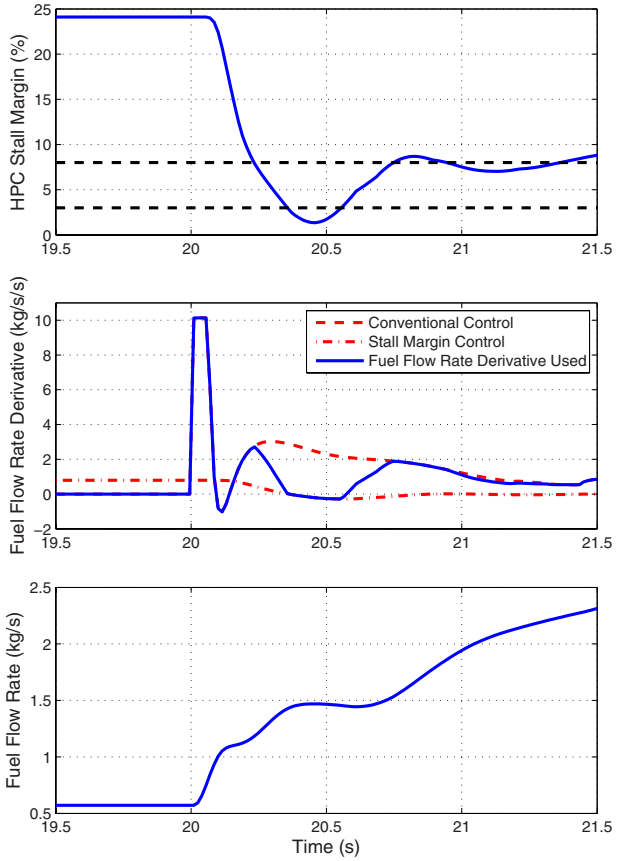

Fig. 17 Independent stall margin mode (degraded engine): stall margin controller activation limits; mode switching through blending; fuel flow command after integration

Figure 17 offers more insight into the interactions between the stall margin mode and the rest of the engine control system. Note that in order to focus on the region of low stall margin, the time scale used for all three plots differs from that in the previous results. The first plot shows the HPC stall margin of the degraded engine. The dashed lines demarcate the stall margin values of 8% and 3%. Recall that the stall margin controller is partially active via blending when stall margin is in that range and only fully active below 3%.

The second plot illustrates the mode switching process. The dashed line represents the $\dot{w}_f$ values calculated by the C-MAPSS engine controller while omitting the acceleration limiter. The dashed-dotted line is the $\dot{w}_f$ from the stall margin controller to a constant demanded HPC stall margin of 8%. The actual $\dot{w}_f$ used follows the engine controller output until stall margin falls below 8%. Between 8% and 3%, $\dot{w}_f$ falls between the values calculated by the two control modes, favoring the stall margin controller output as the HPC loses stall margin. Below 3%, $\dot{w}_f$ follows the stall margin controller completely.

The third plot depicts the fuel flow command sent to the fuel actuator after integrating $\dot{w}_f$. There is a slight plateau near the 20.5 s mark corresponding to the fully activated stall margin control mode.

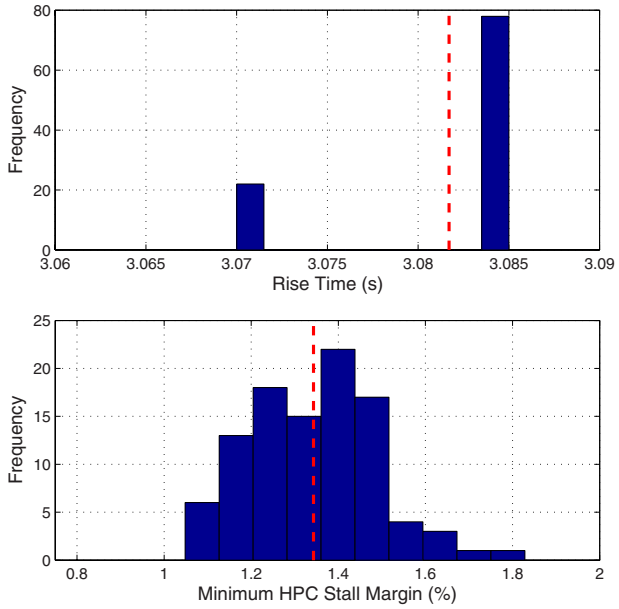

Fig. 18 Active stability management (degraded engine): results of Monte Carlo simulation study. The dashed line represents mean value.

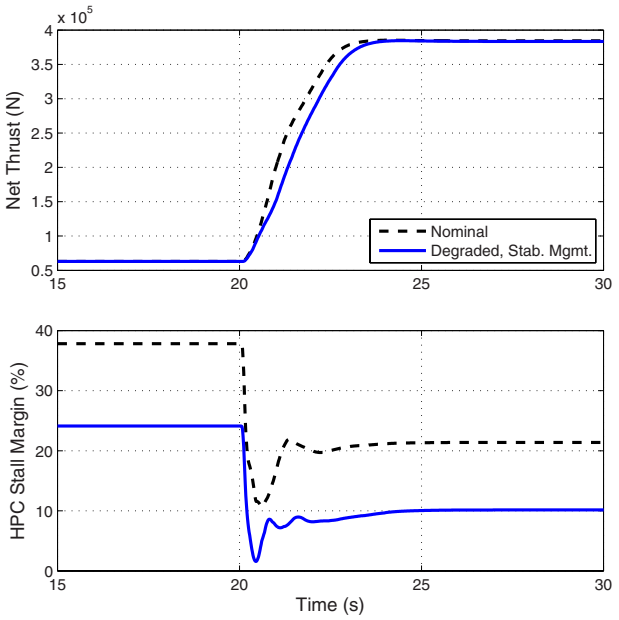

Fig. 19 Active stability management (degraded engine): net thrust and HPC stall margin

7.2 Active Compressor Stability Management. The effectiveness of the stall margin control mode is retained after augmenting the system with the correlation measure. Since the nature of the correlation measure model is not deterministic, a Monte Carlo simulation study is performed. The study consists of running the burst transient with active stability management 100 times while varying the seed value for the pseudo-RNG of the stochastic model. It is expected that 100 trials are sufficient to produce a statistically significant set of results. The values of rise time and minimum HPC stall margin for the 100 runs, presented in histogram form (Fig. 18), are quite consistent. The average rise time (shown as the dashed line) is approximately 3.08 s. The 15 ms separation between the two distinct rise time values corresponds to the update rate of the engine simulation. The average minimum HPC stall margin attained is 1.34%, with no trial reaching 0% or below.

The net thrust and stall margin time histories of a representative case, randomly selected from the 100 trials, are shown in Fig. 19. A comparison with the results shown in Fig. 16 indicates that there is virtually no difference in engine performance between the active stability management system and the independent stall margin control mode.

However, the differences between the control schemes are evident when examining the $\dot{w}_f$ commands (Fig. 20). The plots focus on the low stall margin portion of the transient. The first plot is a time trace of the number of correlation measure events at each controller time-step. The event rate is proportional to the number of events and, hence, follows the same trend. The number of events increases with decreasing stall margin, represented as the dashed-dotted line in the second plot.

The second plot also shows the estimated stall margin obtained from the event rate. The initial disparity between the actual and estimated stall margins prior to the transient is a result of the correlation measure's inability to estimate large stall margin values. The shape of the function relating event rate to stall margin (Fig. 10) is such that the event rate essentially reduces to zero for stall margins above 12%. Thus, this estimate error reflects the fact that stall margins above this value are indistinguishable from one another. Nevertheless, since the stall margin mode is not activated until stall margin reaches 8%, this error does not adversely affect engine control. Below 12%, this estimation method provides a satisfactory level of accuracy for this application.

The high-frequency fluctuations present in the estimated stall margin values are a consequence of the stochastic nature of the correlation measure. Since the estimated values are used for the stall margin controller, as well as the blending process, the transitions between the control modes are not as smooth as in the previous case. As the third plot suggests, the high-frequency portion of the estimated stall margin signal carries over to $\dot{w}_f$ when the estimate lies between 8% and 3%. Regardless, the fluctuations in $\dot{w}_f$ do not noticeably impact the fuel flow command to the fuel actuator due to integration of the signal. Therefore, the fuel flow command for this run is nearly identical to that using true HPC stall margin. By the same token, since thrust is a strong function of fuel flow rate, this explains the similarity in the net thrust response of the two cases.

8 Discussion

The results presented here suggest that it is possible to realistically implement a stall margin control mode by incorporating the correlation measure. With this control mode, it is possible to perform a transient with an engine deteriorated to the point at which its default control system is unable to protect it from compressor instabilities. The level of deterioration chosen for this study is between 3000 and 6000 operational cycles. The minimum HPC stall margin attained while using stability management is approximately 1.3%. In fact, it is possible to accommodate higher levels of degradation and/or increase the minimum stall margin by tuning certain variable parameters in the implementation scheme. Namely, these parameters are the commanded value for the stall margin controller, and the relationship between estimated stall margin and the weighting factor used in the blending process. However, as expected, the acceleration times will increase if these variables are modified in the conservative direction.

It may be noted that the process of blending in the stall margin controller inherently mitigates the impact of "false positives." A false positive for this application is defined as an event observed at relatively high stall margin values. On its own, such an event would incorrectly indicate proximity to the compressor stability limit. However, a false positive would be a relatively isolated incident, yielding a low-event rate and consequently a relatively

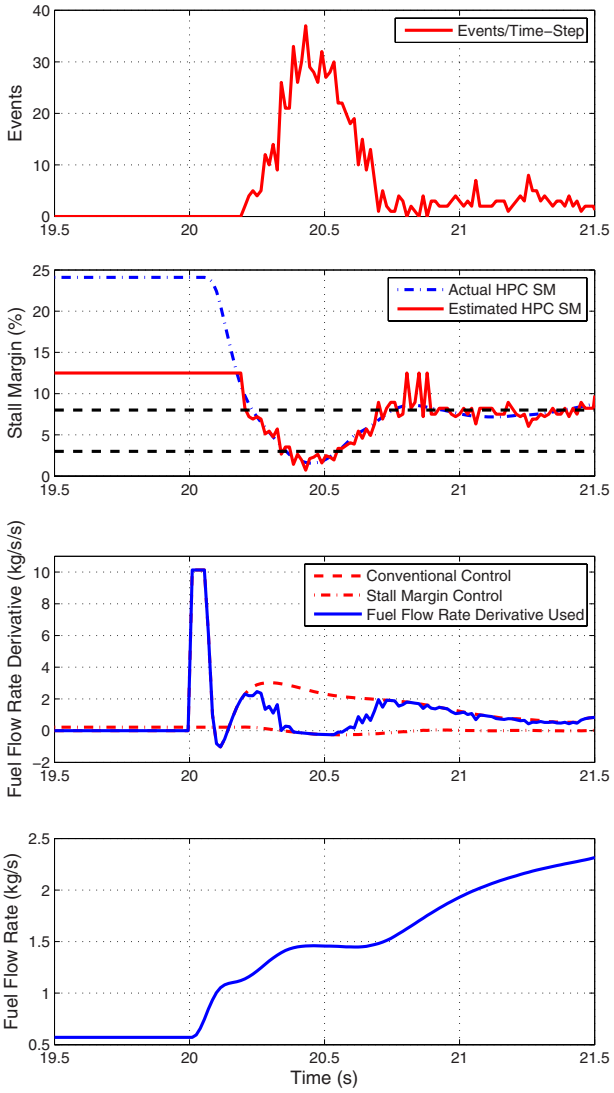

Fig. 20 Active stability management (degraded engine): events at each time-step; estimated stall margin values and controller activation limits; mode switching through blending; fuel flow command after integration

high stall margin estimate. The weighted blending ensures that a false alarm has a negligible impact on the control signal.

This implementation of the stall margin mode is based on the knowledge of the relationship between compressor stall margin and correlation measure event rate. This information is specific to each type of machine and must be obtained from experiments or computational methods. This simulation study assumes a relationship with relatively high event rates. The convenience of such a choice is the greater resolution available to estimate stall margin using simple interpolation/extrapolation methods. Indeed, it is more difficult to obtain an accurate estimate if the difference between stall margins of 0% and 10% is on the order of 10 instead of 1000 events/s. It is possible to partially alleviate the difficulties of a low-event rate scenario by selecting higher threshold values for the correlation measure. As one might expect, a higher threshold increases the event rate for a given compressor loading (Fig. 5). Furthermore, the time window over which the event rate is calculated is variable. Currently, the events are averaged over a single controller time-step. If the time separation between events is greater than that assumed in this work, this time window can be elongated to obtain a more accurate event rate value.

Another important assumption made in this study is that the stall margin-event rate relationship is essentially consistent in the presence of engine deterioration. Specifically, it is assumed that deterioration affects the compressor operating point (as shown in Figs. 14 and 15), and hence stall margin and event rate, but not the general relationship between these latter two parameters. Since the correlation measure has been evaluated using data from several different machines (and hence different levels of deterioration), it is reasonable to expect that the nature of this relationship is consistent. A formal validation, however, will depend on the type of component degradation (i.e., changes in compressor rotor tip clearance) and subsequent experimental or computational analysis.

Finally, a formal stability and robustness analysis of the closed-loop system was not performed for this work. Figure 8 shows at least numerically that for the controller considered (localized at the sea-level static operating point), switching between the conventional and stall margin control modes does not cause instability. Moreover, results from the Monte Carlo study (Fig. 18) indirectly suggest a level of system robustness to the stochastic elements of the correlation measure. However, for a formal validation of overall system stability and robustness, some of the issues that must be addressed include (1) lack of an analytical expression for the nonlinear dynamical system since C-MAPSS utilizes numerous performance maps, (2) blending of the control modes, and (3) nondeterministic nature of the correlation measure model. Such an analysis would be difficult but may be feasible with certain simplifying assumptions, such as linearization of the plant and simplified characterization of the randomness in the feedback signal. The problem may then be cast as the analysis of a linear system with stochastic feedback.

9 Conclusions

The implementation of an active compressor stability management system on a high-bypass turbofan engine with a realistic, conventional control system has been demonstrated in a simulation environment. The stability management system is the integration of two entities: the correlation measure and the stall margin control mode. Past research has established a strong relationship between the correlation measure and operational proximity to the compressor stability limit. The correlation measure, which is rooted in the physics of the flow field over the compressor rotor, is emulated in the simulation environment using a stochastic model that captures its statistical properties. The stall margin control mode is designed using the model-matching, or *KQ*, method. This technique has been previously used in the designs of model-based control systems and a scheduled, multivariable engine controller.

In this work, the model-matching algorithm is used to design a relatively simple single-input, single-output point controller for HPC stall margin. The effectiveness of the stall margin mode is assessed and established by using actual stall margin as a feedback parameter. Stall margin feedback is then substituted with correlation measure-based events, representing a practical implementation of the control mode. The simulation studies show that this resulting active stability management system is successful in preventing compressor instabilities.

The present paper establishes a basic control framework for the integration of a stochastic measure for active compressor stability management and presents results to demonstrate its feasibility. The following describes some items for future work. The stall margin mode for active stability management considered in this study is localized to sea-level static conditions. It is necessary to expand the control mode for operation across the entire flight envelope. Additionally, the case of relatively low-event frequency needs to be assessed by raising the threshold for the correlation measure and/or increasing the window over which the event rate is calculated. Finally, a formal analysis of stability and robustness, though not easily amenable to the current system, is needed to

provide additional confidence in the effectiveness of the proposed stall margin mode controller beyond the current empirical evaluations.

Acknowledgment

The authors would like to acknowledge the NASA Glenn Research Center for developing and providing C-MAPSS. This work is partially funded by GE Aviation through the University Strategic Alliance (GEUSA) program. Y.L. is supported by the National Defense Science and Engineering Graduate Fellowship (NDSEG) program.

Nomenclature

$C(n)$ = correlation measure
i = index
K = controller transfer function
n = sample index
p = pressure signal
Q = desired response transfer function
N = number of samples per shaft rotation
w_f = fuel flow rate (kg/s)
$\dot{w}_f$ = rate of change in fuel flow rate (kg/s/s)
wnd = window size in number of samples

References

[1] Adibhatla, S., Brown, H., and Gastineau, Z., 1992, "Intelligent Engine Control (IEC)," *Proceedings of the 28th AIAA/ASME/SAE/ASEE Joint Propulsion Conference and Exhibit*, Nashville, TN, Paper No. AIAA-92-3484.

[2] Adibhatla, S., and Lewis, T. J., 1997, "Model-Based Intelligent Digital Engine Control (MoBIDEC)," *Proceedings of the 33rd AIAA/ASME/SAE/ASEE Joint Propulsion Conference and Exhibit*, Seattle, WA, Paper No. AIAA-1997-3192.

[3] Parker, K., and Guo, T., 2003, "Development of a Turbofan Engine Simulation in a Graphical Simulation Environment," Technical Report No. TM-2003-212543.

[4] Dhingra, M., Neumeier, Y., Prasad, J. V. R., and Shin, H., 2003, "Stall and Surge Precursors in Axial Compressors," *Proceedings of the 39th AIAA/ASME/SAE/ASEE Joint Propulsion Conference and Exhibit*, Huntsville, AL, Paper No. AIAA-2003-4425.

[5] Christensen, D., Cantin, P., Gutz, D., Szucs, P., Wadia, A., Armor, J., Dhingra, M., Neumeier, Y., and Prasad, J., 2006, "Development and Demonstration of a Stability Management System for Gas Turbine Engines," *Proceedings of the ASME Turbo Expo 2006: Power for Land, Sea and Air*, Barcelona, Spain, Paper No. GT2006-90324.

[6] Dhingra, M., Neumeier, Y., Prasad, J., Breeze-Stringfellow, A., Shin, H., and Szucs, P., 2007, "A Stochastic Model for a Compressor Stability Measure," ASME J. Eng. Gas Turbines Power, **129**(3), pp. 730–737.

[7] Liu, Y., Dhingra, M., and Prasad, J., 2008, "Benefits of Active Compressor Stability Management on Turbofan Engine Operability," *Proceedings of the ASME Turbo Expo 2008: Power for Land, Sea and Air*, Berlin, Germany, Paper No. GT2008-51307.

[8] Frederick, D., DeCastro, J., and Litt, J., 2007, "User's Guide for the Commercial Modular Aero-Propulsion System Simulation (C-MAPSS)," Technical Report No. TM-2007-215026.

[9] Dhingra, M., Armor, J., Neumeier, Y., and Prasad, J., 2005, "Compressor Surge: A Limit Detection and Avoidance Problem," *Proceedings of the AIAA Guidance, Navigation, and Control Conference and Exhibit*, San Francisco, CA, Paper No. AIAA 2005-6449.

[10] Dhingra, M., 2007, "Compressor Stability Management," Ph.D. thesis, Georgia Institute of Technology, Atlanta, GA.

[11] Cramer, H., and Leadbetter, M., 1967, *Stationary and Related Stochastic Processes*, Wiley, New York.

[12] Edmunds, J., 1979, "Control System Design and Analysis Using Closed-Loop Nyquist and Bode Arrays," Int. J. Control, **30**(5), pp. 773–802.

[13] Qi, O., Gawthrop, P., and Maccallum, N., 1992, "Mode-Based Observer: A Gas Turbine Engine Case Study," *Proceedings of the IEEE Conference on Control Applications*, Dayton, OH.

[14] Polley, J., Adibhatla, S., and Hoffman, P., 1989, "Multivariable Turbofan Engine Control for Full Flight Envelope Operation," ASME J. Eng. Gas Turbines Power, **111**, pp. 130–137.

[15] Maciejowski, J., 1989, *Multivariable Feedback Design*, Addison-Wesley, Wokingham, England.

[16] Chatterjee, S., and Litt, J., 2003, "Online Model Parameter Estimation of Jet Engine Degradation for Autonomous Propulsion Control," *Proceedings of the AIAA Guidance, Navigation, and Control Conference and Exhibit*, Austin, TX, Paper No. AIAA-2003-5425.

New Steel Alloys for the Design of Heat Recovery Steam Generator Components of Combined Cycle Gas Plants

Jorge Pinto Fernandes
Project Engineer
ETD, European Technology Development,
ISEL, Instituto Superior de Engenharia de Lisboa;
ETD–6 Axis Centre,
Cleeve Road, Leatherhead,
Surrey KT22 7RD, UK
e-mail: jfernandes@etd1.co.uk

Eduardo Manuel Dias Lopes
R&D Director of Research and Development Division
ISQ, Instituto da Soldadura e Qualidade,
ISEL, Instituto Superior de Engenharia de Lisboa;
ISQ–Rua Dr. Cavaco Silva, no. 33,
Tagus Park 2740-120 Porto Salvo, Portugal
e-mail: edlopes@isq.pt

Vicente Maneta
Manufacturing Engineer Director
Alstom Power,
Estrada Nacional 10-4,
Mitrena 2910-738 Setúbal, Portugal
e-mail: vicente.maneta@power.alstom.com

Demand for power is growing everyday, mainly due to emerging economies in countries such as China, Russia, India, and Brazil. During the last 50 years steam pressure and temperature in power plants have been continuously raised to improve thermal efficiency. Recent efforts to improve efficiency leads to the development of a new generation of heat recovery steam generator, where the Benson once-through technology is applied to improve the thermal efficiency. The main purpose of this paper is to analyze the mechanical behavior of a high pressure superheater manifold by applying finite element modeling and a finite element analysis with the objective of analyzing stress propagation, leading to the study of damage mechanism, e.g., uniaxial fatigue, uniaxial creep for life prediction. The objective of this paper is also to analyze the mechanical properties of the new high temperature resistant materials in the market such as 2Cr Bainitic steels (T/P23 and T/P24) and also the 9–12Cr Martensitic steels (T/P91, T/P92, E911, and P/T122). For this study the design rules for construction of power boilers to define the geometry of the HPSH manifold were applied. [DOI: 10.1115/1.3204563]

Keywords: heat recovery steam generator, Benson once-through technology, finite element modeling, finite element analysis, stress analysis, uniaxial fatigue life assessment, uniaxial creep life assessment, steel alloy mechanical properties, 2 1/4 Cr Bainitic steels, 9–12Cr Martensitic steels

1 Introduction

From the past to the actuality, engineering design process of boiler pressure parts are designed based on codes, e.g., ASME Boiler and Pressure Vessel Code [1], providing basic information to define the dimensioning of piping, headers, manifolds, and boiler valves. Today, with the advancement of technology, creating a better understanding of engineering design concept using stress propagation analysis created and applied, during the design process, not only the rules for construction of power boilers (Section I) and "design-by-rules" approach [2] (Design by Rule Requirement Section VIII division 2), but also the "design-by-analysis" methodology [2] (Design by Analysis Requirements) using the results from stress analysis, providing a better evaluation of the component performance, avoiding plastic collapse, local failure, buckling, or cyclic loading.

Meanwhile, the world is facing new challenges where environmental protection plays the most important rule. New technology techniques improve old power generation systems, creating modern power generation raising power station efficiency, producing more energy, reducing fuel consumption, and gas emissions. In parallel with modern coal power plants, combined cycle gas turbines (CCGTs) achieve one of the most efficient operation condition, where the Benson once-through technology [3–5] is applied to both thermal power plant technologies. Today, the development of gas turbine, heat recovery steam generators, and high-temperature materials give birth to the fourth generation combined cycle plants, reaching 60% or higher efficiency [6].

All the mentioned factors, design, and technology lead the power plant equipments to operate at higher temperatures, raising the metal temperature and creating a push and pull approach through the R&D companies, with the objective of developing new temperature resistant and high strength materials. With the purpose of following these new requirements, European, US, and Asian countries are developing new steel alloys for advanced steam cycle and/or ultrasupercritical pressure power plants, developing the series of 2 % Cr Bainitic Steels (T/P23 and T/P24) and 9–12% Cr Martensitic Steels (T/P91, 92, E911, and T/P122).

To analyze all these factors, a finite element analysis is performed, taking into account the boiler design, operation conditions, and new steel alloy properties, defining the impact of solutions in the mentioned factors.

2 Heat Recovery Steam Generator

A heat recovery steam generator (HRSG) is a recovery boiler that uses the heat from a gas turbine exhaust flow. The heat flow from the exhausted gases is used to produce superheated steam in the HRSG modules, and after this process, superheated steam is used in conventional steam turbines [7]. With this solution, depending on the displacement of the gas turbine, generator, and steam turbine, coupling a gas and a steam turbine in a single shaft provide the generator with a higher kinetic energy in the generator electric shaft, thereby producing in this way an additional fraction of electric energy.

Recently, Alstom Power incorporate Benson once-through evaporator technology [8] developed by Siemens into its new generation of HRSGs, where it will be connected with Alstom's Optimized for Cycling and Constructability (OCC) [9].

The case showed in this study is a triple pressure HRSG with nine modules, five sections with three splitting each section (Fig. 1).

During this study the main focus will be the high pressure superheater (HPSH) module, where the critical elements will be

Contributed by the International Gas Turbine Institute of ASME for publication in the JOURNAL OF ENGINEERING FOR GAS TURBINES AND POWER. Manuscript received March 22, 2009; final manuscript received May 24, 2009; published online March 3, 2010. Review conducted by Dilip R. Ballal. Paper presented at the ASME Gas Turbine Technical Congress and Exposition, Orlando, FL, June 8–12, 2009.

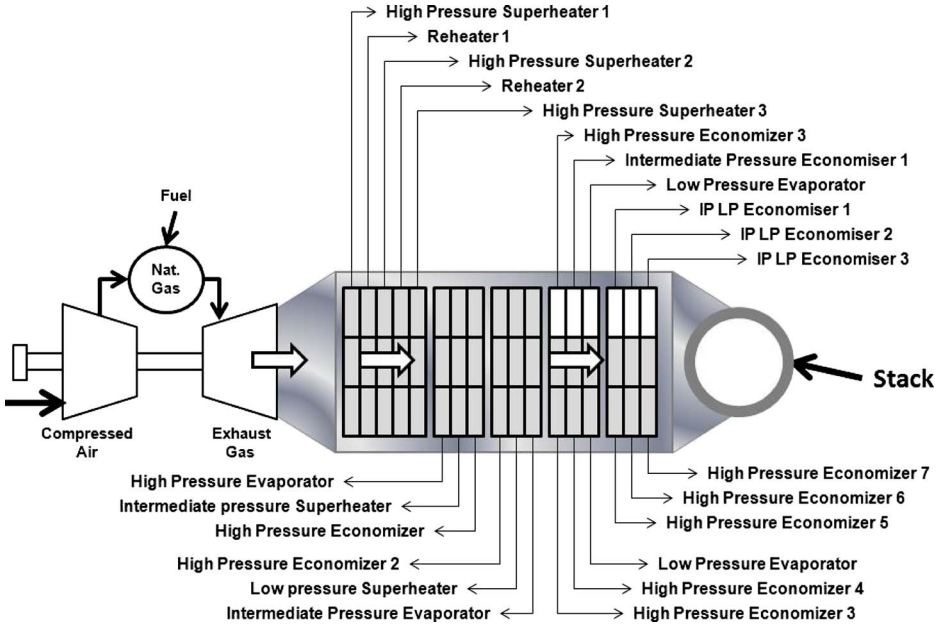

Fig. 1 General representation of the modules displacement of a HRSG

analyzed with especial attention on the HPSH manifold. The design of the HPSH manifold conditions are established in a pressure of 15.4 MPa and with a stamped temperature of 584 °C belonging to a multiunit power station with a capacity of ~400 MW.

3 Design Analysis

The HPSH module (Fig. 2) of a HRSG generally is the first module of the high temperature section, recovering the heat from the exhaust gas of the gas turbine. Therefore, this module is the most solicited because of its exposition to higher temperature, causing high level of stress concentration.

All the module components were designed to meet the minimum thickness requirements in accordance with Section I of ASME Boiler and Pressure Vessel Code, Rules for Construction of Power Boilers. The "diagonal efficiency" and "longitudinal efficiency" were based on an in-house developed method [10,11]. In Ref. [12], an "evaluation of high temperature steel alloys" shown detailed operation conditions of the design process. Table 1 shows a summary of the basic design conditions, geometry, and initial materials used in this component.

The HPSH module shown in Fig. 2 is constituted for some elements that are important for the entire set of components. As mentioned before, this module is a critical component in a HRSG.

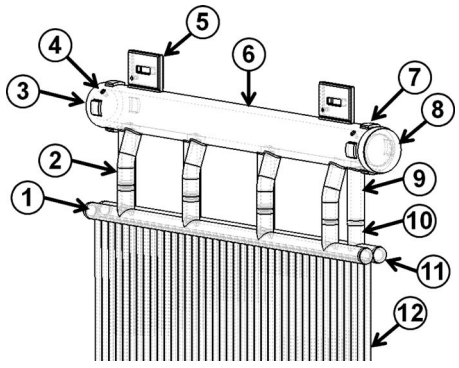

Fig. 2 High pressure superheater module for the finite element analysis purpose

It is designed to be thermal and pressure resistant. The components of the HPSH module are described in Fig. 2 where it is possible to see the (1) header, (2) bending 4″ schedule (SCH) pipe, (3) superheater steam outlet, (4) radiographic hole and plug, (5) manifold support lug, (6) 12″SCH pipe, (7) alignment plates, (8) manifold end plug, (9) strait 4″ SCH pipe, (10) tube to header connection, (11) header end plug, and (12) harps tubing.

Despite the advancement of technology in the field of finite element analysis, complex geometries similar to the one presented in Fig. 2 should be simplified. So the superheater module, constituted by two harps was simplified with the main objective of making the FE simulation more efficient, analyzing only the critical elements (Fig. 3).

One of the most critical elements from a superheater module is the outlet manifold (Fig. 4), where all the superheated steam is collected from the boiler and then sent to the high pressure steam turbine. This critical element was studied separately during the fatigue analysis.

4 Finite Element

According to ASME Boiler and Pressure Vessel code (Section VIII, Division 2) the design-by-analysis is based on the use of the results obtained from a stress analysis of the high pressure superheater manifold, depending on the loading or boundary conditions and defining a thermal analysis; while the design-by-requirements provide design rules for commonly used pressure vessel shapes under pressure loading and the within specified limits, rules, or

Table 1 Design conditions defined using the ASME section I

Design conditions	I.S. units	U.S. units
Design pressure	15.4 MPa	2234 PSIG
Design temperature	584 °C	1083 °F
Manifold outside diameter	323.9 mm	12.75 in.
Manifold nominal thickness	48 mm	1.89 in.
Manifold minimum thickness	29.50 mm	1.16 in.
Pipe outside diameter	114.3 mm	4.5 in.
Pipe minimum wall thickness	14.98 mm	0.59 in.
Pipe average wall thickness	17.12 mm	0.67 in.
Pipe material	SA-335 P91	
Plate material	SA-387 GR22 CL2	

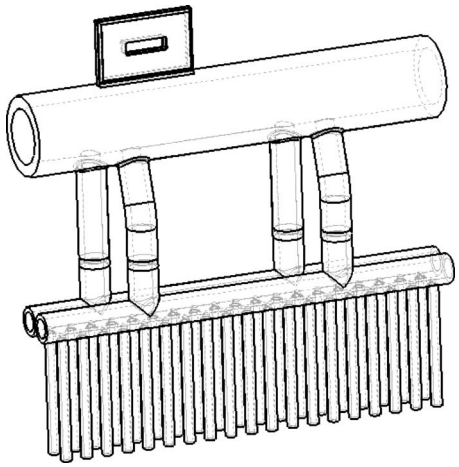

Fig. 3 Simplified high pressure superheater module for the finite element analysis purpose

guidance for treatment of other loadings. Section I of the same code is used to define the dimensioning of the boiler element such as pipes, tubing valves, etc.

Nowadays, the main purposes of finite element are to gather these important design philosophies and unify them, shaping the geometry and bringing the efficiency to the design process.

With the evolution of human necessity and the progress of technology, finite element transformed in two different processes: the modeling process and the analysis process, creating a connection between the SOLIDWORKS and CATIA modeling softwares and multipurpose softwares such as ANSYS. This way it is possible to design complex geometries and define the best procedure to provide a good analysis of the power equipment components.

5 Materials for Power Application

The improvement of thermal efficiency by increasing the operating temperature and pressure of boilers has recently led to the development of new high temperature resistant steel alloys used in thermal power plants.

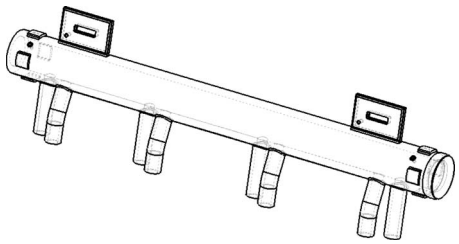

Fig. 4 Trimetric view of the HPSH upper outlet manifold

Table 2 Thermal stress parameters for steam pipe materials

	YT (σ_c) (MPa)	TS (σ_b) (MPa)	Thermal expansion $\times 10^{-6}$/K	Thermal conductivity (W/m K)
P22	205[a]	415[a]	14.3[c]	33.0[c]
P23	400[a]	510[a]	13.9[c]	33.1[c]
P24	415[b]	585[b]	13.7[c]	36.9[c]
P91	415[a]	585[a]	12.9[c]	30.0[c]
$E911_{@600°C}$	285[d]	620[b]	12.0[d]	27.0[d]
$P92_{@600°C}$	368[d]	620[b]	12.0[d]	27.0[d]
$P122_{@584°C}$	265.5[e]	415[e]	14.3[e]	33.0[e]

[a]ASME section II, materials, metric version.
[b]Reference [15].
[c]600°C (Ref. [16]).
[d]Ref. [17].
[e]Extrapolated data.

For 9–12% Cr steels, grade T/P91 (X10CrMoVNb91 according to EN 10216-2), which were developed at the end of the 1970s in the US and first used in the 1980s, marked the starting point for these developments [13,14]. With its excellent mechanical characteristics at elevated temperatures and good workability, it was rapidly adopted worldwide for applications in the field of new power stations in all parts of the world. Today T/P91 type steel is the major subject of discussion in the resurge community. The tube design temperature is limited to around 610°C inside the combustion chamber. This limit depends on factors such as heat flow and corrosion behavior. More recent developments to produce new grades, with improved chemistry (Table 3), such as T/P911 (European E911; X11CrMoWVNb9–1-1) and T/P92, have improved mechanical properties at high temperatures, in particular, an increase in creep strength of 10–20% in 100,000 h at 600°C [18]. This makes it possible to reduce the wall thickness of the pipes and consequently improve their behavior to thermal fatigue. The new grades T/P23 and T/P24 (7CrMoVTiB10–10) are well suited for boiler components working at lower temperatures. While these grades were initially developed for manufacturing water wall panels for ultra super critical boilers (USCB), they are also used for the superheaters and reheaters of conventional boilers and HRSG.

In addition to their excellent workability, they have the advantage of being used without postweld heat treatment (PWHT) in case of welding thin-walled tubes. Furthermore, owing to the good creep properties, they can be used to replace P22 and, for some applications, even P91, with the advantage of lower costs.

Table 2 sets out the characteristics of these new grades that will be used during the FEA. So, resorting to finite element analysis and to develop the geometry, we will analyze the capacity and the behavior of these steel alloys by simulating the operating conditions.

Table 3 Nominal chemical composition of high temperature steel alloys

	Steel alloy					
Element	$T/P23_{[15]}$	$T/P24_{[15]}$	$T/P91_{[18]}$	$E911_{[14]}$	$T/P92_{[19]}$	$T/P122_{[20]}$
C Carbon	0.04–0.10	0.05–0.10	0.08–0.12	0.09–0.13	0.07–0.13	0.11
Si Silicon	≤0,50	0.15–0.45	0.20–0.50	0.10–0.50	0.50	0.1
Mn Manganese	0.10–0.60	0.30–0.70	0.30–0.60	0.30–0.60	0.30–0.60	0.60
Cr Chromium	1.90–2.60	2.20–2.60	8.00–9.50	8.50–9.50	8.50–9.50	12.0
Mo Molybdenum	0.05–0.30	0.90–1.10	0.87–1.13	0.90–1.10	0.30–0.60	0.4
W Tungsten	1.45–1.75	—	—	0.90–1.10	1.5–2.00	2.0
V Vanadium	0.20–0.30	0.20–0.30	1.18–0.25	1.18–0.25	1.15–0.25	0.05
Nb Niobium	0.02–0.08	—	—	0.06–0.10	0.04–0.09	0.05
N Azoth	≤0,030	≤0,01	0.030–0.070	0.040–0.090	0.030–0.070	0.06
B Boron	0.0005–0.006	0.0015–0.007	—	0.0003–0.006	0.001–0.006	0.003

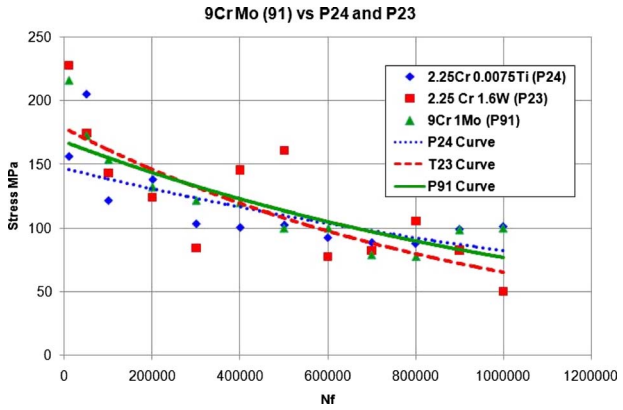

Fig. 5 Representation of stress and number of cycles for P91 and comparison with $2\frac{1}{4}$ Cr steels P24 and P23

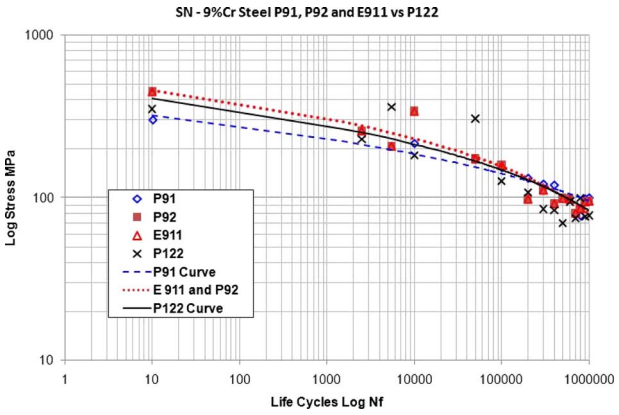

Fig. 7 Logarithmic representation of stress and number of cycles for P122 comparison with 9Cr steel defining one *S-N* curve or Wohler curve

6 Life Assessment Analysis

RLA is a predictive maintenance approach for industrial equipment and other structures with operating methods susceptible to limited life. In specific cases of energy production facilities including conventional thermal power plants, gas turbine combined cycle, cogeneration power plants and other industrial plants such as crude oil refineries, the RLA re-emerged connected with the possibility of exploration activities before the project lifetime finishes, increasing the operation time, pushing the installation to operational and economical limits. In this work we will focus on the behavior of steel alloys in the most important factors for a heat recovery steam generator [19].

7 Uniaxial Fatigue Analysis

Applying the fatigue analysis technique, a general uniaxial fatigue analysis involving the HPSH manifold was developed. The operation condition is identical to the cycle analysis, where the major consideration goes to cold start-up cycle. The FEA data are shown in Fig. 5, where it is possible to compare the mechanical behavior of the new 2% Cr Bainitic steels P23 and P24 and also the 9Cr Martensitic steel P91 submitted in the HPSH manifold.

Analyzing the above diagram below 600,000 cycles, P91 has a good behavior compared with the 2Cr Bainitic P23 and P24 alloys. Meanwhile, above 600,000 cycles, the P91 has a low performance compared with P24, whose capacity to stand high number of cycles during a simulation about 584°C is very good but due to oxidation behavior, the application of P24 is limited to the temperature of 575°C [20]. Figure 6 define the life range for the HPSH manifold geometry, where the right manifold support lug is the element with the lower fatigue life in all the component because it is the restrained support. In future studies, a fixing system must be developed with the objective of improving the data analysis.

P122 is the new Martensitic 12% Chromium steel developed by Japanese experts; nowadays, this steel is being studied in boiler construction as analyzed by Masuyama [21]. A uniaxial fatigue was carried to this steel alloy, comparing with the recent 9Cr Steels P91, P92, and E911 (Fig. 7).

Analyzing the data, the new Grade P122 has a modest fatigue behavior compared with 9% Cr Steels submitted in the HPSH manifold design. But at a higher number of cycles, the performance is higher than in some 9Cr type steels such as P92 and E911. But one fact is that P91 still shows a very good behavior at a high number of cycles, showing a low stress concentration. Meantime, P122 shows a crescent level of thermal conductivity, which is very good for steel with a higher content of chromium. It shows that the thermal expansion grows with the temperature but is not that much significant.

Recent studies present the maximum Cr content of the specification was lowered from 12.50% to 11.50%; the intent was to differentiate the variant due to substantial differences in elevated temperature strength.

Using FEA, a simulation was developed based in the HPSH Manifold, where submitting the geometry of this component to design operation values and using the steel alloy P91 gave the results for the three different fatigue cycles, as presented in Fig. 8.

Regarding the cyclic simulation of steel P91, it is possible to conclude that the applied stress directly influenced the magnitude of the alternating stress or the range of the internal pressure. Comparing the cases of high and small pressure ranges for 1×10^6 cycles (Fig. 8), the only difference between these two operating cases is the magnitude of pressure decay between cycles. Therefore it can be seen that larger alternating stress intensity reduces the allowable stress for the same number of allowable cycles.

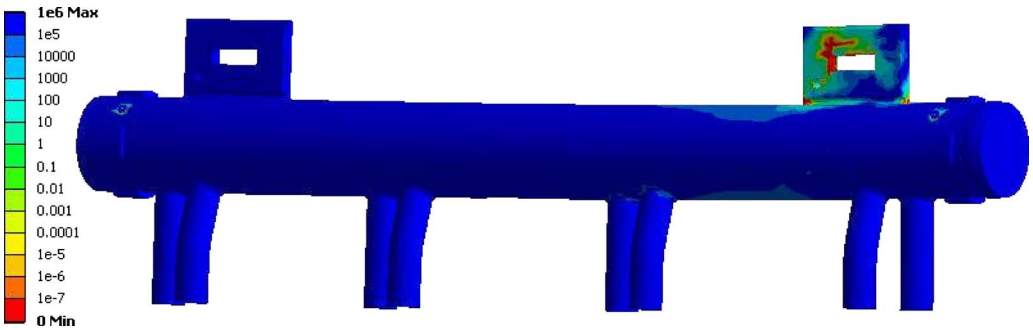

Fig. 6 Number of cycles for SA-335 P91 grade

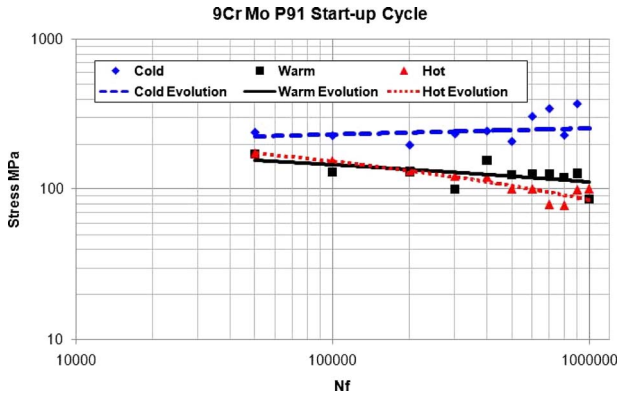

Fig. 8 Fatigue analysis of HPSH manifold subjected to the cyclic loading defining an *S-N* curve

Hence, keeping the alternating stress intensity as small as possible is an important factor for increasing the high cycle fatigue life due to any direct loading.

8 Creep Life Assessment

The master curve for steel alloys represents the average rupture stress values over the range of time, temperature, and stress values used in the prediction of long-term creep-rupture strengths (Fig. 9) for 9Cr steels P91, P92, and E911 as a function of stress and in the form of a time and temperature parameter, following the Manson–Brown Parameter (Eq. (1)), applied by the British Standard Institution (BSI) [22]

$$P_{(\sigma)} = a + b(\log\ \sigma) + c(\log\ \sigma)^2 + d(\log\ \sigma)^3 + e(\log\ \sigma)^4 = \frac{\log\ t - \log\ ta}{(T - Ta)^r} \quad (1)$$

where $P_{(\sigma)}$ is the creep rupture parameter, T is the temperature (K), t is the time to rupture (h), σ is the stress (MPa), r is a temperature exponent, a, b, c, d, and e are constants (see Ref. [22]).

Applying the Manson–Brown Parameter, where the constants for Eq. (2) of the master curve is given in Table 4

$$P_{(\sigma)} = a + b(\log\ \sigma) + c(\log\ \sigma)^2 + d(\log\ \sigma)^3 + e(\log\ \sigma)^4 \quad (2)$$

The master curve shown below (Fig. 9) describe the behavior of 9%Cr steels P91, P92, and E911 (X11CrMoWVNb9–1-1) applied in the design of HPSH module (manifold, header, and tubing). It defines basically the Manson–Brown parameter that we can use during a life assessment analysis. So analyzing the data, the higher

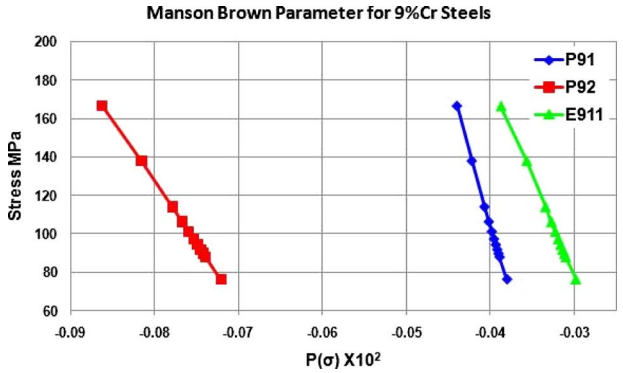

Fig. 9 Master curve for 9% Cr steels P91, P92, and E911 representing the average rupture stress values and the range of Manson–Brown parameter for 584°C

Table 4 Master curve constants

	P91[22]	P92[23]	E911[24]
a	−0.4938277900	−0.921890616	−2.4726
b	0.9749886394	1.94211233	5.1073
c	−0.7671017051	−1.62884569	−3.9845
d	0.2668407261	0.603966355	1.3796
e	−0.03513864124	−0.08465305	−0.17956

the stress in the 9Cr steel pipe is, the smaller the Manson–Brown parameter. Comparing the 9Cr steels, it is easy to conclude that P92 have the lower Manson–Brown parameter and the E911 show the highest values than P91 for the same level of stress.

A similar curve is shown in Ref. [22] for grade 91 on page 87b, but here, we have to consider that the P91 behavior is analyzed with the geometric shape of a high pressure superheater module and not like a simple normalized sample. This element is exposed to a metal temperature of 584°C and a pressure of 15.4 MPa, which induce heavier stresses in the pipe, causing a reduction in its time life. The stress is the equivalent von Misses given by the finite element analysis software.

The equivalent stress is related to the principal stresses (Eq. (3)) as

$$\sigma_e = \left[\frac{(\sigma_1 - \sigma_2)^2 + (\sigma_2 - \sigma_3)^2 + (\sigma_3 - \sigma_1)^2}{2}\right]^{1/2} \quad (3)$$

This equivalent stress σ_e (also called the von Mises stress) is used in design work (Fig. 10) because it allows any arbitrary three-dimensional stress state to be represented as a single positive stress value, making use of the maximum equivalent stress failure theory used to predict yielding in a ductile material. The equivalent stress is also used in the parametric extrapolation techniques for estimation of the long-term creep and rupture strength of materials based on short-duration laboratory tests.

The von Misses or equivalent strain ε is computed (Eq. (4)) as

$$\varepsilon_e = \frac{1}{1+\nu'}\left(\frac{1}{2}[(\varepsilon_1 - \varepsilon_2)^2 + (\varepsilon_2 - \varepsilon_3)^2 + (\varepsilon_3 - \varepsilon_1)^2]\right)^{1/2} \quad (4)$$

where ν' is the effective Poisson's ratio, which is defined as the material Poisson's ratio for elastic and thermal strains computed at the reference temperature. Each material's reference temperature property is used as the reference temperature. If this property does not exist for a material, then the environment's reference temperature uses a coefficient of 0.5 for plastic strains.

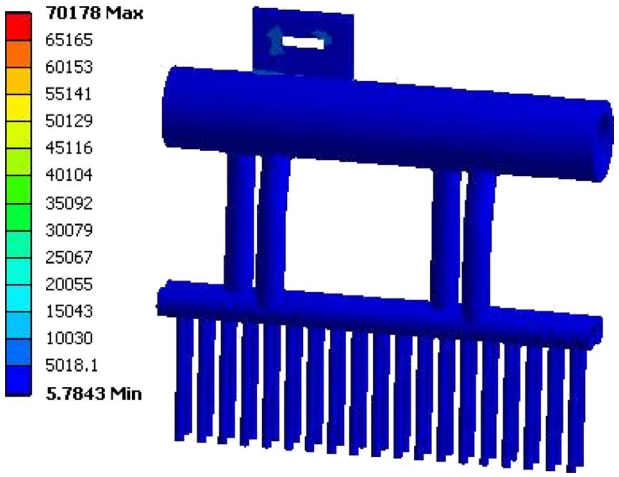

Fig. 10 General equivalent stress representation from the finite element analysis

Table 5 Constants for the parametric equation

	P91[22]	P92[23]	E911[23]
r	1	1	1
ta	370	500	613
Log *ta*	24.75538940	40.5120506	13.3

For reliable predictions, it is necessary to calculate the rupture time, and for that, it is equally necessary for the parametric equation (Eq. (5)) and the constants for this equation, as given in Table 5.

$$P_{(\sigma)} = \frac{\log t - \log ta}{(T - Ta)^r} \tag{5}$$

At the first sign, analyzing the applied constants, we can see that the Manson–Brown parameter transform to the Manson–Haferd parameter. This specific characteristic of the Manson–Brown parameter is very important and valuable because the main objective of parametric extrapolation techniques is extrapolating experimental data, providing the integrity analyzer with reliable and accurate data related with stress concentration and time to rupture. If we force the use of a certain extrapolation technique to a specific steel alloy, the final results will always have an associated error that is considerable if the extrapolation technique chosen is not the best for that specific case. So, the main added value of the Manson–Brown parameter is the possibility to adapt itself to the material and change the form to another extrapolation technique. A similar behavior is detected in the Larson–Miller parameter, when the constant *c* is changed to different steel alloys. But the Manson–Brown parameter goes even further when it simply changes its form according to the steel alloy and the applied constants also follow the material. This characteristic is described by Pinto Fernandes and Dias Lopes [13] when they made the analysis of the Manson–Brown parameter applied to austenitic stainless steel 18Cr 8Ni based on BSI PD 6525.

Related to the Fig. 11 presented below, reductions in stress correspond to higher time to rupture to the specific analyzed component.

Analyzing the data, it is clear that the P92 shows the best behavior when this alloy steel is used in the high pressure superheater module. The development of this new steel alloy P92 suppresses clearly the P91 and shows promissory results when submitted to high and high stress (Fig. 12). With improved chemistry and the same amount of Chromium as P91 the P92, it shows a low stress concentration due to a good thermal conductivity and lower thermal expansion. This characteristic applied to an optimized geometry is prepared to withstand high stresses and gives

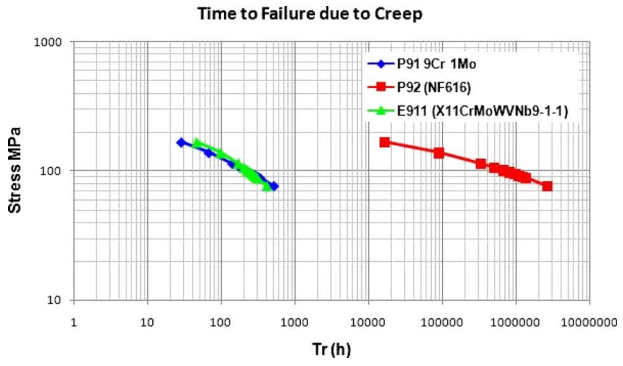

Fig. 11 Master curve for 9% Cr steels P91, P92, and E911 representing the range of stress and the range of rupture time resorts to Manson–Brown extrapolation parameter and HPSH module

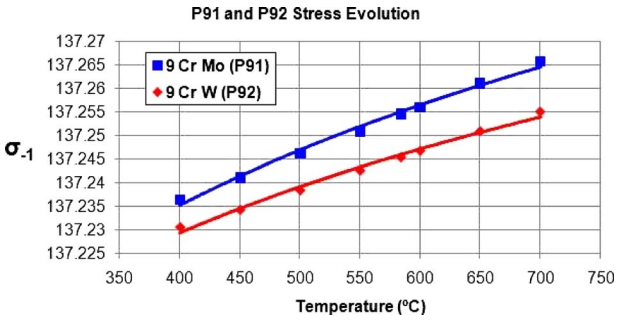

Fig. 12 Stress evolution in the temperature range of 400 –700°C for P91 and P92

birth to a good combination when the most important factors are the possibility to enlarge the predicted life of the component, and consequently, the reliability and possibility of a reduction in probability of forced outage rate due to HPSH manifold failure.

Regarding the European E911 (NF616) during the recent scientific meetings [23] the importance of E911 was discussed and a great number of comparisons between the E911 and P92 was carried on. The results showed that P92 has a better behavior then E911 and in this finite element study regarding the HRSG superheater, the results is not different. P92 shows a better behavior than E911; meanwhile a further discussion and analysis should be made to define clearly the behaviors of P91 and E911.

9 Conclusion

The present paper is a contribution in understanding the use of high alloy type steels for new operating conditions resistant in the new CCGT generation units with improved design and efficiency. The new power generation systems based on CCGT will be, in the medium term, an alternative, and also a complementary solution to the new coming generation of hypercritical coal fired power plants.

During the mechanical design of HPSH manifold, we concluded that design-by-rule (ASME Section VIII, Part 4, Design by Rule Requirements) cannot deal with every possible configurations, and may be unduly restrictive by preferring certain constructions without appropriate justification as we can see in the ASME Code, when we saw some references based only on one type of geometry such as weld joints. The use of design-by-analysis (ASME Section VIII, Part 5, "Design by Analysis Requirements"), employing more elaborate analytical techniques such as finite element models to determine limit loads and reference stresses, can overcome the limitations of design-by-rule for primary loading. To this objective, some codes allow the use of limit load analysis, which can be accomplished using modern finite element analysis softwares that are being developing nowadays, creating a symbiosis between the modeling and simulation/analysis softwares.

Analyzing the behavior of the HPSH manifold and analyzing the HPSH module including headers and tubing, where steel alloys have a strong contribution factor, an exercise was performed, simulating the behavior of this elements by defining the stress, fatigue analysis, and creep strength related with time to rupture.

The 12″ SCH pipe is a component with high stress due to higher thickness and temperature.

Regarding fatigue behavior, normal 4″ SCH pipe is the higher cycled component, but 4″ SCH bending pipe has almost the same parameter values (depending on the material). In the case of 12″ SCH and 4″ SCH pipes operating at 584°C and 15.4 MPa, 9%Cr steel is the best material solution, in the present imposed conditions, to cyclic operation conditions.

During creep assessment P92 show a good performance when submitted to the superheater operation conditions. This result

leads to one of the solutions for the reliability of the high pressure components from the HRSG high temperature section, where the HPSH module as one of the critical modules was designed and constructed to be cyclic efficient, showing a geometry that generates good capability to stand high range of temperatures and good stress distribution. The single row of tubes between the two headers and row-to-row makes this characteristic possible. This unique pressure part arrangement makes this component prepared for faster start-ups handle high thermal stress, creating a combination between these characteristics, and the mechanical behavior of 9Cr W Grade P92 will lead to one of the greatest solutions to increase life and reduce the probability of forced outage rate due to HPSH component failure, preparing the OCGT to be one of the most flexible and adapted unit for cyclic operation and creep resistant unit. In the future new studies, including the new generation of 9Cr steel, should be developed to define the best solution for the Benson once-through technology, defining combinations of geometry and alloy and improving the range of stress and temperature that this type of unit can operate without a substantial life reduction.

The results showed in this paper should be analyzed carefully by the reader. Even now by demonstration that the Manson–Brown parameter is one of the best extrapolation parameters, with a medium difficulty in the calculation process but a high level of flexibility when compared with the common Larson–Miller parameter, the truth is that the constants used in this type of extrapolation are very important; a small change in the constants values can originate a very different result. Beside that, the simulation takes into consideration an entire geometry and not a standard sample, applying new grades of steel alloys that are in the stage of tests to know the creep behavior where long creep-rupture tests are still running.

Regarding the thickness of the pipes and tubing, analyzing the data, we conclude that the 9Cr Steel have a smaller thickness when compared with $2\frac{1}{4}$ Cr steels. The grade P92 is the steel, which presents the best thickness among the analyzed steels. Meanwhile, creep-rupture tests are still running for the new grade P122. Meanwhile, steels like P92 and P122, which show high contents of chromium and at the same time good thermal conductivity and lower expansion, are some of the candidates to replace the Grade P91 in the future.

Acknowledgment

Appreciation to Mahmoud Mostafavi from Bristol University for the discussion of the concept ideas of finite element analysis and explanation of transient analysis and crack grow.

Special thanks to the European Technology Development (ETD) team for their support and motivation.

References

[1] American Society of Mechanical Engineers, 2007, "ASME Boiler and Pressure Vessel Code Section I—Rules for Construction of Power Boilers," American Society of Mechanical Engineers, New York.
[2] American Society of Mechanical Engineers, 2007, "ASME Boiler and Pressure Vessel Code Section VIII—Rules for Construction of Pressure Vessels," American Society of Mechanical Engineers, New York.
[3] Siemens AG Power Generation Group, 2000, *BENSON Boilers for Maximum Cost-Effectiveness in Power Plants*, Erlangen, Germany.
[4] Franke, J., Lenk, U., Taud, R., and Klauke, F., 2000, *Successful Combined Cycle Debut for Novel Horizontal-Flow Vertical-Tube Benson HRSG*, Siemens Power Generation Group, Erlangen, Germany.
[5] Franke, J., and Kral, R., 2000, *Innovative Boiler Design to Reduce Capital Cost and Construction Time*, Siemens Power Generation Group, Erlangen, Germany.
[6] Chase, L. D., 2001, *Combined-Cycle Development Evolution and Future*, General Electric Power Systems, New York.
[7] Garcia Santiago, S., and Moñux Gómez, F., 2006, *Centrales Térmicas de Ciclo Combinado—Teoria y proyecto*, D. de Santos, ed., Edições Díaz de Santos, Spain.
[8] Baumgartner, R., 2004, "Fast Work for the Benson Once-Through HRSG," Mod. Power Syst., UK.
[9] Hess, U., and Bailey, D., 2006, *Second Generation Once-Through HRSG for High Pressure Combined Cycles*, Alstom Power, Besos, Spain.
[10] Maneta, V., 1992, *Calculation of the Demonstration Drum for Renewal of Stamp ASME to be Manufactured in Accordance With ASME Sect. I*, Mague, Alverca, Portugal.
[11] Malek, M. A., 2004, *Power Boiler Design, Inspection, and Repair*, McGraw-Hill, New York.
[12] Pinto Fernandes, J., and Dias Lopes, E., 2009, "Evaluation of High Temperature Steel Alloys Applied to Heat Recovery Steam Generators From Combined Cycle Gas Turbines," Institute of Materials, Minerals & Mining (IOM3), New High Temperature Materials Seminar.
[13] Haarmann, K., Vaillant, J., Vandenberghe, B., Bendick, W., and Arbab, A., 2002, *The T91/P91 Book*, 2nd ed., Vallourec Industries and Mannesmannrohr, France.
[14] Richardot, D., Vaillant, J., Vandenberghe, B., Bendick, W., and Arbab, A., 2002, *The T92/P92 Book*, 2nd ed., Vallourec Industries and Mannesmannrohr, France.
[15] Bendick, B., Gabrel, J., Hanhn, B., and Bendick, W., 2007, "New Low Alloy Heat Resistant Ferritic Steels T/P23 and T/P24 for Power Plant Application," Int. J. Pressure Vessels Piping, **84**, pp. 13–20.
[16] Arndt, J., Haarmann, K., Kottmann, G., and Vaillant, J. C., 2000, *The T23/T24 Book—New Grades for Waterwalls and Superheaters*, 2nd ed., Vallourec Industries and Mannesmannrohr, France.
[17] Starr, F., 2002, "Potential Issues in the Cycling of Advanced Power Plants," OMMI, 1(1).
[18] Pinto Fernandes, J., and Dias Lopes, E., 2008, "Damage Mechanism and Component Life Assessment Applied to Heat Recovery Steam Generators," Expo Mechanic 2008, ISEL Portugal.
[19] Vaillant, J., Vandenberghe, B., Hahn, B., Heuser, H., and Jochum, C., 2008, "T/P23, 24, 911 and 92: New Grades for Advanced Coal-Fired Power Plants—Properties and Experience," Int. J. Pressure Vessels Piping, **85**, pp. 38–46.
[20] Robertson, D., 2008, *T23/P23 and T24/P24 Plant Experience+Fabrication, Welding, Heat Treatment, Oxidation & Damage Mechanisms*, European Technology Development Ltd., London, UK.
[21] Masuyama, F., 2001, "History of Power Plants and Progress in Heat Resistant Steels," ISIJ Int., **41**, pp. 612–625.
[22] British Standard Institution, 1990, "Elevated Temperature Properties for Steels for Pressure Purposes, Part 1. Stress Rupture Properties," BSI Standards PD 6525: Part 1.
[23] WG3A, 2005. "ECCC Data Sheet," European Creep Collaborative Committee.

Computational Design of Corrosion-Resistant Fe–Cr–Ni–Al Nanocoatings for Power Generation

K. S. Chan
Fellow ASME

W. Liang

N. S. Cheruvu

Southwest Research Institute,
6220 Culebra Road,
San Antonio, TX 78238

D. W. Gandy
Electric Power Research Institute,
Charlotte, NC 28262

A computational approach has been undertaken to design and assess potential Fe–Cr–Ni–Al systems to produce stable nanostructured corrosion-resistant coatings that form a protective, continuous scale of alumina or chromia at elevated temperatures. The phase diagram computation was modeled using the THERMO-CALC® software and database (Thermo-Calc® Software, 2007, THERMO-CALC for Windows Version 4, Thermo-Calc Software AB, Stockholm, Sweden; Thermo-Calc® Software, 2007, TCFE5, Version 5, Thermo-Calc Software AB, Stockholm, Sweden) to generate pseudoternary Fe–Cr–Ni–Al phase diagrams to help identify compositional ranges without the undesirable brittle phases. The computational modeling of the grain growth process, sintering of voids and interface toughness determination by indentation, assessed microstructural stability, and durability of the nanocoatings fabricated by a magnetron-sputtering process. Interdiffusion of Al, Cr, and Ni was performed using the DICTRA® diffusion code (Thermo-Calc Software®, DICTRA, Version 24, 2007, Version 25, 2008, Thermo-Calc Software AB, Stockholm, Sweden) to maximize the long-term stability of the nanocoatings. The computational results identified a new series of Fe–Cr–Ni–Al coatings that maintain long-term stability and a fine-grained microstructure at elevated temperatures. The formation of brittle σ-phase in Fe–Cr–Ni–Al alloys is suppressed for Al contents in excess of 4 wt %. The grain growth modeling indicated that the columnar-grained structure with a high percentage of low-angle grain boundaries is resistant to grain growth. Sintering modeling indicated that the initial relative density of as-processed magnetron-sputtered coatings could achieve full density after a short thermal exposure or heat-treatment. The interface toughness computation indicated that the Fe–Cr–Ni–Al nanocoatings exhibit high interface toughness in the range of 52–366 J/m^2. The interdiffusion modeling using the DICTRA software package indicated that inward diffusion could result in substantial to moderate Al and Cr losses from the nanocoating to the substrate during long-term thermal exposures.
[DOI: 10.1115/1.3204651]

1 Introduction

Energy-producing steam and gas turbine components operate in a severe environment at elevated temperatures. For protection against environmental degradation, both *M*Cr and *M*CrAl (where *M*=Fe,Ni,Co, or combination of these elements) are widely used in industry. A large number of oxidation-resistant Ni–Cr–Al coatings are available for protection of gas turbine protection at service temperatures of up to about 1100°C [1–9]. For these Ni-based coatings, the Cr content ranges from 3 wt % to 22 wt % and the Al content ranges from 2 wt % to 20 wt % with no or little Fe. Most of the Ni–Cr–Al coatings are processed using conventional methods and exhibit normal grain sizes. Recently, some investigators processed Ni–Cr–Al coatings with a nanoscaled grain structure [1–8].

Several Fe–Cr–Ni–Al coatings with nanoscaled grain structure are also reported in literature [10–12]. Liu and co-workers [11,12] reported the oxidation characteristics of sputtered-deposited nanocrystalline Fe–Cr–Ni–Al coatings with 25–26 wt % Cr, 19.3 wt % Ni, and 3.4–4.2 wt % Al with and without 1.8 wt % Mn. The compositions of these coatings are essentially those of 310 stainless steels (Fe–25Cr–19.3Ni) with the additions of 3.4–4.2 wt % Al and 1.8 wt % Mn. Nanocoatings based on 304 stainless steel compositions with 3 wt % to 10 wt % Al additions (Fe–18Cr–8Ni–*z*Al, where *z* ranges from 3 wt % to 10 wt %) were also reported [10]. By virtue of a nanoscaled grain structure, these nanocoatings are capable of forming a continuous Al_2O_3 oxide scale in 100 h at 800°C and 900°C [11] and 50 h at 950–1050°C [12]. These authors did not report the oxidation results for longer times of thermal exposure.

He et al. [13] reported the synthesis of microcrystalline Fe–Cr–Ni–Al–Y_2O_3 oxide-dispersion strengthened alloy coatings by electric spark deposition using Fe–20Cr–4.5Al–0.5Ti–0.5Y_2O_3–0.23C–0.002S (in wt %) as an electrode and Fe–1Cr–18Ni–9Ti as a substrate. The coating produced was Fe–18.9%Cr–7.98%Ni–2.41%Al. Because of its relatively low Al content, this particular coating (Fe–18.9%Cr–7.98%Ni–2.41%Al) does not form continuous Al_2O_3 but rather forms a combination of mixed $FeCr_2O_4$ and Cr_2O_3 [13]. Thus, it is unknown whether or not that coating containing low levels of Al provides long-term protection. There are also questions about the long-term stability of the nano-sized grain structure at elevated temperature.

Since elevated temperature tests are expensive, there is a need for an efficient approach to reduce the cost and lead time for developing novel coatings with improved oxidation and corrosion performances. One possible approach is to utilize computational methods to design and optimize the compositions and to interro-

Contributed by the International Gas Turbine Institute of ASME for publication in the JOURNAL OF ENGINEERING FOR GAS TURBINES AND POWER. Manuscript received March 25, 2009; final manuscript received April 3, 2009; published online March 4, 2010. Review conducted by Dilip R. Ballal. Paper presented at the ASME Gas Turbine Technical Congress and Exposition, Orlando, FL, June 8–12, 2009.

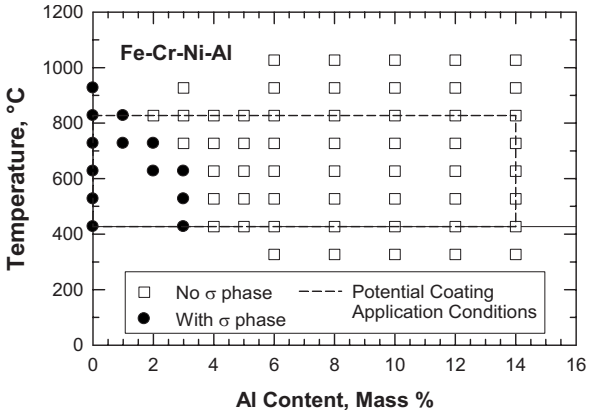

Fig. 1 Computational results of Al contents required to suppress σ-phase formation in Fe–Cr–Ni–Al at a temperature in the range of 327–1027°C

gate the microstructural stability of nanostructured coatings. In this paper, we report the use of an integrated computational approach to develop a stable nanostructured coating that produces a protective, continuous scale of alumina or chromia. The computational efforts included (1) the use of THERMO-CALC® software and database [14,15] for computing pseudoternary phase diagrams for the design of nanocoatings; (2) the use of grain growth model, sintering model, and interface toughness model for optimizing microstructural stability and interface integrity; and (3) the use of DICTRA diffusion code [16] for maximizing the long-term stability of the nanocoatings. The candidate nanocoatings were fabricated by a magnetron-sputtering process.

2 Computational Design of Nanocoating Compositions

Pseudoternary phase diagrams for Fe–Cr–Ni–Al systems were computed using THERMO-CALC Windows version 4 (TCW-4) [14] and TCFE5 [15], which is a thermodynamic database for steels and Fe-based alloys by Thermo-Calc Software, Stockholm, Sweden. This effort was intended to provide guidance on the phase relations of both alumina and chromia formers over the operating temperature range for selected aluminum contents. The intended application of the Fe–Cr–Ni–Al coatings is fossil-fired steam turbine boilers. Since the application temperatures can range from 455°C to 750°C, the pseudoternary phase diagrams were computed from 327°C to 927°C at 100°C increments. The aluminum content was selected to range from 0 wt % to 14 wt % at 2–3 wt % increments. One of the goals of the phase diagram computation is to identify the minimum amounts of Al addition required to suppress σ-phase formation in Fe–Cr–Ni–Al alloys. To achieve this goal, the Fe–Cr–Ni–Al pseudoternary phase diagram was computed for 727°C by increasing the Al content from 0 wt % to 10 wt % at 1 wt % increments.

The computational results have been utilized to establish the minimum Al contents and temperature where σ-phase would be suppressed. The results are presented in Fig. 1, which indicate that a 4 wt % Al addition or greater suppresses the formation of σ-phase in Fe–Cr–Ni–Al at 372–627°C. The amount of Al addition required to suppress σ-phase formation decreases with increase in temperature to about 3 wt % Al at 727°C and to 2 wt % Al at 827°C, as shown in Fig. 1. At Al contents greater than 4 wt %, the microstructures of Fe–Ni–Cr–Al contain ferrite (bcc), austenite (fcc), or a combination of ferrite+austenite. Al is a bcc stabilizer that expands the bcc phase field but diminishes the σ-phase and austenite (fcc) phase fields in Fe–Ni–Cr–Al. Typical pseudoternary phase diagrams for Fe–Ni–Cr–Al at 727°C are presented as a function of Al content in Fig. 2.

The general trend is that the increase in Al content expands the bcc phase field and suppresses the formation σ-phase. Figures 3(*a*)–3(*d*) present the pseudoternary phase diagrams for Fe–Cr–Ni–10 wt %Al for 427°C, 527°C, 627°C, and 827°C, respectively. The corresponding result for 727°C is shown earlier in Fig. 2(*d*). At 427°C, a phase field of two bcc phases (α_1 is Fe-rich and α_2 is Cr-rich) and one fcc phase (γ) exists in the central portion of the phase diagram. The size of this phase field diminishes at 527°C and is completely gone at 627°C. At 627°C, 727°C, and 827°C, the equilibrium phases are α (bcc) and γ (fcc).

Al contents were reported to produce alumina formation in Fe–Ni–Cr–Al alloys [12,17–23]. A minimum of 4–5 wt % Al is required to form a continuous alumina scale on Fe–Ni–Cr–Al alloys. It has been reported that a minimum of 5 wt % Al is required to form a continuous alumina scale on coatings with a normal grain size (>1 μm). The critical Al content is reduced from 5 wt % to 3.5 wt % Al for coating with nano-sized grain size because of a greater Al diffusion kinetics through grain boundaries [12,23]. The critical Al content for Fe–Ni–Cr–Al alloys can be further reduced to the 2.5–4.0 wt % range by controlling the contents of microalloying elements such as Ti, V, and Nb [24–26]. The minimum Al content required for Al_2O_3 formation is also about 3.5 wt % Al for aluminide coatings on Fe-based alloy substrates [27]. To ensure a sufficient Al source, we have tentatively selected 10 wt % Al as the desired Al content for the Fe–Ni–Cr–Al nanocoating compositions.

The candidate nanocoatings were fabricated using a magnetron-sputtering process, which previously produced nanostructured Fe–18Cr–8Ni–xAl coatings for several Al contents as part of a small business technology transfer program [10]. These coatings typically contained a columnar-grained microstructure with small amounts of pores in the as-processed condition. The grain size was in the micrometer range in the columnar grain growth direction but was on the nanometer range (average grain size =350–550 nm) in the transverse direction. Efforts are currently underway to further reduce the grain size by altering the deposition parameters. Computational methods applied to assess the evolution of the microstructure, the durability, and the long-term stability of these nanocoatings are highlighted in Secs. 2.1–2.4.

2.1 Grain Growth Modeling. The expression for grain growth kinetics [28] is generally given by

$$d^2\text{-}d_o^2 = k_g t \tag{1}$$

where d and d_o are the current and initial grain diameter, respectively, t is the time, and k_g is the microstructure parameter [25] given by

$$k_g = \frac{4}{3} M_{gb} \gamma_{gb} (n-6) \tag{2}$$

where M_{gb} and γ_{gb} are the mobility and energy of the grain boundaries, respectively, and n is the number of the grain neighbor. The grain boundary mobility is related to the diffusion coefficient (D) as given by

$$M_{gb} = \frac{\Omega D_o}{\delta_b RT} \exp\left(-\frac{Q}{RT}\right) \tag{3}$$

where Ω is the molar volume, δ_b is the grain boundary thickness, D_o is the pre-exponent coefficient for diffusion, Q is the activation energy for diffusion, R is the universal gas constant, and T is absolute temperature.

The activation energy for grain growth is closely related to the activation energy for the controlling diffusive mechanisms. In Fe-based alloys, the activation energy for grain growth can vary from 91 kJ/mol to 404 kJ/mol [29]. The high value is associated with grain growth in a columnar-grained structure [29].

Equations (1)–(3) were utilized to compute the grain diameter as a function of anneal times for equiaxed and columnar microstructures of as-processed magnetron-sputtered Fe–18Cr–8N–

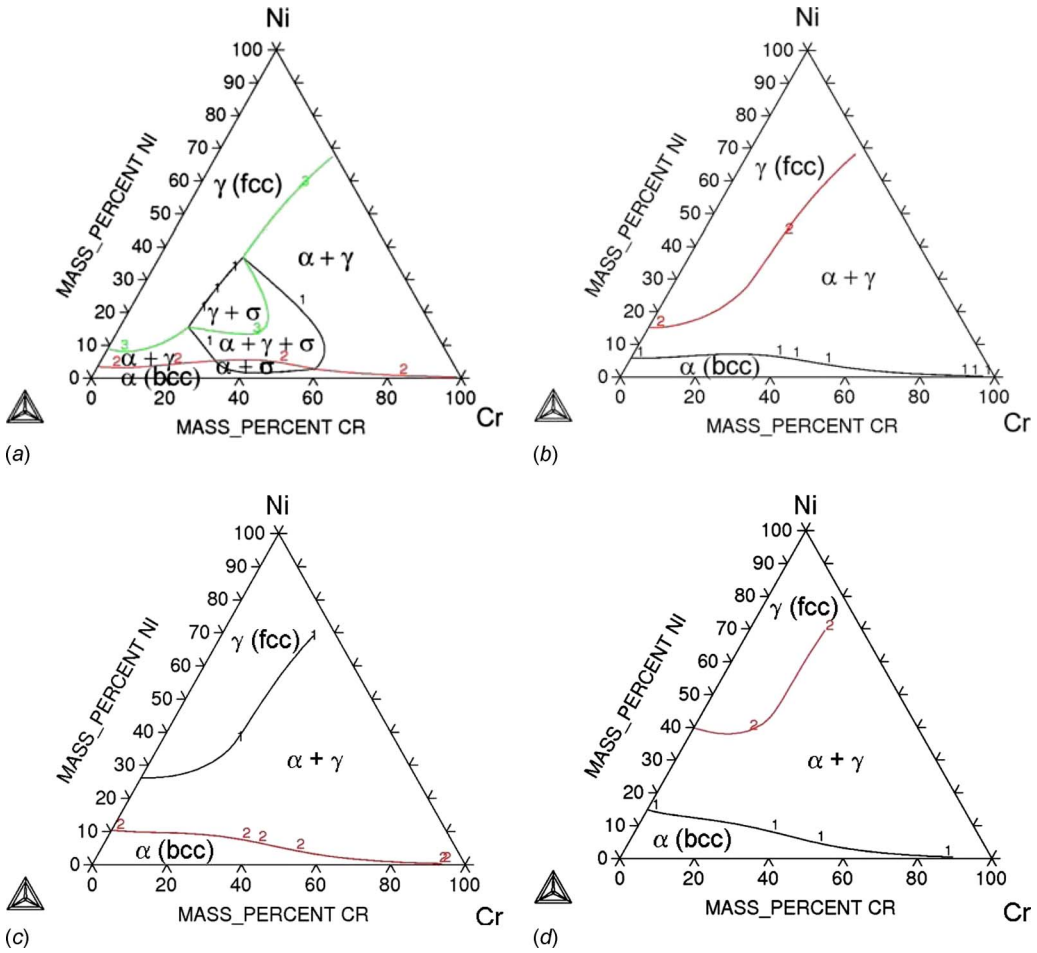

Fig. 2 Computed pseudoternary phase diagrams for Fe–Cr–Ni–Al alloys at 727°C: (*a*) 1 wt % Al, (*b*) 3 wt % Al, (*c*) 6 wt % Al, and (*d*) 10 wt % Al

10Al coating at 750°C. The results are compared against the experimental data for the columnar-grained nanocoating in Fig. 4. The grain sizes of the columnar grain structure in the nanocoatings were measured on a plane normal to the columnar growth direction via orientation image microscopy (OIM). The distribution of the grain diameter for the as-deposited Fe–18Cr–8Ni–10Al nanocoating is presented in Fig. 5. The corresponding mean diameter is 1.23 μm with a standard deviation of 0.43 μm. The theoretical calculation indicates that very little grain growth occurs in the columnar microstructure at 750°C, which is in agreement with the experimental data. In contrast, substantial grain growth occurs in an equiaxed microstructure. The different grain growth kinetics are due to the large difference in the activation energy for grain growth, which is 404 kJ/mol [29] for columnar grain structure and 245 kJ/mol for the equiaxed grain microstructure [29].

To understand the high activation energy for the columnar grain structure, OIM was also utilized to characterize the grain orientation and the grain boundary characters in the Fe–Cr–Ni–Al nanocoatings. Figure 6 shows the color-coded orientation map for the as-processed Fe–18Cr–8Ni–10Al coating, which shows a random distribution of grain orientations. In contrast, the grain boundaries in the columnar structure are mostly low-angle boundaries with 49% of the grain boundaries having less than a 15 deg disorientation angle. Figure 7 shows that about 39% of the grain boundaries are disoriented by 4 deg or less. The distribution is fairly uniform at disorientation angles higher than 4 deg. The higher activation energy for grain growth in the columnar structure appears to be the result of the presence of a large fraction (about 50%) of low-angle boundaries (<15% disorientation) in the microstructure. Thus, a key to maintain a fine-grained structure that resists grain growth is to have a high population of low-angle grain boundaries in the nanocoatings. On the contrary, a high population of high-angle grain boundaries may lower the activation energy for grain growth and promote grain coarsening.

2.2 Sintering Modeling. Connected grain boundary pores are undesirable in coatings because they promote internal oxidation by providing access of oxygen to interior grains. The experimental data indicated the presence of voids and gaps between columnar grains in the as-deposited magnetron-sputtered nanocoatings. The volume fractions of voids ranged from 10% in the as-processed condition to about 2% after cyclic oxidation at 750°C for 1500 one-hour cycles (Fig. 8). The decrease in void density was the result of sintering after high-temperature exposure.

An existing sintering model was utilized to compute the linear shrinkage rate ($\Delta L/L$) according to Ref. [30]

$$\frac{\Delta L}{L} = \left(\frac{15a^4}{r^4}\frac{D\gamma_s}{kT}\right)^{1/3} t^{1/3} \tag{4}$$

where D is self-diffusion coefficient, γ_s is surface energy, r is grain radius, a is lattice parameter, t is time, and k is Boltzmann's constant. The relative density is given in terms of the linear shrinkage rate [30] as

$$\rho = \rho_i\left[1 - \frac{\Delta L}{L}\right]^{-3} \tag{5}$$

where ρ_i is the initial density.

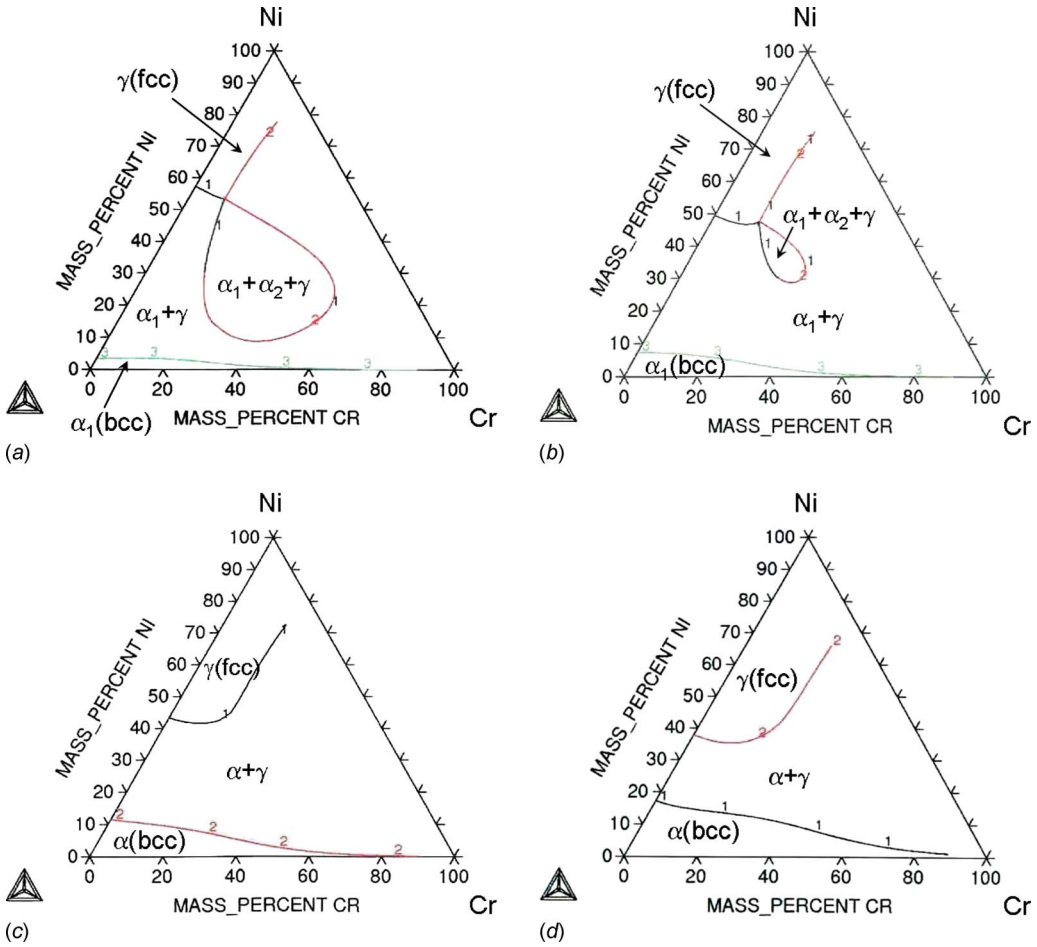

Fig. 3 Computed pseudoternary phase diagrams for Fe–Cr–Ni–Al alloys with 10 wt % Al for various temperatures: (*a*) 427°C, (*b*) 527°C, (*c*) 627°C, and (*d*) 827°C

Using Eqs. (4) and (5), the relative density was computed as a function of time for Fe–Cr–Ni–Al nanocoatings and the results are compared against the experimental data in Fig. 8. The as-coated Fe–18Cr–8Ni–10Al coating was about 90% dense but the relative density increased with increasing times cyclic oxidation to almost 98% dense after about 1373 h of thermal exposure at 750°C. The model prediction is in good agreement with the experimental data. The presence of pores in the coating allows oxygen penetrations and internal oxidation deep inside the nanocoatings. To eliminate oxygen penetration through connected pores, the grain boundary pores must be eliminated or sealed off from the interior grains. The sintering model was utilized to estimate the time required to eliminate the pores. The results indicate that the initial density of the as-fabricated coating must be greater than 98% dense (i.e., less than 2% porosity) in order to eliminate all pores in less than 45 h

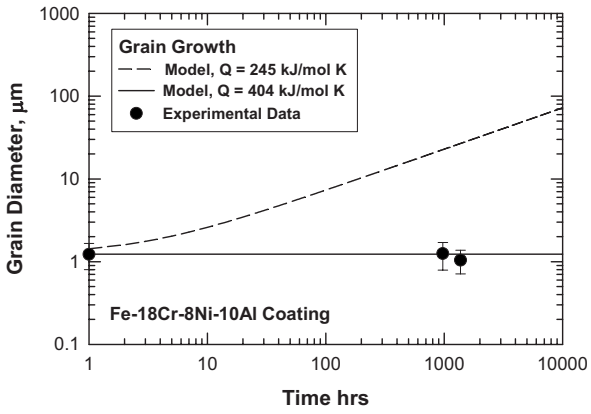

Fig. 4 Predicted grain growth kinetics using the activated energy values for equiaxed and columnar grain structures compared with experimental data for Fe–18Cr–8Ni–10Al nanocoatings with a columnar grain structure at 750°C

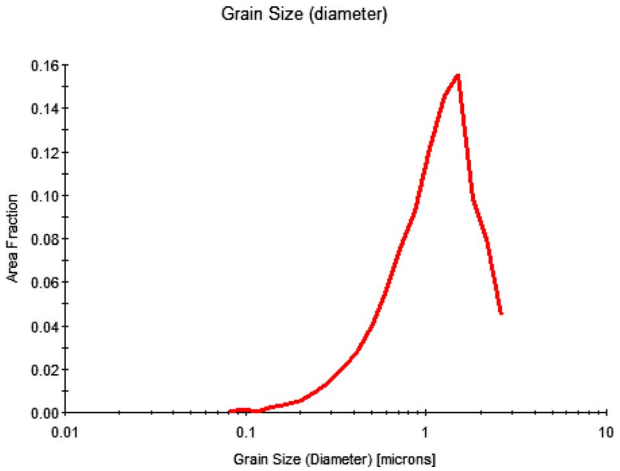

Fig. 5 Grain diameter distribution for Fe–18Cr–8Ni–10Al nanocoating in the as-coated condition

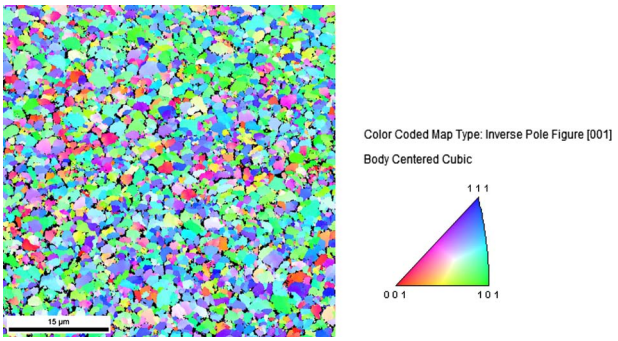

Fig. 6 Colored–coded orientation map for as-coated Fe–18Cr–8Ni–10Al nanocoating on 304 stainless steel substrate

at 750°C. The sintering time increases to 320 h at an initial relative density of 95%. Unlike ceramic coatings, the strain compliance of the metallic nanocoatings is not expected to decrease after sintering to achieve full density since the nanocoatings are inherently ductile.

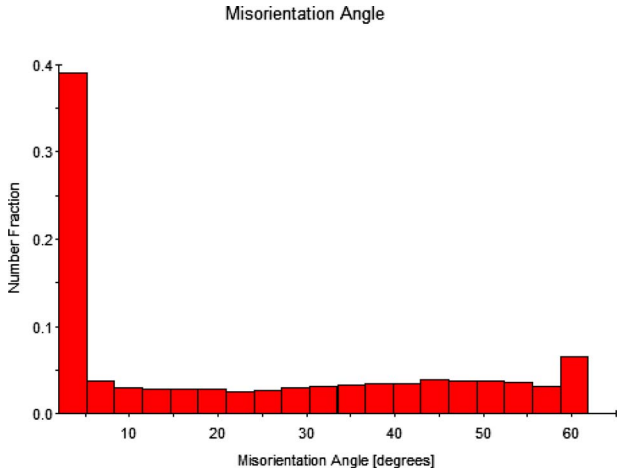

Fig. 7 Distribution of grain boundary disorientation determined by EBSD for as-coated Fe–18Cr–8Ni–10Al nanocoating on 304 stainless steel substrate

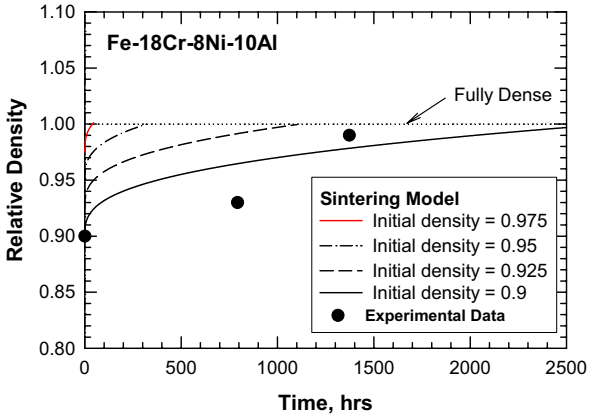

Fig. 8 Theoretical relative density based on the sintering model compared with the experimental data of Fe–18Cr–8Ni–10Al coating on Fe–18Cr–8Ni substrate—the initial relative density of the as-processed coating must be greater than 98% in order to achieve the full density in less than 45 h of exposure at 750°C

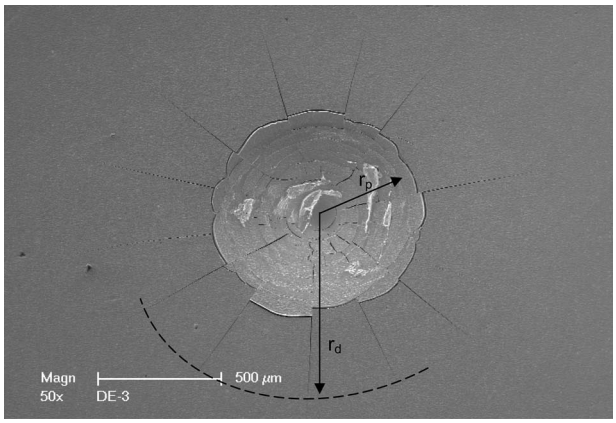

Fig. 9 Rockwell C indentation on a Fe–20Cr–8Ni–10Al nanocoating on Fe–18Cr–8Ni substrate resulted in a circular indent of radius r_p and a cracked/debonded zone of radius r_d—the ratio of r_d/r_p was utilized to deduce the elastic strain energy release rate or interface toughness during steady-state interface debonding using the procedure developed by Drory and Hutchinson [31]

2.3 Interface Toughness. The adhesion and spallation characteristics of the as-deposited nanocoatings were investigated by performed indentation tests using the Rockwell C indenter at 150 kg load. Indentation usually resulted in the formation of a circular indent of radius r_p and a debonded zone of radius r_d, as illustrated in Fig. 9. Results of r_p and r_d for various nanocoatings were measured and the ratios of r_d/r_p are summarized in Table 1. The ratios of r_d/r_p can be utilized to compute the interface toughness (elastic strain energy release rate) during steady-state interface debonding under indentation. Using an established procedure described by Drory and Hutchinson [31], the interface toughness values for Fe–20Cr–8Ni–10Al nanocoatings and the preliminary results were presented in Table 1. In general, the interface toughness of the Fe–20Cr–8Ni–10Al nanocoatings are in the 52–366 J/m^2 range, which are quite high compared with typical values of less than 1–10 J/m^2 for brittle coatings [32] but are consistent with 14–215 J/m^2 for ductile W/Cu coatings [32].

2.4 Interdiffusion Between Coating and Substrate. The microstructural stability of a coating on a particular substrate during long-term high-temperature exposures was evaluated by performing interdiffusion computation treating the coating and the substrate as a diffusion couple. As illustrated in Fig. 10, the coating was taken to be 30 μm on top of a substrate that is considered to be much thicker than the coating. For the purpose of minimizing the computation times, the substrate thickness was taken to be 150 μm. Interdiffusion computation was performed using DICTRA 24 [16] with TCFE5 [15] thermodynamic database and MOB2 mobility database. In these computations, only interdiffusion diffusion due to chemical gradients was considered, but outward diffusion due to oxidation was ignored.

Table 1 Ratios of r_d/r_p and interface toughness of Fe–20Cr–8Ni–10Al nanocoatings processed under various voltage and ion bombardment conditions

Nanocoating	r_d/r_p	Γ_{ss} (J/m^2)
DE-1	1.861 ± 0.230	109.6 ± 65.7
DE-2	1.438 ± 0.083	365.5 ± 96.2
DE-3	1.832 ± 0.084	104.7 ± 26.8
DE-4	2.086 ± 0.146	52.1 ± 21.7
DE-5	1.496 ± 0.031	294.6 ± 29.9

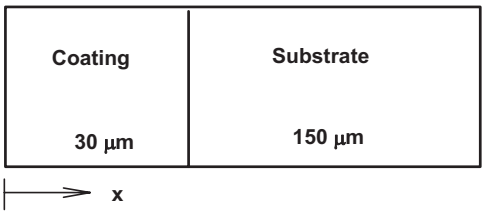

Fig. 10 Diffusion couple used in the interdiffusion computation using DICTRA

Interdiffusion of Al, Cr, and Ni were computed for Fe–18Cr–8Ni–10Al coating on Fe–18Cr–8Ni (304SS) substrate at 750°C for exposure times of 625 h, 825 h, 1250 h, 2500 h, and 8760 h. Figures 11(*a*)–11(*c*) show the concentration profiles for Al, Cr, and Ni, respectively. The initial Al concentration (dotted line) in the coating was 10 wt %. Inward diffusion of Al occurred fairly rapidly and the Al concentration deceased to about 4.1 wt % after 625 h and to 2 wt % after 8760 h (1 year). Al, Cr, and Ni also diffused inwardly into the substrate but their concentration files are more complex, as shown in Figs. 11(*b*) and 11(*c*). The coating contains mostly α (bcc) with about 10–20 mol % γ (fcc). In contrast, the substrate is predominantly γ (fcc) but the mole fraction of α (bcc) phase increases with time as more Al diffuses inwardly into the substrate.

For Fe–25Cr–40Ni–10Al on Fe–18Cr–8Ni at 750°C, inward diffusion of Al, Cr, and Ni into the substrate after 825 h of exposure is presented in Figs. 12(*a*)–12(*c*), respectively. As shown in Fig. 12(*a*), there is some inward diffusion of Al into the substrate but the rate of Al loss to the substrate is considerably lower compared with coatings with lower Cr and Ni contents. In addition, Figs. 12(*b*) and 12(*c*) indicate that the Cr and Ni loss to the substrate is also lower. The phase fraction results indicate that the formation of an fcc layer at the coating/substrate interface. This fcc layer appears to act as a diffusion barrier that limits the inward diffusion of Al and Cr into the substrate at 750°C.

2.4.1 Comparison of Model Computation Against Experiment. Limited efforts were also initiated to compare the theoretical computations against the experimental data of Fe–Cr–Ni–Al coatings produced in a small business technology transfer program [10]. In this program, Fe–18Cr–8Ni–*x*Al coatings were investigated at several Al contents. Without Al additions, Fe–18Cr–8Ni (304 SS) coating showed the presence of σ-phase in the as-deposited and thermally exposed conditions. The microstructure was predominantly bcc ferrite and σ-phases, as shown in Fig. 13(*a*). The σ-phase was suppressed by an Al addition as small as 3 wt % Al. At 10 wt % Al, Fe–18Cr–8Ni–10Al contained mostly ferrite (bcc) with small amounts of austenite (fcc) after 990 one-hour thermal cycles at a peak temperature of 750°C, as shown in Fig. 13(*b*). These experimental findings are in agreement with phase diagram computations obtained via THERMO-CALC®.

The computed concentration profiles of Al, Cr, and Ni based on inward diffusion are compared against experimental data from cyclic oxidation specimens of Fe–18Cr–8Ni–10Al on Fe–18Cr–8Ni (304 SS) substrate tested at a maximum temperature of 750°C. All chemical compositions were determined by energy-dispersive X-ray spectroscopy (EDXS). Figure 14(*a*) shows a comparison of the predicted and measured Al profiles in the coating and in the substrate after 825 h of thermal exposure. In general, the predicted Al profile is in good agreement with the observed profile. The Al content in the coating is predicted to decrease from 10 wt % to 3.7 wt % in the coating. The depth of the interdiffusion zone is predicted to be about 70 μm. Both predictions are in excellent agreement with the experimental data as shown in Fig. 14(*a*). The corresponding concentration profiles for Cr and Ni are compared against the experimental data in Figs. 14(*b*) and 14(*c*), respectively. For both Cr and Ni, the complex profiles detailed by the computations could not be verified by the experimental data. On the other hand, the model predictions of minimal Cr and Ni loss to the substrate by inward diffusion are confirmed in general.

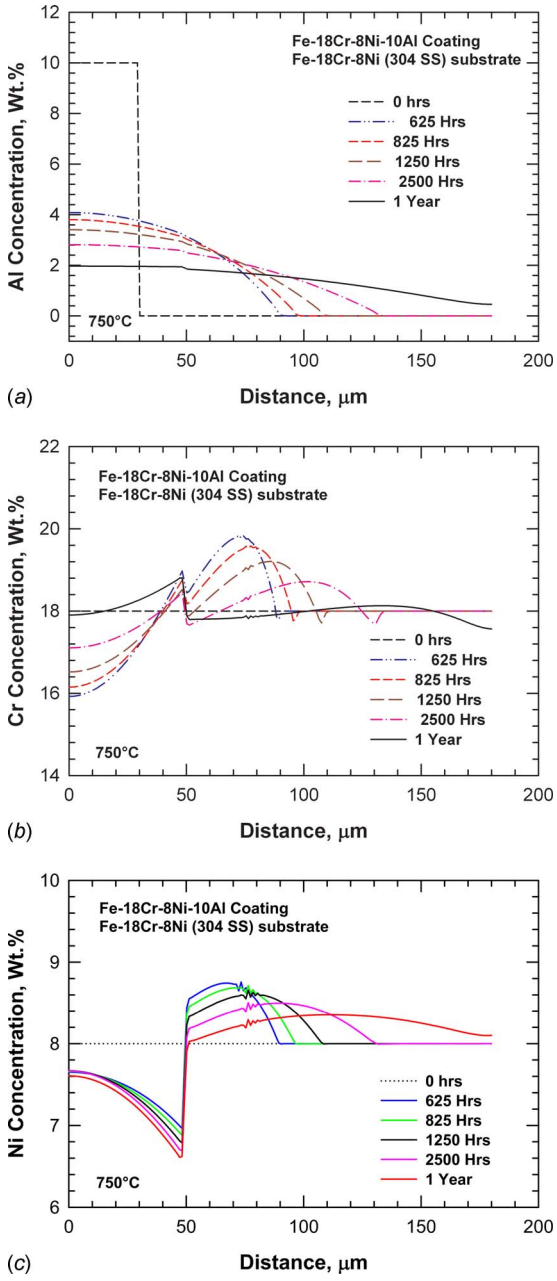

Fig. 11 Computed concentration profiles for Fe–18Cr–8Ni–10Al coating on Fe–18Cr–8Ni substrate after various times of exposure at 750°C: (*a*) Al distribution, (*b*) Cr distribution, and (*c*) Ni distribution

3 Discussion

The oxidation resistance of an Fe–Cr–Ni–Al coating depends on the formation of a continuous alumina layer on the coating surface. A critical Al content in excess of 3–5 wt % is typically required for continuous alumina formation with the critical value of the Al content deceasing with increasing grain sizes in the coating [12,23]. The critical Al content is further decreased to about 2.5 wt % in micro-alloyed Fe–Ni–Cr–Al alloys by eliminating Ti or V additions [24–26]. An estimate of coating life due to Al loss by inward diffusion can thus be made by using an Al

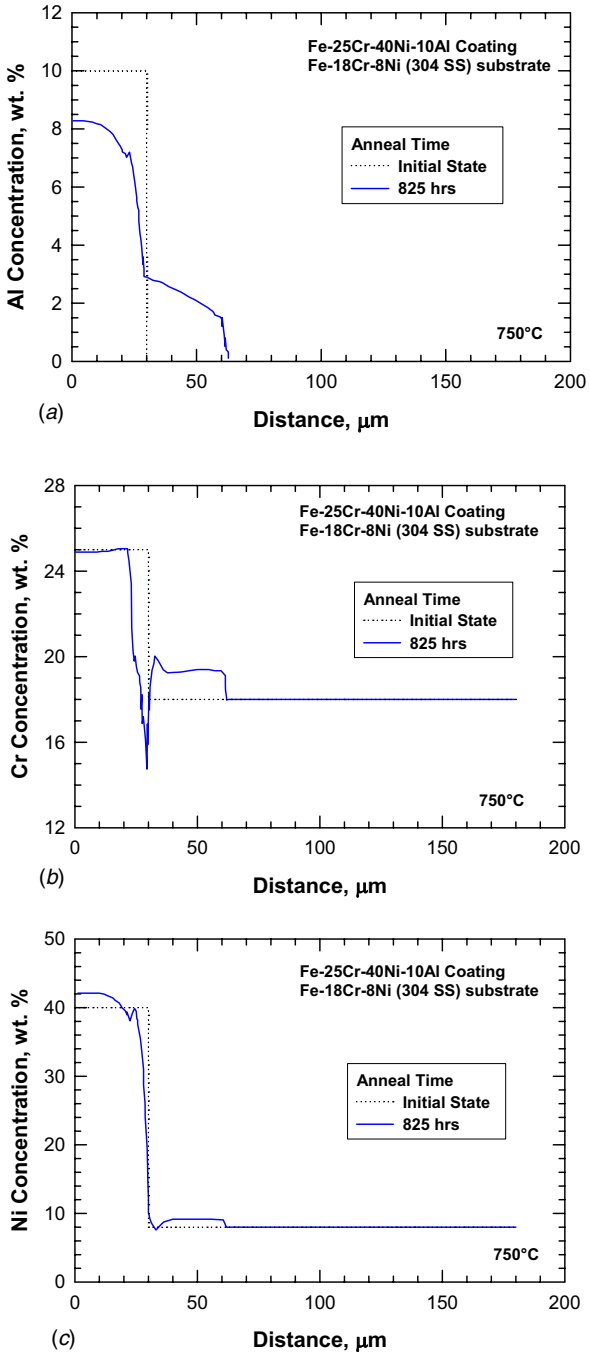

Fig. 12 Computed concentration profiles for Fe–25Cr–40Ni–10Al coating on Fe–18Cr–8Ni (304 SS) substrate after 825 h at 750°C: (*a*) Al concentration, (*b*) Cr concentration, and (*c*) Ni concentration

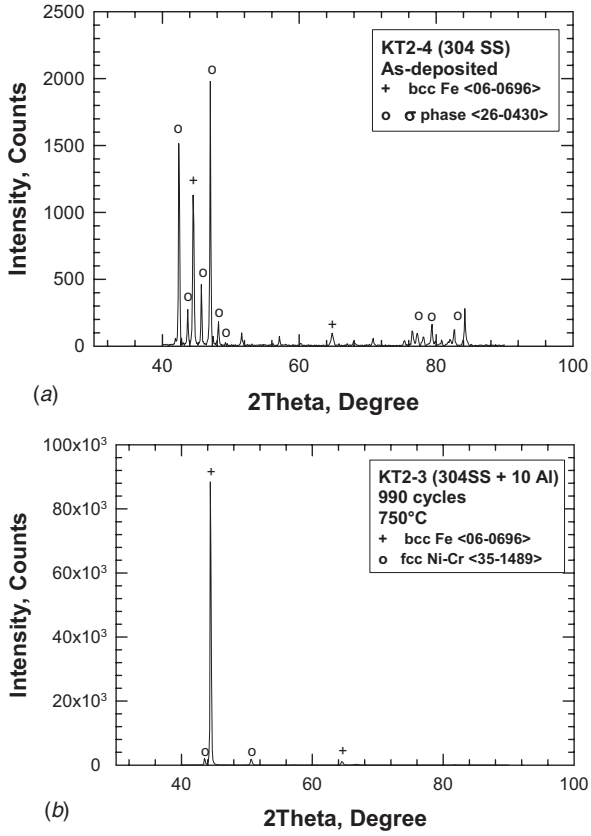

Fig. 13 XRD patterns of Fe–18Cr–8Ni (304SS) and Fe–18Cr–8Ni–10Al (304SS+10Al) show the presence of σ-phase without Al addition in 304 SS and the absence of σ-phase in Fe–18Cr–8Ni–10Al with 10 wt % Al addition—these specimens have been subjected to 990 one-hour thermal cycles at a peak temperature of 750°C

content of 3.5 wt % as the minimum amount required in an oxidation-resistant Fe–Cr–Ni–Al nanocoating [12,23]. For Fe–18Cr–8Ni–10Al on Fe–18Cr–8Ni, the Al content in the coating decreases to less than 3.5 wt % after about 1250 h at 750°C due to inward diffusion (Fig. 11(*a*)). For Fe–25Cr–40Ni–10Al on Fe–18Cr–8Ni, the time to the critical Al content is much larger than 825 h due to the presence of an fcc layer, which acts as a diffusion barrier, at the coating/substrate interface. This finding is consistent with a previous study, which showed that for aluminide coatings on Fe-based substrates, an austenitic substrate acts as a diffusion barrier to the ingress of Al and slows down the interdiffusion [33].

The formation of an interdiffusion barrier layer was also observed in aluminide coatings on Fe-based alloys [33,34]. In the case of aluminide coatings, the interdiffusion barrier layer is comprised of a two-phase microstructure containing bcc ferrites and B2 nickel aluminides [33] or iron aluminides [34]. Thus, the type of interdiffusion barrier layer formed at the coating/substrate depends on both the coating and substrate.

The loss of Al from Fe–Cr–Ni–Al coatings may render them susceptible to excessive oxidation resulting from difficulties in forming a continuous alumina film formation. On the other hand, the presence of a high Cr content in the coatings may provide resistance against oxidation and corrosion. Thus, it is worthwhile to compare the Cr concentration profile against the critical content for chromia formation. The corrosion resistance of an Fe–Cr–Ni coating depends on the formation of a continuous chromia layer on the coating surface. A critical Cr content in excess of 16 wt % is typically required for continuous chromia formation [35] but the critical Cr content also depends on the Ni content [36]. For resistance against type II corrosion, the critical Cr content in excess of 25 wt % is required [37,38]. An estimate of coating life due to Cr loss by inward diffusion can be made by using a Cr content of 16 wt % (or 25 wt %) as the minimum amount required in a corrosion-resistant Fe–Cr–Ni coating. For Fe–18Cr–8Ni–10Al on Fe–18Cr–8Ni, the critical Cr content of 16 wt % for Cr_2O_3 formation and reformation is met in this coating/substrate system over the time periods considered. For Fe–25Cr–40Ni–10Al on Fe–18Cr–8Ni, a Cr content of 16 wt % can be maintained in the coating after 825 h because of the formation of an fcc phase diffusion barrier at the coating/substrate interface (Fig. 12(*b*)). Additional computations to longer time periods are required to pinpoint the oxidation or corrosion life of this coating.

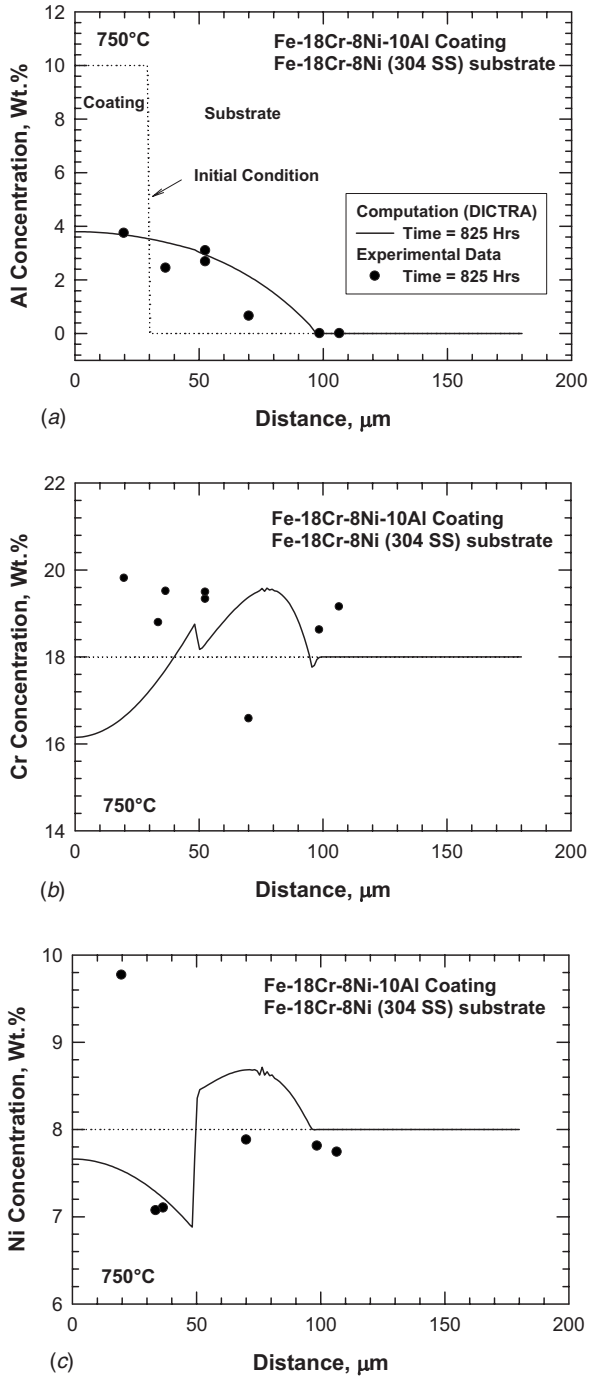

Fig. 14 Calculated concentration profiles compared against experimental data for Fe–18Cr–8Ni–10Al coating on Fe–18Cr–8Ni substrate after 825 h at 750°C: (*a*) Al content, (*b*) Cr content, and (*c*) Ni content

4 Conclusions

The conclusions reached as the results of the computational modeling efforts are as follows:

1. Pseudoternary phase diagrams computed via THERMO-CALC® software provides detailed information on the constituent phases in Fe–Cr–Ni–Al alloys at various temperatures.
2. The formation of σ-phase in Fe–Cr–Ni–Al alloys is suppressed for Al contents in excess of 4 wt % for temperatures in the range of 600–1200 K.
3. Grain growth modeling indicated that the columnar-grained structure observed in Fe–18Cr–8Ni–(4–10)Al nanocoatings is stable and resistant to grain growth because of a high activation energy for grain growth due to a low grain boundary energy resulting from a high percentage of low-angle grain boundaries.
4. Sintering modeling indicated that the initial relative density of the as-processed coating must be greater than 98% in order to achieve full density in less than 2 days of thermal exposure at 750°C.
5. Interface toughness computation indicated that Fe–Cr–Ni–Al nanocoatings produced by magnetron-sputtering at SwRI exhibit high interface toughness in the range of $52-366\ \mathrm{J/m^2}$.
6. Interdiffusion modeling using the DICTRA software package indicated that inward diffusion results in Al and Cr losses from the nanocoating to the substrate during thermal exposure at 750°C.

Acknowledgment

This work was supported by the Department of Energy through Contract No. DE-FC26-07NT439096 and monitored by Ms. Patricia Rawls, Program Manager. The clerical assistance of Ms. L. Mesa in the preparation of the manuscript is likewise acknowledged.

References

[1] Wang, F.-H., 1997, "The Effect of Nanocrystallization on the Selective Oxidation and Adhesion of Al_2O_3 Scales," Oxid. Met., **48**, pp. 215–223.
[2] Liu, Z.-Y., Gao, W., Dahm, K. L., and Wang, F.-H., 1998, "Oxidation Behaviour of Sputter-Deposited Ni–Cr–Al Micro-Crystalline Coatings," Acta Mater., **46**, pp. 1691–1700.
[3] Liu, Z.-Y., and Gao, W., 1998, "Oxidation Behaviours of Microcrystalline Ni–Cr–Al Alloy Coatings at 900°C," Scr. Mater., **38**, pp. 877–885.
[4] Chen, G.-F., and Lou, H.-Y., 1999, "The Effect of Nanocrystallization on the Oxidation Resistance of Ni–5Cr–5Al Alloy," Scr. Mater., **41**, pp. 883–887.
[5] Chen, G.-F., and Lou, H.-Y., 1999, "Oxidation Behavior of Sputtered Ni–3Cr–20 Al Nanocrystalline Coating," Mater. Sci. Eng., A, **A271**, pp. 360–365.
[6] Liu, Z.-Y., Gao, W., Dahm, K. L., and Wang, F.-H., 1998, "Improved Oxide Spallation Resistance of Microcrystalline Ni–Cr–Al Coatings," Oxid. Met., **50**, pp. 51–69.
[7] Chen, G., and Lou, H., 2000, "Oxidation Behavior of Sputtered Ni–Cr–Al–Ti Nanocrystalline Coating," Surf. Coat. Technol., **123**, pp. 92–96.
[8] Chen, G.-F., and Lou, H.-Y., 2000, "Effect of Nanocrystallization on the Oxidation Behavior of a Ni–8Cr–3.5 Al Alloy," Oxid. Met., **54**, pp. 155–162.
[9] Ajdelsztajn, L., Tang, F., Kim, G. E., Provenzano, V., and Shoenung, J. M., 2005, "Synthesis and Oxidation Behavior of Nanocrystalline MCrAlY Bond Coats," J. Therm. Spray Technol., **14**, pp. 23–30.
[10] Cheruvu, N. S., 2008, "Nanostructured Coatings by Pulsed Plasma Processing for Alloys used in Coal-Fired Environments," Department of Energy, Small Business Technology Transfer (STTR) Program, SwRI Fourth Quarterly Report to Karta Technologies, Report No. DE-FG02-5ER 86249.
[11] Liu, Z.-Y., Gao, W., and Li, M.-S., 1999, "Cyclic Oxidation of Sputter-Deposited Nanocrystalline Fe–Cr–Ni–Al Alloy Coatings," Oxid. Met., **51**, pp. 403–419.
[12] Liu, Z., Gao, W., and He, Y., 1999, "Oxidation Behaviour of Nanocrystaliine Fe–Ni–Cr–Al Alloy Coatings," Mater. Sci. Technol., **15**, pp. 1447–1450.
[13] He, Y., Pang, H., Qi, H., Wang, D., Li, Z., and Gao, W., 2002, "Micro-Crystalline Fe–Cr–Ni–Al–Y_2O_3 ODS Alloy Coatings Produced by High Frequency Electric-Spaak Deposition," Mater. Sci. Eng., A, **334**, pp. 179–186.
[14] Thermo-Calc® Software, 2007, THERMO-CALC for Windows Version 4, Thermo-Calc Software AB, Stockholm, Sweden.
[15] Thermo-Calc® Software, 2007, TCFE5, Version 5, Thermo-Calc Software AB, Stockholm, Sweden.
[16] Thermo-Calc® Software, DICTRA, Version 24, Thermo-Calc Software AB, Stockholm, 2007; Version 25, 2008.
[17] Wright, I. G., Pint, P. A., Hall, L. M., and Tortorelli, P. F., 2001, *Lifetimes Modeling of High-Temperature Corrosion Processes*, M. Schutze, W. J. Quadakkers, and J. R. Nicholls, eds., Maney Publishing, London, England, EFC Publications No. 34, pp. 339–358.
[18] Murphy, J. T., Regina, J. R., Deacon, R. M., DuPont, J. N., and Marder, A. R., 2005, "High-Temperature Corrosion Resistance of Candidate FeAlCr Coatings in Low NO_x Environments," *Proceedings of the 19th Annual Conference on Fossil Energy Materials*, Knoxville, TN, May 9–11.
[19] Pivin, J. C., Delaunay, D., Roques-Carmes, C., Huntz, A. M., and Lacombe, P., 1980, "Oxidation Mechanism of Fe–Ni–20–25Cr–5Al Alloys-Influence of Small Amounts of Yttrium on Oxidation Kinetics and Oxide Adherence," Corros. Sci., **20**, pp. 351–373.
[20] Huang, T. T., Richter, R., Chang, Y. L., and Pfender, E., 1985, "Formation of Aluminum Oxide Scales in Sulfur-Containing High Temperature Environ-

ments," Metall. Trans. A., **16A**, pp. 2051–2059.
[21] Karaminezhaad, M., Kordzadeh, E., and Bateni, M. R., 2004, "The Effect of Nickel and Aluminum Addition on Oxidation Behavior of Austenitic Heat Resistance Steels," Journal of Corrosion Science and Engineering, **7**(4), pp. 1–11, Paper 4.
[22] Yamada, S., Tadashi, H., Kawamura, Y., and Saburi, T., 2000, "Alumina Surface Layer Formed by High Temperature Heat-Treatment of Fe-Cr-Ni-Al Alloy Intended for Blade Material," J. High-Temp. Soc., **26**(3), pp. 131–137.
[23] Gao, W., Liu, Z., and Li, Z., 2001, "Nano- and Microcrystal Coatings and Their High-Temperature Applications," Adv. Mater., **13**(12–13), pp. 1001–1004.
[24] Pint, B. A., Peraldi, R., and Maziasz, P. J., 2004, "The Use of Model Alloys to Develop Corrosion-Resistant Stainless Steels," Mater. Sci. Forum, **461–464**, pp. 815–822.
[25] Brady, M. P., Yamamoto, Y., Santella, M. L., and Pint, B. A., 2007, "Effects of Minor Alloy Additions and Oxidation Temperature on Protective Alumina Scale Formation in Creep-Resistant Austenitic Stainless Steels," Scr. Mater., **57**, pp. 1117–1120.
[26] Yamamoto, Y., Brady, M. P., Lu, Z. P., Maziasz, P. J., Liu, C. T., Pint, B. A., More, K. L., Meyer, H. M., and Payzant, E. A., 2007, "Creep-Resistant Al_2O_3-Forming Austenitic Stainless Steels," Science, **316**, pp. 433–436.
[27] Pint, B. A., Zhang, Y., Walker, L. R., and Wright, I. G., 2007, "Long-Term Performance of Aluminide Coatings on Fe-Based Alloys," Surf. Coat. Technol., **202**, pp. 637–642.
[28] Hillert, M., 1965, "On the Theory of Normal and Abnormal Grain Growth," Acta Metall., **13**, pp. 227–238.
[29] Sidor, Y., Kovac, F., and Petrychka, V., 2005, "Secondary Recrystallization in Non-Oriented Electrical Steels," Metabk, **44**(3), pp. 169–174.
[30] Johnson, D. L., and Cutler, I. B., 1963, "Diffusion Sintering: I, Initial Stage Sintering Models and Their Application to Shrinkage of Powder Compacts," J. Am. Ceram. Soc., **46**(11), pp. 541–545.
[31] Drory, M. D., and Hutchinson, J. W., 1996, "Measurement of the Adhesion of a Brittle Film on a Ductile Substrate by Indentation," Proc. R. Soc. London, Ser. A, **452**, pp. 2319–2341.
[32] Volinsky, A. A., Moody, N. R., and Berberich, W. W., 2002, "Interfacial Toughness Measurements for Thin Films on Substrates," Acta Mater., **50**, pp. 441–466.
[33] Bangaru, N. V., and Krutenat, R. C., 1984, "Diffusion Coatings of Steels: Formation Mechanism and Microstructure of Aluminized Heat-Resistant Stainless Steels," J. Vac. Sci. Technol. B, **2**, pp. 806–815.
[34] Zhang, Y., Liu, A. P., and Pint, B. A., 2007, "Interdiffusional Degradatino of Oxidation-Resistant Aluminide Coatings on Fe-Based Alloys," Mater. Corros., **58**, pp. 751–761.
[35] Evans, H. E., Donaldson, A. T., and Gilmour, T. C., 1999, "Mechanisms of Breakaway Oxidation and Application to a Chromia-Forming Steel," Oxid. Met., **52**(5–6), pp. 379–402.
[36] Peraldi, R., and Pint, B. A., 2004, "Effect of Cr and Ni Contents on the Oxidation Behavior of Ferritic and Austenitic Model Alloys in Air With Water Vapor," Oxid. Met., **61**(5/6), pp. 463–483.
[37] Castello, P., Guttmann, V., Farr, N., and Smith, G., 2000, "Laboratory-Simulated Fuel-Ash Corrosion of Superheater Tubes in Coal-Fired Ultra-Supercritical-Boilers," Mater. Corros., **51**, pp. 786–790.
[38] Hack, H., and Stanko, G., 2006, "Update on Fireside Corrosion Resistance of Advanced Materials for Ultra-Supercritical Coal-Fired Power Plants," Presented at the 31st International Technical Conference on Coal Utilization & Fuel Systems, Sand Key Island, FL, May 1–26.

A Cyclic Life Prediction Approach for Directionally Solidified Nickel Superalloys

Roland Mücke

Piyawan Woratat

ALSTOM,
Brown Boveri Strasse 7,
CH-5401 Baden, Switzerland

The performance of heavy duty gas turbines is closely related to the material capability of the components of the first turbine stage. In modern gas turbines single crystal (SX) and directionally solidified (DS) nickel superalloys are applied, which, compared with their conventionally cast version, hold a higher cyclic life and a significantly improved creep rupture strength. SX and DS nickel superalloys feature a significant directional dependence of the material properties. To fully exploit the material capability, the anisotropy needs to be accounted for in both the constitutive and lifing model. In this context, the paper addresses a cyclic life prediction procedure for DS materials with transverse isotropic material symmetry. Thereby, the well-known local approaches to fatigue life prediction of isotropic materials under uniaxial loading are extended toward materials with transverse isotropic properties under multiaxial load conditions. As part of the proposed methodology, a Hill type function is utilized for describing the anisotropic failure behavior. The coefficients of the Hill surface are determined from the actual multiaxial loading, material symmetry, and anisotropic fatigue strength of the material. In this paper we first characterize the anisotropy of DS superalloys. We then present the general mathematical framework of the proposed lifing procedure. Later we discuss a validation of the cyclic life model by comparing the measured and predicted fatigue lives of the test specimens. Finally, the proposed method is applied to the cyclic life prediction of a gas turbine blade. [DOI: 10.1115/1.3205027]

1 Introduction

Improvements in the performance parameters of modern heavy duty gas turbines for electric power generation are driven by the cooling technology [1], as well as the material capability especially for the first turbine stage. In this context, directionally solidified (DS) nickel superalloys were developed for achieving a high fatigue resistance and large creep rupture strength by eliminating the grain boundaries perpendicular to the primary load direction. Moreover, DS turbine blades have a better defect tolerance than single crystal (SX) components [2]. Therefore DS alloys are applied especially for large parts under pronounced rotational loading.

The advanced material capability of DS alloys can only been fully exploited in the design of components when both the constitutive model and life prediction methods appropriately account for the anisotropy of the material. In this context, this paper addresses the procedure for anisotropic cyclic life assessment of DS materials under multiaxial load conditions. Depending on the application, the constitutive anisotropic models, which are not described here, are either based on linear elasticity with an anisotropic Neuber correction [3] or an anisotropic unified viscoplastic model [4].

The physical mechanisms of deformation, fatigue, and fracture have been under intensive investigation for many years. As a result, several cyclic damage models for special types of failure mechanisms and for specific classes of materials have been proposed [5–9]. However, up to date, there is no general, mechanism based damage model, which addresses the most important damage modes such as fatigue, creep, oxidation, and their interactions in a consistent manner. Therefore, for solving complex practical engineering problems, empirical lifetime prediction approaches are still in widespread use. In fact, it has been found and confirmed by several researchers that under the assumption of a stabilized loading cycle, a linear relationship on log-log scale is appropriate for many practical applications to describe the failure of a uniaxial, cyclic loaded material. In this case, the corresponding uniaxial failure equations are of the types

$$N_i = C \cdot \Delta\varepsilon^m \tag{1}$$

$$N_i = C \cdot \Delta\sigma^m \tag{2}$$

for the local strain approach (Coffin–Manson equation) and for the local stress approach (Basquin equation), respectively [5]. Thereby, N_i denotes the number of load cycles relating to a suitable end-of-life criterion, e.g., crack initiation or rupture. The parameters C and m are material constants depending on the temperature, hold time, and further characteristics of an equivalent thermomechanical load cycle. Of course, the parameters C and m in Eqs. (1) and (2) have different numerical values for the strain and stress approaches. Nevertheless, we use the same notation for presentation purpose.

In this paper we propose a generalization of the above equations for application to cyclic life prediction of DS superalloys under multiaxial load conditions. After describing the material symmetry of DS alloys, the mathematical framework of the proposed approach is presented. Later the method is validated by comparing the prediction with additional test results. Finally, the application of the anisotropic procedure to lifetime prediction of gas turbine blades is presented.

2 Anisotropy of Directionally Solidified Materials

Conventionally cast materials develop a polycrystalline microstructure, leading to an isotropic material response on the macroscale (Fig. 1). On the contrary, the columnar grain structure of DS nickel superalloys produces a significant anisotropy in the constitutive and lifing behaviors. Using the definitions in Fig. 1, the response of the DS alloy is isotropic in the x-y plane, whereas it

Contributed by the International Gas Turbine Institute of ASME for publication in the JOURNAL OF ENGINEERING FOR GAS TURBINES AND POWER. Manuscript received April 8, 2009; final manuscript received April 15, 2009; published online March 4, 2010. Review conducted by Dilip R. Ballal. Paper presented at the ASME Gas Turbine Technical Congress and Exposition, Orlando, FL, June 8–12, 2009.

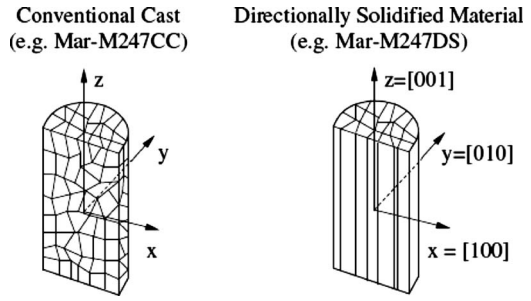

Fig. 1 Sketches of the microstructure of a conventionally cast and a directionally solidified material

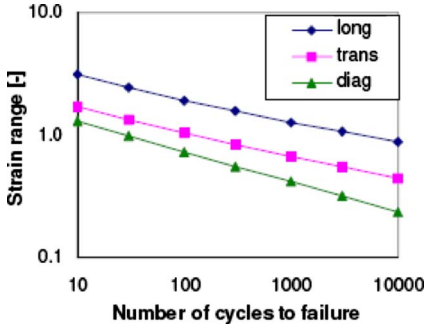

Fig. 3 Example for anisotropy of cyclic strength data of the DS material at elevated temperature

behaves differently in any off-plane direction. In particular, the creep resistance of the alloy is highest in the z-direction, which, throughout the paper, denotes the direction of solidification.

Figure 2 shows the direction dependence of the Young's modulus for a specific temperature. For this purpose the following characteristic directions are introduced:

- longitudinal direction (z-direction, [001], direction of solidification)
- transverse direction (any direction in the x-y plane, e.g., [100])
- diagonal direction (any direction with an off-plane orientation of α=45 deg, e.g., [011])

Note that for typical DS superalloys the elastic anisotropy ratio, i.e., the ratio between the highest and the lowest stiffnesses, approaches from 1.3 to 1.6, depending on the temperature. Note further that the linear elastic model of the DS materials (featuring transverse isotropic material symmetry) is characterized by five independent elastic constants (for details we refer to the Appendix A and to the Refs. [10,11]). The elastic properties of Mar-M247DS have been published in Refs. [12,13].

The anisotropy of the DS alloys can also be observed in the fatigue strength properties (Fig. 3). Considering the cyclic test results in the longitudinal, transverse, and diagonal directions, a significant orientation dependence is observed as a function of temperature and loading. Low cycle fatigue (LCF) properties of Mar-M247DS have been published in Ref. [14].

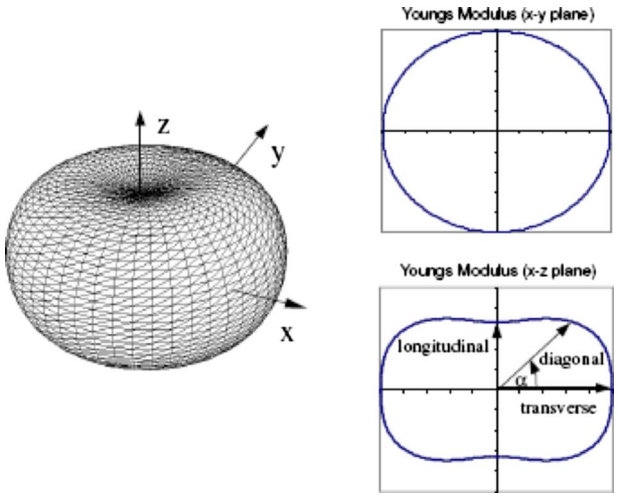

Fig. 2 Anisotropic Young's modulus of the DS materials

3 The Strain Approach of Cyclic Life Prediction for DS Materials

For describing the fatigue behavior of DS materials we consider the fatigue strength in three independent material directions. Typically, material data are available for the longitudinal, transverse, and diagonal directions (Fig. 2). Thus, instead of Eq. (1) for the local strain approach of isotropic materials being used, the following three equations characterize the uniaxial cyclic behavior of the DS materials

$$N_i^{(k)} = C_k \cdot \Delta\varepsilon_k^{m_k} \quad \text{for } k = l,t,d \tag{3}$$

The three pairs of fatigue parameters (C_l, m_l), (C_t, m_t), and (C_d, m_d) are determined by uniaxial cyclic tests in the longitudinal (l), transverse (t), and diagonal (d) material directions. Note that Eq. (3) is sufficient to characterize the fatigue behavior of uniaxial loading in either of the characteristic directions of the DS materials. However, the fatigue assessment of engineering structures additionally requires the following to be accounted for:

- loading in arbitrary directions
- multiaxial load conditions with all possible combinations of strain tensor components

A mere interpolation of individual experimental data of the different loading directions is not sufficient as this only covers the uniaxial load state. To account for multiaxiality, the following procedure is proposed.

3.1 Recovery of the Multiaxial State of Strain. Due to the Poisson effect, a uniaxial load of the material in direction k produces a multiaxial state of strain. Therefore, in the case that the strains are taken as a basis for lifetime prediction (the strain approach), the multiaxial strain state produced by a uniaxial load needs to be determined first. We assume that the loading is proportional, i.e., the ratios of strain components remain constant along the loading path. Therefore, linear elasticity can be used and an applied strain $\Delta\varepsilon_k$ in direction k produces the stress

$$\Delta\sigma_k = E_k \Delta\varepsilon_k \tag{4}$$

with

$$1/E_k = \mathbf{D}_k : \mathbf{H} : \mathbf{D}_k \tag{5}$$

and

$$\mathbf{D}_k = \mathbf{k} \otimes \mathbf{k} \tag{6}$$

where E_k denotes the directional stiffness, $\mathbf{H}$ is the fourth order tensor of elastic compliance, and $\mathbf{D}_k$ represents the direction tensor produced by the dyadic product of the normalized direction vector $\mathbf{k}$ (for details see Appendix A). Further, the uniaxial stress $\Delta\sigma_k$ in direction k produces the stress tensor $\Delta\boldsymbol{\sigma}_k = \mathbf{D}_k \Delta\sigma_k$. Using the generalized Hooke's law $\Delta\boldsymbol{\varepsilon}_k = \mathbf{H} : \Delta\boldsymbol{\sigma}_k$, the recovered state of strain due to a uniaxial strain $\Delta\varepsilon_k$ in direction k yields

$$\Delta\boldsymbol{\varepsilon}_k = \mathbf{H}:\mathbf{D}_k E_k \Delta\varepsilon_k \tag{7}$$

For the load ratio $\mathbf{r}_k$, we obtain

$$\mathbf{r}_k = \frac{\Delta\boldsymbol{\varepsilon}_k}{\Delta\varepsilon_k} = \mathbf{H}:\mathbf{D}_k E_k \tag{8}$$

Note that r_k depends on the elastic constants. Therefore it may slightly change with temperature.

3.2 Generalization of the Uniaxial Strain Approach. For the generalization of the uniaxial strain approach in Eq. (1) the three uniaxial equations (Eq. (3)) are replaced by the general multiaxial formulation

$$N_i = C \cdot f_H(\Delta\boldsymbol{\varepsilon},\mathbf{F})^m \tag{9}$$

where

$$f_H^2(\Delta\boldsymbol{\varepsilon},\mathbf{F}) = \mathbf{q}_\varepsilon^T\mathbf{F} \tag{10}$$

denotes the square of the Hill equivalent strain function. For DS materials featuring transverse isotropic material symmetry with the z-direction as the direction of solidification (Fig. 1), we obtain

$$\mathbf{q}_\varepsilon^T\mathbf{F} = \begin{bmatrix} (\varepsilon_{yy}-\varepsilon_{zz})^2 + (\varepsilon_{zz}-\varepsilon_{xx})^2 + 2\varepsilon_{xy}^2 \\ (\varepsilon_{xx}-\varepsilon_{yy})^2 + 4\varepsilon_{xy}^2 \\ 2(\varepsilon_{yz}^2+\varepsilon_{zx}^2) \end{bmatrix}^T \begin{bmatrix} F \\ H \\ L \end{bmatrix} \tag{11}$$

Note that Eq. (11) involves the three independent Hill parameters $\mathbf{F}=[F,H,L]^T$. For details on the Hill function for different material symmetries see Ref. [11].

Obviously, for uniaxial loadings $\Delta\varepsilon_k$ in one of the characteristic directions k, the general multiaxial approach (Eq. (9)) and the uniaxial formulation (Eq. (3)) have to predict the same number of cycles to failure. Therefore, the following three equations hold

$$\begin{aligned} C_l \cdot \Delta\varepsilon_l^{m_l} &= C \cdot f_H(\Delta\boldsymbol{\varepsilon}_l,\mathbf{F})^m \\ C_t \cdot \Delta\varepsilon_t^{m_t} &= C \cdot f_H(\Delta\boldsymbol{\varepsilon}_t,\mathbf{F})^m \\ C_d \cdot \Delta\varepsilon_d^{m_d} &= C \cdot f_H(\Delta\boldsymbol{\varepsilon}_d,\mathbf{F})^m \end{aligned} \tag{12}$$

where $\Delta\boldsymbol{\varepsilon}_k$ $(k=l,t,d)$ denotes the recovered strain tensor components produced by $\Delta\varepsilon_k$ in the longitudinal (l), transverse (t), and diagonal (d) directions. Further, without loss of generality, the longitudinal direction $k=l$ can be used as reference. Thus, with $C=C_l$ and $m=m_l$, we obtain the three conditions

$$C_k \cdot \Delta\varepsilon_k^{m_k} = C_l \cdot f_H(\Delta\boldsymbol{\varepsilon}_k,\mathbf{F})^{m_l} \quad \text{for } k=l,t,d \tag{13}$$

to describe the three Hill parameters $\mathbf{F}=[F,H,L]^T$.

We now consider the Hill function f_H on the right side of Eq. (13) and replace the strain tensor $\Delta\boldsymbol{\varepsilon}_k$ by the load ratio $\mathbf{r}_k$ according to Eq. (8) as

$$f_H^2(\Delta\boldsymbol{\varepsilon}_k,\mathbf{F}) = f_H^2(\mathbf{r}_k,\mathbf{F}) \cdot (\Delta\varepsilon_k)^2 \tag{14}$$

to obtain

$$f_H^2(\Delta\boldsymbol{\varepsilon}_k,\mathbf{F}) = \boldsymbol{\theta}_k^T\mathbf{F} \cdot (\Delta\varepsilon_k)^2 \tag{15}$$

with

$$\boldsymbol{\theta}_k^T = \begin{bmatrix} (r_{yy}-r_{zz})^2 + (r_{zz}-r_{xx})^2 + 2r_{xy}^2 \\ (r_{xx}-r_{yy})^2 + 4r_{xy}^2 \\ 2(r_{yz}^2+r_{zx}^2) \end{bmatrix}^T \tag{16}$$

Combining the above formulations with Eq. (13) and after squaring the results in

$$C_k^2 \cdot (\Delta\varepsilon_k)^{2m_k} = C_l^2 \cdot (\boldsymbol{\theta}_k^T\mathbf{F})^{m_l} \cdot (\Delta\varepsilon_k)^{2m_l} \tag{17}$$

we obtain

$$\left(\frac{C_k}{C_l}\right)^2 \cdot \Delta\varepsilon_k^{2(m_k-m_l)} = (\boldsymbol{\theta}_k^T\mathbf{F})^{m_l} \tag{18}$$

We now eliminate $\Delta\varepsilon_k$ by assuming that the actual multiaxial load $\Delta\boldsymbol{\varepsilon}$ computed by finite element analysis produces the same damage as a uniaxial load of the same Hill equivalent strain in either of the characteristic directions, that is

$$f_H(\Delta\boldsymbol{\varepsilon},\mathbf{F}) = f_H(\Delta\boldsymbol{\varepsilon}_k,\mathbf{F}) \quad \text{for } k=l,t,d \tag{19}$$

Using Eqs. (11) and (15) immediately gives

$$\Delta\varepsilon_k^2 = \frac{\mathbf{q}_\varepsilon^T\mathbf{F}}{\boldsymbol{\theta}_k^T\mathbf{F}} \tag{20}$$

Finally, with Eq. (18) we arrive at the following governing equations for the unknown Hill parameters

$$\begin{aligned} \phi_1(\mathbf{F}) &:= 1 - (\boldsymbol{\theta}_l^T\mathbf{F})^{m_l} = 0 \\ \phi_2(\mathbf{F}) &:= \left(\frac{C_t}{C_l}\right)^2 \cdot (\mathbf{q}_\varepsilon^T\mathbf{F})^{m_t-m_l} - (\boldsymbol{\theta}_t^T\mathbf{F})^{m_t} = 0 \\ \phi_3(\mathbf{F}) &:= \left(\frac{C_d}{C_l}\right)^2 \cdot (\mathbf{q}_\varepsilon^T\mathbf{F})^{m_d-m_l} - (\boldsymbol{\theta}_d^T\mathbf{F})^{m_d} = 0 \end{aligned} \tag{21}$$

The Eqs. (21) form a nonlinear algebraic system of three equations for the three unknown Hill parameters $\mathbf{F}=[F,H,L]^T$. The system is iterated with a standard Newton method. Details are given below. After iteration for the Hill parameters, the number of cycles to failure is evaluated by

$$N_i = C_l \cdot f_H(\Delta\boldsymbol{\varepsilon},\mathbf{F})^{m_l} \tag{22}$$

where $f_H(\Delta\boldsymbol{\varepsilon},\mathbf{F})$ is defined by Eqs. (10) and (11).

4 The Stress Approach of Cyclic Life Prediction for DS Materials

The stress approach to cyclic life prediction is greatly simplified by the fact that no material model is required for recovering the multiaxial state of load. Indeed, a uniaxial stress $\Delta\sigma_k$ in direction k produces the stress tensor components

$$\Delta\boldsymbol{\sigma}_k = \mathbf{r}_k \Delta\sigma_k \tag{23}$$

where the load ratio $\mathbf{r}_k$ is determined by

$$\mathbf{r}_k = \Delta\boldsymbol{\sigma}_k / \sqrt{\Delta\boldsymbol{\sigma}_k:\Delta\boldsymbol{\sigma}_k} = \mathbf{D}_k \tag{24}$$

and $\mathbf{D}_k$ is defined according to Eq. (6). Further, in the Hill function, we now apply the stress components to give

$$\mathbf{q}_\sigma^T\mathbf{F} = \begin{bmatrix} (\sigma_{yy}-\sigma_{zz})^2 + (\sigma_{zz}-\sigma_{xx})^2 + 2\sigma_{xy}^2 \\ (\sigma_{xx}-\sigma_{yy})^2 + 4\sigma_{xy}^2 \\ 2(\sigma_{yz}^2+\sigma_{zx}^2) \end{bmatrix}^T \begin{bmatrix} F \\ H \\ L \end{bmatrix} \tag{25}$$

Finally, the governing equations for the multiaxial failure surface of the stress approach read

$$\phi(\mathbf{F}) := \left(\frac{C_k}{C_l}\right)^2 \cdot (\mathbf{q}_\sigma^T\mathbf{F})^{m_k-m_l} - (\boldsymbol{\theta}_k^T\mathbf{F})^{m_k} = 0 \tag{26}$$

After iteration for the Hill parameters the number of cycles to failure for the stress approach is obtained by

$$N_i = C_l \cdot f_H(\Delta\boldsymbol{\sigma},\mathbf{F})^{m_l} \tag{27}$$

4.1 Remarks

1. The above governing equations for iterating the Hill parameters (Eqs. (21) and (26)) are general and can be applied for any suitable combination of independent material directions k. Of course, for the sake of stability and accuracy of the numerical procedure, the angle between the applied directions should be as large as possible.

2. For the stress approach the components of $\boldsymbol{\theta}_k$ are independent of the material model. Using the longitudinal $\mathbf{k}_l=[0,0,1]^T$, transverse, $\mathbf{k}_t=[0,1,0]^T$, and diagonal $\mathbf{k}_d=[0,1/\sqrt{2},1/\sqrt{2}]^T$ directions, we immediately obtain $\boldsymbol{\theta}_l=[2,0,0]^T$, $\boldsymbol{\theta}_t=[1,1,0]^T$, and $\boldsymbol{\theta}_d=\left[\frac{1}{4},\frac{1}{4},\frac{1}{2}\right]^T$. Note that for the strain approach, the components of $\boldsymbol{\theta}_k$ depend on the elastic constants (see Eqs. (8) and (16)).
3. In case of $m_l=m_t=m_d$ the anisotropy of fatigue strength is independent of the load level. If one of the fatigue exponents is different, different failure surfaces occur at different load levels.
4. The governing equations (Eqs. (21) and (26)) for DS materials contain the well-known cyclic life prediction approaches for isotropic materials when using $C_l=C_t=C_d$ and $m_l=m_t=m_d$. Further, the equations include the uniaxial formulations (Eqs. (1) and (2)) when using uniaxial load conditions.

5 Details of Implementation

The implementation of the proposed procedure in a cyclic life prediction tool implies the following steps:

1. Calculate the loading ($\Delta\boldsymbol{\varepsilon}$ for the strain approach or $\Delta\boldsymbol{\sigma}$ for the stress approach) by using a (linear or nonlinear) finite element analysis and determine the load vectors $\mathbf{q}_\varepsilon$ and $\mathbf{q}_{\boldsymbol{\sigma}}$ according to Eqs. (11) and (25).
2. Obtain the three pairs of fatigue parameters (C_k,m_k) from the material testing in three independent material directions.
3. Determine the load ratio $\mathbf{r}_k$ for the three independent material directions according to Eqs. (8) and (24) and calculate the corresponding vectors $\boldsymbol{\theta}_k$ according to Eq. (16).
4. Iterate Eqs. (21) and (26) for the unknown Hill parameters.
5. Determine the number of cycles to failure according to Eqs. (22) and (27).

A standard Newton method is used to iterate the governing equations [15]. With the longitudinal direction $k=l$ as reference, we immediately get

$$F=\frac{1-\theta_{l2}H-\theta_{l3}L}{\theta_{l1}} \tag{28}$$

where θ_{li} denotes the components of the vector $\boldsymbol{\theta}_l$. Therefore, we have only two remaining equations to be solved. In view of the computer implementation the logarithmic forms

$$\begin{aligned}2\cdot\log(C_t/C_l)+(m_t-m_l)\cdot\log(\mathbf{q}^T\mathbf{F})-m_t\cdot\log(\boldsymbol{\theta}_t^T\mathbf{F})=0\\ 2\cdot\log(C_d/C_l)+(m_d-m_l)\cdot\log(\mathbf{q}^T\mathbf{F})-m_d\cdot\log(\boldsymbol{\theta}_d^T\mathbf{F})=0\end{aligned} \tag{29}$$

are used. The corresponding entries of the Jacobian matrix then become

$$\begin{aligned}J_{11}&=\frac{m_t-m_l}{\mathbf{q}^T\mathbf{F}}\left(q_2-\frac{q_1\theta_{l2}}{\theta_{l1}}\right)-\frac{m_t}{\boldsymbol{\theta}_t^T\mathbf{F}}\left(\theta_{t2}-\frac{\theta_{t1}\theta_{l2}}{\theta_{l1}}\right)\\ J_{12}&=\frac{m_t-m_l}{\mathbf{q}^T\mathbf{F}}\left(q_3-\frac{q_1\theta_{l3}}{\theta_{l1}}\right)-\frac{m_t}{\boldsymbol{\theta}_t^T\mathbf{F}}\left(\theta_{t3}-\frac{\theta_{t1}\theta_{l3}}{\theta_{l1}}\right)\\ J_{21}&=\frac{m_d-m_l}{\mathbf{q}^T\mathbf{F}}\left(q_2-\frac{q_1\theta_{l2}}{\theta_{l1}}\right)-\frac{m_d}{\boldsymbol{\theta}_d^T\mathbf{F}}\left(\theta_{d2}-\frac{\theta_{d1}\theta_{l2}}{\theta_{l1}}\right)\\ J_{22}&=\frac{m_d-m_l}{\mathbf{q}^T\mathbf{F}}\left(q_3-\frac{q_1\theta_{l3}}{\theta_{l1}}\right)-\frac{m_d}{\boldsymbol{\theta}_d^T\mathbf{F}}\left(\theta_{d3}-\frac{\theta_{d1}\theta_{l3}}{\theta_{l1}}\right)\end{aligned} \tag{30}$$

where q_i denotes the components of the vector $\mathbf{q}$. Using the longitudinal, transverse, and diagonal material directions, we have not experienced numerical problems in solving the nonlinear equations.

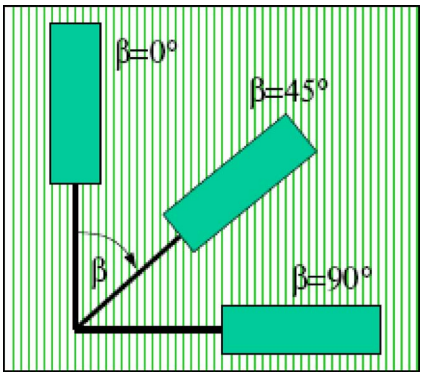

Fig. 4 Definition of the crystallographic orientation of uniaxial specimens

6 Validation

6.1 Uniaxial Loading in Different Directions. For validation of the proposed procedure we first consider the predicted cyclic life of uniaxial specimens in different loading directions (Fig. 4). To this end, uniaxial thermomechanical fatigue (TMF) tests have been carried out in the longitudinal ($\beta=0$ deg), diagonal ($\beta=45$ deg), and transverse ($\beta=90$ deg) directions for describing the anisotropic failure surface of the material. Further, additional TMF tests in $\beta=25$ deg and $\beta=70$ deg directions are performed for comparing the fatigue life predictions for these orientations with the additional experimental data.

The following procedure has been processed to obtain Fig. 5.

- The fatigue parameters (C_β,m_β) have been determined from TMF tests on different load levels in the following load directions: longitudinal ($\beta=0$ deg), transverse ($\beta=90$ deg), diagonal ($\beta=45$ deg), $\beta=25$ deg, and $\beta=70$ deg.
- The cyclic life prediction procedure for the strain approach has been followed on each load level and for each load angle between 0 deg$\leq\beta\leq$90 deg in increments of 1 deg. To this end, the recovered strain components $\Delta\boldsymbol{\varepsilon}_\beta$ of the applied loading $\Delta\varepsilon_a$ (to be used in Eq. (11)) have been evaluated as function of β by

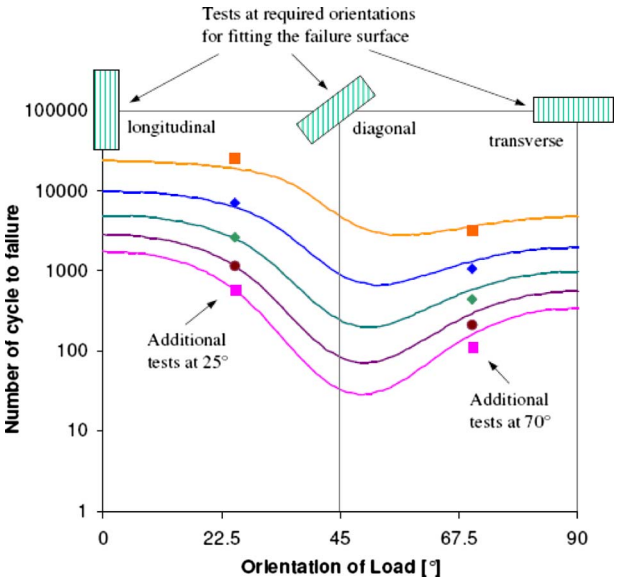

Fig. 5 Comparison of predicted and experimental uniaxial test results for the strain approach

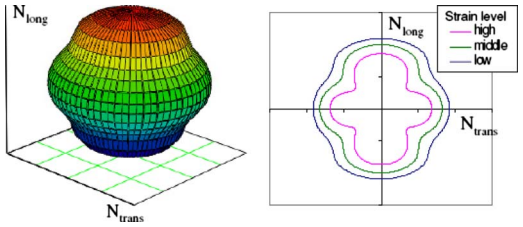

Fig. 6 Cycles to failure (failure surface) for constant strain in logarithmic scale

$$\Delta\boldsymbol{\varepsilon}_\beta = \mathbf{H}:\mathbf{D}_\beta E_\beta \Delta\varepsilon_a$$

where $\mathbf{D}_\beta = \mathbf{k}_\beta \otimes \mathbf{k}_\beta$ with $\mathbf{k}_\beta = [\sin\beta, \cos\beta, 0]^T$, and E_β denotes the directional stiffness in direction $\mathbf{k}_\beta$.

- The predicted number of cycles to failure is plotted for different load levels together with the results of the additional TMF tests in one diagram.

Figure 5 shows a good agreement of the predicted and the measured cyclic life results. Note that for the investigated material the fatigue resistance is highest for the longitudinal direction, followed by the transverse and diagonal directions. Figure 6 presents the failure surface, i.e., the number of cycles to failure for a constant uniaxially applied strain as function of the orientation.

In addition, Figs. 7 and 8 show the corresponding results for the stress approach. Note that the shape of the failure surface is different from the strain approach because of the orientation dependence of the strain-stress transformation for the DS materials.

6.2 Notch Specimens. In the second example we compare the predicted and measured cyclic life of notch specimens. In contrary to the uniaxial loading in the above case, we now address biaxial load conditions produced by the notch effect. The load conditions of the notch specimen tests are listed in Table 1 and illustrated in Fig. 9, where $\Delta\sigma_{\text{av,notch}}$ denotes the average stress and $\Delta\varepsilon_{\text{av,notch}}$ is the average strain in the notch section.

Figures 10 and 11 show the distributions of axial stress (σ_{33}), Hill stress, and equivalent (Hill) strain, as well as the predicted cyclic life. Note that the distributions are axial-symmetric because the direction of material solidification matches the specimen axis

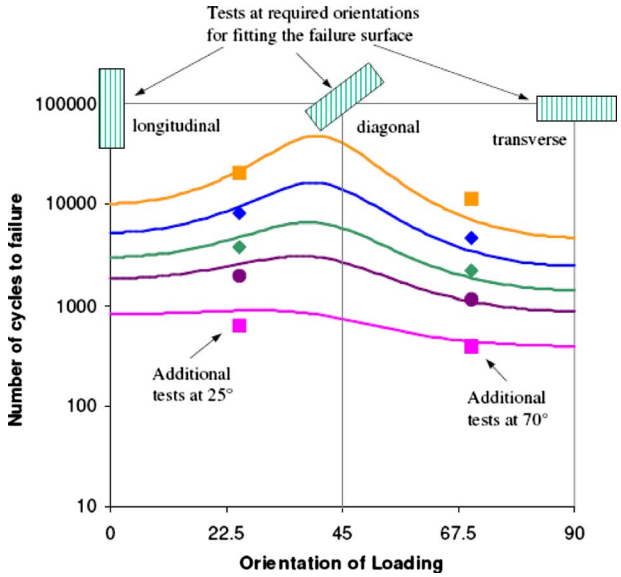

Fig. 7 Comparison of predicted and experimental uniaxial test results for the stress approach

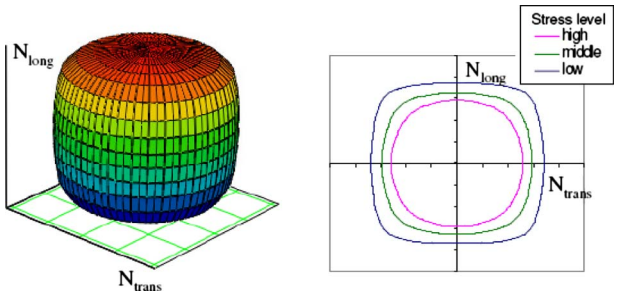

Fig. 8 Cycles to failure (failure surface) for constant stress in logarithmic scale

(Fig. 9). Note further that because of anisotropy, the maximum load and therefore the minimum predicted cyclic life occur on the flank rather than on the ground of the notch.

Figure 12 displays an example of a strain-stress hysteresis for the first and tenth (stabilized) load cycle predicted by an anisotropic viscoplastic constitutive law (for details see Ref. [4]).

Table 2 shows the predicted cyclic life (strain approach) when using the isotropic lifing approach either with transverse or longitudinal material data as well as the results of the proposed anisotropic lifing procedure.

Table 3 then compares the test results with the predicted cyclic

Table 1 Test conditions and measured cyclic life of notch specimen testing

Load conditions	Load levels	Measured cyclic life
LCF, $R_\sigma=-1$, load controlled	$\Delta\sigma_{\text{av,notch}}=400$ MPa $T=1000\,^\circ$C	616
LCF, $R_\sigma=-1$, load controlled	$\Delta\sigma_{\text{av,notch}}=460$ MPa $T=1000\,^\circ$C	313
TMF, $R_\varepsilon=-1$, displ. controlled	$\Delta\varepsilon_{\text{av,notch}}=0.45\%$, $T=400-1000\,^\circ$C	612
TMF, $R_\varepsilon=-1$, displ. controlled	$\Delta\varepsilon_{\text{av,notch}}=0.55\%$, $T=400-1000\,^\circ$C	252

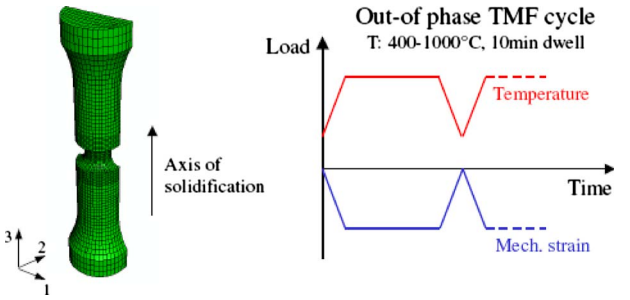

Fig. 9 Details on notch specimen testing

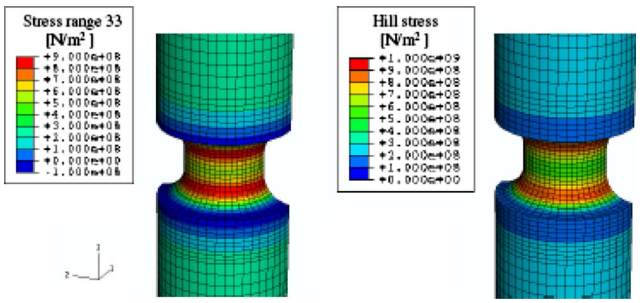

Fig. 10 Axial stress range and Hill stress

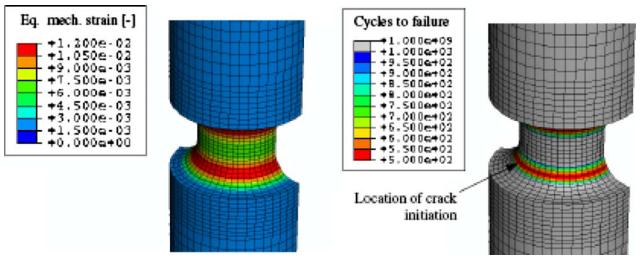

Fig. 11 Hill equivalent mechical strain and predicted number of cycles to failure

life using the anisotropic procedure. Note that the predictions and measurements are close. Note further that under the investigated conditions the prediction tends to give conservative results.

7 Application to Turbine Components

The anisotropic procedure for cyclic life prediction of the DS materials has been implemented in a lifetime analysis tool. The tool is applied as postprocess after the finite element analysis of the turbine components. The lifing process is therefore characterized (Fig. 13) as follows:

1. A heat transfer analysis evaluates the metal temperature of the part.
2. A structural analysis (based on either nonlinear or linear constitutive models) calculates the stress or strain amplitudes.
3. A lifetime analysis tool predicts the cyclic life of the component.

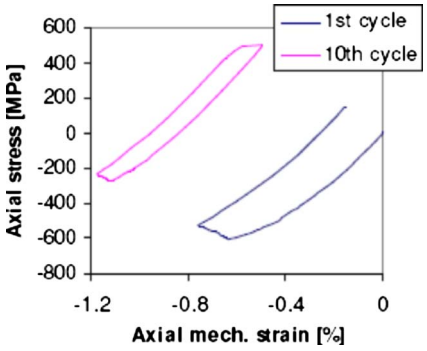

Fig. 12 Predicted first and stabilized tenth load cycles

Table 2 Predicted cyclic life using isotropic and anisotropic procedures (strain approach)

Load case	Isotropic with transverse data	Isotropic with longitudinal data	Anisotropic procedure
LCF: 400 MPa	202	421	520
LCF: 460 MPa	95	234	286
TMF: 0.45%	167	362	454
TMF: 0.55%	61	174	232

Table 3 Predicted cyclic life using the anisotropic procedure and test results

Load case	Predicted life in load cycles	Test results in load cycles
LCF: 400 MPa	520	616
LCF: 460 MPa	286	313
TMF: 0.45%	454	612
TMF: 0.55%	232	252

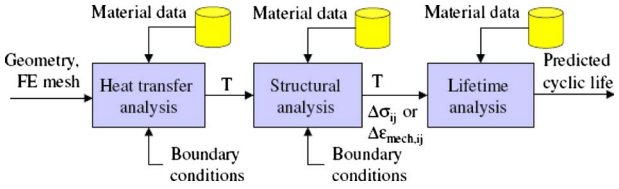

Fig. 13 Lifetime prediction analysis

Note that the cyclic life analysis is performed as a postprocessing step after the structural analysis, i.e., in the current version of the tool the fatigue damage is not considered in the constitutive model (as done in classical continuum damage mechanics [16]). As an advantage of this simple procedure the cyclic life analysis is fast and additional iterations with the finite element model due to fatigue damage evolution are avoided. For most practical applications this approach gives results with sufficient accuracy.

As an example, Fig. 14 shows the metal temperature, Hill equivalent mechanical strain, and predicted cyclic life using the proposed anisotropic lifing approach. In addition, a specific location has been selected for presenting typical results of lifetime prediction for the stress and strain approaches (Table 4). For common details on turbine blade analysis, we refer to Refs. [17,18] among others.

8 Summary

A cyclic life prediction procedure for DS alloys with transverse isotropic material symmetry has been presented. Therefore, the well-known strain and stress based cyclic lifing approaches for isotropic materials have been extended toward materials with transverse isotropy as it occurs, e.g., in directionally solidified nickel superalloys.

The described mathematical framework is consistent, i.e., the isotropic and uniaxial lifing approaches are inherently included when using isotropic fatigue strength properties and uniaxial load conditions. The implementation of the anisotropic lifing approach is straightforward. The proposed method is applied to lifetime prediction of turbine components made of DS alloys. Thus, the benefit of using DS material in turbine design is exploited by considering the anisotropy of the material in the lifing procedure.

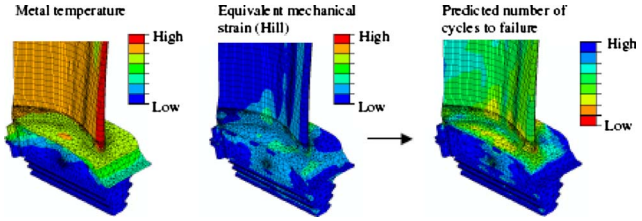

Fig. 14 Example of application to turbine components

Table 4 Specific results for strain and stress approaches

	Strain approach	Stress approach
Load tensor components (%)/(MPa)	$\begin{pmatrix} -0.18 & 0 & -0.10 \\ 0 & -0.05 & 0 \\ -0.10 & 0 & 0.42 \end{pmatrix}$	$\begin{pmatrix} 120 & 0 & -120 \\ 0 & 305 & 0 \\ -120 & 0 & 705 \end{pmatrix}$
Equivalent load	$\Delta\varepsilon_{Hill}=0.462\%$ $\Delta\varepsilon_{Mises}=0.548\%$	$\Delta\sigma_{Hill}=609$ MPa $\Delta\sigma_{Mises}=558$ MPa
Hill parameters	$F=0.257$ $H=2.226$ $L=6.551$	$F=0.500$ $H=1.636$ $L=2.224$
Predicted cyclic life	$N_\varepsilon=11.8\times10^6$	$N_\sigma=9.7\times10^6$

Nomenclature

- LCF = low cycles fatigue
- $\boldsymbol{\varepsilon}$ = strain tensor
- $\Delta\varepsilon_k$ = applied uniaxial strain range in direction k
- $\Delta\boldsymbol{\varepsilon}_k$ = strain tensor produced by $\Delta\varepsilon_k$
- $\Delta\sigma_k$ = applied uniaxial stress range in direction k
- $\Delta\boldsymbol{\sigma}_k$ = stress tensor produced by $\Delta\sigma_k$, $\Delta\boldsymbol{\sigma}_k=\mathbf{D}_k\Delta\sigma_k$
- C_k, m_k = fatigue parameters for direction k
- $\mathbf{D}_k$ = direction tensor, $\mathbf{D}_k=\mathbf{k}\otimes\mathbf{k}$
- $\mathbf{k}$ = normalized direction vector
- f_H = Hill function
- $\mathbf{F}$ = Hill parameters, $\mathbf{F}=[F,H,L]^T$
- $\mathbf{H}$ = tensor of elastic compliance
- $\mathbf{q}_\varepsilon$ = load vector for strain approach
- $\mathbf{q}_\sigma$ = load vector for stress approach
- T = metal temperature
- R_ε, R_σ = load ratio in the cyclic test, $R_\varepsilon=\varepsilon_{\min}/\varepsilon_{\max}$, $R_\sigma=\sigma_{\min}/\sigma_{\max}$

Subscripts

- l = longitudinal direction, [001]
- t = transverse direction, e.g., [100], [010]
- d = diagonal direction, e.g., [011], [101]
- k = l,t,d

Further symbols are explained in the text. Throughout the paper bold symbols denote tensors and vectors. The term "strain" denotes the mechanical strain, i.e., the difference between the total and thermal strains.

Appendix A: Elastic Properties and Directional Stiffness of DS Materials

A.1 Matrix of Elastic Compliance. For the purpose of presentation we use the index transformation $(x,y,z)=>(1,2,3)$. Further, the Voigt notation is applied [10], which transfers the components of the fourth order tensor $\mathbf{H}$ of the elastic compliance into a 6×6 matrix using

$$\begin{bmatrix} H_{11} & H_{12} & H_{13} & H_{14} & H_{15} & H_{16} \\ & H_{22} & H_{23} & H_{24} & H_{25} & H_{26} \\ & & H_{33} & H_{34} & H_{35} & H_{36} \\ & S & & H_{44} & H_{45} & H_{46} \\ & & Y & & H_{55} & H_{56} \\ & & & M & & H_{66} \end{bmatrix} = \begin{bmatrix} H_{1111} & H_{1122} & H_{1133} & 2H_{1123} & 2H_{1113} & 2H_{1112} \\ & H_{2222} & H_{2233} & 2H_{2223} & 2H_{2213} & 2H_{2212} \\ & & H_{3333} & 2H_{3323} & 2H_{3313} & 2H_{3312} \\ & S & & 4H_{2323} & 4H_{2313} & 4H_{2312} \\ & & Y & & 4H_{1313} & 4H_{1312} \\ & & & M & & 4H_{1212} \end{bmatrix}$$

Therefore, for transverse isotropy (with $z=3$ as the reference direction (Fig. 1)) we obtain the following matrix of elastic compliance

$$[H_{ij}]=\begin{bmatrix} 1/E_1 & -\nu_{12}/E_1 & -\nu_{23}/E_1 & 0 & 0 & 0 \\ & 1/E_1 & -\nu_{23}/E_1 & 0 & 0 & 0 \\ & & 1/E_3 & 0 & 0 & 0 \\ & S & & 0 & 1/G_{23} & 0 \\ & & Y & & & 1/G_{23} \\ & & & M & & 2(1+\nu_{12})/E_1 \end{bmatrix}$$

Note that the five independent material constants E_1, E_3, G_{23}, ν_{12}, and ν_{23} (E_x, E_z, G_{yz}, ν_{xy}, and ν_{yz}, respectively) define the elastic behavior of the material.

A.2 Directional Stiffness. We assume that $\mathbf{k}=[k_1,k_2,k_3]^T$ are the components of an arbitrary normalized direction vector. Using Eq. (5), the stiffness E_k in the direction k is then given by

$$1/E_k = H_{11}k_1^4 + H_{22}k_2^4 + H_{33}k_3^4 + 2(H_{23}k_2^2k_3^2 + H_{13}k_1^2k_3^2 + H_{12}k_1^2k_2^2) + H_{44}k_2^2k_3^2 + H_{55}k_1^2k_3^2 + H_{66}k_1^2k_2^2$$

Using the back transformation of indices $(1,2,3)=>(x,y,z)$ we obtain

$$\frac{1}{E_k}=\frac{1}{E_x}(k_x^4+k_y^4)+\frac{1}{E_z}k_z^4+\frac{2}{E_x}k_x^2k_y^2+\left(\frac{1}{G_{yz}}-2\frac{\nu_{yz}}{E_x}\right)(k_x^2k_z^2+k_y^2k_z^2)$$

In particular with $\mathbf{k}_l=[0,0,1]^T$ for the longitudinal direction, $\mathbf{k}_t=[0,1,0]^T$ for the transverse direction, and $\mathbf{k}_d=[0,1/\sqrt{2},1/\sqrt{2}]^T$ for the diagonal direction, we obtain the following directional stiffness:

$$E_l = E_z$$

$$E_t = E_x$$

$$\frac{1}{E_d}=\frac{1}{4}\left(\frac{1-2\nu_{xy}}{E_x}+\frac{1}{E_y}+\frac{1}{G_{xy}}\right)$$

References

[1] Krückels, J., Arzel, T., Kingston, T. R., and Schnieder, M., 2007, "Turbine Blade Thermal Design Process Enhancements for Increased Firing Temperatures and Reduced Coolant Flow," ASME Paper No. GT2007-27457.

[2] Sims, C. T., Stoloff, N. S., and Hagel, W. C., 1987, *Superalloys II, High Temperature Materials for Aerospace and Industrial Power*, Wiley, New York.

[3] Mücke, R., and Bernhardi, O.-E., 2003, "A Constitutive Model for Anisotropic Materials Based on Neuber's Rule," Comput. Methods Appl. Mech. Eng., **192**, pp. 4237–4255.

[4] Robinson, D. N., 1984, "Constitutive Relationships for Anisotropic High-Temperature Alloys," Nucl. Eng. Des., **83**, pp. 389–396.

[5] Suresh, S., 1994, *Fatigue of Materials*, Cambridge University Press, Cambridge.

[6] Tipton, S. M., and Nelson, D. V., 1997, "Advances in Multiaxial Fatigue Life Prediction for Components With Stress Concentrations," Int. J. Fatigue, **19**, pp. 503–515.

[7] Schütz, W., 1996, "A History of Fatigue," Eng. Fract. Mech., **54**, pp. 263–300.

[8] Wang, Y.-Y., and Yao, W.-X., 2004, "Evaluation and Comparison of Several Multiaxial Fatigue Criteria," Int. J. Fatigue, **26**, pp. 17–25.

[9] Schijve, J., 2003, "Fatigue of Structures and Materials in the 20th Century and the State of the Art," Int. J. Fatigue, **25**, pp. 679–702.

[10] Cowin, S. C., and Mehrabadi, M. M., 1995, "Anisotropic Symmetries of Linear Elasticity," Appl. Mech. Rev., **48**(5), pp. 247–285.

[11] Lemaitre, J., and Chaboche, J.-L., 1990, *Mechanics of Solid Materials*, Cambridge University Press, Cambridge.

[12] Kuhn, H.-A., and Sockel, H.-G., 1989, "Elastic Properties of Textured and Directionally Solidified Nickel-Based Superalloys Between 25 and 1200°C ," Mater. Sci. Eng., A, **112**, pp. 117–126.

[13] Hasebe, T., Sakane, M., and Ohnami, M., 1992, "Elastic Anisotropy of Directionally Solidified Superalloys," ASME J. Eng. Mater. Technol., **114**, pp. 141–148.

[14] Hasebe, T., Sakane, M., and Ohnami, M., 1992, "High Temperature Low Cycle Fatigue and Cyclic Constitutive Relation of Mar-M247 Directionally Solidified Superalloy," ASME J. Eng. Mater. Technol., **114**, pp. 162–167.

[15] Press, W. H., Teukolsky, S. A., Vetterling, W. T., and Flannery, B. P., 1992, *Numerical Recipes*, Cambridge University Press, Cambridge.

[16] Lemaitre, J., 1996, *A Course on Damage Mechanics*, 2nd ed., Springer, New York.

[17] Olschewski, J., Haftaoglu, C., and Noack, H.-D., 1993, "Thermo-Mechanical 3D-FE-Analysis of a Cooled Turbine Blade Using an Unified Constitutive Model," *Proceedings of the Post-SMiRT Seminar No. 5, Inelastic Analysis, Fatigue and Life Prediction*, Paris, France.

[18] Mücke, R., 1998, "Finite Element Methods for the Structural Analysis of Gas Turbine Blades," *Proceedings of the 25th Finite Element Congress*, Baden-Baden, Nov. 16–17, 1998.

Overcoming of a Resonance Stall and the Minimization of Amplitudes in the Transient Resonance of a Vibratory Machine by the Phase Modulation Method

J. Michalczyk
e-mail: michalcz@agh.edu.pl

Ł. Bednarski
e-mail: lukaszb@agh.edu.pl

Faculty of Mechanical Engineering and Robotics,
University of Science and Technology (AGH),
30-059 Krakow, Poland

The present paper elucidates the difficulties faced in the practical implementation of phase modulation methods in the form that was presented by Wang et al. and in the actual systems where the motor driving moment is the control value. A more general model, which takes into consideration the impact of machine vibrations on the rotor angular velocity, was developed. The modification of the phase modulation method is also proposed. The usefulness of such an approach for shaping the transient resonance of the machines with an unbalanced rotor is proven by means of a simulation and an experiment. [DOI: 10.1115/1.3204503]

1 Problem Overview and the Objectives

The system that is shown in Fig. 1 will be considered as the first one. This figure corresponds to the "half" model of the over-resonance vibratory machine, e.g., a screen with forcing by means of two counter-rotating imbalances. The rotor in the rotor-housing assembly must be accelerated through the natural circular frequency $\omega_n=\sqrt{(m_0+m)/k}$ before reaching its steady operating speed as well as during the rundown.

The phenomenon of the excitation of the intensive resonance vibrations of elastically supported systems, when subjected to harmonic forcing with the continually changing frequency, constitutes one of the principal problems in the design of vibratory machines (e.g., screens and concrete mix vibration tables), vibration insulation systems of rotor and piston machinery, turbines with long rotors, etc.

Industrial practice in this regard is currently based upon the works of Lewis [1] and Kac [2], who analyzed the resonance vibration escalation phenomenon on the model of the harmonic oscillator, which was subjected to harmonic forcing with a frequency linearly variable over time. More recent works [3–5] generally do not significantly differ as to the methods of problem formulation. However, the method for integrating the motion equations is different. Whereas Lewis adopted the constant amplitude of the exciting force, Kac assumed the amplitude proportional to the rpm square, as in the case of the inertial character of the exciting force.

On the grounds of the vibrations envelope, as determined by Lewis and Kac, the monograms were developed [6], serving for the determination of the maximum amplitudes in the states of start-up and coasting. However, Michalczyk [7] showed that the values of the amplitudes, when determined in such a way, for the coasting were overestimated several times. Michalczyk, as well as Agranowska and Blechman, provided more accurate estimates for these amplitudes [7,8]. The reason for the inaccuracy of the solutions of Lewis and Kac is the phenomenon of the strong back effect of the body vibrations in the resonance on the run of the unbalanced rotor [7]. In addition, the analysis of the solutions of Lewis and Kac showed only one method for reducing the maximum amplitudes: by the angular acceleration increase of the rotor in the resonance zone, which leads to the application of oversized and costly motors that display less efficiency in the steady-state operation.

Most recently several works that discuss the problem of reducing these amplitudes by various methods have been published [9,10]. The authors of these respective papers indicate that there is a possibility of reducing the amplitudes in the transient resonance by changing the direction of the power flow in the system. This change can be done by means of the modulation of the angle between the direction of the machine body mass center velocity and the direction of the inertial force exerted on it (referred to by the authors as the "phase angle") by the rotor angular velocity control.

The practical usefulness of these works is limited since it is only possible to directly control the forcing moment and not the angular velocity. The relation between the angular velocity and forcing moment is significantly influenced by the additional moment acting on the rotor due to the movement of the rotor axis. (Its essence is similar to the phenomenon of excitation or stopping the pendulum rotary motion by means of the excitation of the vibration of its axle.) In addition, phase control may constitute an efficient tool enabling one to overcome the resonance stall of the driving system, the power of which is selected from the steady-state operation condition [11].

The objective of the present paper is the application of the phase modulation method for the desired shaping of the transient resonance by means of controlling the rotor driving moment.

2 Design Model

This task requires the building of a model of the system, with the incorporation of the additional degree of freedom, describing the rotor angular motion under the influence of the driving moment as well as the reactions arising from the vibrations of the machine body.

Manuscript received November 25, 2008; final manuscript received May 27, 2009; published online March 3, 2010. Review conducted by Jaroslaw Szwedowicz.

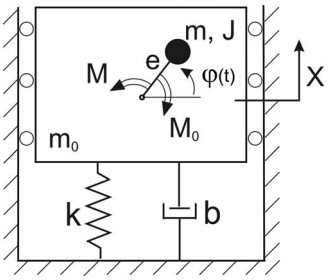

Fig. 1 Calculation model; assumption for the model (*a*) rigid-rotor and rigid bearings producing the first rotor critical speed ω_n that is substantially below a running speed and (*b*) one direction motion for the housing

The equations for the model (Fig. 1) motion are as follows:

$$(m_0 + m)\ddot{x} + b\dot{x} + kx = \dot{\varphi}^2 me \sin\varphi - \ddot{\varphi} me \cos\phi \quad (1a)$$

$$J\ddot{\varphi} = M - M_0 - \ddot{x} me \cos\varphi \quad (1b)$$

It is denoted

$$-\ddot{x} me \cos\varphi = M_w \quad (1c)$$

$$\dot{\varphi}^2 me \sin\varphi - \ddot{\varphi} me \cos\varphi = F_x(t) \quad (1d)$$

The expression M_w (1*c*), coupling the equation of the rotor rotary motion (1*b*) with the vibratory motion of the body $x(t)$ and having the sense of the rotary moment will be called, throughout this paper, as the *vibratory moment* [12]. In order to picture the impact of this moment on the motion of the rotor, Fig. 2 shows the typical behavior of the angular velocity of the unbalanced rotor in the course of free coasting, following drive disengagement. Curve a in Fig. 2 corresponds to the system without the vibratory moment (coasting under the influence of the resistance of motion M_o), while curve b in Fig. 2 corresponds to the entire system (coupled with the body motion by means of M_w).

The calculations were carried out for the following parameter values:

$$m_0 = 2700 \text{ kg}, \quad m = 50 \text{ kg}, \quad e = 0.085 \text{ m},$$

$$k = 999{,}000 \text{ N/m}, \quad b = 700 \text{ N s/m}$$

These charts indicate the essential role exerted by the body vibrations $x(t)$ on the $\dot{\varphi}(t)$.

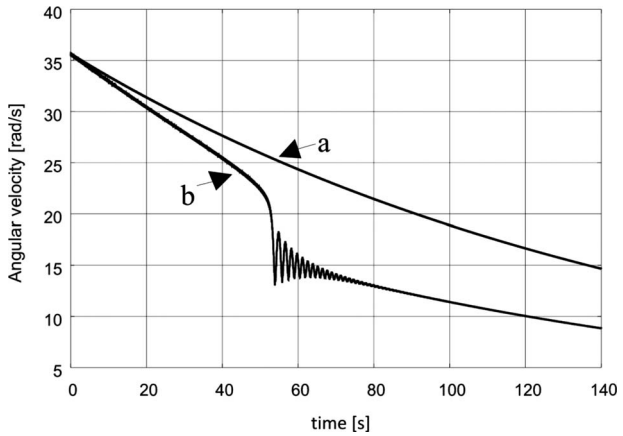

Fig. 2 The impact of the vibratory moment on the free run-down that was obtained by the numerical solution of Eq. (1) for *M*=0; curve a: system without a vibratory moment and curve b: system with a vibratory moment

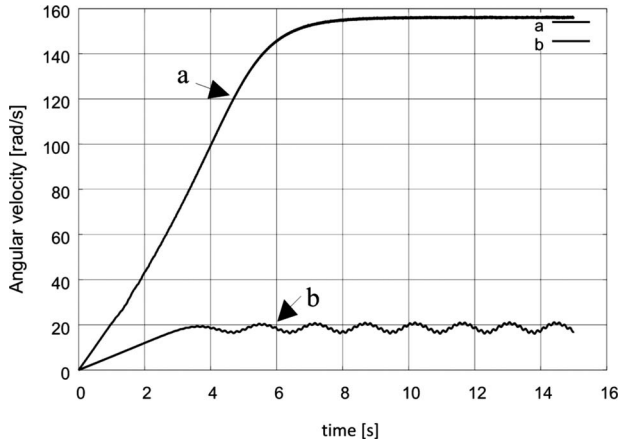

Fig. 3 The impact of the vibratory moment on the occurrence of the resonance stall during start-up (obtained for the numerical solution of Eq. (1) for curve a: $M > M_0 - M_w$ and curve b: $M < M_0 - M_w$)

These interactions also appear in the course of the start-up. If the motor driving moment is too low, they may lead to stopping the rpm of the rotor at the resonance velocity, wherein the intensification of the vibrations of the body occurs and M_w becomes an essential braking moment. This phenomenon is shown in Fig. 3, where curve (a) describes $\dot{\varphi}$ for the start-up with the induction motor of an appropriately large driving moment, while curve (b) illustrates the behavior of a motor that is clearly too weak [11].

3 Phase Control as the Method for Enabling the System to Overcome the Resonance Stall

The possibility of applying motors with less power is the decisive factor for the efficiency of the system in the steady-state operation, while the necessity of overcoming the resonance stall frequently imposes requirements that are larger than the technological process implementation.

In order to show the usefulness of the method, the phase angle for the state of the stall will be defined in a way that is slightly different from what was provided in Refs. [5,10], where it was understood as the angle between the vectors of force and velocity. In the present paper, the phase angle shall be deemed the angle γ of displacing two periodic functions: force $F_x(t)$ (1*d*) and body displacement $x(t)$, where $F_x(t)$ describes forcing in Eq. (1*a*).

Under a steady-state condition of the systems, with vibratory moment assisted coupling, the angular velocity $\dot{\varphi}$ is not constant and slightly fluctuates around the average value ω_{AV} [12,13]

$$\dot{\varphi} = \omega_{AV} + \Delta_2 \cos(2\varphi) + \Delta_4 \cos(4\varphi) + \Delta_6 \cos(6\varphi) + \cdots \quad (2)$$

where the distribution factors Δ_i are expressed by means of elliptic integrals

$$\omega_{AV} = \frac{\omega_{\min}}{2\pi} \int_0^{2\pi} \frac{d\varphi}{\sqrt{1 - C\cos^2\varphi}}$$

$$\Delta_2 = \frac{\omega_{\min}}{2\pi} \int_0^{2\pi} \frac{\cos 2\varphi d\varphi}{\sqrt{1 - C\cos^2\varphi}} \quad (3)$$

$$\Delta_4, \Delta_6 \ll \Delta_2 \ll \omega_{AV}$$

where

$$C = \frac{m^2 e^2}{J(m_0 + m)}$$

This phenomenon accounts for a sinusoidal variation in the angular velocity with circular frequency $2\omega_{AV}$, as seen in Figs. 2 and

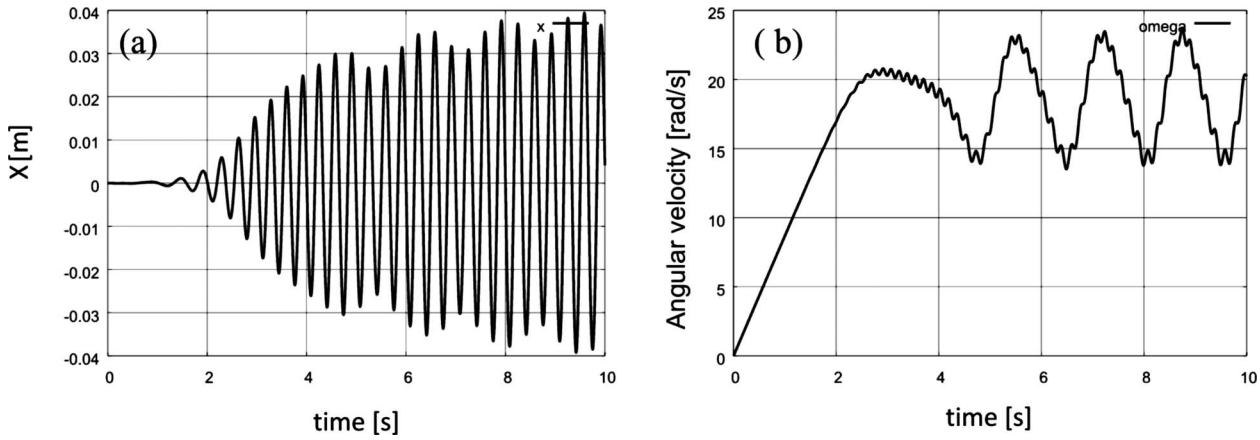

Fig. 4 Resonance stall (obtained from numerical calculations); (*a*) body vibrations and (*b*) motor angular velocity

3. The low-frequency oscillation, as seen in the simulation results of curve b in Fig. 3, will be discussed hereinafter in the present section.

Due to the small and rapidly decreasing value of the coefficients in the trigonometric functions, there will be a limit, in the first approach, to the approximated form of the integral of Eq. (1*b*): $\dot{\varphi}_{\mathrm{AV}}=\omega_{\mathrm{AV}}$ (with an unknown value) and in combining it with Eq. (1*a*), its particular integral will be determined

$$x(\omega t) = A\,\sin(\omega_{\mathrm{AV}} t + \gamma) \tag{4}$$

where

$$A = \frac{\dfrac{m}{m_0+m} e \left(\dfrac{\omega_{\mathrm{AV}}}{\omega_n}\right)^2}{\sqrt{\left[1-\left(\dfrac{\omega_{\mathrm{AV}}}{\omega_n}\right)^2\right]^2 + \left(\dfrac{b\omega_{\mathrm{AV}}}{k}\right)^2}} \tag{5}$$

$$\omega_n = \sqrt{\frac{k}{m_0+m}} \tag{6}$$

$$tg\,\gamma = \frac{\dfrac{b}{k}\omega_{\mathrm{AV}}}{\left(\dfrac{\omega_{\mathrm{AV}}}{\omega_n}\right)^2 - 1}, \quad \gamma \in [-\pi, 0] \tag{7}$$

In this solution, the values of ω_{AV} and amplitude A—dependent on them—are not known. In order to determine value A, the equation of the balance of energy that is delivered and dissipated by the vibrating system for the period of vibrations will be used

$$2\pi(M - M_0) = \pi A^2 b \omega_{\mathrm{AV}} \tag{8}$$

where M and M_o may—in general—constitute the functions ω_{AV}, hence

$$A = \sqrt{\frac{2(M-M_0)}{b\omega_{\mathrm{AV}}}} \tag{9}$$

If $M-M_o$ can be treated as constant near the resonance frequency, then equating Eqs. (5) and (9) deliver the equation in the form of Eq. (10*a*) allowing one to arrive at the ω_{AV}

$$\frac{b}{\omega_n{}^4}\frac{m^2e^2}{(m_0+m)^2}\omega_{\mathrm{AV}}{}^5 - \frac{2(M-M_0)}{\omega_n{}^4}\omega_{\mathrm{AV}}{}^4 + \left(\frac{2}{\omega_n{}^2} - \frac{b^2}{k^2}\right) \times 2(M-M_0)\omega_{\mathrm{AV}}{}^2 - 2(M-M_0) = 0 \tag{10a}$$

In the case of natural attenuation arising from the deflection of the system support (without additional attenuation units attached)

$$b = \frac{\psi k}{2\pi\omega}$$

where

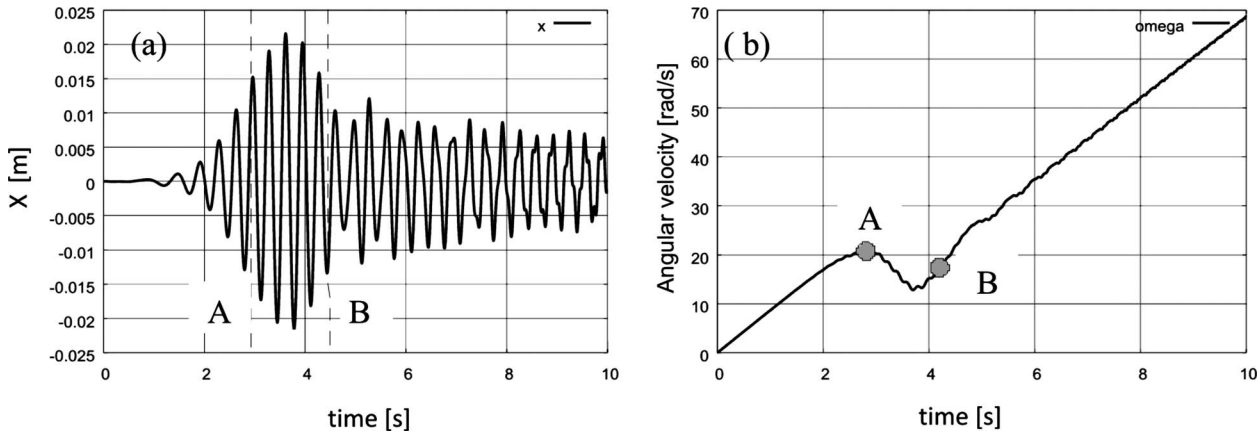

Fig. 5 Overcoming resonance stall (obtained from numerical calculations); (*a*) vibrations of machine body and (*b*) angular velocity of motor; A is the motor disengagement instant and B is the motor engagement instant

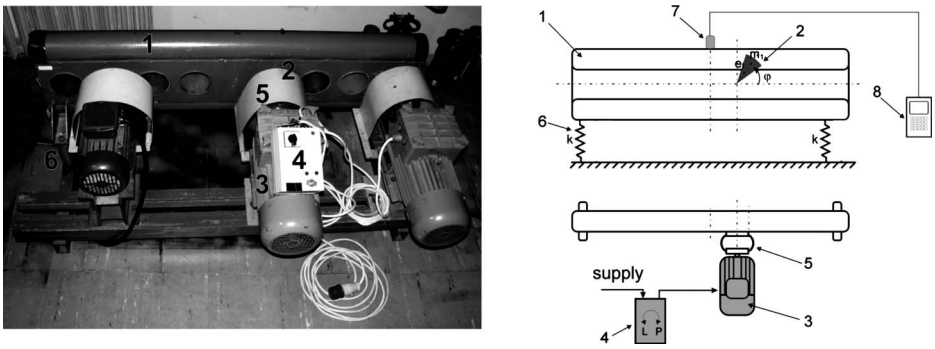

Fig. 6 View and scheme of the experimental stand; 1 is the vibratory machine body, 2 is the vibrator with constant unbalancing, 3 is the electric motor (three-phase, asynchronous, and slip ring), 4 is the changeover switch (left; stop-right), 5 is the yoke clutch, 6 is the body suspension, 7 is the vibration detector, and 8 is the HP logger

$$\psi = \frac{\text{energy dissipated per cycle}}{\text{maximum amount of energy stored during a cycle}}$$

where b is an equivalent viscous damping coefficient, ensuring the equivalence of the energy losses in a linear system and in a system with hysteric damping for a vibration period.

Therefore

$$\frac{b^2}{k^2} = \frac{\psi^2 k^2}{4\pi^2 \omega_n{}^2} \frac{1}{k^2} = \frac{\psi^2}{4\pi^2 \omega_n{}^2} \tag{10b}$$

for the typical elastic elements $\psi < 0.5$ [7], which leads to the inequality $2/\omega_n{}^2 > b^2/k^2$. Similarly, $M > M_o$, which entirely ensures the sequence of signs of the coefficients of Eq. (10*a*) to be compliant with the form of this equation.

Then, the Cartesian rule provides that Eq. (10*a*) has either one or three positive radicals, whereas a physical analysis of the phenomenon shows that the first and third radicals correspond to the stable states, and the second one to the unstable state. The sought after stall frequency corresponds to the lowest radical, if there are three of them (if Eq. (10*a*) has only one radical, a stall does not occur). This allows one to present the approximated particular integral (4) of Eq. (1*a*).

Then, in the stall state, the vibratory moment appearing in Eq. (1*b*) is expressed by the relation

$$M_w = -me\ddot{x}\cos\varphi = meA\omega_{\mathrm{AV}}{}^2 \sin(\omega_{\mathrm{AV}} t + \gamma)\cos(\omega_{\mathrm{AV}} t) \tag{11}$$

Taking into consideration the mean value of the vibratory moment for the period of motion T, yields

$$M_{w\mathrm{AV}} = \frac{1}{T}\int_0^T M_w(t)dt = \frac{\omega_{\mathrm{AV}}}{2\pi} \times \int_0^{2\pi/\omega_{\mathrm{AV}}} meA\omega_{\mathrm{AV}}{}^2 \sin(\omega_{\mathrm{AV}} t + \gamma)\cos(\omega_{\mathrm{AV}} t)dt = \frac{\omega_{\mathrm{AV}}{}^3 meA}{2\pi} \times \int_0^{2\pi/\omega_{\mathrm{AV}}} \sin(\omega_{\mathrm{AV}} t + \gamma)\cos\ \omega_{\mathrm{AV}} t dt = \frac{\omega_{\mathrm{AV}}{}^2 meA}{2}\sin\ \gamma \tag{12}$$

In the stall state, the body of the machine performs high amplitude vibrations with a frequency corresponding to the system natural frequency. This vibration is excited through the resonance phenomenon, while the motor driving moment is used for its sustainment (balancing $M_o - M_{w\mathrm{AV}}$). A fast transition of the rotor to a position different than the steady-state by $+\pi$ or $-\pi$ (with the restoration of the previous value of an angular velocity) is possible to be done by means of the binary control of the motor with the use of a high moment value. Then, the phase angle between the vibrating motion of the body and the vibrator force will also change with this value, as the body (similarly to the resonance escalation of vibrations) requires time for changing its motion.

As can be seen in Eq. (12), the vibratory moment will then change its sign. This means the change in the direction of a power flow in the system, which will start flowing in the opposite direction, in turn collecting the energy of the motion of the vibrating body, which will thereby lead to the reduction in the amplitude of the body vibrations. This allows for, after the restoration of the previous value of a driving moment, an easy passage of the system through the resonance zone (small value of the vibratory moment).

Forcing and maintaining the appropriate phase angle in the system are difficult to implement and require both an advanced measuring system and a sophisticated motor control system. A much simpler way that is capable of being used in industrial applications is the control method involving the use of changes of the phase angle in the system that naturally occur near the resonance frequency of the system.

The period of the oscillation of the phase angle may be arrived at by calculating the "coefficient of elasticity" of the vibratory moment

$$K_o = \frac{dM_{w\mathrm{AV}}}{d\gamma} = \frac{\omega_n^2 meA}{2}\cos\ \gamma \tag{13}$$

In the case of the subresonance stall of the slightly attenuated system (typical situation), the average value of the angle γ—slightly negative, allows for the adoption of the approximation of $\cos\ \gamma \approx 1$, which gives the possibility of estimating the oscillation frequency of the angular velocity of the system as

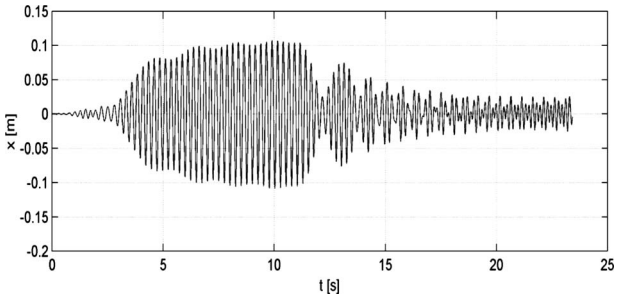

Fig. 7 Machine body vibrations—full cycle of a machine motion (the result of the experiment). Start-up and stall in the resonance and passing through the stall zone as a result of the applied motor control.

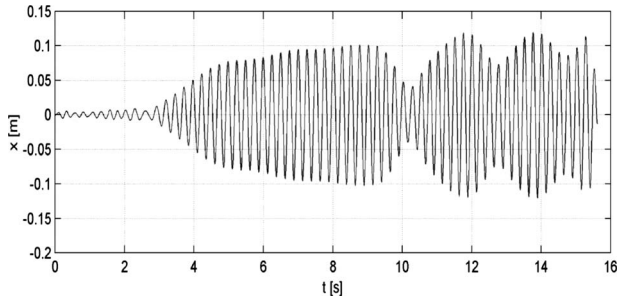

Fig. 8 Machine body vibrations—motor switching inappropriately performed (on purpose). The system remains in the resonance zone (the result of the experiment).

$$\omega_\gamma \approx \sqrt{\frac{|K_o|}{J}} = \omega_n \sqrt{\frac{meA}{2J}} \tag{14}$$

The use of the self-acting changes of the phase angle involves the deactivation and activation of the motor at the appropriate time instant. It should be highlighted here that the phenomenon of the phase angle change is a low-speed phenomenon compared with the vibrations performed by the machine body. The period of oscillations of the phase angle depends on the system parameters and amounts to 1.6 s for the model examined (curve b in Fig. 3 and Fig. 4). Relatively slow changes of the phase angle enable the application of the changeover switch assisted control of the motor without any concern about the dynamic phenomena occurring therein.

The theoretical considerations were confirmed by simulations and experiments. The control system that is being proposed will be shown in an example of the machine, which is illustrated in Fig. 1, while the motion equations have the form of Eqs. (1*a*) and (1*b*).

The selected motor driving moment is lower than the minimum driving moment, ensuring the passing through of the resonance zone. When the too-low driving moment is applied, the motor stalls at frequencies near the natural frequency of the system (Fig. 4).

If the power of the driving motor is too low it renders it impossible for passing through the resonance zone. During the resonance stall, the angular velocity of the motor oscillates at the frequency ω_γ around the value corresponding to the frequency of the natural vibrations of the system, amounting to 19.7 rad/s. Thus far, the only method that allows the resonance stall to be overcome was the application of a larger power driving motor.

Using the phenomenon of the change in the energy flow direction in the vibrator-machine body system, due to the change in the phase angle, a resonance stall may be overcome by means of a small power motor (Fig. 5).

The proposed control involves engaging and disengaging the motor at the appropriate time. In order for the control to be performed most efficiently, the instant of motor disengagement should correspond to the instant of collapsing the motor angular velocity (point A, Fig. 5(*b*)). The engagement should take place in half of the first escalating slope of the motor angular velocity (point B, Fig. 5(*b*)). The control presented hereby allows a resonance stall to be overcome with the use of the small power motor. If the deficiency of the motor power is too large, the control procedure should be repeated several times.

The possibility of overcoming the resonance stall with the use of a small power motor was confirmed experimentally (Fig. 6). The experiment was performed at the experimental stand for vibrator's self-synchronization testing in the Department of Mechanics and Vibroacoustics of the University of Science and Technology, AGH (Krakow, Poland). During the experiment, the central driving motor was only used. The driving moment of the motor was reduced (through the insertion of additional resistors into the rotor winding) in such a way that the normal start-up of the equipment was prevented.

During the experiment, the start-up of the machine was performed. Following activation, the motor stalled in the resonance zone (the resonance vibrations escalated and then became steady), and then the motor was disengaged and engaged. As a result of the control applied, the motor overcame the resonance zone, which was manifested by decreasing the vibration amplitude and the increase in their frequency (Fig. 7). When the times of disengagement and engagement of the motor were wrongly selected (on purpose), the motor was unable to pass through the resonance zone (Fig. 8).

4 The Use of Impulse-Phase Control for the Minimization of the Vibration Amplitudes During the Resonance Zone Being Passed Through

The control method that is presented in this paper can be successfully used for the reduction in the maximum amplitude of machine body vibrations during the passing through of the resonance zone. The start-up of the machine performed by the motor

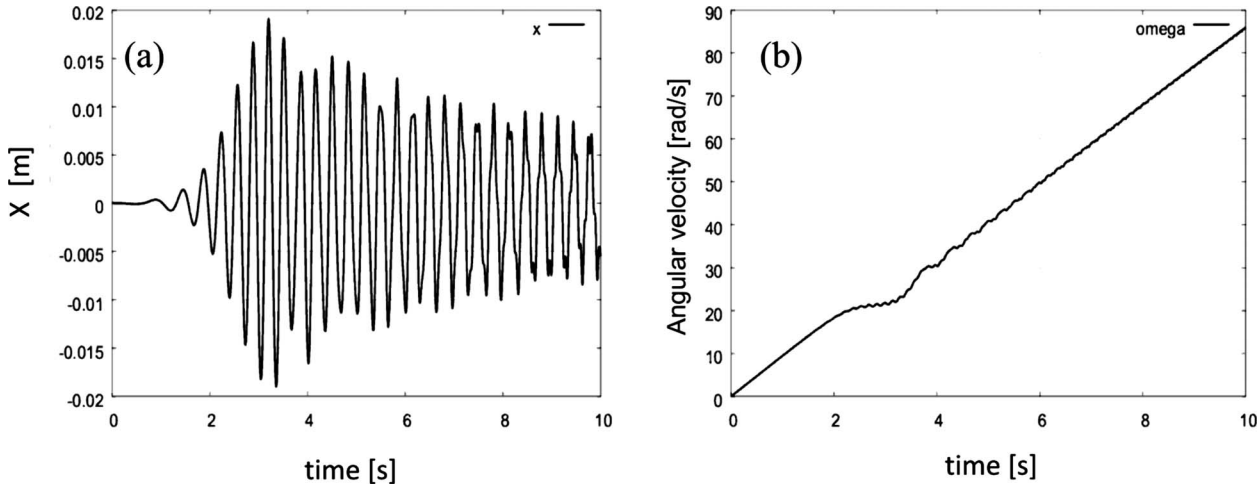

Fig. 9 Passing through the resonance zone during the vibration machine start-up (obtained from numerical calculations); (*a*) body vibrations and (*b*) vibrator angular velocity

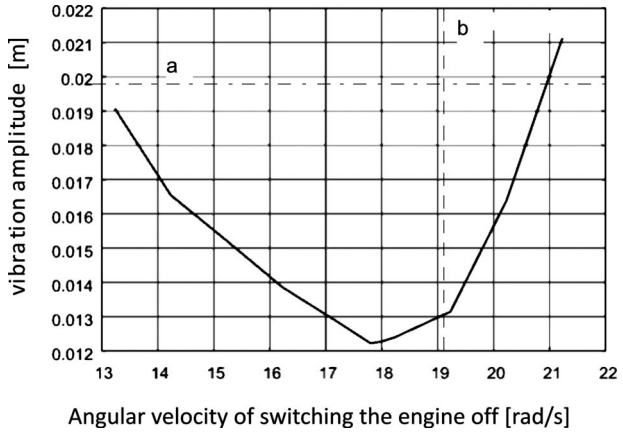

Fig. 10 Dependence of the vibration maximum amplitude on the motor disengagement instant (obtained from numerical calculations). The vibration maximum amplitude without any control was equal to 0.019965 for line "a" and resonance frequency 19.23 rad/s for line "b."

without any control (Fig. 9) is adopted to act as the reference value.

The maximum vibration amplitude during the start-up with a motor without the control system is equal to 0.0199 m.

The efficiency of the impulse-phase method depends on the times of the deactivation and reactivation of the driving motor. The impact of the motor deactivation instant on the value of the maximum vibration amplitude is shown in Fig. 10. For the system tested, with a natural frequency of 19.23 rad/s, the best effect is obtained when the motor deactivation takes place at a motor angular velocity of 17.8 rad/s.

The most advantageous condition used in order to overcome a stall as well as to decrease a vibration amplitude will be created when the applied driving torque is added to the maximum positive mean value of the vibratory torque. This causes a maximum angular acceleration of the vibrator, which—in turn—allows for the passage of the system through the resonance zone in the most effective way. As shown in Fig. 11, the instant when the vibratory torque mean value is at its maximum takes place during the first increasing slope of the motor angular velocity curve. The application of control results in a change in the phase angle, as shown in Fig. 12.

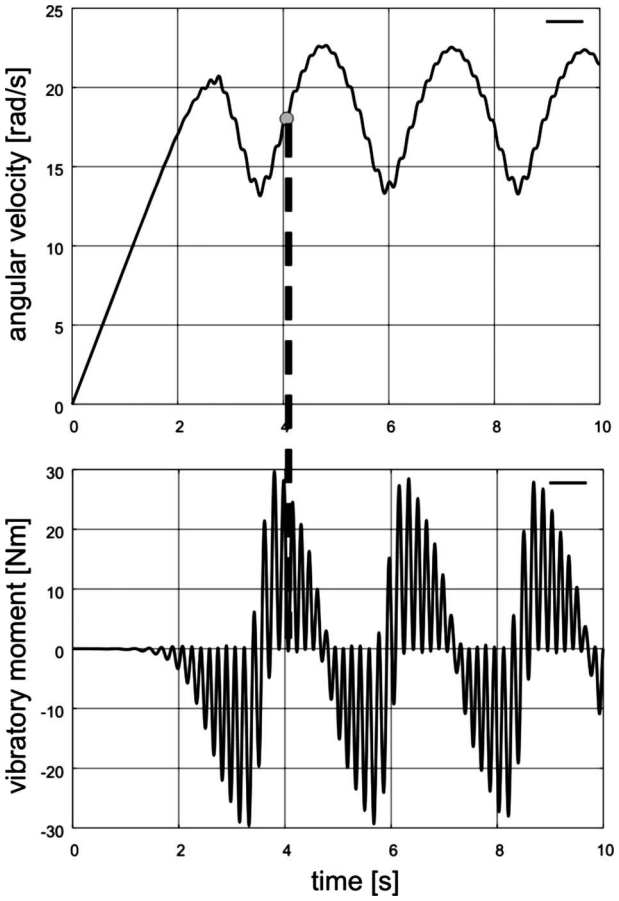

Fig. 11 Determination of the motor restarting instant. The maximum mean value of the vibratory moment takes place in half of the first escalating slope of the motor angular velocity curve.

As a result of applying the phase control in the course of the start-up, the reduction in the vibration maximum amplitude to the level of 0.0122 m is achieved. It means that there was 39% reduction in the vibration maximum amplitude in the course of the

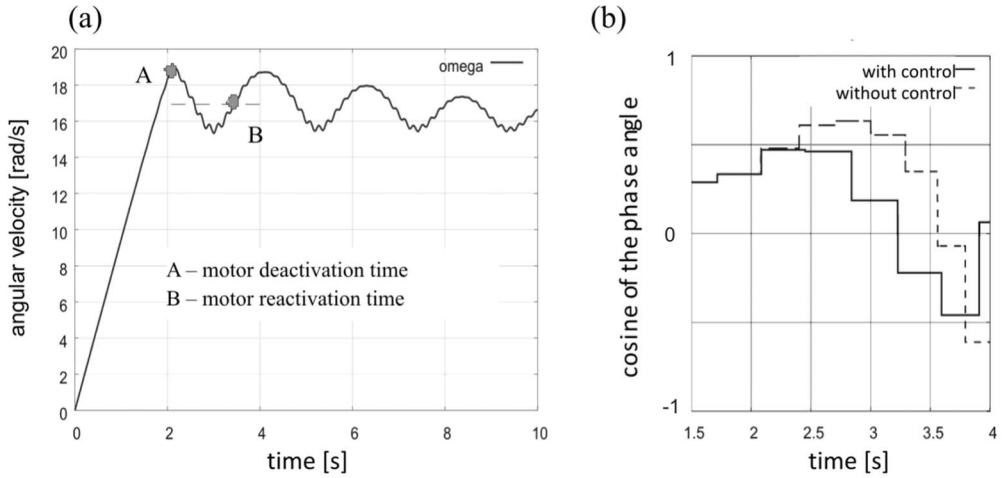

Fig. 12 (*a*) Angular velocity of the vibrator following disengagement of the driving moment (at a frequency of 19 rad/s) and (*b*) change in the phase angle (defined in Ref. [10]) in the resonance zone as a result of the applied control (obtained from numerical calculations)

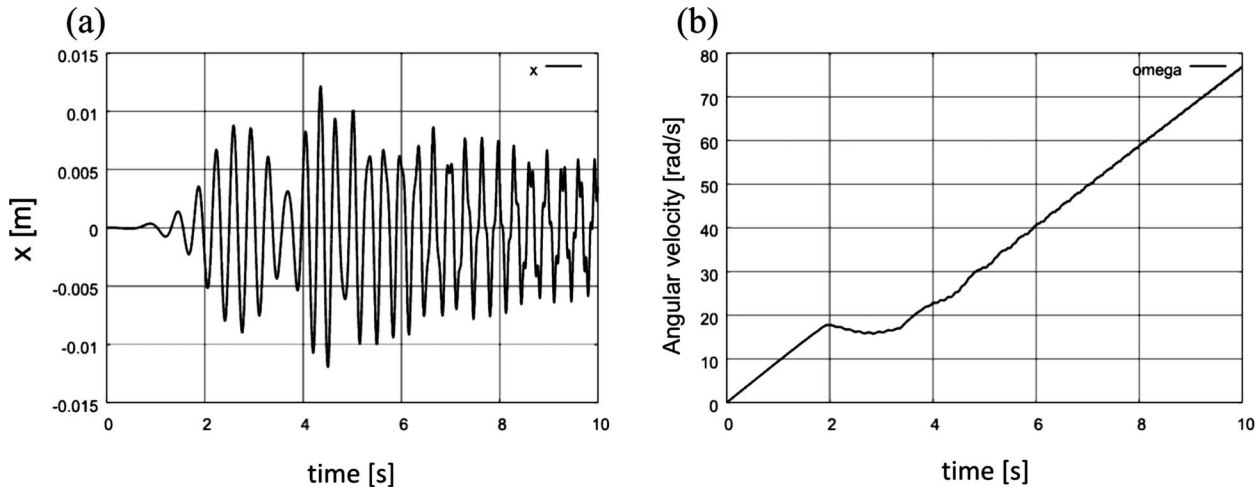

Fig. 13 Transition through the resonance zone in the course of the vibration machine start-up with the motor disengagement and engagement at the most advantageous time (obtained from numerical calculations); (*a*) body vibrations and (*b*) vibrator angular velocity

start-up without any control. Figure 13 shows the transition of the system through the resonance zone for the most advantageous instant of control.

5 Conclusions

1. Strong coupling occurring in the actual systems between the machine body vibrations and the rpm of the rotor imposes the necessity of changing the phase control in relation to what was proposed in other papers [9,10]. The driving moment is the control parameter, whose impact on the rotor angular velocity may only be accessed by means of the system analysis with an additional degree of freedom for the rotor (incorporating the vibratory moment).
2. The present paper describes the modified version of the phase modulation method, taking full advantage of the natural oscillations of the system phase angle. The presented method provides the possibility of reducing the value of the maximum amplitude during transient resonance and enables one to overcome the resonance stall by using a low power motor.

Nomenclature

F_x = force (N)
J_c = central moment of the inertia of the vibrator (kg m^2)
$J=J_c+me^2$ = moment of the inertia of the vibrator (kg m^2)
K_o = coefficient of elasticity of the vibratory moment (N m/rad)
M = motor electromagnetic moment (N m)
M_0 = rotary motion resistance moment (N m). Usually for the rolling bearings and inertial loading; $M_0=M_0(\dot{\varphi})=c_1+c_2\dot{\varphi}^2$, where c_1 and c_2 are constants dependent on the bearing system type, c_1 (N m) and c_2 (N m s^2)
M_w = vibratory moment (N m)
$M_{w\mathrm{AV}}$ = vibratory moment averaged in the period of oscillation (N m)
b = coefficient of the viscous damping of the machine support (N s/m)
e = eccentricity (m)
k = coefficient of the elasticity of the body support (N/m)
m_0 = mass of the body (kg)
m = eccentric mass (kg)
$x(t)$ = absolute body displacement (m)
φ = absolute rotation angle of the eccentric mass (rad)
ω_{AV} = average value of the vibrator angular velocity (rad/s)
ω_n = natural circular frequency of the machine $\omega_n=\sqrt{(m_0+m)/k}$ (rad/s)
$\omega_{\min}$ = minimum value of the vibrator angular velocity in the stationary motion (rad/s)
ω_γ = natural circular frequency of the system: vibrator-vibratory moment (rad/s)

References

[1] Lewis, F., 1932, "Vibration During Acceleration Through a Critical Speed," Trans. ASME, **54**, pp. 253–261.
[2] Kac, A. M., 1947, "Forced Vibration During the Resonance Passage," Inzynierny Sbornik, **2**(3).
[3] Market, R., and Seidler, M., 2001, "Analytically Based Estimation of the Maximum Amplitude During Passage Through Resonance," Int. J. Solids Struct., **38**(10–13), pp. 1975–1992.
[4] Yanabe, S., and Tamura, A., 1980, "Vibration of a Rotating Shaft Passing Through Critical Speed," *Vibration in Rotating Machinery*, I Mech E Conference Publications.
[5] Iwatsubo, T., 1976, "Vibration of Rotors Through Critical Speed," Shock Vib. Dig., **8**, p. 89.
[6] Harris, C., 1957, *Handbook of Noise Control*, McGraw-Hill, New York.
[7] Michalczyk, J., 1995, "Vibratory Machines," *Dynamic Calculations, Vibrations, and Noise*, WNT, Warsaw, Poland.
[8] Agranowskaja, E. A., and Blechman, I. I., 1969, "Estimating the Resonance Amplitudes During the Overrun of Systems of Many Degrees of Freedom," *Dynamics of Machines*, Nauka, Moscow.
[9] Millsaps, K. T., and Reed, G. L., 1998, "Reducing the Lateral Vibrations of a Rotor Passing Through Critical Speed by Acceleration," ASME J. Eng. Gas Turbines Power, **120**, pp. 615–620.
[10] Wang, S. M., Lu, Q. S., and Twizell, E. H., 2003, "Reducing the Lateral Vibration of a Rotor Passing Through Critical Speed by Phase Modulating," ASME J. Eng. Gas Turbines Power, **125**, pp. 766–771.
[11] Michalczyk, J., Cieplok, G., and Bednarski, L., 2006, *Forcing the Start-Up of Vibratory Machines by Means of Small Power Motors*, The Archive of Mechanical Engineering, Krakow, Poland.
[12] Bychowskij, I., 1969, *Bases of the Theory of the Vibratory Technique*, Maszynostrojenie, Moscow.
[13] Michalczyk, J., 1984, "Selected Problems of Over-Resonance Vibratory Machines Dynamics," Mechanika, **5**, Krakow, Poland.

An Active Auxiliary Bearing Control Strategy to Reduce the Onset of Asynchronous Periodic Contact Modes in Rotor/Magnetic Bearing Systems

Iain S. Cade[1]
e-mail: i.s.cade@bath.ac.uk

M. Necip Sahinkaya
e-mail: m.n.sahinkaya@bath.ac.uk

Clifford R. Burrows
e-mail: c.r.burrows@bath.ac.uk

Patrick S. Keogh
e-mail: p.s.keogh@bath.ac.uk

University of Bath,
Bath BA2 7AY, UK

To prevent rotor/stator contact in a rotor/magnetic bearing system, auxiliary bearings may be located along the shaft and at the magnetic bearings. Rotor responses after a contact event may include periodic trapped modes where repeated contact may lead to highly localized thermal stresses. This paper considers an active auxiliary bearing system with a control strategy designed to limit the trapped contact modes in a rotor/magnetic bearing system that are induced by rotor unbalance. The controller is evaluated from a system model and its responses to short duration contact events. An active auxiliary bearing model is introduced to the system where the dynamic response of the bearing is dependent on the controller. From a harmonic decomposition of rotor/bearing contact, dynamic controllers are sought, which limit the numbers of possible periodic solutions for a given rotor unbalance and operating speed. A case study is performed considering a simple two degree of freedom system with passive and active auxiliary bearings. Recovery of a rotor trapped in an asynchronous contact mode is shown with variation of the auxiliary bearing controller parameters. [DOI: 10.1115/1.3204644]

1 Introduction

During normal operation, the rotor in a rotor/magnetic bearing system levitates without contact with stator structures. However, during a fault condition, the rotor orbit may be sufficiently large to induce rotor/stator contact. Such fault conditions include unexpected changes in rotor unbalance, base motion inputs, and power/sensor system failures. Auxiliary bearings are used to prevent rotor/stator contact. It is important to assess the rotor response during and after a contact event since the forces involved together with high initial slip speeds may lead to significant mechanical and thermal stresses.

The behavior of a rotor during and after a contact event has received much attention in the open literature. Responses of a rigid rotor in two sliding retainer bearings were predicted by Fumagalli et al. [1]. Circular orbit responses with constant rub were discussed in Refs. [2,3]. Wang and Noah [4] identified the steady state rotor responses for a rotor/auxiliary bearing interaction. Backward whirl responses were identified by Bartha [5]. Periodic responses at subharmonics of the synchronous frequency were identified in Refs. [6,7]. Chaotic rotor vibration was identified by Muszynska and Goldman [8], particularly with looseness in the system. Cole and Keogh [9] identified synchronous periodic responses, in which a periodic auxiliary bearing contact occurs, often referred to as trapped contact modes. Their approach considered energy conservation during idealized short duration contact events, and the results were compared with previously published experimental responses. Rotor drop was considered in Ref. [10]. A transient response calculation was presented, and rotor drop responses were evaluated from which the influence of support damping was assessed. Thermal stresses arising from rotor/bearing contact were also discussed by Keogh and Yong [11].

Various control strategies have been presented to recover the rotor from a trapped contact mode or persistent contact [9,12–14]. These methods, in general, involve applying synchronous control signals through the active magnetic bearings, taking account of amplitude and phase variation in the rotor vibration due to contact. During fault conditions, the limited load capacity of the magnetic bearings may not be sufficient to retrieve the rotor from contact or rub responses. Furthermore, nonlinear system dynamics may cause instability for linear control strategies. An active auxiliary bearing solution may also be sought to reduce rotor/bearing contact forces. References [15,16] consider an auxiliary bearing controlled by electromechanical actuators to reduce contact forces. Ginzinger and Ulbrich [16] used electromechanical actuators to match the position and phase of rotor vibration in order to minimize contact forces before the onset of a full annular rub.

This paper presents a control strategy for an active auxiliary bearing. In principle, such systems could be achieved using piezoelectric/electromagnetic actuation and have been proposed in the open literature [15,17,18]. The techniques adopted in Ref. [9] are expanded to consider nonidealized contact events dictated by the performance of an active auxiliary bearing. From consideration of the dynamic behavior of the rotor during and after a contact event, control strategies for the active auxiliary bearing are identified.

2 Rotor Dynamics

The dynamic characteristics of a flexible rotor, operating at a rotational speed Ω, can be described by a second order system with appropriate mass, **M**, damping, **C**, gyroscopic, **G**, and stiffness, **K**, matrices [19],

$$\mathbf{M}\ddot{\mathbf{q}} + (\mathbf{C} + \Omega\mathbf{G})\dot{\mathbf{q}} + \mathbf{K}\mathbf{q} = \mathbf{d}_d + \mathbf{d}_u + \mathbf{d}_c \quad (1)$$

where $\mathbf{q}$ is the displacement vector referred to a fixed reference frame and the effect of gravity can be compensated for using

[1]Corresponding author.

Contributed by the International Gas Turbine Institute of ASME for publication in the JOURNAL OF ENGINEERING FOR GAS TURBINES AND POWER. Manuscript received March 24, 2009; final manuscript received March 26, 2009; published online March 3, 2010. Review conducted by Dilip R. Ballal. Paper presented at the ASME Gas Turbine Technical Congress and Exposition, Orlando, FL, June 8–12, 2009.

appropriate control forces. It can be described in terms of nodal lateral and angular displacements $\mathbf{q}=[x_1, y_1, \theta_1, \phi_1, \ldots, x_N, y_N, \theta_N, \phi_N]^T$. $\mathbf{d}_d$, $\mathbf{d}_u$, and $\mathbf{d}_c$ are vectors containing disturbance, control, and contact forces acting on the rotor, respectively. Rotor auxiliary bearing contact will occur if the radial displacement of the rotor, say, at node j, equals or exceeds the clearance gap,

$$[x_j^2 + y_j^2]^{1/2} \geq c_j \tag{2}$$

The rotor states, $\mathbf{q}$, can be converted to a synchronously rotating reference frame, with lateral and angular displacements given by $\mathbf{r}=[u_1, v_1, \vartheta_1, \zeta_1, \ldots, u_N, v_N, \vartheta_N, \zeta_N]^T$, using a transformation $\mathbf{q}=\mathbf{T}\mathbf{r}$, where

$$\mathbf{T} = \mathbf{I}_r^T \mathbf{S} \mathbf{I}_r, \quad \mathbf{S} = \begin{bmatrix} \cos(\Omega t + \phi) & -\sin(\Omega t + \phi) \\ \sin(\Omega t + \phi) & \cos(\Omega t + \phi) \end{bmatrix} \tag{3}$$

with $\mathbf{I}_r=[\mathbf{I}, \mathbf{I}, \ldots, \mathbf{I}]$ being a $2\times 4N$ matrix of adjacent 2×2 unit matrices. It therefore follows that the rotor dynamics governed by Eq. (1) can be converted to a synchronously rotating reference frame as

$$\mathbf{M}_\Omega \ddot{\mathbf{r}} + \mathbf{C}_\Omega \dot{\mathbf{r}} + \mathbf{K}_\Omega \mathbf{r} = \mathbf{f}_d + \mathbf{f}_u + \mathbf{D} \tag{4}$$

where

$$\mathbf{f}_d = \mathbf{T}^T \mathbf{d}_d, \quad \mathbf{f}_u = \mathbf{T}^T \mathbf{d}_u, \quad \mathbf{D} = \mathbf{T}^T \mathbf{d}_c \tag{5}$$

and

$$\mathbf{M}_\Omega = \mathbf{T}^T \mathbf{M} \mathbf{T}$$

$$\mathbf{C}_\Omega = 2\Omega \mathbf{T}^T \mathbf{M} \hat{\mathbf{T}} + \mathbf{T}^T (\mathbf{C} + \Omega \mathbf{G}) \mathbf{T}$$

$$\mathbf{K}_\Omega = -\Omega^2 \mathbf{M}_\Omega + \Omega \mathbf{T}^T (\mathbf{C} + \Omega \mathbf{G}) \hat{\mathbf{T}} + \mathbf{T}^T \mathbf{K} \mathbf{T} \tag{6}$$

$$\hat{\mathbf{T}} = \mathbf{I}_r^T \mathbf{R} \mathbf{S} \mathbf{I}_r$$

$$\mathbf{R} = \begin{bmatrix} 0 & -1 \\ 1 & 0 \end{bmatrix}$$

The synchronously rotating frame lateral and rotational displacements can be extracted from $\mathbf{r}$ and converted to a complex notation using the transformation $\mathbf{r}=\mathbf{T}_c\mathbf{z}$, where $\mathbf{z}=[u_1+iv_1, \vartheta_1+i\zeta_1, \ldots, u_N+iv_N, \vartheta_N+i\zeta_N]^T$. Then,

$$\mathbf{M}_c \ddot{\mathbf{z}} + \mathbf{C}_c \dot{\mathbf{z}} + \mathbf{K}_c \mathbf{z} = \mathbf{T}_c^T \mathbf{f}_d + \mathbf{T}_c^T \mathbf{f}_u + \mathbf{T}_c^T \mathbf{D} \tag{7}$$

where

$$\mathbf{M}_c = \mathbf{T}_c^T \mathbf{M}_\Omega \mathbf{T}_c, \quad \mathbf{C}_c = \mathbf{T}_c^T \mathbf{C}_\Omega \mathbf{T}_c, \quad \mathbf{K}_c = \mathbf{T}_c^T \mathbf{K}_\Omega \mathbf{T}_c \tag{8}$$

3 Periodic Rotor Contact Dynamics

3.1 Periodic Vibrations. The contact dynamic response of the rotor may be periodic and persistent. The rotor response depends strongly on the initial conditions of the rotor and bearing, together with their physical properties. This work considers an active auxiliary bearing to influence the contact forces. It may be possible to use the active auxiliary bearing control strategy to prevent the onset of trapped or persistent contact modes. To understand the problem, it is advisable to perform an analysis of the rotor/magnetic bearing/active auxiliary bearing system. The approach considers a model incorporating a variable duration contact event with a dynamically varying contact force. Since an active auxiliary bearing can impart energy to the system, an energy absorption factor is introduced. The energy absorption factor can be varied to assess whether the auxiliary bearing acts to absorb or input energy into the system.

If the disturbance force is synchronous with the reference frame, e.g., rotor unbalance, then steady state solutions for $\mathbf{z}$ will be stationary. Periodic solutions, which correspond to contact modes, may also exist. The rotor/auxiliary bearing contact force, $\mathbf{D}(t)$, can be varied and depends on the auxiliary bearing control strategy used. In general, the rotor/bearing contact force at node j can be expressed as $D_j(t)=-(d_n+id_p)$, where d_n and d_p are the normal and tangential contact force components, respectively. For periodic contact events, with period τ, the rotor contact force at node j can be expressed in the time domain as

$$D_j(t) = -(1 + i\mu) \sum_{k=-\infty}^{\infty} \psi(t - k\tau) \tag{9}$$

where $\psi(t)$ is the radial contact force for a single contact event and is dependent on the active auxiliary bearing control strategy. In Eq. (9), $d_p=\mu d_n$, where μ is the dry sliding friction. For short duration events, the friction coefficient is assumed to be constant. For long duration events or a persistent rub, a dynamic friction model may also be used. For periodic solutions $\psi(t)=\psi(t-k\tau)$, and $\omega_\tau=2\pi/\tau$ is the frequency between contacts. The complex rotor displacement, $\mathbf{z}$, can be represented using a complex Fourier series as

$$\mathbf{z} = \sum_{n=-\infty}^{\infty} \zeta_n e^{in\omega_\tau t} \tag{10}$$

Similarly, the rotor/auxiliary bearing contact force can be expressed as a complex Fourier series,

$$D_j(t) = -(1 + i\mu) \sum_{n=-\infty}^{\infty} \Phi_n e^{in\omega_\tau t} \tag{11}$$

where the complex Fourier contact force coefficients for periodic contact events are evaluated from

$$\Phi_n = \frac{\omega_\tau}{2\pi} \int_0^\tau \psi(t) e^{in\pi t/\tau} dt \tag{12}$$

From Eq. (10),

$$\dot{\mathbf{z}} = \sum_{n=-\infty}^{\infty} in\omega_\tau \zeta_n e^{in\omega_\tau t}, \quad \ddot{\mathbf{z}} = \sum_{n=-\infty}^{\infty} -n^2 \omega_\tau^2 \zeta_n e^{in\omega_\tau t} \tag{13}$$

Substituting Eqs. (10), (11), and (13) into Eq. (7) gives

$$\sum_{n=-\infty}^{\infty} [-n^2 \omega_\tau^2 \mathbf{M}_c + in\omega_\tau \mathbf{C}_c + \mathbf{K}_c] e^{in\omega_\tau t}$$

$$= \mathbf{T}_c^T \mathbf{f}_u + \mathbf{T}_c^T \mathbf{f}_d - \mathbf{T}_c^T (1 + i\mu) \sum_{n=-\infty}^{\infty} \Phi_n e^{in\omega_\tau t} \tag{14}$$

Now, define

$$\Lambda_n(\omega_\tau) = [-n^2 \omega_\tau^2 \mathbf{M}_c + in\omega_\tau \mathbf{C}_c + \mathbf{K}_c]^{-1} \mathbf{T}_c^T (1 + i\mu) \Phi_n \tag{15}$$

When $n=0$, which corresponds to the steady state solution, both contact and rotor unbalance forces are present. It is assumed that the control forces applied to the rotor by the active magnetic bearing to compensate for rotor unbalance are also stationary in the rotating reference frame. The steady state deviation of the rotor due to disturbance and control forces is therefore given by $\mathbf{K}_c^{-1}(\mathbf{T}_c^T \mathbf{f}_d + \mathbf{T}_c^T \mathbf{f}_u)$. When $n \neq 0$, only the contact forces are present. It therefore follows that the complete Fourier coefficients of harmonic rotor displacement are given by

$$\zeta_n = \begin{cases} \Lambda_0(\omega_\tau) + \mathbf{K}_c^{-1}(\mathbf{T}_c^T \mathbf{f}_d + \mathbf{T}_c^T \mathbf{f}_u), & n = 0 \\ \Lambda_n(\omega_\tau), & n \neq 0 \end{cases} \tag{16}$$

The harmonic rotor displacement is therefore dependent on $\Lambda_n(\omega_\tau)$. Since $\Lambda_n(\omega_\tau)$ is related to Φ_n, then ζ_n is related to the contact event profile and magnitude given by $\psi(t)$.

3.2 Periodic Contact Condition. The rotor displacement magnitude can be evaluated from a complex rotating reference plane colocated with the contact plane as

$$r_j(t) = (u_j^2 + v_j^2)^{1/2} \tag{17}$$

Rotor bearing contact occurs if the condition specified in Eq. (2) is met. Therefore, for periodic contact events, $r_i(t) = r_i(k\tau) = c_i$, which satisfies

$$\mathbf{z}_i(k\tau) = \sum_{n=-\infty}^{\infty} \zeta_n e^{in\omega_\tau k\tau} \tag{18}$$

Since n and k are integer values, then $e^{in\omega_\tau k\tau} = 1$. Substituting Eq. (16) for ζ_n into Eq. (18) and rearranging gives

$$(\mathbf{T}_c^T\mathbf{f}_d + \mathbf{T}_c^T\mathbf{f}_u) = \mathbf{K}_c^{-1}\left[c_j - \sum_{n=-\infty}^{\infty} \Lambda_n(\omega_\tau)\right] \tag{19}$$

$(\mathbf{T}_c^T\mathbf{f}_d + \mathbf{T}_c^T\mathbf{f}_u)$ represents the residual rotor synchronous forcing due to the active magnetic bearing control action and initial rotor unbalance.

3.3 Energy Loss During Impact. The start time of a contact event can be defined as t_-. Similarly, t_+ can be defined as the end time. The rotor lateral displacement in a synchronously rotating reference frame can be defined in a complex form as

$$\mathbf{w} = \mathbf{u} + i\mathbf{v} = (\mathbf{x} + i\mathbf{y})e^{-i(\Omega t + \phi)} \tag{20}$$

where

$$\mathbf{x} = [x_1, x_2, \ldots, x_N]^T, \quad \mathbf{y} = [y_1, y_2, \ldots, y_N]^T$$
$$\mathbf{u} = [u_1, u_2, \ldots, u_N]^T, \quad \mathbf{v} = [v_1, v_2, \ldots, v_N]^T \tag{21}$$

The change in the momentum, $\Delta\mathbf{p}$, of the rotor during a contact event is related to the contact force and event duration as

$$\Delta\mathbf{p} = (1 + i\mu)\mathbf{B}_c \int_{t_-}^{t_+} \psi(t)dt \tag{22}$$

where $\mathbf{B}_c$ is a distribution matrix used to map the dimension of $\psi(t)$ to that of $\mathbf{w}$. Since the rotor mass is conserved, only the rotor velocity changes. The change in the rotor vibrational velocity is therefore

$$\Delta\dot{\mathbf{w}} = -(1 + i\mu)\mathbf{M}_l^{-1}\mathbf{B}_c \int_{t_-}^{t_+} \psi(t)dt \tag{23}$$

where $\mathbf{M}_l$ contains the rows and columns of $\mathbf{M}_c$ that correspond to lateral rotor displacements. For harmonic rotor vibrations,

$$\mathbf{w} = \sum_{n=-\infty}^{\infty} \hat{\zeta}_n e^{in\omega_\tau t} \tag{24}$$

and

$$\dot{\mathbf{w}} = \sum_{n=-\infty}^{\infty} in\omega_\tau \hat{\zeta}_n e^{in\omega_\tau t} \tag{25}$$

where $\hat{\zeta}_n$ contains elements of ζ_n that correspond to lateral rotor displacements. Therefore,

$$\dot{\mathbf{w}}(t_-) = \sum_{n=-\infty}^{\infty} in\omega_\tau \hat{\zeta}_n e^{in\omega_\tau t_-}$$
$$\dot{\mathbf{w}}(t_+) = \sum_{n=-\infty}^{\infty} in\omega_\tau \hat{\zeta}_n e^{in\omega_\tau t_+} - (1 + i\mu)\mathbf{M}_l^{-1}\mathbf{B}_c \int_{t_-}^{t_+} \psi(t)dt \tag{26}$$

Table 1 Predicted modeled contact frequencies, ω_τ, and experimentally determined values [20]

Rotor angular velocity (rad/s)	Experimental ω_τ (rad/s)	Predicted ω_τ (rad/s)
114.1	240	240.0
115.2	241	241.1

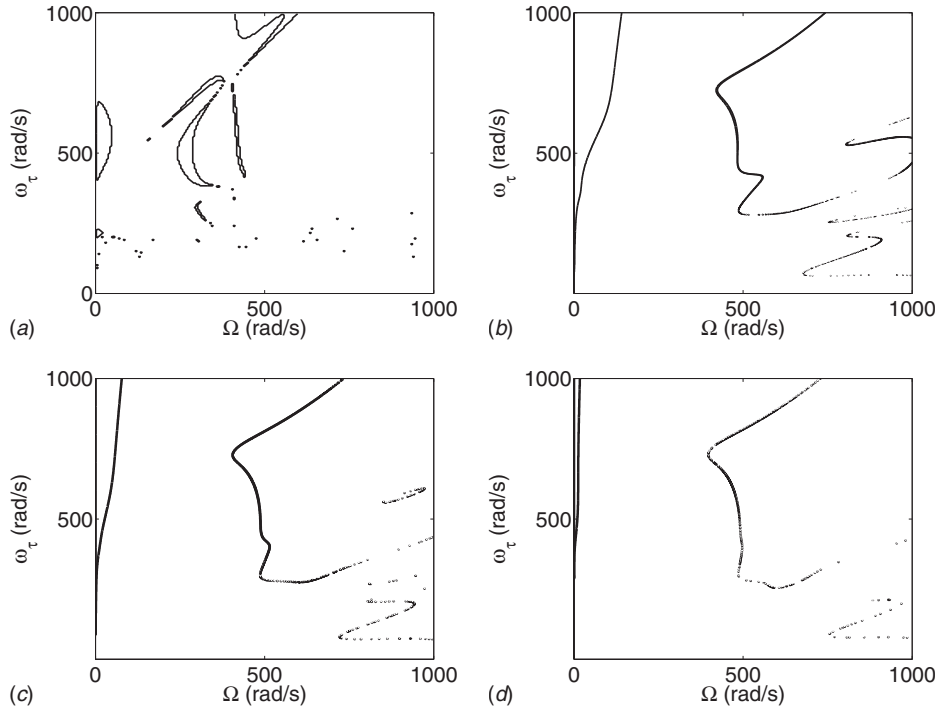

Fig. 1 Contact mode maps for different auxiliary bearing controller configurations. The same effective stiffness, k_b=1 MN/m, is used for all cases. Effective damping values are (*a*) 10 N s/m, (*b*) 50 N s/m, (*c*) 100 N s/m, and (*d*) 500 N s/m.

The total kinetic energy, J, of the rotor during a contact event can be evaluated from $J=J_n+J_p$, where J_n and J_p correspond to the kinetic energy due to motion normal and parallel to the contact location, respectively. For a passive auxiliary bearing undergoing a perfectly elastic rotor impact, the vibrational energy of the rotor before and after the contact event will be identical. However, in reality a small amount of energy will be lost and can be attributed to a coefficient of restitution, β. The initial and final rotor energies in a direction normal to the contact zone, $J_n(t_-)$ and $J_n(t_+)$, respectively, can therefore be related as $J_n(t_+)=\beta J_n(t_-)$. For an active auxiliary bearing, it may be possible for the auxiliary bearing controller to both absorb energy and input energy into the system. The relation between initial and final energies for an active auxiliary bearing is therefore $J_n(t_+)=\Upsilon J_n(t_-)$, where Υ is an energy absorption factor. The kinetic energy of the rotor can be evaluated from the velocities at the rotor nodes as

$$J = \tfrac{1}{2}[\dot{\mathbf{x}}^T\mathbf{M}_l\dot{\mathbf{x}} + \dot{\mathbf{y}}^T\mathbf{M}_l\dot{\mathbf{y}}] \tag{27}$$

From Eq. (20),

$$\dot{\mathbf{x}} = \mathrm{Re}[(\dot{\mathbf{w}} + i\Omega\mathbf{w})e^{i(\Omega t+\phi)}]$$
$$\dot{\mathbf{y}} = \mathrm{Im}[(\dot{\mathbf{w}} + i\Omega\mathbf{w})e^{i(\Omega t+\phi)}] \tag{28}$$

Equation (27) becomes

$$J = \tfrac{1}{2}[\mathrm{Re}[(\dot{\mathbf{w}} + i\Omega\mathbf{w})e^{i(\Omega t+\phi)}]^T\mathbf{M}_l\,\mathrm{Re}[(\dot{\mathbf{w}} + i\Omega\mathbf{w})e^{i(\Omega t+\phi)}]] + \tfrac{1}{2}[\mathrm{Im}[(\dot{\mathbf{w}} + i\Omega\mathbf{w})e^{i(\Omega t+\phi)}]^T\mathbf{M}_l\,\mathrm{Im}[(\dot{\mathbf{w}} + i\Omega\mathbf{w})e^{i(\Omega t+\phi)}]] \tag{29}$$

It therefore follows that J_n can be evaluated from J as

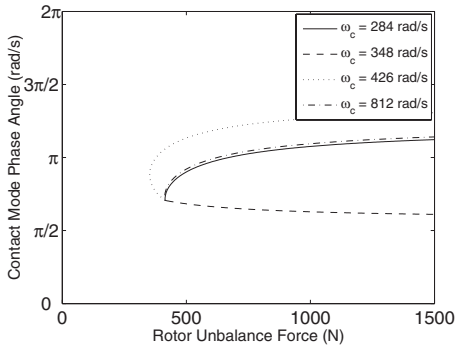

Fig. 2 Contact mode phase angle in the rotating reference frame for different unbalance conditions

$$J_n = \tfrac{1}{2}[\mathrm{Re}[(\dot{\mathbf{w}} + i\Omega\mathbf{w})e^{i(\Omega t+\phi)}]^T\mathbf{M}_l\,\mathrm{Re}[(\dot{\mathbf{w}} + i\Omega\mathbf{w})e^{i(\Omega t+\phi)}]] \tag{30}$$

Since $J_n(t_+)=\Upsilon J_n(t_-)$, solutions can be sought for the equation $J_n(t_+)-\Upsilon J_n(t_-)=\Gamma(\omega_\tau,t_-,t_+,\psi)=0$, hence, asynchronous periodic contact cases. Using Eqs. (30), (26), and (24), it is possible to show that

$$\Gamma(\omega_\tau,t_-,t_+,\psi) = [\mathbf{P}(\omega_\tau,t_-) + \mathbf{Q}(\omega_\tau,t_-)]^T\mathbf{M}_l[\mathbf{P}(\omega_\tau,t_-) + \mathbf{Q}(\omega_\tau,t_-)] - \Upsilon[\mathbf{P}(\omega_\tau,t_+) + \mathbf{Q}(\omega_\tau,t_+) - \mathbf{K}_2]^T\mathbf{M}_l[\mathbf{P}(\omega_\tau,t_+) + \mathbf{Q}(\omega_\tau,t_+) - \mathbf{K}_2] \tag{31}$$

given that

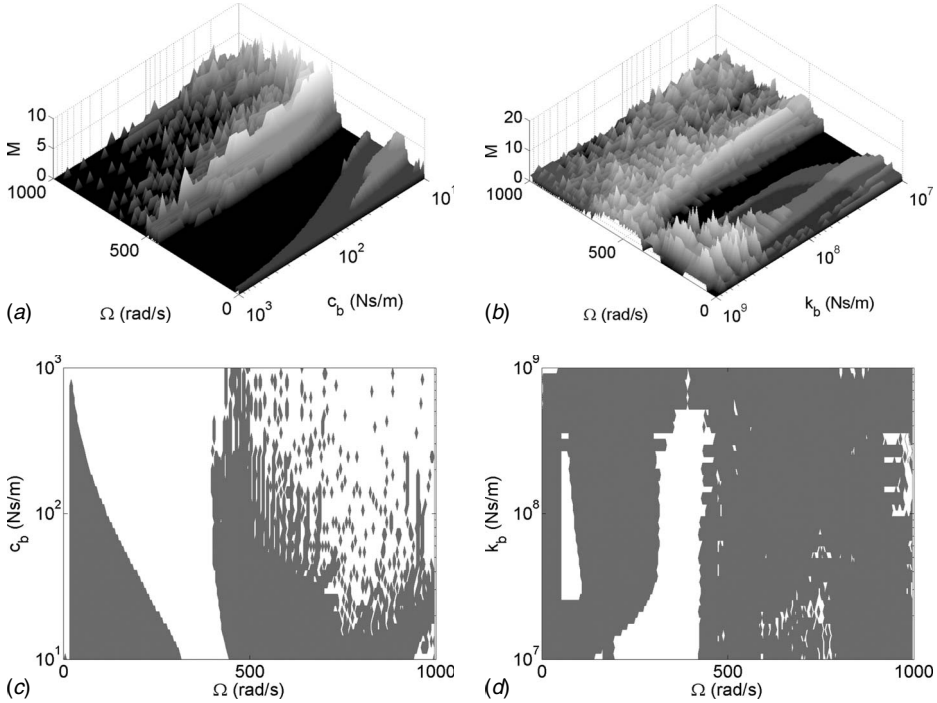

Fig. 3 (*a*) Number of contact modes, *M*, in the range $0<\omega_\tau<1000$ rad/s for different effective damping terms. Effective stiffness $k_b=1$ MN/m. (*b*) Number of contact modes, *M*, in the range of $0<\omega_\tau<1000$ rad/s for different effective stiffness terms. Effective damping $c_b=10$ N s/m. (*c*) Minimum contact modes (white) in the range of $0<\omega_\tau<1000$ rad/s for different effective damping terms. Effective stiffness $k_b=1$ MN/m. (*d*) Minimum contact modes (white) in the range of $0<\omega_\tau<1000$ rad/s for different effective stiffness terms. Effective damping $c_b=10$ N s/m.

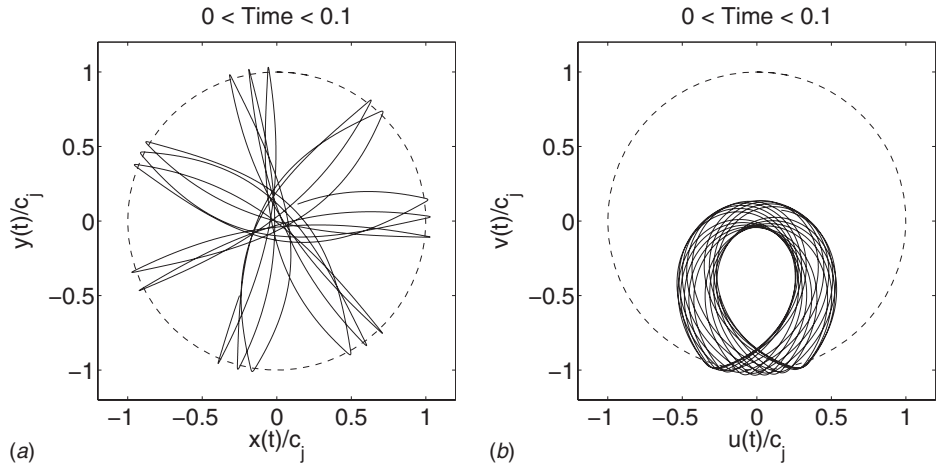

Fig. 4 Rotor orbit within normalized clearance circle: (*a*) fixed frame and (*b*) synchronous rotating frame. The dashed line shows the clearance circle.

$$\mathbf{P}(\omega_\tau t) = \mathrm{Re}\left[\sum_{n=-\infty}^{\infty} (in\omega_\tau + i\Omega[e^{i(n\omega_\tau t+\Omega t+\phi)} - 1])\Lambda_n(\omega_\tau)\right] \tag{32}$$

$$\mathbf{Q}(\omega_\tau t) = \mathrm{Im}\left[c_j\Omega\mathbf{K}_c^{-1}\sum_{n=-\infty}^{\infty} e^{i(n\omega_\tau t+\Omega t+\phi)}\right] + \mathrm{Re}\left[c_j\mathbf{K}_c^{-1}\sum_{n=-\infty}^{\infty} in\omega_\tau e^{i(n\omega_\tau t+\Omega t+\phi)}\right]$$

where

$$\mathbf{K}_2 = (1+i\mu)\mathbf{M}_l^{-1}\mathbf{B}_c\int_{t_-}^{t_+}\psi(t)dt \tag{33}$$

Periodic contact frequencies can therefore be found by searching for roots of Eq. (31). The solution is dependent on the energy absorption factor, Υ, contact time and duration, t_- and $t_+ - t_-$, and the contact force profile $\psi(t)$. Since these parameters can be varied by the choice of active auxiliary bearing control strategy, it may be possible to design a controller to limit the number of asynchronous periodic contact frequencies for a given operating condition. Furthermore, it may be possible to vary the auxiliary bearing controller to retrieve the rotor from an asynchronous contact mode.

4 Active Auxiliary Bearing Control Strategy

It is assumed for an active auxiliary bearing that the bearing displacement is small compared with the clearance gap, and contact occurs between the bearing and rotor when $(x(t)^2+y(t)^2)^{1/2} = r(t) = c_j$. An active auxiliary bearing can be configured to provide effective stiffness and damping forces during rotor/bearing contact, which leads to

$$\psi(t) = -(1+i\mu)[K_b(r(t)-c_j) + C_b(r(t)-c_j)] \tag{34}$$

where

$$K_b = \begin{cases} k_b, & r(t)-c_j \geq 0 \\ 0, & \text{otherwise} \end{cases} \tag{35}$$

and

$$C_b = \begin{cases} c_b, & r(t)-c_j \geq 0, \quad \dot{r}(t) > 0 \\ 0, & \text{otherwise} \end{cases} \tag{36}$$

In this paper, the active auxiliary bearing is considered to be a smart system that can be reconfigured to change the system dynamics. The auxiliary bearing is characterized by effective stiffness and damping terms, which are governed by the bearing controller. In reality, to achieve these characteristics, an active system may be required to provide appropriate control forces during rotor/bearing contact. In principle, an active auxiliary bearing could also apply additional forces to the rotor; however, this case is not considered here.

To reduce the onset of asynchronous periodic contact modes, an active auxiliary bearing can be configured to operate with the minimum number of possible contact modes in a specified operating range. An example may be to avoid specific contact frequencies, such as $\omega_\tau = \Omega$ in this case, to prevent accumulated thermal stress associated with rotor/bearing contact forces on the same locations.

On the detection of a contact mode, it is possible to reconfigure the controller to change the contact frequency and phase. This paper considers a control strategy to escape from trapped contact modes when the steady state response of the rotor could lie within the clearance gap.

A two stage solution is proposed. An initial variation in the auxiliary bearing controller is performed to induce forward rub and to minimize the rotor/auxiliary bearing contact force. Once forward rub is established, the auxiliary bearing may be reconfig-

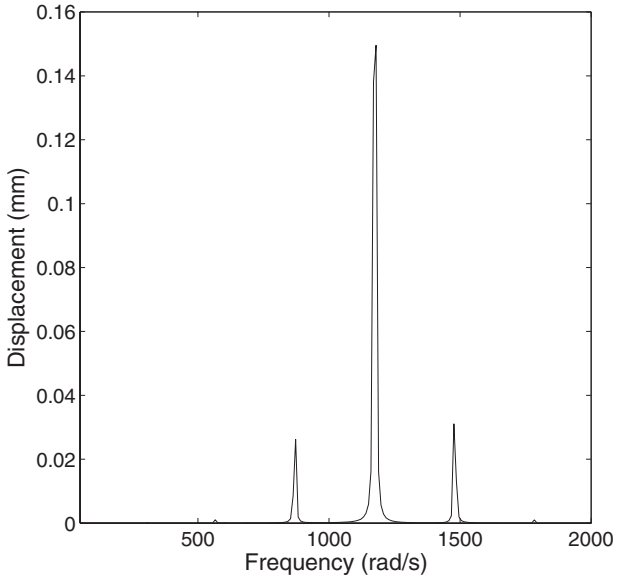

Fig. 5 Rotor vibration frequency content

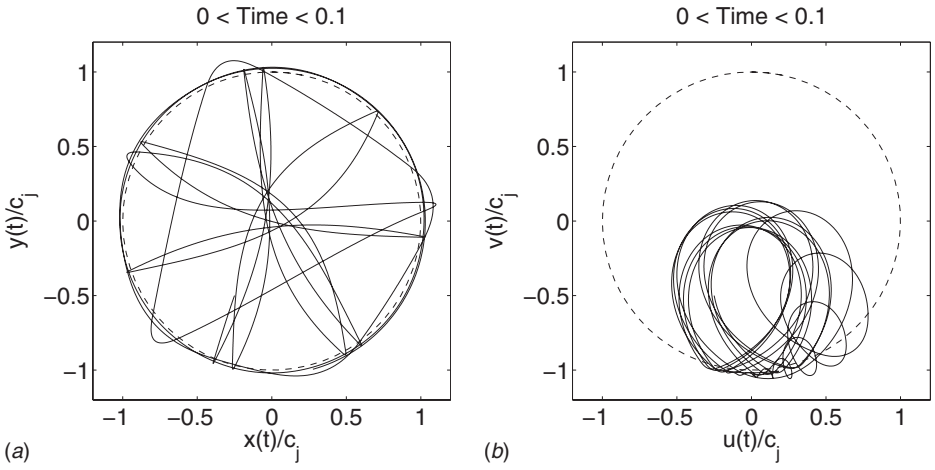

Fig. 6 Rotor orbit within normalized clearance circle: (*a*) fixed frame and (*b*) synchronous rotating frame. After 0.02 s, the controller was changed to induce forward whirl. The dashed line shows the clearance circle.

ured to a controller that minimizes the change in phase due to contact forces. The auxiliary bearing must still provide sufficient force to prevent rotor/stator contact. This puts a limit on the choice of auxiliary bearing controllers that may be used.

5 Results and Discussion

5.1 Model Validation. To validate the model, a comparison is made with experimentally determined results [20]. Tamura et al. [20] identified four trapped contact modes, each occurring at a different operating speed. In two cases, $\Omega=114.1$ rad/s and $\Omega=115.2$ rad/s, the contact frequencies are identified. In the other two cases, $\Omega=119.4$ rad/s and $\Omega=130.9$ rad/s, the contact frequency is unidentified. Table 1 shows asynchronous periodic contact frequencies for specific rotor angular velocities along with the predicted values. The corresponding auxiliary bearing effective stiffness and damping terms were 1.02 MN/m and 56 N s/m, respectively. A dry sliding friction coefficient of $\mu=0.3$ and an absorption factor of $\Upsilon=0.99$ were used.

5.2 Different Auxiliary Bearing Parameters. A simplified two degree of freedom rotor model can be used to demonstrate how the variation in contact event profile and auxiliary bearing parameters vary the contact modes of a system. The modeled system consists of a 6.5 kg rotor supported by two active magnetic bearings with effective stiffness and damping values of 500 kN/m and 750 N s/m, respectively. Figures 1(*a*)–1(*d*) show maps detailing possible trapped contact modes for different rotor angular frequencies. Variations in the auxiliary bearing effective stiffness and damping are seen to change the contact modes present in the system. Figure 2 shows rotor unbalance force and the corresponding trapped contact mode phase angle in the rotating reference frame for the case when $k_b=1$ MN/m and $c_b=50$ N s/m. In the case of $\omega_\tau=426$ rad/s, unbalance forces below 410 N result in two possible contact mode phases.

When designing a rotor/magnetic bearing system, it is therefore possible to consider the number of contact modes present in a specified operating range. Considering the ranges $0<\Omega<1000$ rad/s and $0<\omega_\tau<1000$ rad/s, the number of possible contact modes that exist is shown in Fig. 3. An active auxiliary bearing can therefore be used to select controllers that limit the number of contact modes at each running speed; hence, the control strategy can be varied to maintain the minimum number of contact modes as the rotor speed varies. Suitable effective stiffness and damping terms are shown in Figs. 3(*c*) and 3(*d*). It can be seen that a passive bearing would be unable to offer the minimum number of contact modes across the whole running speed range.

5.3 Case Study. An active auxiliary bearing system can be varied not only to minimize the number of possible contact modes, but also once a contact mode has become established. Objectives for such action include varying the contact mode frequency, ω_τ, inducing continuous contact (forward whirl), and terminating the contact mode so the rotor returns to a noncontacting orbit.

For the case study, a system with auxiliary bearing effective stiffness and damping terms, $k_b=100$ kN/m and $c_b=10$ N s/m, and $\Upsilon=0.99$ is considered. For this system, an asynchronous periodic contact mode, $\omega_\tau=1210$ rad/s, is present at the operating speed $\Omega=500$ rad/s. On detection of the contact mode, variation in the effective stiffness and damping characteristics of the auxiliary bearing can be used to change the rotor response. Three different cases are considered. An unbalance force of 375 N was chosen to excite the asynchronous periodic contact mode at $\omega_\tau=1210$ rad/s, where the steady state rotor response, if no auxiliary bearing was present, is within the clearance circle. Three

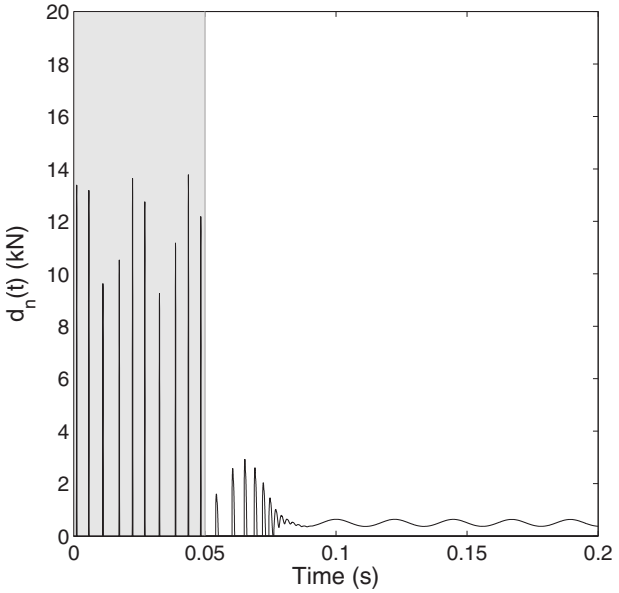

Fig. 7 Rotor/auxiliary bearing contact force variation. After 0.02 s, the controller was changed to induce forward whirl (unshaded region).

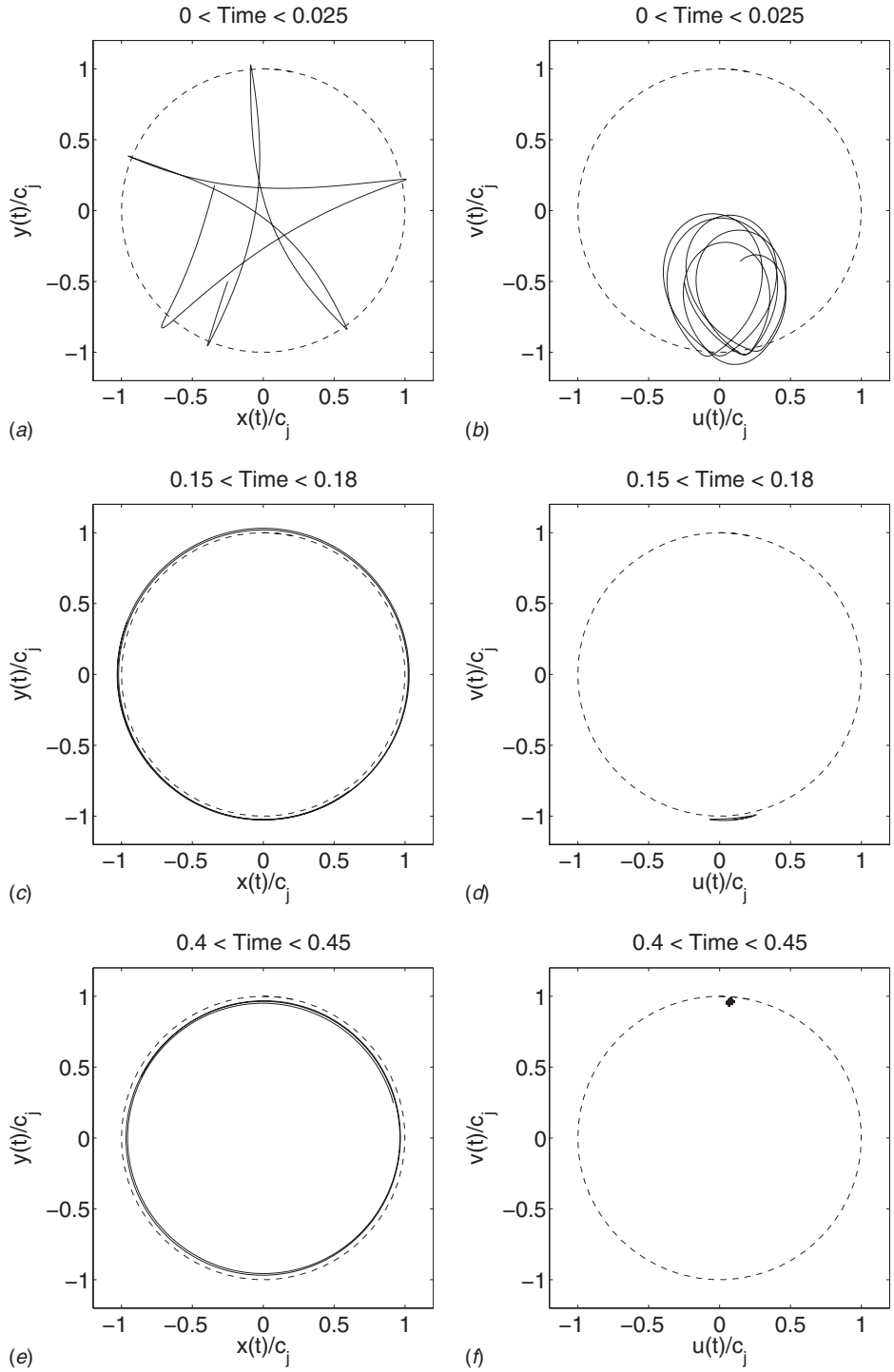

Fig. 8 Rotor displacement in (*a*) a fixed and (*b*) a synchronous rotating reference frame with the case 1 auxiliary bearing controller. (*c*) and (*d*) show the displacement in fixed and synchronous rotating reference frames with the case 2 auxiliary bearing controller. (*e*) and (*f*) show the displacement in fixed and synchronous rotating reference frames with the case 3 auxiliary bearing controller. The dashed line shows the clearance circle.

different approaches are considered. The rotor was initially configured to operate in a state of perfect balance before step change in the unbalance occurring at 0 s.

5.3.1 Case 1. The first case considers the active auxiliary bearing controller providing effective stiffness and damping of $k_b = 100$ kN/m and $c_b = 10$ N s/m, respectively. This is in effect a passive strategy. Figure 4 shows the rotor orbit in fixed and synchronously rotating reference frames. Then, the rotor is seen to orbit with periodic contact between the rotor and auxiliary bearing. An analysis of the frequency content of the rotor vibration (Fig. 5) shows a peak at 1210 rad/s and is consistent with the predicted contact mode. The dominant peak corresponds with the time period between successive contacts. The side peaks are associated with the transient behavior in the rotor response. Contact

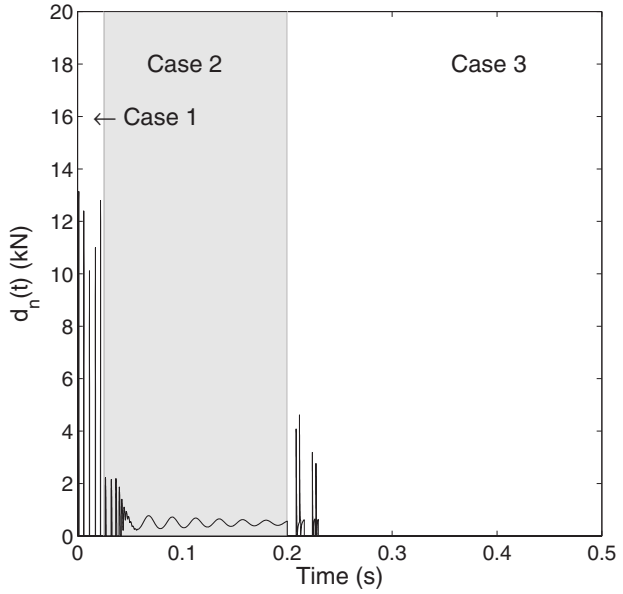

Fig. 9 Rotor/auxiliary bearing contact forces variation under case 1–3 controllers

forces and durations are approximately 13 kN and 0.8 ms, respectively.

5.3.2 Case 2. The second case considers the same system with the same initial auxiliary bearing controller as case 1. On the detection of a periodic contact mode, the auxiliary bearing controller is reconfigured (after 0.05 s) to provide different effective stiffness and damping characteristics where the established contact mode contact frequency is not permitted. The modified auxiliary bearing effective stiffness and damping terms are $k_b = 50$ kN/m and $c_b = 100$ N s/m, respectively. The rotor orbits in a fixed and synchronously rotating reference frames are shown in Fig. 6. The modified auxiliary bearing dynamics are seen to reduce the rotor/bearing contact force before the rotor enters a forward rub (Fig. 7).

5.3.3 Case 3. In the third case, once a trapped contact mode is detected, the auxiliary bearing controller is reconfigured to induce a forward rub response. The new auxiliary bearing effective stiffness and damping terms are $k_b = 50$ kN/m and $c_b = 100$ N s/m, respectively. Once forward rub is established, the auxiliary bearing is reconfigured to add additional damping to the rotor to return it to an orbit within the clearance circle. The final auxiliary bearing controller is designed with a minimal phase difference between the steady state noncontacting and the continuing forward rub rotor responses. Here, the auxiliary bearing controller parameters are $k_b = 50$ kN/m and $c_b = 1.5$ kN s/m and the corresponding phase angle between rotor orbit and unbalance force is 19 deg.

Initially, the rotor enters an asynchronous contact mode. After 0.025 s, the auxiliary bearing is reconfigured to induce the rotor into the forward rub. Once the forward rub is established, the auxiliary bearing is again reconfigured, at 0.2 s, to provide sufficient rotor damping to return the rotor to an orbit within the clearance circle. Several more rotor/auxiliary bearing contact events occur before the rotor settles into a noncontacting steady state orbit. This response may be caused by transient dynamics excited by the sudden change in system parameters. Figures 8(*a*) and 8(*b*) show the initial asynchronous contact mode. Figures 8(*c*) and 8(*d*) correspond to the forward rub response. Figures 8(*e*) and 8(*f*) show the rotor orbit within the clearance circle. Figure 9 shows the rotor/auxiliary bearing contact force. The initial periodic rotor bearing contact is seen in region 1 (left). In region 2 (middle), the continuous contact force corresponding to the forward rub is present. The third region (right) shows the rotor returning to an orbit within the clearance circle, hence, zero contact force. This approach is seen to initially reduce the rotor/bearing contact forces before successfully returning the rotor to a contact free orbit.

6 Conclusions

A method of reducing the onset of asynchronous periodic contact modes in rotor/magnetic bearing auxiliary/bearing systems is presented. A theoretical method to identify asynchronous periodic contact modes is used to consider finite duration contact.

An auxiliary bearing controller design is centered on the minimization of the number of possible contact modes at a given operating speed. Furthermore, on the detection of a contact mode, the auxiliary bearing controller is switched to one that prohibits the continuation of the contact mode. Results indicate that a two stage strategy can be used to return the rotor to a noncontact orbit once a trapped contact mode is established. The strategy initially reconfigures the auxiliary bearing to induce a forward rub. Once the forward rub is established, the bearing is reconfigured to increase the damping on the rotor while minimizing the phase difference between the rotor orbit and the unbalance force vector. This is shown to return the rotor to an orbit within the clearance circle.

Acknowledgment

The authors gratefully acknowledge the funding support of the Engineering and Physical Sciences Research Council through Grant No. EP/D031389/1.

Nomenclature

$\mathbf{B}_c$ = distribution matrix
c_j = rotor/auxiliary bearing clearance gap at node j
$\mathbf{D}$ = fixed reference frame rotor contact force vector
$\mathbf{d}_{d,u,c}$ = fixed reference frame rotor disturbance, control, and contact force vector
D_j = rotor/auxiliary bearing contact force at node j
$d_{n,p}$ = rotor/auxiliary bearing contact force normal and parallel to the contact patch
$\mathbf{f}_{d,u}$ = fixed reference frame rotor disturbance and control force vector
i = $\sqrt{-1}$
J = rotor kinetic energy
j = nodal index
k_b, c_b = auxiliary bearing effective stiffness and damping
k, n = integers
$\mathbf{M}$, $\mathbf{C}$, $\mathbf{G}$, $\mathbf{C}$ = fixed reference frame rotor mass, damping, gyroscopic and stiffness matrices.
$\mathbf{M}_c$, $\mathbf{C}_c$, $\mathbf{K}_c$ = rotating reference frame rotor complex mass, damping, and stiffness matrices
$\mathbf{M}_\Omega$, $\mathbf{C}_\Omega$, $\mathbf{K}_\Omega$ = rotating reference frame rotor mass, damping, and stiffness matrices
$\mathbf{p}$ = rotor momentum vector
$\mathbf{q}$ = fixed reference frame rotor displacement vector
$\mathbf{r}$ = rotating reference frame rotor displacement vector
r_j = radial rotor displacement
t = time
u_N, v_N = rotating reference frame rotor lateral displacement at node j
$\mathbf{w}$ = rotor lateral displacement vector in a synchronously rotating reference frame
x_j, y_j = rotor lateral displacement at node j
$\mathbf{z}$ = rotating reference frame complex rotor displacement vector
β = coefficient of restitution

ζ_n = rotor/displacement complex Fourier coefficient
ϑ_N, ζ_N = rotating reference frame rotor angular displacement at node j
θ_N, ϕ_N = rotor angular displacement at node j
μ = coefficient of friction
τ = contact period
Υ = energy absorption factor
ϕ = unbalance phase angle
Φ_n = periodic rotor/auxiliary bearing contact force complex Fourier coefficient
$\Psi(t)$ = radial contact force profile
Ω = rotor angular velocity
$\omega_t = 2\pi/\tau$

References

[1] Fumagalli, M., Feeny, B., and Schweitzer, G., 1992, "Dynamics of Rigid Rotors in Retainer Bearings," *Proceedings From the Third International Symposium on Magnetic Bearings*, pp. 157–166.
[2] Black, H. F., 1968, "Interactions of a Whirling Rotor With a Vibrating Stator Across a Clearance Annulus," J. Mech. Eng. Sci., **10**(1), pp. 1–12.
[3] Lawen, J. L., and Flowers, G. T., 1997, "Synchronous Dynamics of a Coupled Shaft/Bearing/Housing System With Auxiliary Support From a Clearance Bearing," Trans. ASME J. Eng. Gas Turbines Power, **119**, pp. 430–435.
[4] Wang, X., and Noah, S. T., 1998, "Nonlinear Dynamics of a Magnetically Supported Rotor on Safety Auxiliary Bearings," Trans. ASME, J. Vib. Acoust., **120**, pp. 596–606.
[5] Bartha, A. R., 1998, "Dry Friction Induced Backwards Whirl: Theory and Experiment," *Proceedings of the Fifth IFToMM Conference on Rotor Dynamics*, pp. pp. 757–767.
[6] Ehrich, F. F., 1988, "High Order Subharmonic Response of High Speed Rotors in Bearing Clearance," Trans. ASME, J. Vib., Acoust., Stress, Reliab. Des., **110**, pp. 9–16.
[7] Childs, D. W., 1979, "Rub Induced Parametric Excitation in Rotors," ASME J. Mech. Des., **10**, pp. 640–644.
[8] Muszynska, A., and Goldman, P., 1993, "Chaotic Vibrations of Rotor/Bearing/Stator Systems With Looseness or Rubs," ASME Vibration and Noise Conference, Nonlinear Vibrations, Vol. 54, pp. 187–194.
[9] Cole, M. O. T., and Keogh, P. S., 2003, "Asynchronous Periodic Contact Modes for Vibration Within an Annular Clearance," Proc. Inst. Mech. Eng., Part C: J. Mech. Eng. Sci., **217**, pp. 1101–1115.
[10] Ishii, T., and Kirk, G. R., 1996, "Transient Response Technique Applied to Active Magnetic Bearing Machinery During Rotor Drop," Trans. ASME, J. Vib. Acoust., **118**, pp. 154–163.
[11] Keogh, P. S., and Yong, W. Y., 2007, "Thermal Assessment of Dynamic Rotor/Auxiliary Bearing Contact Events," Trans. ASME, J. Tribol., **129**, pp. 143–152.
[12] Cole, M. O. T., and Keogh, P. S., 2003, "Rotor Vibration With Auxiliary Bearing Contact in Magnetic Bearing Systems—Part 2: Robust Synchronous Control for Rotor Position Recovery," Proc. Inst. Mech. Eng., Part C: J. Mech. Eng. Sci., **217**(4), pp. 393–409.
[13] Abulrub, A. G., Sahinkaya, M. N., Keogh, P. S., and Burrows, C. R., 2006, "Experiments on ROLAC to Recover Rotor Position Following Contact," The Tenth International Symposium on Magnetic Bearings, Martigny, Switzerland, Aug. 21–23.
[14] Schlotter, M., and Keogh, P. S., 2007, "Synchronous Position Recovery Control for Flexible Rotors in Contact With Auxiliary Bearings," Trans. ASME, J. Vib. Acoust., **129**, pp. 550–558.
[15] Ulbrich, H., Chavez, A., and Dhima, R., 2004, "Minimization of Contact Forces in Case of Rotor Rubbing Using an Actively Controlled Auxiliary Bearing," *Proceedings of the Tenth International Symposium on Transport Phenomena and Dynamics of Rotating Machinery*, pp. 10–31.
[16] Ginzinger, L., and Ulbrich, H., 2008, "Simulation-Based Controller Design for an Active Auxiliary Bearing," *Proceedings From the 11th International Symposium on Magnetic Bearings*, Nara, Japan, Aug. 26–29.
[17] Palazzolo, A. B., Lin, R. R., Alexander, A. F., Kascak, R. M., and Montauge, J., 1991, "Test and Theory for Piezoelectric Actuator-Active Vibration Control of Rotating Machinery," Trans. ASME, J. Vib. Acoust., **113**, pp. 167–175.
[18] Cade, I. S., Sahinkaya, M. N., Burrows, C. R., and Keogh, P. S., 2008, "On the Design of an Active Auxiliary Bearing for Rotor/Magnetic Bearing Systems," *Proceedings From the 11th International Symposium on Magnetic Bearings*, Nara, Japan, Aug. 26–29.
[19] Nelson, H., and McVaugh, J., 1976, "The Dynamics of Rotor-Bearing Systems Using Finite Elements," ASME J. Eng. Ind., **98**, pp. 593–600.
[20] Tamura, K., Shiraki, K., Awa, K., and Watanabe, Y., 2002, "Vibration Behaviour of Rotating Shaft Due to Contact With Casing," *Proceedings From the Sixth International Conference on Motion and Vibration Control*, Urawa, Japan, Aug. 26–29.

The Numerical and Experimental Characteristics of Multimode Dry-Friction Whip and Whirl

Jason C. Wilkes
Graduate Research Assistant
e-mail: jasonwilkes@tamu.edu

Dara W. Childs
Leland T. Jordan Professor of Mechanical Engineering
e-mail: dchilds@tamu.edu

Benjamin J. Dyck
Graduate Research Assistant
e-mail: bjdyck@chevron.com

Stephen G. Phillips
Research Engineer
e-mail: sphillips@tamu.edu

Turbomachinery Laboratory,
Texas A&M University,
College Station, TX 77802

The nature of dry-friction whip and whirl is investigated through experimental and numerical methods. A test rig was designed and constructed to demonstrate and record the character of multimode dry-friction whip and whirl. These tests examined steady-state whip and whirl characteristics for a variety of rub materials and clearances. A simulation model was constructed using tapered Timoshenko beam finite elements to form multiple-degree-of-freedom rotor and stator models. These models were reduced by component mode synthesis to discard high-frequency modes while retaining physical coordinates at the rub location to model rotor-stator interaction using a nonlinear contact model with Coulomb friction. Simulations were performed for specific test cases, and compared against experimental data; these comparisons are favorable. Experimental data analysis showed multiple whirl and whip regions, despite claims of previous investigators that these regions are predicted analytically but not produced in simulations or experiments. Spectral analysis illustrates the presence of harmonic sidebands that accompany the fundamental whirl solution. These sidebands are more evident in whip, and can excite higher-frequency whirl solutions. [DOI: 10.1115/1.3204658]

1 Introduction

Rubbing occurs regularly in turbomachinery, and generally, does not cause serious problems. One of the most destructive rubbing phenomena occurs when a rotor, upon contact with the stator across a radial clearance, is forced by traction into a backward precessional orbit. This motion falls into the following two regimes.

- *Dry-friction whirl*. The rotor is rolling-without-slipping on the surface of the stator with a backward precession frequency governed by the radius-to-clearance ratio at the contact location.
- *Dry-friction whip*. The rotor slips continuously on the stator surface with a backward precession frequency governed by the combined natural frequency of the connected rotor-stator system.

Dry-friction whip and whirl have been produced in several test rigs but rarely occurs in real machines. One incident reported by Rosenblum [1] cited a catastrophic failure associated with whip. No troubles have been reported related to whirl until recent problems occurred during the start up tests on the advanced liquid hydrogen (ALH) turbopump. Those problems led to the test/simulation program relayed here.

1.1 Literature Review. In 1962, Johnson [2] established a basic framework for the analysis of rotor-stator interaction. Johnson [2] states that the solution must be real, the reaction must be positive, and the equilibrium must be stable. In 1965, Billett [3], proposed that the occurrence of slip between the rotor and stator explained why shafts whirled close to their natural frequency throughout a wide range of running speeds. Using a Jeffcott rotor with a clearance at one bearing, he showed that the simple model cannot whirl faster than its first natural frequency without pulling away from the stator. In addition, Billett [3] solved for the friction coefficient that is required to sustain steady reverse whirl, which he used to determine the whirl frequency at which the friction coefficient needed to sustain steady whirling is greater than the rotor-stator Coulomb friction coefficient, thus resulting in a transition to whip.

In 1967 and 1968, Black [4,5] extended the methods employed by Johnson [2] and Billett [3] to include contact with a compliantly mounted stator. Black [4,5] developed a general model for synchronous rubbing, and reduced it to investigate dry-friction counter whirl. Black [4,5] concluded that dry-friction whirl is only possible in the frequency band, extending from an individual rotor/stator natural frequency to the next higher combined system natural frequency. This range is further reduced by the condition placed on the traction angle, which Black [4,5] resolved into a plot having a characteristic U-shape that separates regions of whirl and whip

In 1988, Zhang [6] accounted for multiple rotor modes in dry-friction whip and whirl by applying Black's model to a long-cantilevered disk. Zhang [6] identified the same whirl regions as Black [4,5], asserting the validity of Black's results when correctly applied. In addition, Zhang [6] presented a condition for the critical contact velocity required to initiate dry-friction whirl.

In 1990, Lingener [7] and Crandall [8] revisited the analytical and experimental work of Black [4,5]. Their analysis indicated that Black's model was generally valid in predicting whirl ranges; however, Lingener [7] concludes that "it is impossible, to run through any resonance of the joined system, excited by reverse whirl," despite this prediction using Black's model. This feat was accomplished recently by Choi [9] and Dyck [10].

In 2000, Bartha [11,12] validated the critical impact velocity given by Zhang [6], but concluded that numerical simulations using Black's model were unstable without accounting for the relative surface velocity at the contact location, and noticed differences between whirl ranges predicted using Black's model and measured results.

In 2007—following statements by Bartha [11,12] and Yu et al. [13] that Black's whirl model predicted erroneous whirl ranges when applied to their experimental apparatus—Childs and Bhattacharya [14] applied Black's methods with MDOF models of the rotor of Bartha [11,12] and Yu et al. [13], and found that (1) accurate whirl-range predictions require an accurate rotor-stator

Contributed by the International Gas Turbine Institute of ASME for publication in the JOURNAL OF ENGINEERING FOR GAS TURBINES AND POWER. Manuscript received March 30, 2009; final manuscript received May 12, 2009; published online March 4, 2010. Review conducted by Dilip R. Ballal. Paper presented at the ASME Gas Turbine Technical Congress and Exposition, Orlando, FL, June 8–12, 2009.

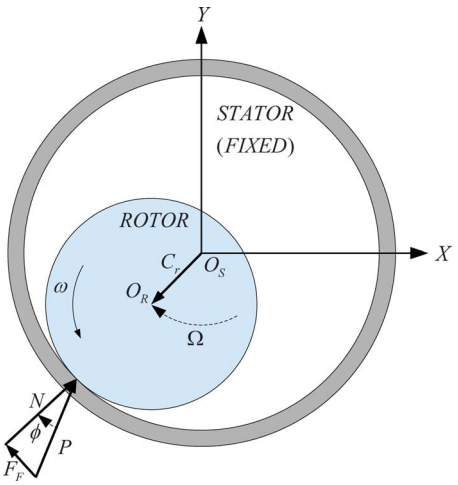

Fig. 1 Geometric model governing rotor-stator contact

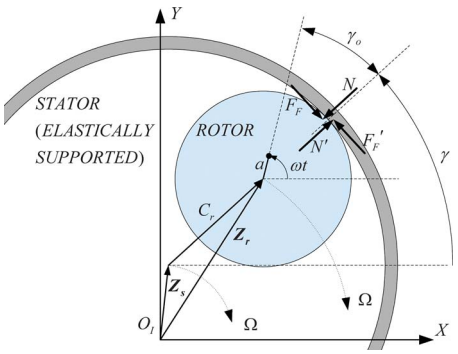

Fig. 2 Rotor-stator interaction model after Ref. [14]

model, which may require the use of multiple rotor/stator modes (Black [4,5] and Zhang [6] cited this necessity; however, Black [4,5] did not extend his whirl-whip method to multimode rotor-stator interaction, and Zhang [6] failed to produce multiple whirl regions), and (2) a multimode rotor-stator model produces several U-shaped curves, thus predicting several possible whirl regions. Although Childs and Bhattacharya [14] predicted multiple regions, only the first whirl region and its whip frequency could be produced in simulations.

1.2 Background on the ALH. In 1995, the U.S. Air Force Research Laboratory (AFRL), Space and Missile Propulsion Division, Edwards AFB, CA, commissioned Pratt & Whitney (P&W) Liquid Space Propulsion to design and build the ALH. The P&W design features a one-piece rotor with unshrouded impellers to be supported by hydrostatic journal bearings and a single hydrostatic thrust bearing. The hydrostatic bearings are supplied by the pump discharge, which results in little or no rotor support during startup.

From 1998 through 2002, 20 tests were performed on 11 different builds of the ALH; only the first of these ran according to plan. Following test 1, the development of large supersynchronous vibrations at low speeds overpowered the drive capabilities of the turbopump, and retarded the rotor. The supersynchronous motion "tracked" running speed, i.e., they largely stayed at a fixed multiple of ω. Hardware inspection showed visual signs of rubbing at several locations, specifically on the surfaces of the radial and thrust bearings [15].

In 2004 Texas A&M Turbomachinery Laboratory (TAMU-TL) was contacted regarding the low speed ALH results. Childs [16] stated that dry-friction whip and whirl were consistent with the observed supersynchronous tracking motion; however, the multiplicity of tracking frequencies present in the vibration spectrum had not previously been reported. A research program was initiated at TAMU-TL to develop a test rig to explain these results; the experimental and numerical exploration of this test rig is the focus of this paper.

2 Mathematical Model

Using a model similar to the one given in Fig. 1, Den Hartog [17] proposed the following kinematic constraint between the precessional velocity Ω of the rotor's whirl orbit and rotor speed ω:

$$\Omega = \frac{R}{C_r}\omega = \Gamma\omega \tag{1}$$

Here, Γ is the precession frequency ratio (PFR). A rotor that is rolling-without-slipping within the stator clearance circle is said to be exhibiting dry-friction whirl.

Following Black [4,5], the equations of motion can be derived from the free-body diagram of Fig. 2, and stated as

$$\begin{aligned} m_r\ddot{\mathbf{Z}}_\mathbf{r} + c_r\dot{\mathbf{Z}}_\mathbf{r} + k_r\mathbf{Z}_\mathbf{r} &= \begin{cases} -(N+jF_F)e^{j\gamma} + m_r a\omega^2 e^{j\omega t} & |\mathbf{Z}_\mathbf{r}-\mathbf{Z}_\mathbf{s}| = C_r \\ m_r a\omega^2 e^{j\omega t} & |\mathbf{Z}_\mathbf{r}-\mathbf{Z}_\mathbf{s}| < C_r \end{cases} \\ m_s\ddot{\mathbf{Z}}_\mathbf{s} + c_s\dot{\mathbf{Z}}_\mathbf{s} + k_s\mathbf{Z}_\mathbf{s} &= \begin{cases} (N+jF_F)e^{j\gamma} & |\mathbf{Z}_\mathbf{r}-\mathbf{Z}_\mathbf{s}| = C_r \\ 0 & |\mathbf{Z}_\mathbf{r}-\mathbf{Z}_\mathbf{s}| < C_r \end{cases} \end{aligned} \tag{2}$$

where

$$\mathbf{Z}_\mathbf{r} = X_r + jY_r, \quad \mathbf{Z}_\mathbf{s} = X_s + jY_s$$

Neglecting the effect of rotor imbalance, Eq. (2) reduces to

$$\begin{aligned} m_r\ddot{\mathbf{Z}}_\mathbf{r} + c_r\dot{\mathbf{Z}}_\mathbf{r} + k_r\mathbf{Z}_\mathbf{r} &= -(N+jF_F)e^{j\gamma} \\ m_s\ddot{\mathbf{Z}}_\mathbf{s} + c_s\dot{\mathbf{Z}}_\mathbf{s} + k_s\mathbf{Z}_\mathbf{s} &= (N+jF_F)e^{j\gamma} \end{aligned} \tag{3}$$

Their steady-state properties follow from assuming the periodic solution

$$\mathbf{Z}_\mathbf{r} = \mathbf{z}_\mathbf{r}e^{-j\Omega t}, \quad \mathbf{Z}_\mathbf{s} = \mathbf{z}_\mathbf{s}e^{-j\Omega t}, \quad \gamma = -\Omega t + \gamma_o \tag{4}$$

Plugging the assumed solution and its derivatives into Eq. (3) nets

$$\begin{aligned} (k_r - m_r\Omega^2 - jc_r\Omega)\mathbf{z}_\mathbf{r}e^{-j\Omega t} &= \frac{\mathbf{z}_\mathbf{r}e^{-j\Omega t}}{\boldsymbol{\alpha}_{\mathbf{11}}(-\Omega)} = -(N+jF_F)e^{j\gamma} \\ (k_s - m_s\Omega^2 - jc_s\Omega)\mathbf{z}_\mathbf{s}e^{-j\Omega t} &= \frac{\mathbf{z}_\mathbf{s}e^{-j\Omega t}}{\boldsymbol{\beta}_{\mathbf{11}}(-\Omega)} = (N+jF_F)e^{j\gamma} \end{aligned} \tag{5}$$

where Black [4,5] introduced the rotor and stator receptances $\boldsymbol{\alpha}_{\mathbf{11}}(-\Omega)$ and $\boldsymbol{\beta}_{\mathbf{11}}(-\Omega)$. For continuous contact, the model is completed by the constraint equation

$$C_r e^{j\gamma} = \mathbf{Z}_\mathbf{r} - \mathbf{Z}_\mathbf{s} = (\mathbf{z}_\mathbf{r} - \mathbf{z}_\mathbf{s})e^{-j\Omega t} \tag{6}$$

Substituting from Eq. (5) into Eq. (6) nets first

$$C_r e^{j\gamma_o} = \mathbf{z}_\mathbf{r} - \mathbf{z}_\mathbf{s} = -[\boldsymbol{\alpha}_{\mathbf{11}}(-\Omega) + \boldsymbol{\beta}_{\mathbf{11}}(-\Omega)](N+jF_F)e^{j\gamma_o} \tag{7}$$

and then

$$(N+jF_F) = -C_r[\boldsymbol{\alpha}_{\mathbf{11}}(-\Omega) + \boldsymbol{\beta}_{\mathbf{11}}(-\Omega)]^{-1} \tag{8}$$

The required friction coefficient μ that satisfies Eq. (8) is

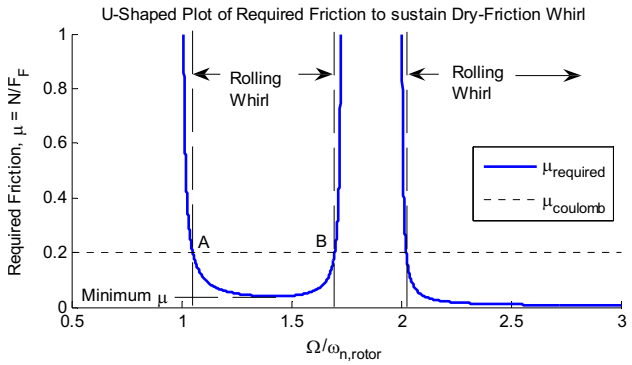

Fig. 3 General case of the U-shaped plot attributed to black

$$\mu = \frac{F_F}{N} = -\frac{\mathrm{Im}[\alpha_{11}(-\Omega) + \beta_{11}(-\Omega)]}{\mathrm{Re}[\alpha_{11}(-\Omega) + \beta_{11}(-\Omega)]} \tag{9}$$

In addition, the real part of Eq. (8) yields the normal force

$$N = -C_r\,\mathrm{Re}[\boldsymbol{\alpha_{11}}(-\Omega) + \boldsymbol{\beta_{11}}(-\Omega)]^{-1} \tag{10}$$

From Eq. (9), Black [4,5] generated a plot having a characteristic U-shape to differentiate between regions of whip and whirl. An example of the U-shaped plot is given in Fig. 3.

Below the left side of the U-shape curve dry-friction whirl is not possible for any finite Coulomb friction coefficient, and within the U-shaped curve whirl is it only possible, given the sufficient Coulomb friction. The right hand side of the U-shaped curve defines the transition from whirl to whip for which the rotor will precess at the combined rotor-stator natural frequency

$$\omega_{n,\mathrm{comb}} = \sqrt{\frac{k_r + k_s}{m_r + m_s}} \tag{11}$$

otherwise known as the whip frequency.

Extending Black's model to include multiple rotor-stator modes, Childs and Bhattacharya [14,15] produced the predictions for Bartha's test rig given in Fig. 4. Using only one rotor mode to predict whirl, Bartha [11,12] predicted a transition to whip at 1600 Hz. When he observed a transition to whip at 600 Hz, Bartha [11,12] attributed the discrepancy to a flaw in Black's whirl solution. Childs and Bhattacharya [14,15] showed that a multimode extension of Black's model predicts whip at 650 Hz, very close to the actual whip frequency.

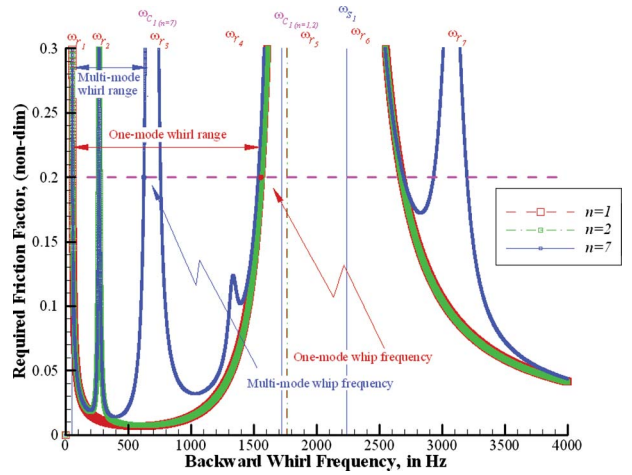

Fig. 4 Multimode dry-friction whirl prediction for Bartha's rig [14]

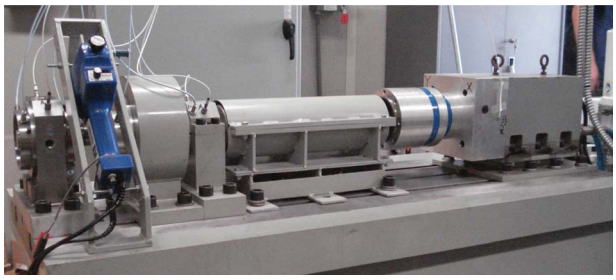

Fig. 5 Picture of the TAMU whip and whirl test rig

3 TAMU Dry-Friction Whip and Whirl Test Rig

3.1 General Description. The TAMU whip and whirl test rig is shown in Figs. 5 and 6.

Figure 6 shows that the rotor is supported from the right by two adjacent angular-contact ball bearings. On the left, an impact hammer initiates contact between the test rotor and a replaceable rub insert. Motion was observed by four pairs of proximity probes, located along the shaft, plus a pair of accelerometers on each pedestal. The proximity probes and accelerometers can be seen in Fig. 7, and were oriented 45 deg from the horizontal and vertical directions. Not shown is a 64:1 encoder on the motor to detect the rotor speed. All of the data were recorded using data acquisition boards with a 20 kHz sample rate, and were postprocessed.

Because whip and whirl testing was performed for ω from 0 rpm to 250 rpm, the shaft was driven by a 22 kW (29.5 hp) motor through a gear reducer to provide high torque at low speeds. The drive system was connected to the test rotor through a spline shaft to minimize misalignment between the test rotor and drive system. These components were all mounted and aligned on a heavy,

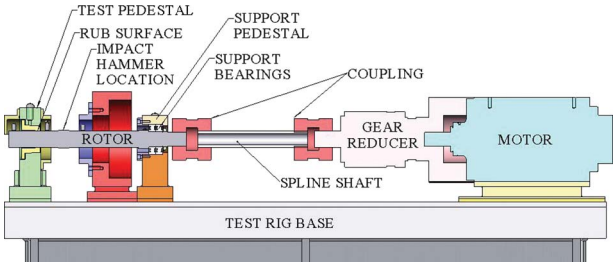

Fig. 6 Section view of the TAMU whip and whirl test rig

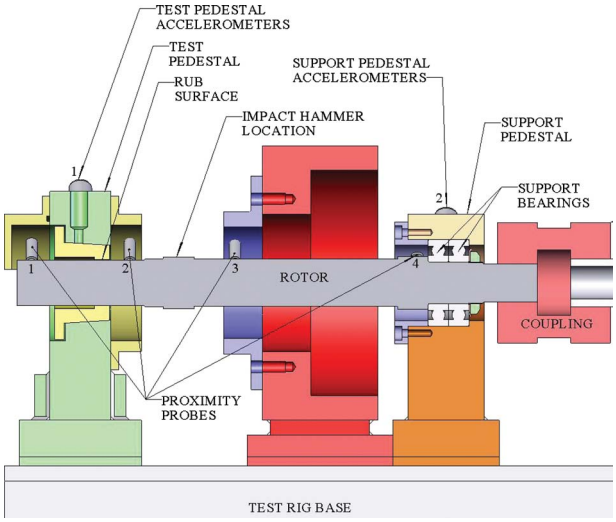

Fig. 7 Section view of the TAMU whip and whirl test rig rotor

Table 1 Properties of rotor-stator pairs at the rub location

Bearing	R/C_r	Material	Hardness (HB)	Friction coefficient [18,19]
S1,S2	517.1	660 Bronze	65	0.1–0.5
L1	245.8	660 Bronze	65	0.1–0.5
B1	517.1	Babbitt	24	0.25–0.6
T1	348.7	AISI 4140	197	0.25–0.7

softly mounted test base, which reduced the influence of base motion due to high-frequency whip/whirl, and significantly reduced orthotropy in the bearing support.

3.2 Test Rotor. The AISI 4140 steel shaft has an average diameter of 38.1 mm (1.5 in), and a length of 0.433 m (17.08 in). With these dimensions and ball bearings with predicted stiffness of 80.6 MN/m (480,000 lb/in), the lowest three calculated natural frequencies of the shaft are 40.9 Hz, 418.5 Hz, and 810.6 Hz, where 40.9 Hz represents the rigid-body conical mode, and the latter two represents the bending modes. Figure 7 provides more detail on the location of probes, accelerometers, and rubbing contact.

The center of the rub surface was 70.87 mm (2.79 in) from the free end of the rotor, and had a length of 12.7 mm (1/2 in). The measured diameter of the rotor at this location was 38.09 mm (1.4997 in). Four different stator inserts were machined to test the effects of clearance and material at the rubbing-contact location. These properties are summarized in Table 1.

3.3 Base of Test Stand and Rotor Support. Table 2 gives the lowest horizontal and vertical natural frequencies of each pedestal resulting from impact tests.

These pedestal natural frequencies are in the range of excitation frequencies, and their associated modes must be included in the model. The higher vertical-direction natural frequency than horizontal-direction natural frequency indicates pedestal-support orthotropy. These pedestals were mounted on a 2500 lbs test stand, having horizontal and vertical natural frequencies of approximately 3–6 Hz. Because these frequencies are significantly lower than those excited during tests, the motion of the base can be eliminated from the model

3.4 Test Series and Data Analysis. Several test series were executed for each stator insert, consisting of increasing and/or decreasing linear speed profiles within the range from 20 rpm to 240 rpm. The tests consisted of exciting whirl with the impact hammer, and then traversing the speed range. Test durations were 30–90 s, which generated a sufficient number of data points in proximity to discrete rotor speeds for frequency analysis.

4 Simulation Model

Simulations were performed using XLTRC^2, a component mode, finite element program that uses tapered Timoshenko beam finite elements to generate a rotor and stator model [20]. The resulting dynamic system has both modal coordinates that enables the user to discard higher-frequency modes, and retain physical coordinates at nonlinear rotor-stator contact locations. Simulations were executed in a manner similar to experimental tests using a fixed-step Runge–Kutta method.

Table 2 First horizontal and vertical natural frequencies of the support and test pedestals

	Support pedestal	Test pedestal
Vertical direction	1620 Hz	1240 Hz
Horizontal direction	1000 Hz	615 Hz

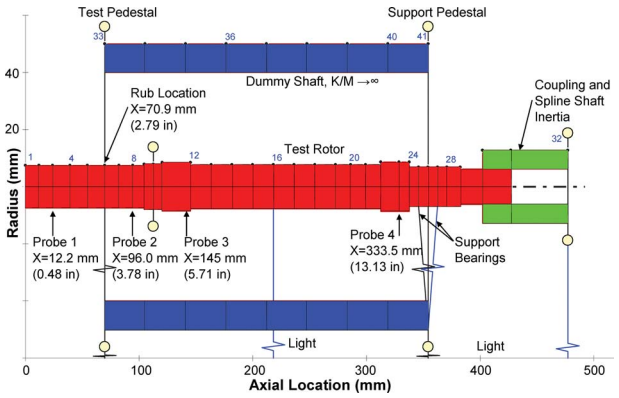

Fig. 8 XLTRC^2 simulation model for the TAMU whip and whirl rig

4.1 Structural Model. The simulation model shown in Fig. 8 consists of the test rotor that is connected to the test pedestal at station 6, and the support pedestal at stations 25 and 27.

The test pedestals were modeled using a dummy shaft, comprised of rigid massless elements to yield uncoupled point mass pedestals. Stiffness coefficients for each pedestal were determined using finite element analysis, and an assumed mode for the lowest horizontal and vertical natural frequencies was used to estimate an appropriate point mass for each pedestal. Light viscous damping was added to the model at both pedestals and stations 16 and 32 to prevent excessive vibration amplitudes in whip. Table 3 presents the resulting individual and combined natural frequencies and damping ratios. Neglecting damping, Table 3 suggests that the possible whirl ranges are 40.9–381.2 Hz, 429.6–565.7 Hz, and 606.5–786.0 Hz.

4.2 Nonlinear Connection. As suggested by Bartha [11,12], nonlinear interaction at the rub location was modeled using a modified form of the coefficient-of-restitution model of Hunt and Crossley [21]. The normal force was given by

$$N = k_{\mathrm{nl},1}\delta + k_{\mathrm{nl},2}\delta^2 + c_{\mathrm{nl}}\dot{\delta}\delta \tag{12}$$

where $k_{\mathrm{nl},1}$, $k_{\mathrm{nl},2}$, and c_{nl} are the nonlinear stiffness and damping coefficients, and δ represents the deflection of the rub surface. This yields a transverse contact force

$$F_F = \mu_d N \,\mathrm{sgn}(V_t) \tag{13}$$

The nonlinear stiffness coefficients were determined from the derivative of the Hertzian contact force with respect to penetration depth, and the damping coefficient was obtained by scaling the

Table 3 Individual and combined natural frequencies for the simulation model

Individual		Combined	
ω_n (Hz)	ζ (%)	ω_n (Hz)	ζ (%)
40.9	1.41	381.2	1.03
418.5	0.81	392.3	0.93
429.6	0.73	565.7	2.23
606.5	2.47	786.0	1.07
810.6	1.01	868.0	0.48
918.2	0.22	1142.3	2.45
1174.4	1.26	1164.1	1.40
1222.7	2.47	1612.7	2.01
1613.1	2.00	2264.5	1.42

Table 4 Nonlinear stiffness and damping coefficients used in simulations for a 660 Bronze bearing

Nonlinear stiffness $k_{nl,1}$ (N/m, lb/in)	Nonlinear stiffness $k_{nl,2}$ (N/m^2, lb/in^2)	Nonlinear damping c_{nl} ($N\,s/m^2$, $lb\,s/in^2$)	Friction Coefficient μ_d
$9.99\times10^8(5.71\times10^6)$	$7.10\times10^{13}(1.03\times10^{10})$	$1.65\times10^9(2.40\times10^5)$	0.3–0.4

experimentally determined parameters given by Bartha [11,12] to yield comparable contact damping. The parameters used in numerical simulations are given in Table 4.

5 Results

In this section, results for experimental whip and whirl motion will be presented, discussed, and compared to simulations. Test data will be presented first to illustrate the fundamental aspects of the whirl-whip motion, as well as some characteristics previously unseen in the literature. Unless noted otherwise, results are presented for test bearings composed of 660 Bronze. This will be followed by a review of the simulation results and the model's validity in simulating whip and whirl for the experimental apparatus.

5.1 Experimental Dry-Friction Whip and Whirl Characteristics. A representative dry-friction whip and whirl test case is shown in Figs. 9 and 10. Figure 9, illustrating the primary (backward) whirl frequency and amplitude recorded at the rub surface (probe 1), shows that the rig readily passed through several whip regions. The first three whip frequencies shown here are at 400 Hz, 630 Hz, and 708 Hz.

Figure 10 shows harmonic sidebands that accompany the main backward whirl/whip component. The forward component at one, times the main backward component ($-1\ \Omega$), could be caused by support orthotropy; multiples of the backward component could be caused by contact location nonlinearities or by partial rubbing [22]. Despite their cause, these sidebands may have a special impact on multimode dry-friction whip and whirl. Results show that when the rotor speed is ascending in a whip region, these harmonic sidebands often excite the next whirl range.

Figure 11 illustrates the most apparent difference between increasing and decreasing speed profiles, namely, the variability and extent of whirl regions excited with decreasing speed, in contrast to the abrupt jumps between whip regions seen with increasing speed.

These results raise the following questions. (1) Why does the system appear to excite two whip regions when traversing down but four on the way up? (2) If the first/lowest whip orbit is stable/attractive, why does increasing ω result in a jump to a higher whirl frequency, and what causes this jump? The former question is explained by the small gap between whirl ranges surrounding the pedestal natural frequency. Although whip is excited for both accelerating and decelerating cases, it is only apparent when the accelerating rotor locks into whip, and fails to jump to the admissible whirl orbit, having a slightly higher precession frequency. The first step towards answering the second question is to examine the nature of the harmonic sidebands present in the frequency spectrogram in Fig. 12. An additional set of sidebands is excited in the first whip region at 110 rpm. As the rotor approaches 137.5 rpm, the $11/2\ \Omega$ harmonic sideband begins to migrate towards the whirl solution, possibly due to increasing μ_d occurring with reduced surface velocity. At 142.5 rpm, the sideband reaches this whirl frequency, and begins to excite it. At 147.5 rpm, whirl is fully excited and predominant, and the whip frequency no longer exists.

Figure 13 shows the dominant whirl amplitude as a function of the rotor speed at all four probes. Although μ_d may be changing

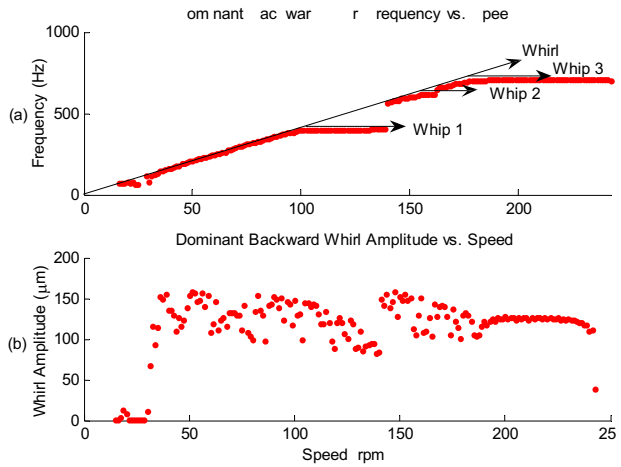

Fig. 9 Measured (*a*) frequency and (*b*) amplitude of the primary backward whirl component at probe 1 for a test case having $R/C_r=246$

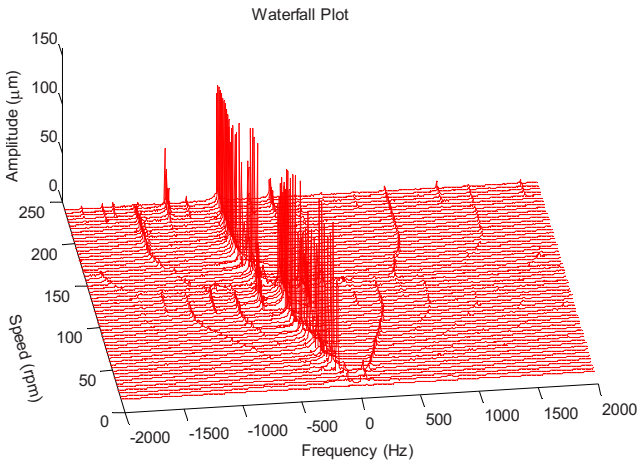

Fig. 10 Two-sided FFT of probe 1 measurements for a speed decreasing case of dry-friction whip and whirl, recorded during a test case having $R/C_r=246$

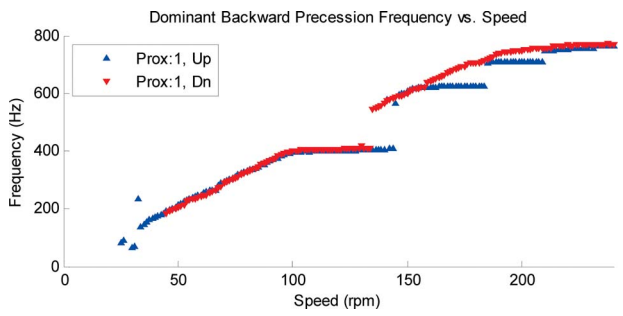

Fig. 11 Measured backward precession frequency versus rotor speed at probe 1 for a test case having $R/C_r=238$

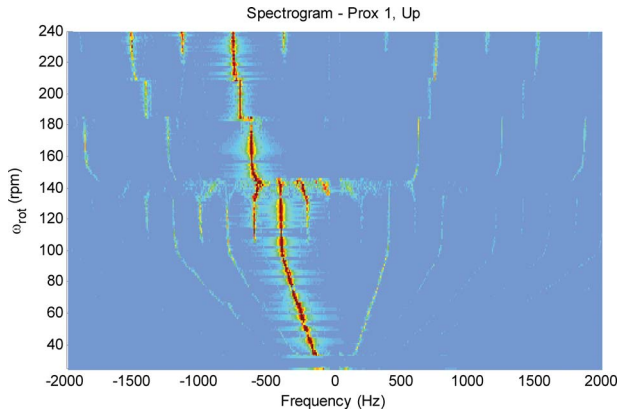

Fig. 12 Spectrogram for speed increasing whirl/whip for a test case having R/C_r=238, showing excitation of higher whirl modes by sideband harmonics

during tests, the whirl-orbit magnitude should not depend on the available friction coefficient. Why are the amplitudes changing so drastically?

The probe amplitudes relative to probe 1, illustrated in Fig. 14, show that the relative magnitudes of the probes do not vary in a given whirl region, and indicate that the primary mode in a given whirl range is dominant. How do the relative magnitudes recorded during whip compare to those predicted by the model's combined

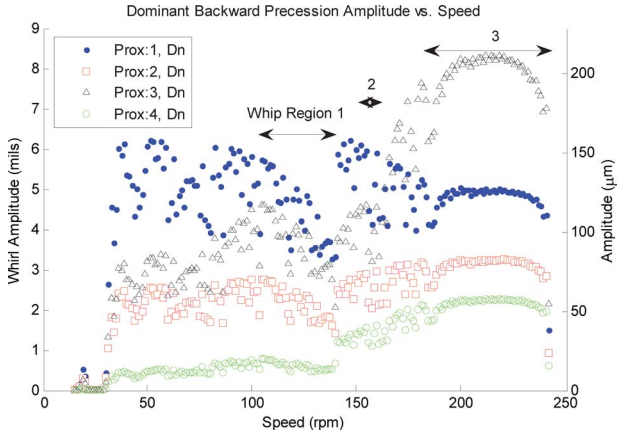

Fig. 13 Measured backward precession amplitude versus speed for a test case having R/C_r=246

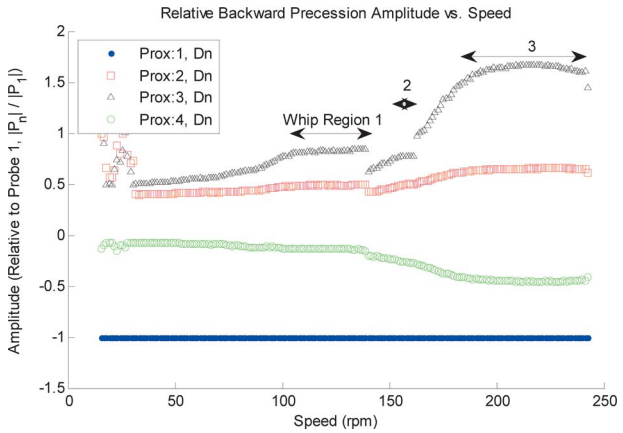

Fig. 14 Measured backward precession amplitude relative to probe 1 versus speed for a test case having R/C_r=246

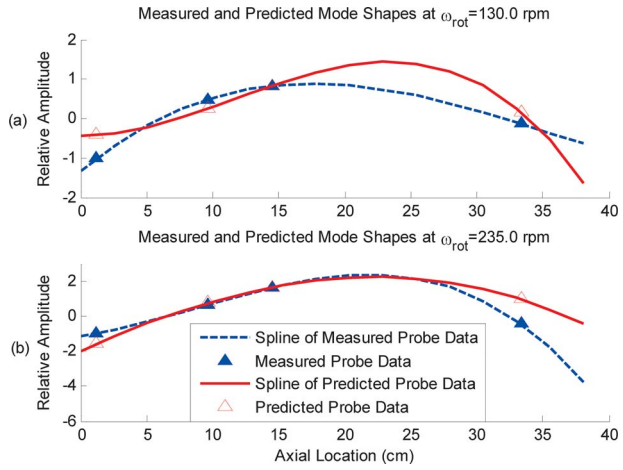

Fig. 15 Measured and predicted relative mode shapes at (*a*) 130 rpm and (*b*) 235 rpm for a test case having R/C_r=246

rotor-stator mode shapes? Figure 15 illustrates the measured and predicted modes in the first and third regions of whip shown in Fig. 14. The agreement between measured and predicted relative modes in the first whip region is weak; however, the third relative mode closely resembles test rig measurements. The model's comparatively weak prediction of the first mode might be attributed to the models lack of pitch and yaw mobility for the test pedestal. Because the rub surface is located at the edge of the test pedestal, large contact forces could induce angular deflections, and skew the measurements of probes 1 and 2.

Figure 16 shows the physical orbits captured by the probes and accelerometers for case 20 in the first and third whirl regions at Fig. 16(*a*) 50 rpm and Fig. 16(*c*) 165 rpm, and after transitioning to whip at Fig. 16(*b*) 100 rpm and Fig. 16(*d*) 210 rpm. At the time of this test, probe 2 in the *X* direction and accelerometer 1 in the *X* direction were not functioning properly, and accelerometer orbits were constructed by integration with respect to the fundamental whirl frequency. Steady repeated orbits in both whirl and whip are presented. In Fig. 16(*d*), probe 3 and accelerometer 2 show highly elliptical orbits with major axes in the horizontal direction (horizontal on the test rig at −45 deg). This may have prevented the rotor from transitioning to the higher-frequency whirl solution

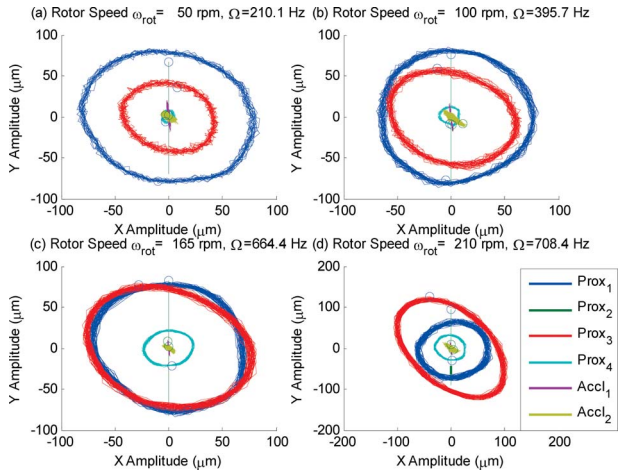

Fig. 16 Measured probe and accelerometer orbits in (*a*) the first whirl region, (*b*) the first whip region, (*c*) the third whirl region, and (*d*) the third whip region for a test case having R/C_r=246

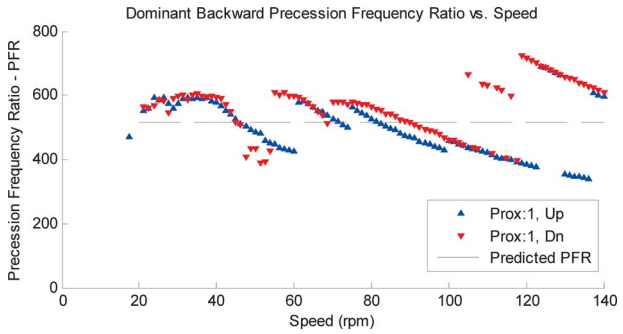

Fig. 17 Measured PFR versus rotor speed for 660 Bronze bearing with a measured R/C_r=517

at 760 Hz that was excited in the case shown in Fig. 11.

Figure 17 shows the measured PFR for a bearing, having a predicted PFR of 517, given by the radius-to-clearance ratio at the contact location; this prediction results from rotor and stator measurements accurate to ± 2.54 μm (0.1 mil) prior to testing. Though one might assume that the measured PFR would be lower than predicted due to deflections at the rub surface, Fig. 17 shows the predicted PFR is exceeded in this case by 15–20%.

In general, the relationship between the predicted and observed PFR becomes increasingly nonlinear with the radius-to-clearance ratio, resulting in a difference of only 7% for R/C_r=238. Is the nonlinearity of this parameter an effect of increased sensitivity and measurement error as clearance approaches zero, or is there some other explanation for this behavior? While the former is certainly true, Fig. 18 illustrates a test case for the Babbitt bearing, in which the measured PFR rapidly increases to more than twice the predicted value.

Although the reason for this unprecedented increase in observed PFR is unknown, deviations seen in other cases had more rational explanations. Test cases having large increases in bearing clearances due to material removal had a lower PFR towards the end of the case, while decreases in clearance due to thermal effects saw a higher PFR when descending. In some cases, clearance changes due to wear were as large as 25.4 μm (1 mil); this resulted in dry lubrication of the contact surfaces and ultimately diminished or prevented subsequent dry-friction whirl.

5.2 Simulation Validation. The first comparison between experimental and simulation data will be the dominant backward precession frequency versus the rotor speed. Figure 19 shows the predicted and measured primary backward whirl frequency for the rotor-stator contact having R/C_r of 385.

The difference between the measured and predicted precession frequency is evident, with slightly higher precession frequencies for the test case. Even though this difference affects whirl frequencies, the predicted and measured transition-to-whip frequencies are very close, deviating only at frequencies above 800 Hz. The simulation model does not produce the second whirl/whip region, despite the observation of this mode in test data. This whirl region is located from 429.6 Hz to 565.7 Hz, and lies between the first and second bending modes of the rotor. This mode is characterized by large deflections at the pedestals, which were lightly damped in the model to ensure that motion was within reasonable limits. The increased damping of this vibration mode could explain the absence of this whirl region in simulations.

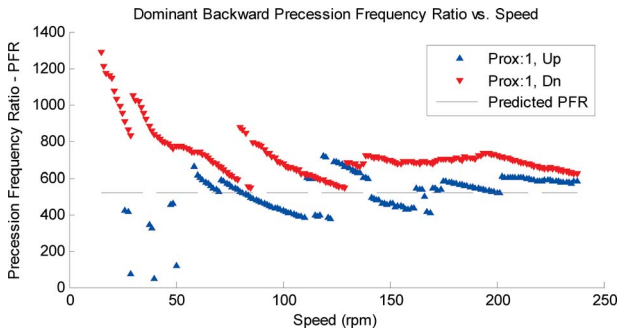

Fig. 18 Measured PFR versus rotor speed for Babbitt bearing with R/C_r=517

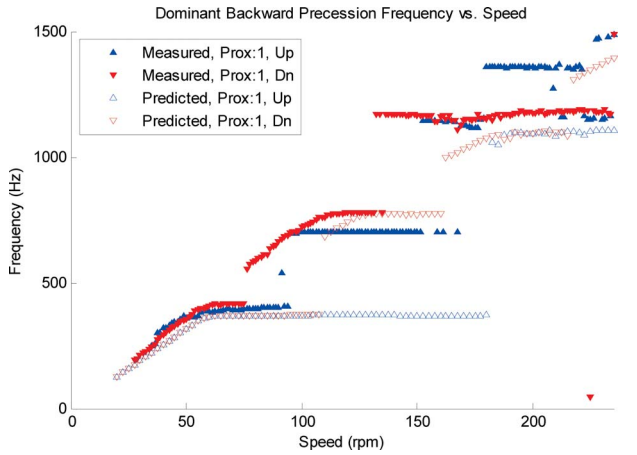

Fig. 19 Comparison of measured and predicted backward precession frequencies for a 660 Bronze bearing having R/C_r =385

Figure 19 shows a predicted vibration waterfall plot from simulation 2. As compared to experiments, the simulation frequency spectra predicts harmonic sidebands during whip, but not during whirl. In addition, the sidebands seem to be drastically different during higher-frequency whip regions than observed in experiments. Overall, the spectra show a good resemblance to their experimental counterpart.

Figure 21 shows simulated probe amplitudes for the bearing used in the test case presented in Fig. 13. In comparison to measured amplitudes given in Fig. 13, predicted amplitudes are slightly larger but less erratic.

6 Summary and Conclusions

The present paper looks at characteristics unique to the phenomena of multimode dry-friction whip and whirl, and the ability of modern simulation tools to accurately model them. This section will reiterate accomplishments of the research, and recommend focal points for future investigations.

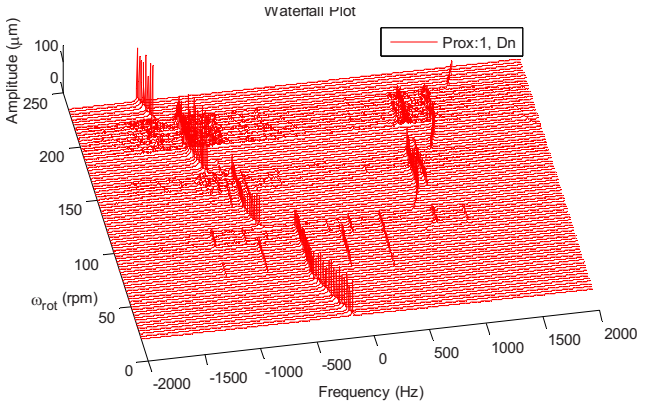

Fig. 20 Frequency spectra for simulation of 660 Bronze bearing having R/C_r=385 at probe 1

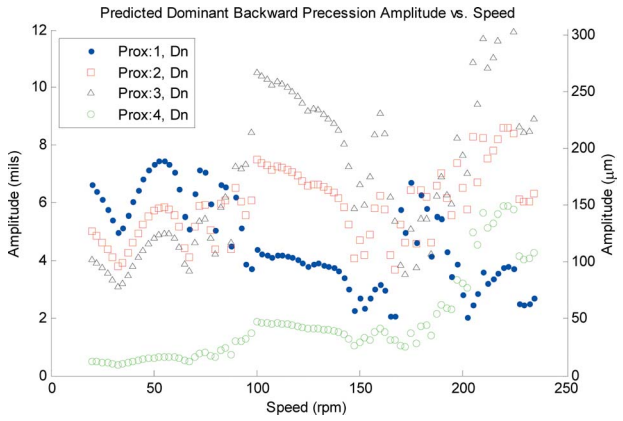

Fig. 21 Predicted backward precession amplitude versus speed for a 660 Bronze bearing having $R/C_r=385$

6.1 Experimental Achievements. A dry-friction whip and whirl test rig was designed and constructed that accurately demonstrated and recorded the nature of multimode dry-friction whip and whirl. The design of the test rig enabled the testing of several rub surfaces to examine the effect of the bearing material and clearances.

6.2 Multimode Dry-Friction Whip and Whirl. Analysis of experimental data provided by the test rig confirms that dry-friction motion falls into the following regions.

- Dry-friction whirl in which the precession frequency ratio is roughly proportional to the radius-to-clearance ratio at the contact location.
- Dry-friction whip in which the rotor precesses at a frequency close to a combined natural frequency of the connected rotor and stator system.

These regions were not solely defined by the rotor speed due to the existence of multiple attractive orbits at a given rotor speed. The rotor speed can increase and decrease through regions characterized by whip, terminating with jumps to different whirl/whip frequencies. These frequencies are usually close to the predicted whirl frequency, which corresponds to a rolling-without-slipping condition at the contact location. Dry-friction whip and whirl testing on different bearing configurations resulted in a variety of precession frequency ratios and whirl ranges; however, the frequencies at which the shaft whipped were constant for all test cases.

Sidebands were seen in the frequency spectrum provided by probe data, and are suspected to result from structural asymmetry of the test pedestals in combination with the nonlinear properties of the rub location. These harmonics became more prevalent in whip, and often played a role in exciting higher whirl frequencies.

The measured PFR for most test cases was significantly greater than that predicted by the radius-to-clearance ratio at the contact location. For the Babbitt bearing, several instances occurred in which the measured PFR rapidly increased to more than double of that predicted by the radius-to-clearance ratio.

6.3 The Validity of the Simulation Model. To produce accurate whip and whirl characteristics, the simulation model requires an accurate structural-dynamics model and a valid contact model. Simulations accurately predicted the first few fundamental modes of the test rig, resulting in quite accurate whip and whirl region predictions through the second rotor mode at 800 Hz. Although there were deviations between predicted and observed motions, improvements would require the development of a more sophisticated structural model of the housing and pedestals. Amplitudes on the test rig were slightly smaller than those in simulations, possibly due to simplifications in the structural model. A nonlinear Hunt and Crossley contact model with Coulomb friction adequately approximates the rotor-stator contact. The simulations closely tracked the whirl frequency, as predicted by the radius-to-clearance ratio at the contact location, deviating only slightly when approaching whip.

Why did Childs and Bhattacharya fail to produce higher whirl ranges using a contact model similar to the one described here? The difference between results may correspond to the method of inducing rotor-stator contact. In simulations presented here, contact was induced by exciting the rotor with a radial impulse force; whereas, Childs and Bhattacharya employed initial conditions arising from the steady-state whirl solution.

6.4 Future Work. Necessary improvements to the rub model include modeling damping due to rolling friction, and the effect of thermal changes and wear on clearance and friction coefficient. These efforts may produce a more accurate prediction of whip and whirl frequency spectrums, but changes in predicted whirl ranges are unlikely.

Acknowledgement

I would like to thank Northrop Grumman Space Technology, Redondo Beach, CA and Air Force Research Laboratory, Propulsion Directorate, Edwards Air Force Base, CA for the opportunity to partake in what will hopefully become the technology, and inspiration, for future generations. Special recognition is extended to Chuck Papesh, Gordon Dressler, and Alan Sutton for helpful suggestions. This research was performed with AFRL/RZS under Grant No. FA9300-04-C-0016, and can be reviewed in greater detail in Ref. [23].

Nomenclature

C_r = radial clearance at the rub surface (m, in)
F_F = friction force at contact location (N, lb)
FFT = fast-Fourier transform
N = normal force at the contact location (N, lb)
NGST = Northrop Grumman Space Technology
$\mathbf{P}$ = complex contact force (N, lb)
R = rotor radius at the contact location (m, in)
V_t = relative tangential surface velocity at contact (m/s, in/s)
$\mathbf{Z_r}$, $\mathbf{Z_s}$ = complex rotor and stator displacements (m, in)
a = rotor mass imbalance (m, in)
c_{nl} = nonlinear contact damping (N s/m^2, lb s/in^2)
c_r, c_s = rotor and stator damping coefficients (N s/m, lb s/in)
e = shorthand for exponential function $e^{\ln(x)}=x$
j = imaginary unit $j=\sqrt{-1}$
$k_{\mathrm{nl},1}$, = nonlinear contact stiffness (N/m, N/m^2)
$k_{\mathrm{nl},2}$ = (lb/in, lb/in^2)
k_r, k_s = rotor and stator stiffness (lb/in, N/m)
m_r, m_s = rotor and stator mass (kg, lb s^2/in)
t = time (s)
x_r, x_s = rotor and stator displacements along the x-axis (m, in)
y_r, y_s = rotor and stator displacements along the y-axis (m, in)
$\mathbf{z_r}$, $\mathbf{z_s}$ = complex rotor and stator solutions satisfying (m, in); ICs at $t=0$
$\boldsymbol{\alpha_{11}}$, $\boldsymbol{\beta_{11}}$ = complex rotor and stator receptances (m/N, in/lb) $\alpha_{11}(-\Omega)=1/k_r-m_r\Omega^2-jc_r\Omega$
$\delta, \dot{\delta}$ = normal contact displacement and velocity (m, m/s, in, in/s)
γ = angle between clearance vector x-axis (rad)
γ_o = angle between imbalance vector and clearance (rad)

Vector

μ = friction coefficient which satisfies whirl
μ_d = dynamic Coulomb friction coefficient
Ω = rotor precession frequency (rad/s)
ω = rotor speed (rad/s)
$\omega_{n,\text{comb}}$ = combined natural frequency of the rotor-stator (rad/s)

System

ϕ = traction angle at contact location $\phi=\sin^{-1}(\mu)$ (rad)
ξ = angle between clearance and imbalance vector (rad)

References

[1] Rosenblum, V. I., 1995, "Entstehung mehrfacher Wellenbrüche nach dem Bruch einer Laufschaufel oder Radscheibe bei Dampfturbinen," Allianz Report, **68**(5), pp. 176–179.
[2] Johnson, D. C., 1962, "Synchronous Whirl of a Vertical Shaft Having Clearance in One Bearing," J. Mech. Eng. Sci., **4**(1), pp. 85–93.
[3] Billett, R. A., 1965, "Shaft Whirl Induced by Dry Friction," The Engineer, **29**, pp. 713–714.
[4] Black, H. F., 1967, "Synchronous Whirling of a Shaft Within a Radially Flexible Annulus Having Small Radial Clearance," Proc. Inst. Mech. Eng., **181**(4), pp. 65–73.
[5] Black, H. F., 1968, "Interaction of a Whirling Rotor With a Vibrating Stator Across a Clearance Annulus," J. Mech. Eng. Sci., **10**(1), pp. 1–12.
[6] Zhang, W., 1988, "Dynamic Instability of Multi-Degree-of-Freedom Flexible Rotor Systems Due to Full Annular Rub," Proc. Inst. Mech. Eng., IMechE Conf., **C252**(88), pp. 305–308.
[7] Lingener, A., 1990, "Experimental Investigation of Reverse Whirl of a Flexible Rotor," *Proceedings of the 3rd IFToMM International Conference on Rotordynamics*, Lyon, France, pp. 13–18.
[8] Crandall, S., 1990, "From Whirl to Whip in Rotordynamics," *Proceedings of the 3rd IFToMM International Conference on Rotordynamics*, Lyon, France, pp. 19–26.
[9] Choi, Y. S., 2002, "Investigation on the Whirling Motion of Full Annular Rub," J. Sound Vib., **258**(1), pp. 191–198.
[10] Dyck, B. J., 2007, "Experimental Study of Dry-Friction Whirl and Whip for a Rotor Supported by and Annular Rub Surface," NGST Project Report.
[11] Bartha, A. R., 1998, "Dry Friction Induced Backward Whirl: Theory and Experiment," *Proceedings of the Fifth IFToMM Conference on Rotor Dynamics*, Vieweg Publishers, Braunschweig, Germany, pp. 756–767.
[12] Bartha, A. R., 2000, "Dry Friction Backward Whirl of Rotors," Dissertation ETH Paper No. 13817, ETH Zurich.
[13] Yu, J. J., Goldman, P., and Bently, D., 2000, "Rotor/Seal Experimental and Analytical Study of Full Annular Rub," ASME Paper No. 2000-GT-389.
[14] Childs, D. W., and Bhattacharya, A., 2007, "Prediction of Dry-Friction Whirl and Whip Between a Rotor and a Stator," ASME J. Vibr. Acoust., **129**, pp. 355–362.
[15] Grabowski, R., Chapman, L., Crease, G., Friant, J., Gualtieri, G., Kmiec, T., Kincaid, K., and Rodriguez, J., 2000, "Testing of an Advanced Liquid Hydrogen Turbopump," Paper No. AIAA-2000-3678.
[16] Childs, D. W., 2004, private correspondence.
[17] Den Hartog, J. P., 1956, *Mechanical Vibrations*, 4th ed., McGraw-Hill, New York.
[18] Lu, X., and Khonsari, M. M., 2007, "An Experimental Study of Grease-Lubricated Journal Bearings Undergoing Oscillatory Motion," Trans. ASME, J. Tribol., **129**(3), pp. 640–646.
[19] Bijak-Zochowski, M., and Marek, P., 1997, "Residual Stress in Some Elasto-Plastic Problems of Rolling Contact With Friction," Int. J. Mech. Sci., **39**(1), pp. 15–32.
[20] Nelson, H. D., 1980, "A Finite Rotating Shaft Element Using Timoshenko Beam Theory," ASME J. Mech. Des., **102**(4), pp. 793–803.
[21] Hunt, K. H., and Crossley, F. R., 1975, "Coefficient of Restitution Interpreted as Damping in Vibroimpact," ASME J. Appl. Mech., **42**, pp. 440–445.
[22] Beatty, R. F., 1985, "Differentiating Rotor Response Due to Radial Rubbing," ASME J. Vib., Acoust., Stress, Reliab. Des., **107**, pp. 151–160.
[23] Wilkes, J. C., 2008, "A Perspective on the Numerical and Experimental Characteristics of Multi-Mode Dry-Friction Whip and Whirl," M.S. thesis, Texas A&M University, College Station, TX.

Forced Response of Mistuned Bladed Disks in Gas Flow: A Comparative Study of Predictions and Full-Scale Experimental Results

Evgeny Petrov
e-mail: y.petrov@imperial.ac.uk

Luca Di Mare
e-mail: l.di.mare@imperial.ac.uk

Department of Mechanical Engineering,
Imperial College London,
Exhibition Road, SW7 2AZ, UK

Holger Hennings
German Aerospace Center,
Institute of Aeroelasticity,
Bunsenstrasse 10, Göttingen, Germany
e-mail: holger.hennings@dlr.de

Robert Elliott
Rolls-Royce plc,
P.O. Box 31 Derby,
DE24 8BJ, UK
e-mail: robert.elliott@rolls-royce.com

An integrated experimental-numerical study of forced response for a mistuned bladed disk has been performed. A full chain for the predictive forced response analysis has been developed including data exchange between the computational fluid dynamics code and a code for the prediction of the nonlinear forced response for a bladed disk. The experimental measurements are performed at a full-scale single stage test rig with excitation by aerodynamic forces from gas flow. The numerical modeling approaches and the test rig setup are discussed. Comparison of experimentally measured and predicted values of blade resonance frequencies and response levels for a mistuned bladed disk without dampers is performed. A good correspondence between frequencies at which individual blades have maximum response levels is achieved. The effects of structural damping and underplatform damper parameters on amplitudes and resonance frequencies of the bladed disk are explored. It is shown that the underplatform damper significantly reduces scatters in values of the individual blade frequencies and maximum forced response levels. [DOI: 10.1115/1.3205031]

1 Introduction

The key components necessary for a predictive forced response analysis of mistuned bladed disks can be identified as (i) determination of the aerodynamic excitation forces and the characteristics of aerodynamic damping and coupling; (ii) accurate modeling and description of the mechanical properties of a bladed disk including blade mistuning; (iii) modeling of friction contacts in bladed disk assemblies (if such contacts are present and significant); and (iv) an efficient method using high-fidelity aerodynamic and structural models and allowing the performance of such calculations for a mistuned bladed disk in practical design timescales.

Measurements of excitation forces for cases of subsonic gas flow were carried out in Refs. [1,2]. The excitation in transonic turbines was studied in Refs. [3,4] and the mechanical and the aerodynamic damping in bladed disks were experimentally investigated in Ref. [5] on a test rig with one-stage rotor containing actual engine vanes and rotor blades. A comparison between computational fluid dynamics (CFD) predictions and measured nozzle guide vane (NGV) outlet flow field for this rig was performed in Ref. [6] using three different methods although no attempt was made to evaluate the corresponding blade vibration amplitudes.

In Ref. [7], the experimental verification of predictions for the aerodynamic forces, damping, and stresses for blades without mistuning is performed. The results of measurements and predictions of gas flow and structural vibrations for a compressor blisk excited by strut wakes are discussed in Ref. [8]. A small number of blades were instrumented here, which restricts the use of experiments for mistuning prediction validation. Experimental validation of the technique for identification of blade mistuning in blisks was performed in Ref. [9] using a rotating test rig with structural vibrations excited by an array of permanent magnets. A measurement system developed for tests on industrial gas-turbine high-pressure buckets is described in Ref. [10]. Assessment of the accuracy of experimental predictions for structures with friction interfaces is usually performed in test rigs (e.g., Refs. [11,12]). Methods for analysis of structural vibrations of mistuned bladed based on different approaches for reduction in mistuned bladed disk models were developed in Refs. [13–17].

Recently developed methods for the forced response analysis of mistuned bladed disks including aerodynamic and friction contact effects [18,19] and methods for the analysis of bladed disk aerodynamic forces and damping [20–23] provide sophisticated capabilities for predictive studies. Although these methods were validated by some representative test cases [24–27], the validation was performed for the structural and computational fluid mechanics solvers separately.

The goal of the studies reported in this paper was to explore the state-of-the-art predictive capabilities for a whole chain of the predictive tools from a CFD analysis code to a structural vibration analysis code. These capabilities are applied to an analysis of a mistuned bladed disk with aerodynamic excitation, which is due to struts, NGV wakes, and predefined variation in the vane geometry and then compared with experimental results obtained on a rotating test rig. All blades of the bladed disk were strain-gauged in order to compare with the predictions for the mistuning assembly. Such integrated analysis of forced response combined with the experimental validation has not been reported for mistuned bladed disks in literature.

An experimental investigation was conducted at DLR using a single high-pressure turbine stage test rig [28]. The turbine stage was designed and manufactured for the European research project Aeroelastic Design of Turbine Blades (ADTurB) [29,30]. In the experiments, gas flow characteristics and bladed disk vibration levels are measured. The gas flow pressure and velocity provide data for CFD analysis and strain gauge measurements are used for the comparison of measured and predicted amplitude values.

The aerodynamic excitation forces and aerodynamic damping

Contributed by the International Gas Turbine Institute of ASME for publication in the JOURNAL OF ENGINEERING FOR GAS TURBINES AND POWER. Manuscript received April 8, 2009; Final manuscript received April 15, 2009; published online March 5, 2010. Review conducted by: Dilip R. Ballal. Paper presented at the ASME Gas Turbine Technical Congress and Exposition, June 8–12, 2009, Orlando, FL.

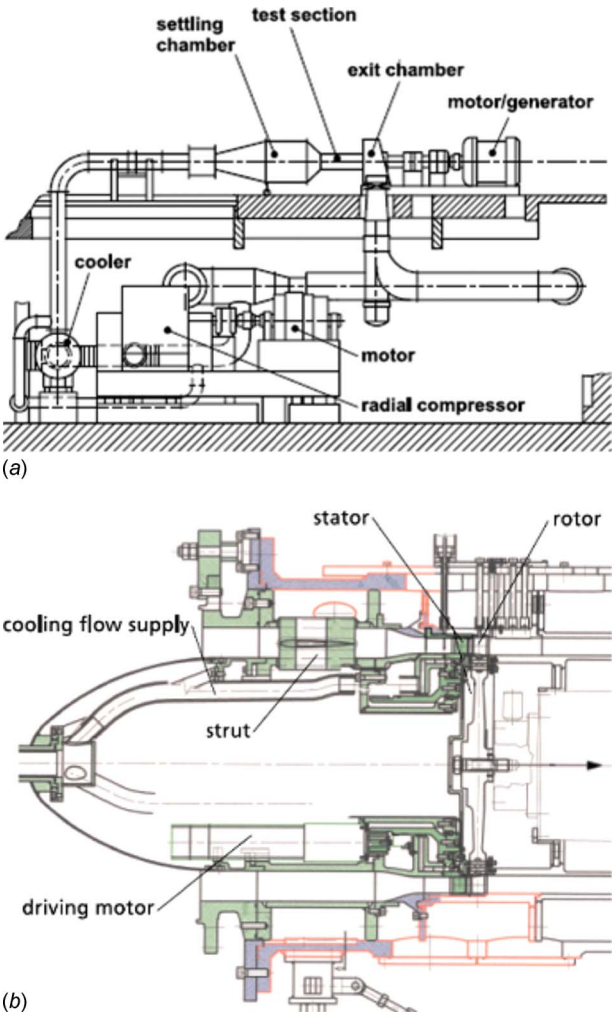

Fig. 1 RGG wind tunnel at DLR: (*a*) a general view and (*b*) a configuration of a stage analyzed

factors are determined using aerodynamic parameters of gas flow at the test rig intake. The predicted values are then used in the forced response predictions for a mistuned bladed disk. The large-scale finite element structural model of the mistuned bladed disk is used in the analysis, which is performed by a high-fidelity method allowing the inclusion of aerodynamic damping, coupling, and excitation determined as a result of CFD analysis. Predictive analysis for the bladed disk with and without underplatform dampers (UPD) is performed. The analysis of the effects on the forced response of contact interface parameters, excitation levels, the spectrum of the multiharmonic excitation, structural damping, and completeness of the aerodynamic data have been explored. The correspondence between numerical results and the experimental data obtained from forced response measurements is established for a bladed disk without dampers.

2 Experimental Measurements

2.1 Test Facility. The facility used for the measurements is the wind tunnel for rotating cascades (RGG) operated by the Institute of Propulsion Technology of DLR, Göttingen, Germany. The RGG (see Fig. 1(*a*)) is a closed circuit wind tunnel that allows continuous running. It is driven by a four-stage radial compressor with a variable speed allowing a constant flow rate of up to 15.5 m^3/s and a maximum pressure ratio of 6. Mach and Reynolds number can be varied independently within a certain range.

The turbine stage studied (Fig. 1(*b*)) here includes an NGV set, which comprises 43 vanes and a high-pressure turbine bladed disk mounted on a rotor. The low engine order (EO) excitation was intentionally introduced in the test rig by 2% and 4% variation in vane geometry. The amplitudes of NGV throat area variations chosen should be regarded as typical values for a newly built gas-turbine engine under ordinary operation. To produce 5EO and 7EO excitation two NGV sets were manufactured with five and seven sinusoidal waves of the vane throat variation along NGV annulus. The rotor is driven by an electric motor/generator with a maximum power of 500 kW. Rotation speeds between 0 rpm and 10,000 rpm can be achieved and the stage aerodynamics conditions can be chosen independently from the rotation speed.

2.2 Instrumentation. Figure 2(*a*) gives a view of the rotor outside the rig. The rotating bladed disk was instrumented by strain gauges located at a blade tang (see Fig. 2(*b*)). In addition the rotor has a limited number of pressure transducers to measure the unsteady pressures on the blades. The total number of blades in the bladed disk is 64. The instrumentation was as follows: 57 blades with one strain gauge, three blades with three strain gauges, and four blades with one strain gauge and 18 pressure transducers overall. Several strain gauges failed after the experiments had been started and, hence, measurements could not be obtained for seven blades for the whole program of the experiments.

The strain gauges make use of the piezo-resistance effect. The pressure transducers have been designed with the membrane directly embedded in the surface of the blades. The resonant frequency of the pressure transducer is 500 kHz.

The calibration coefficients are used to determine displacements at the blade tip from the strain gauge measurements.

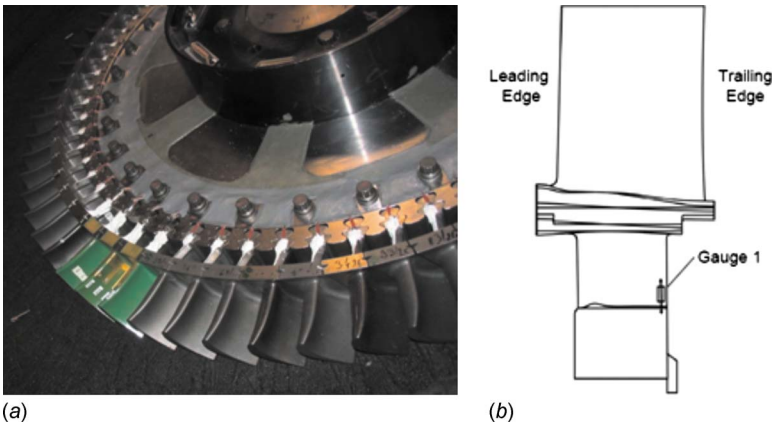

Fig. 2 Rotor outside of the rig (*a*) and strain gauge location (*b*)

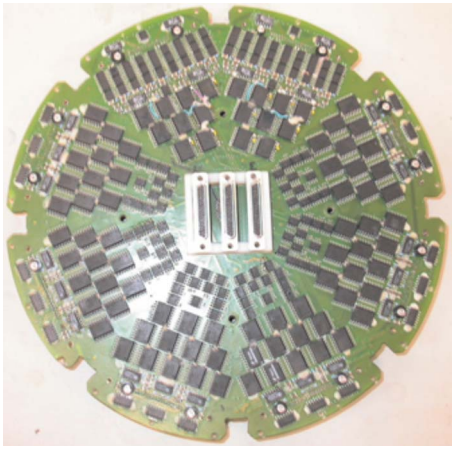

Fig. 3 The electronic board of the data acquisition system

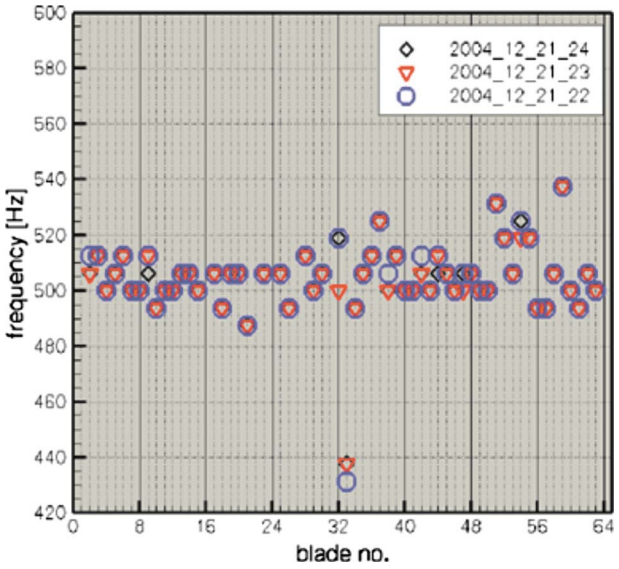

Fig. 5 Repeatability of the measurements for blade resonance frequencies

2.3 Measurement Chain and Data Acquisition. The data transmission system used to transfer signals from the rotating to the stationary system is a 100 channel high precision slip ring system together with pre-amplifying electronics in the rotating system.

The main advantage of such a slip ring system is to have the signals available at the same time. The disadvantage of slip ring systems is usually a significant noise level. To compensate for this, a pre-amplifying electronic board was designed, manufactured, and mounted directly on the rotor. Figure 3 shows the electronics board separately.

In the stationary frame the signals were digitized by a data acquisition system that allows a maximum sampling frequency of 196 kHz.

2.4 Measurement Results. The results obtained from the measurement are derived in the way documented in Ref. [28]. Some of these results are shown in Figs. 4–6. The Campbell diagram determined from measurements is plotted in Fig. 4 and results illustrating the repeatability of blade resonance frequency and amplitude measurements in three sequential tests are shown in Figs. 5 and 6.

3 CFD Analysis

3.1 Method. The computations are based on a finite volume compressible flow solver. The flow modeling is based on the 3D Favre-averaged Navier–Stokes equations. Unsteady cases are computed using unsteady Reynolds-averaged Navier–Stokes (RANS) equations with the basic assumption that the frequencies of interest are far removed from the frequencies of turbulent flow structures. The flow variables are represented on the nodes of a generic unstructured grid and numerical fluxes are computed along the edges of the grid. The numerical fluxes are evaluated using Roe's flux vector difference splitting coupled to Jameson's pressure switch to prevent the appearance of spurious oscillations in the solution.

The solution method is implicit, with second order accuracy in space and time. For steady-state gas flow computations the solution is advanced in pseudotime using local time stepping while for unsteady computation dual time stepping is used to preserve

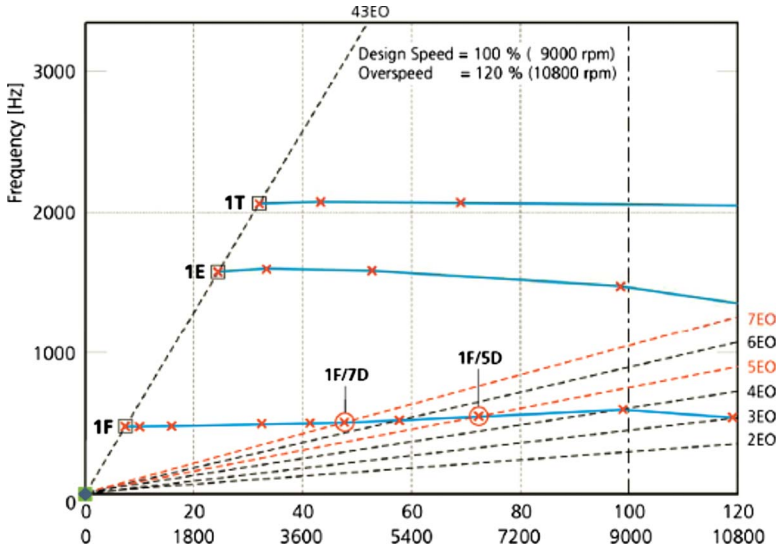

Fig. 4 Experimentally determined Campbell diagram

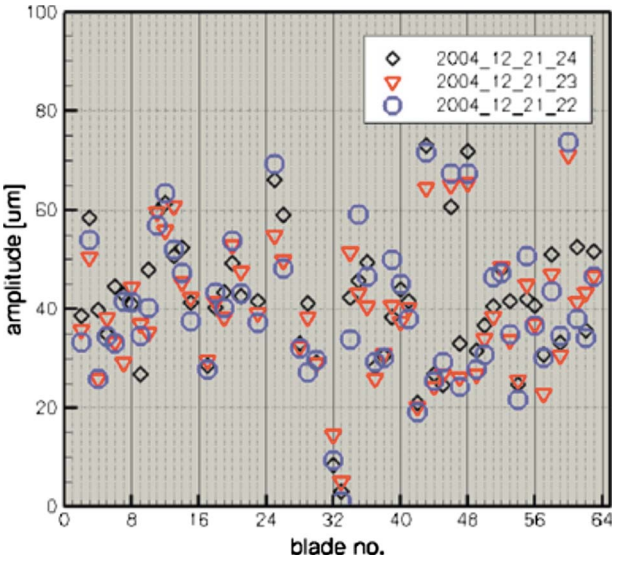

Fig. 6 Repeatability of the measurements for blade maximum amplitudes

stability at high Courant numbers. The method is described in detail in Refs. [20,27].

The grids used for this study are semistructured, following the procedure described in Ref. [21], with hexahedral elements around the aerofoil in the boundary layer region and prismatic elements in the passage. The radial grid distribution is stretched toward hub and casing to allow representation of the end-wall boundary layers.

For the present study, numerical solutions for steady gas flow have been obtained for a domain including three blade rows in the rig: struts, NGV, and rotor. The boundary conditions applied are measured total temperature, pressure and flow angles at the strut inlet and static pressure at the rotor outlet. Each blade row is represented for steady-state analysis by a single passage with mixing planes used to model the interblade row boundaries.

Two separate sets of aerodynamic unsteady computations have been performed for each condition studied: (i) a computation that includes the NGV and rotor blade row and (ii) a computation including the rotor only.

The computations in the first set are used to provide modal forces for the forced response analysis. In this set, the whole strut outlet flow field is used as an NGV inlet boundary condition with a sliding plane connecting the NGV and rotor domains. The sources of unsteady forcing on the rotor blades modeled are strut wakes providing 4EO component of the excitation, throat area variations (5EO and 7EO), and NGV wakes (43EO). Modal forces required for the forced response analysis are obtained by integrating the pressure field computed over the blade surface at each time step. The time histories of the modal force variation are collected and then fast Fourier transform (FFT) analysis is performed to extract amplitudes of the engine order excitation [20,22,27].

The modal forces and modal damping have been calculated for two rotation speeds: 4210 rpm and 6320 rpm, i.e., at rotations speeds corresponding to experimentally observed resonance regimes with 7EO and 5EO, respectively.

The computations in the second set are used to provide aerodamping estimates. In these computations, the mass-averaged NGV outlet profiles are imposed as boundary conditions at rotor inlet. For aerodynamic damping computations, the modal forces evaluated at each time step are used to determine the magnitudes of modal displacements and velocities. The initial conditions for motion of the structure are set by specifying the modal velocity for each structural mode considered. The values of the modal velocity are selected to be small enough to satisfy the mesh integrity requirement and large enough to overcome round-off error in the computations. In the present computations, the initial velocity chosen corresponds to a maximum physical displacement on the blade surface of 80 μm. For each aerodamping computation, all the nodal diameters of each family are included so that the dependence of aerodamping from nodal diameter can also be assessed. The modal displacements are used to update the position of the grid points on the blade surface and, then, via a spring-analogy mesh motion algorithm, in the rest of the computational domain. The final computation of the damping factor is performed fitting an exponential function to the envelope of the time history of modal displacements. The details of the damping evaluation procedure are explained in Ref. [23].

3.2 Grid Convergence Study and Comparison With Measured Wakes. A grid convergence study has been performed on all three blade rows. Particular attention has been devoted to the grid independence of the solution on the NGV.

For the purpose of the grid convergence study, the grid resolution is parameterized in terms of a number of points along blade chord for each radial section and a number of layers (in a direction normal to the blade surface) in the boundary layer grid.

A preliminary study has shown that the static pressure distribution around the NGV is not affected by grid resolution if more than 80 points clustering near trailing edge are used along the aerofoil chord. Therefore, in the present study, the calculations have been performed with 120 points along NGV chord and matching resolution in the blade-to blade direction away from the blade.

The resolution for the boundary layer and wake has been determined comparing solutions obtained with 14, 18, 22, and 26 layers in the *O*-grid and grid spacing in the wake matching the wall-normal grid spacing at the *O*-mesh edge. The grids chosen have yielded wall distances between 5 and 15 and it has been found that no appreciable change in the boundary layer profiles can be seen in the boundary layer and wake profiles computed with the two finest grids. Hence, all computations have been performed with 22 layers in the *O*-mesh and as expansion ratio of 1.2. NGV suction side boundary layer profiles from four grids are compared at four stations along chord in Fig. 7.

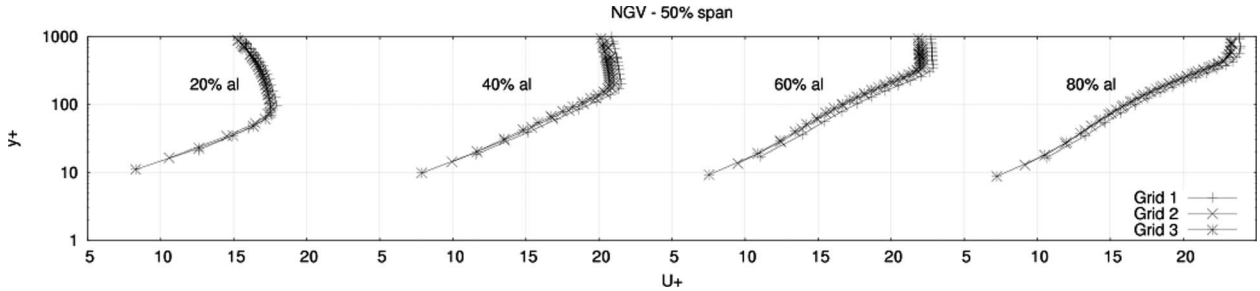

Fig. 7 NGV suction side boundary layer profiles from grid convergence study

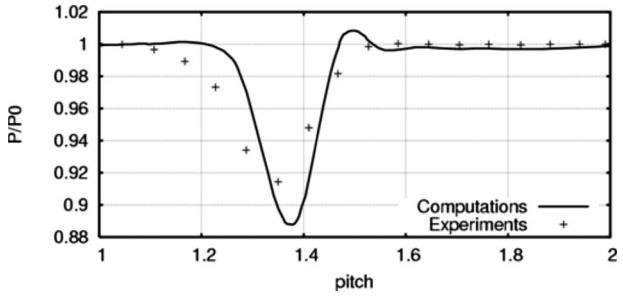

Fig. 8 Comparison of computed and measured NGV wakes at 50% span

Studying both NGV blade loading and wake amplitudes at 128% of NGV axial chord for the datum (no throat area variation) case it has been found that good match can be obtained with measured data at 50% span (see Fig. 8) although the agreement deteriorates at 90% span (see Fig. 9).

In order to explain this behavior a separate study has been conducted to assess the effect of the 100 μm gap between the NGV sitting at the top center position in the assembly and the casing. This clearance is due to the presence of an optically flat window for laser measurements. When the clearance is included in the computational model a far better agreement is found between measured data and computed data in terms of wake position and strength (Fig. 9). As this window is blanked during rotor vibration measurements, no tip clearance is introduced in the rotor-stator interaction computations

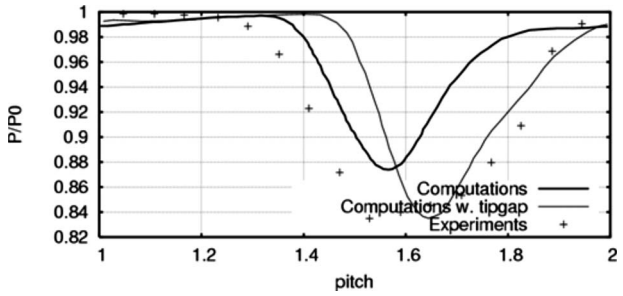

Fig. 9 Comparison of computed and measured NGV wakes at 90% span: computed values showing an effect of 0.1 mm gap for L2F optical window

The grid resolution requirement for the rotor and the strut has been determined in a similar fashion to the NGV study. However, in view of the need to perform rotor-stator interaction computations, the blade-to-blade resolution in the rotor domain needs to match to the wake resolution in the NGV domain, the requirement of correctly representing the NGV wakes being more stringent than the basic steady flow requirement for the rotor itself.

The grid sizes determined from the grid convergence study are 0.9 M points for each NGV passage and 0.4 M points for each rotor passage.

4 Mistuned Forced Response Analysis

4.1 Analysis Method. For the analysis of forced response of the mistuned bladed disk a method developed in Refs. [17–19] is applied. The method is based on: (i) an exact relationship between the responses of tuned and mistuned assemblies derived from Ref. [17], (ii) an approach allowing accurate description of aerodynamic coupling and damping developed in Ref. [18], and (iii) a method for the analysis of nonlinear vibration of mistuned bladed disk with friction dampers presented in Ref. [19].

The analysis allows the use of a large-scale detailed FE model for a mistuned bladed disk. A single industrial-size sector FE model is applied to obtain natural frequencies and mode shapes of a tuned bladed disk and then to generate a forced response function (FRF) matrix for a whole bladed disk. Mistuning due to blade frequency scatter and friction contact interface scatters is modeled by modification and friction contact elements. The FRF matrix can include the full effects of aerocoupling, aerodamping, and bladed disk stiffening effects due to gas flow.

The method is applicable to cases of high mechanical coupling of blade vibration through a flexible disk and, possibly shrouds, and to cases with stiff disks and low mechanical coupling. The

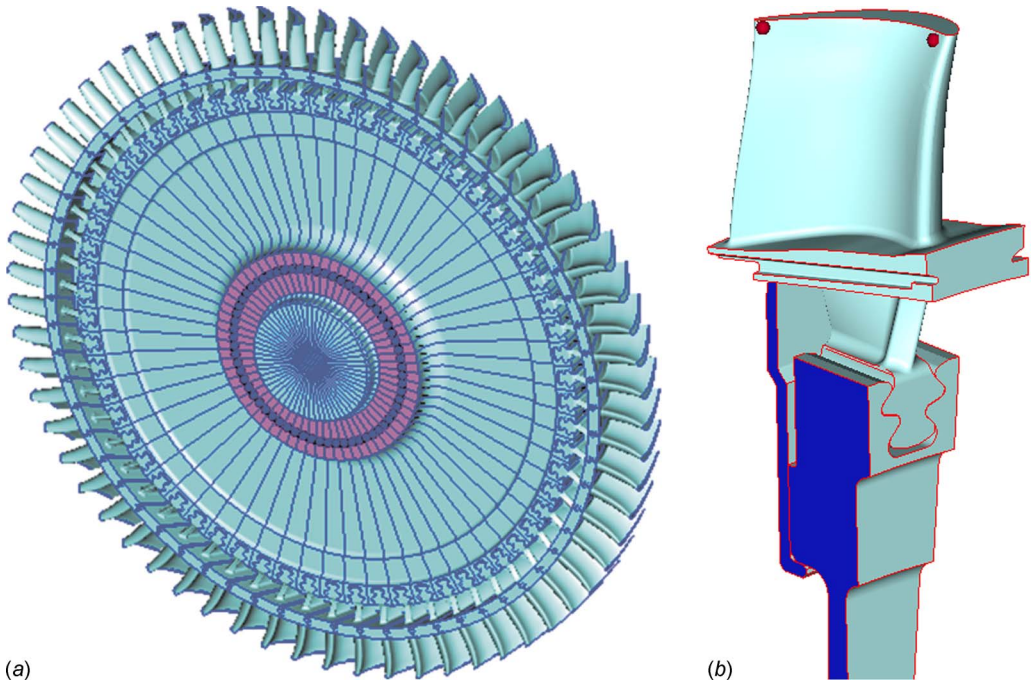

Fig. 10 General view of the whole mistuned assembly (*a*) and nodes where mistuning elements are applied (*b*)

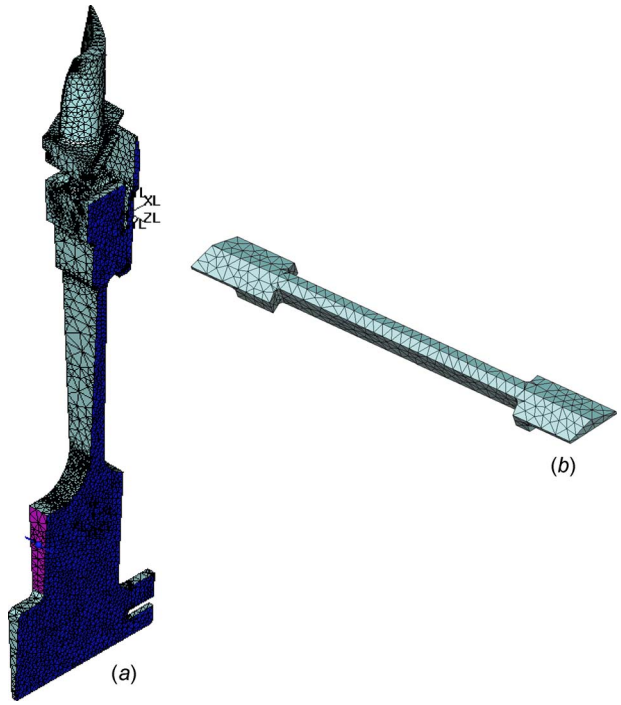

Fig. 11 FE models of a bladed disk sector (*a*) and an underplatform damper (*b*)

interaction of different families of bladed disk modes and frequency veering effects are included in the analysis.

4.2 Bladed Disk Model. The bladed disk analyzed contains 64 blades (Fig. 10(*a*)). The forced response is calculated at the blade tip trailing node (Fig. 10(*b*)). The modal characteristics of a tuned bladed disk and underplatform dampers are determined using large-scale finite element models. An FE model of one sector comprises more than 220,000 DOFs and an FE model of an UPD has 9500 DOFs (Fig. 11).

The first 48 natural frequencies and mode shapes of the bladed disk are calculated for each of the possible nodal diameter values from 0 to 32. All these modes are included in the mistuning analysis. For underplatform damper modeling the first 48 mode shapes and natural frequencies are also determined to generate an FRF matrix for the damper.

The mistuned response is analyzed for the first flapwise mode (1*F*) family of modes excited by 7EO and 5EO. Bladed disk modal characteristics are affected by the rotation mostly through centrifugal forces. Because of this, the modal characteristics are determined for two rotation speeds: 441 rad/s and 662 rad/s corresponding to the resonances excited by 7EO and 5EO, respectively, and the respective modal characteristics are used for each EO analyzed. The lower natural frequencies of the bladed disk are plotted in Fig. 12.

The frequency-nodal diameter diagram in Fig. 12 shows that this frequency range includes frequency veering modes, where modes of first and second families can interact but these two families of modes are separated significantly from higher modes. Hence, the aerodynamic damping was calculated for the first five modes for all possible values of traveling wave index values from −31 to +32. Positive indices correspond to the forward traveling waves and negative—to backward traveling wave modes of vibrations.

The modal damping factors used in the analysis are presented in Fig. 13.

In addition to the aerodynamic damping, the bladed disk analysis has a significant level of structural damping due to friction at blade root joints; damping provided by the bladed disk instrumentation, including strain gauge wiring, and by friction contact surface close to the disk hub. Exact values of structural damping produced by such sources were not available and, hence, cases with different structural damping levels were explored in the analysis. In the calculations the structural damping was added to the aerodynamic modal damping factors. The damping produced by the underplatform dampers is not included in the structural damping factors and is determined directly as a result of calculation.

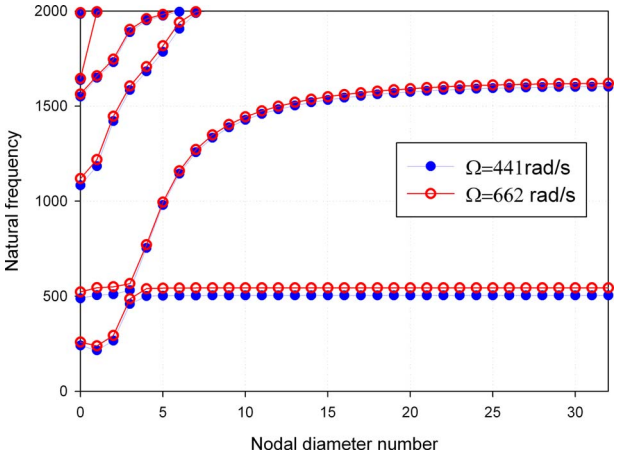

Fig. 12 Natural frequencies of the bladed disk

Excitations by 7EO and 5EO components of aerodynamic forces are of major interest. In order to facilitate use of the results of CFD calculation the aerodynamic pressure was projected on bladed disk mode shapes and modal excitation forces are calculated for all mode shapes involved in the analysis. The modal forces determined from the CFD analysis are plotted in Fig. 14

Blade frequency mistuning is modeled by mass elements located at blade tip nodes that are close to leading and trailing airfoil edges and shown in Fig. 10(*b*). The measured blade-alone frequencies formed an irregular random-like mistuning pattern with all blade frequencies located within a range of −5% to +8%.

Forced response of the bladed disk is performed for two major cases: (i) a case of a bladed disk without UPDs and (ii) a case of a bladed disk with UPDs. The numerical results obtained are discussed in the following sections.

4.3 A Mistuned Bladed Disk Without Dampers. Forced response analysis of the blade disk without dampers has been performed for cases of 7EO and 5EO excitation. The envelope of the

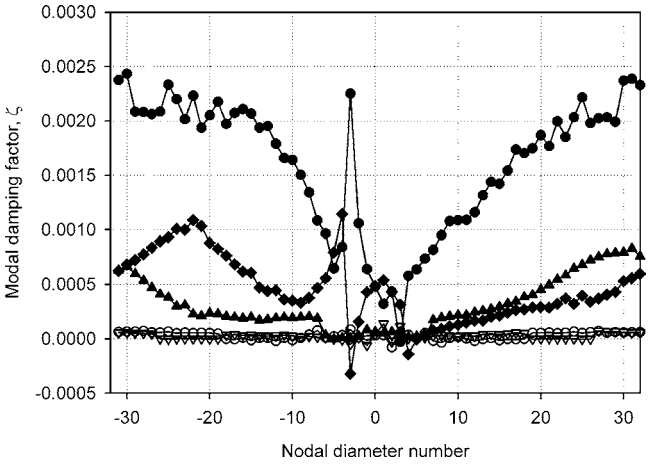

Fig. 13 Aerodynamic modal damping factors

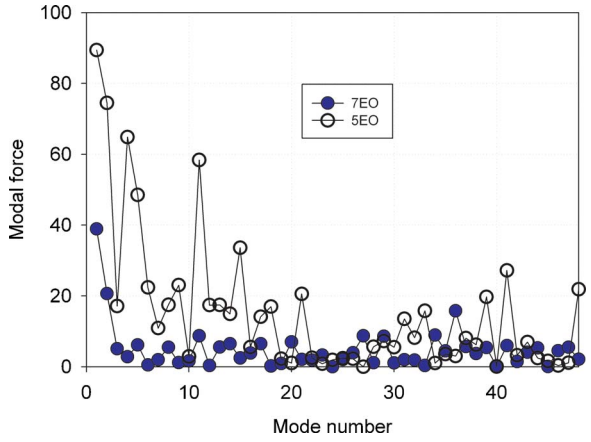

Fig. 14 Excitation aerodynamic modal forces

maximum blade amplitude calculated for different levels of structural damping added to the aerodamping is plotted in Fig. 15 for a case of 7EO.

Frequencies at which each individual blade has the maximum value of the forced response amplitude over the whole frequency range are compared in Figs. 16 and 17 with those obtained from experimental measurements for cases of 7EO and 5EO, respectively. For a case of 5EO two experimental measurements are plotted, which were recorded on the same day.

One can see that for the bladed disk analyzed the maximum response frequencies are not affected by the structural damping and there is a good correspondence between predicted and measured frequency values. Values of blade resonance frequencies for 7EO and 5EO are slightly different, which is due to blade coupling through disk and gas flow. If the blades were uncoupled then these resonance frequencies would coincide with the blade-alone frequencies and the centrifugal forces, which are different for cases of 5EO and 7EO would simply scale the resonance frequency pattern.

Comparison of maximum response levels is made for a case of 7EO excitation in Fig. 18. The predicted value of the maximum forced response achieved over all blades is close to the experimental measurements, but the distribution of blade maximum amplitudes differs, which is likely to be a result of different damping produced by the disk instrumentation, which is not accounted for in the calculation and inherent variability of measurements (see Fig. 6).

4.4 A Tuned Bladed Disk With Dampers. The analysis of the effects of excitation and friction contact interface parameters of forced response of the bladed disk with underplatform dampers

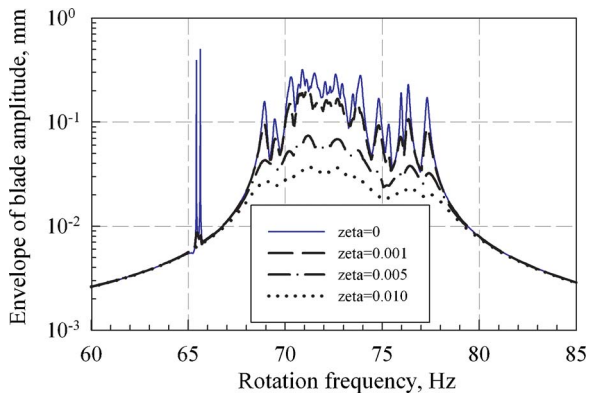

Fig. 15 Envelope of the bladed disk forced response: a case 7EO excitation without dampers

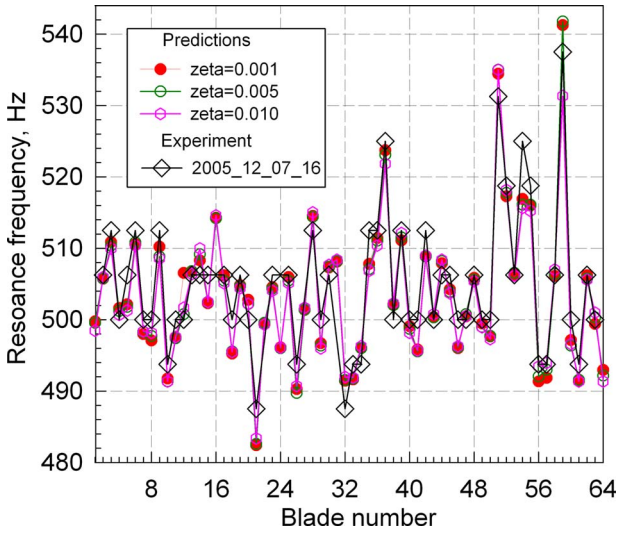

Fig. 16 Frequencies providing maximum response levels for individual blades: a case of 7EO without dampers

was performed first for a case when all blades are tuned. For a tuned bladed disk assembly, a method for using cyclic symmetry properties in nonlinear forced response analysis [31] is used, which exactly reduces the analysis of a whole bladed disk to an analysis of its repetitive part: a sector including a single blade and adjusted disk sector. The use of sector models allows decreasing time of calculation by several orders of magnitudes compared with that required for mistuned analysis.

Vibrations in a bladed disk with friction dampers are inherently nonlinear and, therefore, in contrast to linear vibration, the superposition principle cannot be applied, i.e., vibration response excited simultaneously by many excitation harmonics generally cannot be obtained as a sum of responses excited by each harmonic. Since at operating conditions the excitation is usually multiharmonic, the effects of the cumulative action of many excitation harmonics on the forced response is estimated for the bladed disk analyzed. For forced response calculations the dominant excita-

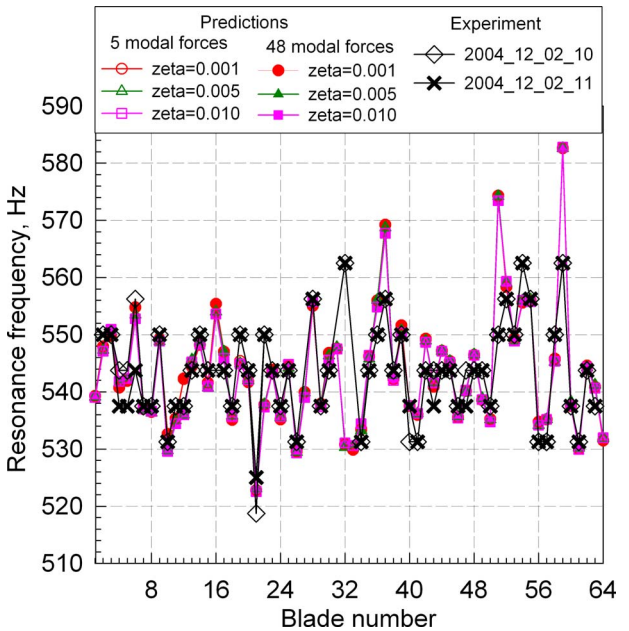

Fig. 17 Frequencies providing maximum response levels for individual blades: a case of 5EO without dampers

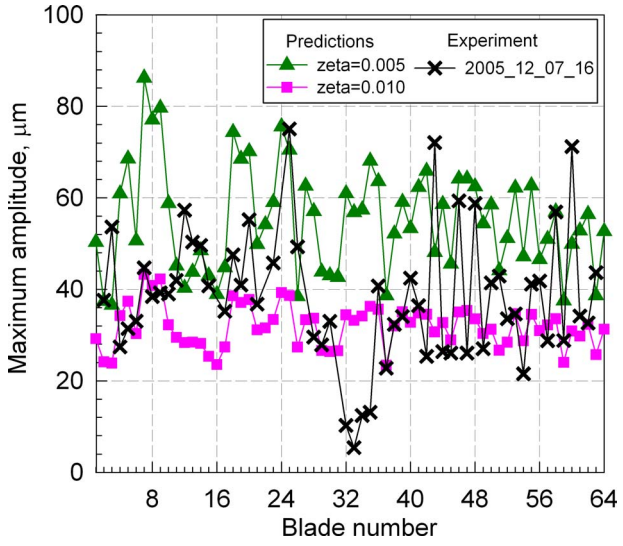

Fig. 18 Comparison of predicted and measured maximum response levels for individual blades for a case of 7EO without dampers

tion harmonics were selected from a list of values obtained from CFD analysis. The dominant harmonic numbers were 7EO, 36EO, 43EO, 50EO, and 86EO, which, as expected, are multiples and combinations of the number of NGVs (i.e., 43), and the number of waves along NGV annulus for the NGV throat area variation (seven in this case). Forced response calculated with different numbers of the multiharmonic excitation is shown in Fig. 19.

One can see that, for the considered case, in the vicinity of the resonance peak of interest the responses obtained with single 7EO excitation and with multiharmonic excitation are close. Therefore, in most calculations for this bladed disk, only a single EO excitation was considered, which allows significant reduction in the computation time.

The effect of the excitation level on the forced response of the bladed disk is illustrated in Fig. 20.

The modal forces obtained from CFD analysis for nominal conditions are multiplied by factors indicated in this figure. For comparison, the forced responses of a bladed disk without dampers and with stuck dampers are also plotted here. It is evident that the underplatform dampers efficiently reduce two resonance peak response levels (at rotation speed frequencies 70 Hz and 168 Hz) for all excitation levels considered here.

For higher excitation levels ($f=10$ and 16), a resonance peak is also observed at a frequency that is close to the resonance frequency of a bladed disk without dampers. For these excitation levels the damper is too light and is subjected to a high level of macroslip motion, hence its stiffening effect is negligible. Moreover, for high excitation levels we can see that the resonance peak frequency value is smaller than that for a bladed disk without dampers, which is owing to damper inertia added to the system.

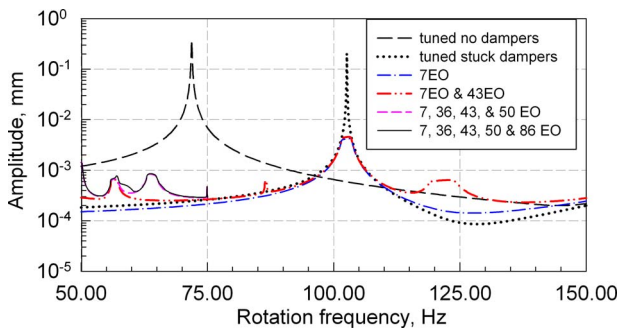

Fig. 19 Effect of number of excitation harmonic applied simultaneously on the forced response

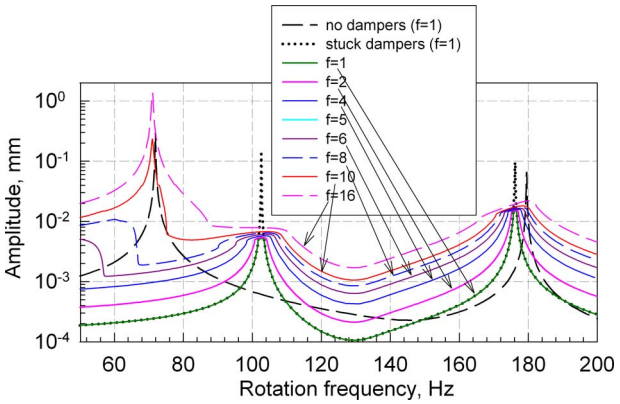

Fig. 20 Effect of excitation level on the forced response

Effects on the forced response of the parameters of damper friction contact parameters: (i) friction coefficient and (ii) rough surface contact stiffness coefficient are shown in Fig. 21. One can see that the forced response becomes insensitive to the variation in the contact stiffness coefficient value when it is higher than 10^4, since the damper body flexibility is then dominant. Smaller friction coefficient values provide smaller resonance peak amplitudes for the level of excitation and damper weight considered here: i.e., when the damper is heavy and reduction in the friction coefficient increases time over a vibration period when the damper is slipping and decreases time when it is stuck.

4.5 A Mistuned Bladed Disk With Dampers. For analysis of the mistuned bladed disk with underplatform dampers the following parameters were used: friction coefficient 0.3, contact stiffness due to roughness 10^5 N/mm^3, and excitation level—nominal (i.e., $f=1$). For the results plotted in Fig. 22 the forced response

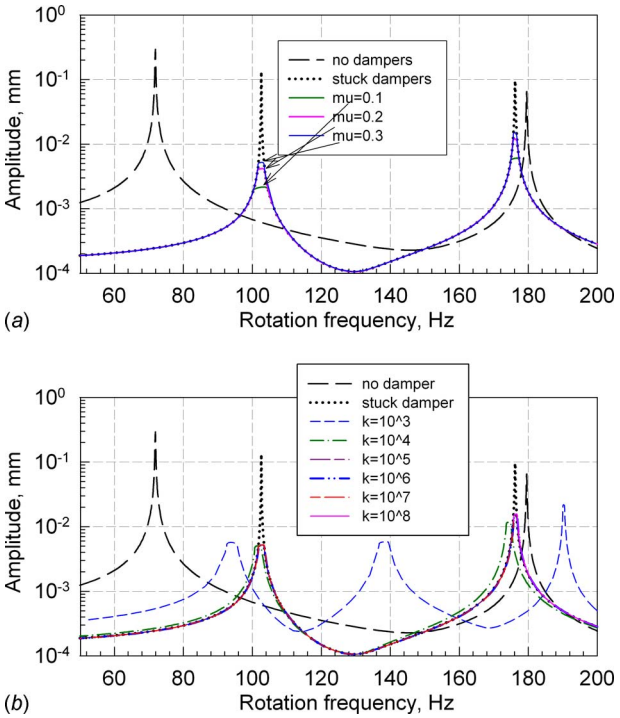

Fig. 21 Effect of contact interface parameters of forced response: (*a*) friction coefficient and (*b*) contact stiffness

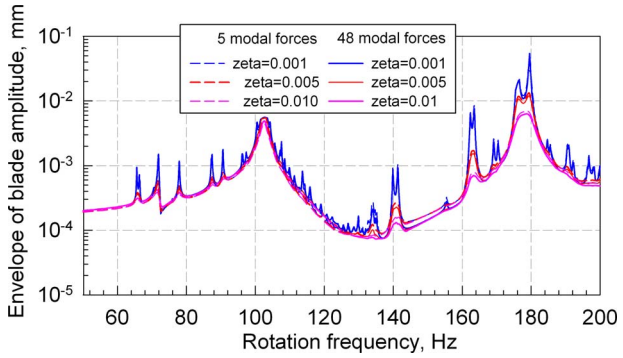

Fig. 22 Envelope of the mistuned forced response (7EO)

was calculated for two cases: (i) a case of five modal forces and (ii) a case of 48 modal forces included in the analysis. For each of these cases three levels of structural damping are studied.

One can see 48 modal forces produce higher response levels although the difference is less than 20%. The effects of the underplatform dampers on reduction in the resonance response are dominant and the forced response levels differ a little for the values of the structural damping factor analyzed: ζ=0.001, 0.005, and 0.01. For the second resonance peak the background structural damping contribute significantly to the amplitude reduction.

Forced response of the mistuned bladed disk with dampers produced by different excitation levels is plotted in Fig. 23.

One can see that the dampers make the first resonance peak response almost unaffected by variation in the excitation level, as it was observed for a tuned bladed disk (see Fig. 20), while the second resonance peak is much more sensitive to excitation variation.

The frequencies at which individual blades reach their maximum response levels and the values of these response levels are plotted in Figs. 24 and 25, respectively. Comparing these plots with those corresponding to the bladed disk without dampers (see Figs. 17 and 18) one can see that the dampers significantly reduce scatter in the values of response frequencies and levels.

5 Conclusions

In the paper, an integrated experimental-numerical study of forced response for a mistuned bladed disk has been performed.

A full chain for the predictive forced response analysis has been developed including data exchange between CFD code and a code for nonlinear forced response prediction.

The experimental study of mistuned bladed disk vibration amplitudes has been performed in a wind tunnel with a full-scale rotating bladed disk and aerodynamic excitation by nozzle guide vanes. Measured parameters of gas flow on the inlet and outlet of

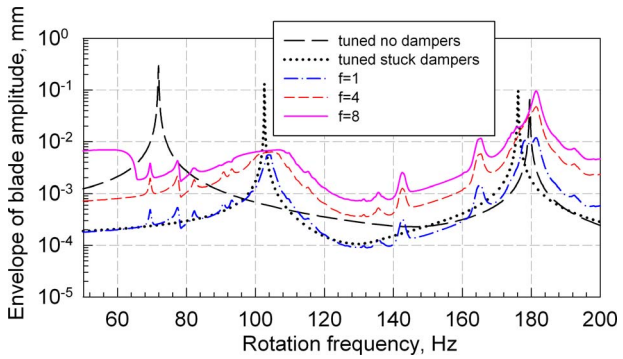

Fig. 23 Envelope of the mistuned forced response excited by 7EO with different levels of excitation

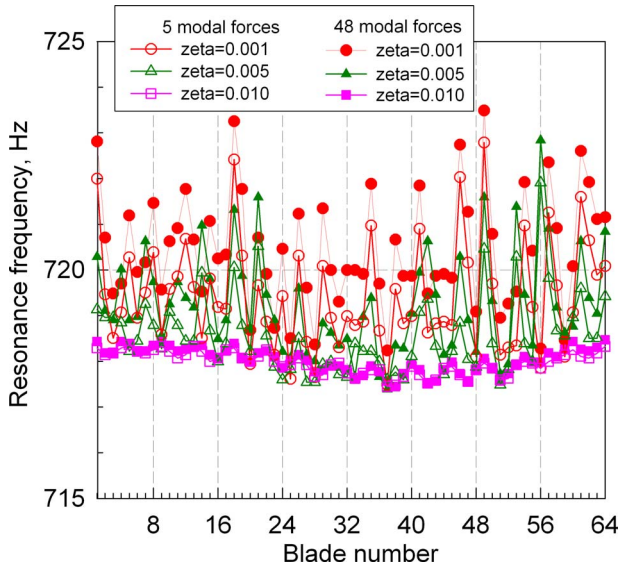

Fig. 24 Frequencies providing maximum response levels for individual blades: a case of 7EO with dampers

the turbine stage are used as boundary conditions in the CFD analysis to calculate unsteady pressures and to determine modal excitation forces and modal aerodynamic damping factors. Forced response analysis is performed, using the aerodynamic data, for two cases of the bladed disk design: (i) without underplatform dampers and (ii) with underplatform dampers.

Comparison of experimentally measured and predicted values for the mistuned bladed disk without dampers shows a good correspondence between frequencies at which individual blades have maximum values.

Numerical studies for a bladed disk with underplatform dampers demonstrate, for the considered structure, little sensitivity of the forced response resonance amplitude to the variation in the excitation force. The resonance amplitude remains at an almost constant value under tenfold increase of the excitation level.

It is shown that the underplatform damper significantly reduces scatter in values of the individual blade response frequencies and maximum forced response levels.

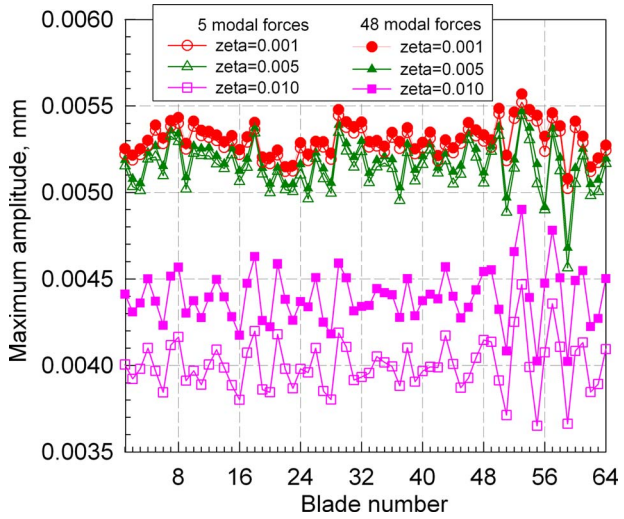

Fig. 25 Maximum response levels for individual blades for a case of 7EO with dampers

The study indicates on possibility of using the state-of-the-art predictive method for quantitative estimates of forced response characteristics for mistuned bladed disks.

Acknowledgment

The first two authors are grateful to Rolls-Royce plc for providing financial support toward this project and for giving permission to publish this paper. The test rig used in the study was created with the aid of financial support from the European Community in a framework of the ADTurB project [30].

References

[1] Manwaring, S. R., and Wisler, D. C., 1993, "Unsteady Aerodynamics and Gust Response in Compressors and Turbines," ASME J. Turbomach., **115**, pp. 724–740.
[2] Johnston, D. A., and Fleeter, S., 1998, "Measured Rotor Wake and Potential Forcing Functions, Including Blade Row Interactions," J. Propul. Power, **14**, pp. 191–198.
[3] Kurkov, A. P., and Lucci, B. L., 1997, "Measurements of Gust Response on a Turbine Cascade," ASME J. Turbomach., **119**, pp. 238–246.
[4] Weaver, M., Manwaring, S. R., Abhari, R. S., Dunn, M. G., Salay, M. J., Frey, K. K., and Heidegger, N., 2000, "Forcing Function Measurements and Predictions of a Transonic Vaneless Counter Rotating Turbine," ASME Paper No. 2000-GT-0375.
[5] Kielb, J. J., and Abhari, R. S., 2003, "Experimental Study of Aerodynamic and Structural Damping in a Full-Scale Rotating Turbine," ASME J. Eng. Gas Turbines Power, **125**(1), pp. 102–112.
[6] Jöcker, M., Kessar, A., Fransson T. H., Kahl, G., and Rehder, H.-J., 2003, "Comparison of Models to Predict Low Engine Order Excitation in a High Pressure Turbine Stage," Tenth ISUAAT Conference, Sept. 7–11.
[7] Ning, W., Moffat, S., Li, Y., and Wells, R. G., 2003, "Blade Forced Response Prediction for Industrial Turbines: Verification and Application," ASME Paper No. GT2003-38642.
[8] Lombard, J.-P., Sharma, V., Dumas, M., Dupont, C., and, Seinturier, E., 2005, "Calibration of Aeroelastic Prediction Methods: Comparison With Experimental Results on a Single Stage Compressor Blisk," *Proceedings of NATO AVT-121 Symposium on Evaluation, Control and Prevention of High Cycle Fatigue in Gas Turbine Engines*, Granada, Spain, Oct. 3–7.
[9] Feiner, D. M., and Griffin, J. H., 2005, "Exploring the Use of FMM ID for Engine Health Monitoring," *Proceedings of NATO AVT-121 Symposium on Evaluation, Control and Prevention of High Cycle Fatigue in Gas Turbine Engines*, Granada, Spain, Oct. 3–7.
[10] Del Turco, P., D'Ercole, M., Gamberi, F., De Prosperis, R., Pieroni, N., and Mariotti, M., 2007, "Modelling and Measuring Experiences to Evaluate the Modal Behaviour of an Industrial Turbine High Pressure Bucket," ASME Paper No. GT2007-27459.
[11] Sextro, W., 2000, "The Calculation of the Forced Response of Shrouded Blades With Friction Contacts and Its Experimental Verification," ASME Paper No. GT2000-540.
[12] Szwedowicz, J., Gibert, C., Sommer, T. P., and Keller, R., 2006, "Numerical and Experimental Damping Assessment of a Thin-Walled Friction Damper in the Rotating Set-Up With High Pressure Turbine Blades," ASME Paper No. GT2006-90951.
[13] Yang, M.-T., and Griffin, J. H., 2001, "A Reduced-Order Model of Mistuning Using a Subset of Nominal System Modes," ASME J. Eng. Gas Turbines Power, **123**, pp. 893–900.
[14] Bladh, R., and Pierre, C., 2002, "Dynamic Response Predictions for a Mistuned Industrial Turbomachinery Rotor Using Reduced-Order Modeling," ASME J. Eng. Gas Turbines Power, **124**, pp. 311–324.
[15] Moyroud, F., Fransson, T., and Jacquet-Richardet, G., 2002, "A Comparison of Two Finite Element Reduction Techniques for Mistuned Bladed Disks," ASME J. Eng. Gas Turbines Power, **124**, pp. 942–952.
[16] Feiner, D. M., and Griffin, J. H., 2002, "A Fundamental Model of Mistuning for a Single Family Of Modes," ASME J. Turbomach., **124**, pp. 597–605.
[17] Petrov, E. P., Sanliturk, K. Y., and Ewins, D. J., 2002, "A New Method for Dynamic Analysis of Mistuned Bladed Discs Based on Exact Relationship Between Tuned and Mistuned Systems," ASME J. Eng. Gas Turbines Power, **124**(3), pp. 586–597.
[18] Petrov, E., 2009, "A Method for Forced Response Analysis of Mistuned Bladed Discs With Aerodynamic Effects Included," ASME Paper No. GT2009-59634.
[19] Petrov, E. P., and Ewins, D. J., 2005, "Method for Analysis of Nonlinear Multiharmonic Vibrations of Mistuned Bladed Discs With Scatter of Contact Interface Characteristics," ASME J. Turbomachinery, **127**(1), pp. 128–136.
[20] Sayma, A. I., Vahdati, M., and Imregun, M., 2000, "An Integrated Nonlinear Approach for Turbomachinery Forced Response Prediction. Part I: Formulation," J. Fluids Struct., **14**(1), pp. 87–101.
[21] Sayma, A. I., Vahdati, M., Sbardella, L., and Imregun, M., 2000, "Modeling of Three-Dimensional Viscous Compressible Turbomachinery Flows Using Unstructured Hybrid Grids," AIAA J., **38**(6), pp. 945–954.
[22] Breard, C., Green, J. S., and Imregun, M., 2003, "Low-Engine-Order Excitation Mechanisms in Axial-Flow Turbomachinery," J. Propul. Power, **19**(4), pp. 704–712.
[23] Vahdati, M., Sayma, A. I., Marshall, J. G., and Imregun, M., 2001, "Mechanisms and Prediction Methods for Fan Blade Stall Flutter Source," J. Propul. Power, **17**(5), pp. 1100–1108.
[24] Sever, I., Petrov, E.P. and Ewins, D.J., 2008, "Experimental and Numerical Investigation of Rotating Bladed Disk Forced Response Using Under-Platform Friction Dampers," ASME J. Eng. Gas Turbines Power, **130**, p. 042503.
[25] Sever, I., 2004, "Experimental Validation of Turbomachinery Blade Vibration Predictions," Ph.D. thesis, Imperial College London, UK.
[26] Sever, I., Stanbridge, A. B., and Ewins, D. J., 2006, "Experimental Validation of Mistuned Bladed Disc Vibration Predictions," Seventh IFToMM Rotor Dynamics Conference, Vienna, Austria, Sept. 25–28.
[27] Vahdati, M., Sayma, A. I., and Imregun, M., 2000, "An Integrated Nonlinear Approach for Turbomachinery Forced Response Prediction. Part II: Case Studies," J. Fluids Struct., **14**(1), pp. 103–125.
[28] Hennings, H., and Elliott, R., 2002, "Forced Response Experiments in a High Pressure Turbine Stage," ASME Paper No. GT-2002-30453.
[29] Green, J. S., 2001, "An Overview of a European Collaborative Programme for Forced Response," Sixth National Turbine Engine High Cycle Fatigue Conference, Jacksonville, FL.
[30] 2001, Aeromechanical Design of Turbine Blades (ADTurB), Project funded by the European Community Under the Industrial and Material Technologies Programme (Brite-EuRam III), Contract No. BRPR-CT95-0124, ADTurB Synthesis Report.
[31] Petrov, E. P., 2004, "A Method for Use of Cyclic Symmetry Properties in Analysis of Nonlinear Multiharmonic Vibrations of Bladed Discs," ASME J. Turbomach., **126**(1), pp. 175–183.

Jacob Laborenz[1]
e-mail: laborenz@ids.uni-hannover.de

Christian Siewert

Lars Panning

Jörg Wallaschek

Institute of Dynamics and Vibration Research,
Leibniz Universität Hannover,
30167 Hannover, Germany

Christoph Gerber

Pierre-Alain Masserey

ALSTOM Power, Steam Turbines and Generators,
5401 Baden, Switzerland

Eddy Current Damping: A Concept Study for Steam Turbine Blading

In gas and steam turbine applications a common approach to prevent the blades from high cycle fatigue failures due to high vibration amplitudes is the usage of friction damping elements. Besides the intended amplitude reduction this procedure also features some possibly unwanted side effects like a shift in resonance frequencies due to stiffening effects caused by the contact. Thus, as an alternative an eddy current based noncontacting damping concept for the application in turbomachinery is investigated. In this paper two different types of eddy current dampers are considered. Theoretical models for both are established by applying electromagnetic-mechanical theory. The theoretical models are compared with forced response measurements that are performed at a stationary test rig. [DOI: 10.1115/1.3205032]

1 Introduction

Gas and steam turbine blades are subjected to high static and dynamic loads due to thermal and centrifugal loads as well as dynamic excitation forces. The resulting vibration amplitudes in combination with the high static loads can lead to high cycle fatigue failures. Thus, the avoidance of high cycle fatigue failures is of great importance. To meet those concerns a common solution is the usage of coupling devices such as underplatform dampers, lacing wires, and tip shrouds, which provide additional damping through energy dissipation in friction contacts. The disadvantage of those friction dampers is that the design is complex since the required physical contact parameters are difficult to evaluate and alter under operating conditions through wear. Furthermore, the coupling of the blades and in particular, the geometric properties of the friction damping device changes the dynamic characteristics such as eigenfrequencies and mode shapes. Sanliturk et al. [1] investigated the damping effect of a wedge damper and observed a considerable frequency shift depending on the normal load of the damping element in addition to the intended amplitude reduction. Firrone et al. [2] investigated the damping effect of cylindrical damping elements and stated that besides the intended amplitude reduction the resonance frequencies are effected by the damping device. Panning et al. [3,4] compared several underplatform damper geometries in numerical and experimental approaches. These analyses revealed that besides the contact parameters the geometry has a strong influence on the damped resonance frequencies.

As an alternative solution a noncontact damping mechanism based on eddy current damping is investigated. In this approach eddy currents are generated in an electrical conductor through movement relative to a permanent magnet. The interaction of this current flow with the flux field produces a force that is proportional to the velocity of the conductor such that linearized behavior of the assembly corresponds to a viscous dashpot damper. By this means a high damping potential can be achieved with very little change in the dynamic characteristics of the undamped system since no direct coupling occurs.

1.1 Review on the Eddy Current Damping Research. In the field of braking technologies the retardation effect of eddy currents has been known for a long time [5] and has been investigated in many cases to brake rotating structures [6,7]. In the actual generation of German high speed trains (ICE 3), a linear eddy current brake is used in addition to conventional brakes. It consists of electromagnets that can be lowered close to the rail and therefore provides a retardation that does not depend on the wheel-rail-contact and is free from wear [8].

According to Sodano [9], one main focus in the former research on eddy current damping has been the suppression of lateral vibrations of rotors. For example Kligerman et al. [10] analyzed a system very similar to an eddy current brake consisting of an electrical conducting disk fixated at the rotor as to follow its rotation and vibration, and a horseshoe magnet which induces a magnetic field parallel to the rotor's axis in the conducting disk. They showed theoretically and experimentally that a considerable amount of damping can be achieved but also stated that it could lead to instability under specific operation conditions which would happen due to the braking effect of that setup. By decoupling the disk with a bearing from the rotation they eliminated the braking effect and proved their assumption experimentally.

In the field of the eddy current based damping of structural vibrations the damping concepts can be classified depending on their functional principle. Graves et al. [11] compared in a theoretical approach the efficiency of two novel dampers for a vehicle suspension system, one generating eddy currents due to a relative motion between a magnet and a conductor referred to as "motional electromotive force (EMF)," and the other one generating eddy currents through a time-varying magnetic field linking a stationary conductor referred to as "transformer electromotive force." They stated that both principles could be used in vibration damping but that in most cases motional EMF devices would result in a higher efficiency when using the same conductor volume and the same maximum field strength. Kwak et al. [12] proposed an eddy current based damping element for the suppression of beam vibrations consisting of an electrical conductor fixated at the tip of the beam and two permanent magnets, which are connected with a flexible linkage to the beam in such way that the conductor moves through the axial field between the two magnets

[1]Corresponding author.

Contributed by the International Gas Turbine Institute of ASME for publication in the JOURNAL OF ENGINEERING FOR GAS TURBINES AND POWER. Manuscript received April 8, 2009; final manuscript received April 15, 2009; published online March 5, 2010. Review conducted by Dilip R. Ballal. Paper presented at the ASME Turbo Expo 2009, Orlando, FL.

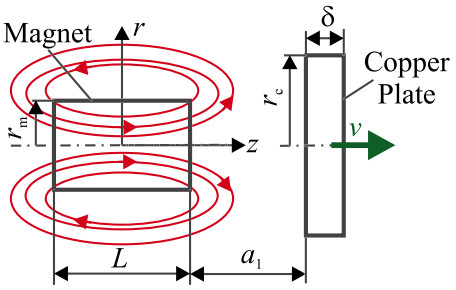

Fig. 1 Schematic sketch of first damping configuration

in case of vibrations and, therefore, dissipates energy due to motional EMF. Tests revealed a considerable amplitude reduction for different beam modes in a wide frequency range. However, the damping element leads to an enormous change in the beam's dynamic behavior as another DOF is added due to the additional masses connected via a flexible linkage. Bae et al. [13] modified the theoretical model established by Kwak et al. [12] and achieved a good agreement between tests and simulation in time and frequency domain. To the author's knowledge, Sodano et al. [14] have been the first who proposed a motional EMF device, which utilizes the radial component of a cylindrical permanent magnet for the vibration suppression of a beam. Contrary to previous approaches magnet orientation and vibration direction are parallel to each other resulting in a simple set up: A copper conductor is fixated at the beam's profile and a cylindrical permanent magnet is placed in it's vicinity in such way that the air gap between conductor and magnet changes in case of vibrations inducing motional EMF (Fig. 1). Tests revealed a considerable damping effect with very little change in the beam's dynamic behavior due to its noncontacting operation method and low additional masses. The simulations were in good agreement for small air gaps but with an increase in the gap the approximation became less accurate. By utilizing two magnets facing each other with their like-poles, Sodano et al. [15] improved the damping effect up to critical damping of the beam's first mode. Ebrahimi et al. [16] proposed a magnetic spring-damper consisting of two repellent permanent magnets and a ring-shaped aluminum plate between them all lined up coaxially. One magnet and the conductor plate are stationary, whereas the other magnet executes an oscillating motion in case of vibrations. Motional EMFs are generated due to the relative motion of the conductor and the magnet, whereas transformer EMFs are generated due to the change in flux density linking the conductor caused by a modification of the magnets' air gap. The spring behavior arises due to the repulsive force between the two magnets.

In further approaches, noncontact active control systems for the vibration suppression based on eddy current effects have been investigated. By placing the permanent magnet on a shaker, sensing the beam's deflection and controlling the magnet's position Sodano et al. [17] expanded their setup to a passive-active magnetic damper. In Refs. [18,19], Sodano and Inman investigated a noncontact magnetic control system based on an electromagnet, sensing the beam's velocity and controlling the electromagnet's feeding current. Tests revealed an amplitude reduction of about 97.5% for the first and 96.5% for the second bending mode. Tonoli et al. [20] investigated a semi-active eddy current damper based on transformer EMF for the damping of beam vibrations. It consists of a stationary horseshoe electromagnet, which is fed with constant voltage and an anchor fixated at the beam. In the case of vibrations the air gap between magnet and anchor alters and therefore changes the flux within the coil dissipating energy via the induced current. The authors indicate a considerable damping effect but also state that this setup contains a negative mechanical stiffness, which has to be compensated with a spring to guarantee stability.

In the field of eddy current damping of turbine blading different approaches have been made. Ernst et al. [21] patented an application for the damping of turbine blade vibrations based on eddy currents. It consists of permanent magnets placed in the snubber or shroud of turbine blades inducing eddy currents in adjacent blades in case of vibrations and, therefore, damping the blades' vibration without contact. Siewert et al. [22] also investigated the damping of turbine blades using eddy currents. A test rig has been set up to investigate the damping of beam vibrations. Forced response measurements showed a considerable damping effect and simulations were in good agreement with the experimental results. Further numerical investigations concerning the damping potential of a real turbine blade revealed an amplitude reduction of about 70% for a circumferential vibration mode caused by an engine order six excitation.

In this paper two types of eddy current dampers for the damping of turbine blade vibrations are investigated. In the first configuration energy dissipation is obtained by relative movement of a permanent magnet with respect to a copper plate, initiating motional electromotive forces as already published in Refs. [14,22]. In this paper the damping effect of that kind of assembly is investigated when acting relatively between two vibrating structures as damping of complex vibration modes against the inertial frame is difficult to realize on rotating machinery. Furthermore, another eddy current damping element is proposed consisting of two assemblies each composed of a copper plate and a permanent magnet. In this case the relative movement of the permanent magnets causes a time-varying magnetic field within the copper plates and therefore generates transformer electromotive forces. A theoretical model for the second damping concept is established resulting in equivalent mechanical parameters and forced response measurements and simulations are carried out to validate the setup.

2 Mathematical Model of Eddy Current Dampers

2.1 Equivalent Viscous Damping Coefficient of First Configuration. The first damping configuration consists of a cylindrical copper plate and a cylindrical permanent magnet, which is axially polarized (Fig. 1). To attain its damping effect cylindrical coordinates are appropriate and a mathematical description of the flux density of the magnet is required. The flux density can be obtained in a concise form utilizing the magnetic vector potential **A**. According to Lehner [23], for a cylindrical permanent magnet it consists only of a tangential component and reads as

$$\mathbf{A} = A_r\mathbf{e}_r + A_\varphi\mathbf{e}_\varphi + A_z\mathbf{e}_z = A_\varphi\mathbf{e}_\varphi$$

$$A_\varphi = \frac{\mu_0 M_0}{2\pi}\int_{-L/2}^{L/2}\frac{1}{r}\sqrt{(r+r_m)^2+(z-z')^2}\cdot\left(\left(1-\frac{k^2}{2}\right)K\left(\frac{\pi}{2},k\right) - E\left(\frac{\pi}{2},k\right)\right)dz' \tag{1}$$

where μ_0 denotes the magnetic permeability, M_0 denotes the magnetization, r_m denotes the magnet's radius, k denotes the modul, and E and K denote elliptic integrals of the first and second kind [24] with

$$k^2 = \frac{4rr_m}{(r+r_m)^2+(z-z')^2}$$

$$K\left(\frac{\pi}{2},k\right) = \int_0^{\pi/2}\frac{1}{\sqrt{1-k^2\sin^2\psi}}d\psi \tag{2}$$

$$E\left(\frac{\pi}{2},k\right) = \int_0^{\pi/2}\sqrt{1-k^2\sin^2\psi}\,d\psi$$

With the relation between the magnetic vector potential and the flux density

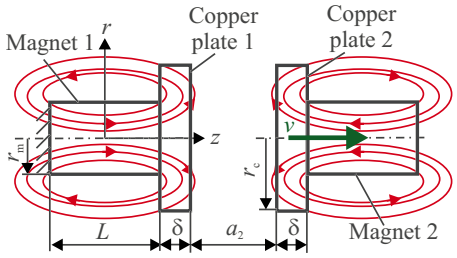

Fig. 2 Schematic sketch of second damping configuration

$$\mathbf{B} = \nabla \times \mathbf{A} \tag{3}$$

the radial component of the flux density which is essential for the damping mechanism reads as

$$B_r = -\frac{\partial A_\varphi}{\partial z} = -\frac{\mu_0 M_0}{2\pi}\int_{-L/2}^{L/2} \frac{(z-z')}{r\sqrt{(r+r_m)^2+(z-z')^2}} \cdot \left(K - \left(1+\frac{k^2}{2(1-k^2)}\right)E\right)dz' \tag{4}$$

According to Sodano [14] the resulting damping force in z-direction for the first damping configuration is given by

$$F_{d,1,z} = -\int_V \sigma v B_r^2 dV = -2\pi\sigma v \int_{a_1(t)+L/2}^{a_1(t)+L/2+\delta}\int_0^{r_c} rB_r^2 dr dz \tag{5}$$

where σ denotes the conductivity, v denotes the conductor's velocity, and V denotes the conductor's volume. When regarding small vibrations compared with the air gap $\Delta a_1(t) \ll \overline{a_1}$ and therefore neglecting a change in the current position through the movement

$$a_1(t) = \overline{a_1} + \Delta a_1(t) \Rightarrow a_1(t) \approx \overline{a_1} \tag{6}$$

a linear viscous damping coefficient c_1 can be defined as follows:

$$c_1(a_1) = 2\pi\sigma \int_{a_1+L/2}^{a_1+L/2+\delta}\int_0^{r_c} rB_r^2 dr dz \tag{7}$$

2.2 Equivalent Viscous Damping Coefficient of Second Configuration. The second damping configuration consists of two assemblies each composed of a copper plate and a permanent magnet, which experience a relative motion in case of vibrations (Fig. 2). To obtain its damping behavior the description of the magnetic vector potential and the magnetic flux density of two equal permanent magnets whose like-poles face each other is required. The resulting magnetic vector potential $\mathbf{A}_{\text{res}}$ can be obtained by superimposing the fields of the two magnets since linearity is given

$$\mathbf{A}_{\text{res}} = A_{\varphi,\text{res}}\mathbf{e}_\varphi = (A_{\varphi,1} + A_{\varphi,2})\mathbf{e}_\varphi \tag{8}$$

The magnetic vector potential $A_{\varphi,1}$ equals the one of the first configuration and is given by Eq. (1). The magnetic vector potential of the second magnet can be derived from Eq. (1) when substituting the position of the magnet from the origin to its new position,

$$z_2 = z - (L + 2\delta + a_2) \tag{9}$$

and flipping the magnet's orientation. It then reads as

$$A_{\varphi,2} = -\frac{\mu_0 M_0}{2\pi}\int_{-L/2}^{L/2} \frac{1}{r}\sqrt{(r+r_m)^2+(z-(L+2\delta+a_2)-z')^2} \cdot \left(\left(1-\frac{k_2^2}{2}\right)K_2\left(\frac{\pi}{2},k_2\right) - E_2\left(\frac{\pi}{2},k_2\right)\right)dz' \tag{10}$$

with

$$k_2^2 = \frac{4rr_m}{(r+r_m)^2+(z-(L+2\delta+a_2)-z')^2}$$

$$K_2 = K\left(\frac{\pi}{2},k_2\right) \tag{11}$$

$$E_2 = E\left(\frac{\pi}{2},k_2\right)$$

Again, the radial component of the magnetic flux density can be obtained by deriving the magnetic vector potential $\mathbf{A}_{\varphi,\text{res}}$ with respect to z,

$$\begin{aligned} B_{\text{res},r} &= B_{1,r} + B_{2,r} = -\frac{\partial}{\partial z}A_{\varphi,1} - \frac{\partial}{\partial z}A_{\varphi,2} \\ &= -\frac{\mu_0 M_0}{2\pi}\int_{-L/2}^{L/2} \frac{(z-z')}{r\sqrt{(r+r_m)^2+(z-z')^2}} \cdot \left(K - \left(1+\frac{k^2}{2(1-k^2)}\right)E\right)dz' \\ &\quad + \frac{\mu_0 M_0}{2\pi}\int_{-L/2}^{L/2} \frac{(z-(L+2\delta+a_2)-z')}{r\sqrt{(r+r_m)^2+(z-(L+2\delta+a_2)-z')^2}} \cdot \left(K_2 - \left(1+\frac{k_2^2}{2(1-k_2^2)}\right)E_2\right)dz' \end{aligned} \tag{12}$$

Due to the symmetrical composition of the damping element the energy dissipated in the two copper plates is identical. Therefore, to obtain the damping coefficient of the second configuration caused by relative motion, the left assembly of magnet and copper plate is considered as still standing (Fig. 2), whereas the right assembly is considered as moving with the velocity v. To derive the damping coefficient the energy dissipated in the still standing copper plate 1 is regarded. According to Kupfmüller et al. [25], an electric field $\mathbf{E}_{\text{ind}}$ is induced which causes a current density $\mathbf{J}$ when the copper plate with the conductivity σ experiences a change in the magnetic vector potential

$$\mathbf{J} = \sigma\mathbf{E}_{\text{ind}} = -\sigma\frac{d\mathbf{A}}{dt} \tag{13}$$

Therefore, the conductor is affected by a Lorentz force $\mathbf{F}_1$, which reads as

$$\mathbf{F}_1 = \int_V \mathbf{J}\times\mathbf{B}dV = -\int_V \sigma\left(\frac{d\mathbf{A}}{dt}\right)\times\mathbf{B}dV \tag{14}$$

The total derivative of the vector potential $\mathbf{A}$ with respect to the time for a point p of the stationary copper plate 1 can be simplified to

$$\frac{d}{dt}\mathbf{A}(\mathbf{x}_p,t) = \frac{\partial\mathbf{A}}{\partial t} + \underbrace{v_p}_{0}\nabla\mathbf{A} = \frac{\partial\mathbf{A}}{\partial a_2}\frac{\partial a_2}{\partial t} = \frac{\partial\mathbf{A}}{\partial a_2}v \tag{15}$$

and therefore only depends on the velocity of the other assembly v and the rate of change in the vector potential with respect to the air gap a_2. When taking into account that the vector potential of the stationary magnet does not depend on the position of the moving magnet the partial derivative can be simplified to

$$\frac{\partial A_\varphi}{\partial a_2} = \frac{\partial A_{\varphi,1}}{\partial a_2} + \frac{\partial A_{\varphi,2}}{\partial a_2} = \frac{\partial A_{\varphi,2}}{\partial a_2} = -\frac{\partial A_{\varphi,2}}{\partial z} = B_{2,r} \tag{16}$$

Hence, the resulting damping force which acts on the first copper plate of the damping element when moving the second magnet can be expressed by

Table 1 Parameters of the damping element

Symbol	Value	Unit	Description
$B_{r,\max}$	1.21	T	Residual induction
μ_0	$4\pi\times10^{-7}$	(m kg/s^{2}A^2)	Permeability (vacuum)
M_0	$\frac{B_{r,\max}}{\mu_0}$	(A/m)	Magnetization
L	10	mm	Magnet length
r_m	7.5	mm	Magnet radius
r_c	12.5	mm	Plate radius
δ	3	mm	Plate thickness
σ	5.88×10^7	(1/Ω m)	Conductivity

$$F_{d,2,z} = 2\pi\sigma v \int_{L/2}^{L/2+\delta}\int_0^{r_c} rB_{2,r}B_{\mathrm{res},r}\,dr\,dz \tag{17}$$

which leads to an equivalent viscous damping coefficient

$$c_2(a_2) = 4\pi\sigma \int_{L/2}^{L/2+\delta}\int_0^{r_c} rB_{2,r}B_{\mathrm{res},r}\,dr\,dz \tag{18}$$

when taking the heating in both copper plates into account.

Since the integrals which describe the flux distributions (Eqs. (4)–(12)) do not have analytical solutions the estimation of the damping coefficients can only be solved numerically. This is done for the two configurations using an adaptive Lobatto quadrature and using the parameters given in Table 1. Figure 3 shows the equivalent viscous damping coefficients for both configurations against the static air gap.

2.3 Equivalent Stiffness Coefficient of Second Configuration. The second damping configuration consists of two magnets facing each other with their like-poles. Hence, besides damping effects conservative magnetic forces between the two magnets occur. As those forces depend on the air gap they show characteristics of a nonlinear spring element, which can be approximated with an equivalent stiffness coefficient depending on the air gap.

To attain the magnetic force between the two magnets the magnetization of the second magnet can be substituted by an equivalent current density $\mathbf{J}_m$, which causes the same flux distribution as the primal permanent magnet [26]. By this means again the magnetic force can be estimated with use of the Lorentz force (Eq. (14)). The distribution of the equivalent current density $\mathbf{J}_m$ of the second magnet equals its lateral surface and can be expressed utilizing the well-known delta-function δ_{di}

$$\mathbf{J}_m = -M_0\cdot\delta_{\mathrm{di}}(r-r_m)\mathbf{e}_\varphi;\quad L_0 - L/2 < z < L_0 + L/2 \tag{19}$$

where L_0 denotes the distance between the magnets' centroids

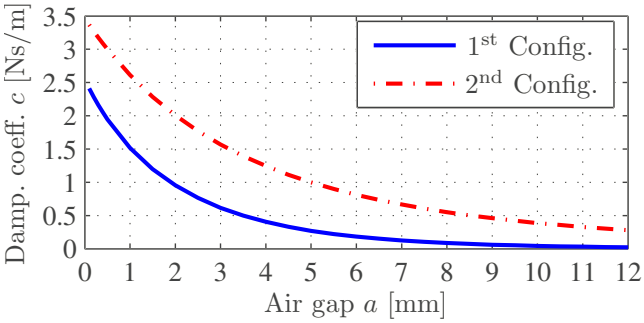

Fig. 3 Numerically estimated equivalent viscous damping for both configurations

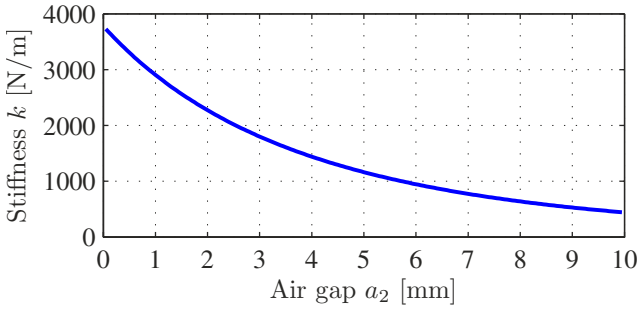

Fig. 4 Numerically estimated equivalent stiffness coefficient for second damping configuration

$$L_0 = L + 2\delta + a_2 \tag{20}$$

Due to this the integral in the calculation of the Lorentz force can be simplified yielding

$$\mathbf{F}_{\mathrm{mag}} = \int_V \mathbf{J}_m\times\mathbf{B}\,dV = -\int_{L_0-L/2}^{L_0+L/2} M_0\int_0^{2\pi}(r_m d\varphi)\mathbf{e}_\varphi\times\mathbf{B}\,dz \tag{21}$$

which leads to a magnetic force in z-direction

$$F_{\mathrm{mag},z}(a_2) = -2\pi M_0 r_m\int_{L/2+2\delta+a_2}^{3L/2+2\delta+a_2} B_r(r_m,z)\,dz \tag{22}$$

When regarding only small changes Δa_2 at the static operating point $a_{2,\mathrm{stat}}$, the magnetic force $F_{\mathrm{mag},z}$ can be linearized by expanding it in a Taylor series and neglecting higher-order terms,

$$F_{\mathrm{mag},z} \approx F_{\mathrm{mag},z}(a_{2,\mathrm{stat}}) + \underbrace{\left.\frac{\partial F_{\mathrm{mag},z}}{\partial a_2}\right|_{a_{2,\mathrm{stat}}}}_{k}\Delta a_2 \approx F_0 + k\Delta a_2 \tag{23}$$

where k denotes the equivalent stiffness coefficient of the second damping configuration.

To estimate the equivalent stiffness coefficient against the static air gap, the magnetic force F_{mag} is computed first by integrating Eq. (22) numerically with the parameters given in Table 1 using an adaptive Lobatto quadrature. To obtain the equivalent stiffness coefficient (Fig. 4), the partial derivative of the magnetic force with respect to the air gap is computed using a differential quotient.

3 Description of the Test Rig

The test rig is depicted in Fig. 5. It consists of a pair of dummy blades which are made of creep resistant steel (X 20 CrMoV 12 1) and which are clamped hydraulically on an isolation table, a shaker, a laser scanning vibrometer, and the eddy current damping

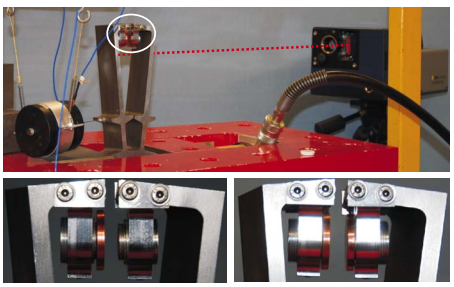

Fig. 5 Test rig consisting of two dummy blades, hydraulic clamping, shaker, laser vibrometer, and damping element in two configurations

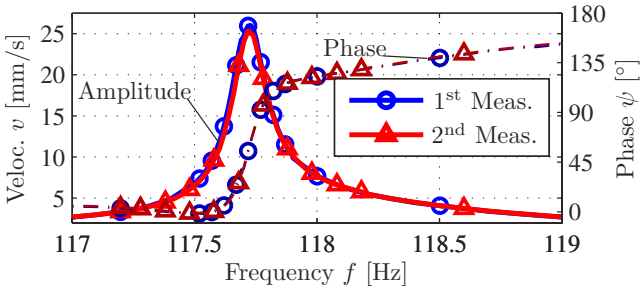

Fig. 6 Repeatability of measurements: amplitude and phase of first configuration with an air gap of a_1=1 mm

element in two configurations. The first setup consists of two aluminum mounts, a samarium cobalt magnet (Sm_2Co_{17}) which is glued into a threaded aluminum bushing, and a copper plate which is glued on a threaded aluminum bolt. That way the damping element can be fixated at the dummy blade with only little disturbance of the magnetic field through the surrounding iron material of the dummy blades and the air gap can be adjusted gradually. In the second setup permanent magnets in threaded bushings with copper plates glued on are applied in both mountings. When measuring the undamped system dummies of equivalent weight are applied to eliminate the frequency shift due to the additional masses.

To estimate the damping effect forced response, measurements are carried out using a force controlled stepped sine excitation and capturing the velocity of the blades with the vibrometer. Due to the low internal damping of the dummy blades, a frequency resolution as high as Δf=0.01 Hz is used resulting in an excellent repeatability in amplitude and phase (Fig. 6).

4 Forced Response Calculations

To validate the developed electromechanical model of the damper, a numerical forced response analysis is performed and compared with the measurements. The computation is based on a modal description applied to the finite element model of the dummy blade pair. Therefore, modal analyses of the dummy blades with the different additional masses are carried out extracting 20 eigenvalues $\omega_{0,i}$ and eigenvectors $\boldsymbol{\varphi}_i$ for the nodes at which excitation, measurement, or damping takes place, comprised in the concise modal matrix Φ. The present eigenfrequencies of the dummy blades without additional damping are identified with an impact test. As the deviation between measured and computed eigenfrequencies of the first bending modes is less than 3% (influence of moving mass of shaker) the modal base is adjusted to the measured eigenfrequencies to guarantee optimal conditions to evaluate the influence of the eddy current damping device. To estimate the material damping a fraction of critical damping $\xi = 1.41 \times 10^{-4}$ is used for all modes, which is identified by applying the half power method on the measurements in which no additional damping was applied. Since the measured response of the system is the velocity, modal velocities are calculated using the mechanical impedance:

$$\mathbf{v} = \boldsymbol{\Phi}\left[\mathrm{i}\Omega\mathbf{E} + \mathbf{diag}(2\omega_{0,i}\xi) + \boldsymbol{\Phi}^{\mathrm{T}}\mathbf{C}_{\mathrm{mag}}\boldsymbol{\Phi} - \frac{\mathrm{i}}{\Omega}(\mathbf{diag}(\omega_{0,i}^2) + \boldsymbol{\Phi}^{\mathrm{T}}\mathbf{K}_{\mathrm{mag}}\boldsymbol{\Phi})\right]^{-1}\boldsymbol{\Phi}^{\mathrm{T}}\mathbf{f}_e \tag{24}$$

where $\mathbf{C}_{\mathrm{mag}}$ denotes the viscous damping matrix which is obtained when applying the equivalent viscous damping between two opponent DOF on both dummy blades and $\mathbf{K}_{\mathrm{mag}}$ denotes the additional stiffness matrix of the second configuration.

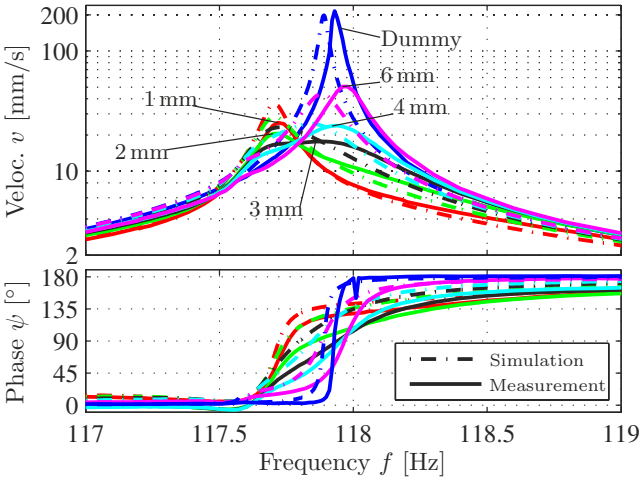

Fig. 7 Comparison of measurements and simulations: forced response functions for different static air gaps in first damping element

5 Comparison of Measurements and Simulations

5.1 First Configuration. In Fig. 7 the measured forced response of the first damping element is depicted when varying the static air gap a_1. The response belongs to a measurement point at the blade tip of the excited dummy blade and shows the response in the frequency range of the first bending modes. The blue curve corresponds to the system without the eddy current damper since only dummy masses of equal weight are applied. When applying a real damping element with an air gap a_1=6 mm, a considerable amplitude reduction can be observed. When decreasing the air gap the amplitude reduction increases at first but reaches an optimum with an air gap of a_1=3 mm. A further decrease in the air gap leads to a new peak, which differs slightly from the initial resonance frequency and even increases more with smaller air gaps. It is remarkable that the highest damping coefficient does not lead to the least resonance amplification. Choosing the optimum an amplitude reduction in more than 20 dB from 215 mm/s to 18 mm/s can be observed.

The simulated frequency response functions (FRF) are in good agreement with the measurements. They show the same characteristic curves and the amplitude reductions due to additional damping fits well. Again an air gap of 3 mm leads to the lowest resonance amplification and a further decrease in the air gap causes an increase in amplitude with a frequency shift of about 0.3 Hz, which equals 0.25%.

To comprehend the observed phenomena of an optimal damping coefficient a consideration of the modes in the examined frequency range is revealing. In Fig. 8 it is depicted that the dummy

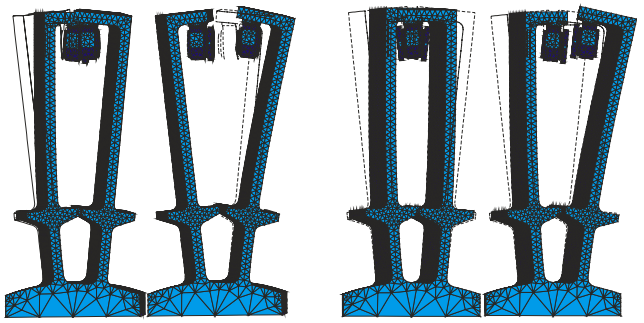

Fig. 8 First bending modes of dummy blades. Left: first setup (117.6 Hz and 117.9 Hz) and right: second setup (115.008 Hz and 115.068 Hz)

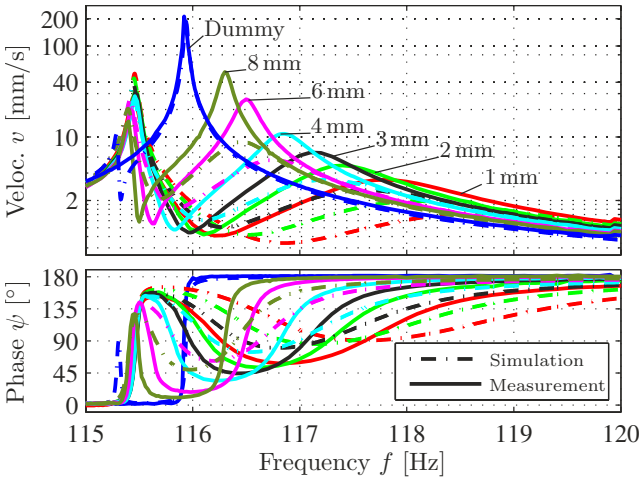

Fig. 9 Comparison of measurements and simulations: forced response functions for different static air gaps in damping element using the second set up

blades possess an in-phase and an out-of-phase bending mode with very similar eigenfrequencies. Due to a small deviation of the weight of both parts of the damping element in the first configuration those modes degenerate into two modes, where only one blade is mainly in motion. Therefore, when exciting the left blade without additional damping its response is much stronger because the corresponding mode shape (117.9 Hz) is mainly excited by the applied excitation. When installing a damper between the two blades the excitation of the second blade increases due to the damping force. Therefore, when decreasing the air gap the second resonance appears as a small peak in the amplitude response (cyan curve at approximately 117.6 Hz) which rises with a further decrease. In the case of the least resonance amplification the smoothest curve is present. A further increase in the damping coefficient leads to a mode coupling of the two modes so that both blades vibrate more in phase which results in less energy dissipated and leads to a new resonance which is damped more weakly and differs in its frequency. This is also in good agreement with the measured and simulated phase response functions. The undamped system shows the steepest phase shift, with an increase in the damping the phase shift flattens but when exceeding the optimal damping the gradient increases again.

5.2 Second Configuration. In Fig. 9 the measured and simulated forced responses for the second configuration are depicted. They also belong to a measurement point on the left blade. Again the blue curve corresponds to the undamped system. Here it becomes obvious that all damped curves consist of two maxima and one minimum. The frequency of the first maximum rises slightly with a decrease in the air gap, the frequency of the minimum and the second maximum rises considerably. The amplitude of the second peak decreases strongly, whereas the amplitude of the first peak increases slightly.

These phenomena appear due to two additive effects. As depicted in Sec. 2.3 the effect of the second damping element can be regarded as a parallel connection of a viscous dashpot damper and a spring element with nonlinear characteristics. Therefore, when exciting one blade and measuring its amplitude the second blade acts as a damped vibration absorber since it is connected via a stiffness and no external excitation is applied on that dummy blade. This results in a maximum of in-phase motion of both blades, a minimum where most vibration energy is located in the second blade and a maximum of out-of-phase motion. When increasing the coupling stiffness the frequency of antiresonance and out-of-phase mode increase considerably whereas the frequency of the in-phase motion only changes slightly.

Furthermore, the damping rises heavily with a decrease in the static air gap. But since the damping element acts only relatively between the two blades only the out-of-phase resonance can be affected. When taking only the out-of-phase mode into account for the estimation of the damping effect an amplitude reduction of 34 dB can be denoted. The observed phenomena also correspond well with the phase response. In case of a large air gap, it is dominated by the stiffness where the antiresonance corresponds to a phase jump. With a decrease in the air gap the damping influence is superimposed.

The simulated forced response functions feature the same curve characteristics consisting of an in-phase maximum, a minimum, and an out-of-phase maximum and, therefore, correspond qualitatively with the measured FRFs. So the existence of the proposed superposition of damping and stiffness effect could be shown. However, a small deviation between simulation and measurement has to be denoted: The frequencies of minimum and out-of-phase maximum in the simulation are higher than the measured ones for all air gaps. Besides this the amplitudes of the out-of-phase maximum are smaller for all air gaps. Hence, it has to be stated that stiffness and damping coefficient are overestimated for this configuration in the simulations. Therefore, further investigations seem appropriate to improve the quality of modeling.

6 Conclusions

In this paper two types of eddy current based damping elements for the suppression of turbine blade vibrations have been investigated in a numerical as well as in an experimental analysis. The first configuration consists of a permanent magnet and a copper plate. In this paper the damping effect of that kind of assembly has been investigated when acting relatively between two vibrating structures as it is difficult to realize damping against the inertial frame on rotating machinery. Forced response measurements were taken out at a stationary test rig evaluating the damping effect in this configuration. In simulations the eddy current damping effect was estimated with an equivalent viscous damping coefficient, which resulted in a good agreement between the forced response calculations and the measurements. It revealed that for this test assembly an amplitude reduction of more than 20 dB can be realized with only a slight shift in resonance frequency of about 0.25%.

Furthermore, a second type of eddy current damping element has been analyzed in this paper. It consists of two magnets facing each other with their like-poles and two electrical conductors fixated at the magnets' front surfaces. In case of vibrations, those two assemblies experience a relative motion causing a time-varying magnetic field within the copper plates and, therefore, generating transformer EMF which lead to energy dissipation. A theoretical model of the proposed assembly has been established by applying electromagnetic-mechanical theory resulting in an equivalent stiffness coefficient to describe conservative magnetic forces and an equivalent damping coefficient to describe nonconservative magnetic forces. The tests confirm the existence of conservative as well as nonconservative magnetic forces, which lead to a considerable amplitude reduction. Simulations utilizing the equivalent parameters match qualitatively the forced response measurements.

Contrary to the previous studies on eddy current damping where damping was realized against the inertial frame it became apparent that in the case of a relative damping it is not the highest damping coefficient which provides the least resonance amplification. Those phenomena occur due to mode coupling effects caused by the viscous damping and, therefore, depend strongly on the vibrating structure indicating that the results may be transferred with care on a cyclic structure. Hence, in future work further investigations based on the results presented in Ref. [22] and in this paper concerning the eddy current damping on cyclic structures will be considered.

References

[1] Sanliturk, K. Y., Ewins, D. J., and Stanbridge, A. B., 2001, "Underplatform Dampers for Turbine Blades: Theoretical Modelling, Analysis and Comparison With Experimental Data," J. Eng. Gas Turbines Power, **123**, pp. 919–929.

[2] Firrone, C. M., Allara, M., and Gola, M. M., 2008, "A Contact Model for Nonlinear Forced Response Prediction of Turbine Blades: Calculation Techniques and Experimental Comparison," ASME Paper No. GT2008-51231.

[3] Panning, L., Sextro, W., and Popp, K., 2000, "Optimization of Interblade Friction Damper Design," ASME Paper No. GT-2000-0541.

[4] Panning, L., Popp, K., Sextro, W., Götting, F., Kayser, A., and Wolter, I., 2004, "Asymmetrical Underplatform Dampers in Gas Turbine Bladings: Theory and Application," ASME Paper No. GT-2004-53316.

[5] Walter, H. E., 1892, "Electro-Magnetic Brake," U.S. Patent No. 467,243.

[6] Schieber, D., 1975, "Optimal Dimensions of Rectangular Electromagnet for Braking Purposes," IEEE Trans. Magn., **11**(3), pp. 948–952.

[7] Lee, K., and Park, K., 2002, "Modeling Eddy Currents With Boundary Conditions by Using Coulomb's Law and Method of Images," IEEE Trans. Magn., **38**(2), pp. 1333–1340.

[8] Meier-Credner, W.-D., 2000, "Die lineare Wirbelstrombremse-Entwicklung und Einsatz im ICE 3," Eisenbahntechnische Rundschau, **49**(6), pp. 412–418.

[9] Sodano, H. A., 2005, Development of Novel Eddy Current Dampers for the Suppression of Structural Vibrations," Ph.D. thesis, Virginia Polytechnic Institute and State University, Blacksburg, Virginia.

[10] Kligerman, Y., and Gottlieb, O., 1998, "Dynamics of a Rotating System With a Nonlinear Eddy-Current Damper," Trans. ASME, J. Vib. Acoust., **120**, pp. 848–853.

[11] Graves, K., Toncich, D., and Iovenitti, P., 2000, "Theoretical Comparison of Motional and Transformer EMF Device Damping Efficiency," J. Sound Vib., **233**, pp. 441–453.

[12] Kwak, M., Lee, M., and Heo, S., 2003, "Vibration Suppression Using Eddy Current Damper," Korean Society for Noise and Vibration Engineering, **13**(10), pp. 760–766.

[13] Bae, J., Kwak, K., and Inman, D., 2005, "Vibration Suppression of a Cantilever Beam Using Eddy Current Damper," J. Sound Vib., **284**(3-5), pp. 805–824.

[14] Sodano, H., Bae, J., Inman, D., and Belvin, W., 2005, "Concept and Model of Eddy Current Damper for Vibration Suppression of a Beam," J. Sound Vib., **288**, pp. 1177–1196.

[15] Sodano, H., Bae, J., Inman, D., and Belvin, W., 2006, "Improved Concept and Model of Eddy Current Damper," ASME J. Vib. Acoust., **128**, pp. 294–302.

[16] Ebrahimi, B., Khamesee, M. B., and Golnaraghi, M. F., 2008, "Design and Modeling of a Magnetic Shock Absorber Based on Eddy Current Damping Effect," J. Sound Vib., **315**, pp. 875–889.

[17] Sodano, H., Inman, D., and Belvin, W., 2006, "Development of a New Passive-Active Magnetic Damper for Vibration Suppression," ASME J. Vib. Acoust., **128**, pp. 318–327.

[18] Sodano, H., and Inman, D., 2007, "Non-Contact Vibration Control System Employing an Active Eddy Current Damper," J. Sound Vib., **305**, pp. 596–613.

[19] Sodano, H. A. and Inman, D. J., 2008, "Modeling of a New Active Eddy Current Vibration Control System," ASME J. Dyn. Syst., Meas., Control, **130**, p. 021009.

[20] Tonoli, A., 2008, "Transformer Eddy Current Dampers for the Vibration Control," ASME J. Dyn. Syst., Meas., Control, **130**, pp. 031010.

[21] Ernst, P., Hunziker, R., and Rhyner, J., 1999, "Magnetische Vorrichtung zur Dämpfung von Schaufelschwingungen bei Turbomaschinen," Patent No. DE 199 37 146 A 1.

[22] Siewert, C., Panning, L., Hohl, A., Bürge, A., and Gerber, C., 2007, "Damping of Structural Vibrations Using an Electromotive Eddy Current Damper," Proc. Appl. Math. Mech., **7**, pp. 4040039–4040040.

[23] Lehner, G., 2005, *Elektromagnetische Feldtheorie: Für Ingenieure und Physiker*, 5th ed., Springer, New York.

[24] Bronshtein, I., Semendyayev, K., Musiol, G., and Muehlig, H., 2007, *Handbook of Mathematics*, Springer-Verlag, New York, Vol. 5.

[25] Kupfmüller, K., Mathis, W., and Reibiger, A., 2005, *Theoretische Elektrotechnik: Eine Einführung*, 17th ed., Springer-Verlag, Berlin.

[26] Cheng, D., 1989, *Field and Wave Elektromagnetics*, 2nd ed., Addison-Wesley, Reading, MA.

Assessment of Multiobjective Genetic Algorithms With Different Niching Strategies and Regression Methods for Engine Optimization and Design

Yu Shi

Rolf D. Reitz

Engine Research Center,
University of Wisconsin–Madison,
1500 Engineering Drive,
Madison, WI 53706

*In a previous study (Shi, Y., and Reitz, R. D., 2008, "Assessment of Optimization Methodologies to Study the Effects of Bowl Geometry, Spray Targeting and Swirl Ratio for a Heavy-Duty Diesel Engine Operated at High-Load," SAE Paper No. 2008-01-0949), nondominated sorting genetic algorithm II (NSGA II) (Deb, K., Pratap, A., Agarwal, S., and Meyarivan, T., 2002, "A Fast and Elitist Multiobjective Genetic Algorithm: NSGA-II," IEEE Trans. Evol. Comput., **6**, pp. 182–197) performed better than other popular multiobjective genetic algorithms (MOGAs) in engine optimization that sought optimal combinations of the piston bowl geometry, spray targeting, and swirl ratio. NSGA II is further studied in this paper using different niching strategies that are applied to the objective space and design space, which diversify the optimal objectives and design parameters, accordingly. Convergence and diversity metrics are defined to assess the performance of NSGA II using different niching strategies. It was found that use of design niching achieved more diversified results with respect to design parameters, as expected. Regression was then conducted on the design data sets that were obtained from the optimizations with two niching strategies. Four regression methods, including K-nearest neighbors (KNs), kriging (KR), neural networks (NNs), and radial basis functions (RBFs), were compared. The results showed that the data set obtained from optimization with objective niching provided a more fitted learning space for the regression methods. KNs and KR outperformed the other two methods with respect to prediction accuracy. Furthermore, a log transformation to the objective space improved the prediction accuracy for the KN, KR, and NN methods, except the RBF method. The results indicate that it is appropriate to use a regression tool to partly replace the actual CFD evaluation tool in engine optimization designs using the genetic algorithm. This hybrid mode saves computational resources (processors) without losing optimal accuracy. A design of experiment (DoE) method (the optimal Latin hypercube method) was also used to generate a data set for the regression processes. However, the predicted results were much less reliable than the results that were learned using the dynamically increasing data sets from the NSGA II generations. Applying the dynamical learning strategy during the optimization processes allows computationally expensive CFD evaluations to be partly replaced by evaluations using the regression techniques. The present study demonstrates the feasibility of applying the hybrid mode to engine optimization problems, and the conclusions can also extend to other optimization studies (numerical or experimental) that feature time-consuming evaluations and have highly nonlinear objective spaces.*
[DOI: 10.1115/1.4000144]

1 Introduction

More stringent emission regulations and increasing petroleum prices are requiring the engine industry to seek optimum engine designs. As a result, many advanced combustion concepts emerged and were applied to engine designs recently such as premixed charge compression ignition (PCCI) [1] and modulated kinetics (MK) [2] engines. These advanced strategies use many parameters (injection pressure, number of injection pulses, EGR rate, boost, etc.) to fine tune the combustion process in order to achieve ultra-low emissions and fuel consumption. The vast number of variables in these combustion strategies results in a large number of iterations required to achieve an optimal engine design. Therefore, the expense of experimentally optimizing and calibrating engine designs is becoming more and more costly.

With the increasing prediction ability of engine simulation tools, engine design aided by relatively low cost CFD modeling is becoming more popular in both industry and academia. Because of their simplicity, applicability, and parallel ability, genetic algorithms are widely applied in optimizing engineering design. For example, Wickman et al. [3] and Bergin et al. [4] used a single objective genetic algorithm to optimize engine systems, and achieved improved combustion and reduced emissions for small engines. Genzale et al. [5] and Shi and Reitz [6] optimized heavy-duty engines under different operating conditions using different multiobjective genetic algorithms (MOGAs). In their studies, the KIVA CFD code with a relatively simple and efficient combustion model (characteristic time combustion model) was employed to evaluate engine performances, and the optimization processes

Contributed by IC Engine Division of ASME for publication in the JOURNAL OF ENGINEERING FOR GAS TURBINES AND POWER. Manuscript received April 30, 2009; final manuscript received May 25, 2009; published online March 5, 2010. Editor: Dilip R. Ballal.

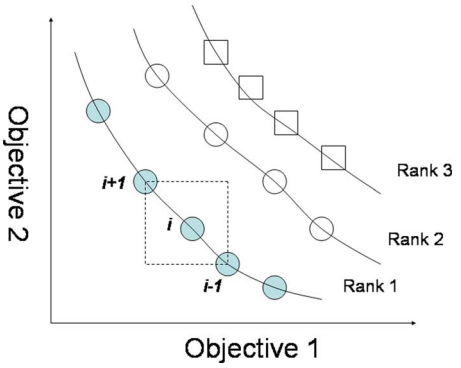

Fig. 1 Illustrations of Pareto solutions, ranking, and crowding distance

were terminated at a certain generation, based on the previous experience.

Using a single objective genetic algorithm, the convergence of the optimization process can be monitored by observing the monotonically increasing or decreasing objective function only. But for a MOGA, it is impossible to justify the convergence of the optimization process by just observing one or even a few objectives. Instead, all objectives need to be considered systematically. Therefore, it is necessary to define an explicit convergence curve that is produced during the optimization process for using MOGAs in engine optimization. In addition, from the viewpoint of designers, in most cases, more diversified designs are desirable, and this can be achieved by implementing a niching method to the original MOGA. In order to assess the diversity of the optimum results in either objective or design space, a diversity metric is also needed.

In the study of Shi and Reitz [6,7], a MOGA, NSGA II [8], was found to perform better for engine optimization in terms of efficiency and optimality of the results, and an efficient multidimensional CFD tool with detailed chemistry was also developed [9,10]. Combining the efficient algorithm and the CFD tool with the efficient chemistry solver, engine optimization using CFD tools with detailed chemistry becomes practical, but the calculation still requires a large number of processors. In order to further save computational resources, several regression methods were compared in the present study to assess their capacity of partly replacing real evaluations from the CFD tools. It was found that a dynamical learning strategy is able to maintain prediction accuracy using selected regression methods. Details of optimum engine designs are therefore not the main subject of this paper. Focus is placed on the discussion of optimization and regression methods to improve efficiency and to save computational resources for engine optimization problems.

2 Models and Methodologies

2.1 Pareto Optimum and NSGA II With Different Niching Strategies. Typical engineering design problems always involve multiple possibly contradicting objectives, in which optimizing one of the objectives usually results in deteriorating the others. Thus, it is necessary to define the term "optimum." The notion of optimum that is most commonly adopted is referred as the Pareto optimum, as in Ref. [11]. As illustrated in Fig. 1, the solid symbols consist of Pareto optimal cases because they are not outperformed by other cases (open symbols) in this problem, which aims to minimize both objectives. A strict mathematical definition of the Pareto optimum can be found in Ref. [11]. It can be stated that there are two goals in multiobjective optimizations: (1) to find a set of solutions as close as possible to the Pareto optimal front, and (2) to find a set of solutions as diverse as possible.

The first goal is obvious in the sense that better solutions are always desired. The second goal can be further explained by an example of engine optimization. For instance, in-cylinder clean combustion techniques are usually combined with aftertreatment methods for the reduction in emissions. In this case, optimal solutions of in-cylinder combustion can guide the selection of aftertreatment devices. This requires that the optimization process provides solutions with diversified objective functions such as emission results. However, under other circumstances, more diversified parameters of the solutions indicate that it is more likely to obtain a design that can minimize the changes to the current baseline design in order to save redesigning costs such as the piston geometry of engines. The diversity of optimal designs may focus on different aspects (either on the objective space or design space), based on the requirements of customers and designers. This can be achieved by performing different niching strategies with MOGA, as shown next.

NSGA II employs both the elite-preserving strategy, as well as an explicit diversity-preserving mechanism. The algorithm first randomly generates a predefined size (N) population, which undergoes conventional selection, crossover, and mutation procedures to produce offspring for the next generation. From the second generation, the parent generation (size N) competes with its offspring generation (size N) to introduce elitism. In this procedure, the crowding tournament selection is used, and two rules are applied to the selection operator: (1) Solutions with higher ranks are given preference to be selected, and (2) if they have the same rank, the less crowding distance cases are assigned a higher priority. The second rule is essentially equivalent to the niching strategy in many other MOGAs, such as the adaptive range multiobjective genetic algorithm (ARMOGA) [12]. Although it is applied with different methodologies in different MOGAs, the niching strategy is a method that can detect whether optimal designs are forming a crowded cluster, and if so, to guide the MOGA to produce more diversified designs based on the previous information.

Figure 1 illustrates the concepts of rank and crowding distance. As shown in this figure, the solid circles are the Pareto cases that dominate (outperform) other cases. However, they do not dominate each other, and thus, they form a nondominated front, defined as the first rank. The same procedure can be applied to the rest of the solutions to find a second rank, and so on until every solution is assigned a rank. The crowding distance is defined by the average distance of a solution to its nearest neighbors. For example, the crowding distance of solution i in Fig. 1 is the average side length of the rectangle (the dashed box). The mathematical definition of the crowding distance can obviously be applied to higher dimensions, although it is only shown in a 2-D plot here for a clear view. Therefore, N populations will be selected from $2N$ combined populations based on the aforementioned competition rules. In this way, a crowded cluster of solutions can be prevented from evolving into the next generation, and the optimal solutions can be distributed on the Pareto front more uniformly. In the original NSGA II [13] source code, such niching strategy is applied to the objective space, which ensures that diversified objective functions are produced during the optimization process. In the present study, the NSGA II source code has been modified to integrate the niching strategy to the design space so that more diverse design parameters can be expected. It was thought that performing both niching strategies concurrently to the objective and design spaces would reduce the optimization efficiency, and thus, either the objective niching or the design niching was performed for each of the case studies as follows.

2.2 Convergence and Diversity Metrics

2.2.1 Convergence Metric. Observation on the movement of the Pareto front as the optimization proceeds indicates if the optimization process moves towards convergence. However, if the

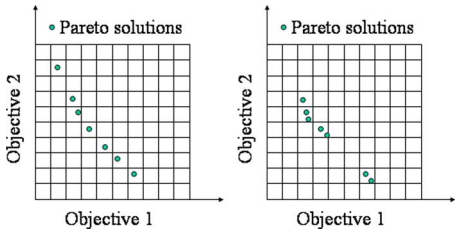

Fig. 2 Illustration of diversity metric

number of objectives exceeds three, the visualization of the Pareto front becomes impossible. Therefore, a convergence metric of the optimization process using MOGAs has to be defined in order to better monitor the optimization process. Equally speaking, defining a convergence metric can be regarded as reducing the dimensionality of the Pareto front to one dimension. The present study adopted the method of Deb and Jain [14], which was also modified for the current engine optimization study, and the method is described in the following steps.

1. Identify the Pareto (nondominated) solutions of each generation that has been done, and those n solutions form a solution pool P.
2. From the second generation, the Pareto solutions of the current generation can be compared with solutions in the pool P that is formed by the previous generation(s) in Step 1. For each Pareto solution of the current generation, calculate the smallest normalized Euclidean distance to the n solutions of the pool P using

$$d_i = \min_{j=1}^{n} \sqrt{\sum_{k=1}^{M} \left(\frac{f_{k,i} - f_{k,j}}{f_k^{\max} - f_k^{\min}} \right)^2} \tag{1}$$

   where M is the total number of objectives, and $f_k^{\max}$ and $f_k^{\min}$ are the maximum and minimum values of the k-th objective from all n solutions in the pool P, respectively.
3. A convergence metric is determined by averaging the normalized distance for all nn Pareto solutions of the current generation

$$C^N = \frac{1}{nn} \sum_{i=1}^{nn} d_i \tag{2}$$

4. In order to keep the value of the convergence metric within [0,1], [0,1] is normalized by its maximum value after all N generations, being assigned a convergent value from Step 3, that is

$$\bar{C}^j = C^j / \max(C^i, i = 1, \ldots, N), \quad j = 1, \ldots, N \tag{3}$$

   Usually, the maximum value is from the beginning generations.

2.2.2 Diversity Metric. In order to assess the diversity of the Pareto solutions in either the objective space or design space, a corresponding metric is needed. Although more complicated methods were employed in Refs. [14,15], this paper introduces a simplified method for measuring the diversity, which is proper for the present engine optimization and similar engineering problems as well. Taking the objective space for example, the method divides the space into many subgrids based on the user-specified spans, and if more subgrids contain sole or few Pareto solutions, the results are deemed to be more diverse. As further illustrated by Fig. 2, the set of the Pareto solutions in the left figure is better than the right one in terms of the diversity of the two objectives. The method can also be extended to study more objectives. However, since the number of Pareto solutions is usually of the order of 100 in typical engine optimization problems [5–7], it is suggested that the number of studied objectives should not exceed 3, and the number of spans of each objective should not exceed 10, in order to keep the total subgrids of the order of 1000. Obviously, the same method can be applied to investigate the design space as well.

To further quantify the diversity metric, different weights are assigned to the subgrids that contain different numbers of Pareto solutions, and these subgrids containing fewer solutions are given higher weights ($1/n$, where n is the number of Pareto solutions that are located in that grid). Therefore, the averaged weighting summation for all subgrids that include the Pareto solutions represents a quantified diversity metric, and a larger value indicates more diversified solutions (maximum value is 1).

2.2.3 Regression Methods. Using regression methods, response surfaces of the objective functions to the design parameters can be built based on the knowledge learned from existing data sets, and then the response surfaces can be employed to approximate the objectives of a design corresponding to the value of the design parameters. If a design that is evaluated experimentally or numerically with designing software, e.g., KIVA, is defined as a real design, the one that is evaluated based on the response surfaces built from regression methods can be regarded as a virtual design, accordingly. Using the same inputs of design parameters, the closer the objectives of the virtual design are to those of the real design, the better the regression method is. It is expected that regression methods that produce reliable virtual designs (with much less cost) can partly replace the functionality of CFD tools or experiments in engineering optimization problems if the confidence of the fidelity of such methodology can be proved through an a priori study. Four regression methods, including K-nearest neighbor (KN), kriging (KR), neural network (NN), and radial basis function (RBF) methods, were used to explore their capacity of data mining for engine optimization. They were chosen because of their popularity [16–19], and also due to the fact that they were integrated into the commercial optimization software MODEFRONTIER™ 4.0 [20], which was used in the current study. A detailed mathematical description of these regression methods is not the subject of this paper, and thus, only brief introductions are given.

The KN method is a very simple regression method, which estimates the value of the objective functions of the evaluated design based on its KN designs (10 in this study). The distance between the evaluated design and its neighbors can be used to weight the neighbors' contribution, so that the nearer neighbors contribute more to the average than the more distant ones. The method is not computationally intensive, so it is suitable also for very large databases, i.e., greater than 1000. But it is poorly informative and highly localized on small data sets, and thus, its prediction ability is limited, especially for data extrapolation. KR belongs to the family of linear least-squares estimation algorithms, and was originally the main tool for making previsions employed in geostatistics (named after Professor Daniel Krige). Its behavior is controlled by a covariance function, called a variogram (Gaussian in this study), which rules the correlation between the values of the function at different points. A function can be rougher or smoother, can exhibit large or small ranges of variation, can be affected by a certain amount of noise, and all these features can be embodied in a variogram model [20]. The KR method is particularly applicable for highly nonlinear responses, but it is relatively computationally expensive. The neural network methods have been widely and successfully applied to engineering problems. The one available in MODEFRONTIER™ 4.0 is based on classical feed forward NNs with one hidden layer, and with an efficient Levenberg–Marquardt back propagation training algorithm. The initialization of the network's parameters is based on the proper initialization approach by Nguyen and Widrow [20,21]. RBFs are a powerful tool for multivariate scattered data interpolation. The values of those functions only depend on the distance from a specified reference origin, and representative RBFs are Gaussian (used in this study), multiquadric, polyharmonic spline,

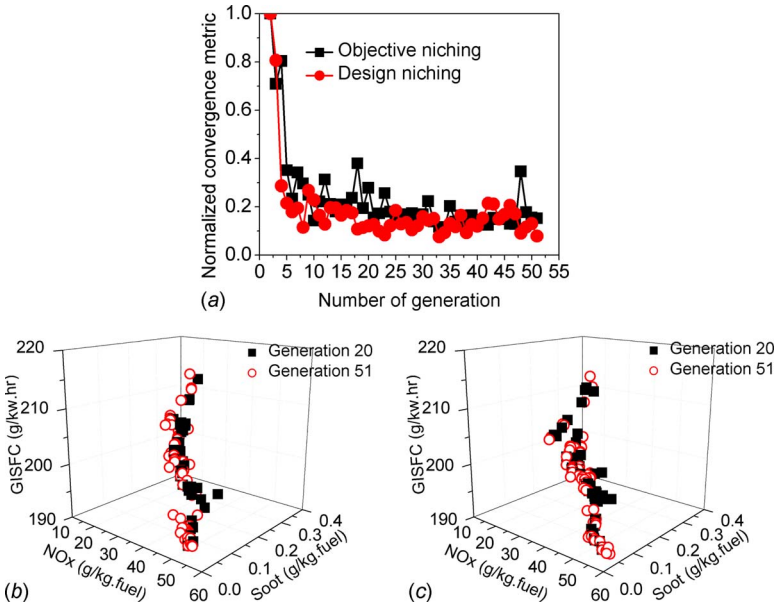

Fig. 3 Comparison of (*a*) convergence metric, (*b*) Pareto front from the optimization using the objective niching, and (*c*) Pareto front from the optimization using the design niching

and thin plate spline functions. They can be used to build an approximation function that is represented as a sum of N radial basis functions, each associated with a different center and weight. The weights can usually be estimated based on linear least-squares.

3 Results and Discussion

3.1 Results of Convergence and Diversity Metrics. Optimization results from using KIVA3V2 [22] and NSGA II with two niching strategies are compared in terms of their convergence and diversity metrics and performance. Discussion of the submodels of the KIVA3V2 code and the algorithm relevant parameters of NSGA II is found in Refs. [6,7]. The population size was set to 24, and a total of 51 generations were evaluated for each group, which corresponds to 1224 cases. Typical operation run time was 25 days for a complete optimization cycle on 24 processors of an SGI Origin 2000 [6]. Nine design parameters were optimized in order to obtain optimum designs with three improved objectives (reduced NO_x, soot emissions, and the fuel consumption indicated by gross indicated specific fuel consumption (GISFC)) for a heavy-duty diesel engine, operated under high-load. The nine design parameters include the start-of-injection timing (SOI), swirl ratio, spray angle, and six other parameters that define the piston geometry using an automated grid generator, Kwickgrid [3]. The details of these parameters can be found in Ref. [6] as well.

Figure 3(*a*) shows normalized convergence metrics using objective niching and design niching. The fluctuations that appear in both curves imply that the later generations in the optimization process do not necessarily produce solutions better than the previous ones. However, in general, the value of the convergence metric becomes smaller as the optimization proceeds. It is seen that both optimization processes converge very fast (in the first ten generations), and after about 20 generations, the curves become relatively flat, which indicates that the Pareto front does not move significantly from generation 20 to the end of the optimization. To further illustrate this, Pareto fronts in the objective space of generations 20 and 51 for the two niching strategies are depicted in Figs. 3(*b*) and 3(*c*), respectively. It is observed that the Pareto fronts of generation 20 and 51 overlap in many places, and their relative locations with respect to the origin are very close as well. The consistency in Figs. 3(*a*)–3(*c*) also proves the fidelity of the present method of calculating the convergence metric for MOGAs. Figure 3 also concludes that the objective niching and the design niching perform similarly in terms of their convergent rates. The results discussed here reveal the significance of dynamically generating the convergence metric in optimization, because the designer can have sufficient confidence to terminate the optimization process if it is seen that further evaluations are redundant.

Since the study of convergence metrics of the two niching methods merely represents their historic performance (comparison between the later generations and previous generations), it is important to also compare the two methods directly in terms of the optimality of their Pareto solutions. The same method described in Ref. [7] was used to assess their performance by comparing two quantities. The mean distance to the Pareto front (MDPF) indicates how close the current Pareto front is to the ideal set of optimum solutions, and the smaller the better. The number of Pareto solutions (NPS) shows how many Pareto solutions have been produced so far, and a larger value is desirable. The comparison is given in Fig. 4, which shows that the two niching methods perform closely with respect to these two quantities, although, it is seen that the design niching method generated slightly better results since its MDPF values are a little smaller than those with objective niching.

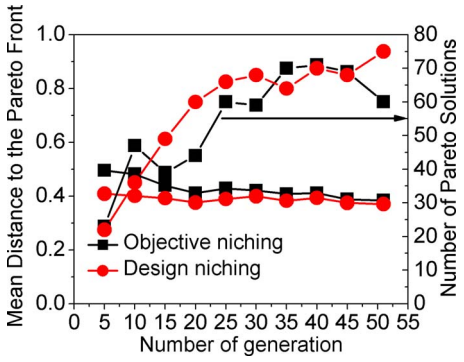

Fig. 4 Comparison of performance

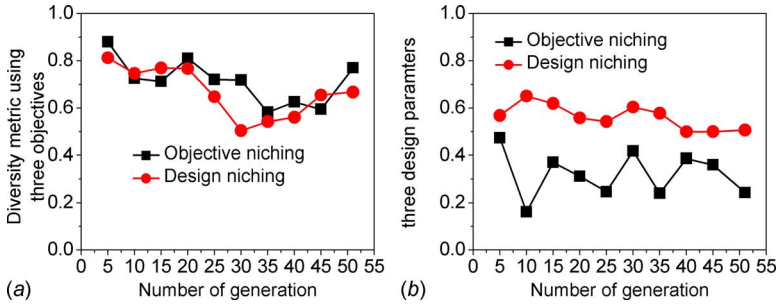

Fig. 5 Comparison of (*a*) diversity metric in the objective space, and (*b*) diversity metric in the design space

The diversity metric was analyzed based on the values of the objectives and design parameters of the Pareto solutions of the optimizations using the two niching methods. For the objectives, the investigated ranges were determined automatically by the maximum and minimum values of that objective from all Pareto solutions, up to the current generation, and the ranges were discretized with ten spans (this corresponds to 1000 grids in the three-dimensional objective space). For the design parameters, the investigated boundaries were prespecified prior to the optimization, and in this paper, only three parameters, which are the SOI, swirl ratio, and spray angle, were analyzed. Because the investigated range of the start of injection was limited to −12 to −15 aTDC [6], it was discretized by three spans, and ten spans were used for the other two parameters, which are in ranges of 0.5–2.0 and 60.0–85.0 for swirl ratio and spray angle, respectively [6].

Figure 5(*a*) shows that the diversity metrics in the objective space for the two niching methods are close, which further indicates that using both niching strategies can produce similar sets of Pareto solutions with respect to the diversified objectives, i.e., emissions and fuel consumption. But by simply altering the objective niching to design niching, the optimization process produced more diversified designs, as seen in Fig. 5(*b*). At the end of the optimization for objective niching, there was no grid in the design space containing just one Pareto solution, and there was one grid containing two Pareto solutions, and the undesirable result was that 27 Pareto solutions were clustered on one grid. For the design niching, there were six grids containing only one Pareto solution, and a maximum of 14 Pareto solutions were found in one grid. The results proved the superiority of design niching when implemented into the NSGA II code.

3.2 Comparison of Regression Methods. Four regression methods were tested, and data sets calculated from KIVA were used to train those regression methods in order to generate corresponding response surfaces that reflect the relationships between the design parameters and the objectives. Predictions of an entire GA generation (24 cases with the present population size), based on the response surfaces (virtual design), were compared with the results calculated by the KIVA code (real design), and the relative errors between the objectives of the virtual and real designs were used to quantify the performance of each regression method. To gain more statistical information, the mean, maximum, median, and minimum values of the error are reported, as well as the standard deviation of the error.

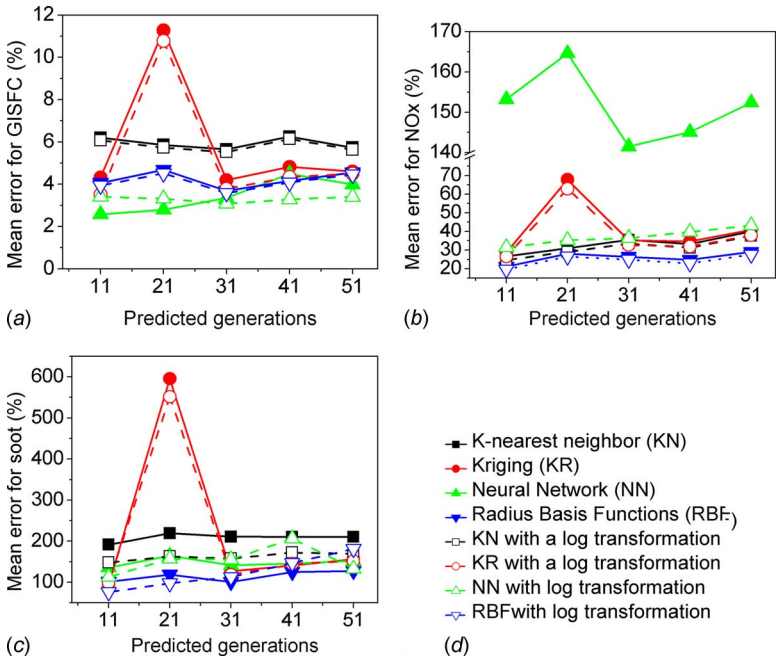

Fig. 6 Comparison of regression methods trained with a data set generated with a DoE method: (*a*) mean %error for GISFC, (*b*) mean %error for NO_x, (*c*) mean %error for soot, and (*d*) legend

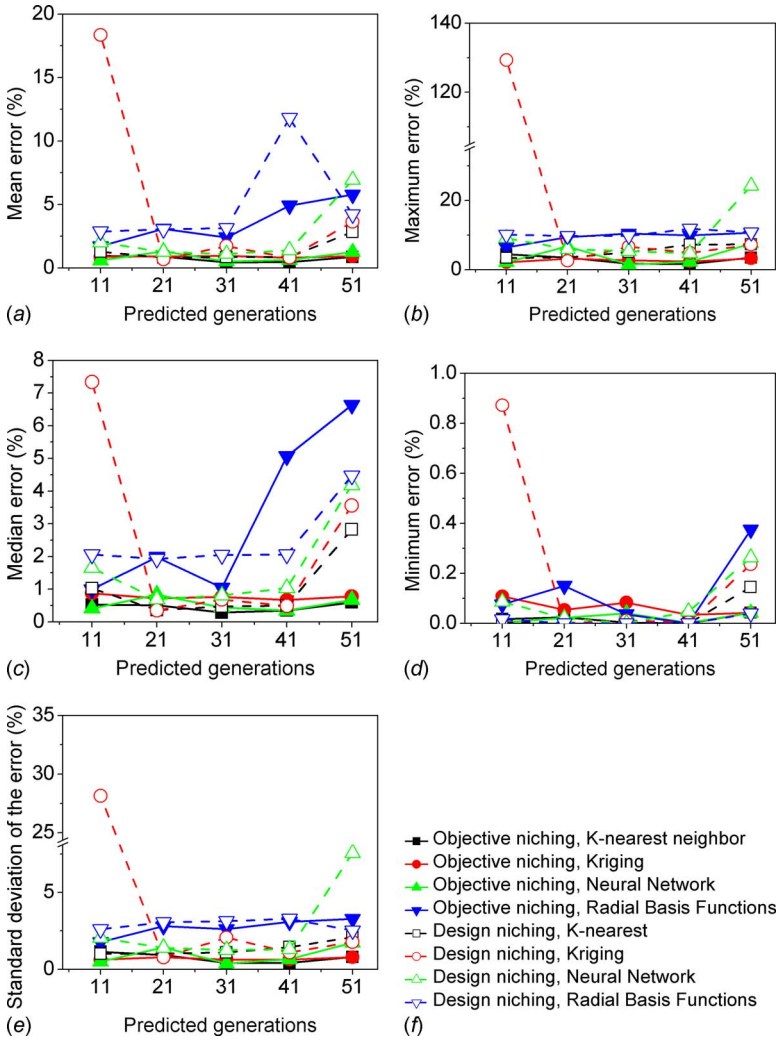

Fig. 7 Comparison of regression methods trained with data sets from the optimization process using different niching strategies: %errors of GISFC, (*a*) mean %error, (*b*) maximum %error, (*c*) median %error, (*d*) minimum %error, (*e*) standard deviation of the %error, and (*f*) legend

As a preliminary test, a design of experiment (DoE) method, the optimum Latin hypercube method, was used to produce a set of design parameters. A total of 120 cases were created based on the investigated range [6] of the design parameters, and KIVA code was first run to obtain the objectives of these cases. This process created a data pool (more uniformly distributed than the GA generated data pool) to train the regression methods. Since KIVA results are available from the previous optimization studies, several generations were selected to test the performance of the regression methods, and without losing generality, only generations from the group using objective niching are considered here. According to Brahma et al. [18] and the authors' experience, a logarithmic transformation (similar to the concept of Box-Cox transformation [23]) was applied to the objectives, i.e., the objectives (NO_x, soot, and GISFC) of the trained data set were transformed by a logarithm function, and correspondingly, the predicted results based on this data set need to undergo a power of ten transformations before comparing with KIVA results. It is noted that the values of soot emissions ranged from 10^{-3} g/kg to 10^{1} g/kg of fuel in the present study, and if a logarithmic transformation was directly applied, the resulting values could be negative and positive. In the authors' experience, this deteriorates the prediction accuracy of the virtual designs, and thus, the logarithm transformation for soot emissions was given by

$$\text{soot}_{\log} = 1 - \log(\text{soot})$$

to ensure positive soot values after logarithmic transformation. Another advantage of using this formula is that it prevents unrealistic negative soot values from being produced for the virtual designs.

The generated response surfaces, using the four regression methods, were used to predict the objectives for the cases from five generations (11, 21, 31, 41, and 51) of the group using the objective niching, and only the mean errors were reported here. It is seen in Fig. 6 that the mean error of the GISFC is the smallest, which implies that the relationship between the GISFC (i.e., engine power since the amount of injected fuel was fixed) and the design parameters is less complicated than that of emissions, and thus, can be well captured by the regression methods. The complicated influences of the design parameters on the soot emissions cause unsatisfactory prediction accuracy, as shown in Fig. 6(*c*). In general, the mean errors of all regression methods for each objective are of the same order of magnitude, and the RBF method performs slightly better than the others on the emissions, which could be due to its suitability for scattered data (generated by DoE here) interpolations. Further observation shows that the implementation of the logarithm transformation improves the prediction accuracy for most of the cases, especially for soot emissions, al-

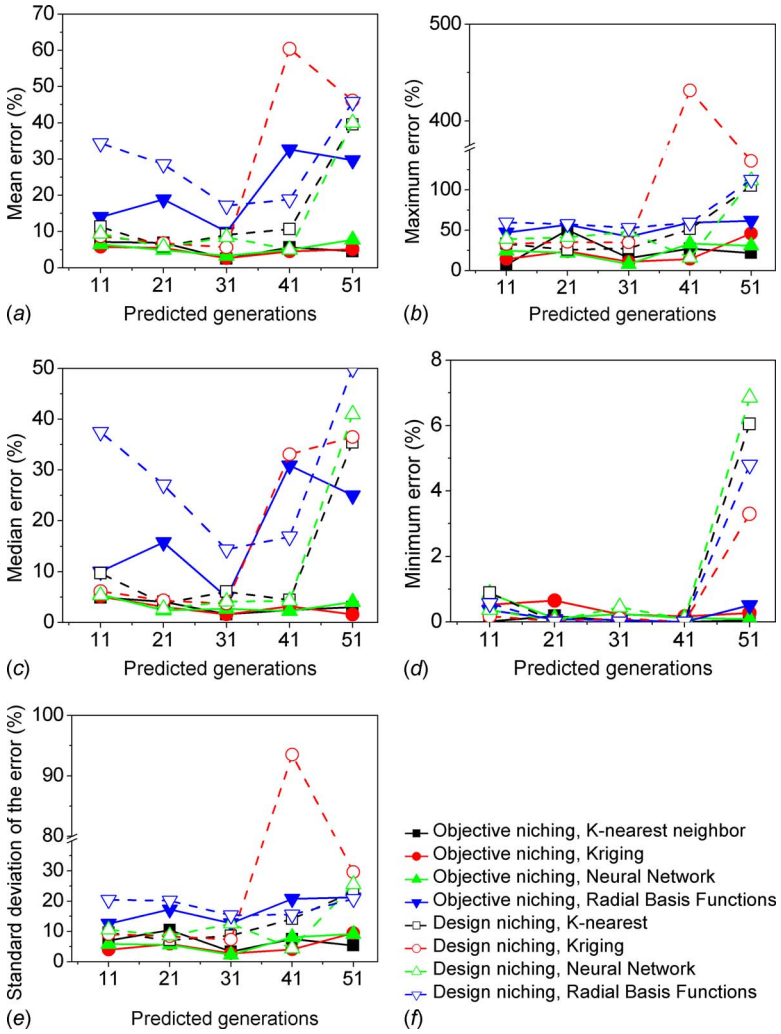

Fig. 8 Comparison of regression methods trained with data sets from the optimization process using different niching strategies: %errors of NO_x, (*a*) mean %error, (*b*) maximum %error, (*c*) median %error, (*d*) minimum %error, (*e*) standard deviation of the %error, and (*f*) legend

though this is not true for the RBF method, which could be due to the use of the Gaussian function (the exponential transformation is already applied intrinsically) in the RBF.

As stated before, the ultimate goal is to explore the feasibility of using a regression method to partly replace actual computationally expensive CFD simulations. The next comparisons aim at this purpose, and the methodology is described as follows.

As can be seen in Fig. 6, the prediction accuracy of the emissions is not satisfactory for replacing a part of the real CFD simulations. This can be understood, because it is somewhat unreasonable to expect that 120 DoE-generated designs with nine parameters over such wide ranges can reveal all complicated relationships between the design and objective spaces for the current engine design problem. However, the inherent characteristics of the genetic algorithm provide a method for possible improvement of utilizing regression methods. Since any of the cases in a GA generation inherits design features from the previous generations, it is expected that this could benefit the learning process of regression methods if all previous generations were trained to form the response surfaces, which are then used to predict the next generation.

It is also of interest to compare results trained on these two niching groups to investigate how the niching method influences the training process by producing different data pools for the regression methods. The logarithmic transformation helped to improve the prediction accuracy for the KN, KR, and NN methods, and thus, it was adopted for them, but for the RBF method, no transformation was applied.

Statistical studies of the relative errors between virtual designs predicted by the regression methods and the real designs from KIVA simulations are reported in Figs. 7–9 for GISFC, NO_x, and soot, respectively. Five generations (11, 21, 31, 41, and 51) were analyzed for each group. For each analyzed generation, all of its previous generations were used as the training data set. The solid lines with solid symbols represent the error of the regression methods trained with the data set from the optimization process using objective niching, and the dashed lines with open symbols represent design niching.

Compared with the results of Fig. 6, the regression methods trained with data sets from the optimization processes show a similar trend that the mean error of GISFC is the smallest, and is followed by NO_x and soot. But the absolute values of the mean errors are much smaller, which indicates that it is important to dynamically learn previous data sets in order to better predict the next. Results predicted using regression methods trained with the data set from the optimization process using objective niching are much better than those with design niching. This is most likely

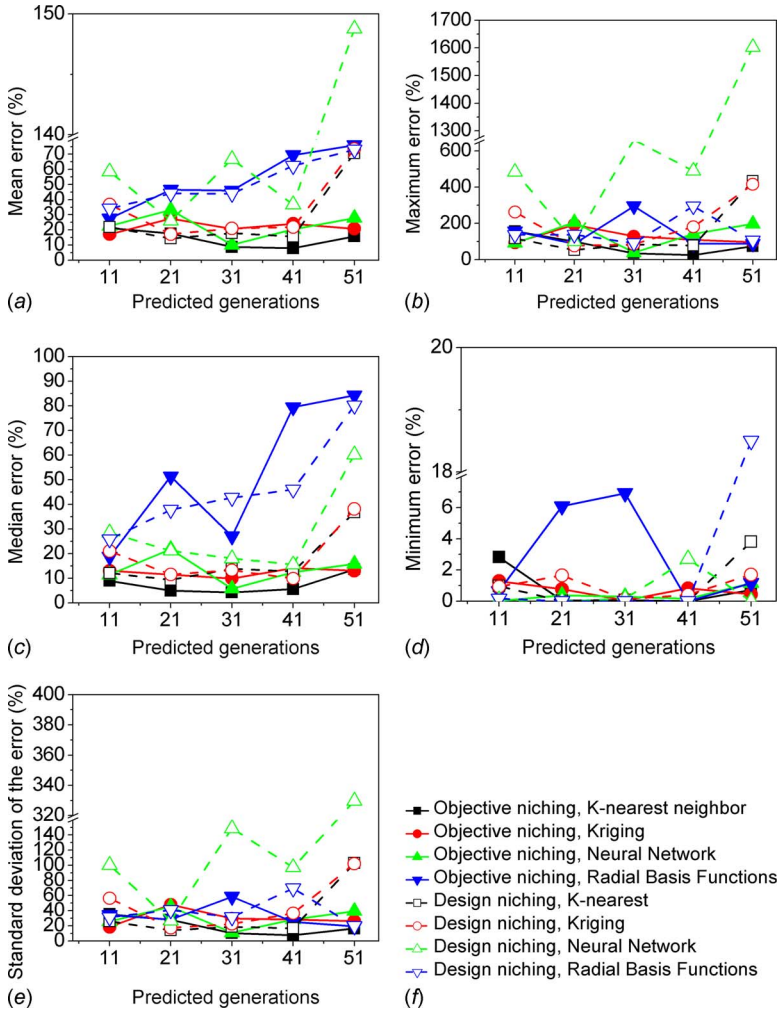

Fig. 9 Comparison of regression methods trained with data sets from the optimization process using different niching strategies: %errors of soot, (*a*) mean %error, (*b*) maximum %error, (*c*) median %error, (*d*) minimum %error, (*e*) standard deviation of the %error, and (*f*) legend

due to the proximity of designs in the data set using objective niching since it is also seen in the figures that the KN method (indicated by the black squares) performs the best in most of the cases, followed by the KR method. It is conjectured that the performance of interpolation of the regression method is more important than that of extrapolation, if it is trained with data sets from the MOGA optimization processes. Figures 7–9 also show that the errors increase with the size of the trained data set, especially for the NN and RBF methods. A possible cause is bad fitting or overfitting data, which could be more likely produced as the size of the trained data set increases, and the exact reason still needs further exploration in order to determine the size of the data set for better dynamic training. Furthermore, different from training with a scattered data set in Fig. 6, the RBF method did not predict satisfactory results. The NN method behaved unexpectedly poor in the prediction of soot emissions. Another important finding is that for all objectives, the median errors are less than the mean errors. The median errors of the KN and KR methods are below 1%, 5%, and 15% for GISFC, NO_x, and soot, if they are trained with the data sets from the optimization using objective niching, as shown in Figs. 7(*c*), respectively. This indicates that half of the real KIVA simulations could be possibly replaced by virtual designs predicted using a reliable regression method, which promises savings in computational resources.

Remaining questions are: (1) Does the computational expense of using a regression method could exceed that of KIVA evaluations because the number of trained cases increases as the optimization proceeds? (2) Prior to each generation, how can one determine which cases are calculated from the regression methods, and which should use KIVA in order to minimize the errors? Having the concern of the computational time, it was observed that by using the response surface methods (RSMs) package of MODEFRONTIER™ 4.0, the learning time of the KN method and the KR method increases approximately linearly with the number of trained data, and is about quadratic for the RBF method, and cubic for the NN method. However, even with over a thousand cases, none of the learning times exceeded the running time of KIVA cases. This means that just one processor is needed to complete learning and evaluation of N virtual designs, and thus, $N-1$ processors can be saved for every generation. Regarding the second concern, error control should be based on the proximity of the cases in the current generation to the trained previous cases. It is unnecessary to fix the number of virtual designs in each generation. Instead, it can be determined adaptively, based on the proximity. The detailed methodology will be the subject of the followup research.

4 Conclusions

This paper explores engine optimization processes using a MOGA, NSGA II, together with different niching strategies. Con-

vergence and diversity metrics were defined to better monitor the optimization process and to analyze the optimum results. Four regression methods such as KN, KR, NN, and RBF, were assessed in order to explore the feasibility of using results predicted from the regression methods to partly replace real CFD evaluations. Conclusions are as follows.

1. The niching strategy does not influence the performance of NSGA II in terms of convergence and optimality of the results. The present convergence metric is able to indicate when the optimization process can be terminated. Using design niching, more diversified design parameters were produced, as shown by the diversity metric.
2. When trained by a data set generated by a DoE method, investigated regression methods could not produce satisfactory results. However, by dynamically learning from all previous generations in the GA optimization process, regression methods, especially the KN and KR methods, predicted results in good agreement with KIVA evaluations for the next generation. A logarithm transformation in the objective space improved the prediction accuracy for the KN, KR, and NN methods, but not for the RBF method. These findings promise a proposed methodology that part of the real evaluations can be replaced by virtual designs through learning from previously existing data. The methodology of determining which cases are suitable for evaluation by the regression method still needs further study.

Acknowledgment

The authors would like to thank the Department of Energy for its financial support of this work (Grant No. DEFC26-06NT42628). We also thank ESTECO for providing the optimization software, MODEFRONTIER™.

Nomenclature

DoE = design of experiment
EGR = exhaust gas recycle
GISFC = gross indicated specific fuel consumption
KN = K-nearest neighbors
KR = kriging
MDPF = mean distance to the Pareto front
MK = modulated kinetics
MOGA = multiobjective genetic algorithm
NN = neural networks
NPS = number of Pareto solutions
NSGA II = nondominated sorting genetic algorithm II
PCCI = premixed charge compression ignition
RBF = radius basis functions
RSM = response surface method

References

[1] Lee, S., Gonzalez, M. A., and Reitz, R. D., 2007, "Effects of Engine Operating Parameters on Near Stoichiometric Diesel Combustion Characteristics," SAE Paper No. 2007-01-0121.
[2] Kimura, S., Aoki, O., Kitahara, Y., and Aiyoshizawa, E., 2001, "Ultra-Clean Combustion Technology Combining a Low-Temperature and Premixed Combustion Concept for Meeting Future Emission Standards," SAE Paper No. 2001-01-0200.
[3] Wickman, D. D., Senecal, P. K., and Reitz, R. D., 2001, "Diesel Engine Combustion Chamber Geometry Optimization Using Genetic Algorithms and Multi-Dimensional Spray and Combustion Modeling," SAE Paper No. 2001-01-0547.
[4] Bergin, M. J., Hessel, R. P., and Reitz, R. D., 2005, "Optimization of a Large Diesel Engine Via Spin Spray Combustion," SAE Paper 2005-01-0916.
[5] Genzale, C. L., Reitz, R. D., and Wickman, D. D., 2007, "A Computational Investigation Into the Effects of Spray Targeting, Bowl Geometry and Swirl Ratio for Low-Temperature Combustion in a Heavy-Duty Diesel Engine," SAE Paper No. 2007-01-0119.
[6] Shi, Y., and Reitz, R. D., 2008, "Optimization Study of the Effects of Bowl Geometry, Spray Targeting and Swirl Ratio for a Heavy-Duty Diesel Engine Operated at Low- and High-Load," Int. J. Engine Res., **9**, pp. 325–346.
[7] Shi, Y., and Reitz, R. D., 2008, "Assessment of Optimization Methodologies to Study the Effects of Bowl Geometry, Spray Targeting and Swirl Ratio for a Heavy-Duty Diesel Engine Operated at High-Load," SAE Paper No. 2008-01-0949.
[8] Deb, K., Pratap, A., Agarwal, S., and Meyarivan, T., 2002, "A Fast and Elitist Multiobjective Genetic Algorithm: NSGA-II," IEEE Trans. Evol. Comput., **6**, pp. 182–197.
[9] Shi, Y., Hessel, R. P., and Reitz, R. D., 2009, "An Adaptive Multi-Grid Chemistry (AMC) Model for Efficient Simulation of HCCI and DI Engine Combustion," Combust. Theory Modell., **13**, pp. 83–104.
[10] Shi, Y., and Reitz, R. D., 2009, "Efficient Multidimensional Simulation of HCCI and DI Engine Combustion With Detailed Chemistry," SAE Paper No. 2009-01-0701.
[11] Deb, K., 2001, *Multi-Objective Optimization Using Evolutionary Algorithms*, Wiley, New York.
[12] Arakawa, M., and Hagiwara, I., 1998, "Development of Adaptive Real Range (ARRange) Genetic Algorithms," JSME Int. J., Ser. C, **41**, pp. 969–977.
[13] http://www.iitk.ac.in/kangal/codes.shtml
[14] Deb, K., and Jain, S., 2002, "Running Performance Metrics for Evolutionary Multi-Objective Optimization," Kanpur Genetic Algorithm Laboratory Report No. 2002004.
[15] Farhang-Mehr, A., and Azarm, S., 2002, "Diversity Assessment of Pareto-Optimal Solution Sets: An Entropy Approach," Proceedings of the World Congress on Computational Intelligence, pp. 723–728.
[16] Ge, H.-W., Shi, Y., Reitz, R. D., Wickman, D. D., Zhu, G., Zhang, H., and Kalish, Y., 2009, "Heavy-Duty Diesel Combustion Optimization Using Multi-Objective Genetic Algorithm and Multi-Dimensional Modeling," SAE Paper No. 2009-01-0716.
[17] Angelo, S. D., and Minisci, E., 2007, "Multi-Objective Evolutionary Optimization of Subsonic Airfoils by Meta-Modelling and Evolution Control," Proc. Inst. Mech. Eng., Part G: J. Aerosp. Eng., **221**, pp. 805–814.
[18] Brahma, J., Sharp, M. C., Richter, I. B., and Frazier, T. R., 2008, "Development of the Nearest Neighbour Multivariate Localized Regression Modelling Technique for Steady State Engine Calibration and Comparison With Neural Networks and Global Regression," Int. J. Engine Res., **9**, pp. 297–324.
[19] He, Y. and Lin, C.-C., 2007, "Development and Validation of a Mean Value Engine Model for Integrated Engine and Control System Simulation," SAE Paper No. 2007-01-1304.
[20] User manuals of MODEFRONTIER™ 4.0, http://www.esteco.com
[21] Nguyen, D., and Widrow, B., 1990, "Improving the Learning Speed of 2-Layer Neural Networks by Choosing Initial Values of the Adaptive Weights," Proceedings of International Joint Conference on Neural Network, Vol. 3, pp. 21–26.
[22] Amsden, A. A., 1993, "KIVA-3: A KIVA Program With Block-Structured Mesh for Complex Geometries," Los Alamos National Laboratory Report No. LA-12503-MS.
[23] Draper, N. R., and Smith, H., 1981, *Applied Regression Analysis*, Wiley, New York.

A Numerical Investigation of Transient Flow and Cavitation Within Minisac and Valve-Covered Orifice Diesel Injector Nozzles

Won Geun Lee

Rolf D. Reitz

Engine Research Center,
University of Wisconsin-Madison,
1500 Engineering Drive,
Madison, WI 53706

Cavitating flow within diesel injector passages has been investigated numerically using the homogeneous equilibrium model (HEM), which uses the barotropic assumption and the variable speed of sound of the mixture. To apply the HEM, the KIVA-3V code was modified to implement a generalized equation of state, and injector needle movement is simulated by the arbitrary Lagrangian-Eulerian (ALE) approach and the snapper algorithm. It is demonstrated that the model can predict the effect of nozzle passage geometry on the flow structure and cavitation. The model is able to reproduce the transient fuel injection rate as a function of the needle lift profile. Special interest is focused on the transient behavior during the nozzle closing period, which shows that the fast decrease in flow rate can increase the cavitation in the nozzle passage. The effects of the pressure difference and environment pressure on cavitation augmentation at the end-of-injection were also investigated. Flow characteristics due to different shapes of the nozzle flow passage in axisymmetric single hole nozzles and multihole nozzle configurations (minisac and valve-covered orifice eight-hole nozzles) were compared with emphasis on the end-of-injection period. [DOI: 10.1115/1.4000145]

1 Introduction

Increase of injection pressure and precise control of the injection event have contributed greatly to the reduction in pollutant emissions from diesel engines. As the injection pressure in the diesel injector increases, the flow velocity increases and the high speed flow and curved streamlines reduce the static pressure below the vapor pressure and can cause cavitation to occur.

Since cavitation reduces the maximum attainable flow rate and may damage the nozzle surface by erosion, there has been much research to investigate the mechanisms of cavitation initiation and its development with the aim to find optimal geometries to minimize cavitation. Cavitation also influences the spray process, and for the spray modeling the existence of cavitation increases uncertainty about the initial conditions at the nozzle exit.

Even though experimental efforts have substantially helped reveal the mechanism of cavitation [1], most of them simply visualize the flow inside an increased size injector and operate under the condition of reduced pressure difference. Therefore, the extremely high speed flow inside a real-sized injector has been a challenging topic largely confined to computational analyses.

Several approaches have been proposed for the simulation of highly transient, cavitating flow. One of them is the single-fluid approach. Based on the homogeneous equilibrium model of Wallis [2], a barotropic equation of state of the mixture of fuel vapor and liquid is established. The method treats the two-phase mixture as one compressible fluid. This HEM has been applied to simulate cavitation phenomena in the two-dimensional nozzle passage geometries by Schmidt et al. [3,4]. Their study introduced novel features like higher-order time marching, highly accurate convection schemes, and Navier–Stokes characteristic boundary conditions (NSCBCs) [5]. The HEM method was successfully implemented into the KIVA code and developed as a code named CAVIF [6,7]. Using the code, three-dimensional computations with needle movement have also been successfully demonstrated [7]. The code was used to solve laminar flows with the Navier–Stokes equations without solving for the pressure correction using the SIMPLE method. Instead, the pressure was calculated directly from the equation of state.

A recent application of this method has been reported by Ning et al. [8], in conjunction with the Eulerian-Lagrangian spray atomization (ELSA) model [9]. The method was also implemented in the KIVA code, and a new equation for pressure was proposed that is derived from the continuity equation. After solving for the flow in the nozzle passage, the results were used as the inlet boundary condition for the ELSA approach. However, that application was limited to two-dimensional cases.

Other approaches have been proposed to use the results from injector flow simulation as an inlet boundary condition, and the results have also been used for engine combustion simulations with an Eulerian two-phase flow approach [10]. Other examples are the three-fluid approach of Grogger and Alajbegovic [11] that is used to improve spray calculations [12], and the cavitation bubble-tracking model of Gavaises et al. [13]. However, a single-fluid model is relatively easy to implement into existing codes, and with some modifications, it can be combined with turbulence and spray models. Thus, the single-fluid HEM was used in the present study.

A generalized implementation of the HEM approach is presented in this study. As an application, special focus on the transient end-of-injection (EOI) event was selected. It is widely known that the spray behavior near the end-of-injection affects significantly diesel engine pollutant emissions. However, the details of the spray behavior after the end-of-injection are still not clear. Recently an important engine study on end-of-injection mixing was performed by Musculus et al. [14]. They investigated

Contributed by the IC Engine Division of ASME for publication in the JOURNAL OF ENGINEERING FOR GAS TURBINES AND POWER. Manuscript received April 30, 2009; final manuscript received May 14, 2009; published online March 5, 2010. Editor: Dilip R. Ballal.

the end-of-injection event and suggested the hypothesis that in the limit of a gradual ramp down of injection velocity, the jet structure remains, leaving fuel rich zones near the injector. In the limit of a very sharp end-of-injection, momentum would carry the trailing edge of the jet downstream, leaving in its wake a region free of fuel near the injector. They showed evidence of lean combustion very near the injector. In the present study, an attempt to investigate the phenomena inside the nozzle at the end-of-injection was performed to help understand these flows.

2 Numerical Model

2.1 CFD Code. The CFD code was based on the KIVA-3V RELEASE 2 code [15] with improvements developed at the Engine Research Center, University of Wisconsin-Madison. The code uses the ALE approach, an explicit time marching scheme, and a quasi-second order upwind scheme for the convection flux. In these calculations, the pressure gradient and viscous terms are treated using a fully explicit scheme. Pressure boundaries were set at both the inlet and exit of the injector geometry. To reduce acoustic wave reflection, the pressure at the exit boundary face was set as if the environment pressure was constant at a certain distance ($\approx$ nozzle radius in the present study) outside the boundary [16]. The injector needle movement is implemented in an analogous way to the standard KIVA two stroke engine simulation with intake and exhaust ports. The mesh cells in the gap between the needle and housing were added or eliminated by the snapper algorithm to resolve the transient needle movement.

2.2 Generalized EOS. The standard KIVA code adopts an equation of state (EOS) based on the ideal gas assumption

$$P = \rho RT \tag{1}$$

This relation is used in many subroutines of the code to calculate specific heats, temperature boundary conditions, Lagrangian volume changes due to pressure, etc. To consider the departure from ideal gas behavior in gases under high pressure and temperature, a generalized equation of state was introduced by Trujillo et al. [17]. In their method, several modifications were made to the specific heat and the energy equation. One of the most important changes is the Lagrangian volume correction due to the pressure correction

$$V^C = V^P - \frac{V^P}{\gamma P^P}(P^C - P^P) \tag{2}$$

which is converted to the generalized form

$$V^C = V^P + \left.\frac{\partial V^P}{\partial P}\right|_S (P^C - P^P) \tag{3}$$

$$\left.\frac{\partial V^P}{\partial P}\right|_S = -\frac{M}{\rho^2}\left.\frac{\partial \rho^P}{\partial P}\right|_S = -\frac{V}{\rho}\left.\frac{\partial \rho^P}{\partial P}\right|_S = -\frac{V}{\rho}\frac{1}{a_S^2} \tag{4}$$

where a_s is the isentropic speed of sound.

This correction was used in the present model, with the assumption of the HEM for the speed of sound in the liquid-vapor mixture. In this study temperature variation inside the injector was neglected and the isothermal acoustic speed was used.

2.3 Homogeneous Equilibrium Model. Since it is not possible to capture the interface between liquid and vapor on cavitation bubbles within computational meshes of a practical size, the two-phase flow was assumed to be one homogeneous mixture of vapor and liquid with the homogeneous equilibrium model. In this study the barotropic equation of state by Wallis [2] was used. Under the assumption of constant temperature, the acoustic speed of the two-phase flow is expressed as

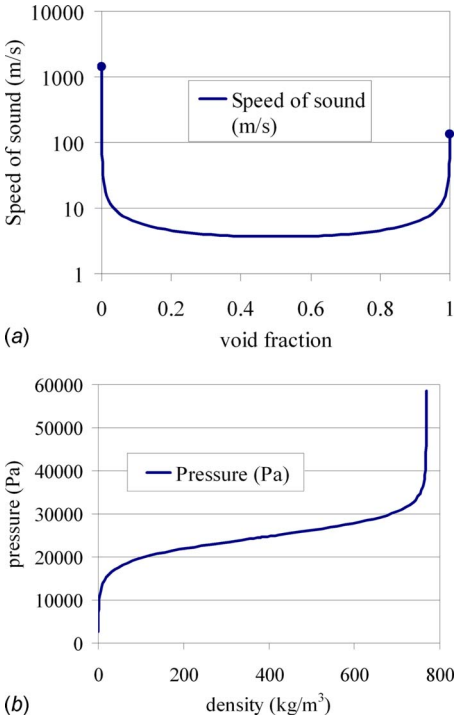

Fig. 1 (*a*) Speed of sound of the HEM and (*b*) the pressure-density relation in the liquid-vapor mixture

$$\frac{1}{a^2} = [\alpha\rho_v + (1-\alpha)\rho_l]\left[\frac{\alpha}{\rho_v a_v^{\,2}} + \frac{1-\alpha}{\rho_l a_l^{\,2}}\right] \tag{5}$$

where α is the void fraction, defined as

$$\alpha = \frac{\rho_l - \rho}{\rho_l - \rho_v} \tag{6}$$

With the typical properties of the No. 2 diesel fuel, this relation is plotted in Fig. 1(*a*). The variation in the acoustic speed is seen to be large, and once cavitation happens in a computational cell, the flow can be locally supersonic.

The pressure can be integrated directly from the equation

$$dP = a^2 d\rho \tag{7}$$

resulting in Ref. [3]

$$P = \rho a_v^{\,2}, \quad \text{if } \rho \le \rho_v \tag{8}$$

$$P = P_l^{\text{sat}} + P_{vl}\log\left[\frac{\rho_v a_v^{\,2}(\rho_l + \alpha(\rho_v - \rho_l))}{\rho_l(\rho_v a_v^{\,2} - \alpha(\rho_v a_v^{\,2} - \rho_l a_l^{\,2}))}\right], \quad \text{if } \rho_v < \rho < \rho_l \tag{9}$$

$$P = P_l^{\text{sat}} + (\rho - \rho_l)a_l^2, \quad \text{if } \rho \ge \rho_l \tag{10}$$

where

$$P_{vl} = \frac{\rho_v a_v^{\,2}\rho_l a_l^{\,2}(\rho_v - \rho_l)}{\rho_v^{\,2} a_v^{\,2} - \rho_l^{\,2} a_l^{\,2}} \tag{11}$$

$$P_l^{\text{sat}} = P_v^{\text{sat}} - P_{vl}\log\left[\frac{\rho_v^{\,2} a_v^{\,2}}{\rho_l^{\,2} a_l^{\,2}}\right] \tag{12}$$

With the assumption that the acoustic speed is constant in both pure substances, the pressure-density relation of pure vapor and pure liquid is linear. However, the relation is nonlinear for the mixture of vapor and liquid, as shown in Fig. 1(*b*).

In previous research [3,4,6,7] the above equations were used for

Table 1 Typical diesel fuel properties at 373 K

ρ_v	1.41×10^{-3} kg/m^3
a_v	135 m/s
P_v^{sat}	2,560 Pa
ρ_l	768 kg/m^3
a_l	1400 m/s
P_l^{sat}	58,600 Pa

single-fluid cavitation simulations. The pressure gradient in the momentum equation was calculated directly with Eqs. (8)–(10) and the flow inside the injector was regarded as a laminar flow.

In this study the standard coupled solver in the KIVA code for the corrected pressure, corrected volume, and corrected face velocity was used with the volume correction equations (3) and (4), and the above equation of state was applied only for calculating the absolute pressure. The inverse function of Eqs. (8)–(10) was derived and used to set the boundary values of the density

$$\rho = P/a_v^2, \quad \text{if } P \le P_v^{sat} \tag{13}$$

$$\rho = \frac{\exp(P/P_{vl})\rho_l(\rho_l^2 a_l^2 - \rho_v^2 a_v^2)}{\exp(P_l^{sat}/P_{vl})(\rho_l - \rho_v)\rho_v a_v^2 + \exp(P/P_{vl})\rho_l(\rho_l a_l^2 - \rho_v a_v^2)}, \quad \text{if } P_v^{sat} < P < P_l^{sat} \tag{14}$$

$$\rho = (P - P_l^{sat})/a_l^2 + \rho_l, \quad \text{if } P \ge P_l^{sat} \tag{15}$$

2.4 Physical Properties. The fuel physical properties were adopted from the fuel library in the KIVA code. At a given temperature, the saturated vapor pressure P_v^{sat} was interpolated from the fuel library. Then the density of the saturated vapor ρ_v was calculated using the ideal gas assumption, and the isothermal acoustic speed was set as

$$\rho_v = \frac{P_v}{R_u T/M_f} \tag{16}$$

$$a_v = \sqrt{R_u T/M_f} \tag{17}$$

Since a_l, ρ_l, and P_l^{sat} are coupled, there is no explicit formula for the density of the saturated liquid ρ_l. These values were calculated in an iterative manner using the following equations:

$$\rho_l = \rho_f - (P_{1\ atm} - P_l^{sat})/a_l^2 \tag{18}$$

$$P_l^{sat} = P_v^{sat} - P_{vl}\log\left[\frac{\rho_v^2 a_v^2}{\rho_l^2 a_l^2}\right] \tag{19}$$

where fuel density at given temperature and atmospheric pressure was $\rho_f = 844 - 0.9(T - 289)$ kg/m^3 [18] and a constant representative value of a_l was set as 1400 m/s.

The properties for the fuel at 373 K are shown in Table 1.

For the viscosity in the momentum equation, the classical formulation for the viscosity of the mixture was chosen

$$\mu = \alpha\mu_v + (1-\alpha)\mu_l \tag{20}$$

where μ_v is given in the KIVA code and μ_l is set from the fuel library data. Even though the flows in this paper were regarded as laminar for simplicity, the present method can be extended to consider turbulent flow because this approach is fully compatible with the original KIVA method.

3 Nozzle Geometry and Test Conditions

3.1 Nozzle Geometry. Computational meshes were generated for axisymmetric single hole nozzles, a three-dimensional minisac (MS) nozzle and a valve-covered orifice (VCO) nozzle. The typical shape and mesh for the single hole nozzle is shown in Fig. 2.

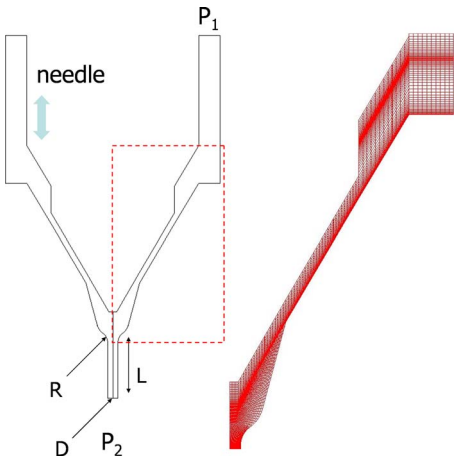

Fig. 2 Typical shape and mesh for single hole nozzles

A 0.5-deg sector mesh was used for the single hole nozzle.

The injector dimensions are characterized by the nozzle passage length L, hole diameter D, nozzle hole inlet rounding radius R due to hydrogrinding, and the K-factor that expresses the difference between the inlet and outlet diameters ($K=(D_{inlet}-D_{exit})/10$ μm). To investigate the effect of nozzle shape on cavitation strength, two types of nozzle passage were generated: one a highly hydroground converging nozzle and the other a less hydroground diverging nozzle.

The three-dimensional meshes are shown in Fig. 3. The MS and VCO eight-hole nozzle geometries were modeled and 1/8 sector, 45-deg meshes were generated. Nozzle hole inlet rounding was not considered in this geometry, and the important dimensions are shown in Table 2.

3.2 Needle Lift Profile and Test Condition. A typical measured needle lift profile was modeled, as shown in Fig. 4. Since at least two layers of computational cells are required between the needle and housing, the minimum needle lift was 10 μm. The

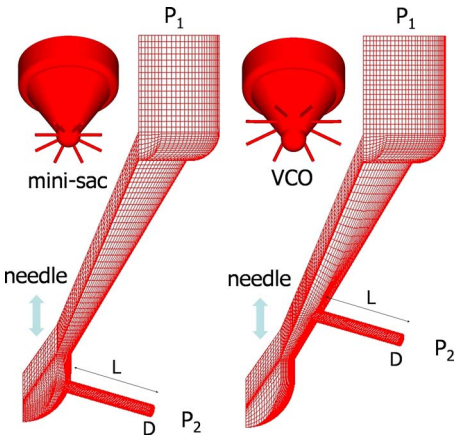

Fig. 3 Meshes for MS and VCO nozzles

Table 2 Nozzle specifications

Nozzle	No. of holes	D (mm)	L (mm)	R (mm)	K
Sng-1	1	0.18	1.15	0.2	1.5
Sng-2	1	0.18	1.15	0.02	−1.5
MS	8	0.127	1.1	0	0
VCO	8	0.127	1.1	0	0

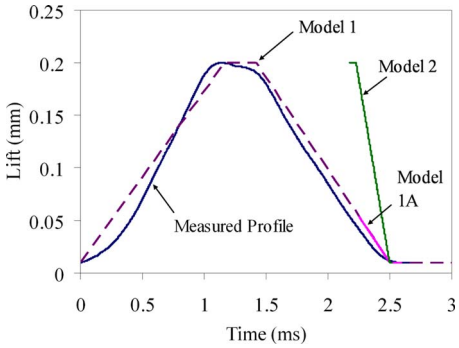

Fig. 4 Needle lift profiles

total injection duration was 2.5 ms, and the calculation was continued for a 0.167 ms period with the 10 μm lift, to study the flow after the needle is fully closed. The profile was also simplified to a linear ramp like model 1. The average opening speed was about 0.16 m/s and the closing speed was about 0.175 m/s. In some cases, calculations were not performed for the whole injection period to save computation time. In these cases, the calculation was started during the later part of whole profile (model 1A). The needle closing speed is a unique characteristic of an injector, which is determined by many parameters like the return fuel flow passage geometry and the return spring stiffness, and this results in different needle lift profiles. Typical closing speeds are around 0.175–0.2 m/s [12,14], but others are about 0.8–1 m/s [7,13]. To investigate the effect of needle closing speed, a new closing profile (model 2) was designed to have a four times faster (=0.70 m/s) closing speed than the original one.

Two different conditions were studied. One had an injection pressure difference ΔP of 1500 bars and exit pressure P_2 of 5 bars (CN=301), and the other had 1100 bars pressure difference and 60 bars exit pressure (CN=18.3), which is regarded as practical in real engines, where $CN=\Delta P/(P_2-P_v)$ and ΔP is the nominal pressure difference between the inlet supply passage and the exit. Temperatures were set constant as 373 K in both cases.

3.3 Coefficients to Evaluate Results. The flow inside an injector is basically a pressure-driven flow. If there is no restriction or loss, the exit velocity should be the "Bernoulli velocity" defined by

$$U_b = \sqrt{\frac{2\Delta P}{\rho}} \tag{21}$$

However, the nozzle flow expresses pressure losses due to area changes and viscous work, and the exit velocity profile is not uniform. To evaluate those effects, several classical coefficients were defined and examined.

The mass flow rate, momentum flux, and actual average velocity is defined as

$$\dot{m} = \int \rho u dA \tag{22}$$

$$\dot{M} = \int \rho u^2 dA \tag{23}$$

$$\bar{u} = \int u dA/A \tag{24}$$

From the relation $\dot{M}=\dot{m}u_n$, the average velocity for a contracted flow area at the nozzle exit is defined as

$$u_n = \dot{M}/\dot{m} \tag{25}$$

The area contraction ratio C_a represents the velocity deficit due to the no-slip wall boundary condition. If the speed is very high, C_a approaches unity because the boundary layer is thin and the velocity profile at the exit is almost uniform. At low speed, C_a is less than unity and

$$C_a = \bar{u}/u_n \tag{26}$$

The velocity coefficient C_v represents pressure loss due to area change and friction

$$C_v = u_n/U_b \tag{27}$$

The discharge coefficient is defined as

$$C_d = \frac{\dot{m}}{\rho U_b A} \tag{28}$$

If the fluid density is constant everywhere, then

$$C_d = \bar{u}/U_b = C_a C_v \tag{29}$$

$$C_a = \frac{\dot{m}^2}{\dot{M}A\rho} \tag{30}$$

However, in the diesel injector nozzle, due to the very large pressure difference and cavitation, the density is no longer constant in both the axial and cross-sectional directions. With an acoustic speed of 1400 m/s, a pressure difference of 1000 bars give a 51 kg/m^3 difference in the density of the fuel, which is about 7% of the base density. Therefore, new definitions were introduced, which are slightly different from the traditional ones. First, the densities in the Bernoulli velocity and C_d definition are chosen using the nominal pure liquid density ρ_f at the exit pressure

$$U_b = \sqrt{\frac{2\Delta P}{\rho_f}} \tag{31}$$

$$C_d = \frac{\dot{m}}{\rho_f U_b A} \tag{32}$$

The actual pressure difference and the density at the nozzle exit may vary due to the flow condition. Thus, C_a should be defined using the density ρ_m determined from the mass flux

$$C_a = \frac{\dot{m}^2}{\dot{M}A\rho_m} \tag{33}$$

where

$$\rho_m = \dot{m}/(\bar{u}A) \tag{34}$$

Then the equation for C_d is

$$C_d = \frac{\dot{m}}{\rho_f U_b A} = \frac{\rho_m \bar{u} A}{\rho_f U_b A} = \frac{\rho_m}{\rho_f}\frac{\bar{u}}{u_n}\frac{u_n}{U_b} = C_\rho C_a C_v \tag{35}$$

Here we define a new coefficient C_ρ as

$$C_\rho = \rho_m/\rho_f = \frac{C_d}{C_a C_v} \tag{36}$$

4 Single Hole Nozzle Results

4.1 Conditions at the Nozzle Exit at Steady State. The velocity at the nozzle exit and the density distribution under $\Delta P/P_2=1100/60$ bars in axisymmetric single hole nozzles at full lifts are shown in Fig. 5. The flow structure reached quasisteady state in about 20 μs and at that condition, $C_d=0.86$, $C_a=0.95$, $C_v=0.90$, and $C_\rho=1.00$ for the Sng-1 nozzle and $C_d=0.65$, $C_a=0.91$, $C_v=0.97$, and $C_\rho=0.74$ for the Sng-2 nozzle. In the Sng-2 nozzle, C_a is 4% lower than in the Sng-1 nozzle due to increased

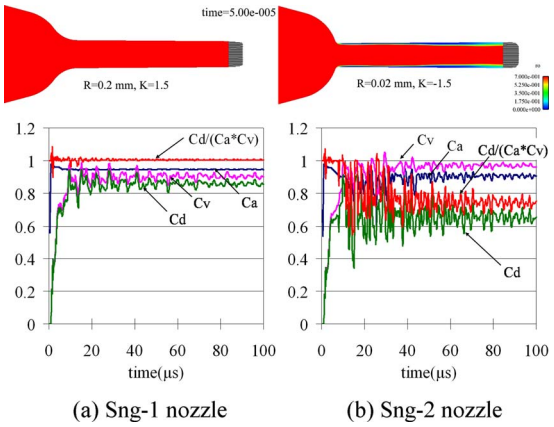

Fig. 5 Flow and cavitation inside single hole nozzles under $\Delta P/P_2$=1100/60 bars reaches quasisteady state

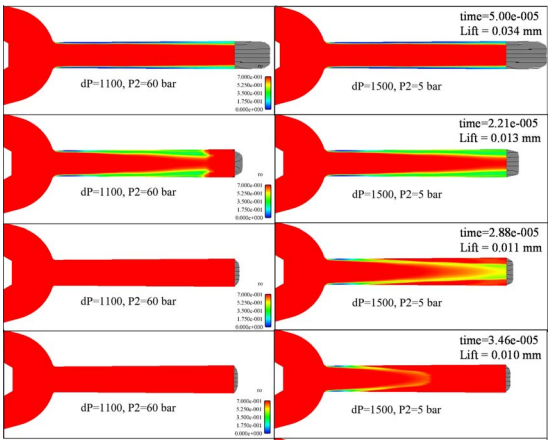

Fig. 7 Cavitation collapsed due to the gradual decrease in exit velocity at the end-of-injection (closing speed=0.175 m/s)

loss from the nonuniform velocity profile, but C_v is 7% higher because the actual exit pressure is lower in the flow with cavitation. Therefore, the lower C_d in the Sng-2 nozzle is mainly due to the lower density due to cavitation, which is also evidenced by the high frequency fluctuations in the discharge coefficient.

The exit condition of the Sng-1 nozzle was calculated with the measured lift profile and is shown in Fig. 6. At the end-of-injection, (t=2.5 ms), C_a decreased due to the nonuniform velocity distribution that resulted from decreased flow speed, and C_v decreased quickly because the pressure loss increased as the needle lift decreased. However, C_ρ remained unity, which implies no cavitation occurs around the EOI.

4.2 End-of-Injection Stage. To save computation time, only the later parts of the end-of-injection event were calculated in most cases. This was justified because the flow converges to its steady state very quickly (in about 20–50 μs), as shown in Fig. 5.

As shown in Fig. 6, no cavitation occurred in the Sng-1 nozzle at the EOI in which the needle was closing at the speed of 0.175 m/s. In the Sng-2 nozzle, cavitation already exists before the EOI, and slowly closing the nozzle made the exit pressure increase gradually and the cavitation collapsed, as shown in Fig. 7.

If the needle closing speed is increased, the flow rate decreases faster. In this case, the flow speed at the exit is faster than the flow speed in the middle of the nozzle, so that the average pressure inside the nozzle drops and the flow is easier to cavitate. Therefore, a faster needle closing speed promotes cavitation around EOI, which then collapses, as shown in Fig. 8. Similar flow characteristics are seen for the two injector and ambient pressure conditions.

To clarify this, the average density and pressure inside the nozzle are plotted in Fig. 9. In the fast closing nozzle, the density coefficient ($C_\rho = C_d/(C_a \times C_v)$) at the exit drops as the flow rate decreases quickly ($C_d \rightarrow 0$), whereas it returns to unity in the slowly closing nozzle. The averaged pressure and density inside the nozzle shows a similar trend.

Figure 10 shows that faster needle closing can cause cavitation even in the highly hydroground converging nozzle Sng-1, which does not otherwise have cavitation in most conditions.

5 Multihole Nozzle Results

5.1 Flow Patterns in Steady State. The velocity fields and flow patterns in two eight-hole nozzles (minisac and VCO) were simulated and are shown in Fig. 11. When the valve lift is high to medium, the flow in the minisac nozzle is supplied mainly from the upper supply passages and cavitation occurs predominantly on the upper wall of the nozzle. However, when the valve lift is small, the flow from the upper region decreases and most of the flow is supplied from the sac volume. Cavitation then occurs on the lower wall. For the VCO nozzle, the portion of the flow supplied from the sac volume increases as the needle lift decreases, but not as much as for the minisac nozzle.

Even though these nozzles are not hydroground, the present result shows not much cavitation occurs inside the nozzle. This is because the hole diameters of the nozzles are relatively small, so that L/D is about 8.7. It is reported that a larger L/D suppresses cavitation [12]. The larger L/D leads to higher pressure loss between the nozzle exit and the nozzle entrance, which increases the pressure level at the nozzle entrance where cavitation initiates.

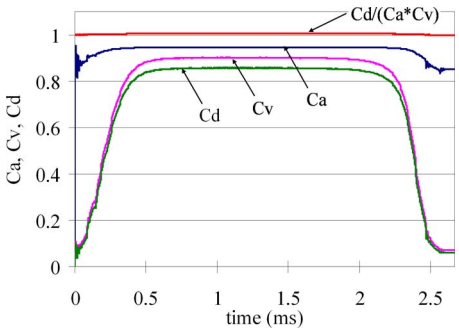

Fig. 6 Coefficients representing the exit condition of the Sng-1 nozzle, $\Delta P/P_2$=1100/60 bars

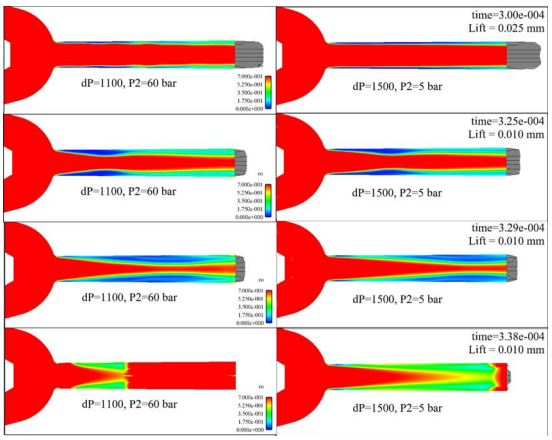

Fig. 8 Cavitation enhanced due to the fast decrease in exit velocity at the end-of-injection (closing speed=0.7 m/s)

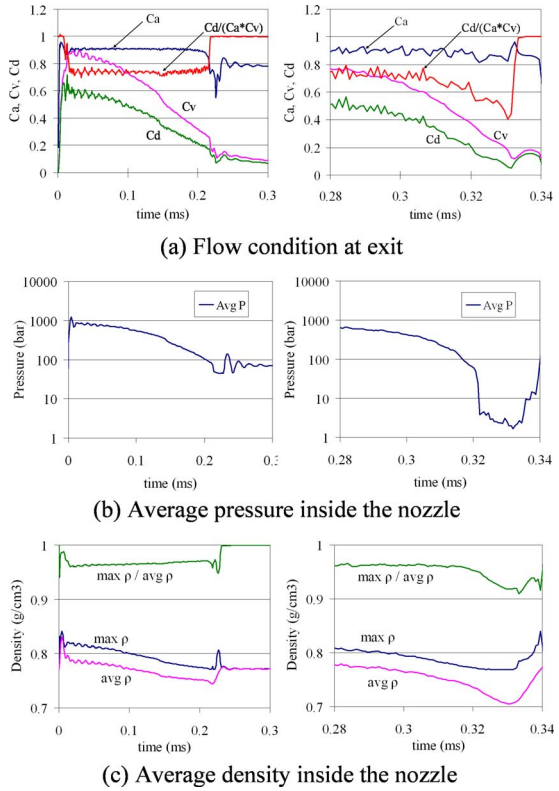

Fig. 9 Comparison of flow conditions at the nozzle exit, and pressure and density inside the nozzle, $\Delta P/P_2=1100/60$ bars (needle closing speed: left=0.175 m/s and right=0.70 m/s)

5.2 End-of-Injection Stage. The flow structures of the eight-hole nozzles at the end-of-injection stage were also investigated. Similar to the axisymmetric nozzle cases, it was observed that the cavitation phenomena do not increase much when the needle is closed at a relatively slow speed (0.175 m/s). The results are shown for both the minisac and VCO nozzles in Figs. 12 and 13, respectively.

At the condition of $\Delta P/P_2=1100/60$ bars, cavitation regions in both the minisac and VCO nozzles collapse. However, at $\Delta P/P_2=1500/5$ bars, cavitation regions increase slightly while the exit velocities decrease quickly and then collapse after the exit velocity decreased. In Fig. 14 it is seen that the density coefficient at the nozzle exit and the average density inside the nozzle decrease at around $t=0.2$ ms, due to increased cavitation.

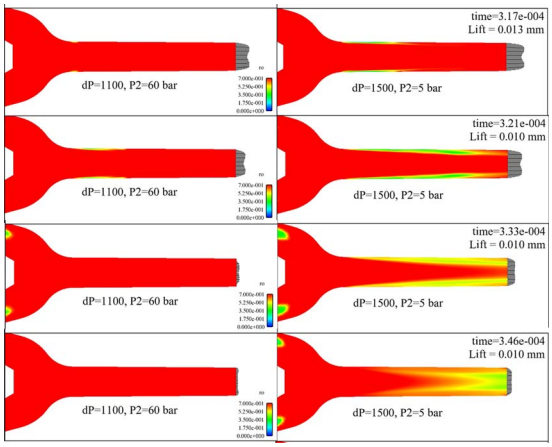

Fig. 10 Cavitation generation in a Sng-1 nozzle at the end-of-injection with a needle closing speed of 0.7 m/s

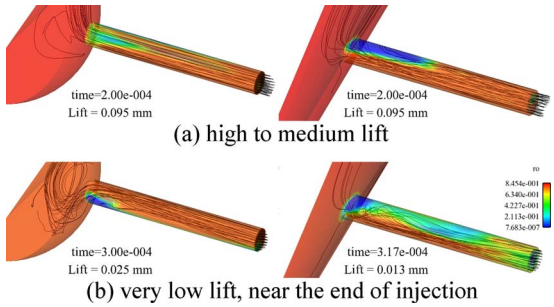

Fig. 11 Flow patterns in minisac (left) and VCO nozzles (right)

When the needle closing speed is higher (0.7 m/s), similar trends with the axisymmetric nozzle cases were found again at the condition of $\Delta P/P_2=1500/5$ bars. As shown in Figs. 15–17, faster needle closing increases cavitation significantly during the end-of-injection period.

During the end-of-injection event, the pressure at the nozzle exit recovers to the ambient pressure level and cavitation inside the nozzle collapses. Actually, some backflow (or "hydraulic flip") happens at this stage. The backflow would be expected to be a mixture of environment gas, fuel vapor, and liquid. However, the density boundary condition for the backflow in the present method was set as the density from the HEM EOS (Eqs. (13)–(15)) using

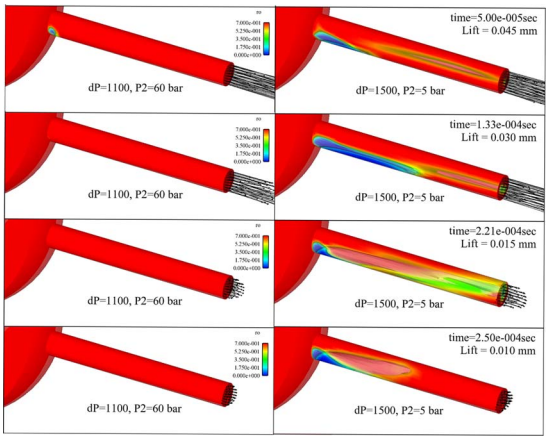

Fig. 12 Cavitation in the minisac nozzle at the end-of-injection (closing speed=0.175 m/s)

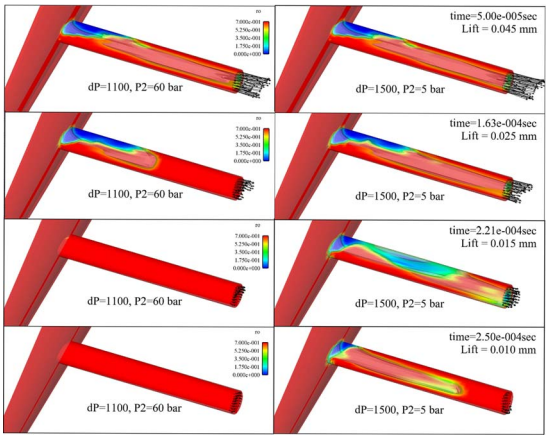

Fig. 13 Cavitation in the VCO nozzle at the end-of-injection (closing speed=0.175 m/s)

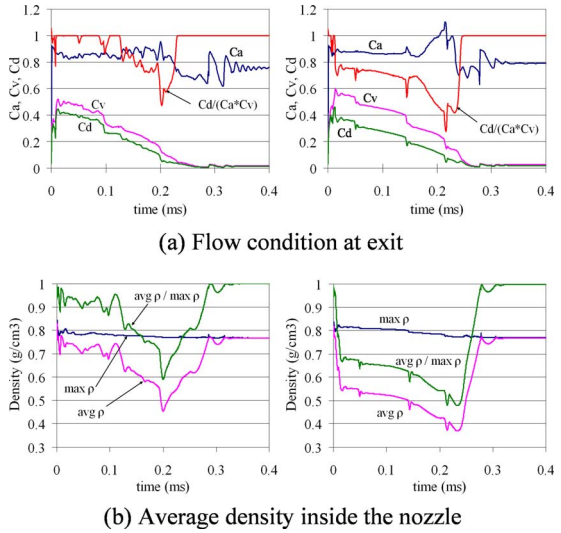

Fig. 14 Flow conditions at the nozzle exit and density inside the nozzle, $\Delta P/P_2=1500/5$ bars, needle closing speed of 0.175 m/s (left=minisac and right=VCO)

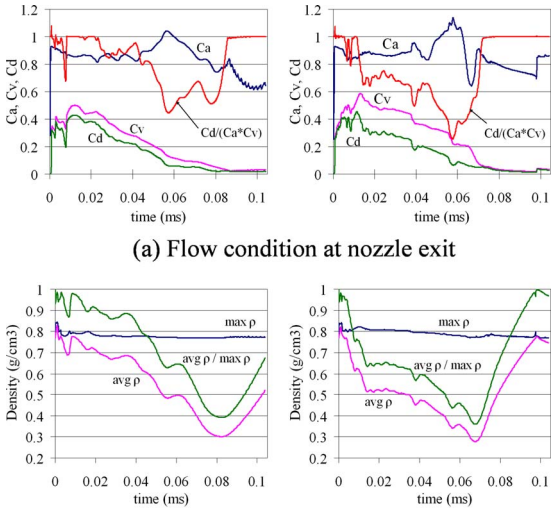

Fig. 17 Flow conditions at the nozzle exit and density inside the nozzle, $\Delta P/P_2=1500/5$ bars, needle closing speed of 0.70 m/s (left=minisac and right=VCO)

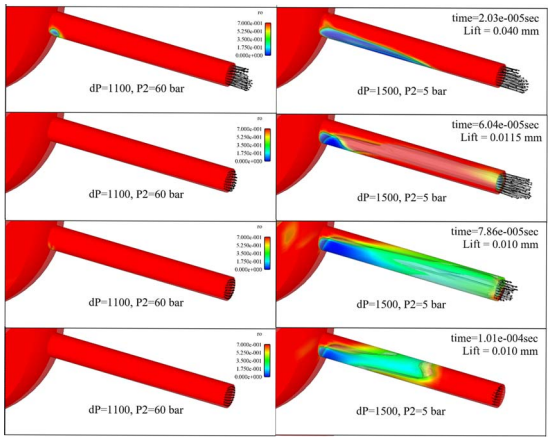

Fig. 15 Cavitation in the minisac nozzle at the end-of-injection (closing speed=0.70 m/s)

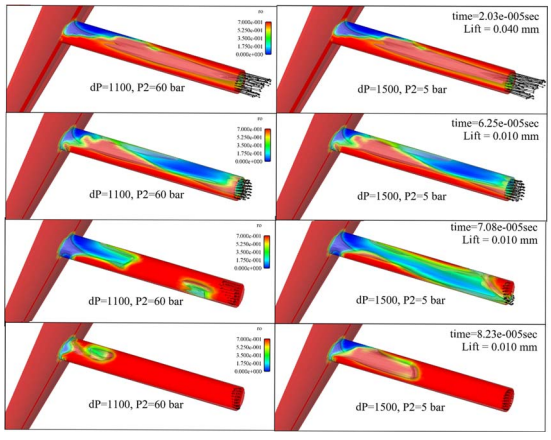

Fig. 16 Cavitation in the VCO nozzle at the end-of-injection (closing speed=0.70 m/s)

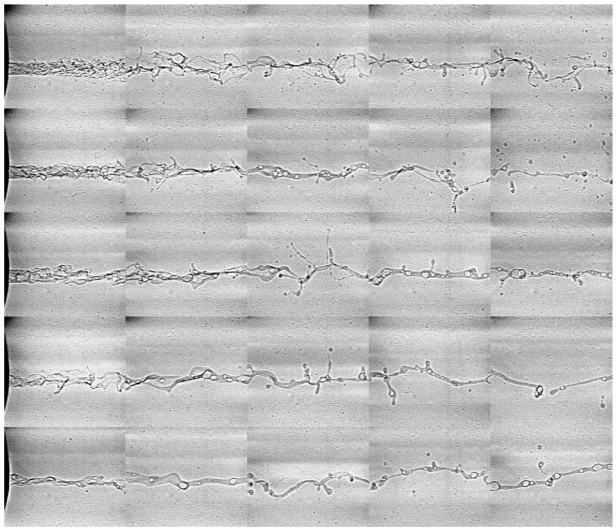

Fig. 18 X-ray image of the fuel spray evolution at the end-of-injection (courtesy of the Argonne National Laboratory)

the pressure at the boundary cell. This results in the liquid backflow eventually. Further research is needed to consider the mixture composition in the backflow.

Figure 18 shows an X-ray image visualization of the spray during the end-of-injection event obtained by the Argonne National Laboratory. The spray was injected at the pressure of 400 bars into stagnant nitrogen gas of 1 bar. The pictures were taken at intervals of 20 μs. It shows that the spray structure changes from a jet to a detached liquid column as the flow speed decreases. The liquid flow in the bottom frame contains large bubbles, and the downstream jet is thinner than the upstream jet at the nozzle exit. This implies that the flow is stretched because of the decreasing flow rate and the fact that it is mixed with cavitation vapor and air, consistent with the interpretation of the model results.

6 Concluding Remarks

The homogeneous equilibrium model was implemented into the KIVA-3V RELEASE 2 code with modifications for the generalized

equation of state. A generalized algorithm for pressure and volume correction was used. The flow within diesel injector nozzle passages was treated as laminar flow in this study. But since the approach is general, the method can be extended easily to consider turbulent flow in the future.

With the present model, the flow structures inside various types of injectors around the end-of-injection event were investigated numerically. It was shown that the cavitation inside the nozzle passage increased temporarily before it collapses if the needle closing speed is relatively high (0.7 m/s). The fast closing of the needle can cause cavitation to occur even in nozzles that do not exhibit cavitation in most conditions. If the needle is closed slowly (0.175 m/s), the cavitation collapsed at the end-of-injection in all of the nozzles investigated in this study. This suggests that there is some optimum lift profile in the needle closing movement.

Acknowledgment

The authors acknowledge the financial support of Cummins, Inc. The measurement data of the shape and needle lift of the axisymmetric nozzle provided by Dr. L. Pickett of the Sandia National Laboratory and the visualization image of the spray at the nozzle exit by Dr. J. Wang of the Argonne National Laboratory are greatly appreciated.

Nomenclature

A = area at nozzle exit
a = speed of sound
a_s = isentropic speed of sound
a_l = speed of sound in pure liquid
a_v = speed of sound in pure vapor
C_a = area contraction coefficient
C_d = discharge coefficient
C_ρ = coefficient for density ratio
C_v = velocity coefficient
M = mass of a cell
M_f = molar mass of a fuel
$\dot{m}$ = mass flux
$\dot{M}$ = momentum flux
P = pressure
P_1 = pressure at the inlet of an injector
P_2 = pressure at the exit of a nozzle
ΔP = $P_1 - P_2$
P^C = corrected pressure
P^P = predicted pressure
R = gas constant
R_u = universal gas constant
T = temperature
u = velocity
U_b = Bernoulli velocity
u_n = average velocity for a contracted area
$\bar{u}$ = actual average velocity at the nozzle exit
V = Lagrangian volume
V^C = corrected Lagrangian volume
V^P = predicted Lagrangian volume
α = void fraction of mixture
γ = specific heat ratio
μ = viscosity
μ_l = viscosity of fuel liquid
μ_v = viscosity of fuel vapor
ρ = density
ρ_f = nominal pure liquid density of fuel
ρ_m = density determined from mass flux
ρ_l = liquid density of fuel
ρ_v = vapor density of fuel

References

[1] Roth, H., Gavaises, M., and Arcoumanis, C., 2002, "Cavitation Initiation, Its Development and Link With Flow Turbulence in Diesel Injector Nozzles," SAE Paper No. 2002-01-0214.
[2] Wallis, G. B., 1969, *One-Dimensional Two-Phase Flow*, McGraw-Hill, New York.
[3] Schmidt, D. P., Rutland, C. J., and Corradini, M. L., 1997, "A Numerical Study of Cavitating Flow Through Various Nozzle Shapes," SAE Trans., **106**(3), pp. 1664–1673.
[4] Schmidt, D. P., Rutland, C. J., and Corradini, M. L., 1999, "A Fully Compressible Two-Dimensional Model of High Speed Cavitating Nozzles," Atomization Sprays, **9**, pp. 256–276.
[5] Poinsot, T. J., and Lele, S. K., 1992, "Boundary Conditions for Direct Simulations of Compressible Viscous Flows," J. Comput. Phys., **101**, pp. 104–129.
[6] Dumont, N., Simonin, O., and Habchi, C., 2001, "Numerical Simulation of Cavitating Flows in Diesel Engine Injectors by a Homogeneous Equilibrium Modeling Approach," Paper No. CAV2001-B6.005.
[7] Habchi, C., Dumont, N., and Simonin, O., 2008, "Multidimensional Simulation of Cavitating Flows in Diesel Injectors by a Homogeneous Mixture Modeling Approach," Atomization Sprays, **18**, pp. 129–162.
[8] Ning, W., Reitz, R. D., Diwakar, R., and Lippert, A. M., 2008, "A Numerical Investigation of Nozzle Geometry and Injection Condition Effects on Diesel Fuel Injector Flow Physics," SAE Paper No. 2008-01-0936.
[9] Blokkeel, G., Barbeau, B., and Borghi, R., 2003, "A 3D Eulerian Model to Improve the Primary Breakup of Atomizing Jet," SAE Paper No. 2003-01-0005.
[10] Suzzi, D., Kr, C., Blessing, M., Wenzel, P., and Weigand, B., 2008, "Validation of Eulerian Spray Concept Coupled With CFD Combustion Analysis," SAE Paper No. 2007-24-0444.
[11] Grogger, H., and Alajbegovic, A., 1998, "Calculation of the Cavitating Flow in Venturi Geometries Using Two Fluid Model," *Proceedings of the 1998 ASME Fluids Engineering Division Summer Meeting*, Jun. 21–25.
[12] Nagaoka, M., Ueda, R., Masuda, R., von Berg, E., and Tatschl, R., 2008, "Modeling of Diesel Spray Atomization Linked With Internal Nozzle Flow," *Proceedings of the THIESEL 2008.*
[13] Gavaises, M., Papoulias, D., Andriotis, A., Giannadakis, E., and Theodorakakos, A., 2007, "Link Between Cavitation Development and Erosion Damage if Diesel Fuel Injector Nozzles," SAE Paper No. 2007-01-0246.
[14] Musculus, M. P. B., Lachaux, T., Pickett, L. M., and Idicheria, A. I., 2007, "End-of-Injection Over-Mixing and Unburned Hydrocarbon Emissions in Low-Temperature-Combustion Diesel Engines," SAE Paper No. 2007-01-0907.
[15] Amsden, A. A., 1999, "KIVA-3V, RELEASE 2, Improvements to KIVA-3V," Los Alamos National Laboratory Report No. LA-UR-99-915.
[16] Amsden, A. A., O'Rourke, P. J., and Butler, T. D., 1989, "KIVA-II: A Computer Program for Chemically Reactive Flows With Sprays," Los Alamos National Laboratory Report No. LA-11560-MS.
[17] Trujillo, M. F., Torres, D. J., and O'Rourke, P. J., 2004, "High-Pressure Multicomponent Liquid Sprays: Departure From Ideal Behavior," Int. J. Engine Res., **5**(3), pp. 229–246.
[18] Naber, J. D., and Siebers, D. L., 1996, "Effects of Gas Density and Vaporization on Penetration and Dispersion of Diesel Sprays," SAE Paper No. 960034.

A Study on an Automatically Variable Intake Exhaust Injection Timing Turbocharging System for Diesel Engines

Shiyou Yang
Engine Research Center,
University of Wisconsin-Madison,
1500 Engineering Drive,
Madison, WI 53706

Kangyao Deng

Yi Cui

Hongzhong Gu

School of Mechanical Engineering,
Shanghai Jiao Tong University,
1954 Hua Shan Road,
Shanghai 200030, China

A new turbocharging system, named automatically variable intake exhaust injection timing (AVIEIT), is proposed. Its main purpose is to improve the performance of low-speed high torque operating conditions and improve the economy of high-speed operating conditions for high-speed supercharged intercooled diesel engines. The principle of the AVIEIT turbocharging system is presented. A control mechanism for the proposed AVIEIT system used for a truck diesel engine is introduced. An engine simulation code has been developed. In this code, a zero-dimensional in-cylinder combustion model, a one-dimensional finite volume method-total variation diminishing model for unsteady gas flow in the intake and exhaust manifolds, and a turbocharger model are used. The developed code is used to simulate the performances of diesel engines using the AVIEIT system. Simulations of a military use diesel engine "12V150" and a truck diesel engine "D6114" using the AVIEIT system have been performed. Simulation results show that the in-cylinder charge air amount of the diesel engine with the AVIEIT system is increased at low-speed high torque operating conditions, and the fuel economy is improved at high-speed operating conditions. In order to test the idea of the AVIEIT system, an experiment on a truck diesel engine D6114 equipped with an AVIEIT control mechanism has been finished. The experiment results show that the AVIEIT system can improve the economy of high-speed operating conditions. Both the simulation and experiment results suggest that the AVIEIT system has the potential to replace the waste-gate and variable geometry turbocharger turbocharging systems. [DOI: 10.1115/1.4000146]

Keywords: diesel engine, turbocharging system, variable valve timing, engine simulation

1 Introduction

Some high-speed supercharged intercooled diesel engines for military use, railway use, marine use, or truck use have problems at low-speed high torque operating conditions or high-speed operating conditions [1]. These problems include in-cylinder charge air amount insufficiency at low-speed high torque operating conditions, and limited charge air pressure at high-speed operating conditions due to the speed limit of turbocharger. The in-cylinder charge air amount insufficiency at low-speed high torque operating conditions may cause combustion deterioration, increase the exhaust gas temperature, and cause thermal load aggravation. The limited charge air pressure at high-speed operating conditions may limit further increase in rated power. The main reason for these problems is that the match between the diesel engine and turbocharger cannot satisfy all the operating conditions from low speed to high speed [2]. If the match between the diesel engine and the turbocharger is done at a rated speed, the turbocharger cannot supply sufficient air for the diesel engine at low-speed high torque operating conditions, while if the match is done at low speed, the revolution speed of turbocharger and the maximum in-cylinder pressure rise are very high. Many measures have and are being proposed for improving the performance of both low-speed high torque and high-speed operating conditions for supercharged intercooled diesel engines. Such measures include the waste–gate, by-pass, sequential turbocharging (STC), variable geometry turbocharger (VGT), and hyperbar systems [3–6], for improving the performance of low-speed and high-speed operating conditions. However, these measures have more or less shortcomings. Although they can solve the problems at low-speed high torque and high-speed operating conditions, they always sacrifice other aspects of performances of diesel engines. In the waste-gate system, to avoid too much high revolution speed of turbocharger at high-speed operating conditions, part of the exhaust gas before turbine is by-passed to the exhaust pipe after turbine, and thus some of the useful energy are wasted, causing high fuel consumption. The VGT can avoid the shortcomings of the waste-gate system, but the control of the VGT is complicated and the expenses of a diesel engine are increased. Also the STC can solve the problems at low-speed high torque operating conditions, but the structure of the STC is more complicated than the VGT and thus expenses are higher than the VGT. In 1990, Gu [7] proposed a turbocharging system, named "Gu-system," which can well solve the problems at both high-speed and low-speed operating conditions without sacrificing other aspects of performances. In the Gu-system, the variations of the intake, exhaust, and injection timings are controlled by three different eccentrics, which carry three rollers on different cams to move their positions. However, the structure of the Gu-system is still complicated for some compact high-speed diesel engines.

In this paper, a new turbocharging system with a simple structure, named automatically variable intake exhaust injection timing (AVIEIT), is proposed to improve the performances of both high load and low load operating conditions of high-speed supercharged intercooled diesel engines. At first we describe the principle of this turbocharging system in detail. A selected control mechanism for the AVIEIT system is introduced. Then the models used in an engine simulation code for modeling diesel engines

Contributed by the IC Engine Division of ASME for publication in the JOURNAL OF ENGINEERING FOR GAS TURBINES AND POWER. Manuscript received April 30, 2009; final manuscript received May 24, 2009; published online March 5, 2010. Editor: Dilip R. Ballal.

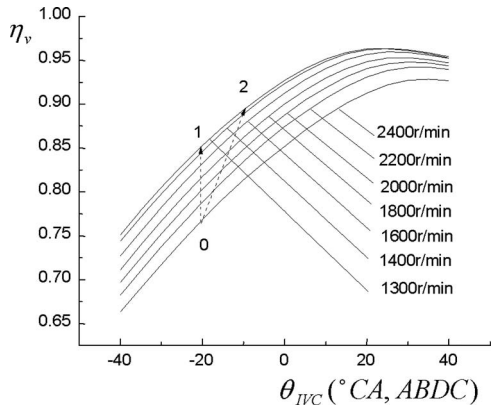

Fig. 1 Correlations between η_V and θ_{IVC}, n

using the AVIEIT system are introduced. To validate the idea of the proposed system, both simulation results and experimental results are presented.

2 The Principle of AVIEIT System

2.1 The Effect of Intake Valve Closing Timing on Volumetric Efficiency. Figure 1 shows the volumetric efficiency η_V as a function of intake vale closing timing θ_{IVC} at different engine revolution speeds of a truck diesel engine [8]. From Fig. 1, it is seen that when the intake valve closes after the 40°CA ABDC, the difference of η_V between the high speed and low speed is very small, but when the intake valve closes at an early crank angle, e.g., before the BDC, the difference of η_V between the low speed and high speed is increased. For example, when the IVC is 20°CA before the BDC, the η_V of 2400 rpm is 0.77, whereas the η_V of 1300 rpm is 0.86. The earlier the intake valve closes before the BDC, the larger the difference of η_V between the high speed and low speed is. At the same engine speed, if the intake valve closing timing is moved from before the BDC to after the BDC, η_V will be increased further. From the above observations, an idea is formed that if the intake valve closes before the BDC at high speed, and the intake valve closes after the BDC at low speed, then η_V will be improved. This process is shown as the dotted line $0 \rightarrow 2$ in Fig. 1. From this idea the AVIEIT system is proposed. In this system a control mechanism is used to realize the automatic intake valve timing change from $0 \rightarrow 2$. At high speed, since the intake valve closes before the BDC, the charge air pressure should be increased. For this purpose, the waste-gate is not necessary, and thus the useful exhaust energy can be saved.

2.2 The Basic Principle of AVIEIT System. The "built-in" type injection timing advance device is used for the control mechanism of the AVIEIT system. The advance device is put inside the camshaft transfer gear. The control mechanism construction is comparatively simple. The gear transfer system and the whole engine arrangement will not be changed. The built-in automatic timer has the self-locked function. The force from valves will not cause timing variation, and the timing variation is nearly linear with engine speed. The AVIEIT system is more suitable for high-speed supercharged diesel engines. The valve timing variations of the AVIEIT system are shown in Fig. 2.

At rated speed, the intake valve closes before the BDC. At low speed, the intake valve closing, exhaust valve opening, and injection timings are retarded with a crank angle relative to the timing at high speed. Generally speaking, at the speed of 40% of full load, the intake, exhaust, and injection timings are retarded 8–12°CA [8]. The AVIEIT system is different with the Gusystem [7], in which each timing variation is not the same, especially the intake valve closing timing can be changed by 12–15°CA. For the IVC timing, at low speed, retarding a crank

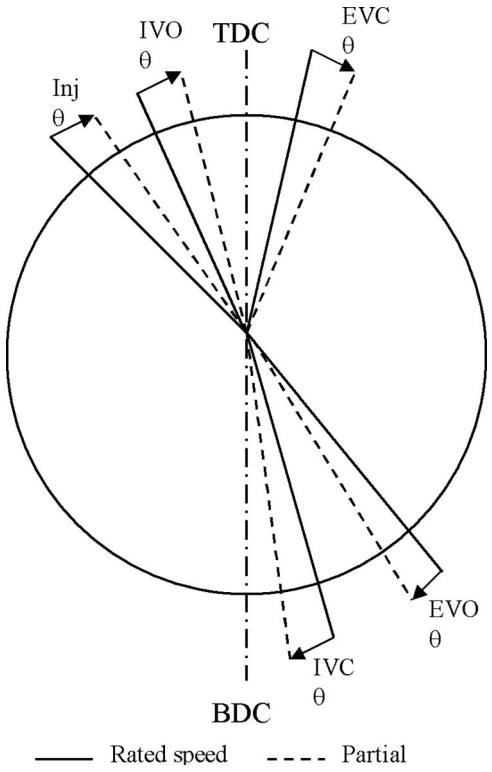

Fig. 2 Valve timing variations of the AVIEIT system

angle can increase volumetric efficiency η_V and, thus, can increase the in-cylinder charge air amount. In the AVIEIT system, the variation of the intake valve closing timing is restricted by the variation of the exhaust valve opening timing, but for high-speed supercharged diesel engines, even an 8–12°CA variation of intake valve closing timing is enough and can generate a big variation of volumetric efficiency η_V, and, thus, the in-cylinder charge air amount can be increased by 10–15% [8]. Due to the intake valve closing before the BDC, it is possible to realize in-cylinder expansion low temperature cycle and decrease emissions. The retarded exhaust valve opening timing at low speed may decrease the in-cylinder pumping loss. The retarded injection timing at low speed causes the reduction in the maximum in-cylinder pressure rise rate $(dp/d\varphi)_{\max}$ and, thus, can decrease engine vibration and combustion noise. The value of retarding the intake, exhaust, and injection timings is determined by the engine type, and it is a function of engine revolution speed.

2.3 The Control Mechanism for AVIEIT System. Figure 3 shows one selected control mechanism of the AVIEIT system designed for a truck diesel engine "D6114." As shown in Fig. 3, the driving torque of the engine is transmitted from camshaft transfer gear 1 to flying block 8, and then flying block 8 transmits the torque to sleet block 7. Sleet block 7 transmits the torque to straight pin 5, which is fixed on driven plank 2, and then the driving torque is transmitted to driven plank 2. Camshaft is driven by driven plank 2. When the diesel engine works at a fixed revolution speed, the relative position between driven plank 2 and camshaft transfer gear 1 is fixed, and there exist certain intake, exhaust, and injection timings. When the engine speed increases, the centrifugal force of flying block 8 increases; as a result, it overcomes the spring force and torque resistance to move flying block 8 outward in radial direction, and sleet block 7 also moves relative to the sleeting in the sleet groove of flying block 8. The movement of sleet block 7 drives straight pin 5, and then straight pin 5 drives driven plank 2 to advance an angle relative to camshaft transfer gear 1 in the rotating direction, until a new balance

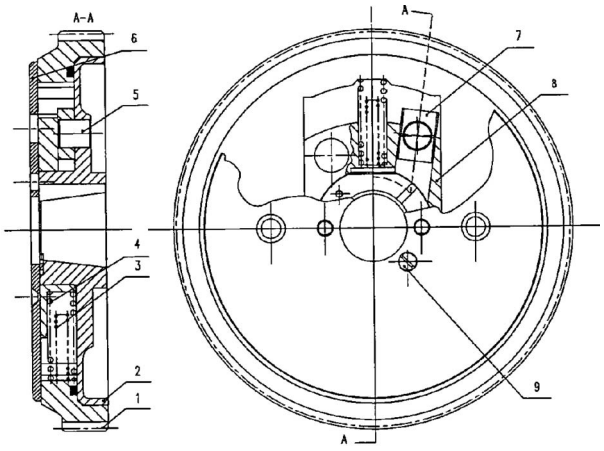

1: camshaft transfer gear; 2: driven plank; 3,4: spring; 5: straight pin; 6: cover board; 7: sleet block; 8: flying block; 9: fastening screw

Fig. 3 A selected control mechanism of the AVIEIT

position is reached. For this kind of control mechanism, the valve timing variation angle is a function of engine speed: $\theta=f(n)$.

3 Models Used in Simulation

3.1 In-Cylinder Models. The energy conservation of in-cylinder is shown in Fig. 4. The temperature change rate of the in-cylinder can be derived as [9]

$$\frac{dT_z}{d\varphi}=\left(\frac{dQ_f}{d\varphi}+\frac{dG_s}{d\varphi}I_s-\frac{dG_e}{d\varphi}I_e-\frac{dQ_w}{d\varphi}-AP_z\frac{dV_z}{d\varphi}-c_{vmz}T_z\frac{dG_z}{d\varphi}\right)\frac{1}{G_z c_{vz}} \tag{1}$$

where T_z is the in-cylinder temperature, φ is the crank angle, $dQ_f/d\varphi$ is the combustion heat release rate, $dG_s/d\varphi$ is the mass flow rate through the intake valve, I_s is the enthalpy of inlet gas, $dG_e/d\varphi$ is the mass flow rate through the exhaust valve, I_e is the enthalpy of outlet gas, $dQ_w/d\varphi$ is the heat transfer rate to the cylinder wall, A is the piston area, P_z is the in-cylinder gas pressure, $dV_z/d\varphi$ is the cylinder volume change rate, c_{vmz} is the in-cylinder average specific heat at constant volume, G_z is the in-cylinder mass, and c_{vz} is the in-cylinder specific heat at constant volume. The double-Weibe curve heat release law [9] is used to calculate $dQ_f/d\varphi$. Woschni formulation [10] is used to calculate $dQ_w/d\varphi$. The calculation of the other terms in Eq. (1) can be found in Ref. [9].

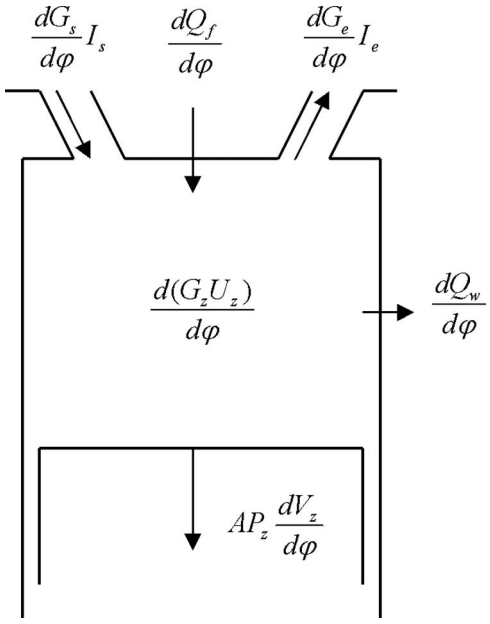

Fig. 4 The energy conservation of in-cylinder

3.2 Exhaust Gas Flow Models. Considering the tradeoff between accuracy and computational intensity, an explicit finite volume method (FVM) plus a second-order total variation diminishing (TVD) scheme of Harten [11] are used to simulate the one-dimensional unsteady exhaust gas flow in this paper. The governing equations for the one-dimensional unsteady gas flow of a compressible fluid in a pipe with variable cross section area A, wall friction f, and heat transfer q are written in vector form as follows [12]:

$$\frac{\partial \mathbf{W}}{\partial t}+\frac{\partial \mathbf{F}(\mathbf{W})}{\partial x}=\mathbf{S}(\mathbf{W}) \tag{2}$$

where

$$\mathbf{W}=\begin{bmatrix}\rho\\ \rho u\\ \rho\left(e+\frac{u^2}{2}\right)\end{bmatrix},\quad \mathbf{F}(\mathbf{W})=\begin{bmatrix}\rho u\\ \rho u^2+p\\ \rho u\left(\frac{u^2}{2}+e+\frac{p}{\rho}\right)\end{bmatrix}$$

$$\mathbf{S}(\mathbf{W})=\begin{bmatrix}-\frac{\rho u}{A}\frac{dA}{dx}\\ -\frac{\rho u^2}{A}\frac{dA}{dx}-\rho G\\ -\left(\frac{\rho u^2}{2}+p\frac{\gamma}{\gamma-1}\right)\frac{u}{A}\frac{dA}{dx}+\rho q e\end{bmatrix}$$

where ρ, u, p, e, and γ are the density, flow velocity, pressure, internal energy, and specific heat ratio, respectively. t is the time and x is the length. The wall heat transfer q can be calculated as $q=(2f/D)(\gamma/(\gamma-1))R|u|(T_w-T_g)$, where f, D, R, T_W, and T_g are the wall friction coefficient, the pipe diameter, the gas constant, the wall temperature, and gas temperature, respectively. $G=f(u|u|/2)(4/D)$ is the friction term, and the term $u|u|$ is used to ensure that the pipe wall friction always oppose the fluid motion.

The second-order accuracy TVD scheme is described by

$$\mathbf{W}_i^{n+1/2}=\mathbf{W}_i^n-\frac{\Delta t}{2\Delta x}(\mathbf{F}_{i+1/2}^n-\mathbf{F}_{i-1/2}^n)+\frac{\Delta t}{2}\mathbf{S}_i^n \tag{3}$$

$$\mathbf{W}_i^{n+1}=\mathbf{W}_i^n-\frac{\Delta t}{\Delta x}(\mathbf{F}_{i+1/2}^{n+1/2}-\mathbf{F}_{i-1/2}^{n+1/2})+\Delta t\mathbf{S}_i^{n+1/2} \tag{4}$$

where Δt and Δx are the time step and space step, respectively, i is the mesh number, and n is the time level. For subsonic flow, the flux and source terms are calculated based on the upstream scheme [13]

$$\mathbf{F}_{i+1/2}=\frac{(u_{i+1/2}+a_{i+1/2})\mathbf{F}(\mathbf{W}_{i+1/2}^L)-(u_{i+1/2}-a_{i+1/2})\mathbf{F}(\mathbf{W}_{i+1/2}^R)}{2a_{i+1/2}}+\frac{(u_{i+1/2}+a_{i+1/2})(u_{i+1/2}-a_{i+1/2})}{2a_{i+1/2}}(\mathbf{W}_{i+1/2}^R-\mathbf{W}_{i+1/2}^L) \tag{5}$$

$$\mathbf{S}_{i+1/2} = \frac{(u_{i+1/2} + a_{i+1/2})\mathbf{S}(\mathbf{W}_{i-1/2}) - (u_{i+1/2} + a_{i+1/2})\mathbf{S}(\mathbf{W}_{i+1/2})}{2a_{i+1/2}} \tag{6}$$

where a represents the speed of sound. The values at the midgrid points are calculated based on the arithmetic mean values of the following terms:

$$\mathbf{W}^L_{i+1/2} = \mathbf{W}_i + \tfrac{1}{2}\Phi(\theta_i)(\mathbf{W}_{i+1} - \mathbf{W}_i) \tag{7}$$

$$\mathbf{W}^R_{i+1/2} = \mathbf{W}_{i+1} - \tfrac{1}{2}\Phi(\theta_{i+1})(\mathbf{W}_{i+2} - \mathbf{W}_{i+1}) \tag{8}$$

where $\theta = (\mathbf{W}_i - \mathbf{W}_{i-1})/(\mathbf{W}_{i+1} - \mathbf{W}_i)$ and $\Phi(\theta) = (|\theta| + \theta)/(1 + |\theta|)$.

3.3 Turbocharger Models. The radial turbine efficiency η_T is calculated as [9]

$$\frac{\eta_T}{\eta_{T\max}} = -0.105 + 2.685 \times \left(\frac{u}{c_0}\right) - 0.76 \times \left(\frac{u}{c_0}\right)^2 - 1.17 \times \left(\frac{u}{c_0}\right)^3 \tag{9}$$

where $\eta_{T\max}$ is the maximum turbine efficiency, and u/c_0 is the ratio of turbine circumferential velocity to the exhaust gas velocity before turbine. The mass flow rate through the turbine G_T is calculated as [9]

$$G_T = \mu_T \times F_{\text{res}} P_T / \sqrt{R_T T_T} \times \sqrt{2g \frac{K_T}{K_T - 1}\left[\left(\frac{1}{\pi_{T,\text{eq}}}\right)^{2/K_T} - \left(\frac{1}{\pi_{T,\text{eq}}}\right)^{(K_T+1)/K_T}\right]} \tag{10}$$

where μ_T is the mass flow rate coefficient, F_{res} is the equivalent turbine nozzle area, P_T is the exhaust gas pressure before turbine, R_T is the exhaust gas constant, T_T is the exhaust gas temperature before turbine, K_T is the specific heat ratio of exhaust gas, and $\pi_{T,\text{eq}}$ is the equivalent exhaust gas expansion ratio. $\pi_{T,\text{eq}}$ is calculated as [9]

$$\pi_{T,\text{eq}} = \pi_T \left(1 - \frac{u_T^2}{\dfrac{gK_T}{K_T - 1} R_T T_T}\right) \tag{11}$$

where π_T is the exhaust gas expansion ratio $P_T/P_{T\text{amb}}$, and u_T is the turbine circumferential velocity. The mass flow rate coefficient μ_T can be calculated as [9]

$$\mu_T = 1.1787 - 1.6074/(20\pi_{T,\text{eq}} - 16) + 4.608e^{-18(\pi_{T,\text{eq}} - 1.01)} \times (\pi_{T,\text{eq}} - 1.05) \tag{12}$$

The calculation of other terms in Eqs. (9)–(12) can be found in Ref. [9].

4 Simulation Results and Analysis

4.1 Simulation of a Military Use Diesel Engine "12V150" Using the AVIEIT System. A military use diesel engine 12V150 has 12 cylinders, and the cylinder diameter is 150 mm. This engine originally matches with the turbocharger at rated speed operating condition. But at low-speed high torque operating conditions the in-cylinder air amount is not sufficient, causing high exhaust temperature. This engine using the proposed AVIEIT system has been simulated. Figures 5(*a*)–5(*f*) show the performance comparison between the engine with the AVIEIT system and without the AVIEIT system.

In Fig. 5(*a*), the excess combustion air ratio is defined as the actual air fuel ratio divided by the stoichiometric air fuel ratio. It is a very important parameter to evaluate the in-cylinder charge air amount in engine simulation. In the simulation we still match the diesel engine with the turbocharger at rated engine speed (2200 rpm). The excess combustion air ratio of 2200 rpm is kept the same as that of the base engine (without using the AVIEIT). Because the IVC is before the BDC at 2200 rpm, to keep the in-cylinder charge air amount unchanged the charge air pressure should be increased, as shown in Fig. 5(*b*). A smaller size of turbocharger can be matched to increase the charge air pressure.

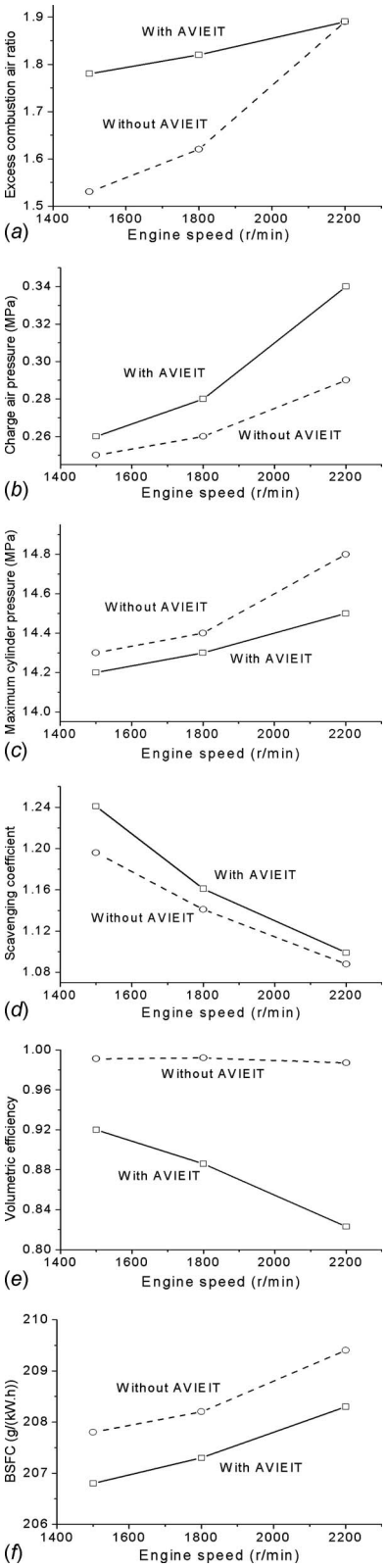

Fig. 5 Comparison between with the AVIEIT system and without the AVIEIT system: (*a*) excess combustion air ratio, (*b*) charge air pressure, (*c*) maximum in-cylinder pressure, (*d*) scavenging coefficient, (*e*) volumetric efficiency, and (*f*) brake specific fuel consumption

From Fig. 5(*a*), it is seen that the excess combustion air ratio of the AVIEIT system at 1800 rpm is 1.83, and at 1500 rpm is 1.73. For this diesel engine if the excess combustion air ratio is above 1.7 the performances including exhaust gas temperature and emissions are good enough, while the excess combustion air ratio values of the base engine at 1800 rpm and 1500 rpm are lower than 1.65. That is the reason why the base diesel engine has higher thermal load and dark smoke at low-speed operating conditions. The excess combustion air ratio values of the AVIEIT system are enough higher than those of without the AVIEIT system. The reason for the higher excess combustion air ratio is that in the AVIEIT system the IVC is retarded with a crank angle at low-speed operating conditions, and, thus, the volumetric efficiency is increased, as shown in Fig. 5(*e*), while the volumetric efficiency of the base engine does not change form low speed to high speed. So, with respect to improving the in-cylinder charge air amount at low-speed operating conditions, the AVIEIT system is better than the original diesel engine without the AVIEIT system. The other parameters shown in Figs. 5(*c*), 5(*d*), and 5(*f*), the maximum in-cylinder pressure, the scavenging coefficient, and the brake specific fuel consumption of the AVIEIT system, are all better than those of without the AVIEIT system. The reason for the lower maximum in-cylinder pressure and brake specific fuel consumption is that the IVC is before the BDC, and, thus, a low temperature and pressure in-cylinder cycle is realized. The scavenging coefficient is defined as the ratio of the air amount passing through the intake valve to the air amount left in the cylinder. From Fig. 5(*d*), it is seen that the higher scavenging coefficient of the AVIEIT system is helpful in reducing the exhaust gas temperature before the turbine.

4.2 Simulation of a Truck Diesel Engine D6114 Using the AVIEIT System. A truck diesel engine D6114 has six cylinders, and the cylinder diameter is 114 mm. This engine originally matches with the turbocharger at the maximum torque operating condition. At high-speed conditions the waste-gate system is used to avoid high in-cylinder pressure and high revolution speed of turbocharger. The main purpose to match the diesel engine with the turbocharger at low-speed operating conditions is to supply sufficient combustion air amount at the maximum torque operating condition (1300 rpm). The excess combustion air ratio of 1300 rpm is 1.63, which is good for this engine at this condition. However, the economy characteristic is poor at high speeds due to the waste of useful energy. The brake specific fuel consumption at rated speed (2400 rpm) reaches 252.10 g/kWh. Simulation of this engine using the AVIEIT system has been performed. Figures 6(*a*)–6(*f*) show the performance comparison between with the AVIEIT system and the original waste-gate system.

In the simulation we still match the diesel engine with the turbocharger at the maximum torque speed (1300 rpm). But the waste-gate is always closed at high speeds, because in the AVIEIT system the IVC is before the BDC. From Fig. 6(*b*) it is seen that because the waste-gate is always closed in the AVIEIT system the charge air pressure of the AVIEIT is always higher than that of the waste-gate. Because in the AVIEIT the charge air pressure is increased the excess combustion air ratio varies from 1.93 at a rated speed to 1.64 at the maximum torque speed, as shown in Fig. 6(*a*). Nearly at all speeds, the excess combustion air ratio of the AVIEIT system is apparently higher than that of the waste-gate system. Due to sufficient charge air amount for combustion and low temperature cycle the exhaust gas temperature of the AVIEIT is lower than that of the waste-gate, as shown in Fig. 6(*d*). From Fig. 6(*c*) it is seen that because of the increased charge air pressure the maximum in-cylinder pressure of the AVIEIT is higher than that of the waste-gate at high engine speeds. Although the maximum in-cylinder pressure is increased, it is still below the limit of the maximum in-cylinder pressure of this engine. Because the waste-gate system is removed in the AVIEIT, the BSFC of

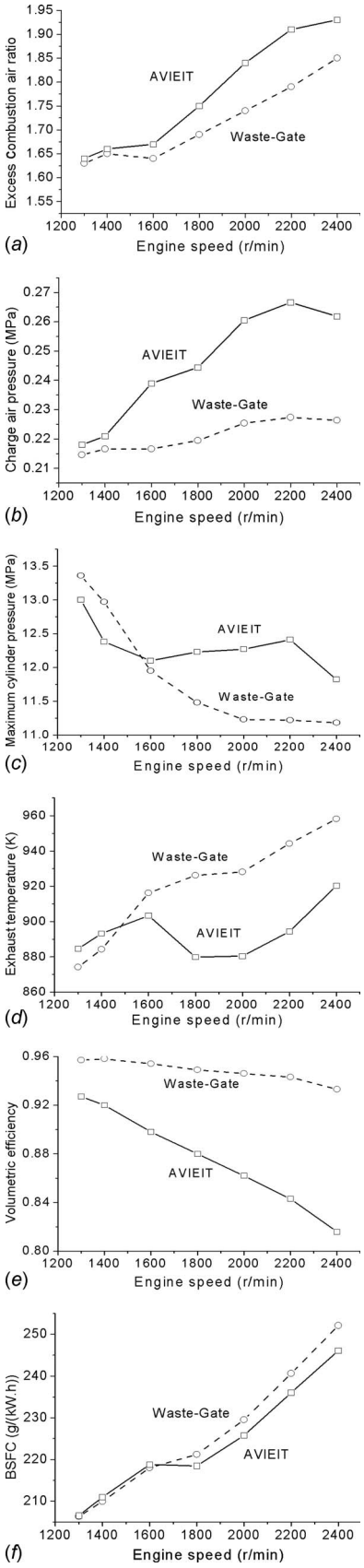

Fig. 6 Comparison between the AVIEIT system and the waste-gate system: (*a*) excess combustion air ratio, (*b*) charge air pressure, (*c*) maximum cylinder pressure, (*d*) exhaust gas temperature, (*e*) volumetric efficiency, and (*f*) brake specific fuel consumption

Table 1 Intake exhaust injection timing of each engine speed

Operating condition	2400 rpm	2200 rpm	2000 rpm	1800 rpm	1600 rpm	1400 rpm	1300 rpm
EVO (BBDC)	67.5	66.5	65.5	64.5	63.5	61.5	59.5
IVC (ABDC)	−8	−7	−6	−5	−4	−2	0
EVC (ATDC)	25.5	26.5	27.5	28.5	29.5	31.5	33.5
IVO (BTDC)	22.5	21.5	20.5	19.5	18.5	16.5	14.5
INJ (BTDC)	20	19	18	17	16	14	12

Table 2 Experiments on a truck diesel engine D6114 with a waste-gate system

n (rpm)	N_e (kW)	BSFC (kWh)	G_s (kg/s)	α	P_s (MPa)	T_s (K)	P_T (MPa)	T_T (K)	Smoke (PSU)	P_{max} (MPa)	η_V	NO_x (ppm)	CO (ppm)	HC (ppmc)
1300	146.9	210.2	0.188	1.533	0.205	309.6	0.167	898	3.35	13.40	0.941	785	100	94.5
2400	205	253.6	0.371	1.849	0.227	319.8	0.239	957	2.25	11.05	0.907	345	120	96

Table 3 Experiments on a truck diesel engine D6114 with an AVIEIT system

n (rpm)	N_e (kW)	BSFC (kWh)	G_s (kg/s)	α	P_s (MPa)	T_s (K)	P_T (MPa)	T_T (K)	Smoke (PSU)	P_{max} (MPa)	η_V	NO_x (ppm)	CO (ppm)	HC (ppmc)
1300	146.9	210.0	0.195	1.566	0.214	308.5	0.169	906	3.80	13.80	0.90	720	95	81
2400	205	247.6	0.385	1.965	0.295	328.3	0.295	924	2.15	11.70	0.74	242	120	90

high speed is decreased. The BSFC of rated speed is decreased by 6 g/kWh, as can be seen in Fig. 6(*f*). The volumetric efficiency comparison in Fig. 6(*e*) is similar with Fig. 5(*e*).

5 Experiments on a Diesel Engine With AVIEIT System

5.1 The Design of Control Mechanism of AVIEIT System Equipped on a Truck Diesel Engine D6114. According to the simulation results of a truck diesel engine D6114 using the AVIEIT system as described above, a control mechanism of the AVIEIT system equipped on this diesel engine has been designed. It is shown in Fig. 3. By computation, the intake, exhaust, and injection timings that this AVIEIT control mechanism can realize at each engine speed are shown in Table 1.

5.2 Experiments on an Engine With a Waste-Gate System. A truck diesel engine D6114 is companied with waste-gate. An experiment of the waste-gate system at the maximum torque speed and rated speed has been completed. The experimental results are shown in Table 2.

5.3 Experiments on an Engine With an AVIEIT System. The control mechanism of the AVIEIT system designed above was equipped on a truck diesel engine D6114, and then an experiment at the maximum torque speed and rated speed has been completed. Because the intake valve closing timing is at the BDC at the maximum torque operating condition, a small diameter entrance turbine is used to increase the charge air pressure to ensure that the excess combustion air ratio is identical with that of the waste-gate system at the maximum torque operating condition. Because the intake valve closing timing is before the BDC at the rated speed operating condition, the waste-gate valve can be closed. This action can save useful energy. The experimental results are shown in Table 3.

5.4 Analysis of Experimental Results. The meaning of each symbol in Tables 2 and 3 can be found from Nomenclature and Sec. 3. From Tables 2 and 3, it is seen that with the AVIEIT system, because a small diameter entrance turbine is used, at the maximum torque operating condition, the charge air pressure and air mass flow rate are higher than that of the waste-gate system. Although the intake valve closing timing is at the BDC at the maximum torque condition, the cylinder excess combustion air ratio of the AVIEIT can maintain the same value as that of the waste-gate. Other parameters, such as BSFC, temperature after intercooler, exhaust pressure before turbine, exhaust temperature before turbine, and smoke, are nearly unchanged.

At rated speed, because the waste-gate is removed, the supercharged air pressure is increased. Correspondingly the air mass flow rate, excess combustion air ratio, and exhaust air pressure are increased. Because of the saved useful energy and realizing low temperature in-cylinder cycle, the BSFC is decreased by 6g/kWh, and exhaust temperature, smoke, and emissions are all decreased.

From the above analysis, a conclusion can be drawn out that under the case that the performance of the AVIEIT is nearly the same as that of the waste-gate at the maximum torque operating condition, the AVIEIT can replace waste-gate at rated speed to decrease fuel consumption and emissions.

6 Conclusions

By simulating a military use diesel engine 12V150 with and without the AVIEIT system, a conclusion can be drawn that the AVIEIT system has the function of improving the excess combustion air amount at low-speed high torque operating condition of high-speed supercharged intercooled diesel engines. By simulating a truck diesel engine D6114, a conclusion can be drawn that the AVIEIT system can replace the waste-gate system for decreasing BSFC.

Experiment comparison between the AVIEIT system and the waste-gate system shows that under the case that the performance of the AVIEIT is nearly the same as that of the waste-gate at the maximum torque operating condition, the AVIEIT can replace the waste-gate at rated speed to decrease fuel consumption and emissions.

Acknowledgment

This work was supported by Shanghai Diesel Engine Co. of China. The authors thank Dr. You Zhang and Dr. Hanlin Yang for

helpful discussions and comments. Shanghai Diesel Engine Co. of China is thanked for providing experiments for validating the AVIEIT system proposed in this paper.

Nomenclature

ABDC = after bottom dead center
ATDC = after top dead center
BBDC = before bottom dead center
BDC = bottom dead center
BSFC = brake specific fuel consumption
BTDC = before top dead center
CA = crank angle
EVC = exhaust valve close
EVO = exhaust valve open
INJ = injection timing
IVC = intake valve close
IVO = intake valve open
rpm = revolutions per minute
TDC = top dead center
n = engine speed
N_e = power
G_s = mass flow rate
α = excess combustion air ratio
P_s = boosted air pressure
T_s = boosted air temperature
$P_{\max}$ = maximum in-cylinder pressure

References

[1] Gu, H., 1998, *Research on Performance of Turbocharged Diesel Engines*, Shanghai Jiao Tong University, Shanghai, China.
[2] Watson, N., 1982, *Turbocharging the Internal Combustion Engine*, Macmillan, London.
[3] Walsham, B. E., 1990, "Alternative Turbocharger Systems for the Automotive Diesel Engine," IMechE Conference on Turbo-Charging and Turbochargers, London, May, Paper No. C405/036.
[4] Borilla, Y. G., 1986, "Some Aspects of Performance Optimization of the Sequentially Turbocharged Highly-Rated Truck Diesel Engine With Turbochargers of Unequal Site and a Pulse Converter," IMechE, Paper No. C105186.
[5] Hashimoto, T., Okada, K., and Oikawa, T., "ISUZU New 9.81 Diesel Engine With Variable Geometry Turbocharger," Paper No. SAE860460.
[6] Andre-Talamon, T., 1983, "Supercharged Engine Used for High Performance Ship Main Power," 15th CIMAC Congress, Paper No. D12.1.
[7] Gu, H., 1990, "A New System for Recovering Surplus Exhaust Gas Energy," discussion on the ISME Fourth International Marine Engineering Conference, Japan, Discussion No. PD7-1, p. 10.
[8] Gu, H., 1997, "Some New Systems for Improving the Partial Load Performance of High and Medium Speed Turbocharged Diesel Engines," International Conference on I. C. Engines, Wuhan, China, Oct.
[9] Gu, H., 1985, *Simulation of Turbocharged Diesel Engines*, Shanghai Jiao Tong University, Shanghai, China.
[10] Woschni, G., "Universally Applicable Equation for the Instantaneous Heat Transfer Coefficient in the Internal Combustion Engine," Paper No. SAE 670931.
[11] Harten, A., 1983, "High Resolution Schemes for Hyperbolic Conservation Laws," J. Comput. Phys., **49**, pp. 357–393.
[12] Yang, S., Deng, K., and Cui, Yi., 2007, "Simulation and Experimental Research on a Mixed Pulse Converter Turbo-Charging System," Proc. Inst. Mech. Eng., Part D (J. Automob. Eng.), **221**(2), pp. 215–223.
[13] Chalet, D., Chesse, P., and Hetet, J. F., 2008, "Boundary Conditions Modeling of One-Dimensional Gas Flows in an Internal Combustion Engine," Int. J. Engine Res., **9**, pp. 267–282.

In-Cylinder Flow Computational Fluid Dynamics Analysis of a Four-Valve Spark Ignition Engine: Comparison Between Steady and Dynamic Tests

Damian E. Ramajo
e-mail: dramajo@santafe-conicet.gov.ar

Norberto M. Nigro

International Center for Computational Methods in Engineering (CIMEC), INTEC-Universidad Nacional del Litoral-CONICET, Güemes 3450, S3000GLN Santa Fe, Argentina

Numerical and experimental techniques were applied in order to study the in-cylinder flow field in a commercial four-valve per cylinder spark ignition engine. Investigation was aimed at analyzing the generation and evolution of tumble-vortex structures during the intake and compression strokes, and the capacity of this engine to promote turbulence enhancement during tumble degradation at the end of the compression stroke. For these purposes, three different approaches were analyzed. First, steady flow rig tests were experimentally carried out, and then reproduced by computational fluid dynamics (CFD). Once CFD was assessed, cold dynamic simulations of the full engine cycle were performed for several engine speeds (1500 rpm, 3000 rpm, and 4500 rpm). Steady and cold dynamic results were compared in order to assess the feasibility of the former to quantify the in-cylinder flow. After that, combustion was incorporated by means of a homogeneous heat source, and dynamic boundary conditions were introduced in order to approach real engine conditions. The combustion model estimates the burning rate as a function of some averaged in-cylinder flow variables (temperature, pressure, turbulent intensity, and piston position). Results were employed to characterize the in-cylinder flow field of the engine and to establish similarities and differences between the three performed tests that are currently used to estimate the engine mean flow characteristics (steady flow rig, and cold and real dynamic simulations). [DOI: 10.1115/1.4000265]

Keywords: dynamic engine simulation, steady flow rig tests, CFD, tumble, turbulence

1 Introduction

In-cylinder charge motion has been steadily gaining importance since the introduction of new technologies such as gasoline direct injection (GDI) or homogeneous charge compression ignition (HCCI). Understanding the behavior of in-cylinder flow structures is the first step to efficiently control fuel stratification, turbulence generation, and heat losses. These factors play a crucial role on fuel economy, emissions, and engine performance.

For years, engine development has been mainly supported by experimental tests such as dynamometric and steady flow rig tests. Latterly, the evolution of optical techniques has allowed sights of the inside of optical access engines. However, this kind of tests are tedious, expensive, and limited to low engine speeds. Moreover, they are restricted to a small portion of the whole cylinder. On the other hand, steady rig tests are easier, faster, and cheaper, but they yield limited information about engine performance and in-cylinder flow characteristics under real conditions.

Engine research by computational techniques started by means of zero-/one-dimensional (0D/1D) simulators. Nowadays, they are massively employed to study the overall engine gas dynamics, but in-cylinder studies are gaining more relevance due to the necessity to improve combustion and reduce emissions. For this reason, computational fluid dynamics (CFD) became a useful tool to design complex engine components such as combustion chambers, manifolds, and injectors. During the last years CFD has been significantly improved, especially thanks to high performance computing (HPC), allowing more real engine simulations. Nowadays, efforts are focused on simulating injection of fuel, combustion, and chemical species evolution for emission control. But, on the other hand, experimental techniques such as steady rig and cold dynamic tests (optical) are daily employed. Several papers report CFD simulations of intake-compression or compression-expansion strokes [1–8], but only a few deal with whole engine cycles [9–14]. One possible explanation might be found on the difficulty to handle the extreme mesh deformations around valves and the topological changes during valve opening and closing. Moreover, combustion model estimations are far from accurate, so cold in-cylinder simulations are the first step to understand in-cylinder flow dynamics.

In this work experimental and CFD steady tests were carried out. Subsequently, the in-cylinder flow behaviors under cold and real dynamic conditions were solved by CFD and results were compared with the steady ones, concluding about the usefulness of steady and dynamic tests.

2 Methodology

A commercial 16-valve four-cylinder spark ignition Fiat Torque engine was employed. Table 1 consigns the main constructive and operative characteristics of the engine. Crank angles (CAs) are given with reference to the top dead center (TDC) at the beginning of the intake stroke. Steady test conditions are not standardized, so it is important to describe the methodology to carry on the different tests. As regards to the performed steady test simulations, they reproduced the experimental conditions as exactly as possible.

Three kinds of steady tests were carried out as follows: flowmeter, swirl, and tumble tests. For all tests, a constant pressure drop of 6227 Pa (equivalent to 25 in. of water) (SuperFlow SF-

Contributed by the IC Engine Division of ASME for publication in the JOURNAL OF ENGINEERING FOR GAS TURBINES AND POWER. Manuscript received March 5, 2009; final manuscript received September 7, 2009; published online March 5, 2010. Editor: Dilip R. Ballal.

Table 1 Constructive and operative data of the engine

Cylinder		Valves characteristics		
Fuel	Gasoline		Intake	Exhaust
Number of cylinders	4	Diameter (mm)	30.4	29.9
Piston displacement	1582 cm^3	Maximum lift (mm) at CA	9 mm at 102.5 deg	8.5 mm at 618.5 deg
Bore	87 mm			
Stroke	68 mm	Opening period (CA)	255 deg	253 deg
Compression ratio	10.5:1	OVA (CA)	25 deg	48 deg
Connecting rod length	118 mm	CVR (CA)	50 deg	25 deg

600) was applied to the cylinder head to induce flow. A rotating-honeycomb swirl meter (SM) (AUDIE Technology) was employed to perform the angular momentum measurements.

2.1 Experimental Procedure: Steady Tests. As regards to flow discharge coefficients, both the intake and the exhaust systems were studied. Flow entered the cylinder through the intake system, and left the cylinder through the exhaust. In order to reduce flow turbulence and wave effects, a 100 mm cylinder was placed between the cylinder head and flowbench. Additionally, a nozzle and a diffuser were placed at the beginning and at the end of the intake and exhaust ducts, respectively.

For swirl tests the swirl meter was inserted between the cylinder and flowbench. As regards to tumble tests, they were performed through a L-shape tumble bench (Fig. 1) of our own design and based on CFD analysis [15].

The employed tumble bench has some interesting characteristics. First, the lateral duct has a diameter larger than the cylinder bore, thus reducing tumble loss. Moreover, tumble loss is fairly linear along the lateral duct. Second, the fact that the tumble bench has only one lateral duct produces more intense angular momentum. Third, the tumble loss at the joint between the cylinder and the lateral duct is negligible, so tumble below the cylinder head can be estimated by linear extrapolation with two measurements along the lateral duct (P_2 and P_4, for example). Finally, in general, L-shape benches are asymmetric with respect to the cylinder mean plane, so one of the intake valves produces more tumble than the other [16]. This can be observed by measuring the tumble generated while one of both valves is kept closed. However, no difference was experimentally observed for this tumble bench. That is, both valves produced the same tumble regardless of which one was closed. That might be explained by the significant distance that exists from the lateral duct to the bridle (30 mm), and the fact that the joint between the cylinder and the lateral duct is symmetric. From the experimental results, it was found that this tumble bench introduces a pressure drop, reducing the mass flow rate at maximum valve lift in 7%.

3 Numerical Procedure

3.1 Computational Model. Due to the narrow dimensions of the engine ports, in order to obtain the engine geometry, it was necessary to make positive replicas from the intake and exhaust ports (low-contraction silicone) and the combustion chamber (high-rigid polyester resin). Afterwards, replicas were measured by means of a three-dimensional rotary laser scanner (Roland LPX-250), obtaining around 550,000 points over the surfaces of replicas. Pathlines were drawn from selected points (GID 7.2) and then exported to ANSYS-ICEM 10.0 to generate the overall surface by adding small patches (Fig. 2).

The meshes were generated in ANSYS-ICEM 10.0. The optimum element size (1.1 mm) [15] was obtained through a mesh convergence study. Around 2×10^6 tetrahedral elements were required to get an accurate description of the layout of the steady rig tests.

3.1.1 Steady Test Simulations. Results were obtained by using the incompressible and isothermal Navier–Stokes equations. Although air is clearly a compressible fluid, due to the relatively low flow velocities close to the valves (maximum Mach number of around 0.2), the compressible effects on the air are less than 4%; therefore, incompressible formulation is appropriate in this context. Turbulence was modeled through a standard k-ε model. Simulations were unsteady, so a suitable time step was obtained through a time-convergence study, this being 5×10^{-5} s [15]. At least 1000 time steps were solved for each valve lift. Results were obtained as a time average of 10 solutions in time along the simulated period.

Steady test simulations reproduced the experimental conditions. Cylinder head was subjected to a pressure drop that was progressively increased from 0 Pa to 6227 Pa (25 in. of water) in order to avoid overflow problems.

A boundary condition of total pressure was fixed at the inlet, while an opening condition was employed for the outlet (this al-

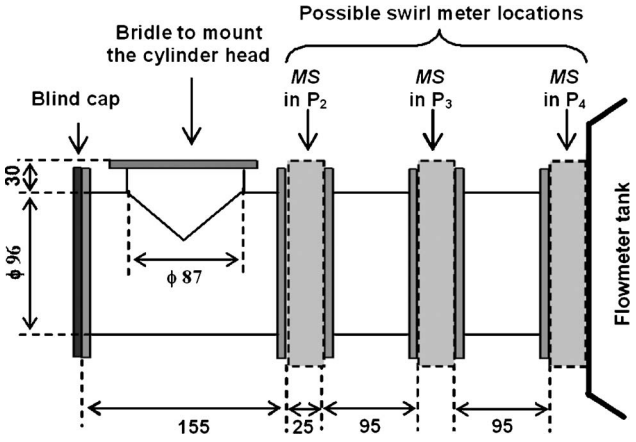

Fig. 1 Sketch of the tumble bench employed

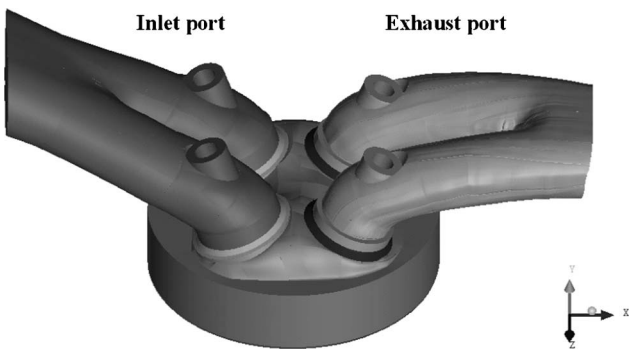

Fig. 2 Computational model

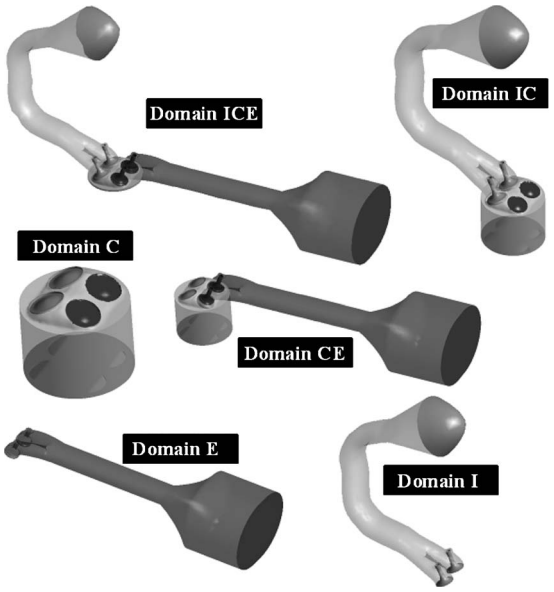

Fig. 3 Different kinds of domains employed to simulate the whole engine cycle

lows the flow to leave or to enter the domain according to pressure conditions). A no-slip boundary condition was fixed at walls, and a roughness of 0.2 mm was applied at the intake and exhaust duct walls.

Models were solved with distributed calculus in a Beowulf cluster with 20 single-core processors; around 24 h were necessary to obtain each valve lift result.

3.1.2 Dynamic Test Simulations. For dynamic test simulations the compressible Navier–Stokes equations were solved, including the thermal equation for both cold and real dynamic simulations. Cold dynamic simulations were performed under atmospheric pressure and room temperature conditions at the inlet and outlet boundaries, and room temperature was also set at the engine walls. Although these engine test conditions are far from the real ones, experimental tests under these conditions are usually carried on in order to visualize the in-cylinder flow patterns and measure the vortex dynamics, so cold versus real dynamic simulations can be useful to extract conclusions about the suitability of the firsts.

Tackling the dynamic simulation of the whole engine cycle involves at least two main difficulties: the mesh deformation and the topological changes in the geometry. Mesh deformation was handled by a Laplacian algorithm, which, at each time step, computes the displacement of the inner nodes due to the imposed motions at some boundary walls. Moreover, that was combined with remeshing after several time steps, thus preserving mesh quality. Seventeen remeshes were needed to complete the whole engine cycle. The mesh deformation algorithm of ANSYS-CFX 10.0 did not prove to be robust enough, so better algorithms, such as the one introduced by Lopez et al. [17], are being considered in order to reduce the remeshing steps from 17 to only 4.

Simulations start at the TDC when all valves are opened and the intake and exhaust systems are connected to the cylinder (domain *ICE* at Fig. 3). Then, the exhaust valves close and the exhaust duct is disconnected to the cylinder. After that, the exhaust system is solved separately. Six different *IC* domains are needed to represent the intake process (from 0 CA to 208 CA). Once the intake valves are completely closed (at 208 CA), three isolated domains are solved (*I*, *C*, and *E*). At 492 CA deg, the exhaust valves are opened, connecting the exhaust duct to the cylinder (domain *CE*), so initial conditions have to be fed from the isolated domains *C* and *E*. For this purpose, a user external Fortran routine (UEFR) was incorporated to ANSYS-CFX. This routine uses a directed-search algorithm to find the cell of the *C* domain or *E* domain, where each one of the nodes of the assembled *CE* domain is located. Then, a finite element interpolation is employed to find initial conditions for temperature, pressure, and turbulence [15]. The assembled methodology is also applied when the intake valves are opened.

The extreme deformation of the mesh around the valve seats is a really hard problem for the mesh deformation algorithm. So, the minimum valve lift was limited to 0.6 mm. That is, the domains were connected or disconnected when the valve lifts reached a lift threshold of 0.6 mm. Although this reduces the valve opening period, the mass flow rate at low valve lifts can be neglected.

Even though the simulation of several isolated domains is laborious, it allows the use of an increased time step to simulate the intake and exhaust systems due to the low gas velocity inside ducts, thus reducing the cost of simulations without introducing convergence problems.

The real valve displacements were computed through the well-known crank-slider mechanism expression [18] and then introduced to simulations through an UEFR.

The time step at 1500 rpm was 5×10^{-5} s (the same as for steady tests), while it was reduced to 2.5×10^{-5} s at 3000 rpm and 1.66×10^{-5} s at 4500 rpm in order to keep the Courant number almost constant.

Depending on the mesh sizes, between 8 and 20 cluster processors were employed to solve the dynamic simulations. The simulation of one engine cycle at 1500 rpm demanded about 40 h, this value increasing to 80 h at 3000 rpm and to 120 h at 4500 rpm.

3.1.3 Combustion Model. For homogeneous charge spark ignition (HCSI) engines, combustion takes place in a very thin zone (a few millimeters), where flame propagation is fairly laminar. Turbulence distorts, stretches, and corrugates the thin combustion zone, increasing the flame front surface area and enhancing the mixing of reactants. Combustion phenomenon can be classified under the turbulent premixed combustion flamelet regime. This regime has the advantage of allowing the flow behavior and the combustion phenomenon to be solved separately, only introducing the combustion effect by means of a heat source in the energy balance equation [7,19].

In this work, a phenomenological simple combustion model was implemented in order to roughly quantify the effect of combustion (change in temperature, pressure, and gas properties) over the in-cylinder flow behavior. As expected, combustion increases the gas temperature and pressure, affecting mainly the gas viscosity, thermal conductivity, and heat capacity. But the most evident effect is that the in-cylinder pressure increment affects the in-cylinder mass flow rate during the intake and exhaust processes, modifying the in-cylinder flow structures. The combustion model was incorporated through a UEFR. This takes into account the main in-cylinder flow variables (average pressure and temperature and the turbulence quantities k and ε), applying a simple fractal model to estimate the turbulent burning velocity (S_t)

$$\frac{S_t}{S_l}=\frac{A_t}{A_l}\approx\left(\frac{l_e}{l_i}\right)^{D_3-2} \tag{1}$$

where S_l is the laminar burning velocity, A_t and A_l are the turbulent and laminar flame front surface areas, and l_e and l_i are the outer and inner turbulent spatial cutoff scales, respectively [20]. Finally, D_3 is a fractal dimension. The scales l_e and l_i are related to the biggest and the smallest turbulent structures of the flow, respectively. l_e and l_i were assumed as the integral scale and the Kolmogorov one, respectively. The fractal dimension D_3 was calculated through a correlation proposed by North and Santavicca [21] as

$$D_3=C_1\frac{u'}{u'+S_l}+C_2\frac{S_l}{u'+S_l} \tag{2}$$

In Eq. (2), u' is the turbulent intensity, and C_1 and C_2 are model constants (C_1=2.35 and C_2=2.0). Returning to Eq. (1), the well-known correlation proposed by Meghalchi and Keck [22] was employed to estimate the laminar burning velocity (S_l) as

$$S_l = S_{l0}\left(\frac{T_u}{T_0}\right)^{\alpha}\left(\frac{p}{p_0}\right)^{\beta}(1-1.5Y_{\text{res}}) \tag{3}$$

where S_{l0} is a reference laminar burning velocity related with the fuel and the stoichiometric ratio of the mixture, T_u is the temperature of the unburned gas, and Y_{res} is the residual gas fraction. S_{l0}, α, and β are obtained from

$$S_{l0} = B_1 + B_2(\tilde{\varphi} - \varphi_0)^2$$

$$\alpha = 2.18 - 0.8(\tilde{\varphi} - 1)$$

$$\beta = -0.16 + 0.22(\tilde{\varphi} - 1) \tag{4}$$

Due to the combustion model not being a true multizone model, there is no real interface separating the burned and unburned gases. So, an algebraic estimation of the laminar flame front surface area (A_l) must be performed, assuming that an imaginary flame is spherically growing from the spark plug (S_l is isotropic). Then, the estimation of A_l must be performed in order to know how much fuel is being burned at each time step due to the flame front advance. That allows the introduction of a homogeneous heat source $\dot{x_b}$ in the Navier–Stokes equations. $\dot{x_b}$ has the following form:

$$\dot{x_b} = S_t A_l Q_{\text{fuel}} = S_t A_l \frac{m_{\text{fuel}} E_{\text{fuel}}}{V_{\text{cyl}}} \tag{5}$$

where m_{fuel} is the mass of fuel at the ignition time, E_{fuel} is the specific heat of the fuel, and V_{cyl} is the current volume of the combustion chamber ($V_{\text{cyl}}=f(t)$)

Fluid properties notoriously change with temperature variations, so some suitable correlations were introduced to estimate the constant pressure heat capacity (C_p), thermal conductivity (λ), and dynamic viscosity (μ).

As it was previously mentioned, cold dynamic simulations were performed under atmospheric conditions at inlet and outlet. However, for real dynamic simulations, constant boundary conditions are far from realistic because combustion induces significant temperature and pressure waves inside the ducts. Moreover, the computational model considers only a fraction of the overall engine, so the influence of the other cylinders has to be properly represented. For these two reasons, the overall engine was modeled by 0D/1D engine software of our own development [23,24]. The 0D/1D engine simulator allows to handle the overall layout of pluri cylinder engines, modeling ducts by one-dimensional mass, momentum, and energy Euler equations, adding appropriate terms for taking into account heat transfer and frictional losses, and solving by finite element method. As for cylinders, plenums, and tanks, they are approximated by zero-dimensional mass and energy balances. Finally, the in-cylinder heat release (combustion) is modeled by the Wiebe function [18]. 0D/1D simulator parameters were tuned by fitting the power and torque curves of the engine along the overall engine speed range (1000–6500 rpm), using typical SI engine parameters for the Wiebe equation (a=2.0, m=5.0, $\Delta\phi$=80 CA, and ϕ^0=340 CA). Once a good agreement was reached, dynamic boundary conditions (pressure, temperature, and turbulence) were extracted from the 0D/1D results and incorporated to the 3D computational model by means of an UEFR. 3D simulations were carried on and the combustion durations estimated from the CFD combustion model were feed on the 0D/1D simulator to improve the estimation of the dynamic boundary conditions for the 3D simulations.

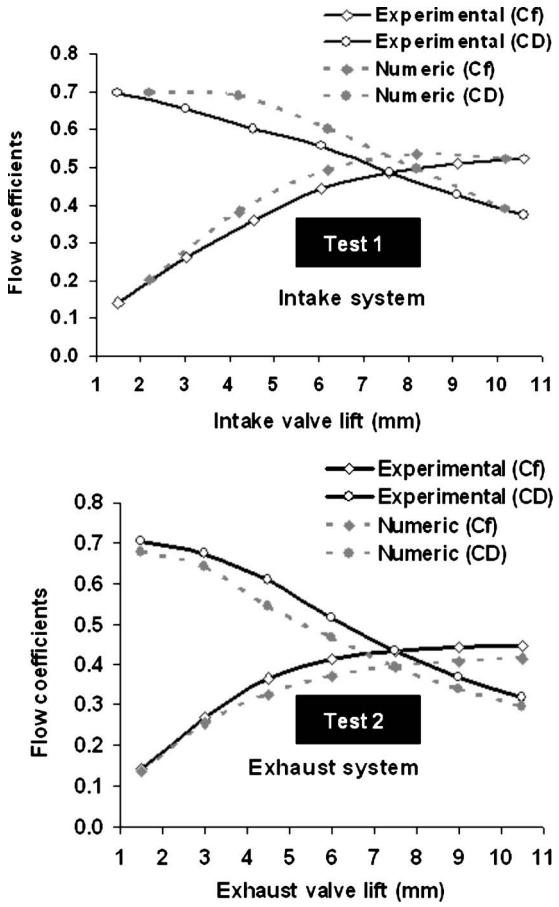

Fig. 4 Discharge coefficients (C_D and C_f); upper: intake system; bottom: exhaust system

4 Results and Discussion

This section shows numerical and experimental steady test results. Then, the results concerning dynamic test simulation are presented, focusing on describing the main flow characteristics and averaged flow quantities. Finally, steady and dynamic results are compared so as to evaluate the suitability of the former and the in-cylinder flow behavior.

4.1 Numerical and Experimental Steady Rig Tests

4.1.1 Flow Meter Tests. Figure 4 shows numerical and experimental results of flow discharge coefficients for the intake (called Test 1) and exhaust (called Test 2) systems. Note that an acceptable concordance is obtained between CFD and experimental results. Differences are bigger at the mean valve-lift range, the average relative errors being closer to 6.5%, and the maximum relative errors around 10%. Both the discharge (C_D) and flow (C_f) coefficients are displayed because the former has more sensitivity at low valve lifts (C_D is calculated based on the current valve curtain area), while the latter better reflects the behavior of the overall system at high valve lifts (C_f is calculated based on the constant cross section area of the valve seat) [25].

A comparison of the flow coefficients (C_f) of both systems showed that the exhaust one has a better efficiency at low valve lifts (below 4.5 mm), while the intake system is 17% more efficient at maximum valve lift. For this engine, the maximum valve lifts are 9 mm and 8.5 mm for the intake and exhaust systems, respectively (Table 1). Regarding the flow efficiency, these valve timings seem to be close to the optimum. The gain in mass flow

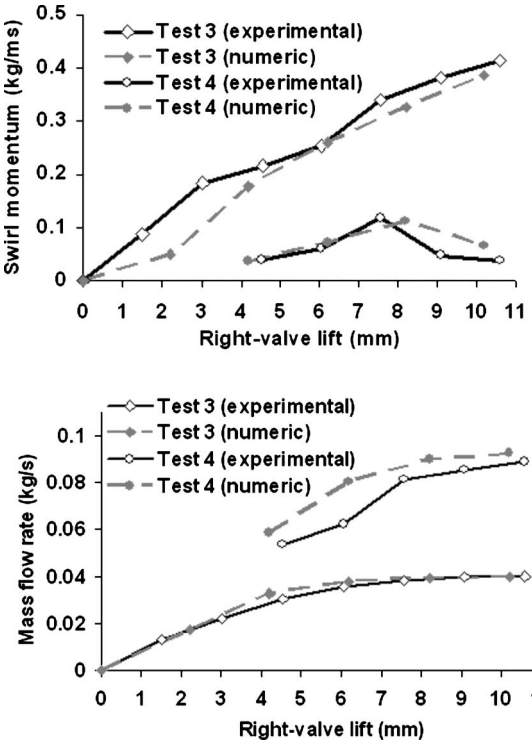

Fig. 5 Numerical and experimental results from swirl tests; upper: swirl momentum; bottom: mass flow rate

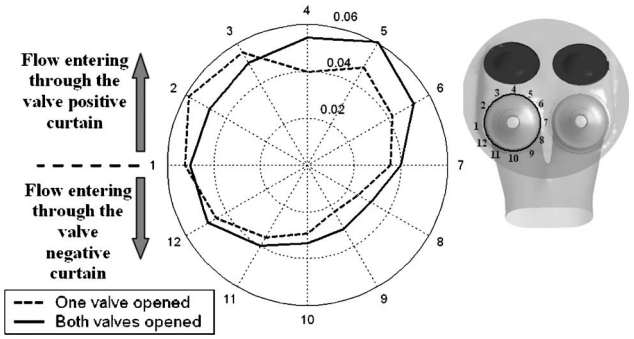

Fig. 6 Mass flow rate distribution around one valve curtain when only one valve is opened (dashed line) and when both valves are equally opened (solid line)

rate is only 2.5% when the intake valve lift is increased from 9.09 mm to 10.6 mm, while for the exhaust system the improvement on C_f is less than 1%.

4.1.2 Swirl Tests. Typical four-valve cylinder engines produce negligible swirl, so two timing strategies were employed to explore the potentiality of this cylinder head to produce swirl. First, one intake valve was kept completely closed while the other was opened (called Test 3). Second, both valves were opened but one of them was opened 1.51 mm more than the other (called Test 4). In order to compare the numerical and experimental results, the measured angular honeycomb speed from the swirl meter was converted to the volume-average angular momentum (kg/ms), applying the rigid body assumption for the in-cylinder flow

$$M_s = \int_{\text{vol}} \rho V_t r dV = \int_0^R 2\pi r l \rho r \omega r dr = \pi l \rho \omega \frac{\text{Bo}^4}{32} \tag{6}$$

where Bo is the cylinder bore, ρ is the fluid density, and l is the cylinder height (100 mm) [15]. Figure 5 shows the swirl and mass flow rate results of both timing strategies.

Correlation between numerical and experimental data is good enough. However, differences on mass flow rate increase for the second timing strategy (Test 4). A look at the upper part of Fig. 5 shows that swirl generation is fairly linear when only one valve is opened (Test 3), even though at high valve lifts the mass flow rate keeps almost constant. One possible explanation for this could be found in the flow redistribution around the valve curtains while the valve lift is increased. Small valve lift differences between the intake valves (Test 4) induce little swirl at medium valve lifts, but once the valve lift reaches 7.57 mm (starting the asymptotic mass flow rate zone), the mass flow rate through both valves becomes almost the same and swirl generation falls down. Grimaldi et al. [26] obtained similar results in experimental tests and Mahrous et al. [14] found that valve-lift differences greater than 100% are required to induce significant swirl by means of dynamic tests (CFD).

Figure 6 shows numerical results of the mass flow distribution around one valve curtain at 10.6 mm. Note that, if only one valve is opened (Test 3), flow turns to the 2–3 direction, clearly influenced by the corresponding intake duct. On the other hand, if both valves are equally opened (Test 1), the flow turns to the middle zone between valves. Similar conclusions have also been reported in other papers [3,16].

The honeycomb of the swirl meter introduces negligible pressure drop. A comparison of the results obtained with and without the device showed that the mass flow rate loss at maximum valve lift was less than 0.4% [15].

4.1.3 Tumble Tests. Figure 7 shows numerical and experimental results obtained at two locations (P_2 and P_4 in Fig. 1) along the lateral duct of the tumble bench. Tests 5 and 6 refer to P_2 and P_4 locations, respectively. A good agreement at low valve lifts at both locations is found. Moreover, the tumble fall at medium valve lifts is also well predicted by CFD. However, at location P_2 (Test 5) tumble is significantly overestimated, being the maximum relative error closer to 61% (at 7.57 mm valve lift) and the average relative error 25%. As regards position P_4 (Test 6), the maximum relative error reaches 32% (also at 7.57 mm valve lift), and the average one is 32%. Note that even though discrepancies between numerical and experimental results are noticeable, similar numerical investigations had yielded errors closer to 100% [16,27]. Simulations showed that the tumble falling effect also occurs inside the cylinder, but curiously it is weaker than that measured in the lateral duct of the tumble bench. The results at P_2 and P_4 positions show a similar behavior, indicating that momentum loss is fairly linear along the lateral duct of the tumble bench.

Note that the tumble generation is almost linearly proportional to valve lift, except at medium valve-lift range, where the tumble

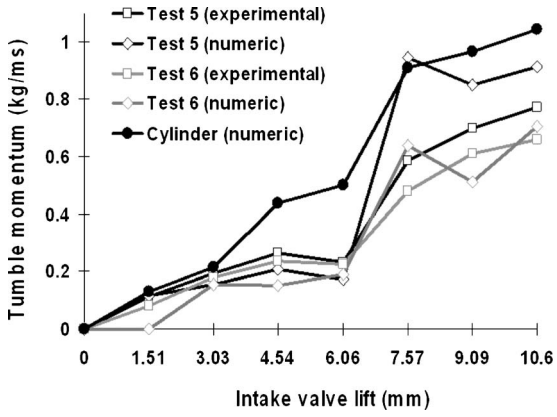

Fig. 7 Numerical and experimental results from tumble tests for P_2 and P_4 measurement positions

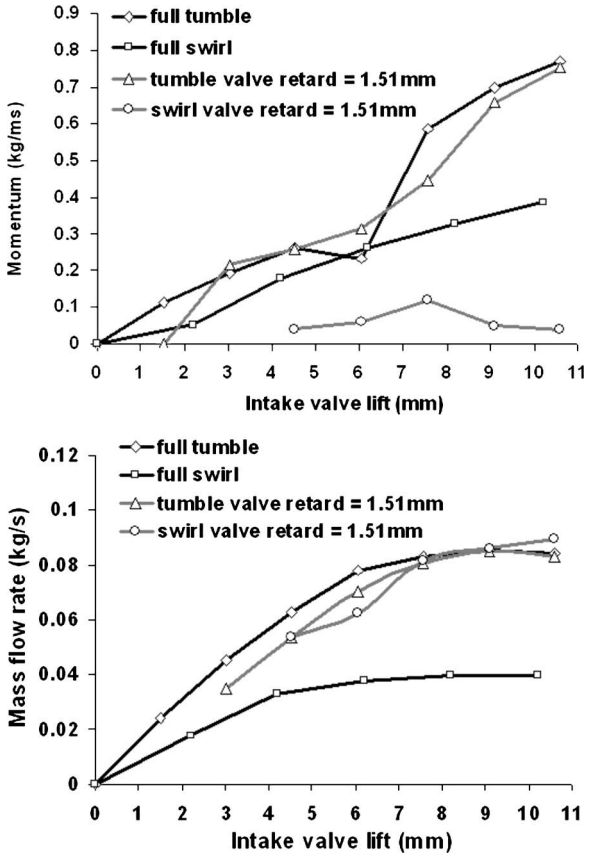

Fig. 8 Numerical results for four strategies to produce angular momentum (swirl or tumble); upper: angular momentum; bottom: mass flow rate

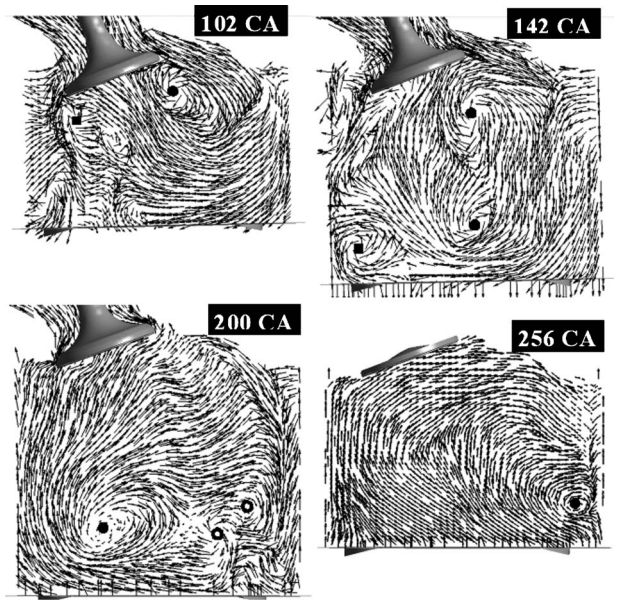

Fig. 9 Evolution of flow during the intake and compression strokes on a plane cutting one intake valve

falling effect takes place.

Figure 8 displays the numerical results from four strategies to produce angular momentum (swirl or tumble) using different timing configurations.

The full tumble strategy (valves equally opened) seems to be the most effective option to induce momentum. On the other hand, a small lift difference (of 1.51 mm) smooths tumble production at mean valve lifts, but also produces a significant reduction in mass flow rate at low and medium valve lifts. If only one valve is opened (full swirl), the maximum momentum is less than half of that for the full tumble strategy. Also, the mass flow rate reduces more than 50%. This comparative analysis allows us to estimate the intensity of the flow structures (tumble and swirl) that might be induced using variable valve lift (VVL). As shown in several papers, steady tests are the first step to design valve timing strategies to control the in-cylinder flow motion [5,16,26,28–30].

Any valve opening configuration that improves tumble or swirl will probably affect the volumetric efficiency of the engine negatively. On the other hand, the effect of introducing adjustable tumble deflectors inside the intake port of this engine has been numerically evaluated [15], enhancing tumble by 18%, but reducing the mass flow rate by 10%. In regards of swirl, the use of a swirl deflector produced swirl values closer to the previously reported for Test 3, but enhancing the mass flow rate by 46% with respect to Test 3.

4.2 Numerical Dynamic Tests

4.2.1 Cold Dynamic Simulations. Three engine speed simulations were performed to cover almost the whole engine speed range (1500 rpm, 3000 rpm, and 4500 rpm). Initial conditions were atmospheric over a quiescent flow, but steady results were quickly obtained after the fourth cycle. Of course, this fast convergence probably will be slower for multicylinder engines, due to the combination of pressure waves generated by each cylinder inside the intake and exhaust systems.

Figure 9 shows the evolution of the velocity pattern on a cutting plane at the intake valve, during the intake and compression strokes. Note that vortex dynamics is very complex. Structures are constantly created and destroyed. In Fig. 9, the main structures have been identified using circles for clockwise rotation sense vortexes (positive tumble) and squares for counterclockwise ones (negative tumble). Moreover, structures are classified according to its size (big with solid; small with hollow).

Figure 10 shows the average tumble momentum M_T (m^2/s) along with the turbulent kinetic energy k (m^2/s^2) for the last simulated engine cycle. M_T is negative until the first 50 CA. Then, tumble quickly increases, reaching the maximum at 150 CA. Subsequently, tumble evolution linearly decreases until 280 CA, and it quickly decreases at the end of the compression stroke. After that, during the expansion stroke, the tumble is negligible, but negative tumble is produced between 630 CA and 720 CA due to the flow evacuation when the piston rises.

Turbulent kinetic energy k is mainly produced due to two mechanisms: first, frictional efforts, flow detachment around valve vortexes, and large strain gradients during the intake and exhaust strokes; second, tumble degradation at the end of the compression stroke. The first mechanism explains the peak of k around 170 CA, and the second causes the significant increment of k around 360 CA (TDC), this being the maximum k of the whole engine cycle. k keeps almost null during the expansion stroke and the first stages of the exhaust stroke. Finally, little turbulence is produced during the gas evacuation.

The generation of coherent macrovortex structures guarantees the conservation of a large amount of kinetic energy of the entering flow until the end of the compression stroke. Then, the destruction of the macrovortices transfers the kinetic energy from the mean flow to smaller turbulent structures (microeddies), causing the peak of turbulence close to the spark ignition time. That increases the burning velocity (S_t) and improves the overall combustion process [5,31–33].

Table 2 highlights the effect of the engine speed over M_T and k. For low engine speeds (increment from 1500 rpm to 3000 rpm), M_T and k increase more than the engine speed. M_T increases between 150% and 300% while k grows over 350%. However, when

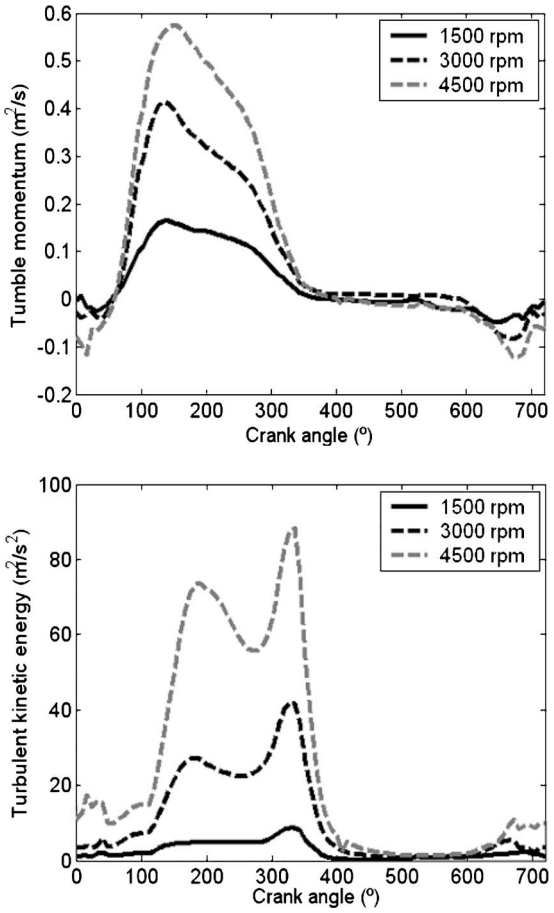

Fig. 10 Tumble momentum (upper) and turbulent kinetic energy (bottom) for the three engine speeds

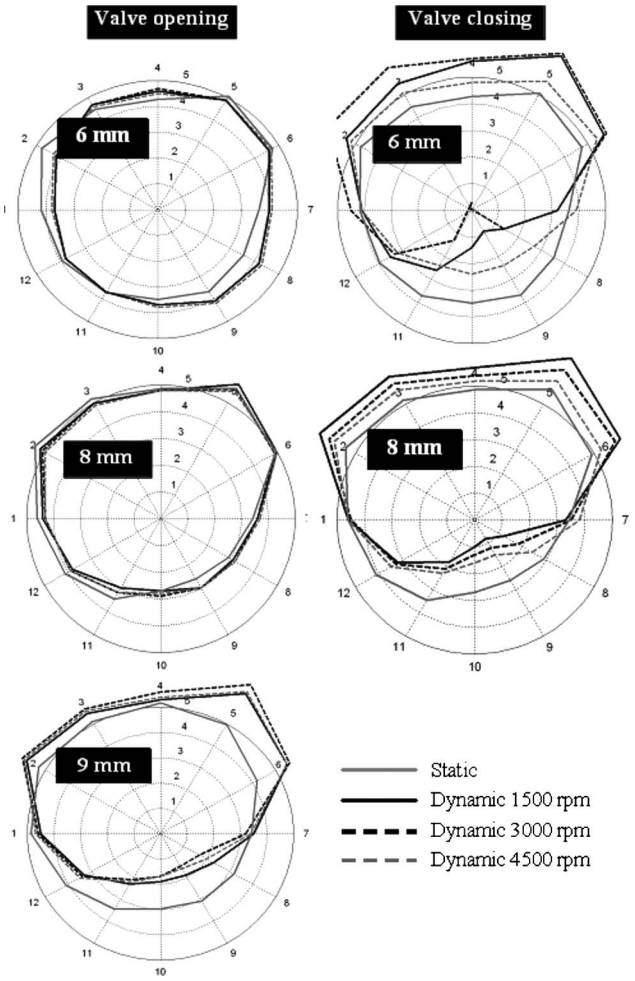

Fig. 11 Mass flow distribution around one valve curtain for several valve lifts and steady and cold dynamic simulations

the engine speed is incremented from 3000 rpm to 4500 rpm, M_T is scarcely incremented, and at 360 CA, the increment is negligible. On the other hand, k increases similarly to the engine speed. So, the increment of k at high engine speed seems to be caused by strain and squish than by tumble degradation.

4.2.2 Steady Versus Cold Dynamic Simulations. It is interesting to compare the mass flow distribution around one valve curtain for steady (tumble Test 5) and dynamic cases at different valve lifts. Figure 11 shows the mass flow distribution (percentage) at 6 mm, 8 mm, and 9 mm during valve opening and closing. In the same graphics, distributions corresponding to steady tests are also included. Naturally, for steady tests, the opening and closing events are the same. In the polar diagrams, the flow crossing the upper segment from 1 to 7 produces positive tumble momentum, so this segment is called the positive curtain of the valve. The bottom segment from 1 to 7 is called the negative curtain of the valve.

Table 2 Increments of tumble momentum M_T and turbulent kinetic energy k by increasing engine speed

Engine speed increments	Percentage increments (%)					
	Maximum		at 342 CA		at 360 CA	
	M_T	k	M_T	k	M_T	k
1500–3000	153	387	157	350	300	365
3000–4500	38	111	39	119	5	100
1500–4500	250	929	257	889	320	830

Note that for the three engine speeds flow distributions for dynamic tests are fairly similar during opening and also for the maximum valve lift. However, they completely change during the closing phase. Steady distributions are roughly similar to dynamic ones when valves are opening, but the differences become significant once the maximum valve lift is reached and start the closing phase. The orientation of the flow at the middle zone between the intake valves is more evident for the dynamic cases. At maximum valve lift the entering flow through the negative curtain of the valve diminishes with respect to the steady case.

The significant change in flow distribution at high valve lifts for dynamic tests enhances tumble generation with respect to the steady estimations. Moreover, the mass flow rate entering through the negative curtain is reduced even more during valve closing, improving tumble production.

Figure 12 in its upper part, shows the tumble generation while valves are opened as a function of the valve lift. Note that positive tumble appears after 7 mm valve lift in the opening phase, even though the mass flow rate before this valve lift is quite significant, as shown at the bottom of Fig. 12. The negative tumble at the beginning of the cycle might be explained by the flow leaving the cylinder through the exhaust valves at the end of the previous cycle, and due to the significant fraction of flow entering through the negative curtain of the intake valves at valve lifts below 7 mm. The fast production of positive tumble after 7 mm can be due to the change in flow distribution around the valve curtains. Curiously, for the three engine speeds analyzed, around 70% of the

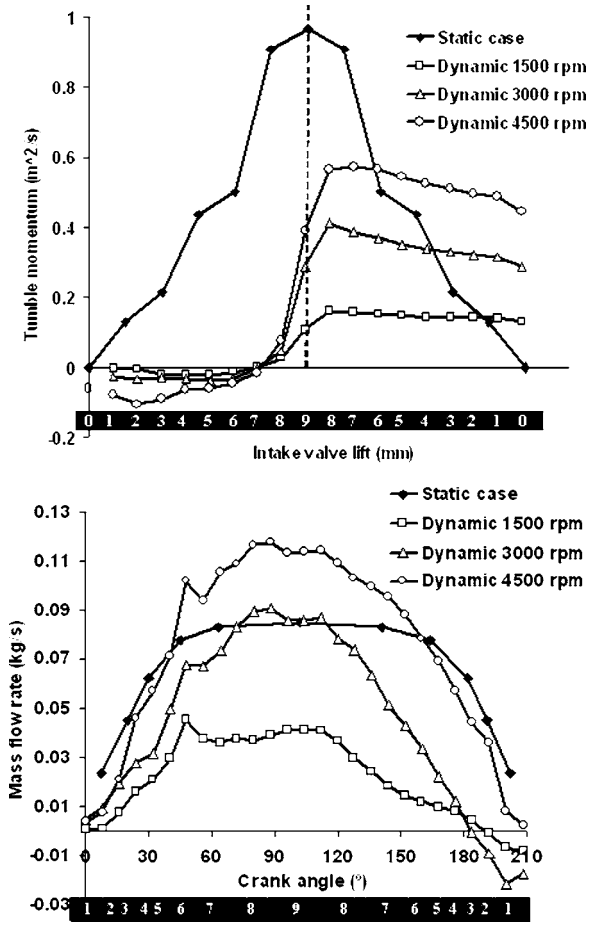

Fig. 12 Upper: tumble momentum as a function of valve lift for steady and dynamic tests; bottom: mass flow rate along the intake process

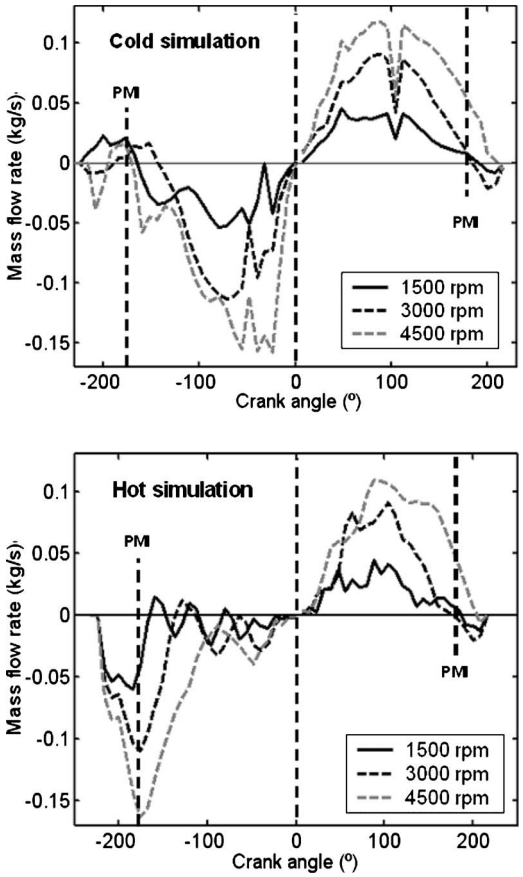

Fig. 13 Mass flow rate for cold (upper) and real (bottom) dynamic simulations

maximum tumble is reached at the maximum valve lift and the maximum tumble is reached at 8 mm valve lift (while valves are closing). Thereafter, tumble decreases almost linearly during valve closing.

As regards to the mass flow rates, no conclusions can be drawn about the relationship between the steady and cold dynamic behaviors of the engine because it is difficult to do both experiments at the same operation conditions. While steady tests are performed under constant pressure drops with a flow completely developed, in cold dynamic tests, the cylinder pressure continuously changes, depending on piston and valve motion with a significant influence to the flow field.

Flow discharge coefficients obtained through steady tests are quite independent of the pressure drop [25,27]. In order to compare steady versus dynamic results it is valid to scale the steady curve of mass flow rate in such a way that it matches the dynamic one at maximum valve lift (9 mm) for each engine speed. Then, it is possible to see the overestimation in mass flow rate predicted by steady tests with respect to the dynamic ones, especially during valves closing. As previously observed in Fig. 11, differences between steady and dynamic results are bigger during valve closing than during valve opening.

4.2.3 Real Versus Cold Dynamic Simulations. Dynamic boundary conditions extracted from 0D/1D simulation were achieved and a phenomenological combustion model was implemented in order to perform more real dynamic simulations. Results for the same three engine speeds (1500 rpm, 3000 rpm, and 4500 rpm) were obtained, these highlighting the differences with respect to cold dynamic tests.

As for the mass flow rate, the main differences between cold and real hot simulations are found at the beginning and at the end of the cycles. Under real engine conditions, flow motion is mainly governed by pressure differences, but for cold dynamic tests, flow is pushed or sucked by the piston motion (Fig. 13). Note that the intake process is fairly similar for cold and real simulations, but significant differences appear when exhaust valves are opened. The maximum mass flow rate for cold dynamic tests takes place close to the maximum exhaust valve lift, while for real dynamic tests, it immediately occurs once the valves open.

Comparing Figs. 10 and 14, the evolution of tumble is quite similar for cold and real simulations, although the maximum tumble increases for real tests (20% at 1500 rpm, 18% at 3000 rpm, and only 4% at 4500 rpm). An oscillatory behavior is found at the end of the cycles for real dynamic tests, possibly due to the variations in mass flow rate caused by pressure waves at the intake and exhaust systems.

Turbulent kinetic energy k for real dynamic simulations is greater than for cold ones, and differences become more significant as the engine speed is increased. The first peak during the intake stroke gains importance during real dynamic simulations, and for 4500 rpm, it becomes the highest, indicating that tumble degradation at the end of the compression stroke produces less turbulence than the strain efforts during the intake stroke.

Table 3 consigns the increments of M_T and k (percentage) after the introduction of the combustion process. Note that the effect of combustion over tumble diminishes with engine speed increment, but tumble is always bigger than that for the cold tests. Similar conclusions can be reached by analyzing the turbulent kinetic energy.

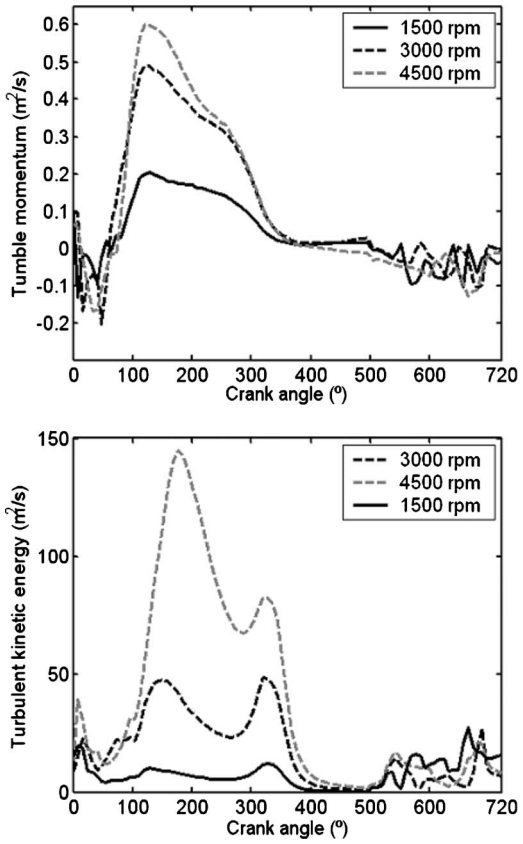

Fig. 14 Tumble momentum M_T (upper) and turbulent kinetic energy k (bottom) for the three engine speeds

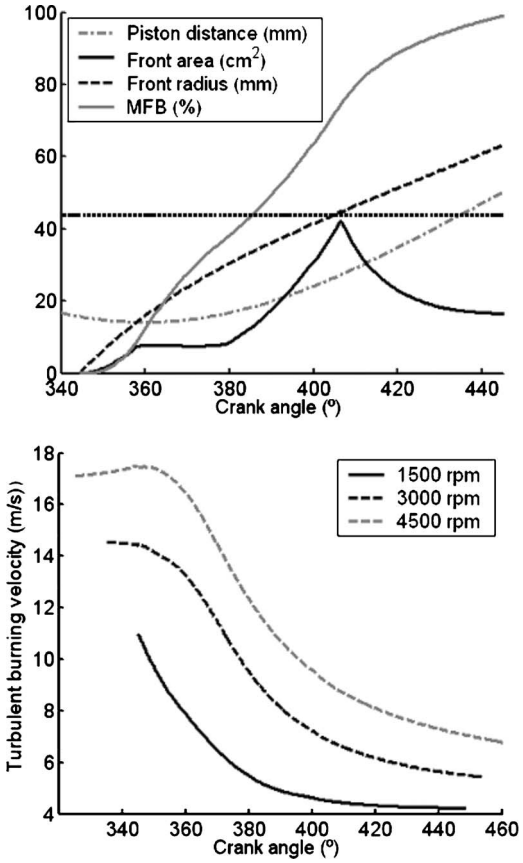

Fig. 15 Combustion variables for 1500 rpm (upper) and burning velocity (bottom) the for three engine speeds

4.2.4 Combustion Behavior. Figure 15 on the upper part, displays the evolution of the main characteristic variables with the implemented combustion model (at 1500 rpm), while on the bottom part, the turbulent burning velocity (S_t) for the three engine speeds is drawn. The flame front radius is the time-integrate turbulent burning velocity. Note that the flame front area changes when the flame front reaches the piston crown surface (around 355 CA) and the cylinder surface (around 405 CA). Although the implemented combustion model is a rough simplification of the complex combustion phenomenon, it is still adequate to estimate the influence of turbulence due to tumble degradation. As shown in Fig. 15, S_t is directly related with turbulence enhancement, but S_t quickly diminishes after the TDC. Moreover, the increment on S_t due to turbulence is not enough to compensate the increment in engine speed, and combustion process is extended during the expansion stroke.

Table 3 Increments of M_T and k (percentage) as a result of introducing the combustion process

	Percentage increments (%)					
	Maximum		at 342 CA		at 360 CA	
Engine speed	M_T	K	M_T	k	M_T	k
1500	22	37	71	33	190	26
3000	18	16	39	17	40	19
4500	4	64	0	4	5	3

5 Conclusion

In this work numerical and experimental tests were performed over a commercial engine. Some mean flow characteristics of this engine such as mass flow discharge coefficients and tumble and swirl productions were investigated. About steady tests, the following conclusions were reached:

(a) CFD proved to be adequate to capture the tumble falling effect at medium valve lifts, making it possible to relate this effect with the vortex dynamic below the intake valves.
(b) Considering exclusively the generation of swirl, the greater the differences between valves lifts, the greater the swirl production, not taking into account the loss of volumetric efficiency produced.
(c) There is a cooperative effect between the intake valves, improving significantly the discharge coefficients when both of them are opened.

Cold dynamic simulation results allow us to find the following conclusions:

(a) The steady-state engine conditions are reached after no more than four cycles. Probably, more cycles are necessary for multicylinder engines
(b) Positive tumble dominates the whole cycle, starting to grow after 50 CA, and reaching a peak around 144 CA. Then, a fast vortex degradation takes place from 280 CA to 360 CA, enhancing turbulence. After 630 CA, negative tumble is induced by gas evacuation.
(c) The abrupt increment of tumble nearby the maximum valve lift is mainly consequence of the change in the mass flow rate distribution around the valves curtains.

(d) k has two peaks: the first one during the intake process, and the other one due to tumble degradation near to the TDC at the end of the compression stroke.
(e) M_T and k are proportional to the engine speed, but their increments are more significant from 1500 rpm to 3000 rpm than from 3000 rpm to 4500 rpm.

Regarding the combustion process, the following conclusions seem appropriate:

(a) Differences between cold and real dynamic simulations are highlighted by drawing the in-cylinder mass flow rates. For cold tests, flow is governed by piston kinematics, while for real tests pressure differences drive the flow dynamics.
(b) M_T is slightly affected by the combustion process. On the other hand, k is substantially increased during the intake stroke. Moreover, at 4500 rpm, the maximum k is not due to tumble degradation but to frictional efforts during the intake process.

Acknowledgment

The authors want to thank CONICET and ANPCyT (Grant Nos. PICT Lambda 12-14573/2003, PME 209/2003). Also, they are grateful to Fiat Argentina for the donation of the engine analyzed in this work.

References

[1] Bailly, O., Buchou, C., Floch, A., and Sainsaulieu, L., 1999, "Simulation of the Intake and Compression Strokes of a Motored 4-Valve SI Engine With a Finite Element Code," Oil Gas Sci. Technol., **54**(2), pp. 161–168.
[2] Weng, V., Gindele, J., Töpfer, G., Spicher, U., Latsch, R., and Kuhnert, D., 1999, "Investigation on the Bowl-Prechamber-Ignition (BPI) Concept in a Direct Injection Gasoline Engine at Part Load," SAE Paper No. 1999-01-3658.
[3] Mattarelli, E., 2000, "Comparison Between two Combustion Chambers for a Motorcycle Racing Engine," SAE Paper No. 2000-01-1894.
[4] Hong, C., and Tarng, S., 2001, "In-Cylinder Tumble Flow Field Measurements and Predictions," ASME J. Eng. Gas Turbines Power, **123**, pp. 139–145.
[5] Li, L., Tao, J., Wang, Y., Su, Y., and Xiao, M., 2001, "Effects of Intake Valve Closing Timing on Gasoline Engine Performance and Emissions," SAE Paper No. 2001-01-3564.
[6] Stan, C., Stanciu, A., Troeger, R., Martorano, L., Tarantino, C., Antonelli, M., and Lensi, R., 2003, "Direct Injection Concept as a Support of Engine Down-Sizing," SAE Paper No. 2003-01-0541.
[7] Tan, Z., and Reitz, R. D., 2006, "An Ignition and Combustion Model Based on the Level-Set Method for Spark Ignition Engine Multidimensional Modeling," Combust. Flame, **145**, pp. 1–15.
[8] Ramajo, D., Zanotti, A., and Nigro, N., 2007, "Assessment of a Zero-Dimensional Model of Tumble in Four-Valve High Performance Engine," Int. J. Numer. Methods Heat Fluid Flow, **17**(8), pp. 770–787.
[9] Bianchi, G., Cantore, G, Mattarelli, E., Guerrini, G., and Papetti, F., 1998, "The Influence of Stroke-to-Bore Ration and Combustion Chamber Design on Formula One Engines Performance," SAE Paper No. 980126.
[10] Johan, Z., Moraes, C. M., Buell, J. C., and Ferencz, R. M., 2001, "In-Cylinder Cold Flow Simulation Using a Finite Element Method," Comput. Methods Appl. Mech. Eng., **190**, pp. 3069–3080.
[11] Fontana, G., Galloni, E., Jannelli, E., and Palmaccio, R., 2003, "Influence of the Intake System Design on a Small Spark-Ignition Engine Performance. A Theoretical Analysis," SAE Paper No. 2003-01-3134.
[12] Cao, L., Zhao, H., and Jiang, X., 2004, "Effects of Intake Valve Timing on Premixed Gasoline Engine With CAI Combustion," SAE Paper No. 2004-01-2953.
[13] Fontana, G., Galloni, E., Palmaccio, R., and Torella, E., 2006, "The Influence of Variable Timing on the Combustion Process of a Small Spark-Ignition Engine," SAE Paper No. 2006-01-0445.
[14] Mahrous, A., Wysznski, M., Xu, H., and Tsolakis, A., 2007, "A CFD Investigation Into the Effects of Intake Valves Events on Airflow Characteristics in a Motored 4-Valve Engine Cylinder With Negative Valve Overlapping," Paper No. 07-NAPLES-74.
[15] Ramajo, D., 2008, "Simulación Computacional de los Procesos Fluido-Dinámicos en el Interior de Motores de Combustión Interna," Ph.D. thesis, Universidad Nacional del Litoral, Santa Fe, Argentina.
[16] Grimaldi, C., Battistone, M., and Uccellani, M., 2004, "Dependence of Flow Characteristics of a High Performance S.I. Engine Intake System on Test Pressure and Tumble Generation Conditions—Part 1: Experimental Analysis," SAE Paper No. 2004-01-1530.
[17] López, E., Nigro, N., and Storti, M., 2008, "Simultaneous Untangling and Smoothing of Moving Grids," Int. J. Numer. Methods Eng., **76**, pp. 994–1019.
[18] Heywood, J. B., 1988, *Internal Combustion Engines Fundamentals*, McGraw-Hill, New York.
[19] Williams, F., 1985, *Turbulent Combustion*, SIAM, Philadelphia, PA.
[20] Gouldin, F. C., 1987, "An Application of Fractals to Modelling Premixed Turbulent Flames," Combust. Flame, **68**, pp. 249–266.
[21] North, G., and Santavicca, D., 1990, "The Fractal Nature of Premixed Turbulent Flames," Combust. Sci. Technol., **72**, pp. 215–232.
[22] Metghalchi, M., and Keck, J. C., 1982, "Burning Velocities of Mixtures of Air With Methanol, Isoctane and Indolene at High Pressure and Temperature," Combust. Flame, **48**, pp. 191–210.
[23] http://www.fceia.unr.edu.ar/fceia1/mecanica/Automotores/laboratorio_de_automotores_index.htm
[24] López, E., Nigro, N., and Storti, M., 2009, "Validation of a 0D/1D Computational Code for the Design of Several Kind of Internal Combustion Engines," LAAR, in press.
[25] Xu, H., 2001, "Some Critical Technical Issues on the Steady Flow Testing of Cylinder Heads," SAE Paper No. 2001-01-1308.
[26] Grimaldi, C., Battistone, M., and Mariani, F., 2005, "Experimental and Numerical Analysis of Charge Motion Characteristics Depending on Intake Valves Actuation Strategies," SAE Paper No. 2005-01-0242.
[27] Grimaldi, C., Battistone, M., and Postrioti, L., 2003, "Flow Characterization of a High Performance S.I. Engine Intake System—Part 1: Experimental Analysis," SAE Paper No. 2003-01-0623.
[28] Wilson, N., Watkins, A., and Dopson, C., 1993, "Asymmetric Valve Strategies and Their Effect on Combustion," SAE Paper No. 930821.
[29] Geiger, J., Grigo, M., Lang, O., Wolters, P., and Hupperich, P., 1999, "Direct Injection Gasoline Engines—Combustion and Design," SAE Paper No. 199-01-0170.
[30] Kim, M. J., Lee, H. S., and Kim, W. T., 2006, "Correlation Study of the Measured Tumble Ratios Using Three Different Methods: Steady Flow Rig, 2-Dimensional PIV, and 3-Dimensional PTV Water Flow Rig," Int. J. of Automotive Technology, **7**(4), pp. 441–448.
[31] Jeon, C., Chang, Y., Cho, K. B., and Kang, K. Y., 1998, "Effects of Intake Ports on In-Cylinder Flow and Lean Combustion in a 4-Valve Engine," SAE Paper No. 981048.
[32] Aleiferis, P. G., Taylor, A. M. K. P., Ishii, K., and Urata, Y., 2004, "The Nature of Early Flame Development in a Lean Burn Stratified-Charge Spark-Ignition Engine," Combust. Flame, **136**, pp. 283–302.
[33] Mariani, F., and Cavalletti, M., 2004, "Dependence of Flow Characteristics of a High Performance S.I. Engine Intake System on Test Pressure and Tumble Generation Conditions—Part 2: Numerical Analysis," SAE Paper No. 2004-01-1531.

Computational Study of a High-Expansion Ratio Radial Organic Rankine Cycle Turbine Stator

John Harinck
Process and Energy Department,
Faculty of Mechanical, Maritime and Materials Engineering,
Delft University of Technology,
2628 CA Delft, The Netherlands
e-mail: j.harinck@tudelft.nl

Teemu Turunen-Saaresti
Fluid Dynamics Laboratory,
LUT Energy, Faculty of Technology,
Lappeenranta University of Technology,
53850 Lappeenranta, Finland
e-mail: teemu.turunen-saaresti@lut.fi

Piero Colonna
Process and Energy Department
Faculty of Mechanical, Maritime and Materials Engineering,
Delft University of Technology,
2628 CA Delft, The Netherlands
e-mail: p.colonna@tudelft.nl

Stefano Rebay
Department of Mechanical Engineering,
University of Brescia,
25123 Brescia, Italy
e-mail: rebay@ing.unibs.it

Jos van Buijtenen
Tri-O-Gen B.V.,
Nieuwenkampsmaten 8,
7472 DE Goor, The Netherlands

*There is a growing interest in organic Rankine cycle (ORC) turbogenerators because they are suitable as sustainable energy converters. ORC turbogenerators can efficiently utilize external heat sources at low to medium temperature in the small to medium power range. ORC turbines typically operate at very high pressure ratio and expand the organic working fluid in the dense-gas thermodynamic region, thus requiring computational fluid dynamics (CFD) solvers coupled with accurate thermodynamic models for their performance assessment and design. This article presents a comparative numerical study on the simulated flow field generated by a stator nozzle of an existing high-expansion ratio radial ORC turbine with toluene as working fluid. The analysis covers the influence on the simulated flow fields of the real-gas flow solvers: FLUENT, FINFLO, and ZFLOW, of two turbulence models and of two accurate thermodynamic models of the fluid. The results show that FLUENT is by far the most dissipative flow solver, resulting in large differences in all flow quantities and appreciably lower predictions of the isentropic nozzle efficiency. If the combination of the $k-\omega$ turbulence model and FINFLO solver is adopted, a shock-induced separation bubble appears in the calculated results. The bubble affects, in particular, the variation in the flow velocity and angle along the stator outlet. The accurate thermodynamic models by Lemmon and Span (2006, "Short Fundamental Equations of State for 20 Industrial Fluids," J. Chem. Eng. Data, **51**(3), pp. 785–850) and Goodwin (1989, "Toluene Thermophysical Properties From 178 to 800 K at Pressures to 1000 Bar," J. Phys. Chem. Ref. Data, **18**(4), pp. 1565–1636) lead to small differences in the flow field, especially if compared with the large deviations that would be present if the flow were simulated based on the ideal gas law. However, the older and less accurate thermodynamic model by Goodwin does differ significantly from the more accurate Lemmon–Span thermodynamic model in its prediction of the specific enthalpy difference, which leads to a considerably different value for the specific work and stator isentropic efficiency. The above differences point to a need for experimental validation of flow solvers in real-gas conditions, if CFD tools are to be applied for performance improvements of high-expansion ratio turbines operating partly in the real-gas regime.*
[DOI: 10.1115/1.3204505]

Keywords: organic Rankine cycle, real gas, high expansion ratio, radial turbine, CFD simulation

1 Introduction

In organic Rankine cycle (ORC) processes, the working fluid is an organic substance, which allows for the efficient application of the Rankine cycle principle, also to the energy conversion of low-temperature heat sources (starting from approximately 90°C) and for low-power output (from few kWe up to few MWe). Current applications of ORC turbogenerators are the electricity generation from low-grade geothermal heat reservoirs, from biomass fuel, the energy recovery from turbogas or reciprocating engines, and from industrial waste heat. The installed power of geothermal ORC plants now totals approximately 1000 MWe [1], and can be considered a mature technology [2]. ORC systems designed for comparatively high-temperature heat sources demonstrated to be a viable technology for small-scale biomass-fired combined-heat-and-power energy conversion [3–6]. The use in the near future of ORC power systems coupled with solar concentrators [7], high-temperature fuel cells [8], and for domestic cogeneration is also very attractive.

The selection of the working fluid is the key to the achievement of high isentropic efficiency of the turboexpander, which is usually in a single stage and often features a low peripheral speed and optimal dimensions. Other advantages include (i) simple cycle configuration even for large sink/source temperature ratio, because of the nonextractive desuperheating regeneration, (ii) dry expansion of the fluid through the turbine is easily achievable and often even without superheating of the vapor at the inlet, (iii) the minimum and maximum pressures of the thermodynamic cycle can be selected independently of the sink/source temperatures (to a certain degree), and (iv) the supercritical cycle configuration can be obtained with low maximum cycle pressure, and also if the heat source is at low temperature [9,10]. In addition, it can be shown that, the heat of vaporization of organic fluids being much lower than that of water, a better match between the heating trajectory of the working fluid and the cooling trajectory of the heat source can be achieved. As a result, the heat source can be cooled to a significantly lower temperature [11]. Classes of substances that are currently employed as working fluids in ORC power plants are the linear or cyclic hydrocarbons, the refrigerants, and the siloxanes. The optimization of a mixture as a working fluid was also proposed [12].

Expansions in ORC turbines are characterized by two distinguishing features. Owing to the use of heavy and molecularly complex substances as working fluids, the expansion features a small specific enthalpy drop, which allows for the adoption of

Manuscript received December 30, 2008; final manuscript received May 8, 2009; published online March 3, 2010. Review conducted by Dilip R. Ballal.

only one or two stages, without running into the problem of high rotational speed and associated penalties on efficiency [9]. As a consequence though, the expansion pressure ratio per stage is typically very high (5–50), especially for radial turbines (50–150), so that the flow through the stator nozzle is highly supersonic [13]. The second important difference with respect to steam and gas turbines is the fact that the initial part of the expansion process takes place comparatively close to the critical point of the working fluid in the so-called dense-gas or real-gas thermodynamic region, where the ideal gas law does not apply. Complex thermodynamic models of organic fluids are therefore required for the correct and accurate (computational) fluid dynamic design and performance evaluation of high-expansion ratio ORC turbines.

The need for fluid dynamic simulations of expansions in the dense-gas region has led to the interfacing of existing finite-volume computational fluid dynamics (CFD) solvers with programs for the estimation of thermodynamic properties of fluids, featuring various degrees of accuracy (see, e.g., Refs. [10,14–22]). Examples of such CFD programs are the FINFLO solver, which was extended to allow for real-gas simulations [16] in order to aid the aerodynamic design of the stator of an ORC turbine [23], and ZFLOW [21, 24, and 22], which was specifically developed with the aim of creating a highly accurate real-gas flow simulation program, capable of treating complex geometries. The commercial CFD code FLUENT can also be interfaced with real-gas thermodynamic models [25]. FINFLO, ZFLOW, and FLUENT were validated for turbomachinery expansions in the ideal-gas thermodynamic region by comparing with the experimental data [10,16,21,26–28]. However, due to the lack of measurements of flows occurring in the dense-gas region, none of the codes have been validated on dense-gas flows. Without proper validation, these programs cannot be used as a predictive tool for the design of ORC turbines.

The aim of the work documented in this article is twofold. On the one hand, the study has the objective of demonstrating the possibility of effectively simulating, using state-of-the-art models, real-gas flows through blade passages of ORC turbine stators characterized by large pressure ratios; on the other hand, the investigation focuses also on the assessment of different flow solvers, turbulence models, and accurate thermodynamic models on the results. The results of the simulations are discussed quite extensively, and the outcome of this study is summarized in the concluding remarks, which also reports plans for future research.

2 The Test Case: The Stator of the Tri-O-Gen Radial Turbine

The test case for this study is the expanding flow of dense toluene ($C_6H_5CH_3$) vapor in the stator nozzle of a radial ORC turbine. This is the main component of the 150 kWe combined-heat-and-power ORC turbogenerator, manufactured by Tri-O-Gen B.V. The turbine and main pump of this ORC system are mounted on the same shaft, together with the high-speed electrical generator, as shown in Fig. 1(*a*). This arrangement allows for a compact and hermetic unit to be effectively integrated with the other components. Selected design specifications of the turbine are listed in Table 1. The aerodynamic design of the Tri-O-Gen turbine [16,23] was performed with the help of the FINFLO solver, interfaced to the thermodynamic property data of toluene, calculated with the model developed by Goodwin [29]. This article presents simulations of the Tri-O-Gen stator performed with a more accurate thermodynamic model developed by Lemmon and Span [30], as well as with the three mentioned CFD solvers (FINFLO, ZFLOW, and FLUENT), and several turbulence models.

2.1 Grid Independency and Convergence Criteria. The flow through the stator nozzle ring is mainly two-dimensional in the radial plane, and the influence of the endwall boundary layers on the flow field is assumed to be small. Coarse and fine 2D

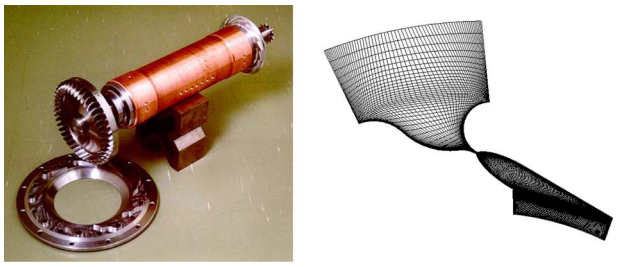

(*a*) (*b*)

Fig. 1 (*a*) The stator and rotor of the Tri-O-gen ORC turbine. The main pump, the rotor of the electrical generator, and the rotor of the turbine are mounted on the same shaft. (*b*) Coarse 2D computational grid (11,264 cells) of the stator nozzle for the viscous simulations. The figure aspect ratio is deformed since the blade design is a confidential property of the manufacturer.

structured computational grids (Fig. 1(*b*)) have been generated, consisting of 11,264 and 26,112 quadrilateral cells, respectively. Since the turbulence models implemented in FINFLO are of the low-Reynolds type, the grids were generated such that the nondimensional wall distance y^+ is of order 1 or smaller at the first cell adjacent to the wall [25]. For the FINFLO simulations, the largest differences between the solutions obtained using the two grids are observed for the density and the pressure at the throat (about 0.4%). The differences observed in the grid-convergence study performed with FLUENT are largest at the outlet of the stator: The pressure and the density calculated with the fine and the coarse grid differ by about 3%, and this corresponds to 2.6 kPa and 0.05 kg/m^3, respectively. It can therefore be concluded that the computational results are grid independent with both FINFLO and FLUENT.

The convergence of the simulations was ensured by monitoring the residuals and the maximum change in the pseudotime of the mass flow entering and leaving the computational domain. The iterations were continued until the scaled residuals decreased to 10^{-3} for all the conservation equations, except for the energy equation, for which the limiting value was set to 10^{-6}. For these values of the residuals, the density does not change anymore, and the difference in mass flow rate is smaller than 0.8%.

2.2 Influence of Real Gas Behavior. The flows of dense gases are different from their ideal gas counterparts, first of all because of the different volumetric relation, leading to quantitative deviations. In addition, for fluids that are complex enough, the dependence of the variation in the speed of sound on the density along isentropes in the dense-gas region is inverted, leading also to significant qualitative differences in the fluid dynamics [22]. The current test case has inlet conditions at reduced pressure and temperature (reduced with their respective critical point values) of 0.77 and 0.99, respectively, corresponding to a compressibility factor of 0.61. Given the common practice, it is important to remark that fluid dynamic simulations of this stator nozzle, based on the polytropic ideal gas model, would lead to strong average deviations from true fluid flow behavior [10,22]. On av-

Table 1 ORC turbine specifications and boundary conditions for the CFD simulations

Total inlet pressure	p_{01} [bar]	31.9
Total inlet temperature	T_{01} [°C]	314.5
Stator static backpressure	p_2 [bar]	0.55
Turbine overall pressure ratio	p_{01}/p_4	120.5
Mass flow rate	$\dot{m}$ [kg/s]	1.24
Working fluid		Toluene

Table 2 Typical percentage differences of area-averaged values obtained for the comparison of the models under investigation. The accurate thermodynamic models are the Goodwin model and the more recent Lemmon–Span model. Ranges are specified for the comparisons of the viscous FLUENT with viscous FINFLO and inviscid FLUENT with inviscid ZFLOW, and for the comparisons of the $k-\varepsilon$ and $k-\omega$ turbulence models compared for each of the two viscous flow solvers. The difference in isentropic efficiency and outflow angles is given in percentage points and degrees, respectively.

		Flow solvers	Turbulence models	Accurate thermodynamic models	Ideal-gas model (from Ref. [22])
Inlet density	ρ_{01}	0	0	0–2	64
Outlet pressure	p_2	6–16	0–1	1	10
Outlet density	ρ_2	6–15	0–1	1	1
Outlet Mach number	Ma_2	2–5	0–1	0	10
Outlet velocity	c_2	2–5	0–1	0	50
Outlet flow angle	α_2 [deg]	1–2	0–1	0	2
Mass flow rate	$\dot{m}$	0–2	0–1	1	15
Isentropic efficiency	η [%-points]	8	0–2	5	n/a
Specific work	$\dot{W}/\dot{m}$	n/a	n/a	6	n/a

erage, these deviations are at least approximately 10% for the Mach number and pressure distributions, 50% for the flow velocity and sound speed (where the sound speed would incorrectly decrease instead of increase), 40% for the density, 15% for the mass flow rate, and 30% for the total pressure loss and the flow exit angles (2 deg).

2.3 Influence of Fluid Thermodynamic Models on Energy Balances. Based on pressure and temperature measurements taken at the turbine inlet of an ORC plant under testing, the calculation using the Goodwin thermodynamic model predicts a specific enthalpy drop due to the expansion through the turbine that is 6.3% higher than the one predicted by means of the Lemmon–Span model. A detailed energy-balance study [31] that relates the enthalpy drop to the measured electrical power output and power absorbed by the main pump showed that the predictions, based on the Goodwin equation of state, would lead to an improbably high estimation of the isentropic efficiency of the turbine (87%), given the very large expansion ratio. The use of the Lemmon–Span thermodynamic model leads to a more realistic isentropic turbine efficiency of 82%. This is expected since closer to the critical point, accurate experimental data are mandatory in order to obtain good estimations with equations of state. The Lemmon–Span model is therefore expected to perform especially better in this thermodynamic region, as it is fitted on data that were not available when the model by Goodwin [29] was developed. The use of the Lemmon–Span thermodynamic model shows that, for the ORC power plant operating at design conditions, 6% less shaft power can actually be obtained with respect to the power output estimated by the design calculations, which relied on the Goodwin thermodynamic model.

3 Simulation Results

Computed flow field solutions obtained using the different models and flow solvers are systematically compared. In all simulations, the pressure and temperature at the stator inlet and pressure ratio are specified. An overview of results is presented in Table 2, which compares the typical differences in relevant flow and performance parameters observed for the various models. For conciseness, only key differences are described in more detail.

3.1 Effect of Flow Solvers. Figure 2 shows the Mach number contours of the flow through the turbine stator, as calculated using FLUENT and FINFLO, both based on the $k-\varepsilon$ turbulence model, the Lemmon–Span thermodynamic model, and the extended corresponding states-based transport property model. As can be noted, the structure of the flow field is similar. An oblique shock emerges

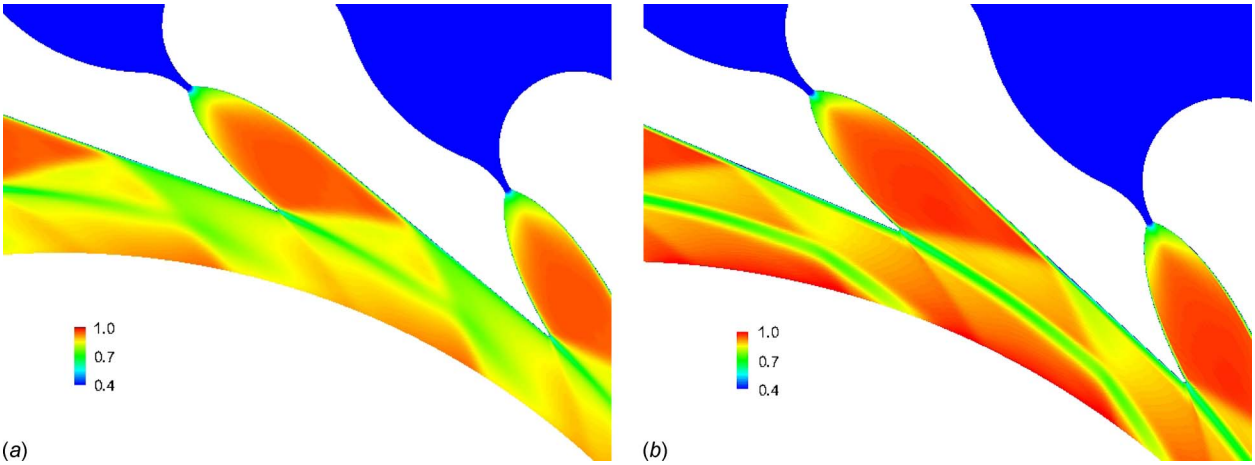

Fig. 2 Comparison of scaled Mach number fields of the flow through the turbine stator nozzle, as calculated by (*a*) FLUENT and (*b*) FINFLO viscous flow solvers, respectively. Both flow solvers employ the $k-\varepsilon$ turbulence model and the Lemmon–Span thermodynamic model for toluene. The Mach number fields are scaled by one outlet value for reasons of confidentiality requested by the manufacturer.

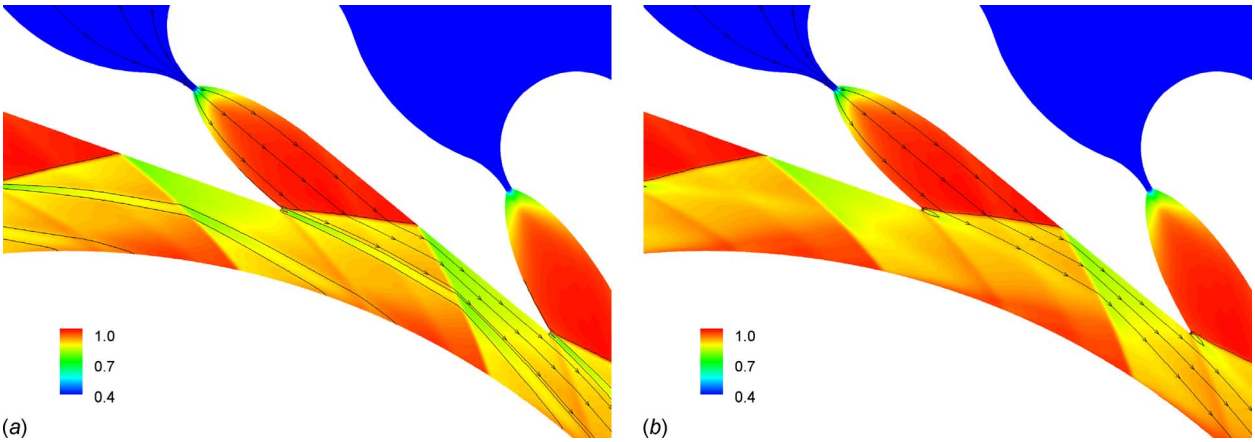

Fig. 3 Comparison of scaled Mach number fields of the flow through the turbine stator nozzle, as calculated by (*a*) inviscid FLUENT and (*b*) inviscid ZFLOW solvers, respectively. Both flow solvers employ the Lemmon–Span thermodynamic model for toluene. The Mach number fields are scaled by one outlet value for reasons of confidentiality requested by the manufacturer. Streamlines and equidistant isolines of total pressure are also indicated.

from the trailing edge of the stator nozzle because the flow entering the mixing region (i.e., the region after the trailing edge) cannot maintain its direction due to the flow coming from the adjacent stator. The flow is turned into itself, which, at supersonic velocities, leads to the emergence of an oblique shock wave. The oblique shock wave is reflected from the opposite stator-vane wall toward the outlet of the computational domain and the turbine-rotor inlet. The flow structure is typical of radial high-expansion ratio turbines.

The Mach number at the stator outlet, as calculated by FINFLO, is higher, and the shock wave calculated with FLUENT is less inclined (i.e., directed more toward the normal of the flow direction). This indicates that the oblique shock predicted by FLUENT is stronger, namely, more dissipative, than the one predicted by FINFLO. This results into a dramatically (8%-point) lower isentropic efficiency than the one obtained using FINFLO, regardless of the thermodynamic and turbulence models. The same difference can be observed in the comparison of the inviscid flow fields simulated using ZFLOW and FLUENT (inviscid solver), see Fig. 3. Here, the shock wave, as predicted by FLUENT, is approximately 6% stronger than the one predicted by ZFLOW in terms of the dimensionless shock strength $(p_B - p_A)/(\rho_A a_A^2)$, where A and B denote pre- and postshock states, respectively. FLUENT also predicts a distinct dissipative wake, which, for inviscid simulations, is purely numerical. These two effects lead to a total pressure loss coefficient $(1 - p_{02}/p_{01})$, which is 32% higher in the case of simulations performed with FLUENT. In fact, all of the deviations in flow quantities resulting from the choice of the flow solver, as shown in Table 2, pertain to the comparisons of either FINFLO or ZFLOW with respect to FLUENT. It is likely that the cause for the consistently more dissipative behavior of FLUENT, compared with FINFLO and ZFLOW, can be found in different numerical schemes employed by the solvers. This could be the result of the design criteria adopted for a commercial software package, where a somewhat more dissipative characteristic could be favored for the sake of robustness and of a better convergence behavior at the cost of accuracy.

3.2 Effect of Fluid Thermodynamic Models. The effect on the flow simulation of using different thermodynamic models, namely, the equations of state of Lemmon and Span [30] and of Goodwin [29], is shown here by comparing results obtained with the FINFLO solver. Relevant results are shown in Table 2. The differences in the calculated flow parameters appear noticeably small, and these are not affected by the choice of the turbulence model. Notice, however, that the Goodwin thermodynamic model

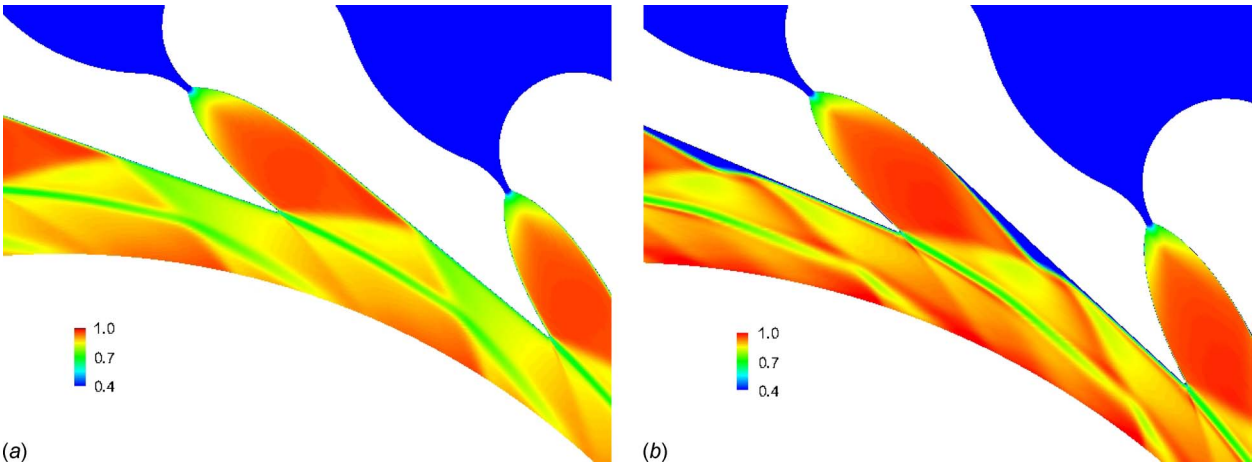

Fig. 4 Comparison of scaled Mach number fields of the flow through the turbine stator nozzle, as calculated by (*a*) FLUENT and (*b*) FINFLO, both employing the $k-\omega$ turbulence model. The latter combination predicts a shock-induced separation bubble.

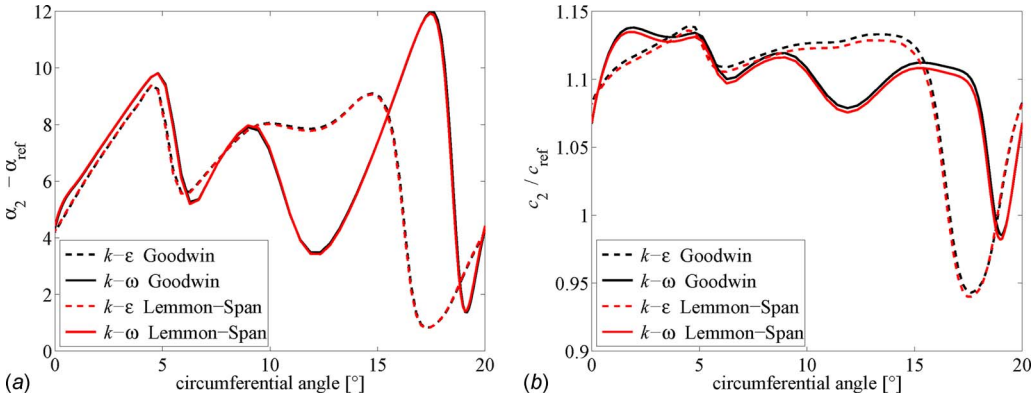

Fig. 5 Comparison of (*a*) the outflow angle and (*b*) outflow velocity, both with respect to a reference value calculated with FINFLO using different turbulence models. Both quantities are plotted as a function of the circumferential rotor angle, where the range corresponds to exactly one periodic stator nozzle outlet. The outflow angle is calculated from the radial direction (the lower the value, the more radial is the flow).

does differ significantly from the more accurate Lemmon–Span thermodynamic model in its prediction of the specific enthalpy difference. This leads to a considerably different value for the specific work and stator isentropic efficiency, as described in Sec. 2.3.

3.3 Effect of Turbulence Models. The comparison of the $k-\varepsilon$ and $k-\omega$ turbulence models is conducted using the viscous flow solvers adopted in this study. As expected, the overall flow structure does not strongly depend on the chosen turbulence model. However, in the simulation performed with FINFLO and the $k-\omega$ turbulence model shown in Fig. 4, a significant difference is observed close to the wall, at the location where the shock wave from the trailing edge is reflected. Here, the $k-\omega$ turbulence model predicts a separation bubble, which does not occur if the flow is simulated by means of FLUENT. A separation bubble is highly unsteady and might exist in the actual flow field. At the boundary layer, where the flow field becomes subsonic, the pressure gradient over the shock wave causes the fluid to flow from the high pressure zone to the low pressure zone. The highest pressure is right after the shock wave, and therefore, the fluid moves upstream in the boundary layer, determining the separation bubble.

The separation bubble affects the direction of both the oblique shock and the trailing edge wake (Fig. 4). Although it does not have an effect on the average values at the stator outlet (see Table 2), it does significantly affect the circumferential distribution of flow quantities at the stator outlet/rotor inlet, as shown in Fig. 5. The maximum periodic change in the flow angle at the rotor inlet increases from 8 deg to 11 deg, and the maximum variation in velocity decreases from 17% to 13%. The effect of the separation bubble on the flow field leads to a 2%-point difference in the isentropic efficiency of the nozzle, depending on the turbulence model, which is small in comparison to the difference caused by the use of two different flow solvers (see Table 2).

4 Conclusions

The work documented in this article demonstrates the ability of simulating high-expansion real-gas flows, which typically occur in ORC turbine stators, using CFD solvers linked to accurate models for the estimation of the thermophysical properties of the working fluid. The influence of different numerical solvers, fluid thermodynamic models, and turbulence models on the simulated flow field has been analyzed.

With respect to the FINFLO and ZFLOW solvers, the commercial FLUENT solver predicts much stronger shock waves and a more dissipative wake, resulting in a dramatically (8%-point) lower isentropic stator efficiency. This could be the result of the design criteria adopted for a commercial software package, where a somewhat more dissipative characteristic could be favored for the sake of robustness and of a better convergence behavior at the cost of accuracy. The two accurate thermodynamic models, namely, the equations of state of Lemmon and Span [30] and of Goodwin [29], lead to small differences in the flow field, especially if compared with the large deviations that would be present if the flow were simulated based on the polytropic ideal gas model. However, the Goodwin thermodynamic model does differ significantly from the more accurate Lemmon–Span thermodynamic model in its prediction of the specific enthalpy difference, which leads to a considerably different (6%) value for the specific work and stator isentropic efficiency. The $k-\varepsilon$ and $k-\omega$ turbulence models have minor influence on the results, except for the $k-\omega$ turbulence model in combination with the FINFLO solver. For this case, a separation bubble is present at the location where the shock wave reflects on the stator wall. The separation bubble affects the shock wave and wake, which in turn affects in particular the variation in the flow velocity and angle along the stator outlet. Averaged quantities are not affected, except for the isentropic nozzle efficiency, which differs by 2%.

The above differences point to a need for experimental validation of the flow solvers by comparison to measurements on flows in dense-gas conditions, if CFD tools are to be applied for performance improvements and design of high-expansion ratio turbines, operating partly in the real-gas regime. A gain of a few percentage points in the isentropic efficiency of the turbine would lead to a relevant increase in the overall conversion efficiency. Such an increase can be obtained at the cost of research and development activities, but has no impact on the capital investment for the power plant.

The extension of the study using three-dimensional viscous-turbulent simulations performed with ZFLOW is planned in the near future. Activities are underway for coupling this flow solver to shape-optimization algorithms. Current plans also include the validation of the CFD code using experimental data obtained with a high-temperature Ludwieg tube for the generation of transonic flows of dense organic vapors, which is in the commissioning phase at the Delft University of Technology.

Acknowledgment

This research is supported by Lappeenranta University of Technology research foundation, Finnish Foundation for Technology Promotion, the Dutch Technology Foundation STW, Applied Science Division of NWO, the Technology Program of the Ministry

of Economic Affairs DSF 6573 and Senter Novem. The authors are grateful to Tri-O-Gen B.V. for providing data of an existing ORC plant and for many interesting discussions.

Nomenclature

a = sound speed
c = flow velocity
k = turbulent kinetic energy
$\dot{m}$ = mass flow rate
Ma = Mach number
p = pressure
T = temperature
$\dot{W}$ = power

Greek

α = outflow angle
ε = dissipation rate of turbulent kinetic energy
ρ = density
ω = specific dissipation rate of turbulent

Subscripts

01 = stator inlet total conditions
02 = stator outlet total conditions
2 = stator outlet conditions
4 = turbine outlet conditions
A = preshock state
B = postshock state

References

[1] Bronicki, L., 2007, "Organic Rankine Cycles in Geothermal Power Plants—25 Years of Ormat Experience," *Proceedings of the GRC 2007 Annual Meeting*, Reno, NV.
[2] Bronicki, L. Y., 1988, "Electrical Power From Moderated Temperature Geothermal Sources With Modular Mini-Power Plants," Geothermics, **17**(1), pp. 83–92.
[3] Bini, R., and Manciana, E., 1996, "Organic Rankine Cycle Turbogenerators for Combined Heat and Power Production From Biomass," *Proceedings of the Third Munich Discussion Meeting on Energy Conversion From Biomass Fuels: Current Trends and Future Systems*, Paper No. 96A00412, pp. 1–8.
[4] Obernberger, I., Thonhofer, P., and Reisenhofer, E., 2002, "Description and Evaluation of the New 1000 kW ORC Process Integrated in the Biomass CHP Plant in Lienz, Austria," Euroheat and Power, **10**, pp. 1–17.
[5] Bini, R., Duvia, A., Schwarz, A., Gaia, M., Bertuzzi, P., and Righini, W., 2004, "Operational Results of the First Biomass CHP Plant in Italy Based on Organic Rankine Cycle Turbogenerator and Overview of a Number of Plants in Operation in Europe Since 1998," *Proceedings of the 2nd World Conference on Biomass for Energy, Industry and Climate Protection*, 10–14 May 2004, Rome, Italy, pp. 1716–1721.
[6] Drescher, U., and Brüggemann, D., 2007, "Fluid Selection for the Organic Rankine Cycle (ORC) in Biomass Power and Heat Plants," Appl. Therm. Eng., **27**, pp. 223–228.
[7] Yamaguchi, H., Zhang, X. R., Fujima, K., Enomoto, M., and Sawada, N., 2006, "Solar Energy Powered Rankine Cycle Using Supercritical CO_2," Appl. Therm. Eng., **26**(17–18), pp. 2345–2354.
[8] Angelino, G., and Colonna, P., 2000, "Organic Rankine Cycles for Energy Recovery From Molten Carbonate Fuel Cells," *Proceedings of the 35th Intersociety Energy Conversion Engineering Conference (IECEC)*, AIAA Paper No. 2000-3052, pp. 1–11.
[9] Angelino, G., Gaia, M., and Macchi, E., 1984, "A Review of Italian Activity in the Field of Organic Rankine Cycles," *VDI Berichte–Proceedings of the International VDI Seminar*, Vol. 539, VDI, Zurich, pp. 465–482.
[10] Colonna, P., Harinck, J., Rebay, S., and Guardone, A., 2008, "Real-Gas Effects in Organic Rankine Cycle Turbine Nozzles," J. Propul. Power, **24**(2), pp. 282–294.
[11] Larjola, J., 1995, "Electricity From Industrial Waste Heat Using High-Speed Organic Rankine Cycle (ORC)," Int. J. Prod. Econ., **41**(1–3), pp. 227–235.
[12] Angelino, G., and Colonna, P., 1998, "Multicomponent Working Fluids for Organic Rankine Cycles (ORCs)," Energy, **23**(6), pp. 449–463.
[13] Verneau, A., 1987, "Supersonic Turbines for Organic Fluid Rankine Cycles From 3 to 1300 kW," *Proceedings of the Small High Pressure Ratio Turbines* (VKI Lecture Series), Jun. 15–18, Von Karman Institute, Rhode-Saint-Genèse, Belgium, Paper No. 1987-07.
[14] Colonna, P., Rebay, S., and Silva, P., 2002, "Computer Simulations of Dense Gas Flows Using Complex Equations of State for Pure Fluids and Mixtures and State-of-the-Art Numerical Schemes," Scientific report, Università di Brescia, Via Branze, Brescia, Italy, Vol. 38, pp. 1–68.
[15] Hoffren, J., 1997, "Adaptation of FINFLO for Real Gases," Technical Report No. 102.
[16] Hoffren, J., Talonpoika, T., Larjola, J., and Siikonen, T., 2002, "Numerical Simulation of Real-Gas Flow in a Supersonic Turbine Nozzle Ring," ASME J. Eng. Gas Turbines Power, **124**(2), pp. 395–403.
[17] Turunen-Saaresti, T., Tang, J., and Larjola, J., 2006, "A Practical Real Gas Model in CFD," Proceedings of the European Conference on Computational Fluid Dynamics (ECCOMAS CFD 2006), P. Wesseling, E. Onate, and J. Périau, eds.
[18] Boncinelli, P., Rubechini, F., Arnone, A., Cecconi, M., and Cortese, C., 2004, "Real Gas Effects in Turbomachinery Flows—A Computational Fluid Dynamics Model for Fast Computations," J. Turbomach., **126**(2), pp. 268–276.
[19] Cinnella, P., and Congedo, P., 2004, "A Numerical Solver for Dense Gas Flows," Proceedings of the 34th AIAA Fluid Dynamics Conference and Exhibit, AIAA Paper No. 2004-2137, pp. 1–12.
[20] Cinnella, P., and Congedo, P., 2007, "Inviscid and Viscous Aerodynamics of Dense Gases," J. Fluid Mech., **580**, pp. 179–217.
[21] Colonna, P., and Rebay, S., 2004, "Numerical Simulation of Dense Gas Flows on Unstructured Grids With an Implicit High Resolution Upwind Euler Solver," Int. J. Numer. Methods Fluids, **46**(7), pp. 735–765.
[22] Harinck, J., Colonna, P., Guardone, A., and Rebay, S., 2010, "Influence of Thermodynamic Models in Two-Dimensional Flow Simulations of Turboexpanders," J. Turbomach., **132**, p. 011001.
[23] Van Buijtenen, J., Larjola, J., Turunen-Saaresti, T., Honkatukia, J., Esa, H., Backman, J., and Reunanen, A., 2003, "Design and Validation of a New High Expansion Ratio Radial Turbine for ORC Applications," *Proceedings of the Fifth European Conference on Turbomachinery*, pp. 1–14.
[24] Colonna, P., Rebay, S., Harinck, J., and Guardone, A., 2006, "Real-Gas Effects in ORC Turbine Flow Simulations: Influence of Thermodynamic Models on Flow Fields and Performance Parameters," *Proceedings of the European Conference on Computational Fluid Dynamics (ECCOMAS CFD 2006)*, P. Wesseling, E. Onate, and J. Périau, eds., pp. 1–18.
[25] FLUENT Inc., 2006, FLUENT 6.3 documentation, Lebanon, NH.
[26] Pan, H., 1993, "Two-Dimensional Navier-Stokes Computations of Subsonic and Supersonic Flows Through Turbine Cascades," Technical Report No. B-40.
[27] Rautaheimo, P., Salminen, E., and Siikonen, T., 1995, "Numerical Simulation of the Flow in the NASA Low-Speed Centrifugal Compressor," Technical Report No. 119.
[28] Pitkänen, H., and Siikonen, T., 1995, "Simulation of Viscous Flow in a Centrifugal Compressor," Technical Report No. B-46.
[29] Goodwin, R., 1989, "Toluene Thermophysical Properties From 178 to 800 K at Pressures to 1000 Bar," J. Phys. Chem. Ref. Data, **18**(4), pp. 1565–1636.
[30] Lemmon, E., and Span, R., 2006, "Short Fundamental Equations of State for 20 Industrial Fluids," J. Chem. Eng. Data, **51**(3), pp. 785–850.
[31] Harinck, J., Turunen-Saaresti, T., and Colonna, P., 2007, "Performance and CFD Analyses of a High-Expansion Ratio Radial ORC Turbine," Scientific Report No. ET-2262.

Laser Beam Welding of Open-Porous Metallic Foams for Application in Cooling Structures of Combined Cycle Power Plants

Uwe Reisgen

Simon Olschok

Stefan Longerich

Welding and Joining Institute (ISF),
RWTH Aachen University,
Aachen NRW D-52062, Germany

Within the Collaborative Research Centre 561, "Thermally highly loaded, porous and cooled multilayer systems for combined cycle power plants," open-porous and high-temperature stable Ni-based structures are being developed for the requirements of effusion cooling. A two-dimensional cooling strategy for the walls of combustion chambers, which allows the outflow of the cooling medium over the complete wall area of the combustion chamber, could be realized by an open-porous metallic foam structure. The open-porous metallic foam is produced by the "slip reaction foam sintering" process, a powder metallurgical process. To join several foams to assemble structural elements, laser beam welding has been used. Different joining strategies have been examined to find out the most suitable method to join these foams. In this paper, the process setups, settings of the different strategies, and results of trials (seam geometry and strength tests) are discussed. The need for graded structures to combine the essential permeability and adequate weldability is also shown.
[DOI: 10.1115/1.3204512]

Keywords: laser beam welding, metallic foams, open porous, production engineering

1 Introduction

The laser beam welding process is a suitable method for the joining of metal foams into a compound structure. This is characterized by a minimum input of energy and, connected with this, a small joining zone. It guarantees that the influence on the mechanotechnological properties of the base material is slight and that only minor distortion of the components occurs [1]. Excessive input of energy, moreover, destroys the porous structure of the foams; i.e., the foam starts sintering by diffusion-induced volume decrease and the high energy input causes liquefaction of the foam and drop development through the surface tension of the molten metal. Another suitable welding process for this application is the capacitor discharge welding. This process has also successfully been applied in SFB 561 research work [2–4]. For the application field of aluminum foam sandwich structures, ultrasonic spot welding has been used successfully [5].

Figure 1(*a*) shows a schematic diagram of the multilayer cooling system consisting of thermal barrier coating with bond coat, an open-porous metallic foam, and a substrate with integrated ducts for the cooling air. The detail in Fig. 1(*b*) shows a micrograph of the joining area of foam and solid material after laser welding. The joining area connects the foam with the substrate. The prevailing temperature level reaches there the temperature of the cooling gas of approximately 420°C [6].

The open-porous foam itself is produced using the slip reaction foam sintering (SRFS) process. This process is based on powder metallurgy and generates a porous cell structure with the aid of a chemical reaction. By varying the different parameters (i.e., the amount of metal powder), the density/porosity of the foam can be adapted to specific needs of permeability or weldability (Fig. 2) [7–9].

The final goal is to determine an appropriate joining strategy to connect the foam structure to a solid material that offers a low energy input into the foam structure to avoid thermal damage to the foam structure. Further, the method should allow an assembly of structures with a homogeneous foam surface without potential "hot spots," which would emerge from noneffusion cooled massive material. It will therefore be necessary to find an appropriate joining additive that slightly penetrates into the foam structure.

2 Experimental Setup

2.1 Material Grades. Foams for the first welding trials were made of a sponge iron powder (NC 100.24). These foams were used only to generally prove the weldability of open-porous structures, which fulfil the requirements of SFB 561. A welded joint between a sponge iron foam and a solid base metal is shown in Fig. 1(*b*). For the trials that are presented in this paper, a nickel-based material Inconel 625 ($NiCr_{22}Mo_9Nb$)[1] was used. Even after the foaming and sintering processes, those foams show an excellent match in the chemical composition compared with the water atomized metal powder the foams are made of (Table 1).

To reach a sufficient mechanical stability, the primary foam pores must not exceed 1.0 mm. Otherwise, the welded structures cannot bear the forces appearing in a turbine, and an accurate bond coat/thermal barrier layer coating is not possible. The secondary pores have to reach up to 0.3 mm for adequate permeability. After sintering, an open porosity of about 80% is received.

As a filler material for the laser beam welding process, a metallurgical identical Inconel 625 wire was used. This wire type is a commercially available welding rod with a diameter of 1.0 mm.

2.2 Laser Beam Welding Setup. The laser beam welding tests were carried out using a TLF 6000 CO_2 laser beam power source from Trumpf Lasertechnik. The unit is a high-frequency-excited, fast axial flow CO_2 high-power laser with an infinitely variable output power from 100 to 6000 W. In the Kugler focusing optics, a molybdenum-coated parabolic mirror with a focal distance of 200 mm focuses the laser beam onto a focal spot with a diameter of approximately 0.6 mm.

3 Joining Strategies

Two different testing arrangements were examined for the welding of nickel-based foams on a solid material. Both variants were welded with a filler material in order to compensate for the shrinkage of the foam during welding (Table 2).

In the first case (see Fig. 3(*a*)), welding was carried out on a butt joint, and a filler wire was used. The wire Inconel 625 is, in its metallurgical composition, identical to the base material of the foams. For the second variation (Fig. 3(*b*)), stepped plates were produced—the projection on the plates was used as a reservoir for the filler material, so no additional filler wire has to be used. The laser beam was shifted specifically into the direction of the solid material so as to keep the thermal load on the foam as low as possible but still realize a partial melt of the foam in the fusion zone to generate a stable connection.

4 Results

4.1 Laser Beam Welding Results. With a foam thickness of 6 mm, full fusion was obtained using both laser beam welding

Manuscript received March 20, 2009; final manuscript received April 27, 2009; published online March 3, 2010. Review conducted by Dilip R. Ballal.

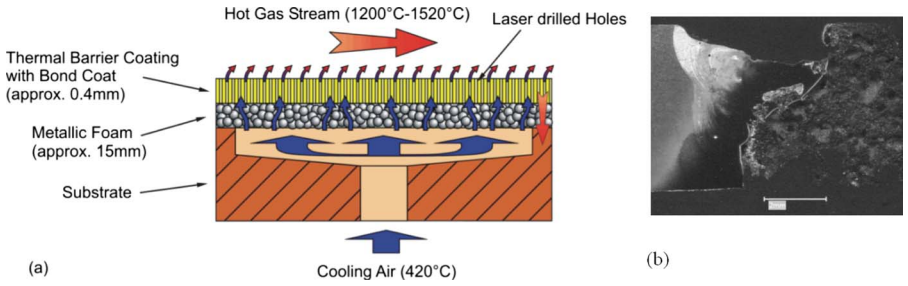

Fig. 1 Schematic diagram of the multilayer cooling system of SFB 561 consisting of thermal barrier coating with bond coat, open-porous metallic foam, and substrate

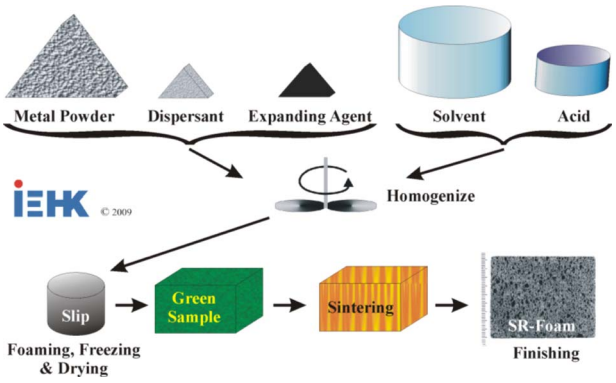

Fig. 2 Scheme of the SRFS process [7]

variations (Figs. 4 and 5). The weld surfaces, however, differ fundamentally. Whereas in the welds of the stepped connecting structures a very flat surface was obtained, the welds made on butt joints show the influence of the porosity very clearly (Fig. 4). In areas where, before welding, larger pores or cavities were found, the welded seams are clearly sunken.

In complementary research projects within the SFB that are dealing with the cooling efficiency of different cooling structures, a minimum foam thickness of 10 mm is required for a homogeneous cooling medium flow through the metal foam and thus a homogeneous transpiration cooling film. For those thick foams, a full-depth weld is not realizable because the energy/heat input of the laser beam, which is necessary for this penetration depth, would be too high and the foam structure would be destroyed. The maximum fusion depth to be reached with the laser beam welding process is about 8 mm; therefore, a foam density not less than 2.6 g cm^{-3} has to be used.

Table 1 Typical chemical composition of Inconel 625 metal powder and chemical composition of sintered foams

	Chemical composition, mass contents in %											
	C	Si	Mn	S	O_2	Al	Cr	Fe	Mo	Nb	Ti	P
Water atomized metal powder	<0.1	<0.5	<0.5	<0.05	⋯	<0.40	20–23	<5.0	8–10	3.15–4.15	<0.40	<0.015
Sintered foam	0.021	1.8	0.06	…	0.5	…	20.9	3.3	8.5	3.5	…	…

Table 2 Welding parameters

	Laser power P_L (kW)	Welding speed v_s (m min^{-1})	Focus position f_z (mm)	Wire feed speed v_W (m min^{-1})	Laser displacement x_L (mm)	Wire displacement $f_{z,\text{wire}}$ (mm)
Variation 1	5.6	1.5	−1.0	3.0	0.8	−0.2
Variation 2	5.6	0.8	−1.0	…	1.4	…

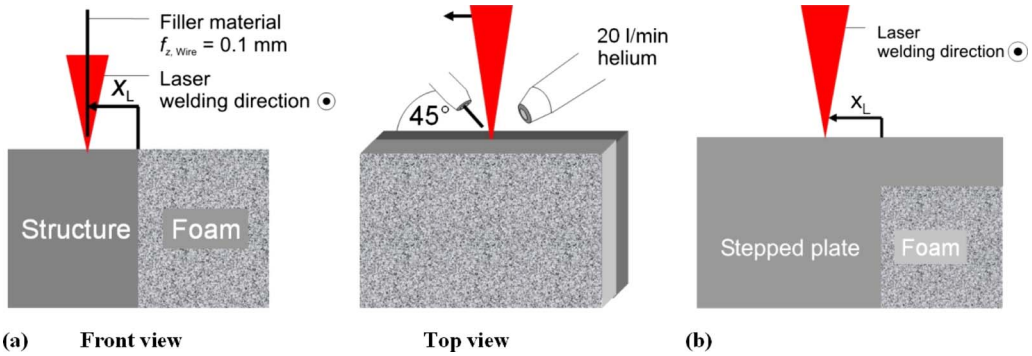

Fig. 3 Process geometry for (*a*) welding variation 1 and (*b*) welding variation 2

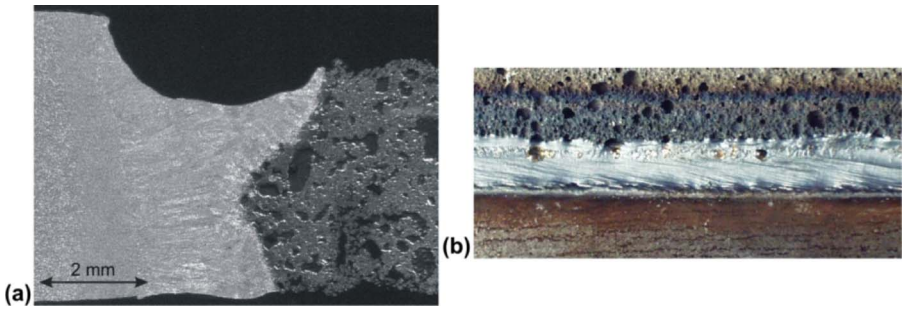

Fig. 4 Specimen welded using variation 1: (*a*) macrosection and (*b*) top view

Independent of the foam thickness, a satisfying fusion between the foam and the solid material was achieved. Figure 5 shows a scanning electron microscopy (SEM) analysis of the region of fusion in detail. Clearly visible is the gradual transition from the base material through the area of molten material into the foam. Some kind of additional clamping between the foam and the resolidified material cannot be excluded, but it is not possible to detect this mechanism in a macrosection.

A specimen welded with variation 2 also shows an excellent weld shape and a gradual transition into the foam (Fig. 6(*a*)). Through the stepped edge of this butt geometry, the joining zone in the foam region is not directly visible. This makes weld defects very hard to determine. Figure 6(*b*) shows a cavity with a size of approximately 70 mm^2, which had been detected only by milling the stepped edges of the solid material. The cavity had developed due to the severe heat effects in the foam. Clearly recognizable is the material of the original foam structure, which has solidified in a droplet shape. The residual weld is, with identical parameters, not objectionable. Still it remains to examine whether these types of weld defects occur with large cavities, which are already existent in the foam.

Welding defects similar to those shown in Fig. 6(*b*) are typical of the welding trials performed with foams with a density less than 2.6 g cm^{-3}, independent of the welding variation. This lower limit of foam density was examined by trials with foams of densities between 1.5 and 3.5 g cm^{-3}. For a suitable cooling medium flow through the foam, a maximum foam density of 1.9 g cm^{-3} is required, so graduated foams slightly more dense at the areas of designated welds are up-to-date object of research.

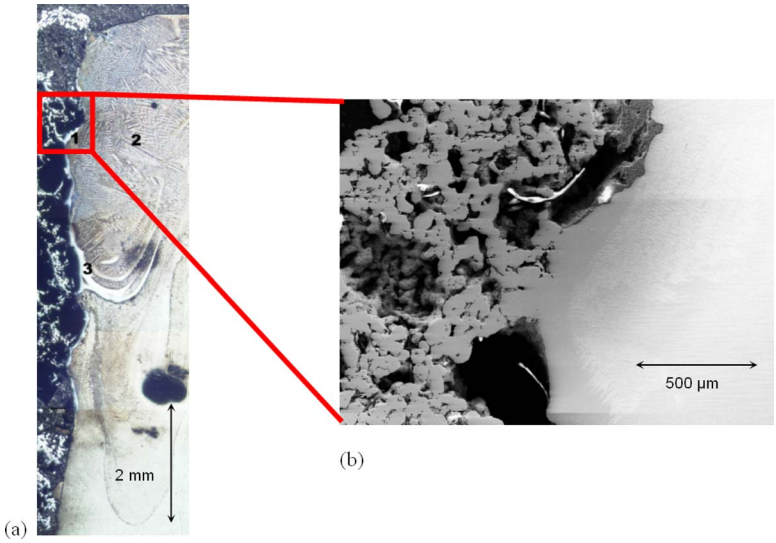

Fig. 5 Specimen welded using variation 1; *t*=15 mm, 8 mm fusion depth: (*a*) macrosection and (*b*) SEM analysis

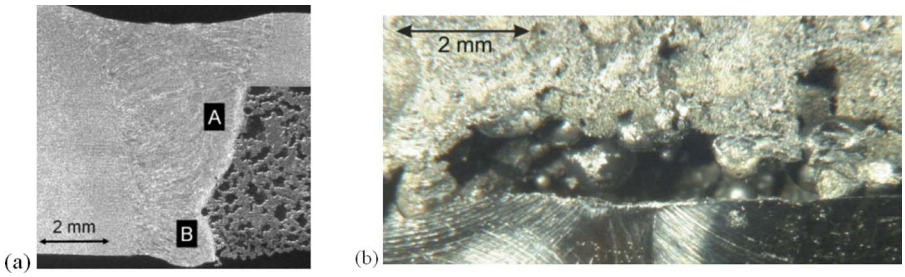

Fig. 6 (*a*) Macrosection of a specimen welded with variation 2. (*b*) Cavity formation through excessive energy input into the foam

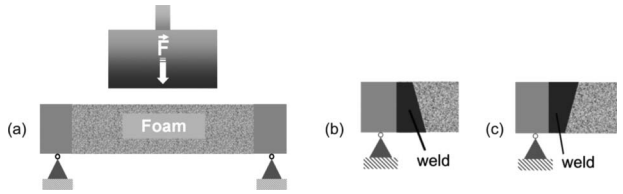

Fig. 7 (*a*) Setup concept for the determination of the shear strength. (*b*) Specimen loading from underneath. (*c*) Specimen loading from the upper side.

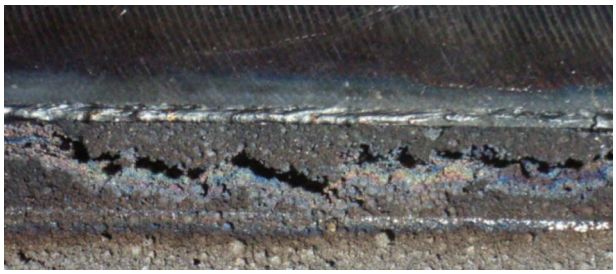

Fig. 9 Typical rupture of the foam, bottom view

4.2 Mechanical Properties of the Welded Joints. Shear strength tests were carried out on the laser beam welded foams. A setup was developed, allowing determination of the shear forces acting in the welds. In this, a rectangular foam specimen is laterally welded to two elements made of a solid material carried on a framework. Loading of the foam is made via a rectangular die (Fig. 7(*a*)). In order to meet the requirements of the asymmetrical welding cross section, the weld specimens were loaded from above and also from below for the determination of a preferential direction (Figs. 7(*b*) and 7(*c*)).

Specimen 2, which is depicted in Fig. 8(*a*), was loaded from below; specimen 1 was loaded from above. The test die was used for all tests; the test speed was 0.5 mm min^{-1}. All specimens broke in the heat-affected zone (HAZ) of the foam (Fig. 9).

Welded joint failure occurs after approximately 4 kN with a cross-sectional area of 250 mm^2. The further rising of the graph is substantiated by the fact that the foams, after the failure of the HAZ, are positioned on the testing device and that, from this moment on, only the mechanical strength of the foam is measured.

The shear tension strength of the specimens with stepped connecting structures was also tested from both sides (Fig. 8(*b*)). Specimen 4 was loaded in such a way that the foam was not supported by the web.

In this, the bearable, very low forces of approximately 1.5 kN are ascribed to the fact that loading of the foams was not absolutely free of flexural moments. Specimen 3 was loaded from below. The supporting effect of the stepped edge increases the strength of the welded joint by far.

The influence of the foam density observed during the weld tests was quite significant for the shear stress. The lower the density of the foams, the larger the pores. This means that the webs and/or cavity walls melt because of the thermal load; large cavities where welding fusion no longer occurs may develop quite easily. With higher densities, the distances between the individual webs are so small that, first, the melting of sporadic webs is not so important and, second, the possible heat dissipation is much higher—so that the thermal load of the foam in the direct environment of the joining zone is not so high. The lower limit of the foam density, as far as weldability is concerned, is found to be approximately at 2.6 g cm^{-3} (see also Sec. 4.1).

5 Conclusion

The weldability of iron- and nickel-based metal foams was proved. Through the testing of different joining strategies, the possibilities and limits of thermal joining of these foams by means of laser beam welding were demonstrated. The different connective structures and the resulting shear strengths allow conclusions about the later design of components. The application of metal foams must be designed, on the one hand, for welding, and the geometry must be adapted to the demands of the porous foam structure. Due to the high flexural susceptibility of the rather thin foam samples tested, attention must be paid to loading that is free of flexural moments. Through a design for welding that, moreover, considers the properties of the foam, the mechanotechnological properties can be specifically improved. The requirements for the foams are a density higher than 2.6 g cm^{-3} (necessary for weldability) and a thickness of at least 10 mm (necessary for homogeneous permeability). Here, the application of graded foams is recommended, allowing the achievement of better mechanical-technological properties in the weld and in the heat-affected zone by adjusting the foam structure to the requirements of the welding process.

The authors gratefully acknowledge the financial support by the Deutsche Forschungsgemeinschaft (DFG) within the Collaborative Research Centre (SFB) 561 "Thermally highly loaded, porous and cooled multilayer system for combined cycle power plants."

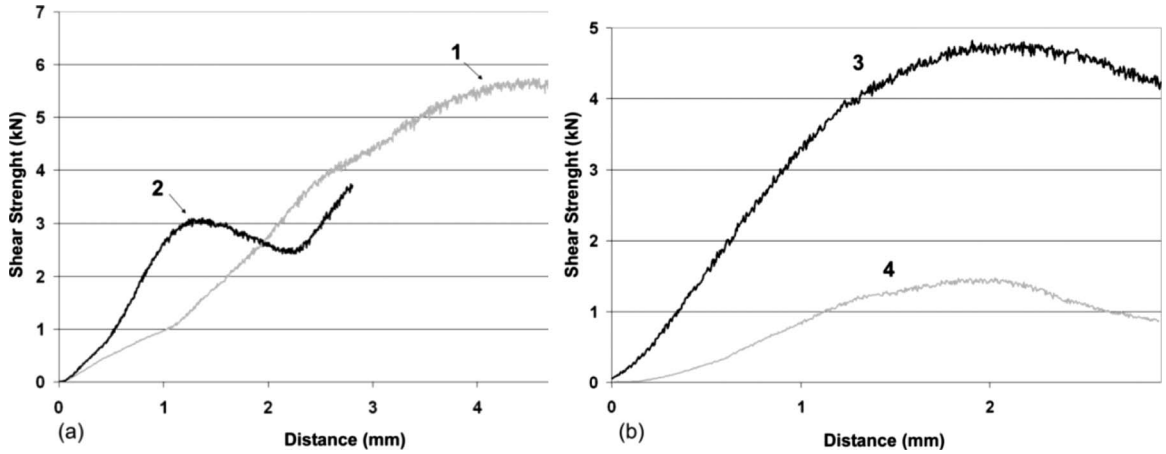

Fig. 8 (*a*) Results of the tensile shear tests of the specimens welded with strategy 1. (*b*) Results of the tensile shear tests of the specimens welded with strategy 2.

References

[1] Dilthey, U., 2006, "Schweißtechnische Fertigungsverfahren—Bd. 1: Schweiß- und Schneidtechnologien (Welding Production Processes—Vol. 1: Welding and Joining Technologies)," Springer, Berlin.

[2] Harms, A., and Longerich, S., 2007, "Schweißen von Hohlstrukturen und offenporösen Metallschäumen für den Einsatz in Kombi-Kraftwerken (Welding of Hollow Structures and Open-Porous Metal Foams for Application in Combined Cycle Power Plants)," Materialwiss. Werkstofftech., **38**(7), pp. 538–543.

[3] Bleck, W., Dilthey, U., Angel, S., Piontek, D., Longerich, S., and Harms, A., 2007, "Joining Strategies for Open Porous Metallic Foams on Iron and Nickel Base Materials," Adv. Eng. Mater., **9**(8), pp. 670–678.

[4] Wang, J., Ohse, P., Wu, S., and Dilthey, U., 2007, "Impulse Capacitor Discharge Welding of Hollow Structure Made of Nickel-Base Alloy," Tsinghua Science & Technology, **12**(4), pp. 453–458.

[5] Born, C., Kuckert, H., Wagner, G., and Eifler, D., 2002, "Joining of Aluminum Foam Sandwich to Sheet Metals by Ultrasonic Welding," Materials Week 2002, International Congress on Advanced Materials, Their Processes and Applications, International Conference on Joining Ceramics, Glass and Metal, München, p. 1.

[6] Bohn, D., 2005, "Technologien für die Gasturbinen der übernächsten Generation (Technologies for Future Generation Gas Turbines)," VGB PowerTech, **85**(7), pp. 65–71.

[7] Scholz, P.-F., 1997, "Verfahren zum pulvermetallurgischen Herstellen und damit hergestellte Bauteile (Method for Powder Metallurcical Production and Produced Components)," German Patent No. DE 197 16 514 C 1.

[8] Angel, S., Bleck, W., and Scholz, P.-F., 2005, "Adjusting the Pore Structure of Open Porous Metallic Foams Produced by the Slip Reaction Foam Sintering (SRFS)-Process," 4th International Conference on Porous Metals and Metal Foaming Technology, MetFoam, H. Nakajima and N. Kanetake, eds., p. 295.

[9] Angel, S., Bleck, W., Scholz, P.-F., and Fend, Th., 2004, "Influence of Powder Morphology and Chemical Composition on Metallic Foams Produced by the Slip Reaction Foam Sintering (SRFS)-Process," Steel Research Int., **75**(7), pp. 483–488.

Technical Brief: Predictions of Flow Field for Circular-Disk Bluff-Body Stabilized Flame Investigated by Large Eddy Simulation and Experiments

Peiqing Guo
e-mail: hopeisendless@hotmail.com

Shusheng Zang

Bing Ge

School of Mechanical Engineering,
Shanghai Jiaotong University,
No. 800, Dongchuan Road,
Shanghai 200240, China

The objective of the current work is to shed light on simulating the flow features of nonpremixed flame stabilized by a circular-disk bluff-body with large eddy simulation technique. Two subgrid scale (SGS) models (Smagorinsky and Germano), combined with a constrained chemical equilibrium model, are applied to simulate this turbulent flame. Validation is made through the particle image velocimetry measurements. The comparison between the numerical simulation and experimental data shows that both models perform well and reproduce most of the significant features of the bluff-body flame, while the Germano SGS model performs better in prediction of turbulent fluctuations. These investigations show that it is possible to describe such flows with relatively simple turbulence and combustion models with moderate grids.
[DOI: 10.1115/1.3205029]

Keywords: large eddy simulation, bluff-body, nonpremixed combustion

1 Introduction

Flows over a bluff-body is a common scene in many engineering applications such as gas turbine combustion chamber due to the enhanced mixing characteristics, improved flame stability, and ease of combustion control [1], because the recirculation of hot gas behind a bluff-body can help to reignite gas mixtures, and thus stabilize the flame. The recirculation zone also has an impact on the velocity distribution and other flow parameters along with the pressure drop in the combustion chamber. On the other hand, inflow swirler component can also be adopted to stabilize the flame in an aerodynamic way. Both bluff-body and swirling flames have received significant attention in recent years. Since the bluff-body geometry provides relatively simple but well-defined initial and boundary conditions when it can maintain the flame stabilization for a wide range of inlet flow conditions, it becomes an ideal geometry for the numerical solution of turbulence/chemistry interactions in turbulent recirculating flows. For example, a wide range of studies have been conducted on Sydney bluff-body flame series: the target flames in the International Workshop on Measurement and Computation of Turbulent Nonpremixed Flames (TNF Workshop) [2]. It was experimentally studied by Dally et al. [1], and has been studied numerically by a number of researchers. Roomina and Bilger [3] and Xu and Pope [4] tested many different combinations of models for flow, mixing, and chemistry. The turbulent flow was simulated by Reynolds-averaged Navier-Stokes (RANS), probability density function (PDF) methods, one-dimensional turbulence, as well as large eddy simulation (LES). Since LES has become a promising simulation tool in investigating processes dominated by unsteady phenomena such as turbulence, mixing, and combustion processes, whose finer details cannot be elucidated by conventional RANS method, LES of Sydney bluff-body flames were also carried out by Raman and Pitsch [5], and Kempf et al. [6]. Raman et al. [7] achieved a hybrid LES/Lagrangian filtered-density-function (FDF) simulation. More recently, bluff-body flame with a swirl in similar configuration was also investigated by some research groups using LES [8–12].

The situation considered in this paper, however, is a bluff-body with a circular disk on its top used in a humid-air combustion chamber. Former studies of nonpremixed flames on this configuration have been done by experiments applying particle image velocimetry (PIV) [13,14], and LES of corresponding nonreactive case was investigated in Ref. [15]. To this end, the present work focuses on the simulation of the methane/air nonpremixed flame burning in this combustion chamber with the circular-disk bluff-body by LES combined with chemical equilibrium/presumed PDF approaches. Since the relatively simple chemical equilibrium/PDF model is adopted in the current simulation, the primary purpose of the present paper focuses on accurate predictions of the mean flow and turbulence by LES. A comparison between two different subgrid scale models is also investigated. However, modeling of more realistic chemical reactions is left for future work.

2 Experimental Setup

The bluff-body flame investigated here is a nonpremixed turbulent flame consisting of a central fuel (methane) jet with a diameter of $D_f=4.0$ mm at a bulk velocity of $U_j=12.5$ m/s, an annular coflowing air provided through a cylindrical pipe with a diameter of $D_a=60$ mm at a bulk velocity of $U_c=12.4$ m/s, and a bluff-body surrounding the central jet with a diameter of $D_{b,l}=22$ mm. Besides, a circular disk with a diameter of $D_{b,u}=D=40$ mm and a height of $H_b=5.0$ mm is installed on the upper side of the original bluff-body, forming a circular-disk bluff-body to further strengthen the recirculation zone behind it and thus further stabilize the flame by the intense mixing between the fuel and air and by the products at high temperature, providing a continuous ignition source inside the recirculation zone. This configuration with all dimensions and coordinate system is shown in Fig. 1.

The test rig has been investigated by our group before, both experimentally and numerically. The experimental results for the velocity statistics were measured through a two dimensional PIV, allowing instantaneous measurements of the flow field for better understanding of how the flame is stabilized in a complex flow field. The PIV (Dantec) system consists of a double pulsed Nd: YAG laser (532 nm output) and a Kodak ES 1.0 digital CCD camera with a resolution of 1008×1018 pixels. A size of 64×64 pixels with a 50% overlap between adjacent interrogation regions is adopted for the interrogation box, resulting to 30 vectors obtained in each direction of the view window. Seeding, supplied by a fluidized bed seeder and in the form of 1 μm MgO, was applied through the central fuel jet as well as coflow air stream. In the present study, experimental data of flow fields measured by using the PIV technique are used as validation data for the LES/PDF calculation. A complete description of the experimental setup and results can be found in Refs. [13–15].

Contributed by the International Gas Turbine Institute of ASME for publication in the JOURNAL OF ENGINEERING FOR GAS TURBINES AND POWER. Manuscript received April 8, 2009; final manuscript received April 28, 2009; published online March 4, 2010. Review conducted by Dilip R. Ballal. Paper presented at the ASME Turbo Expo 2008: Land, Sea and Air (GT2008), Berlin, Germany, June 9–13, 2008.

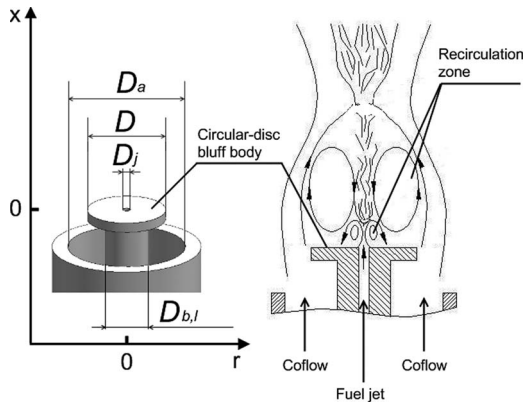

Fig. 1 Circular-disk bluff-body with all dimensions and coordinate system

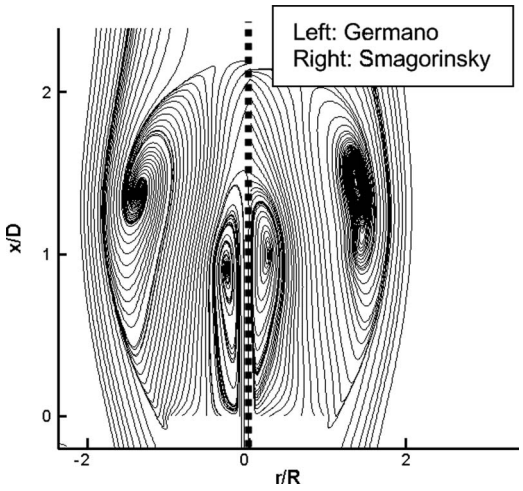

Fig. 2 Streamlines plots of time-averaged velocities for circular-disk bluff-body

3 Numerical Simulation

The three-dimensional features of the reacting flow were examined by performing LES over part of the real combustion chamber, the cylindrical area of $5D$ in the axial direction x, and $3.75D$ in the radial direction r, where D represents the upper diameter of the circular disk. To capture the expected turbulent instability and the recirculation zones, the domain includes portion of the methane and air pipe upstream of the bluff-body. The location selected here allows comparison with measurements by PIV, while the size is selected so that the presence of side walls do not exert any significant influence on the results inside the area of most interest: the recirculation zones located above the bluff-body.

A collocated grid with a cell-centered variable arrangement is used and stretches coarser along both the x- and r-direction, which guarantees a very fine resolution near the bluff-body region. The grid is refined in the recirculation zone downstream of the bluff-body where the flame is anchored and in the shear layer zone, leading to total grid points of 1.5×10^6 throughout the domain. No special wall modeling is adopted for all simulations.

The Reynolds number based on the upper diameter of bluff-body and the inlet velocity is about 29,000. The nominal pressure is 1 atm. At the inlet, the mass flow rate, temperature, and mixture fraction were assumed fixed while pressure was extrapolated. No artificial turbulence was superimposed. Conditions at the outlet boundary are treated by the application of upwinding at boundary adjacent cells combined with zero gradient conditions. Based on the assumption that the flow is dominated by recirculation zones and hence there is no need to resolve the boundary layer, a no slip wall condition is applied on the bluff-body surface and other boundaries.

During the current simulation, the Smagorinsky model with dynamic determination of the constant [16,17] is applied in addition to the standard Smagorinsky SGS model [18] with a constant of $C_S=0.1$. In both cases, the time step was fixed at 0.05 ms and computation was stopped after 5000 time steps corresponding to a physical time of 0.25 s. Simulation with the Germano SGS model was run up to 0.5 s, but no significant changes can be found. In the case of the nonpremixed combustion, chemistry is described by a constrained equilibrium/PDF model with β-PDF shape, parameterized by the filtered mixture fraction and its variance as proposed by Cook and Riley [19]. Numerical results were time-averaged to compare with experimental data.

4 Results and Discussion

4.1 Flow Structures. The flow characteristics of the two different SGS models are first exhibited through the mean streamline plots in Fig. 2. As the recirculation zones downstream of the circular-disk bluff-body are of most interest, streamlines further upstream are not included in the figure. The left half of Fig. 2 represents the streamline plot simulated with Germano SGS model, whereas the right half represents that with the standard Smagorinsky SGS model. Both models indicate the existence of two recirculation zones. The first ring-shaped recirculation zone is just above the circular-disk near the centerline as a result of flow separation at the bluff-body. The second toroidal-shaped recirculation zone is established further downstream away from central axis. It can be found that the two recirculation zones are slightly longer and broader with the Germano model, meaning a more gradual dissipation of momentum in the wake region with respect to the case with the Smagorinsky model.

The core of the ring-shaped recirculation zone can be identified at the location around $x/D=0.95$ and $r/R=0.30$, and $x/D=1.05$ and $r/R=0.30$ for the Germano and Smagorinsky SGS models, respectively. Compared with the experimental measurements ($x/D=1.12$, $r/R=0.45$), the feature is slightly shifted inward in the radial direction and upstream in the axial direction. Relatively moderate grid resolution compared with large gradient of flow in this region may attribute to this deviation. For the second recirculation zone, the positions of the core are at $x/D=1.38$ and $r/R=1.4$ (Germano), and $x/D=1.50$ and $r/R=1.45$ (Smagorinsky). Simulations with both models match the observation in the experiment well; the position of this recirculation zone's core is around $x/D=1.54$ and $r/R=1.45$.

4.2 Velocity Profiles. A more quantitative comparison between the LES prediction and experimental data is obtained. The mean and root mean square (rms) velocity component profiles at axial locations of $x/D=0.2$, 0.7, and 2.5 are shown in Figs. 3 and 4. Note that hereafter, the axial and radial coordinates are nondimensionalized by the diameter and radius of the circular-disk, respectively.

Mean axial and radial velocity profiles are shown in Fig. 3. Figure 3(a) shows a nicely good agreement between the calculated and experimental mean axial velocity profiles at all locations, except that the mean axial velocity is overpredicted near the centerline close to the bluff-body and is underpredicted near the ring-shaped recirculation zone. Difference between the fuel-inlet boundary condition and the actual velocity profile at the central jet inlet may lead to this discrepancy. According to the analysis in Ref. [20], discrepancies at the same region may be caused by the uncertainties during measurements.

As shown in Fig. 3(b), the predicted radial velocity profiles also agree well with the experimental results. Although less satisfactory than the axial mean velocity, at least similar trend is found

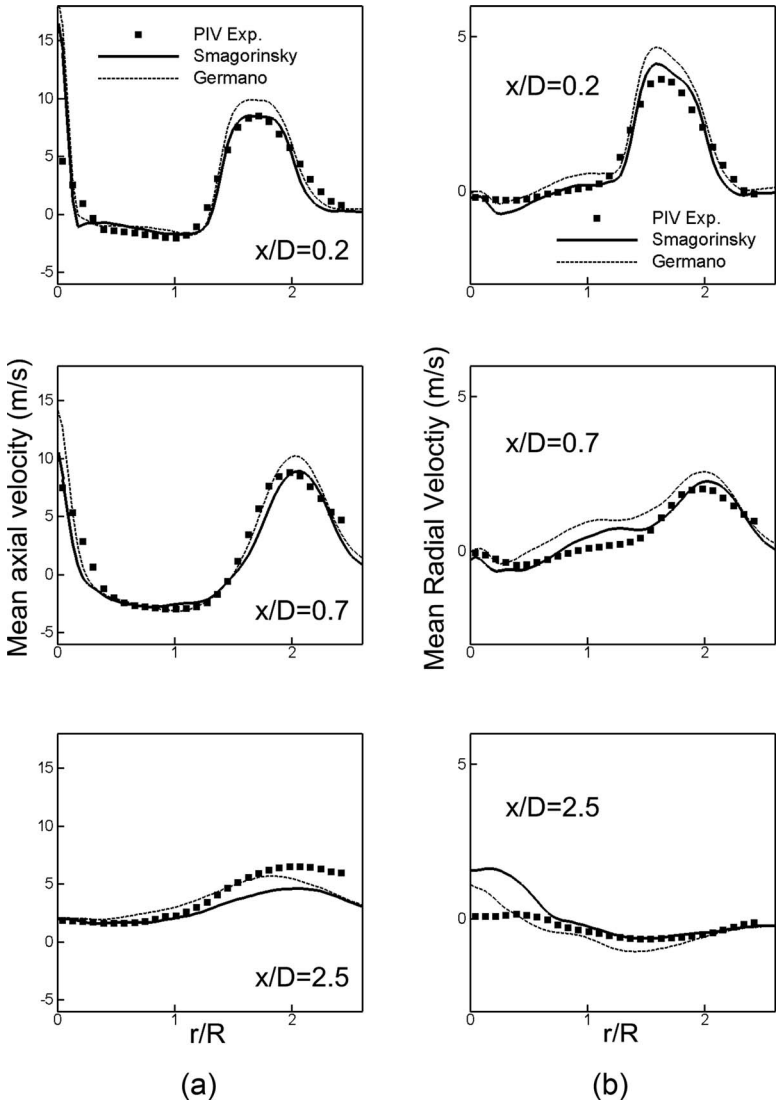

Fig. 3 (*a*) Mean axial and (*b*) radial velocity profiles

between the LES and experiments for the radial velocity components. Considering the difficulty to measure and to calculate the mean radial velocity due to its relatively small magnitude compared with its fluctuating component, which can be found in Fig. 4(*b*), current models calculate the mean radial velocity profiles fairly well when compared with the experimental data. Figure 3 demonstrates that the essential features of the mean combusting flow field can be well captured and reproduced with currently adopted model combination. The results also show that the Smagorinsky model performs better than the Germano model in the region near the bluff-body up to $x/D=0.7$. Further downstream, instead, the Germano model is slightly better.

Figure 4 shows the computed rms profiles of the fluctuating axial and radial velocity components, respectively, compared with the experimental data at different axial locations, where the existence of the unsteady motion of turbulent flame cause the velocity fluctuation. In general, the agreement is reasonable.

As can be seen in Fig. 4(*a*), the axial rms fluctuating velocity is well predicted, especially by the Germano SGS model, although the magnitude of the velocity fluctuation is slightly overestimated at the axial location $x/D=0.7$ and further downstream, where similar trends can still be found. Figure 4(*a*) has shown at least qualitatively good agreement with the experimental data, suggesting that the turbulent shear stress field is better predicted by LES with the Germano SGS model. Radial rms fluctuating velocity profiles are given in Fig. 4(*b*). At least qualitative agreement is obtained by the current simulation. Germano again outperforms the Smagorinsky SGS model, which may benefit more from the grid resolution. As mentioned in Ref. [21], even with expanded computational domain, the effect of confinement due to the side walls cannot be fully neglected, and the existent boundaries may especially affect the prediction of magnitude of the velocity fluctuation.

It is noteworthy that although the average profiles obtained with the two LES models are quite similar, they perform differently with respect to prediction of the velocity fluctuation. For instance, at $x/D=0.2$ in both LES with the Germano model as well as in the experiments, the axial and radial rms fluctuations experience two localized peak around $r/R=1.4$ and 2.0: one near the edge of circular-disk and the other further downstream in the spanwise direction, representing that the shear layer between the wake in the toroidal-shaped recirculation zone and coflow is successfully reproduced by the Germano SGS model. The Smagorinsky model, however, fails to distinguish the two peaks and combines them together. Similar trend can be found further downstream at $x/D=0.7$.

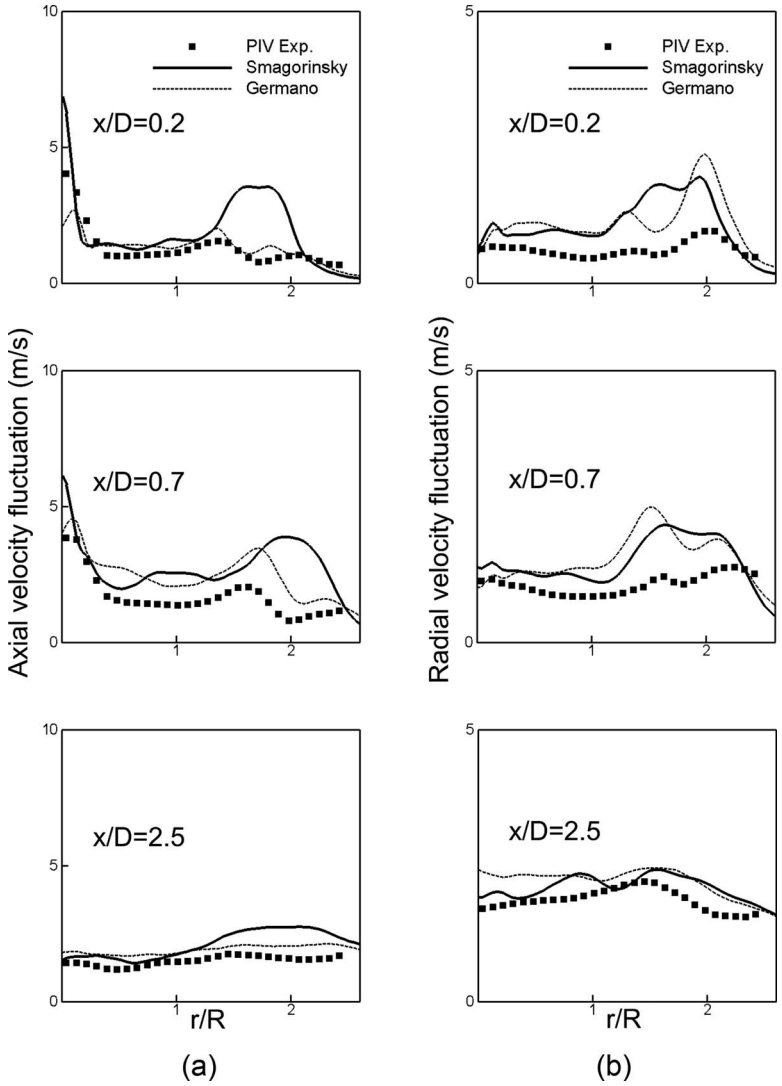

Fig. 4 (*a*) Axial and (*b*) radial velocity fluctuations

4.3 Flow and Flame Structures. A typical instantaneous field of vorticity magnitude at a streamwise plane through the center jet axis is displayed in Fig. 5. The recirculation zone is delimited by a white isoline, where the axial velocity is equal to 0. Large scale vortices exist globally along the borderline of the recirculation zone. The flow regime reveals disorganization and domination features by the presence of elongated vortices.

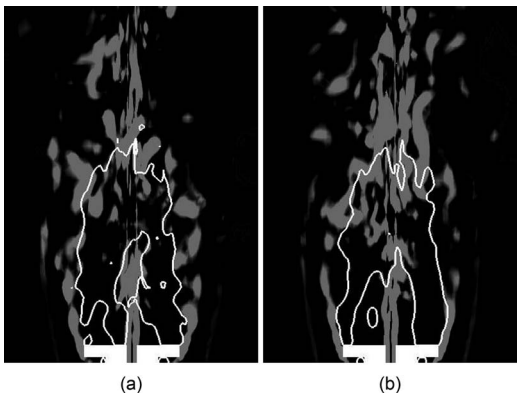

Fig. 5 Instantaneous vorticity distribution: (*a*) Smagorinsky and (*b*) Germano; recirculation zone is denoted by white line

Due to the absence of the concentration field, which precludes the quantitative assessment of current chemical reaction model, an impression of the density distribution for a snapshot at a certain time is given in Fig. 6(*a*). Unsteady structures of turbulent flame can be clearly observed from both SGS models. Besides, both snapshots show steep gradients representing the shape of the flame, which is obviously anchored just above the circular-disk bluff-body. Similar behavior can also be found from the instantaneous temperature field shown in Fig. 6(*b*), showing that having reversed flow offers sufficient assistance for flame stabilization.

Considering the simple SGS and combustion models during the current calculations, the mean velocity and its fluctuation fields, as well as the shape of the flame, are overall well predicted, demonstrating the performance of LES combined with a constrained equilibrium/assumed PDF model in a challenging test case: circular-disk bluff-body combustion. With this test case, the combination confirms its potential to improve prediction by means of expanded computational domain, more refined grid, and more detailed chemical reaction model.

5 Conclusion

Large eddy simulation of a circular-disk bluff-body stabilized nonpremixed flame has been conducted with both the Smagorin-

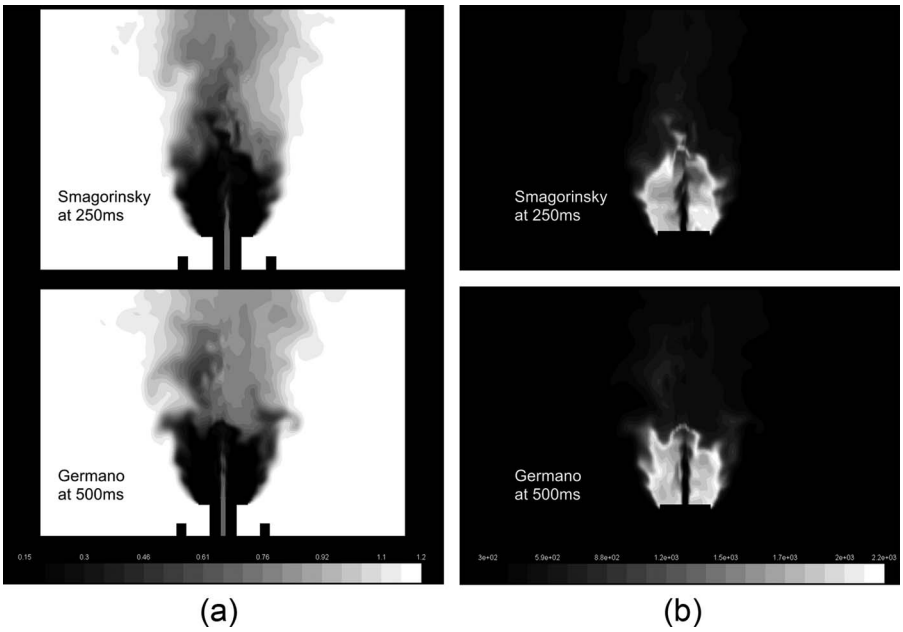

Fig. 6 (*a*) Instantaneous density and (*b*) temperature fields under nonpremixed combustion

sky and Germano SGS models for LES, combined with a constrained equilibrium chemistry model, and the β-PDF method has been adopted for the chemical reaction.

Despite the simple SGS, mixing, and chemistry reaction models used in the simulation, the unsteadiness in this nonpremixed turbulent flame has been well reproduced and overall good agreement of mean and rms velocity profiles has been found between the numerical simulation and experimental measurement. Simulations with both SGS models succeed in predicting the two recirculation zones, which are the main characteristic features in such a reactive flow. Besides, the shear layer between the recirculation zone and the coflow has also been correctly predicted by LES and confirmed by the corresponding experiment. However, due to the confinement effects of the side walls created to reduce computational cost, especially with respect to the velocity fluctuations, there also exists some deviation, such as the magnitude of the radial velocity fluctuation in the flame region, indicating that the level of unsteadiness in the turbulent flame needs to be further investigated.

Results have shown that the overall good agreement can be achieved with both SGS models. The standard Smagorinsky SGS model performs quite well in predicting the mean flow field, although the Germano SGS model provides better agreement with the velocity fluctuation. Therefore, it can be concluded that being inexpensive relative to Germano in terms of CPU requirement, the Smagorinsky SGS model seems a good choice for the simulation of the mean reactive flow, but its prediction of the velocity fluctuations is less adequate.

Acknowledgment

The financial support from the State Key Fundamental Research Program of China under Grant No. G1999022303 is gratefully acknowledged.

Nomenclature

D = diameter
R = radius of upper side of bluff-body
r = radial location
U = bulk velocity
x = axial location

Subscripts

a = air stream
b,u = upper side of the bluff-body
b,l = lower side of the bluff-body
c = coflow
f = fuel stream
j = jet flow

References

[1] Dally, B. B., Masri, A. R., Barlow, R. S., and Fiechtner, G. J., 1998, "Instantaneous and Mean Compositional Structure of Bluff-Body Stabilized Nonpremixed Flames," Combust. Flame, **114**(1–2), pp. 119–148.
[2] 2006, Sandia National Laboratories, Combustion Research Facility website, http://www.ca.sandia.gov/TNF
[3] Roomina, M. R., and Bilger, R. W., 2001, "Conditional Moment Closure (CMC) Predictions of a Turbulent Methane-Air Jet Flame," Combust. Flame, **125**(3), pp. 1176–1195.
[4] Xu, J., and Pope, S. B., 2000, "PDF Calculations of Turbulent Nonpremixed Flames With Local Extinction," Combust. Flame, **123**(3), pp. 281–307.
[5] Raman, V., and Pitsch, H., 2005, "Large-Eddy Simulation of a Bluff-Body-Stabilized Non-Premixed Flame Using a Recursive Filter-Refinement Procedure," Combust. Flame, **142**(4), pp. 329–347.
[6] Kempf, A., Lindstedt, R. P., and Janicka, J., 2006, "Large Eddy Simulation of a Bluff-Body Stabilized Non-Premixed Flame," Combust. Flame, **144**(1–2), pp. 170–189.
[7] Raman, V., Pitsch, H., and Fox, R. O., 2005, "Hybrid Large-Eddy Simulation-Lagrangian Filtered-Density-Function Approach for Simulating Turbulent Combustion," Combust. Flame, **143**(1–2), pp. 56–78.
[8] Sheikhi, M. R. H., Drozda, T. G., Givi, P., Jaberi, F. A., and Pope, S. B., 2005, "Large Eddy Simulation of a Turbulent Nonpremixed Piloted Methane Jet Flame (Sandia Flame D)," Proc. Combust. Inst., **30**(1), pp. 549–556.
[9] Kempf, A., Flemming, F., and Janicka, J., 2005, "Investigation of Lengthscales, Scalar Dissipation, and Flame Orientation in a Piloted Diffusion Flame by LES," Proc. Combust. Inst., **30**(1), pp. 557–565.
[10] Habisreuther, P., Bender, C., Petsch, O., Buchner, H., and Bockhorn, H., 2006, "Prediction of Pressure Oscillations in a Premixed Swirl Combustor Flow and Comparison to Measurements," Flow, Turbul. Combust., **77**(1–4), pp. 147–160.
[11] Olbricht, C., Hahn F., Kuhne, J., Sadiki, A., Janicka, J., Bake, F., and Rohle, I., 2007, "Flow and Mixing in a Model GT Combustor Investigated by LES and Monte-Carlo Filtered PDF Methods," ASME Paper No. GT2007-27270.
[12] Stein, O., and Kempf, A., 2007, "LES of the Sydney Swirl Flame Series: A Study of Vortex Breakdown in Isothermal and Reacting Flows," Proc. Combust. Inst., **31**(2), pp. 1755–1763.
[13] Ge, B., Zang, S. S., and Gu, X., 2007, "Experimental Study on Velocity Characteristic Distribution in Non-Premixed Circular-Disc Stabilized Flames," ASME Paper No. GT2007-27098.
[14] Gu, X., Zang, S. S., and Ge, B., 2006, "Effect on Flow Field Characteristics in

Methane-Air Non-Premixed Flame With Steam Addition," Exp. Fluids, **41**(5), pp. 829–837.
[15] Guo, P. Q., Zang, S. S., and Ge, B., 2008, "LES and Experimental Study of Flow Features in Humid-Air Combustion Chamber With Non-Premixed Circular-Disc Stabilized Flames," ASME Paper No. GT2008-50940.
[16] Germano, M., Piomelli, U., Moin, P., and Cabot, W. H., 1991, "A Dynamic Subgrid-Scale Eddy Viscosity Model," Phys. Fluids A, **3**(7), pp. 1760–1765.
[17] Lilly, D. K., 1992, "A Proposed Modification of the Germano Subgrid-Scale Closure Method," Phys. Fluids A, **4**(3), pp. 633–635.
[18] Smagorinsky, J., 1963, "General Circulation Experiments With the Primitive Equations: I. The Basic Equations," Mon. Weather Rev., **91**(3), pp. 99–164.
[19] Cook, W., and Riley, J. J., 1994, "A Subgrid-Scale Model for Equilibrium Chemistry in Turbulent Flows," Phys. Fluids, **6**(8), pp. 2868–2870.
[20] Muradoglu, M., Liu, K., and Pope, S. B., 2003, "PDF Modeling of a Bluff-Body Stabilized Turbulent Flame," Combust. Flame, **132**(1–2), pp. 115–137.
[21] Giacomazzi, E., Battaglia, V., and Bruno, C., 2004, "The Coupling of Turbulence and Chemistry in a Premixed Bluff-Body Flame as Studied by LES," Combust. Flame, **138**(4), pp. 320–335.